The Pennsylvania State University

The Graduate School

College of Engineering

HYSTERESIS MODEL BASED PREDICTION OF INTEGRAL ABUTMENT BRIDGE BEHAVIOR

A Thesis in

Civil Engineering

by

Kongsak Pugasap

Submitted in Partial Fulfillment
of the Requirements
for the Degree of

Doctor of Philosophy

May 2006

The thesis of Kongsak Pugasap was reviewed and approved* by the following:

Jeffrey A. Laman
Associate Professor of Civil Engineering
Thesis Advisor
Chair of Committee

Andrea J. Schokker
Associate Professor of Civil Engineering

Daniel G. Linzell
Associate Professor of Civil Engineering

Mian C. Wang
Professor of Civil Engineering

Thomas E. Boothby
Professor of Architectural Engineering

Andrew Scanlon
Professor of Civil Engineering
Head of the Department of Civil and Environmental Engineering

*Signatures are on file in the Graduate School

ABSTRACT

Integral abutment (IA) bridge construction has become more common due to desirable performance, however, many design uncertainties still exist, particularly long-term behavior prediction. In order to better understand these design uncertainties, a study of IA bridge behavior through long-term monitoring and numerical modeling has been undertaken. Monitoring and instrumentation consists of three prestressed concrete IA bridges located on I99 in central Pennsylvania. Evaluation of field data reveals hysteretic behavior of IA bridges that may be a significant influence on long-term behavior in addition to creep and shrinkage effects. On the basis of field data and two different problem types; geotechnical and structural, two major sources influencing long-term hysteretic behavior of IA bridges, including soil-structure interaction and yielding of structural connections, are identified. These two hysteretic sources were incorporated in finite element (FE) models using hysteresis elements derived from selected hysteresis models available in the literature for all three instrumented bridges. Also proposed is an alternative condensed hysteresis model in which two selected degrees of freedom at the pile head location are required. Similar types of hysteresis elements employed in the FE models were implemented in the condensed hysteresis models. Equivalent temperature loads to incorporate creep and shrinkage effects by using the AAEM method, ambient temperature loads, and earth pressures were applied to the FE and condensed hysteresis models. Predicted results from all models are compared against field data to evaluate model accuracy. Eight load cases were analyzed with a simulation period of 100 years to determine the relative magnitudes of hysteretic behavior and effects of creep and shrinkage. It is determined from predicted response at the end of the simulation period that the ratios of condensed hysteresis model to 2-D predicted abutment displacements range from 0.81 to 1.08. The ratios of long-term to short-term predicted abutment displacements range from 1.5 to 2.3. The ratios of predicted abutment displacement influenced by hysteretic behavior to short-term predicted abutment displacement are from 1.1 to 1.2 for an elevation near girders, and are from 1.3 to 1.6 for an elevation near abutment bases. These predicted ratios indicate the validity of the condensed hysteresis models and the importance of hysteretic behavior and effects of creep and shrinkage on long-term behavior of IA bridges.

TABLE OF CONTENTS

LIST OF FIGURES

LIST OF TABLES

ACKNOWLEDGEMENTS

I express sincere appreciation to my thesis advisor, Dr. Jeffrey A. Laman, for his time, guidance, and insight throughout this study. Also thanks to my committee members, Dr. Daniel G. Linzell, Dr. Mian C. Wang, Dr. Thomas E. Boothby, Dr. Andrea J. Schokker, and Dr. Andrew Scanlon, who offered guidance and support. I would also like to thank Charles A. Leighty for his insight in setting up the bridge instrumentation. I wish you the best with your endeavors.

Thanks go to the Pennsylvania Department of Transportation for their financial support, providing me the financial means to complete the research project and this thesis study.

Finally, thanks go to my parents, VADM Boonchoo and Mrs. Chailai Pugasap, who endured this long process with me, always offering endless support and love. I would also like to specially thank my wife, Supana Pugasap, for unwavering support and understanding during the many hours we shared and dedicated to achieving this milestone in our lives.

Chapter 1

Introduction

1.1 Background and Motivation

Conventional jointed bridge performance deficiencies due to wheel impact joint damage and water and deicing chemicals leaking through joints has motivated integral abutment (IA) bridge construction. IA bridges exhibit desirable performance with a longer service life and lower maintenance due to joint elimination [**96** and **117**]. Additional benefits of IA bridges include:

- initial material and construction cost savings,
- maintenance cost savings,
- road riding improvement, and
- additional structural redundancies.

A significant number of IA bridges have been constructed and are performing satisfactorily. As design and construction experience has increased, the overall length of IA bridges has also increased. Increased bridge length has accelerated the demand for better understanding of IA bridge behavior and design methodologies. The design uncertainties of IA bridges are primarily a result of complex structural responses due to cyclic temperature changes and material time-dependence including:

- partial longitudinal restraint by intermediate piers,
- creep and shrinkage effects of concrete members,

- earth pressure behind backwalls and abutments,
- nonlinear soil-pile interaction,
- partial rotational rigidity of an abutment-backwall connection,
- pile plastic hinge,
- approach slab effect,
- pile orientation, and
- soil settlement.

The combination of these several uncertainties leads to a very complex problem. In order to gain insight into these issues, a field study of IA bridge structures through long-term monitoring has been undertaken. Data obtained from a range of geometric IA bridge configurations over a period of several years is required to determine a behavior trend. In this study three bridges recently constructed for the I-99 extension in Pennsylvania were selected for testing.

The three instrumented bridges are composite slab on 4-prestressed concrete I-girders with a number of spans ranging from 1 to 3, lengths ranging from 18.9 m (62’) to 52.4 m (172’), and abutment heights ranging from 2.56 m (8.4’) to 4.48 m (14.7’). The numbers of instruments vary from 48 to 64 on each bridge, consisting of:

- extensometers to measure abutment longitudinal displacements,
- tilt meters to measure abutment and girder rotations,
- pressure cells to measure abutment earth pressures from backfill,
- strain gages to measure bending and axial strain of girders and piles, and
- sister bar gages to measure axial strain of approach slabs.

Specific data collection periods, number of spans, bridge length, and abutment heights are provided in Section 1.3.1.

Preliminary evaluation of field data reveals nonlinear and path-dependent effects of IA bridge behavior and motivates this study. Ambient temperature taken at the weather station and extensometer data taken at bridge 203 are plotted on a horizontal and vertical scale shown in Figure 1-1.

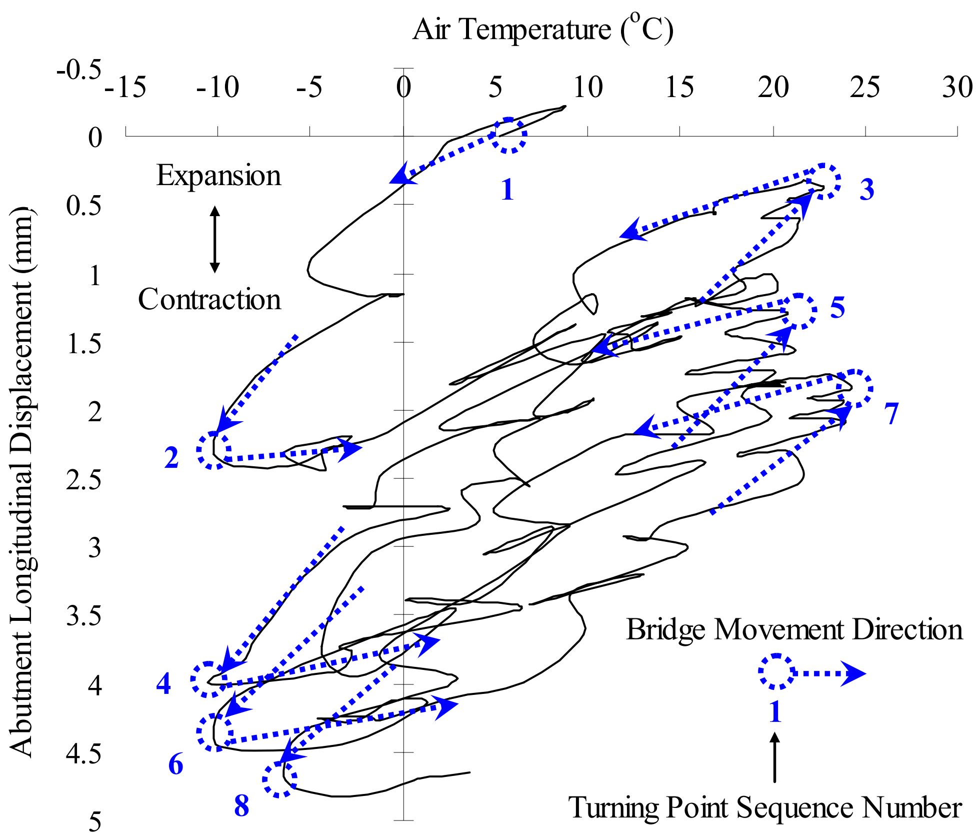

Figure 1-1: Hysteresis Phenomenon of IA Bridges (Bridge 203)

There are eight turning points identified in Figure 1-1: point 1 represents the initial bridge condition; even numbered points (2, 4, 6, and 8) represent winter peaks; and odd numbered points (3, 5, and 7) represent summer peaks. Nonlinear and path-dependent behavior is observed through a comparison of path 1-2 (representing short-term abutment longitudinal displacements) and path 1-2-3-4-5-6-7-8 (representing accumulated longitudinal displacements after 4 winter cycles). It can be observed from Figure 1-1 that the time-history of abutment longitudinal displacements take the shape of an open hysteresis loop at the first spin. Subsequent spinning loops are formed so as to indicate an approaching, stable and closed loop, or steady-state condition.

In addition to nonlinear and path-dependent behavior (hereafter referred to as hysteretic behavior), time-dependent effects due to creep, shrinkage, and strand relaxation are also important factors on IA bridge behavior. Time-dependent effects are non-hysteretic and significantly influence concrete bridge behavior during the first several months. Time-dependent effects are a negligible influence as the bridge matures.

1.2 Problem Statement

The complexity of IA behavior prediction due to the combination of several design uncertainties is, therefore, uncoupled and twofold: hysteretic and non-hysteretic behavior. Hysteretic behavior in IA bridges is primarily a result of nonlinear soil-structure interaction and yielding of certain structural connections. Non-hysteretic behavior involves non-reversing time-dependent effects due to creep, shrinkage, and strand relaxation for prestressed concrete members.

There are two general sources causing hysteresis phenomena in IA bridges: (1) interaction between the structure and soil, a non-recoverable and strongly hysteretic material, and (2) yielding of structurally detailed connections loaded beyond the elastic range. Certain connections and elements for long IA bridges will be forced into the plastic region and, therefore, will not fully recover when unloaded. Both sources of hysteresis phenomenon generally cause bridge behavior to exhibit an open loop at the first spin and are expected to approach steady-state after subsequent spins.

Due to structural continuity in IA bridges, time-dependent effects of creep, shrinkage, and relaxation become indeterminate. Superstructure and substructure components, including supporting abutments and piles, experience stress redistribution resulting from time-dependent effects. Time-dependent effects generally cause significant self-shortening of superstructure components and significant bending of substructure components during the first few years. Time-dependent effects are deemed insignificant after the initial time period of the first few years.

It is evident from field data that the combined effect of hysteretic and non-hysteretic behaviors grows on a logarithmic scale. Therefore, a long-term trend combining these two behaviors is anticipated to approach steady-state within some finite period of time. Because the design bridge life of 75 years is specified by AASHTO LRFD [3] and field data does not span a sufficient time period to reveal the combined long-term trend, a methodology to predict long-term behavior or steady-state, currently unavailable in the literature, is required and developed in this study.

This study proposes a concept of steady-state prediction through the use of hysteresis models for hysteretic behavior and the age-adjusted effective modulus method (AAEM) for non-hysteretic behavior. Two levels of finite element analyses: two-dimensional and three-dimensional, were developed. A procedure to develop a condensed hysteresis model was also devised to provide a simplified analysis methodology. All three models developed for the three instrumented bridges have been calibrated against corresponding field data. After completion of calibration, a steady-state prediction was performed to evaluate long-term behavior of IA bridges.

Methodologies of steady-state prediction are presented in a diagram of Figure 1-2.

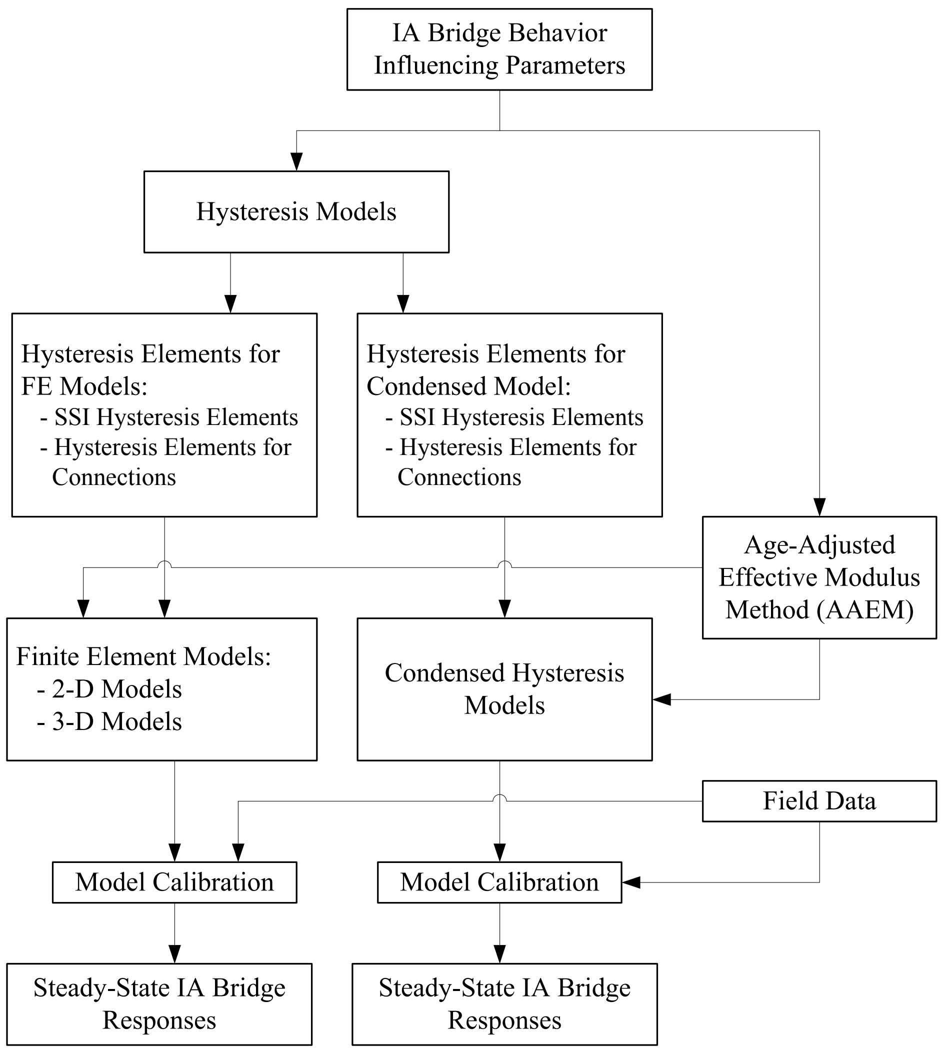

Figure 1-2: Problem Solving Diagram

The development of the methodologies can be described by the following steps:

- establish two approaches: hysteresis models and AAEM, for both hysteresis and non-hysteresis,
- select appropriate hysteresis models to construct hysteresis elements for each of two modeling techniques: FE models and condensed hysteresis models,
- develop FE models and condensed hysteresis models that incorporate: (i) hysteretic behavior by using hysteresis elements, and (ii) non-reversing time-dependent effects by using AAEM,
- calibrate each modeling technique by using field data, and
- predict steady-state from each modeling technique.

1.3 Scope of Research

The scope of this study is composed of three issues: (1) instrumentation, (2) finite element models, and (3) condensed hysteresis models. Instrumentation, descriptions of bridge type, general dimensions, and data collection for all three instrumented bridges are provided in Section **1.3.1**. FE models, methods of applying hysteresis models and time-dependent effects, levels of analysis, number of models, model calibration, and selected software for finite element analysis purpose are discussed in Section **1.3.2**. Condensed hysteresis models, methods of applying hysteresis models and time-dependent effects, general development procedure, and number of models are presented in Section **1.3.3**.

1.3.1 Scope of Instrumentation

Three bridges located on the I-99 extension in Pennsylvania were selected for instrumentation and long-term monitoring. All three instrumented bridges are composite slab on 4-prestressed concrete I-girders with number of spans, bridge length, and abutment heights as summarized in Table 1-1. In addition, one weather station was installed prior to the beginning of bridge construction to collect data of ambient temperature, relative humidity, wind speed, wind direction, solar radiation, air pressure, and precipitation.

The duration of data collection for the three instrumented bridges is also summarized in Table 1-1. Data has been continuously collected every 15 minutes with the corresponding duration as of January 2006. The data collection period at the weather station is 42 months as of January 2006.

Table 1-1: Selected Bridges for Monitoring and Analyses

Bridge Number	Number of Spans	Span Length m (ft)	Total Bridge Length, m (ft)	Abutment Height, m (ft)	Data Collection Duration as of Jan 06 (Month)
203	3	14.3-26.8-11.3 (47-88-37)	52.4 (172)	4.48 (14.7)	39
211	1	34.7 (114)	34.7 (114)	2.56 (8.4)	17
222	1	18.9 (62)	18.9 (62)	2.82 (9.3)	27

Each bridge is equipped with the following five instrument types:

- extensometer to measure abutment longitudinal displacements,
- tilt meter to measure abutment and girder rotations,

- pressure cells to measure abutment earth pressures from backfill
- strain gages to measure bending and axial strain of girders and piles, and
- sister bar gages to measure axial strain of approach slabs.

1.3.2 Scope of Finite Element Models

Because an advanced analysis capability is required for hysteretic behavior, FE models were developed using ANSYS. Two levels of modeling were conducted. The first level is a two-dimensional model consisting primarily of beam elements. A more sophisticated model built in three-dimensional space consisting primarily of shell elements serves as the second modeling level. Two-dimensional ANSYS FE models were developed for each of the three instrumented bridges (203, 211, and 222). In addition, three-dimensional FE models were developed for bridges 203 and 222. A three-dimensional FE model of bridge 211 developed by Laman *et al* [**61**] was also utilized for this study.

Hysteretic behavior by means of nonlinear soil-structure interaction and effects of structural connections was considered by using a one-dimensional, nonlinear, ANSYS element. Nonlinear properties of soil behavior were taken from *p-y* curves and classical earth pressure theory. Moment-curvature relationship based on abutment construction joint details was integrated into the numerical models. Classical plasticity theory was utilized for element properties when unloaded.

Also addressed in FE models are time-dependent effects. In this study a net time-dependent strain after super- and sub-structure continuity is established was determined using the age-adjusted effective modulus method (AAEM). This method is relatively simple but provides a reasonably good estimate. Then, a net time-dependent strain was imposed on the superstructure elements by means of an equivalent temperature loading.

Finally, calibration of the numerical models was performed against available field data. Analyses of FE models through a design life of 100 years were carried out to determine steady-state and long-term bridge response. The difference between short-term and long-term responses was quantified in order to study the importance of the hysteretic effect on IA bridges.

1.3.3 Scope of Condensed Hysteresis Model

A condensed hysteresis model was developed to provide a simple but versatile approach to predict IA bridge response compared to the FE modeling approach. The development of condensed hysteresis models essentially borrows a concept from the FE method, however, only a few inputs and a few outputs are involved. This approach can be used at a practical analysis level with relative ease of implementation.

Abutment movements at the pile head location are identified as the most useful outputs because analysis and design of structural and geotechnical components is typically separated at a convenient boundary. Movements at this location can be substantially used to determine abutment stresses through structural analysis and pile stresses through geotechnical analysis. Therefore, two degrees of freedom at the pile head location; translation and rotation with respect to the longitudinal direction, are selected as desirable outputs to develop a condensed hysteresis model.

The procedure to develop a condensed hysteresis model is demonstrated for a single-span IA bridge. Model assumptions of symmetrical geometry and perfectly rigid abutment and backwall components were applied to introduce constraint conditions and reduce the number of unknowns by using constraint and condensation techniques. Because the developed model was based on a single span bridge applicable to bridges 211 and 222, modified bridge length parameters were proposed to determine model stiffness for the bridge 203 case. The end result appears in a mathematical expression that can be solved by numerical step-by-step integration.

Techniques utilized in FE models such as inclusion of hysteresis behavior, equivalent temperature, and long-term behavior, can also be applied to a condensed hysteresis model. *P-y* curves, classical earth pressure theory, and moment-curvature relationships were utilized to derive condensed hysteresis model properties. Equivalent temperatures used for condensed hysteresis models were taken from the FE model equivalent temperatures. Analyses of condensed hysteresis models through a design life of 100 years were carried out to determine steady-state and long-term bridge response.

1.4 Objectives

The overall objective of this study is to establish the procedure to predict steady-state and long-term IA bridge response due to the combination of hysteretic and non-hysteretic behaviors. Calibrated FE and condensed hysteresis models are used as a crucial step in the procedure to obtain steady-state and long-term response predictions. This prediction procedure is accomplished by achieving the following specific objectives:

1. predict steady-state and long-term responses of all three instrumented integral abutment bridges,
2. develop a condensed hysteresis model,
3. quantify hysteretic effect on IA bridges through a comparison of short-term and predicted long-term bridge responses,
4. determine a correlation of the significant bridge parameters, *i.e.* length and abutment height, to the hysteretic effect, and
5. recommend a methodology to predict a steady-state and long-term IA bridge response/behavior.

1.5 Thesis Organization

This thesis consists of seven chapters. Chapter 2 reviews hysteresis phenomena in IA bridges, a number of hysteresis models from a mathematics and physics perspective, and time-dependent effects on IA bridges. Chapter 3 discusses hysteresis elements derived from Chapter 2 hysteresis models to be applied to FE and condensed hysteresis models. Chapter 4 presents modeling techniques, applied loads, and analysis types for the FE models. Chapter 5 discusses a framework for condensed hysteresis model development and implementation. Chapter 6 presents field data and analysis results obtained from the FE and condensed hysteresis models along with result discussions. Finally, Chapter 7 provides summary, conclusions and recommendations of this study.

Chapter 2

Literature Review

2.1 General

In this chapter relevant past studies of hysteresis in IA bridges as well as a number of selected hysteresis models from a mathematical and physical perspective are reviewed to establish their application to hysteretic behavior of IA bridges. Past studies relating to four identified hysteretic behavior components: (1) soil-pile interaction; (2) soil-abutment interaction; (3) abutment-backwall connection; and (4) pile-abutment connection, are reviewed. The mathematics of hysteresis was primarily developed in an abstract way, intended to be applied to general and multi-dimensional applications. On the other hand, the physics of hysteresis was primarily developed in phenomenological way, intended to be applied to a physical model of limited dimensionality. Most hysteresis models from these two perspectives, however, are generally interconnected and frequently possess the same basic properties. On the basis of past studies and hysteresis model properties, appropriate hysteresis models are selected to represent hysteretic behavior of IA bridges in the ANSYS FE and the condensed hysteresis models.

Time-dependent effects, composed of concrete creep, concrete shrinkage and prestressing steel relaxation, and relevant past studies are also reviewed. The presence of IA bridge structural continuity results in the superposition of time-dependent effects on thermal effects when determining pile and abutment movements. The effects of creep, shrinkage, and steel relaxation are examined herein from a structural mechanics and practical design perspective. A selected analysis method to incorporate time-dependent effects into the FE and condensed hysteresis models is presented. Relevant past studies are also reviewed, particularly in connection with the selected time-dependent analysis method.

This chapter begins with a review of studies relating to each of the hysteretic behavior components in IA bridges. A review of hysteresis models from a mathematical and physical perspective follows. Next, a review of studies relating to time-dependent effects on IA bridges is presented. Concrete creep, concrete shrinkage, and prestressing steel relaxation are described. Finally, an analysis method to incorporate time-dependent effects into the FE and condensed hysteresis models is provided.

2.2 Hysteresis Phenomenon in Integral Abutment Bridges

Past studies of the proposed four components influencing IA bridge hysteretic behavior: (1) soil-pile interaction; (2) soil-abutment interaction; (3) abutment-backwall connection; and (4) pile-abutment connection; are reviewed. The soil-pile and soil-abutment interactions depend on soil-structure interaction behavior, however, the separation of these two components is required due to differences in geometric configurations and general soil resistance behaviors. The abutment-backwall and pile-abutment connections involve yielding of two different types of structural connections loaded beyond their elastic ranges.

2.2.1 Soil-Pile Interaction

Hysteresis phenomenon in IA bridges regarding soil-pile interaction was first discussed by Springman and Norrish [98]. Based on their preliminary test data, under controlled stress cyclic stresses and controlled cyclic strains, soil responses strongly exhibited hysteresis phenomenon as presented in Figure 2-1 [98].

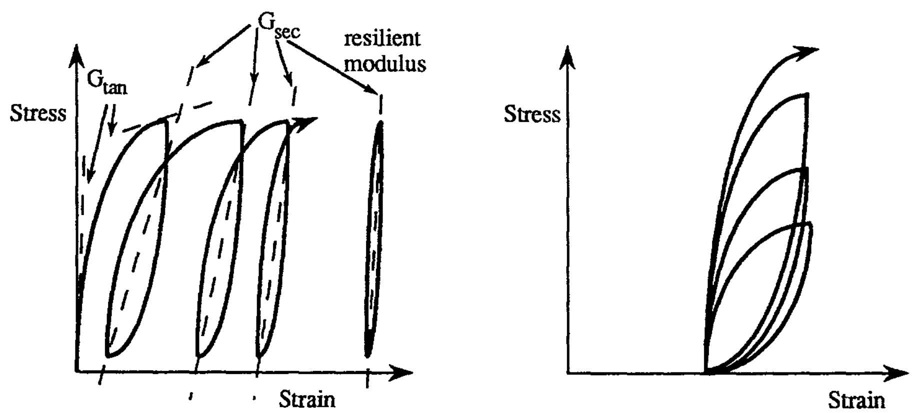

Figure 2-1: Hysteresis Loops of Soil Responses Under Controlled Cyclic Stresses and Controlled Cyclic Strains [98]

In Springman and Norrish studies, a number of scale integral abutment bridge centrifuge tests subjected to cyclic displacements at the deck level were conducted to investigate soil-pile interaction behavior. Results were separated into two cases: small displacement behavior and large displacement behavior. All results consisting of bending moments, shears, and displacements along the length of the pile indicated that cyclic effects are insignificant for small displacement behavior. However, results obtained from large displacement behavior demonstrated strong cyclic effects resulting in larger bending moments and shears as the number of cycles increased. Springman and Norrish [98] also reported that increasing rates of bending moments and shears for large displacement behavior are significantly reduced when the number of cycles is increased. This implies that soil-pile interaction under cyclic loading is dynamic and the mechanism approaches a steady-state when the number of cycles is increased.

Among many methods for predicting soil-structure interaction behavior, the *p-y* curve technique is the most practical due to relative ease of use [**100** and **114**]. This method was developed in the 1970s, well documented in Reese [**92**], and implemented as a microcomputer program by Wang and Reese [**112**].

In addition to the experimental study conducted by Springman and Norrish [**98**], there are several analytical studies concerning IA bridge soil-pile interaction. Although some studies employ a continuum FE model approach (*e.g.* hyperpolic material model with 2D plain strain elements [**12**] and Mohr-Coloumb failure criterion with 3D solid elements [**56**]), nonlinear *p-y* curves have been more commonly used because these curves are simpler and easily modified. Dicleli and Albhaisi [**35** and **36**] performed a push-over analysis and adopted an elasto-plastic stress-strain curve to simplify a *p-y* curve. Faraji *et al* [**41**] carried out a nonlinear analysis with the same simplification as Dicleli's study. Laman *et al* [**60**], Fenemma [**43**], Fenemma *et al* [**44**], Paul [**85**], and Paul *et al* [**86**] applied a multi-linear spring to obtain a better approximated *p-y* curve. However, due to limited software capability of the particular elements used in these studies (SAP2000 [**94**] and STAAD [**99**]), only an initial loading case was evaluated. Thus, no hysteretic behavior was considered.

An unrecoverable property needs to be considered when soil is subjected to cyclic loading. A reduction of soil strength in the classical *p-y* curves to account for cyclic effects was normally utilized [**64** and **112**]. However, this approach cannot be used to capture the transition between initial and final pile behaviors after many loading cycles. In order to bridge this gap, modifications to the classical *p-y* curve were performed by several researchers [18, 64, and 100]. Among these modifications, an elasto-plastic *p-y* curve, proposed and numerically proved by Taciroglu *et al* [100], appears to be the most useful hysteresis model for this study because the desirable characteristics of this model are available in ANSYS. Figure 2-2 presents a qualitative diagram of the elasto-plastic *p-y* curve.

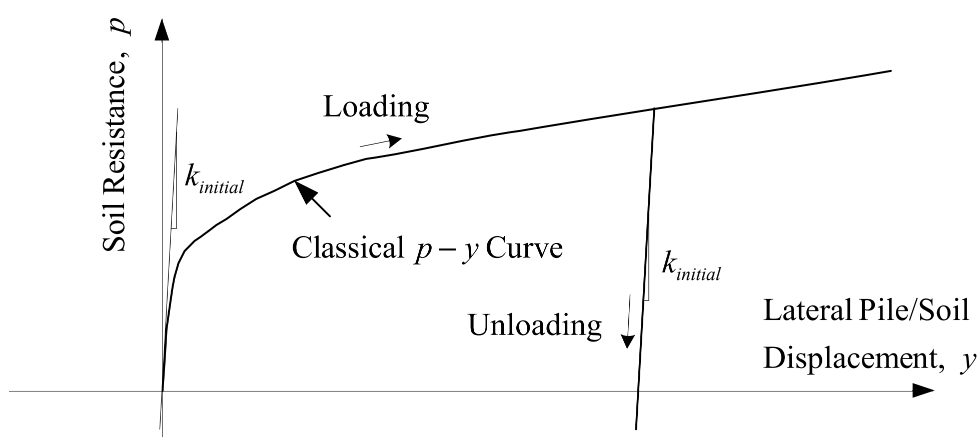

Figure 2-2: Qualitative Diagram of Elasto-Plastic *p-y* Curve

2.2.2 Soil-Abutment Interaction

The difference between soil-abutment interaction and soil-pile interaction depends upon several factors. The most apparent factor is that, regardless of whether temperature rises or falls, abutments receive pressure by backfill in only one direction as a result of the wedged-type failure mode [112]. Piles are prevented from moving in any direction by either of two soil failure modes: wedged-type and local shear around the pile body [112]. Other important factors include structural stiffness and soil properties.

From a practical perspective, classical earth pressure theory is commonly employed to construct a diagram as presented in Figure 2-3 to simulate soil-wall interaction [32, 33, and 39]. A lateral modulus of subgrade reaction, k_h [103], is used to linearly connect the three earth pressure limit states (active, at rest, and passive).

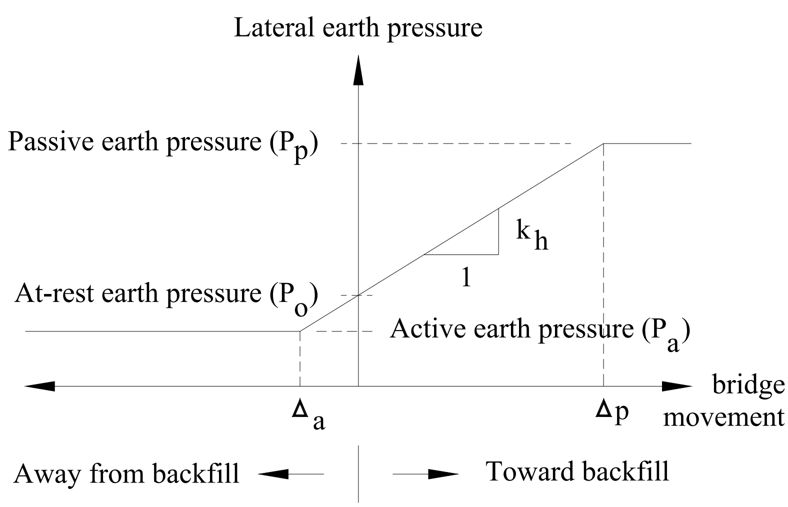

Figure 2-3: Typical Soil-Abutment Interaction Diagram

The diagram presented in Figure 2-3 was adopted by Koskinen [57] to represent backfill behaviors using FE analysis by neglecting the active earth pressure limit state and connecting the lateral soil stiffness slope from the origin to the passive earth pressure limit state. Paul [85] and Paul *et al* [86] employed the same approach as performed by Koskinen [57] to conduct a parametric study on IA bridges. This approach was also adopted by Dicleli [34] to develop computer-aided analysis of IA bridges with several simplified assumptions (*e.g.* identical abutments and soil configuration on both sides, neglecting contribution of substructure resistances, and neglecting an eccentricity of earth pressure resultant forces to the superstructure neutral axis). Only initial loading was evaluated in the above discussed studies, thus, no hysteretic behavior due to unrecoverable soil properties was considered.

Evidence showing that hysteretic behavior exists in soil-abutment interaction of IA bridges is presented in England *et al* [40] and Neil *et al* [77]. A number of tests of a scale semi-integral abutment bridge subjected to cyclic displacement at the deck level were conducted to study soil-wall interaction, settlement, and heave behavior. From experimental data, many hysteresis loops related to soil response were obtained, particularly the relationship between shear/axial strain and a ratio of two principal stresses. However, England and Neil primary focus was to determine recommendations for the design of IA bridges in the UK, therefore, only the extreme values of each loop were extracted and studied.

2.2.3 Abutment-Backwall Connection

Connection joints between abutment and backwall are unavoidable in concrete I-girder IA bridge construction. Reinforcement details for these construction joints vary from state to state. Examples of DOT standard joint details are provided for discussion in Figure 2-4 through Figure 2-7. Pennsylvania Department of Transportation (PennDOT) specifies, presented in Figure 2-4, Ø16 mm @ 250 mm (#5 @ 10″) U-shape rebar as a standard reinforcement detail [17]. As can be observed, the vertical reinforcement across the joint is placed at each face of the wall. Massachusetts Highway Department standard joint detail [21] presented in Figure 2-5 has a similar rebar arrangement.

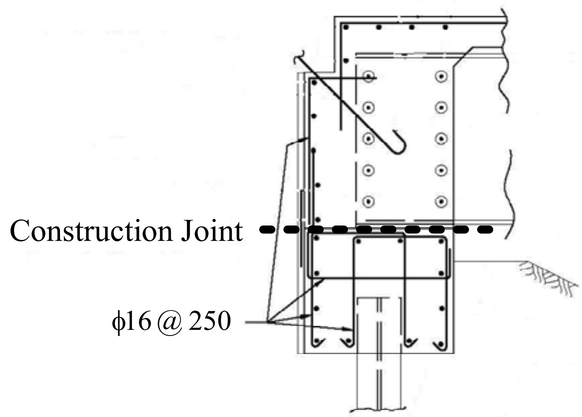

Figure 2-4: PennDOT Standard Integral Abutment Details [17]

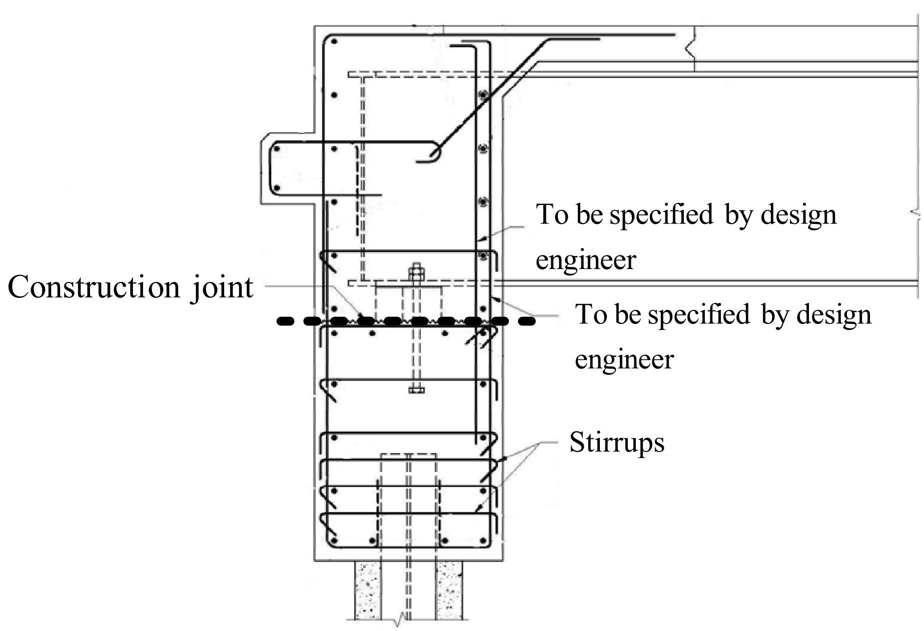

Figure 2-5: MassDOT Standard Integral Abutment Details [21]

Standard joint details for the New Jersey DOT [22] and New York State DOT [20], presented in Figures 2-6 and 2-7, share a common reinforcement arrangement. The apparent difference of the NJDOT and NYSDOT standard details from the PennDOT and MassDOT standard details is that the vertical joint reinforcement has a much shorter moment arm to induce a moment at the joint. However, the use of much larger bar sizes (Ø50 mm @ 300 mm for NJDOT and Ø60 mm @ 300 mm for NYSDOT) compensates for the larger induced moment.

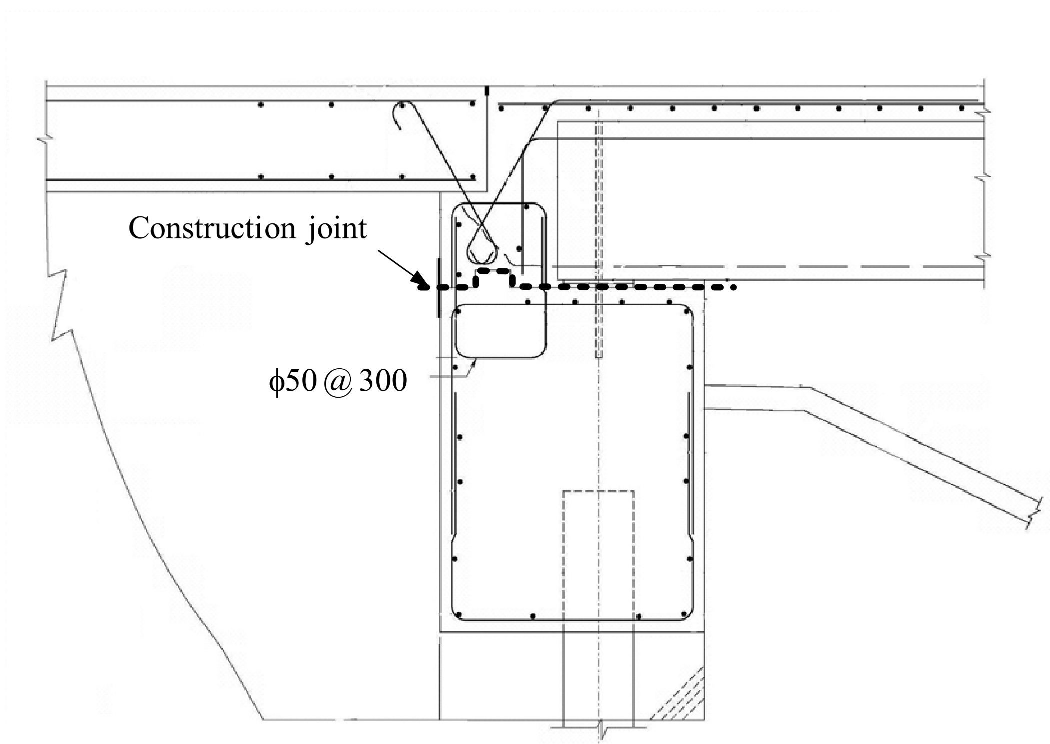

Figure 2-6: NJDOT Standard Integral Abutment Details [22]

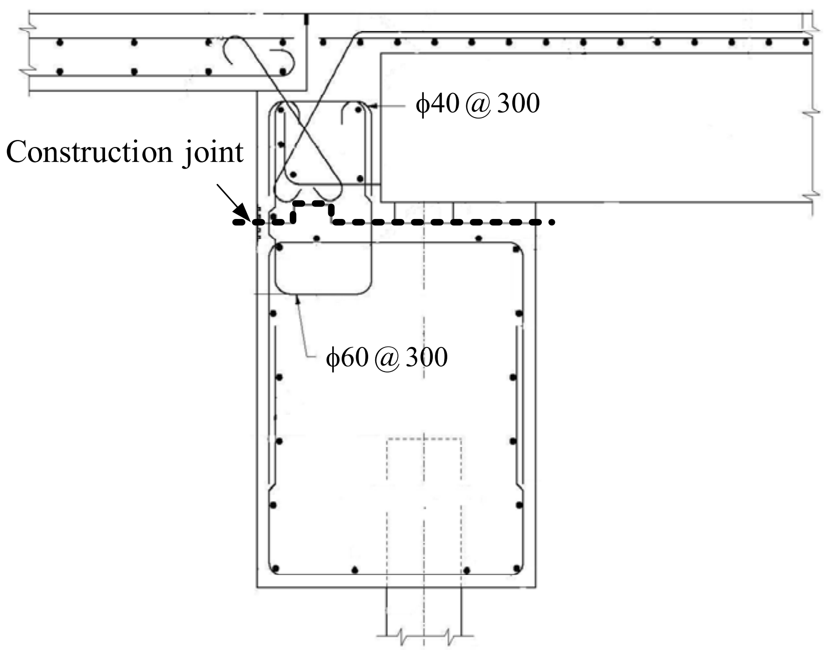

Figure 2-7: NYSDOT Standard Integral Abutment Details [20]

In practical IA bridge design, horizontal construction joints are intended to behave as a rigid connection. However, rotational stiffness of the construction joints is relatively small compared to the stiffness of the abutment and backwall. This is because the joint stiffness relies entirely on reinforcement without contribution from the concrete's modulus of rupture. Based on the PennDOT standard detail, Paul [85] demonstrated that moment strength and initial rotational stiffness of the joint derived from calculated moment curvature are much smaller than those of the abutment derived from calculated abutment moment curvature. An elasto-plastic model was also proposed by Paul [85] to represent the abutment-backwall joint behavior in numerical models.

Due to relatively small rotational stiffness and strength of common abutment and backwall horizontal construction joints, it is expected that medium to long IA bridges will experience movement sufficient to cause yielding in reinforcement. This yielding results in a hysteresis phenomenon.

2.2.4 Pile-Abutment Connection

It is known that steel H-piles in an IA bridge may reach full plastic moment capacity, particularly at the pile-to-abutment connection, when the bridge undergoes sufficient thermal movements. Yielding of steel H-piles at this connection may result in a hysteresis phenomenon similar to yielding of abutment-backwall connection. Therefore, a similar technique used for abutment-backwall connections, *i.e.* elasto-plastic hysteresis model, can be employed to pile-abutment connections. An elasto plastic elements and static push-over analysis was used and studied by Dicleli and Albhaisi [35] to simulate yielding behavior of IA steel H-piles. However, only initial loading was evaluated, thus, no hysteretic behavior was considered.

2.3 Hysteresis Models

2.3.1 Historical Perspective

Hysteresis phenomenon was initially discovered in ferromagnetic materials. According to Visintin [109], Weber, Maxwell, and Wiedemann are pioneers who ascribed this phenomenon to frictional resistance in the late 1800s. However, it was

Ewing in 1882 who was the first to refer to as hysteresis. Hysteresis in plasticity dated back to 1924 by Prandtl [109] who proposed a general scalar model of elasto-plasticity. This model was extended to a tensor framework by Reuss in 1930 [109], which mathematicians labeled a linear Stop Model. Hysteresis phenomenon is also found in many other areas, such as phase transitions, hydrology, chemistry, biology, economics, and many more [89 and 109]. The most recent improvement to hysteresis phenomenon is shape memory alloys.

Although hysteresis phenomenon has existed for more than a century, the mathematics of hysteresis was developed in 1970 by Krasnosel'skiĭ and his co-workers. A monograph written by Krasnosel'skiĭ and Pokrovskiĭ [58] was published in 1983 and translated into English in 1989. The mathematics of hysteresis was then expanded to a partial differential equation framework by Visintin [109]. Their studies covered hysteresis phenomena of many research areas, mainly ferromagnetism and continuum mechanics. Besides the major contribution by Krasnosel'skiĭ, Pokrovskiĭ and Visintin, Mayergoyz [70] published his monographs in 1991 and 2003, devoted entirely to ferromagnetism. Brokate and Sprekels [24] published their monographs in 1995, devoted to an application of thermodynamic phase transitions. Since the 1980s, the number of researchers who study hysteresis has been increasing.

2.3.2 Mathematics of Hysteresis

Mathematics of hysteresis is one of the advanced topics in applied mathematical sciences. As mentioned in Section 2.3.1, there are several textbooks dedicated entirely to the description of the mathematical aspects of hysteresis. The present will not attempt to review all sources but will focus on necessary topics.

Definitions of the basic hysteresis parameters are as follows:

- Input, $x(t)$: A variable that is a function of time, *t*, and acts as an external effect on a system,
- Output, $y(t)$: A variable that is a function of time, *t*, and is the response of a system to the variable $x(t)$ at the same instant of time,
- Hysteresis transducer, $\hat{H}$: A mathematical operator that converts a variable input, $x(t)$, to a variable output, $y(t)$.

The basic relationship between these variables is written in Equation 2-1:

$$y(t) = \hat{H} \cdot x(t) \tag{2-1}$$

Equation 2-1 can also be understood graphically as in Figure 2-8:

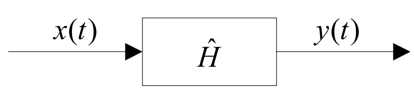

Figure 2-8: Hysteresis Transducer

Prior to discussing the mathematical aspects of hysteresis, it is necessary to present the important hysteresis property of rate-independence. This property implies that rates of input with respect to a time scale, $\dot{x}(t)$, do not affect a hysteresis transducer $\hat{H}$, rates of output $\dot{y}(t)$, or output $y(t)$. Rate-dependent hysteresis is discussed in detail by Brokate [24] and will not be considered here because the relationship of input and output of the present study (temperature and bridge movements) is rate-independent. Further discussion herein is limited to a rate-independent hysteresis model.

In order to demonstrate the mathematical concept of hysteresis, the simplest model of hysteresis, Non-Ideal Relay [58 and 89], is presented in Figure 2-9.

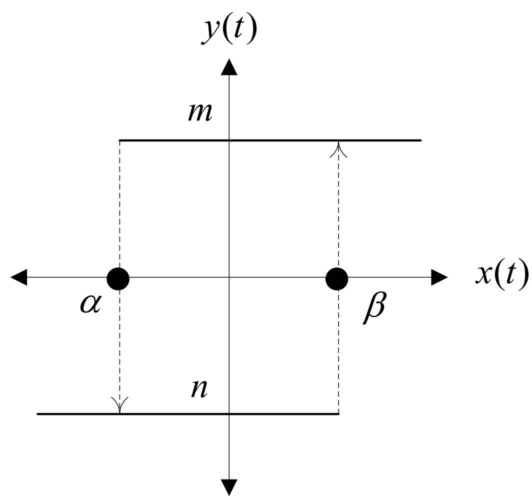

Figure 2-9: Non-Ideal Relay Hysteresis Model

The model in Figure 2-9 allows an output, $y(t)$, to switch only between two specified values, *m* and *n*. There are two threshold points: switch-on point (β) and switch-off point (α) that allow one-way switching from *n* to *m* and *m* to *n*, respectively. For any input values not equal to those threshold points, output will remain constant as either *m* or *n*, regardless of input, $x(t)$. The hysteresis transducer $\hat{H}$ of this model is defined as:

$$y(t) = \hat{H} \cdot x(t) = \begin{cases} y_o, \text{ if } \alpha < x(\tau) < \beta \text{ for all } \tau \in [t_o, t], \\ m, \text{ if there exists } t_1 \in [t_o, t] \text{ such that } x(t_1) \geq \beta, x(\tau) > \alpha \text{ for all } \tau \in [t_1, t], \\ n, \text{ if there exists } t_1 \in [t_o, t] \text{ such that } x(t_1) \leq \alpha, x(\tau) < \beta \text{ for all } \tau \in [t_1, t] \end{cases} \quad (2\text{-}2)$$

where t_o is an initial time and y_o is a value of an output at time t_o (either m or n). Although Equation 2-2 appears awkward, it provides an explicit expression. The hysteresis transducer in Equation 2-2 as well as every mathematical hysteresis model discussed hereafter can be expressed in a complex notation of functional spaces to describe a framework of partial differential equations for multi-dimensional hysteresis models [109]. However, only a one dimensional hysteresis model will be adopted herein so that the use of functional space notation is not required.

There are several available hysteresis models developed by many applied mathematicians. The most widely used hysteresis models include: Preisach Model; Discontinuous Hysteresis Model; Play Model; Stop Model; Prandtl-Ishlinskiĭ Model; and Duhem Model [109].

The Preisach Model is one of the most widely used hysteresis models, however, it is applicable to ferromagnetism and electromagnetism, not mechanics. This is because the model contains a mathematical property, referred to as Wiping-out. Wiping-out agrees with a physical property, referred to as reduced memory sequence, in ferromagnetism [109]. However, there have been attempts in other disciplines to adopt and apply this model to soil-moisture, smart materials, and structural control problems [45, 48, and 93].

The Non-Ideal Relay is commonly classified as a discontinuous hysteresis model. According to Visintin [109], the use of the discontinuous hysteresis model occurs in thermodynamics and phase transitions. Due to the loss of continuity, this model is not suitable for continuum mechanics.

Useful models for a mechanical application; particularly for elasto-plastic, viscoelastic, and elasto-visco-plastic constitutive laws, requires the property of continuity. According to Visintin [109], hysteresis models satisfying the continuity include: Play Model, Stop Model, Prandtl-Ishlinskiĭ Model, and Duhem Model. The following presents the basic concept along with mathematical properties of these hysteresis models.

Play Model

According to Visintin [109], there are two forms of Play Models: (1) linear Play and (2) generalized Play. The linear Play is discussed herein. Figure 2-10 presents a diagram of the Play Model as well as its physical system through a mechanism of a piston and cylinder.

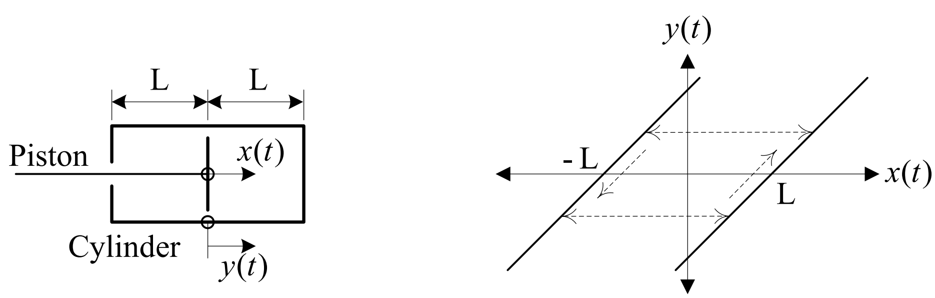

Figure 2-10: Linear Play Model

It is observed from Figure 2-10 that the system represents the action of a piston and cylinder as a driving and driven element. A horizontal displacement is applied to the piston as an input variable *x(t)* while the cylinder displacement represents an output variable *y(t)*. The general equation of an output variable ($t \geq t_o$) corresponding to a monotonic input is given as [58]:

$$y(t) = \hat{H} \cdot x(t) = \begin{cases} y(t_o), & \text{for all } t \text{ such that } y(t_o) - L \leq x(t) \leq y(t_o) + L \\ x(t) - L, & \text{for all } t \text{ such that } x(t) \geq y(t_o) + L \\ x(t) + L, & \text{for all } t \text{ such that } x(t) \leq y(t_o) - L \end{cases} \quad (2\text{-}3)$$

An alternate form of Equation 2-3 is written as:

$$y(t) = \hat{H} \cdot x(t) = \begin{cases} \max\{y(t_o), x(t_o) - L\}, \text{ if } x(t) \text{ is non-decreasing} \\ \min\{y(t_o), x(t_o) + L\}, \text{ if } x(t) \text{ is non-increasing} \end{cases} \quad (2\text{-}4)$$

The domain of the model is given as:

$$\Omega = \{(x, y) \mid -\infty < x < \infty, x - L \leq y \leq x + L\} \quad (2\text{-}5)$$

In order to allow piecewise monotonic inputs, the hysteresis transducer is assumed to be deterministic [58]. A mathematical property, called the semi-group property or semi-group identity, is required such that [58]:

$$\hat{H}[t_o, y(t_o)] \cdot x(t) = \hat{H}\left[t_1, \hat{H}[t_o, y(t_o)] \cdot x(t_1)\right] \cdot x(t) \quad (2\text{-}6)$$

For generalized Play, Krasnosel'skiĭ and Pokrovskiĭ [58] discussed and provided proofs that the model satisfies the Lipschitz condition and monotonicity property. These two basic properties are required to ensure that an output variable is bounded and a change in input and output variables conforms correspondingly. Other mathematical properties, such as continuity and proofs, that allow an extension from piecewise monotonic inputs to an arbitrary continuous input, can be found in Krasnosel'skiĭ and Pokrovskiĭ [58] and Macki *et al* [69].

Stop Model

The Stop Model [58 and 109] is a simple but versatile hysteresis model that can represent a hysteresis phenomenon of elasto-plasticity without strain-hardening. Figure 2-11 presents a simple system having a spring connected to a mass on a rough surface where an external force is applied to the right end of the spring and transmitted to the mass at the left end of the spring. The system maintains its equilibrium by friction between the mass and the surface. The displacement at the right end of the spring and the spring force serves as input and output variables of the system respectively.

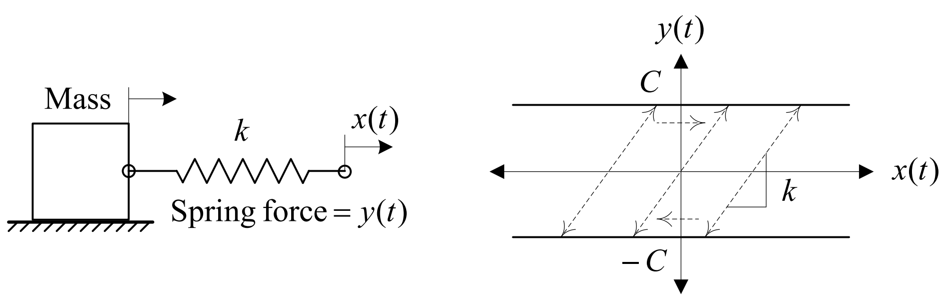

Figure 2-11: Stop Model

Assuming that a threshold value of the friction force is C and spring stiffness is k, an output variable ($t \geq t_o$) is expressed as [58]:

$$y(t) = \hat{H} \cdot x(t) = \begin{cases} \min\{C, k(x(t) - x(t_o)) + y(t_o)\}, & \text{if } x(t) \text{ is non-decreasing} \\ \max\{-C, k(x(t) - x(t_o)) + y(t_o)\}, & \text{if } x(t) \text{ is non-increasing} \end{cases} \quad (2\text{-}7)$$

The domain of the model is defined as:

$$\Omega = \{(x, y) \mid -\infty < x < \infty, -C \leq y \leq C\} \quad (2\text{-}8)$$

As with the Play Model, the semi-group property is required for the Stop Model when piecewise monotonic inputs are used. The Stop Model must also satisfy the Lipschitz condition, monotonicity, and continuity, as determined by Krasnosel'skiĭ and Pokrovskiĭ [58].

Prandtl-Ishlinskiĭ Model

The Prandtl-Ishlinskiĭ Model is a hysteresis model obtained by combining Play and Stop models. Visintin [109] described this hysteresis model as a model of elasto-plasticity with strain-hardening. There are two major forms of the Prandtl-Ishlinskiĭ that can be derived in the following manner [109]:

- Prandtl-Ishlinskiĭ Model, Play-Type: Combination of a Play model and a Stop model in series.
- Prandtl-Ishlinskiĭ Model, Stop-Type: Combination of a Play model and a Stop model in parallel.

Mathematical expressions of these models are of a very complex format, generally expressed in a framework of variational inequalities. The present study primarily addresses a structure subjected to service loading. Yielding of certain structural connections can be sufficiently described using the Stop Model to represent a zero-stiffness plastic region. Therefore, a state beyond the plastic region (strain hardening and necking), which is the primary capability of the Prandtl-Ishlinskiĭ Model, is not a required characteristic for the present study.

Duhem Model

The Duhem Model is primarily constructed from a solution of two families of a smooth function. These two functions, defined as increasing slope f_I and decreasing slope f_D, are defined through the following form of differential equations [58]:

$$\frac{dy}{dx} = f_I(y, x)$$
$$\frac{dy}{dx} = f_D(y, x) \tag{2-9}$$

These two functions must satisfy the Lipschitz condition such that:

$$\begin{aligned}(y_1 - y_2)[f_I(y_1, x) - f_I(y_2, x)] &\leq \lambda(x)(y_1 - y_2)^2 \\ (y_1 - y_2)[f_D(y_1, x) - f_D(y_2, x)] &\geq -\lambda(x)(y_1 - y_2)^2\end{aligned} \tag{2-10}$$

where $\lambda(x)$ is a continuous non-negative function. Figure 2-12 presents a typical graphic representation of the Duhem Model.

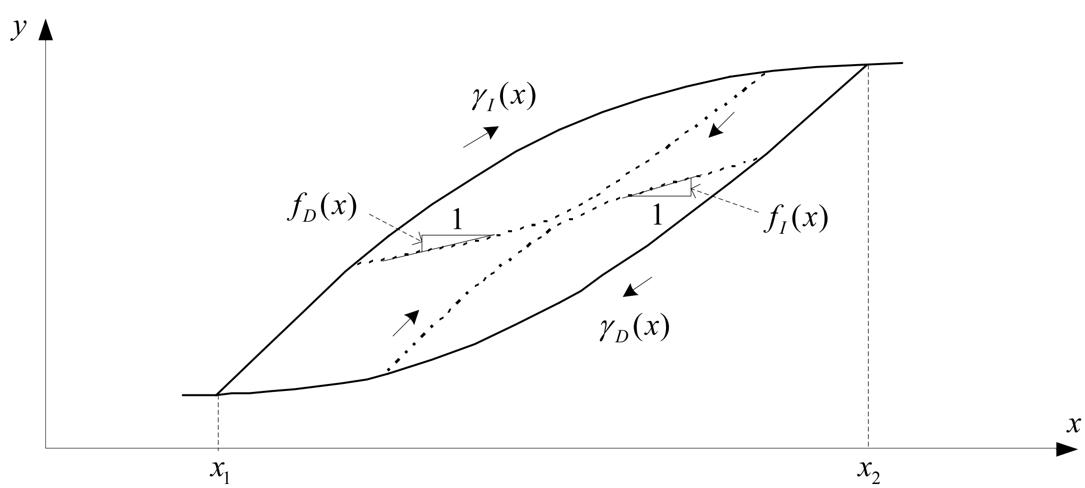

Figure 2-12: Duhem Model

The two slopes, f_I and f_D, are used to construct two trajectory interior C^1 curves bounded inside the hysteresis domain:

$$\Omega = \{(x, y) \mid \gamma_D(x) < y < \gamma_I(x), x \in (x_1, x_2)\} \quad \textbf{(2-11)}$$

where γ_I and γ_D are a C^2 boundary curve [8] with the following properties:

$$\begin{aligned} &\gamma_I(x) > \gamma_D(x), \text{for } x \in (x_1, x_2) \\ &\gamma_I(x) = \gamma_D(x), \text{for } x \notin (x_1, x_2) \end{aligned} \quad \textbf{(2-12)}$$

The relation between the two slopes and the two boundary curves is given as [69]:

$$\left.\begin{aligned} f_I(\gamma_D(x), x) = \max(f_I(\gamma_D(x), x), \gamma'_D(x)) \\ f_D(\gamma_I(x), x) = \max(f_D(\gamma_I(x), x), \gamma'_I(x)) \end{aligned}\right. \text{for } x \in (x_1, x_2) \quad \textbf{(2-13)}$$

$$\left.\begin{aligned} f_I(\gamma_I(x), x) = \gamma'_I(x) \\ f_D(\gamma_D(x), x) = \gamma'_D(x) \end{aligned}\right. \text{for } x \notin (x_1, x_2) \quad \textbf{(2-14)}$$

The hysteresis transducer, $y(t) = \hat{H}[t_o, y_o]x(t)$ for $t \geq t_o$, is a solution of the following Cauchy problem (initial boundary value problem) [58, 69, and 109]:

$$\begin{aligned} &\frac{dy}{dt}(t) = \begin{cases} f_I(y, x)\dot{x}, & \dot{x}(t) \geq 0 \\ f_D(y, x)\dot{x}, & \dot{x}(t) \leq 0 \end{cases} \\ &y(0) = y_o \end{aligned} \quad \textbf{(2-15)}$$

As opposed to the Play and Stop Models, an interior hysteresis loop bounded inside the hysteresis domain, Ω, can be generated every time the sign of $\dot{x}(t)$ is reversed in the Duhem Model. This is because the existence of two curves leads to the loss of the vibro-correctness mathematical property [58 and 69].

2.3.3 Physics of Hysteresis

In this section, hysteresis models developed under a framework of physics are reviewed. As opposed to the mathematics of hysteresis presented in Section 2.3.2, hysteresis models developed in a physics framework are phenomenological, intuitive, and experimental-based. Mathematical properties that play a major role in the mathematics of hysteresis, such as the monotonicity, continuity, semi-group identity, vibro-correctness, and mathematical proofs, are granted less significance in the physics of hysteresis.

In the physics of hysteresis, two model types are generally distinguished: (1) piecewise linear hysteresis and (2) curvilinear hysteresis models [105]. Both model types are discussed in detail below. A hysteresis model requiring a set of obtainable parameters as well as possessing pertinent mathematical properties is the most suitable tool for further use. The pertinent mathematical properties, as generally described in Section 2.3.2, are required to ensure uniqueness and existence of output and to overcome convergence difficulty when approximate method is applied.

Piecewise Linear Hysteresis Model

A piecewise linear hysteresis model is composed of at least two linear segments and, therefore, an abrupt change in each segment connection exists. The most well-known piecewise linear model includes elasto-plastic, bi-linear, and multi-linear hysteresis models.

Elasto-Plastic and Bi-Linear Hysteresis Models

The elasto-plastic and bi-linear hysteresis models are known as one of the simplest and the most widely-used hysteresis models in structural mechanics. The Stop Model is essentially identical to the elasto-plastic hysteresis model. Visualization of the model as a series of spring and friction elements is also similar. In the case of a bi-linear hysteresis model as depicted in Figure 2-13, an additional spring is added and a Coulomb slip element is represented instead of a mass on a rough surface.

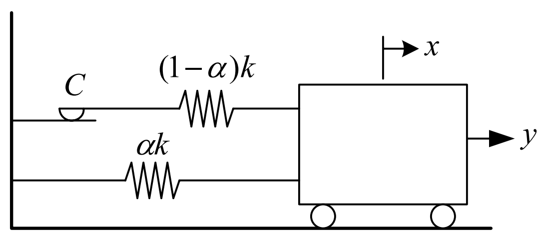

Figure 2-13: Schematic Representation of Bi-Linear Hysteresis Model

By using Stop Model notation, an equation for the restoring force, y, and the displacement, x, for a bi-linear hysteresis model is written as [73, 105]:

$$y = \alpha k x + (1-\alpha)ku \tag{2-16}$$

where u is a relative deformation of a $(1-\alpha)k$ spring, which is a solution of Equation 2-17

$$\dot{u} = \dot{x}\left[H_3(\dot{x}) \cdot H_4\left(u - {}^{C}\!/_{k}\right) + H_2(\dot{x}) \cdot H_1\left(u + {}^{C}\!/_{k}\right)\right] \tag{2-17}$$

with the use of the following Heaviside's unit step functions [73]:

$$H_1(x) = \begin{cases} 1, \text{ for } x \geq 0 \\ 0, \text{ for } x < 0 \end{cases} \quad (2\text{-}18)$$

$$H_2(x) = \begin{cases} 0, \text{ for } x \geq 0 \\ 1, \text{ for } x < 0 \end{cases} \quad (2\text{-}19)$$

$$H_3(x) = \begin{cases} 1, \text{ for } x > 0 \\ 0, \text{ for } x \leq 0 \end{cases} \quad (2\text{-}20)$$

$$H_4(x) = \begin{cases} 0, \text{ for } x > 0 \\ 1, \text{ for } x \leq 0 \end{cases} \quad (2\text{-}21)$$

Note that $\dot{x}$ is positive when x is increasing and $\dot{u}$ is equal to either zero or $\dot{x}$ when the system is in a sliding mode or a non-sliding mode, respectively. Figure 2-14 presents the typical shape of a bi-linear hysteresis model.

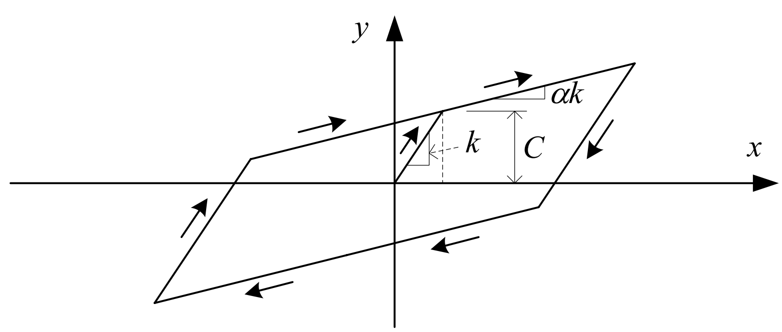

Figure 2-14: Bi-Linear Hysteresis Model

The elasto-plastic hysteresis model can be easily constructed from Equation 2-16 letting $\alpha = 0$.

Multi-Linear Hysteresis Model

A multi-linear hysteresis model is an enhanced version of a bi-linear model that provides better correlation with the actual behavior of many applications. More than two sets of springs and Coulomb slip elements in series are added to configure this model. Figure 2-15 is a diagrammatic representation of a multi-linear hysteresis model,

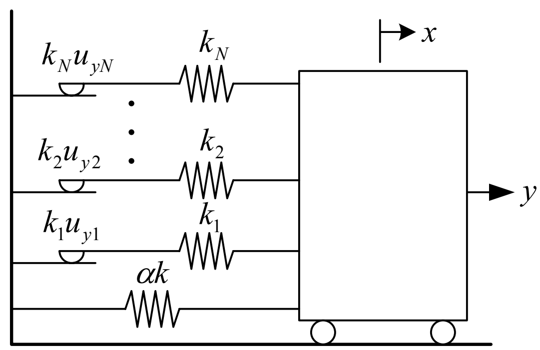

Figure 2-15: Schematic Representation of Multi-Linear Hysteresis Model

where N is the number of spring and Coulomb slip element sets. Because the connection is parallel, an equivalent spring, k_e, is determined by Equation 2-22 [73, 105]:

$$k_e = (1-\alpha)k = \sum_{i=1}^{N} k_i \tag{2-22}$$

An equation for the restoring force, y, and a displacement, x, for this model also appears in the same form as in Equation 2-16. Instead, the relative deformation, u, of an equivalent spring is the solution of the following equations:

$$u = \frac{1}{(1-\alpha)k} \sum_{i=1}^{N} k_i u_i , \tag{2-23}$$

$$\dot{u} = \dot{x}\left[H_3(\dot{x}) \cdot H_4\left(u_i - x_{yi}\right) + H_2(\dot{x}) \cdot H_1\left(u_i + x_{yi}\right)\right] \tag{2-24}$$

Figure 2-16 presents the typical shape of a multi-linear hysteresis model with three sets of springs and Coulomb slip elements. In this particular case, it is assumed that $k_1 u_{y1} < k_2 u_{y2} < k_3 u_{y3}$.

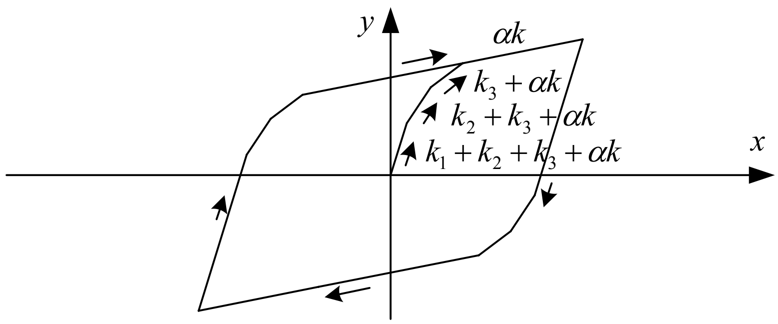

Figure 2-16: Multi-Linear Hysteresis Model

The Prandtl-Ishlinskiĭ Model, Stop-Type, is identical to this model. The Prandtl-Ishlinskiĭ Model, Play-Type, can also be used to construct a multi-linear hysteresis model as performed by Valdman [107].

Curvilinear Hysteresis Model

Hysteretic behavior, in most situations, does not present an abrupt change in slopes. Although a multi-linear hysteresis model is capable of creating a relatively smooth transition, many sets of springs and Coulomb slip elements are generally required to achieve a desirably smooth curve, resulting in an awkward mathematical operation. As a result, the curvilinear hysteresis models have gained wider acceptance when modeling accuracy is concerned. The most widely used curvilinear model includes Bouc-Wen and modified Ramberg-Osgood hysteresis models. In geotechnical applications, a hyperbolic hysteresis model is widely used to represent hysteretic behavior of a soil continuum.

Bouc-Wen Hysteresis Model

The Bouc-Wen Hysteresis Model is the Bouc Model as modified by Wen [115] and discussed in detail by Spencer [97]. The model appears in the form of a first-order differential equation [115]:

$$\dot{y} = A\dot{x} - \beta|\dot{x}||y|^{n-1}y - \gamma\dot{x}|y|^{n} \qquad (2\text{-}25)$$

where $A, \beta, \gamma,$ and n are shape factors. Figure 2-17 demonstrates the shape of a Bouc-Wen hysteresis model with an at rest condition ($x(0) = y(0) = 0$), $n = 1$, $A = 1$, $\beta = 0.8$, and $\gamma = 0.5$.

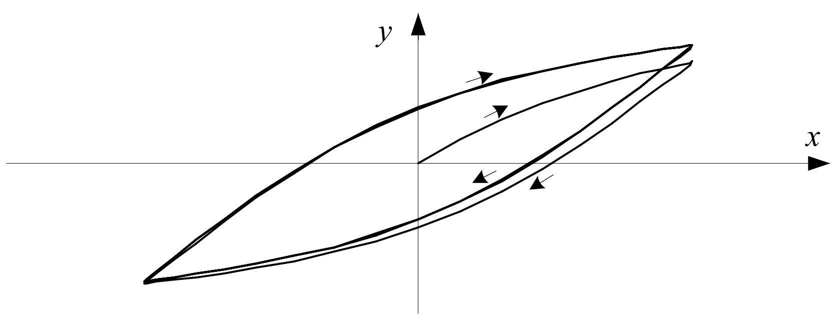

Figure 2-17: Bouc-Wen Hysteresis Model

A numerical approach using a Newton scheme of the form $x_{n+1} = x_n - f(x_n)/f'(x_n)$ was discussed in Haukaas and Kiureghian [49] and the influence of a 4-parameter manipulation to the hysteresis loop shape was presented in Spencer [97]. If n approaches infinity, the smooth transition is removed, yielding a shape similar to the elasto-plastic hysteresis model. Equation **2-25** can be rewritten in the form of Equation **2-26** if two conditions, $\dot{x} \geq 0$ and $\dot{x} \leq 0$, are expressed separately.

$$\frac{dy}{dt}(t) = \begin{cases} \left(A - \beta|y|^{n-1} y - \gamma|y|^n\right)\dot{x}, \dot{x}(t) \geq 0 \\ \left(A + \beta|y|^{n-1} y - \gamma|y|^n\right)\dot{x}, \dot{x}(t) \leq 0 \end{cases} \tag{2-26}$$

Equation **2-26** implies that the Bouc-Wen model (Equation **2-17**) is analogous to the Duhem Model such that $f_I = A - \beta|y|^{n-1} y - \gamma|y|^n$ and $f_D = A + \beta|y|^{n-1} y - \gamma|y|^n$. An initial boundary condition, *i.e.* $x(0) = x_o$ and $y(0) = y_o$, is required to determine $y(t)$. The mathematical equivalence of the Bouc and Duhem models is also discussed in Visintin [**109**].

Over a period of nearly 30 years, a number of parameters have been added to the original 4-parameter Bouc-Wen model. The most recent version of the Bouc-Wen model contains an additional 8 parameters to include strength deterioration, stiffness degradation, and pinching effects [**68**]. However, these effects are not of particular interest to the present study.

Modified Ramberg-Osgood Hysteresis Model

The modified Ramberg-Osgood hysteresis model was developed by Desai and Wu to approximate nonlinear stress-strain soil behavior [cf. **4** and **7**]. This hysteresis model has gained acceptance because of relative ease of use and a simple mathematical form. For monotonic loading, the Modified Ramberg-Osgood hysteresis model is expressed as [4]:

$$y = \frac{kx}{\left(1 + \left|\frac{kx}{y_u}\right|^n\right)^{1/n}} \tag{2-27}$$

where x is the displacement, y is the soil resistance, n is a shape parameter, k is an initial soil stiffness, and y_u is an ultimate soil resistance. For cyclic loading, the modified Ramberg-Osgood hysteresis model is written as [4]:

$$y = y_c + \frac{k(x - x_c)}{\left(1 + \frac{1}{\left|H(\dot{x}) - y_c/y_u\right|}\left|\frac{k(x - x_c)}{y_u}\right|^n\right)^{1/n}} \tag{2-28}$$

To account for path-dependent (memory) effects, x_c and y_c representing displacement and resistance of soil at the last load reversal are included. A Heaviside's unit step function is used and defined as:

$$H(\dot{x}) = \begin{cases} 1, \text{ for } \dot{x} \geq 0 \text{ (Reloading)} \\ -1, \text{ for } \dot{x} \leq 0 \text{ (Unloading)} \end{cases} \tag{2-29}$$

Figure 2-18 demonstrates the typical shape of a modified Ramberg-Osgood hysteresis model with n = 3. As n approaches infinity the smooth transition is removed, yielding a similar shape to the elasto-plastic hysteresis model. It is observed in Figure 2-18 that soil resistances are always bounded by $\pm y_u$.

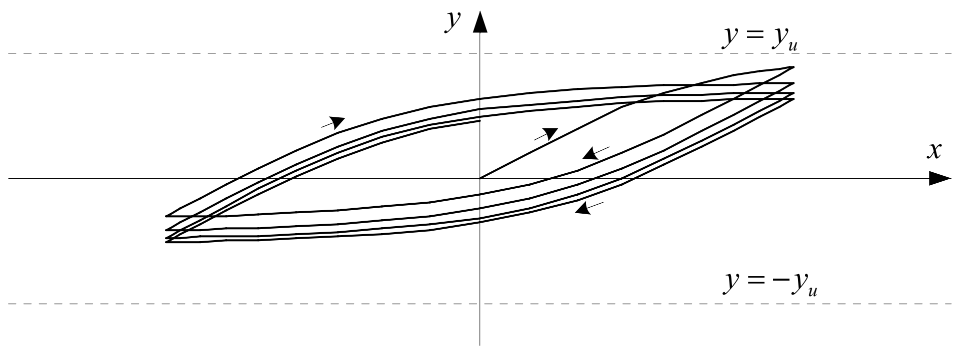

Figure 2-18: Modified Ramberg-Osgood Hysteresis Model

Hyperbolic Hysteresis Model

The hyperbolic hysteresis model is widely used in geotechnical practice, although it may not capture some fundamental aspects of actual soil behavior [90]. This hysteresis model essentially serves as the Mohr-Coulomb shear failure criteria, *i.e.* x and y representing shear strain and shear stress, respectively. The formulation for monotonic loading is similar in form to the modified Ramberg-Osgood hysteresis model [25]:

$$y = \frac{Gx}{1+|x|(G/y_u)} \tag{2-30}$$

where G is the initial shear modulus and x_u is the ultimate shear stress. For unloading and reloading, the Masing Rule, which generates the steady-state response curve based upon initial loading behavior [105], is used and also defines a form similar to the modified Ramberg-Osgood hysteresis model [25]:

$$y = y_c + \frac{G(x - x_c)}{\left(1 + \left|x - x_c\right|\left(G/2y_u\right)\right)} \tag{2-31}$$

where x_c and y_c represent shear strain and shear stress at the last load reversal. This model is more applicable to a continuum modeling technique, therefore, it may not be suitable for use in the present study because one-dimensional hysteresis model is applied.

2.4 Time-Dependent Effects

In this section time-dependent effects of concrete creep, concrete shrinkage, and prestressing steel relaxation on IA bridges as well as relevant past studies are reviewed to establish their application to non-hysteretic behavior. Past studies relating to time-dependent effects of concrete creep, concrete shrinkage, and prestressing steel relaxation on IA bridges are discussed. A review of creep, shrinkage, and prestressing steel relaxation from a structural mechanics and practical design perspective is provided. Finally, a review of the selected time-dependent effect analysis method, age-adjusted effective modulus method (AAEM), is presented in detail to incorporate time-dependent effects into the FE models and the condensed hysteresis models.

2.4.1 Time-Dependent Effects on IA Bridges

Time-dependent effects of concrete creep, concrete shrinkage, and prestressing steel relaxation on IA bridges have long been realized and included in design specifications. However, few studies examining time-dependent effects of concrete creep, concrete shrinkage, and prestressing steel relaxation on IA bridges have been conducted. O'Brien and Flanagan [81] employed the AAEM method in conjunction with the CEB-FIP model code 1990 [27] as a creep and shrinkage model. An experimental test of a scale frame was conducted with data collection over a 27-day period. Results from the experiments demonstrated that the analytical model was conservative for early age but provided good prediction of results from day 7 to day 27. Huang *et al* [51] presented 7 years of data collection through field-instrumentation of a 3-span prestressed concrete I-girder bridge with a total length of 66 m (216′-7″). Strain data measured by a number of strain gages attached to 2 girders (1 interior and 1 exterior) reported time-dependent strains over a range of 175 to 500 micro-strain, leading to a conclusion that time-dependent effects must be included in design. Arockiasamy and Sivakumar [11] also employed the AAEM method to incorporate time-dependent effects in IA bridges. Based on this approach, an equation of time-dependent restrained bending moments was developed for a 2-span continuous bridge with an assumption of fully fixed condition at both ends. An illustrative example of the proposed equation was also provided.

2.4.2 Creep, Shrinkage, and Relaxation of Prestressing Steel

Time-dependent phenomena in typical prestressed concrete structures are generally composed of concrete creep; concrete shrinkage; and relaxation of prestressing steel. These three time-dependent sources are discussed separately as follows:

Creep in Concrete

Creep is a well-known phenomenon in concrete. There are three primary factors influencing this behavior; (1) magnitude and duration of applied stresses; (2) maturity of concrete at the time of loading; and (3) temperature of concrete. A typical creep curve representing concrete subjected to a sustained compressive load is presented in Figure 2-19.

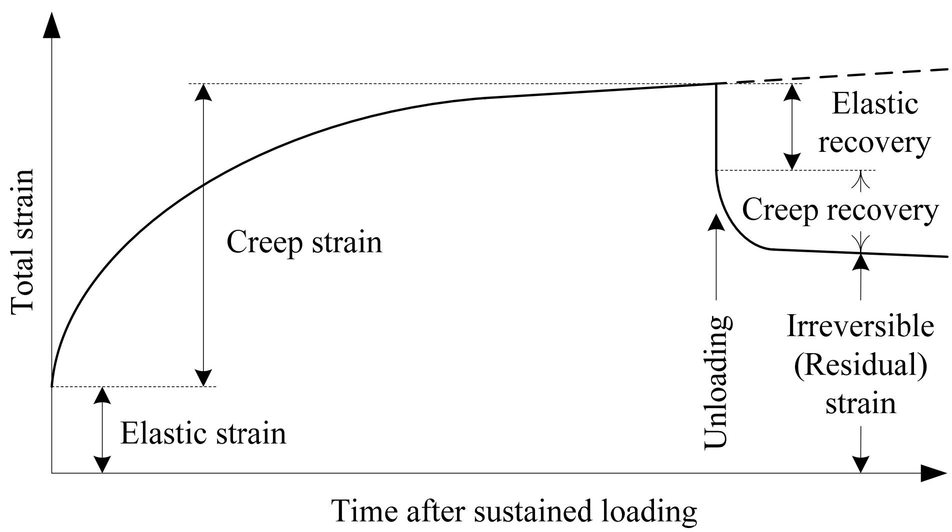

Figure 2-19: Time-Dependent Creep Strain

Mechanics of Creep

From a structural mechanics perspective, creep can be considered and modeled by using a nonlinear, viscoelastic, constitutive law. Nonlinear, viscoelastic material creep can be separated into three components [95]:

$$\varepsilon(t) = \varepsilon_e + \varepsilon_s(t) + \varepsilon_t(t) \quad (2\text{-}32)$$

where $\varepsilon(t)$ is total strain, ε_e is an elastic strain component, $\varepsilon_s(t)$ is a steady creep strain component, and $\varepsilon_t(t)$ is a transient creep strain component. $\varepsilon_s(t)$ and $\varepsilon_t(t)$ are a function of time, typically expressed by either a power law, exponential law, or hyperbolic sine law.

Creep in concrete is strongly associated with maturity at the time of loading known as the aging effect. Creep strain of concrete loaded at a young age is greater than creep strain of concrete loaded at a late age. The aging effect occurs in a structurally unstable material like concrete at a molecular level where chemical reactions cause significant microscopic changes during creep. In addition, creep properties are also influenced by effects of varying stress and temperature.

In order to consider the effects of aging and varying stress, a nonlinear viscoelastic constitutive law based on a time-hardening hypothesis is usually employed for a structurally unstable material. The time-hardening hypothesis postulates a creep strain rate as a function of instantaneous stress and time. The equations of steady creep strain rate and transient creep strain rate may be expressed as [95]:

$$\dot{\varepsilon}_s(t) = \left(\frac{\sigma(t)}{C_1}\right)^{c_2} \qquad \text{(Steady)} \quad (2\text{-}33)$$

$$\dot{\varepsilon}_t(t) = \frac{1}{t_o}\left(\frac{\sigma(t)}{C_3}\right)^{c_4} e^{\left(-t/t_o\right)} \qquad \text{(Transient)} \quad (2\text{-}34)$$

where C_1, C_2, C_3, C_4 are material constants, t_o is retardation time of strain, t is instantaneous time, and e is natural logarithm base.

The effect of temperature on creep strain was studied and a number of creep models were developed by many researchers. For example, one of several creep models based on the time-hardening hypothesis available in ANSYS is expressed as [9]:

$$\varepsilon_c(t) = \underbrace{C_1(\sigma(t))^{C_2} e^{\left(-C_3/T\right)} t}_{\varepsilon_s(t)} + \underbrace{C_4(\sigma(t))^{C_5} e^{\left(-C_6/T\right)} t^{(C_7+1)} /(C_7+1)}_{\varepsilon_t(t)} \qquad \text{(2-35)}$$

where C_1 to C_7 are material constants (different from Equations **2-33** and **2-34**) and T is an absolute temperature. The steady and transient creep strain components of Equation **2-35** are combined and expressed in a single component, denoted as total creep strain, $\varepsilon_c(t)$. An exponential law is used to formulate the equation and a temperature parameter appears on both creep strain components.

Predicted Creep Using Design Specifications

The separation of creep phenomenon into several components in most design specifications for predicting creep and shrinkage is somewhat different from the structural mechanics point of view. This is because creep equations from most design specifications have been exclusively developed for concrete, while creep equations from a mechanics perspective serve as general-purpose models for a wide range of materials. Two components of concrete creep; basic creep and drying creep, are normally distinguished [5]. Basic creep occurs in a condition where moisture is constantly controlled. An uncontrolled condition leads to drying creep that allows moisture in concrete to diffuse to the environment.

Most design specifications use a dimensionless term, called creep coefficient $\varphi(t,t_o)$, to conveniently characterize creep (basic and drying creep). The creep coefficient is defined as the ratio of creep strain at load duration $t-t_o$ to an initial elastic strain at time t_o. Therefore, the total strain can be expressed as [47]:

$$\varepsilon(t)=\frac{\sigma(t_o)}{E(t_o)}\left[1+\varphi(t,t_o)\right] \tag{2-36}$$

where $\varepsilon(t)$ is total strain at time *t*, $\sigma(t_o)$ is an initial stress at time t_o, $E(t_o)$ is concrete modulus of elasticity at time t_o, and $\varphi(t,t_o)$ is creep coefficient at time *t* corresponding to the concrete age at loading t_o.

Numerous creep coefficient equations are available in many well-known design specifications, *e.g.* ACI Committee 209 [5], CEB-FIP MC 90 [27], and Model B3 [16]. Although Model B3 is not a design code, a number of researchers [31, 42, 46, and 55] concluded that this model appears to be the most accurate for predicting creep for a normal weight concrete.

Most design specifications treat aging effects in prestressed concrete members as an important factor in developing creep equations. Aging effects are simplified and incorporated by the use of an aging coefficient, χ. An aging coefficient is taken as a multiplier to a creep coefficient to account for aging effects. An example of the aging and creep coefficients using four well-known design specifications (AASHTO LRFD [3], ACI Committee 209 [5], CEB-FIP MC 90 [27], and Model B3 [16]) for Bridge 222 is provided in Chapter 4. The aging and creep coefficients for all instrumented bridges (Bridges 203, 211, and 222) are presented in Appendix B.

Shrinkage in Concrete

Total shrinkage strain in concrete consists of carbonation shrinkage, plastic shrinkage, autogenous shrinkage, and drying shrinkage. Carbonation shrinkage occurs as a result of chemical reaction of calcium hydroxide from cement paste with atmospheric carbon-dioxide. Carbonation shrinkage is relatively small compared to the total shrinkage and can be neglected. Plastic shrinkage results from loss of water through the surface of fresh concrete during its young age. Plastic shrinkage is also small and can also be neglected. Autogenous shrinkage is caused by chemical reactions during cement hydration. Autogenous shrinkage is normally small but can become significant where high strength concrete with a very low water-cement ratio (0.35 or less) is used [55]. Drying shrinkage occurs after concrete has hardened with ambient humidity as the main influence. Autogenous and drying shrinkages are commonly incorporated into most design specifications.

Figure 2-20 presents a qualitative curve of drying shrinkage strain relative to drying and rewetting ambient conditions. A similar trend of shrinkage strain curves to creep curves can be observed. An example of the shrinkage strain curves based on AASHTO LRFD [3], ACI Committee 209 [5], CEB-FIP MC 90 [27], and Model B3 [16] for Bridge 222 is provided in Chapter 4. The shrinkage strain curves for all instrumented bridges (Bridges 203, 211, and 222) are presented in Appendix B.

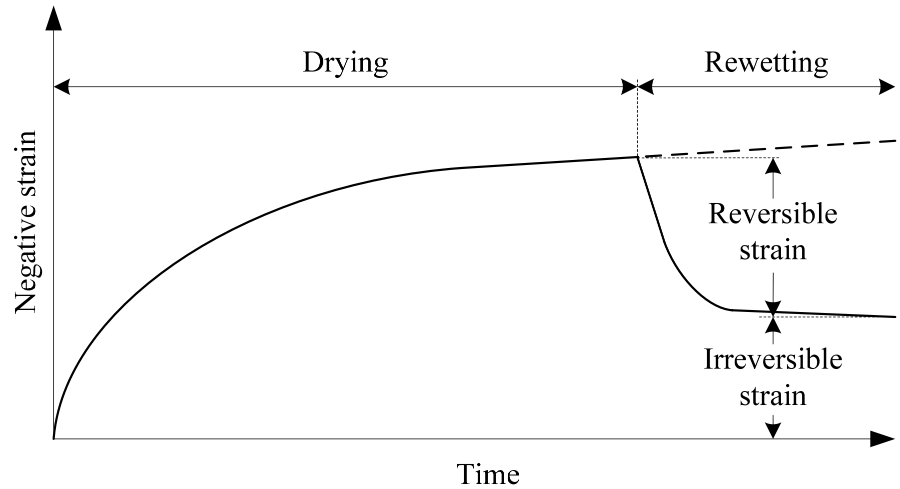

Figure 2-20: Drying Shrinkage Strain

Relaxation of Prestressing Steel

Compared to creep and shrinkage, relaxation of prestressing steel can be predicted more accurately due to a small coefficient of variation. Intrinsic relaxation (relaxation of a constant length subjected to a constant strain) taken from AASHTO LRFD [3] for low-relaxation prestressing strand is expressed as:

$$\Delta f_{RE} = \frac{[\log(24t) - \log(24t_o)]}{40}\left[\frac{f_{pj}}{f_{py}} - 0.55\right] f_{pj} \qquad (2\text{-}37)$$

where Δf_{RE} is an intrinsic relaxation of prestressing steel, t is time at the end of a time interval (day), t_o is time at the beginning of a time interval (day), f_{pj} is stress in the prestressing steel at jacking (ksi), and f_{py} is a specified yield strength of the prestressing steel = 0.90 f_{pu} (ksi).

Intrinsic relaxation occurs where constant strain is imposed on the strand. However, effects of creep and shrinkage immediately after transfer alter the condition where strain and member length are no longer constant. As a result, reduction of intrinsic relaxation is determined by using a dimensionless coefficient of reduced relaxation, χ_r [47 and 77]. The reduced relaxation Δf_R is given as [47]:

$$\Delta f_R = \chi_r \Delta f_{RE} \tag{2-38}$$

The coefficient of reduced relaxation is discussed extensively by Ghali *et al* [47] and Neville *et al* [77]. An approximation of χ_r by Ghali *et al* [47] is adopted here as:

$$\chi_r = \exp\left[(-6.7 + 5.3\lambda)\Omega\right] \tag{2-39}$$

where λ $= \dfrac{\text{steel stress immediately after transfer}}{\text{yield stress of prestressing strand}}$, and

Ω $= \dfrac{\text{total prestress change - intrinsic relaxation}}{\text{steel stress immediately after transfer}}$.

It can be observed from Equation 2-39 that the total prestress change is required, but, this is not known *a priori*. Therefore, it is necessary to employ an iterative procedure to determine the coefficient of reduced relaxation.

2.4.3 Age-Adjusted Effective Modulus Method (AAEM)

There are several analysis methods available to determine time-dependent effects including: the effective modulus method, the rate of creep method, the rate of flow method, the improved Dischinger method, and the age-adjusted effective modulus method (AAEM). The advantages and disadvantages of these methods are discussed in detail by Neville *et al* [77]. Among these methods, the AAEM has gained the widest acceptance because it is capable of solving time-dependent effect problems with relative ease and is in excellent agreement with step-by-step solution methods [55 and 77].

The AAEM method allows an elastic modulus of concrete to vary with time by using creep and aging coefficients. The basic equation of the AAEM method from Jirásek and Bažant [55] is presented in Equation 2-40:

$$\varepsilon(t) = \underbrace{\frac{\sigma(t_o)}{E(t_o)}\left[1+\varphi(t,t_o)\right]}_{\text{strain due to constant stress}} + \underbrace{\frac{(\sigma(t)-\sigma(t_o))}{E(t_o)}\left[1+\chi\cdot\varphi(t,t_o)\right]}_{\text{strain due to varying stress}} + \underbrace{\varepsilon_{sh}(t,t_{sh,o})}_{\text{shrinkage strain}} \qquad (2\text{-}40)$$

where $\sigma(t)$ is the total applied stress at time *t*, χ is the aging coefficient at time *t* corresponding to the concrete age at loading t_o, and $\varepsilon_{sh}(t,t_{sh,o})$ is the total shrinkage strain at time *t*. Notations used are substantially consistent with that of Equation 2-36. Normally, $\bar{E}(t,t_o)$ is used to represent the AAEM of concrete written as:

$$\bar{E}(t,t_o) = \frac{E(t_o)}{\left[1+\chi\cdot\varphi(t,t_o)\right]} \qquad (2\text{-}41)$$

Substituting Equation 2-41 into Equation 2-40 leads to Equation 2-42:

$$\varepsilon(t) = \frac{\sigma(t_o)}{E(t_o)}\left[1+\varphi(t,t_o)\right] + \frac{(\sigma(t)-\sigma(t_o))}{\bar{E}(t,t_o)} + \varepsilon_{sh}(t,t_{sh,o}) \qquad (2\text{-}42)$$

In the present study the basic equation of the AAEM method (Equation 2-40 or Equation 2-42) is used to determine time-dependent strains at any fiber of a section and at any location of a superstructure member.

Uncracked Section Analysis of Superstructure Member

An uncracked section analysis method is required to determine time-dependent strains at a section of a superstructure member under an unrestrained end condition. Analysis method for a superstructure member under a restrained end condition is discussed in the next section. The sign convention and section analysis equations referred to in Ghali *et al* [47] are presented herein. Positive in Figure 2-21 represents tension and a bending moment that produces a tensile strain at the bottom fiber of the superstructure member. The right hand rule is also applied.

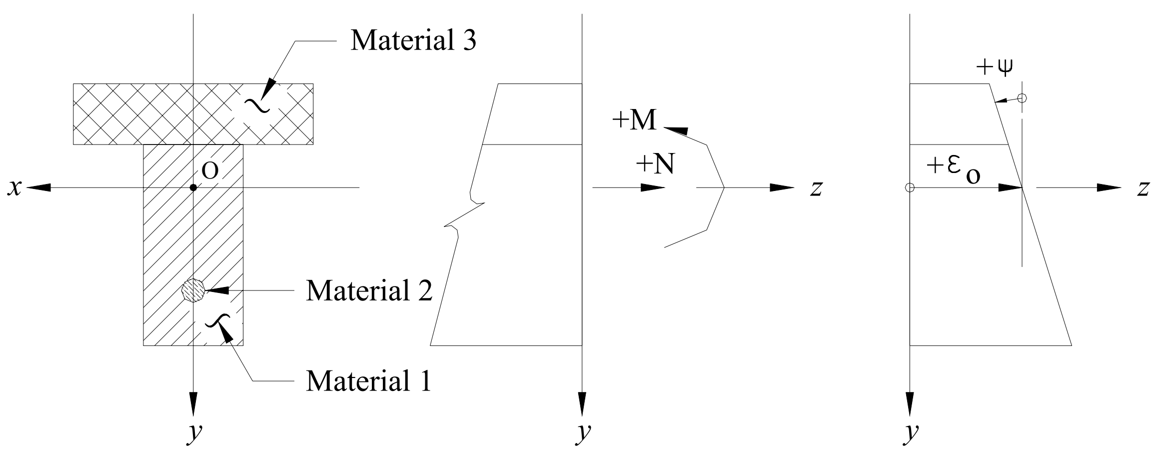

Figure 2-21: Sign Convention for Uncracked Section Analysis

Derivation of a linear-elastic constitutive law based on classical thin beam theory leading to a strain-force relationship was performed by Ghali *et al* [47]. The strain-force relationship in matrix form for a composite section can be written in either Equation 2-43 or Equation 2-44 [47]:

$$\begin{Bmatrix} N \\ M \end{Bmatrix} = E_{ref} \begin{bmatrix} A & B \\ B & I \end{bmatrix} \begin{Bmatrix} \varepsilon_o \\ \psi \end{Bmatrix} \tag{2-43}$$

$$\begin{Bmatrix} \varepsilon_o \\ \psi \end{Bmatrix} = \frac{1}{E_{ref}\left(AI - B^2\right)} \begin{bmatrix} I & -B \\ -B & A \end{bmatrix} \begin{Bmatrix} N \\ M \end{Bmatrix} \tag{2-44}$$

where N = Axial force,

M = Bending moment,

E_{ref} = Modulus of elasticity of the reference material,

A = Area of the transformed section = $\sum_{i=1}^{m}\left(\frac{E_i}{E_{ref}} A_i\right)$,

B = First moment of area about the axis through the reference O

= $\sum_{i=1}^{m}\left(\frac{E_i}{E_{ref}} B_i\right)$,

I = Second moment of area about the axis through the reference O,

= $\sum_{i=1}^{m}\left(\frac{E_i}{E_{ref}} I_i\right)$,

m =Number of parts (different modulus of elasticity),

ε_o = Strain at the axis through the reference O, and

ψ = Strain curvature.

If the axis through the reference O coincides with the elastic neutral axis of a transformed section, the first moment of area B becomes zero, resulting in the classical beam equations as:

$$\varepsilon_o = \frac{N}{E_{ref} A} = \frac{\sigma}{E_{ref}} \tag{2-45}$$

$$\psi = \frac{M}{E_{ref} I} \tag{2-46}$$

Strain at any fiber of the section can be calculated from [47]:

$$\varepsilon = \varepsilon_o + \psi \cdot y \tag{2-47}$$

Section analysis to determine time-dependent strains can be established in the familiar displacement method format. According to Ghali *et al* [47], the superstructure member is artificially restrained and its reaction forces are determined by using Equation 2-43. Based on an initial strain and curvature at time t_o, the increment of restraining force due to creep is expressed in Equation 2-48 [47]:

$$\begin{Bmatrix} \Delta N \\ \Delta M \end{Bmatrix}_{creep} = -\sum_{i=1}^{m} \left\langle \overline{E}(t) \cdot \varphi(t, t_o) \begin{bmatrix} A_c & B_c \\ B_c & I_c \end{bmatrix} \begin{Bmatrix} \varepsilon_o(t_o) \\ \psi(t_o) \end{Bmatrix} \right\rangle \tag{2-48}$$

The subscript, c, in Equation 2-48 represents concrete section properties. Equation 2-48 indicates that creep occurs only in the concrete. Similar to creep, the increment of restraining force for shrinkage is [47]:

$$\begin{Bmatrix} \Delta N \\ \Delta M \end{Bmatrix}_{shrinkage} = -\sum_{i=1}^{m} \left[\overline{E}(t) \cdot \varepsilon_{sh}(t, t_{sh,o}) \begin{Bmatrix} A_c \\ B_c \end{Bmatrix} \right] \tag{2-49}$$

The increment of restraining force for reduced relaxation of prestressing steel is [47]:

$$\begin{Bmatrix} \Delta N \\ \Delta M \end{Bmatrix}_{relaxation} = \sum \begin{Bmatrix} A_{ps} \Delta f_R \\ A_{ps} \Delta f_R y_{ps} \end{Bmatrix} \tag{2-50}$$

where A_{ps} is the prestressing strand area and y_{ps} is the distance between the axis through the reference O to the prestressing strand centroid. The total increment of restraining force is calculated by summing the increments of creep, shrinkage, and prestressing strand relaxation restraining force components [47]:

$$\begin{Bmatrix} \Delta N \\ \Delta M \end{Bmatrix}_{total} = \begin{Bmatrix} \Delta N \\ \Delta M \end{Bmatrix}_{creep} + \begin{Bmatrix} \Delta N \\ \Delta M \end{Bmatrix}_{shrinkage} + \begin{Bmatrix} \Delta N \\ \Delta M \end{Bmatrix}_{relaxation} \tag{2-51}$$

By substituting $\overline{E}(t,t_o)$ and the properties of a transformed section ($\overline{A}$, $\overline{B}$, and $\overline{I}$) into Equation 2-44, the increment time-dependent strain and curvature due to the total increment of all time-dependent effects is computed from Equation 2-52 [47]:

$$\begin{Bmatrix} \Delta \varepsilon_o \\ \Delta \psi \end{Bmatrix} = \frac{1}{\overline{E}(t,t_o)(\overline{A}\overline{I} - \overline{B}^2)} \begin{bmatrix} \overline{I} & -\overline{B} \\ -\overline{B} & \overline{A} \end{bmatrix} \begin{Bmatrix} -\Delta N \\ -\Delta M \end{Bmatrix}_{total} \tag{2-52}$$

After time-dependent strain and curvature are known, the time-dependent concrete stress at any fiber to prevent creep, shrinkage, and prestressing strand relaxation is [47]:

$$\sigma_{restrained} = -\overline{E}(t,t_o)[\varphi(t,t_o)(\varepsilon_o + \psi \cdot y) + \varepsilon_{sh}(t,t_{sh,o})] \tag{2-53}$$

The increment of concrete stress at any fiber for the time duration $t - t_o$ can be calculated as [47]:

$$\Delta\sigma = \sigma_{restrained} + \overline{E}(t,t_o)(\Delta\varepsilon_o + \Delta\psi \cdot y) \tag{2-54}$$

Analysis Method for Indeterminate IA Bridge Superstructures

IA bridge superstructure end restraint in the longitudinal direction prevents free expansion and contraction due to time-dependent effects. The end restraints cause time-dependent stresses to develop, creating additional redundancies in an indeterminate structure. In the present study the displacement method is used to evaluate the statically indeterminate structure due to wide acceptance.

Differences in creep properties of composite section superstructure elments will shift the neutral axis over time. According to Ghali *et al* [47], a convenient way to address this problem is to set a stationary reference axis and introduce a first moment of area *B* (Equations 2-43 and 2-44). For a 2-D frame element, Ghali *et al* [47] introduced a local stiffness matrix of a member in which the neutral axis of a transformed section does not coincide with the reference axis as presented in Equation 2-55.

$$[k]=\bar{E}(t,t_o)\begin{bmatrix} \frac{\bar{A}}{l} & & & & & \\ 0 & \frac{12\left(\bar{A}\bar{I}-\bar{B}^2\right)}{\bar{A}l^3} & & & \mathit{Symm.} & \\ -\frac{\bar{B}}{l} & \frac{6\left(\bar{A}\bar{I}-\bar{B}^2\right)}{\bar{A}l^2} & \frac{4\bar{A}\bar{I}-3\bar{B}^2}{\bar{A}l} & & & \\ -\frac{\bar{A}}{l} & 0 & \frac{\bar{B}}{l} & \frac{\bar{A}}{l} & & \\ 0 & -\frac{12\left(\bar{A}\bar{I}-\bar{B}^2\right)}{\bar{A}l^3} & -\frac{6\left(\bar{A}\bar{I}-\bar{B}^2\right)}{\bar{A}l^2} & 0 & \frac{12\left(\bar{A}\bar{I}-\bar{B}^2\right)}{\bar{A}l^3} & \\ \frac{\bar{B}}{l} & \frac{6\left(\bar{A}\bar{I}-\bar{B}^2\right)}{\bar{A}l^2} & \frac{2\bar{A}\bar{I}-3\bar{B}^2}{\bar{A}l} & -\frac{\bar{B}}{l} & -\frac{6\left(\bar{A}\bar{I}-\bar{B}^2\right)}{\bar{A}l^2} & \frac{4\bar{A}\bar{I}-3\bar{B}^2}{\bar{A}l} \end{bmatrix} \qquad (2\text{-}55)$$

If the neutral axis of a transformed section coincides with the reference axis (through point O), Equation 2-55 reduces to a conventional stiffness matrix.

The presence of time-dependent load effects in the analysis is introduced as a force vector $\{F\}$. Ghali *et al* [47] outlined the procedure as follows:

1. Solve for $\Delta\varepsilon_o$ and $\Delta\psi$, for at least 3 sections (2 sections at ends and 1 section at the mid-span), under an unrestrained end condition using Equation 2-52.
2. Assume a parabolic (or straight line) variation over the span length through the 3 sets of $\Delta\varepsilon_o$ and $\Delta\psi$, and solve for the corresponding rotation increment at each end $\Delta\phi$ and axial deformation increment Δu using the following equations:

$$\begin{Bmatrix} \Delta u \\ \Delta\phi_R \\ \Delta\phi_L \end{Bmatrix} = \frac{l}{6}\begin{bmatrix} 1 & 0 & 4 & 0 & 1 & 0 \\ 0 & 0 & 0 & -2 & 0 & -1 \\ 0 & 1 & 0 & 2 & 0 & 0 \end{bmatrix}\begin{Bmatrix} \Delta\varepsilon_{o1} \\ \Delta\psi_1 \\ \Delta\varepsilon_{o2} \\ \Delta\psi_2 \\ \Delta\varepsilon_{o3} \\ \Delta\psi_3 \end{Bmatrix} \quad \text{(Parabolic variation)} \qquad (2\text{-}56)$$

$$\begin{Bmatrix} \Delta u \\ \Delta\phi_R \\ \Delta\phi_L \end{Bmatrix} = \frac{l}{24}\begin{bmatrix} 6 & 0 & 12 & 0 & 6 & 0 \\ 0 & -1 & 0 & -6 & 0 & -5 \\ 0 & 5 & 0 & 6 & 0 & 1 \end{bmatrix}\begin{Bmatrix} \Delta\varepsilon_{o1} \\ \Delta\psi_1 \\ \Delta\varepsilon_{o2} \\ \Delta\psi_2 \\ \Delta\varepsilon_{o3} \\ \Delta\psi_3 \end{Bmatrix} \quad \text{(Straigth-line variation)} \qquad (2\text{-}57)$$

The development of Equations 2-56 and 2-57 was based on the method of elastic weights that applies a variation over the 3 sets of $\Delta\varepsilon_o$ and $\Delta\psi$ as a pseudo distributed load on a conjugate beam. The notation is presented in Figure 2-22.

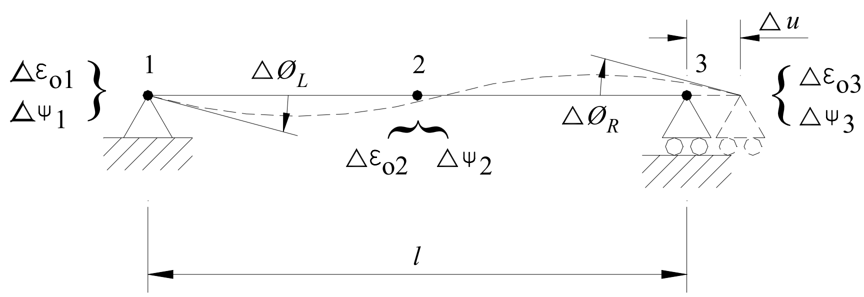

Figure 2-22: Notations for Rotations and Axial Deformation

3. Calculate a force vector $\{\Delta f\}$ using Equation 2-58:

$$\{\Delta f\} \cong \begin{Bmatrix} \Delta N \\ \Delta M_R \\ \Delta M_L \end{Bmatrix} = \frac{\overline{E}(t,t_o)}{l} \begin{bmatrix} \overline{A} & 0 & 0 \\ 0 & 4\overline{I} & 2\overline{I} \\ 0 & 2\overline{I} & 4\overline{I} \end{bmatrix} \begin{Bmatrix} \Delta u \\ \Delta \phi_R \\ \Delta \phi_L \end{Bmatrix} \tag{2-58}$$

4. Arrange the force vector obtained from Equation 2-58 (3x1) into a standard force vector (6x1), transform, and assemble it using the conventional transformation matrix.

To solve for the global (incremental) displacement vector and element forces, a standard procedure of linear or nonlinear analysis is used. For this particular method of forming a force vector, algebraically summing with a reverse sign of $\{\Delta f\}$ is required to obtain final element force results.

Alternatively, a method employing an equivalent temperature has been devised in the present study:

1. Solve for $\Delta\varepsilon_o$ and $\Delta\psi$ as many sections as to ensure that results nearly approach an exact solution.
2. Transform each set of $\Delta\varepsilon_o$ and $\Delta\psi$ to a set of equivalent temperature changes, ΔT, and equivalent temperature gradients, $\Delta T/\Delta y$, by dividing each by a coefficient of thermal expansion α.
3. Apply a set of equivalent temperatures as an input to ANSYS to the corresponding sub-element. A force vector can be generated internally in ANSYS.

For simplicity and efficiency, the equivalent temperature approach is adopted for the FE and condensed hysteresis models. A profile plot of time-dependent strains for all three bridges (203, 211, and 222) at the top and bottom fibers is provided in Appendix B.

2.5 Summary

A review of hysteresis phenomena in IA bridges was presented with respect to four identified components influencing hysteretic behavior in IA bridges: soil-pile interaction, soil-abutment interaction, abutment-backwall connection, and pile-abutment connection. Hysteresis models from a mathematical and physical perspective were reviewed to establish an application to each of the four hysteretic components. The similarity and interconnection between mathematical and physical hysteresis models was also discussed. Detailed development of hysteresis elements to represent hysteretic behavior in the FE and condensed hysteresis models by using the present hysteresis models are deferred to Chapter 3. Concrete creep, concrete shrinkage, prestressing steel relaxation, and the AAEM method were described and used to determine time-dependent strains for IA bridge superstructure members. Time-dependent strain calculations and detailed discussions of applying time-dependent strains as a FE and condensed hysteresis model equivalent temperature are provided in Appendix B and Chapter 4, respectively.

Chapter 3

Hysteresis Elements for FE Models and Condensed Hysteresis Models

3.1 General

This chapter presents hysteresis elements derived from hysteresis models discussed in Chapter 2. These hysteresis elements are used as one of many members in the FE and condensed hysteresis models to represent hysteretic behaviors in IA bridges. A basic property of each hysteresis element is nonlinearity and path-dependency in which different element characteristics are defined for loading and unloading behaviors.

A combination of: (1) soil-pile interaction; (2) soil-abutment interaction; (3) abutment-backwall connection; and (4) pile-abutment connection is a basic component leading to hysteretic behavior as presented in Figure 3-1.

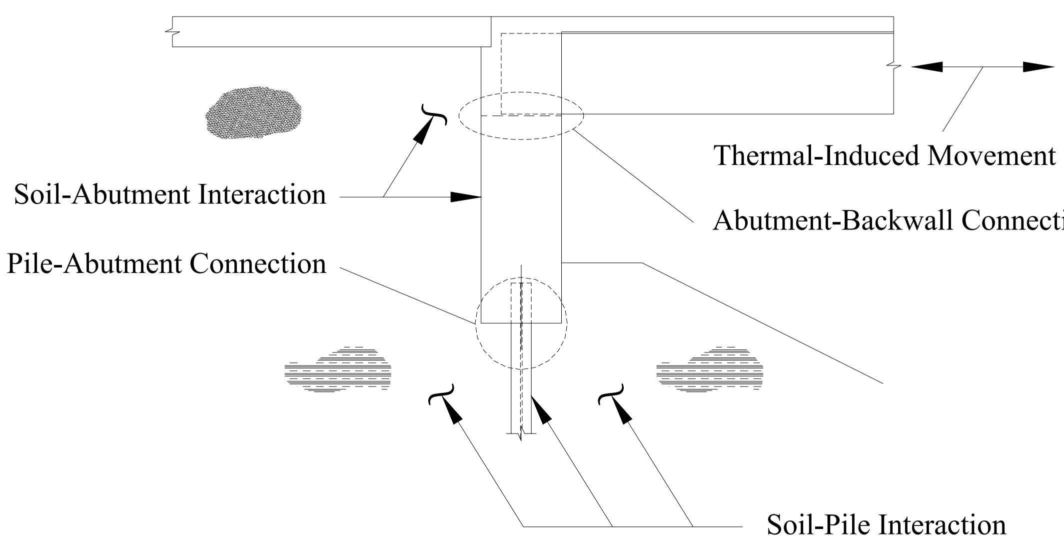

Figure 3-1: Components of Hysteretic Behavior

Soil-pile and soil-abutment interactions, known as soil-structure interaction, are related to geotechnical behavior, while abutment-backwall and pile-abutment connections are related to the yielding of structural connections. Soil-structure interaction generally has more influential parameter than the yielding of structural connections, because soil exhibits nonlinear and hysteretic behavior even over a small range of deformations. Also, the yielding of structural connections may never occur in a lifetime of bridge structures, if properly designed.

This chapter is divided into two parts. The first part discusses various hysteresis elements for the FE models, including hysteresis elements representing soil-pile interaction, soil-abutment interaction, and structural connections presented in Sections **3.2**, **3.3**, and **3.4**, respectively. The second part covers hysteresis elements for the condensed hysteresis models presented in Section **3.5**. The detailed discussions of the FE and condensed hysteresis models are deferred to Chapters 4 and 5, respectively.

3.2 Soil-Pile Interaction Hysteresis Element for FE Models

A hysteresis element for soil-pile interaction hysteretic behavior is presented in this section. The classical *p-y* curve method is adopted to provide a load-deformation curve of laterally loaded soil-pile interaction behaviors. In this study, *p-y* curves will be generated using the COM624P program developed by Wang and Reese [**112**]. All *p-y* curves are considered an input as a multi-linear load-deformation curve in ANSYS that also serves as a loading curve for a soil-pile interaction hysteresis element. Therefore, a validation of an ANSYS pile model against COM624P needs to be performed to ensure model accuracy. Then, a branch of unloading curves in a hysteresis element is constructed using classical plasticity theory. Finally, a convergence study of ANSYS pile model results subjected to cyclic loadings is performed to ensure that this model does not produce divergent results.

This section begins with the discussion of the *p-y* curve method in Section **3.2.1**. Validation of the ANSYS pile model results against COM624P results is conducted in Section **3.2.2**. An application of classical plasticity theory to construct an unloading branch of *p-y* curves is described in Section **3.2.3**. Finally, a convergence study of the proposed hysteresis element is presented in Section **3.2.4**.

3.2.1 *p-y* Curve Method

The *p-y* curve method is one of the soil-structure interaction analysis methods based on the modulus of subgrade reaction approach [**103**]. The *p-y* curve method was originally developed using finite difference techniques to solve an approximate solution of the 4th order governing equation. The substitution of nonlinear *p-y* curve springs on the governing equation was performed instead of using a traditional linear Winkler spring. An iterative solver was implemented to achieve a numerical solution in this transition.

The *p-y* curve method is one of the most widely accepted methods for soil-structure interaction application in practical use [**114**]. Although a nonlinear spring generated from the *p-y* curve method is considered uncoupled, validation of this method was performed against full-scale experiments explicitly to include a continuum effect

[112]. Consistent use by many engineers and researchers for many decades has also proven its validity.

The *p-y* curve method will be used in the present study as a loading curve for a soil-pile interaction hysteresis element. A family of *p-y* curves along the pile length generated by the COM624P program will be taken as a family of multi-linear springs in ANSYS. Validation of results produced by ANSYS against results produced by COM624P will be presented below.

3.2.2 Validation of ANSYS Pile Model

In this section an ANSYS pile model is described and the validation of this ANSYS pile model is performed through result comparisons with COM624P. Samples of *p-y* curves (in dashed lines) generated by COM624P are presented in Figures 3-2 and 3-3.

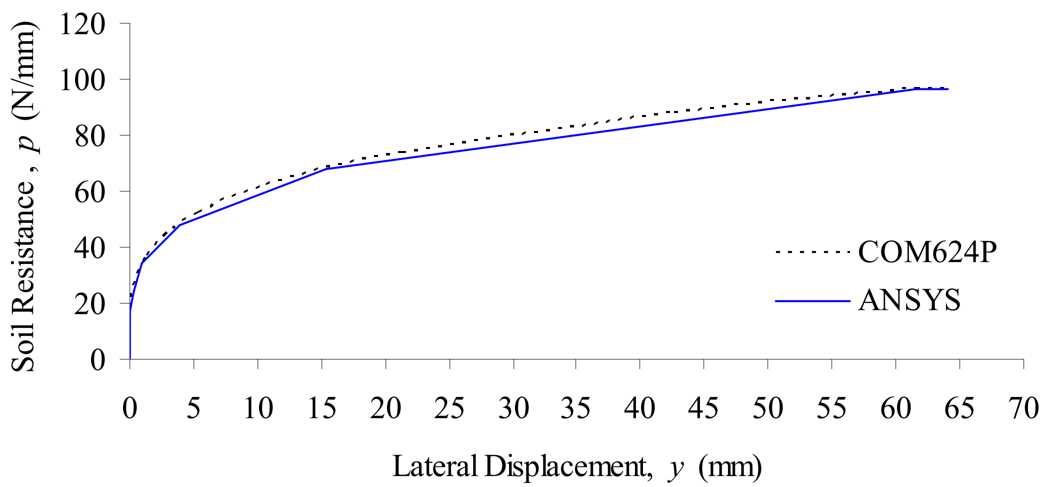

Figure 3-2: *p-y* curve at pile head - clay above water table (Bridge 222)

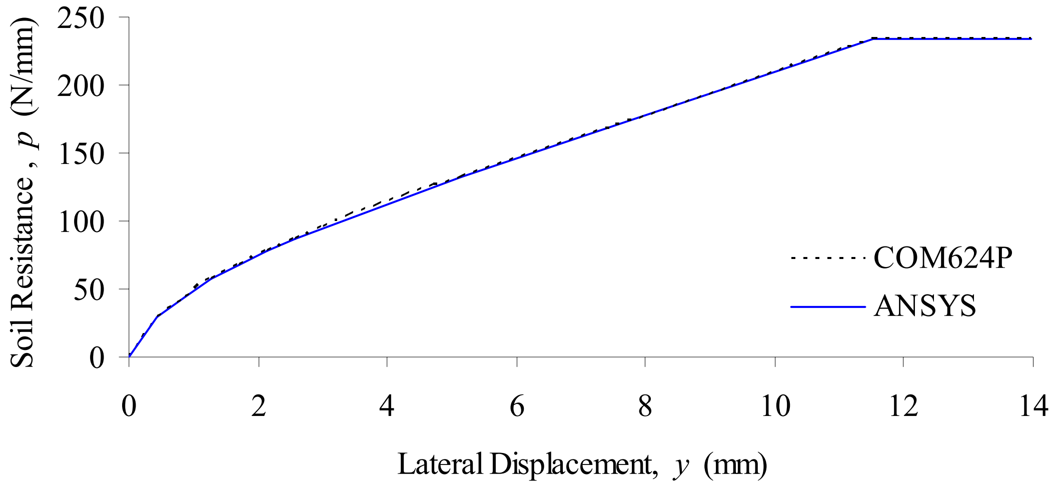

Figure 3-3: *p-y* curve at 3.5 m (11.5') depth - sand (Bridge 222)

Soil parameters were taken from a bridge 222 soil profile for clay above the water table and sand, respectively (see Figure 4-8 in Chapter 4 for bridge 222 soil profile). The multi-linear curves (in solid lines) represent a nonlinear soil spring in ANSYS. The COMBIN39 element type was adopted as the most appropriate nonlinear one-dimensional element available in ANSYS. A lateral force of 44.5 KN (10 kips), which produces a working range of the actual pile movements of bridge 222 and a free end boundary condition, was applied at the pile head. An analysis test case of the ANSYS pile model was performed and validated against COM624P. Prediction of lateral displacements versus depth, bending moments versus depth, and shear forces versus depth using COM624P and ANSYS are presented in Figures 3-4 to 3-6.

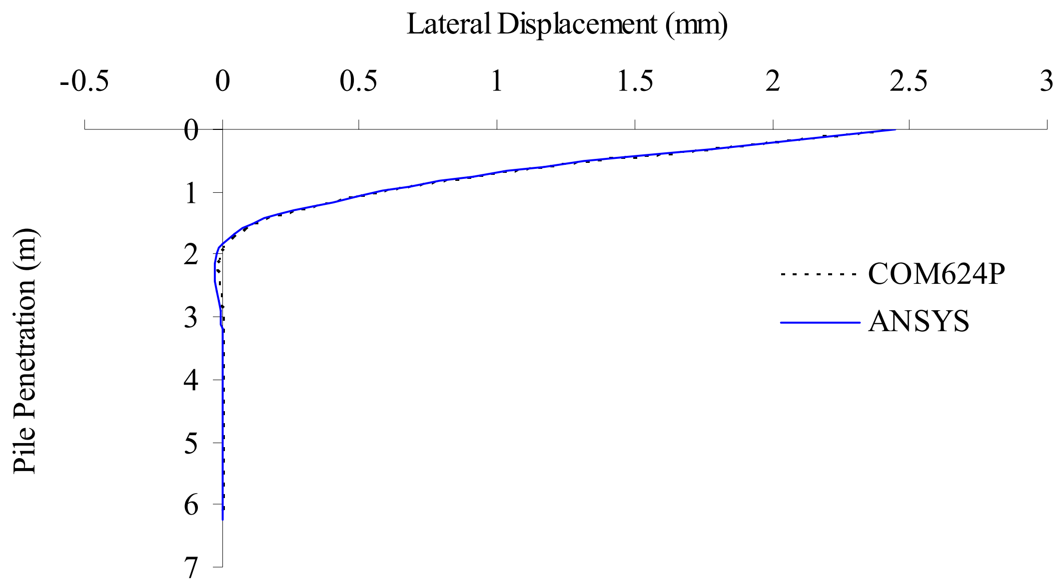

Figure 3-4: Lateral displacement due to 44.5 KN load at pile head (Bridge 222)

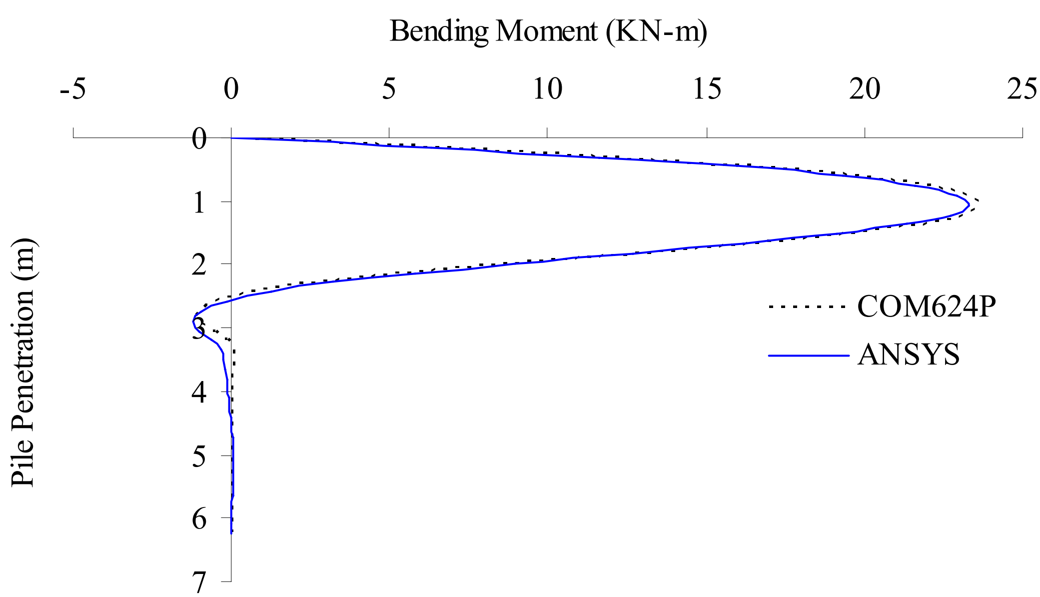

Figure 3-5: Pile bending moment due to 44.5 KN load at pile head (Bridge 222)

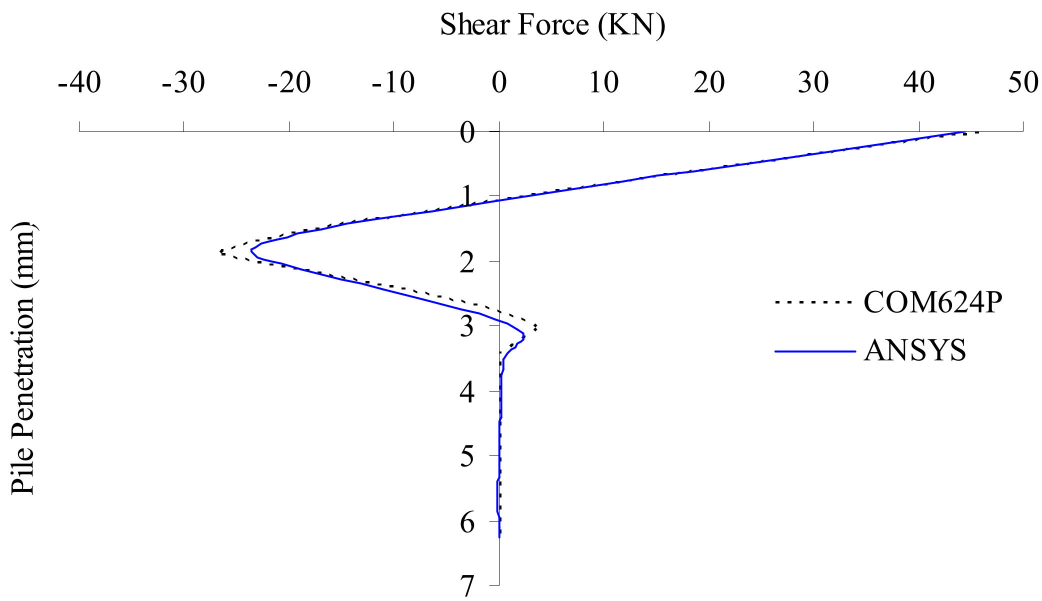

Figure 3-6: Pile shear force due to 44.5 KN load at pile head (Bridge 222)

ANSYS predictions of pile behavior are similar to COM624P with percent differences of 1.4, 1.4, and 2.8 for maximum displacement, maximum moment, and maximum shear, respectively. An element length in the ANSYS pile model is relatively coarse (150 mm – 6″) compared to the length used in COM624P (30 mm – 1.2″). Therefore, some small differences in moments and shears at a depth of approximately 3 m (10′-0″) are expected to appear, where a short distance of two adjacent inflection points occurs. The selection of mesh size based on computation time and accuracy trade-off is considered and predetermined here to further this scheme to a large number of elements used in the 3-D FE models.

3.2.3 Hysteresis Element

In this section a complete hysteresis element for soil-pile interaction hysteretic behavior will be described. Under thermally-induced cyclic loading, soil initially experiences a loading condition following with cycles of unloading and reloading conditions. A non-recoverable property of soil leads to a different response when the direction of loading is reversed. A *p-y* curve is used for the initial loading curve characteristic of this particular hysteresis element. Classical plasticity theory [100] is utilized for the unloading and reloading curve characteristics. Figure 3-7 presents a sample of the loading and unloading curves obtained from the bridge 222 ANSYS pile model for both contraction and expansion cases.

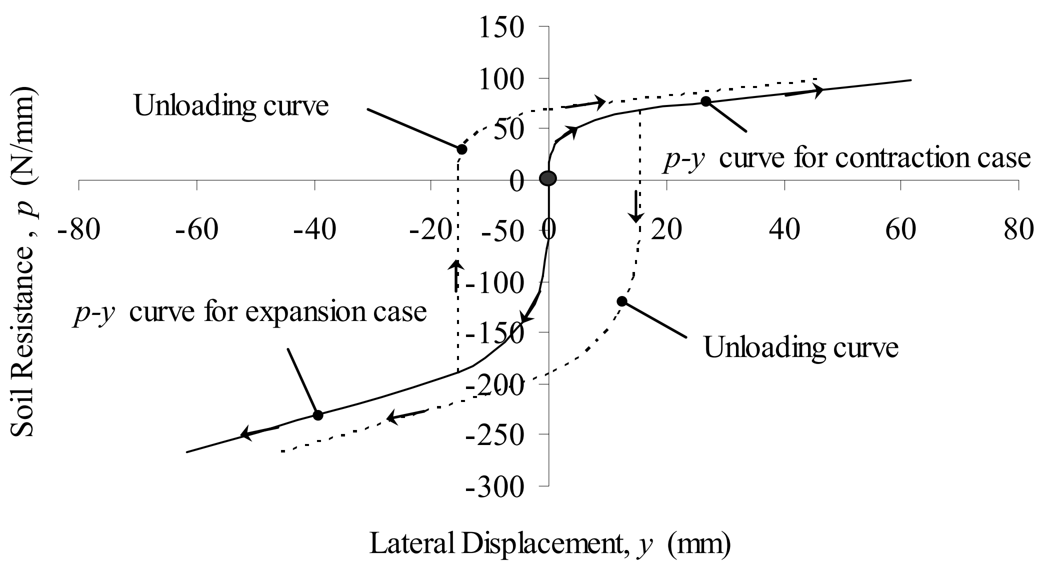

Figure 3-7: Asymmetrical *p-y* curves at pile head (Bridge 222)

Differences in soil resistance magnitudes under bridge expansion and contraction conditions are a result of asymmetrical soil embankment geometry. Resistance magnitude under a bridge contraction condition is much lower due to effects of a shallow soil overburden and downhill slope. Asymmetrical soil embankment geometry, including a shallow soil overburden and downhill slope, is demonstrated in Figure **3-1**. Asymmetrical *p-y* curves are also illustrated in Figure **3-7**.

Effects of asymmetrical p-y curves on lateral displacements at the pile head can be observed and studied. Referring to Figure **3-4**, a lateral displacement of 2.4 mm (0.095″) at the pile head was obtained from an analysis case representing bridge contraction. With respect to the same magnitude of an applied force (44.5 KN), a lateral displacement of 0.56 mm (0.022″) was obtained from an analysis case representing bridge expansion. These two displacement magnitudes indicate that the effect of a downhill slope and the uneven height of soil overburden can produce a significant difference of soil stiffness as high as four times in the bridge 222 pile case.

An unloading branch of the soil-pile interaction hysteresis element for FE models can be defined and constructed internally by COMBIN39. Based on the classical plasticity theory, COMBIN39 provides a capability, called a non-conservative unloading, to define the stiffness of the unloading path. This stiffness, hereafter referred to as an elasto-plastic stiffness k_{ep}, appears in the form of:

$$k_{ep} = \begin{cases} k_i & , F < 0 \\ k_t(y), & F = 0 \end{cases} \tag{3-1}$$

where k_{i} is the initial stiffness of the loading path, $k_t(y)$ is a tangent stiffness (function of deformation), and F is a yield function. The tangent stiffness is taken as the classical *p-y* curve. This parameter for stiff clay above the water table may be written as:

$$k_t(y) = \frac{dp}{dy} = \frac{d}{dy}\left(0.5p_u\left(\frac{y}{y_{50}}\right)^{1/4}\right) = \left(\frac{0.125p_u}{y_{50}^{1/4}}\right)y^{-3/4} \tag{3-2}$$

For a detailed explanation of p_u (ultimate soil resistance) and y_{50} (deformation at one-half p_u), the reader is referred to Wang and Reese [112]. It is observed that p_u and y_{50} are material and geometry dependent and are unchanged in any iterative solution, indicating that displacement y is the only variable. The yield function, F, is defined as:

$$F = \left|p - \overline{\alpha}\right| - p_Y \tag{3-3}$$

where $\overline{\alpha}$ is the hardening variable and p_Y is the yield resistance obtained from solving the equation $p(x) = k_i x$ for x such that:

$$p_Y = k_i\left(\frac{0.5p_u}{k_i y_{50}^{1/4}}\right)^{4/3} \tag{3-4}$$

The hardening variable, $\overline{\alpha}$, is initially zero, representing coexistence of the Cartesian coordinate system origin and the *p-y* curve origin. When the soil resistance p sign is reversed, $\overline{\alpha}$ is updated so as to shift the initial origin of the *p-y* curve to the new origin, revealing an isotropic hardening rule. The only available option of origin transformation is the ANSYS COMBIN39 limitation that does not support a kinematic hardening rule.

The hysteresis element constructed using COMBIN39 is similar to the multi-linear hysteresis model as presented in Chapter 2. This is because *p-y* curves are defined by a number of discrete points in COMBIN39, not by a function.

3.2.4 Convergence Study

There is a necessity to ensure that a hysteresis model shows no trend of divergence and appears to approach a steady-state condition after several cycles. In this section, an analysis using an ANSYS pile model will be performed to investigate numerical convergence of the proposed soil-pile interaction hysteresis element.

With respect to the initial loading and boundary conditions, four general cases are to be investigated: (1) contraction as an initial loading condition with a free head; (2) contraction as an initial loading condition with a fixed head; (3) expansion as an initial loading condition with a free head; and (4) expansion as an initial loading condition with a fixed head. A 50-cycle sinusoidal force function with amplitude of 44.5 KN (10 kips) that produces a working displacement range of 2.4 mm (0.095″) was applied at the pile head for all four cases. The four case analysis results are discussed below and also presented in Figures **3-8** and **3-9**. In both figures, the vertical and horizontal scales represent lateral displacements at the pile head and number of cycles, respectively.

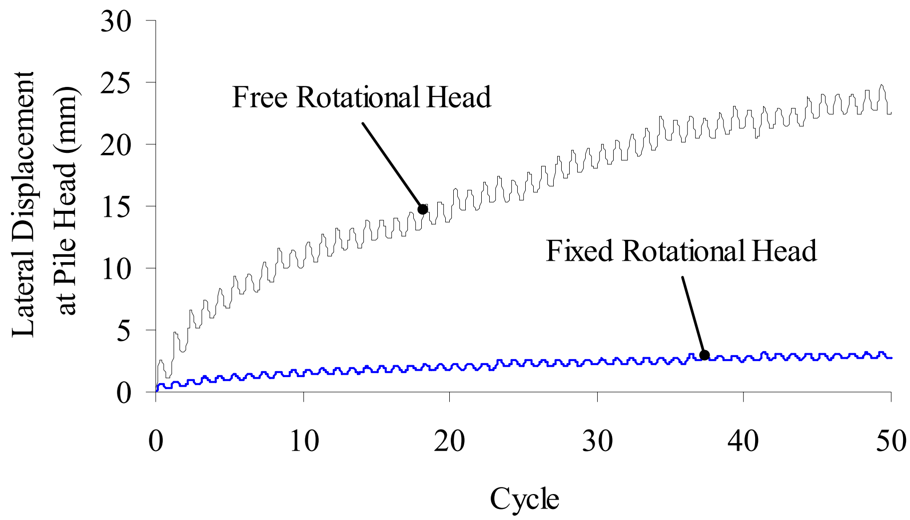

Figure 3-8: Time-History Lateral Displacement for Contraction Case

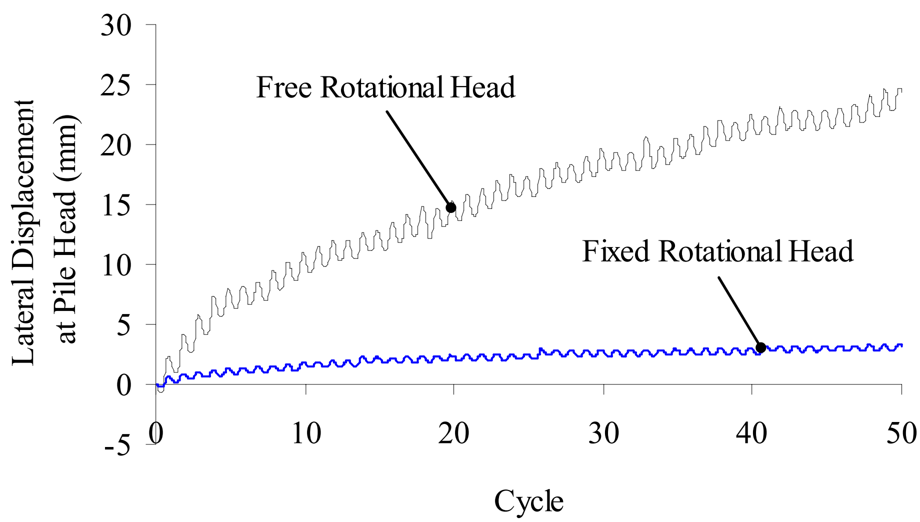

Figure 3-9: Time-History Lateral Displacement for Expansion Case

It is observed that there is strong similarity in terms of trends and magnitudes between contraction and expansion cases for both types of boundary conditions. Therefore, the influence of an initial loading condition can be disregarded. The subsequent investigation will be performed on contraction cases only (cases 1 and 2).

In order to investigate convergence of the analysis results, it is necessary to check whether a sequence of peak-to-peak distances $d(a_m, a_n)$ is a Cauchy sequence. A mathematical definition of Cauchy sequence is written as:

$$\lim_{\min(m,n)\to\infty} d(a_m, a_n) = 0 \tag{3-5}$$

A peak-to-peak distance, in this sense, is the difference in adjacent peak magnitudes of lateral displacement. Figure 3-10 presents a plot of this investigation, taking the difference in adjacent magnitudes of lateral displacements and number of cycles as a vertical and horizontal scale, respectively.

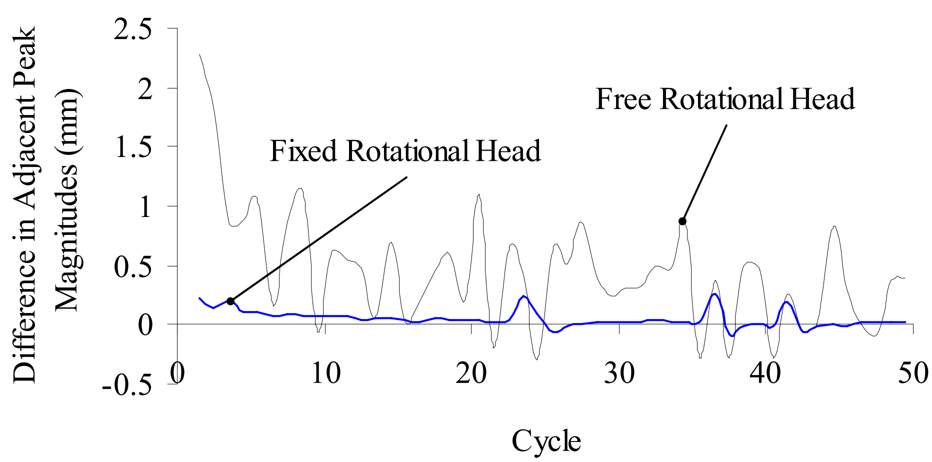

Figure 3-10: Convergence Check using Cauchy Sequence

There is a convergence fluctuation demonstrated in Figure 3-10 for both cases. This numerical fluctuation, known as spurious oscillations or noise [30], is anticipated to occur as a result of the numerical residuals allowed by convergence tolerances and the use of an approximate analysis algorithm. However, there is a convergence tendency observed in both responses presented in Figure 3-10.

It is demonstrated that the convergence fluctuation is significantly improved when the magnitude of loading is reduced. Using 10 percent of the applied load from the previous investigation (4.45 KN), a better convergence tendency is obtained, which can be observed in Figure 3-11.

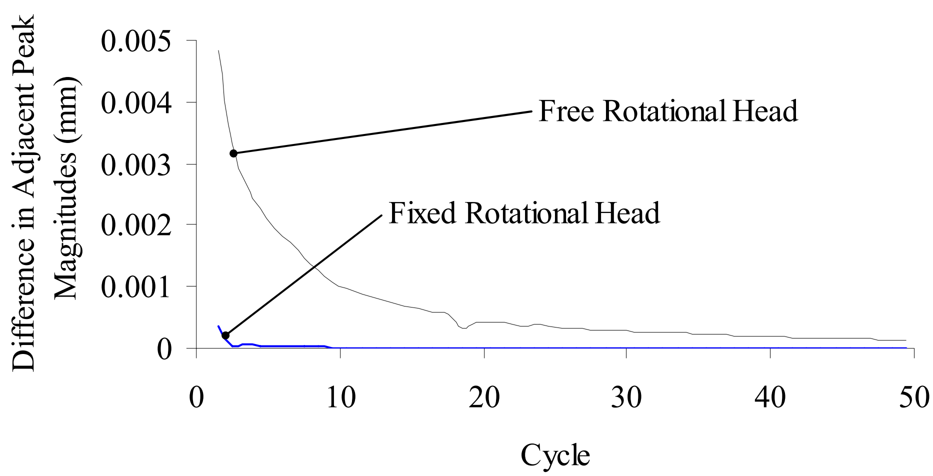

Figure 3-11: Convergence Check Due to Cyclic Load Magnitude of 4.45 KN

Pile heads in an actual IA bridge experience cyclic displacement rather than cyclic force. Therefore, a 50-cycle sinusoidal displacement function with amplitude of 2.4 mm (0.095"), representing a working displacement range, is more realistic to apply at the pile head. Two additional analysis cases were performed and investigated. A convergence check for these two cases is presented in Figure 3-12. It is observed that the numerical noises fluctuate about zero in value of the horizontal axis. The vertical scale for these two cases represents soil reaction at the pile head (summation of all *p-y* spring resistance magnitudes).

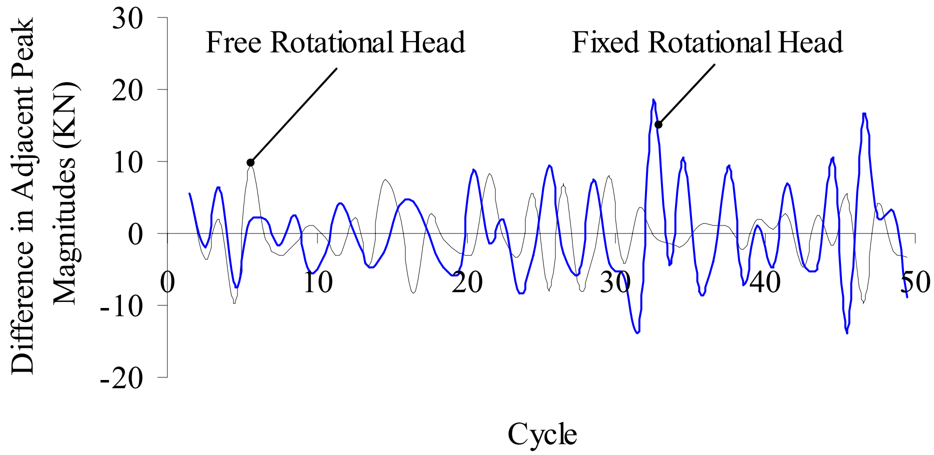

Figure 3-12: Convergence Check Due to Cyclic Displacement Magnitude of 2.4 mm

It is demonstrated that numerical noises are smaller when the magnitude of displacements is reduced. Figure 3-13 presents a similar plot obtained from the case where the applied displacement is 10 percent of the previous investigation (0.24 mm – 0.0095″). The fluctuation amplitude obtained from this case is almost 10 times smaller. A hysteresis loop obtained from the results of this case, where cyclic displacement magnitude is 0.24 mm, is also presented in Figure 3-14. The vertical and horizontal scales in Figure 3-14 represent soil resistances at the pile head and lateral displacements, respectively. A nearly closed loop is observed, which represents the steady state of predicted pile responses. In addition, no tendency for numerical divergence is observed.

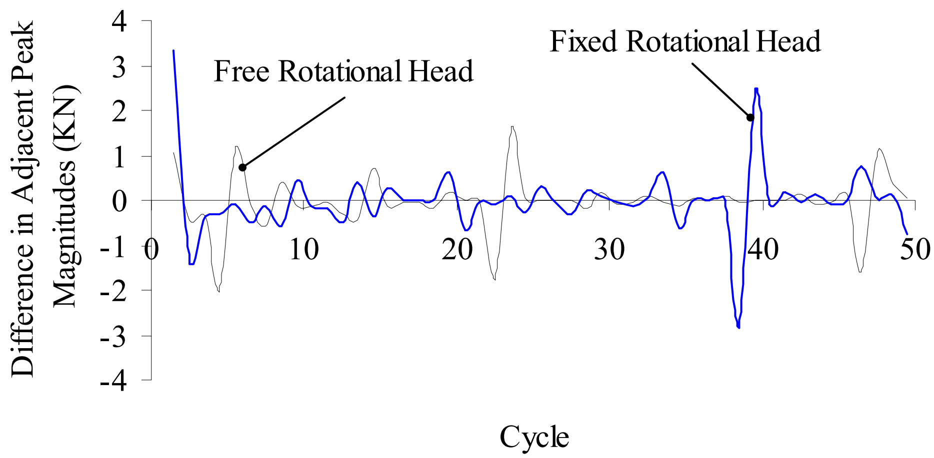

Figure 3-13: Convergence Check Due to Cyclic Displacement Magnitude of 0.24 mm

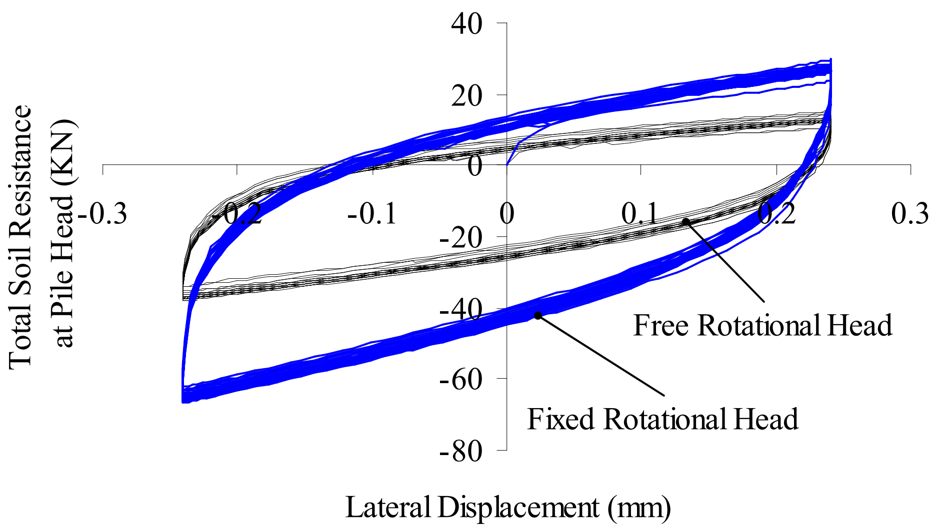

Figure 3-14: Hysteresis Loops of Soil Spring Resistance at Pile Head

3.3 Soil-Abutment Interaction Hysteresis Element for FE Models

Due to wide acceptance and simplicity, the soil model presented in Figure 2-3 will be used as a load response curve for the soil-abutment interaction hysteresis element. The unloading branch is defined as a trajectory parallel to the initial stiffness, k_h, similar to the soil-pile interaction hysteresis element. This hysteresis element for soil-abutment interaction is identical to the Stop and elasto-plastic hysteresis models described in Chapter 2.

The classical elasto-plastic hysteresis model consists of upper and lower bounds that typically appear as opposite signs. However, this characteristic no longer holds for this particular interaction. Passive and active earth pressures are the same sign that impairs the use of ANSYS COMBIN39 elements. This is because only Quadrants 1 and 3 are permitted to have a load-deformation curve defined by the user. Two separated analysis steps in ANSYS are, therefore, required to obtain the desired element characteristics by maintaining the use of COMBIN39. These two steps are hereafter defined as supplementary analysis step and remaining analysis step presented in Sections 3.3.1 and 3.3.2, respectively.

3.3.1 Supplementary Analysis Step

The supplementary step is the first and single analysis step that represents structural behavior immediately after backfilling. At this stage, an at-rest earth pressure P_o is applied to a structural system on the left diagram in Figure 3-15.

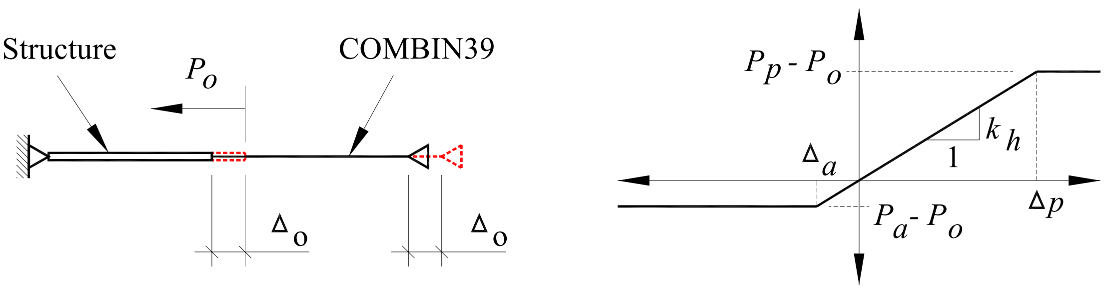

Figure 3-15: Schematic Representation of Supplementary Analysis Step

The COMBIN39 representing the soil-abutment interaction hysteresis element is simultaneously imposed by a prescribed nodal displacement, Δ_o, at the right member end. This prescribed displacement has the same displacement magnitude and direction as the structural system deformation loaded by P_o. After the prescribed displacement is applied, the COMBIN39 is enforced to behave as a rigid body. The net effect of this step is, therefore, due only to the at-rest earth pressure.

Because of element restriction, a load-deformation curve of COMBIN39 presented on the right diagram of Figure 3-15 is required to span from Quadrant 3 to 1. Quadrant 1 represents compression and Quadrant 3 represents tension. The limits of pressure $P_p – P_o$ on Quadrant 1 and pressure $P_a – P_o$ on Quadrant 3 along with a modulus of lateral subgrade reaction, k_h, will be input into ANSYS as upper bound, lower bound, and initial slope parameters. The analysis results for this step will be carried over to the remaining analysis steps through a typical time-history nonlinear analysis procedure.

3.3.2 Remaining Analysis Step

The remaining steps are complete time-history analyses that represent structural behavior immediately after the supplementary step is completed. All pertinent time-history loads, including temperature and time-dependent loads, as well as at-rest earth pressures carried over from the supplementary step, are applied to the structural system as presented on the left diagram in Figure 3-16.

The left diagram in Figure 3-16 presents that time-history deformation, $\Delta(t)$, occurs corresponding to time-history loadings. When the structure is lengthened (or shortened), an additional compressive (or tensile) pressure is reacted by the COMBIN39 element. The relationship of time-history deformation $\Delta(t)$ and the net pressure on the structural system (at-rest pressure plus COMBIN39 reaction) will follow the load-deformation path presented on the right diagram in Figure 3-16.

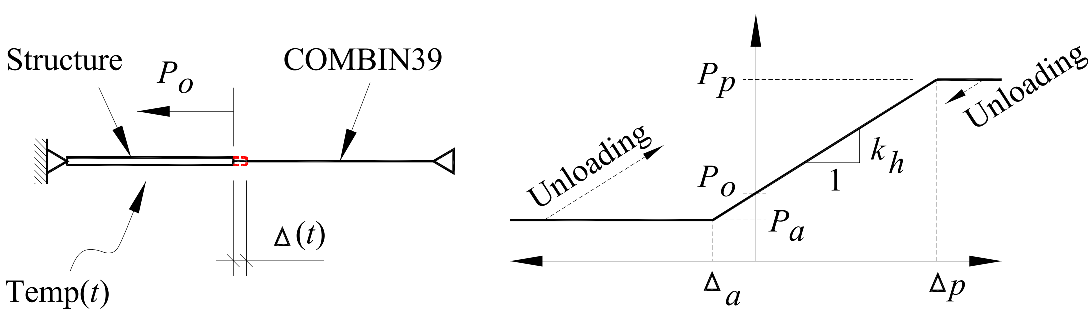

Figure 3-16: Schematic Representation of Remaining Analysis Step

For cases where the structure has been loaded greater than the deformation limits ($\Delta(t) > \Delta_p$ or $\Delta(t) < \Delta_a$), the net compressive or tensile pressures on the structural system become the desired limiting values, i.e. $P_o + (P_p - P_o) = P_p$ and $P_o - (P_o - P_a) = P_a$. When unloaded, a path parallel to the initial slope k_h will be traced at the load reversal point.

The hysteresis element used for the soil-abutment interaction has certain upper and lower bounds; therefore, a divergence problem will not occur.

3.4 Structural Connection Hysteresis Elements for FE Models

The possibility of abutment-backwall and pile-abutment connections being loaded beyond their elastic ranges along a moment-rotation relationship depends on several factors. Length and abutment height are the most important factors, while connection details are considered as a constant parameter, because these connections are typically specified by DOTs. Hysteretic behavior due to the yielding of structural connections for short bridges may never occur during their service lives. Based on analysis results from the FE models, the abutment-backwall connection of the longest instrumented bridge (bridge 203) experienced reinforcement stresses beyond the elastic range. However, the other connections, including the abutment-backwall connections of bridges 211 and 222 and the pile-abutment connections of all instrumented bridges behaved elastically.

The bi-linear hysteresis model as described in Chapter 2 will be used as an abutment-backwall connection hysteresis element. No hysteresis elements will be used for pile-abutment connections, because all predicted moments from the FE models were much smaller than pile moment capacities. Element properties for all hysteresis elements are provided in Chapter 4.

3.5 Hysteresis Elements for Condensed Hysteresis Models

In this section, hysteresis elements for soil-pile interaction, soil-abutment interaction, and abutment-backwall connection for the condensed hysteresis models will be described. All of these hysteresis elements are to be combined to become a single hysteresis operator. Time-history temperatures and two degrees of freedoms (translation and rotation) at the abutment-pile connection location serve as the input and output for the operator, respectively. This particular location is selected based on a practical design perspective in which structural and geotechnical component analysis and design are usually separated at this boundary.

This section begins with outlining the development procedure of a hysteresis element that represents a load-deformation curve of soil-pile interaction at the pile head. A description of hysteresis elements for soil-abutment interaction and abutment-backwall connection follows. A detailed procedure to assemble and condense all hysteresis elements into a single hysteresis operator will be presented in Chapter 5.

3.5.1 Soil-Pile Interaction Hysteresis Element for Condensed Hysteresis Models

This section deals with outlining the development procedure for a soil-pile interaction hysteresis element, using the framework of the Duhem Model as described in Chapter 2. The procedure begins with transformation of a two-dimensional ANSYS pile model to a coupled spring as presented in Figure **3-17**.

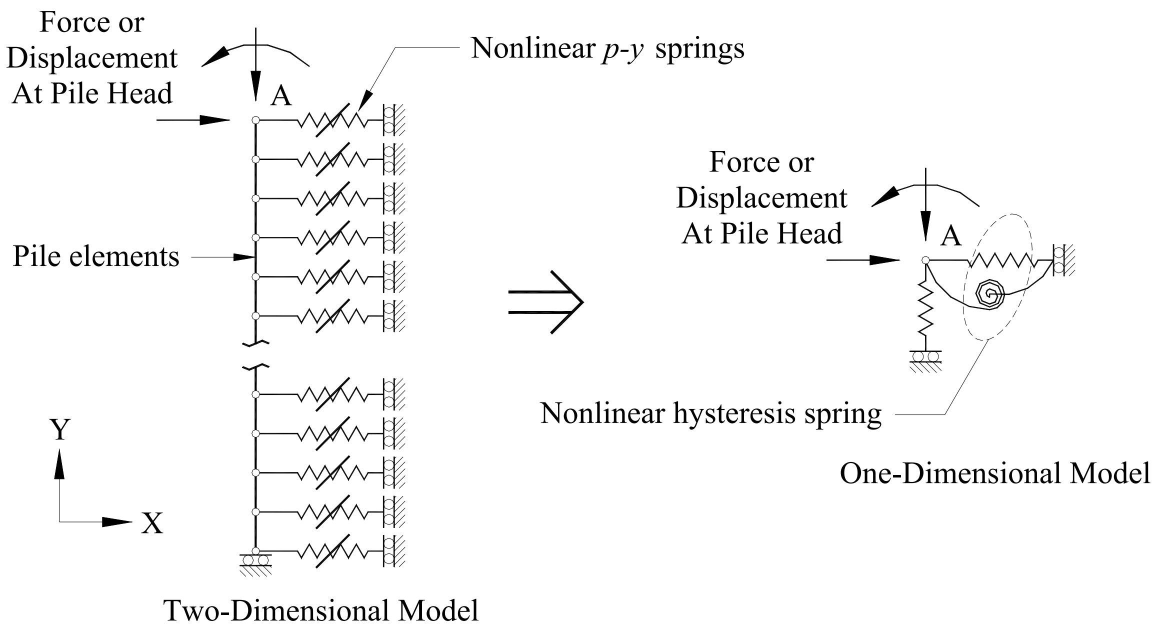

Figure 3-17: Hysteresis Model Representing Pile for One-Dimensional Problem

The nonlinear coupled spring is one of the practical soil-structure interaction analysis methods and is available in the LPILE program [66], known as a foundation stiffness. A method of generating this foundation stiffness essentially involves:

- applying an incremental displacement/rotation to the pile head (node A in Figure 3-17),
- performing a nonlinear analysis, and
- determining a tangent stiffness from the ratio of incremental resulting reaction (force/moment) to incremental displacement/rotation.

A number of incremental analyses is required in this method to determine a continuous curve of nonlinear tangential stiffness.

The nonlinear coupled foundation stiffness, hereafter called nonlinear hysteresis spring H_p, is written in a matrix form as:

$$H_p = \begin{bmatrix} \overline{K}_{11} & 0 & 0 \\ 0 & \overline{K}_{22} & \overline{K}_{23} \\ 0 & \overline{K}_{32} & \overline{K}_{33} \end{bmatrix} \tag{3-6}$$

The following assumptions are required to simplify further development:

- The pile axial deformation is insignificant and, therefore, can be neglected. $\overline{K}_{11}$ is to be replaced by a roller boundary condition.
- The coupled spring stiffness: $\overline{K}_{23}$ and $\overline{K}_{32}$ are insignificant and can be ignored.

The other stiffness components ($\overline{K}_{22}$ and $\overline{K}_{33}$) can be viewed as a single hysteresis element. Using the concept of the Duhem Model (Equations 2-9 and 2-15), each of the stiffness terms can be determined from a solution of the following initial boundary value problem (IBVP):

$$\begin{aligned} \frac{dy}{dt}(t) &= \begin{cases} f_I(y,x)\dot{x} = \dfrac{dy^C}{dx}\dot{x}, \ \dot{x}(t) \geq 0 \\ f_D(y,x)\dot{x} = \dfrac{dy^E}{dx}\dot{x}, \ \dot{x}(t) \leq 0 \end{cases} \\ y(0) &= y_o \\ x(0) &= x_o \end{aligned} \tag{3-7}$$

where $\dfrac{dy^C}{dx}$ is a tangent slope of load-deformation curve at the pile head (contraction case), $\dfrac{dy^E}{dx}$ is a tangent slope of load-deformation curve at the pile head (expansion case), x is a deformation, and y is a restoring force at the pile head. Detailed development of this hysteresis element will be presented in Chapter 5.

3.5.2 Soil-Abutment Interaction Hysteresis Element for Condensed Hysteresis Models

Similar to the hysteresis model used in the FE models (Section 3.3), the elasto-plastic hysteresis model will be adopted for a soil-abutment interaction hysteresis element. Because the classical elasto-plastic hysteresis model creates a similar problem as discussed in Section 3.3, a coordinate transformation is required to obtain the desired element characteristics. Referring to Equation 2-16 through Equation 2-21, a relative deformation, u, prior to a coordinate transformation is a solution of:

$$\dot{u} = \dot{x}\left[H_3(\dot{x}) \cdot H_4\left(u - {(P_p - P_a)}\big/{2k_h} \right) + H_2(\dot{x}) \cdot H_1\left(u + {(P_p - P_a)}\big/{2k_h} \right) \right] \qquad (3\text{-}8)$$

Equation 3-8 can be represented by a diagram presented in Figure 3-18(a) in which variables (x and y) are defined as a small capital letter (before transformation). Figure 3-18(b) presents the desired hysteresis element characteristics in which variables are defined as a big capital letter (after transformation):

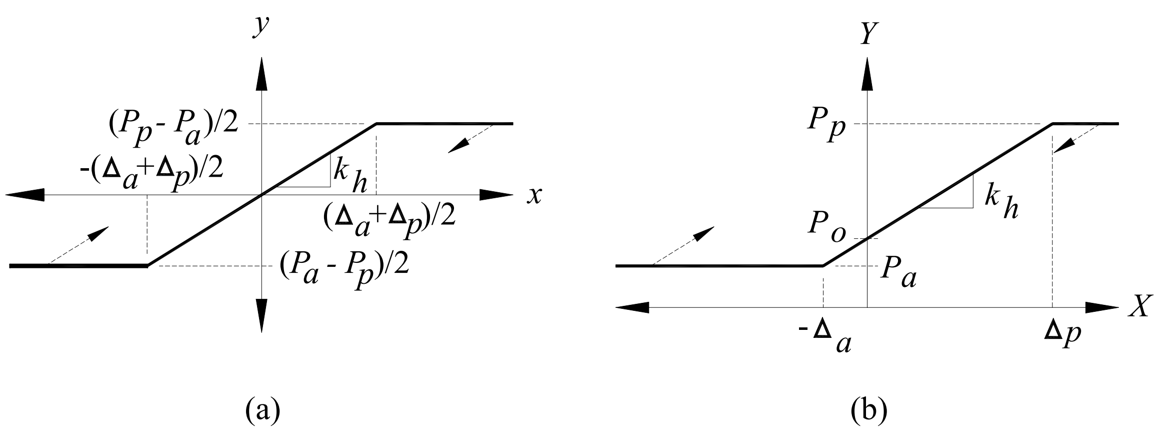

Figure 3-18: Elasto-Plastic Hysteresis Models Before and After Coordinate Transformations

The relationship between deformations x and X can be written as:

$$x = X + \left(\frac{\Delta_a - \Delta_p}{2} \right) = X + \left(\frac{2P_o - P_a - P_p}{2k_h} \right) \quad (3\text{-}9)$$

Similarly, the relationship between restoring forces y and Y is:

$$Y = y + \left(\frac{P_a + P_p}{2} \right) \quad (3\text{-}10)$$

Because both coordinate systems are of the same scale, rates of deformation increments $\dot{x}$ and $\dot{X}$ are identical, i.e. $\dot{x} = \dot{X}$. However, an initial value used in conjunction with Equation 3-8 needs to be transformed:

$$x(0) = X(0) + \left(\frac{2P_o - P_a - P_p}{2k_h} \right) \quad (3\text{-}11)$$

A numerical scheme can be applied to Equation 3-8 with an initial value in Equation 3-11 to determine a solution, u. Restoring force, Y, obtained from substituting Equation 3-10 into Equation 2-16 ($\alpha = 0$) is:

$$Y = k_h u + \left(\frac{P_a + P_p}{2} \right) \quad (3\text{-}12)$$

3.5.3 Abutment-Backwall Connection Hysteresis Element for Condensed Hysteresis Models

The elasto-plastic hysteresis model for abutment-backwall connection will be used to construct a hysteresis element. In order to simplify derivatives of the condensed hysteresis models, the ultimate moment capacity of abutment-backwall connections is assumed to be similar to its yielding moment. Also, differences in yielding moments between contraction and expansion cases are found to be small; therefore, an average yielding moment and rotation can be used. Coordinate transformation is not required for this hysteresis element. All variables are presented with a small capital letter. A relative rotation u is expressed as:

$$\dot{u} = \dot{x}\left[H_3(\dot{x}) \cdot H_4(u - \theta_Y) + H_2(\dot{x}) \cdot H_1(u + \theta_Y)\right] \tag{3-13}$$

Parameters appearing in Equation 3-13 are presented graphically as a simplified moment-rotation shown in Figure 3-19, where M_Y is a yielding moment, θ_Y is a rotation at yielding, x is a rotation, and y is a restoring moment.

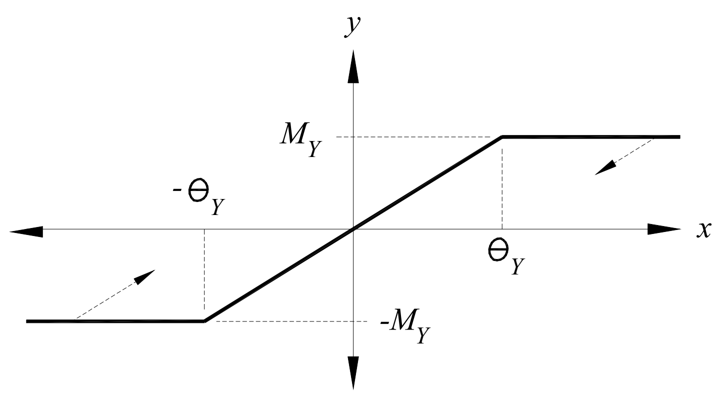

Figure 3-19: Elasto-Plastic Hysteresis Model for Abutment-Backwall Connection

Referring to Equation 2-16 ($\alpha = 0$), a restoring moment y is written as:

$$y = \frac{M_Y}{\theta_Y} u \tag{3-14}$$

Chapter 4

Finite Element Models

4.1 General

Hysteretic behavior in IA bridges transforms a linear static problem into a nonlinear time-history problem. A sophisticated analysis software package is required to achieve this transition. In this study ANSYS is adopted because the program provides an option of many advanced analysis levels and also possesses robust algorithms to overcome convergence difficulties.

Two analysis levels were conducted: two-dimensional and three-dimensional models. A 2-D model is a level 1 analysis, representing a relatively simple analysis level for predictions of extensively long simulation time bridge responses. A 3-D model is a level 2 analysis, representing a sophisticated analysis level for predictions of more accurate bridge responses. The FE models of all three instrumented bridges (203, 211, and 222) were developed using ANSYS for both analysis levels, except for the 3-D model of bridge 211, which was taken from Laman *et al* [61].

Model descriptions in this chapter, including element types, mesh sizes, section properties, and material properties for hysteresis and non-hysteresis elements, are discussed in detail. Loads for the FE models, including earth pressures, temperatures, and time-dependent loads, are described. Finally, an explanation of the analysis method, solution method, and convergence criteria is provided.

4.2 Model Description

In this section descriptions of the FE models for the three-instrumented IA bridges, element types used, and material properties are given. Instrumentation plans and construction details for each bridge are referred to in Appendix A and Laman *et al* [60], respectively. Two major bridge components, including superstructures and substructures, are described separately due to differences in modeling details.

4.2.1 Superstructures

Two-Dimensional Models

Properties of the 2-D models for the superstructure components are described here. A composite slab and 4-girder section for each instrumented bridge was combined and modeled using an ANSYS BEAM3 element. This beam member was subdivided into 10 pieces, all located on a composite elastic neutral axis. An elastic modulus of girders was used as a reference modulus, so that slab and parapet widths were transformed using corresponding modulus ratios. AASHTO LRFD [3] was used to determine a concrete modulus of elasticity based on a girder concrete strength of 55.2 MPa (8 ksi). Table 4-1 summarizes material and section properties for the three bridges.

Table 4-1: Material and Section Properties for 2-D Superstructure Models

Bridge	E_{ref} MPa (ksi)	Area m^2 (in^2)	Moment of Inertia m^4 (in^4)	y_b m (in)	Remark
203	35,536 (5,154)	5.03 (7,802)	2.378 (5,713,283)	1.308 (51.51)	Apply for all three spans
211	35,536 (5,154)	5.34 (8,282)	3.548 (8,525,124)	1.557 (60.60)	
222	35,536 (5,154)	4.37 (6,775)	1.432 (3,440,291)	1.098 (43.22)	

Three-Dimensional Models

Properties of the 3-D models for the superstructure components are described here. All girders, deck slabs, and parapets were modeled using ANSYS SHELL63 elements. A gap between the top flanges of I-girders and slabs that lie in a different plane was connected by a set of rigid links using ANSYS BEAM4 elements. A typical mesh size of shell elements was 0.45 m (18″) for bridge 203 and 0.3 m (12″) for bridges 211 and 222. Aspect ratios and corner angles for shell elements were generally kept to near unity and the right angle, respectively. Figure 4-1 presents two section modeling samples of bridge 203 and bridge 222 superstructures.

Because a bilinear shape function was used in SHELL63, shear locking is susceptible where a membrane action is modeled for bending. In order to avoid model inaccuracy due to shear locking, analyses of a single girder subjected to its own weight were performed under a simple span boundary condition for comparisons with hand calculations. A representative girder deflection of bridge 222 is presented in Figure 4-2.

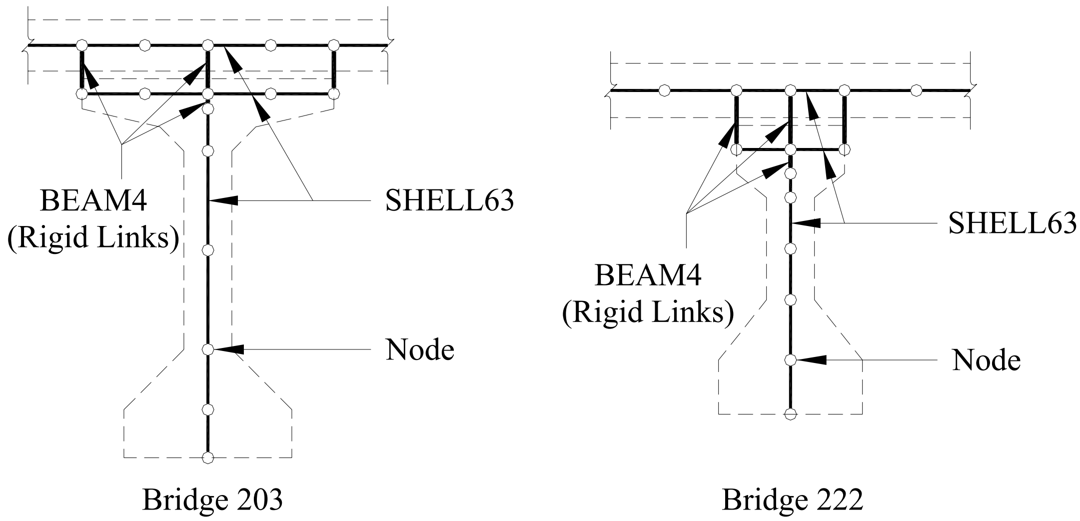

Figure 4-1: Cross Sections of 3-D Superstructure Models

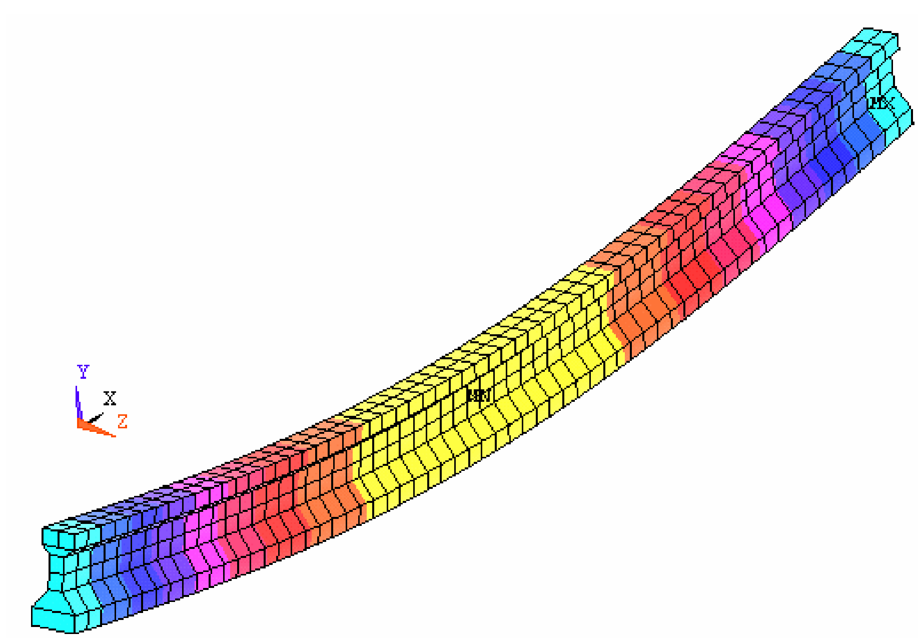

Figure 4-2: Representative Girder Deflection of Bridge 222 Girder Due to Self Weight

Analysis results for all representative girder deflections and comparisons with hand calculations are summarized in Table 4-2.

Table 4-2: Comparisons of ANSYS and Hand Calculation for Girder Deflection

Bridge	Girder Deflection, mm (in)		Span m (ft)	Remark
	ANSYS	Hand Calculation		
203	0.43 (0.017)	0.36 (0.014)	10.8 (35.5)	Integral span
211	25.27 (0.995)	24.59 (0.968)	34.8 (114)	
222	7.06 (0.278)	6.88 (0.271)	18.8 (61.7)	

It is observed that ANSYS results show slightly larger values because shear deformation was included. Material and section properties for three bridges are presented in Table 4-3.

Table 4-3: Material Properties for 3-D Superstructure Models

Component	Elastic Modulus MPa (ksi)	Poisson's Ratio	Coefficient of Thermal Expansion mm/mm/^{o}C (in/in/^{o}F)	Area mm^2 (in^2)	Inertia mm^4 (in^4)	Element Type
Girder	35,536 (5,154)	0.2	9.0E-6 (5.0E-6)	-	-	SHELL63
Slab	25,124 (3,644)	0.2	9.0E-6 (5.0E-6)	-	-	SHELL63
Rigid Link	6.9E7 (1E7)	-	-	6.4E9 (1E7)	4.2E12 (1E7)	BEAM4
Parapet	23,504 (3,409)	0.2	9.0E-6 (5.0E-6)	-	-	SHELL63
Diaphragm	23,504 (3,409)	0.2	9.0E-6 (5.0E-6)	-	-	SHELL63

The thermal expansion coefficient was set at 0.000009 mm/mm/^{o}C (0.000005 in/in/^{o}F) based upon the studies by Ndon and Bergeson [75] and Paul [86]. Rigid link properties were assigned to be much higher than the stiffness of all surrounding elements, but no more than a computer numeric round-off limit to avoid ill-condition [30].

4.2.2 Substructures

Two-Dimensional Models

Properties of the 2-D models for the substructure components are described here. The abutment, backwall, and piles for each instrumented bridge were modeled using an ANSYS BEAM3 element. Four types of hysteresis elements, discussed in Chapter 3, were applied on these bridge components, defined as *H1*, *H2*, *H3*, and *H4* for soil-pile interaction, soil-abutment interaction, abutment-backwall connection, and pile-abutment connection, respectively. An ANSYS COMBIN39 element was used for each hysteresis element.

As presented in Figure 4-3, each *H1* hysteresis element was connected to two adjacent pile elements through a single node to represent soil-pile interaction. One degree of freedom, UX, was utilized for these elements because only longitudinal movement is of particular interest. For the first 3-m (10′) pile depth measured downwards, *H1* elements were typically placed at a spacing of 0.15 m (6″) for all three bridge models, indicating a pile element length. The spacing for a greater depth (and pile element length) was lengthened appropriately, but no more than 0.9 m (3′).

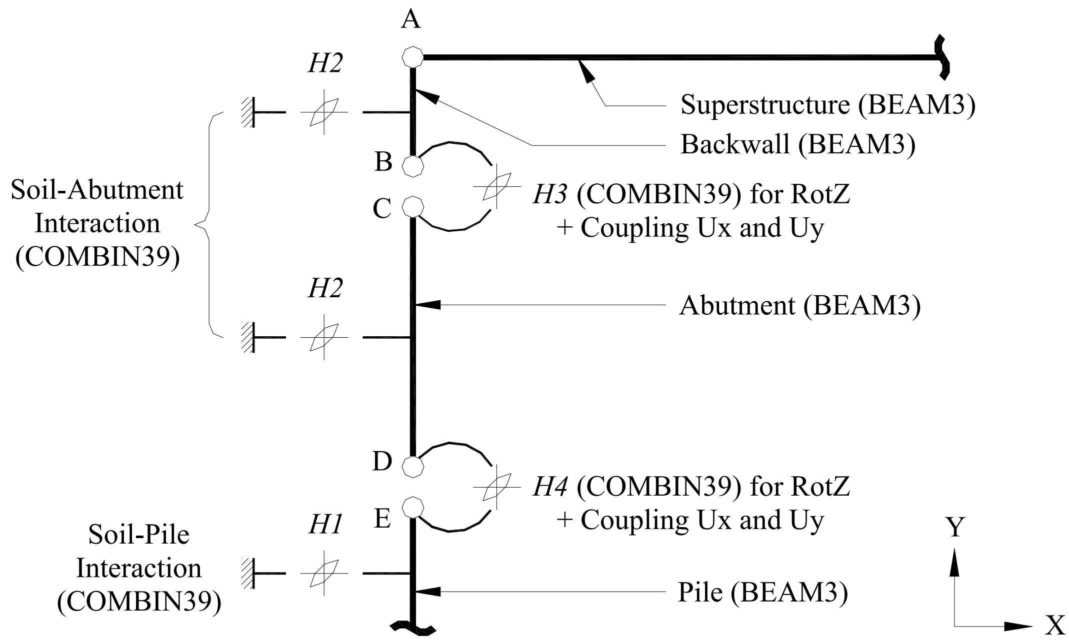

Figure 4-3: Schematic Representation of Substructure Modeling

Similar to the *H1* case, each *H2* hysteresis element was connected to two adjacent abutment elements laid inside the line segment C-D (and two backwall elements laid inside the segment A-B) through a single node to represent soil-abutment interaction. One degree of freedom, UX, was enabled for each *H2* element. An element spacing of approximately 0.3 m (1´), also indicating an abutment and backwall element length, was used for all three-bridge models.

Unlike the *H1* and *H2* cases, a single *H3* hysteresis element was used to connect the bottom of the backwall component (Node B) to the top of the abutment component (Node C). One degree of freedom, RotZ, was utilized for this case to represent hysteretic behavior of the abutment-backwall connection. For the other degrees of freedom, UX and UY, a coupling of nodes B and C was employed. It is noted that nodes B and C essentially coincide.

In case of very long overall bridge length, a *H4* hysteresis element needs to be considered similar to the *H3* case. However, the maximum overall bridge length used in this study is not long enough to produce a rotational plastic hinge to the pile-abutment connections. Therefore, this hysteresis element is not considered in this study.

H1 Properties

Properties of *H1* hysteresis elements were obtained primarily from *p-y* curves, generated by using COM624P [112]. These properties depend on depth, embankment slope, soil overburden, pile stiffness, and soil properties. Figures 4-4 to 4-8 present diagrams of soil profiles and properties for all three bridges.

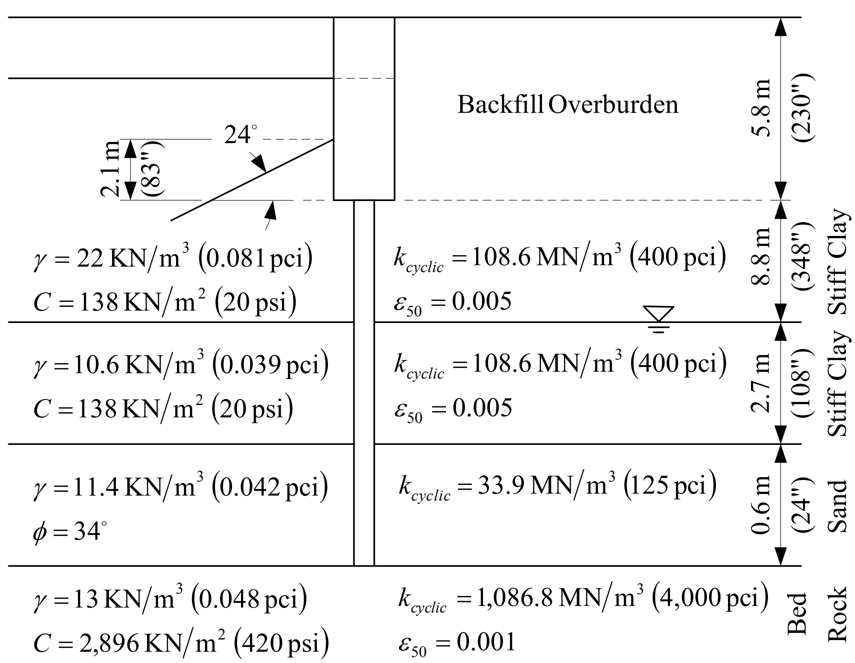

Figure 4-4: Soil Properties for Bridge 203 at Abutment 2

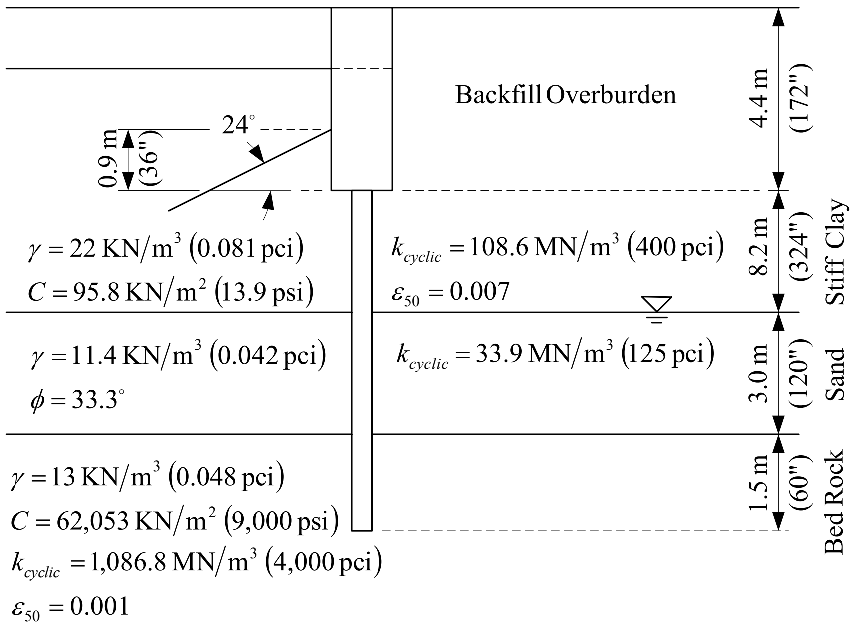

Figure 4-5: Soil Properties for Bridge 211 at Abutment 1

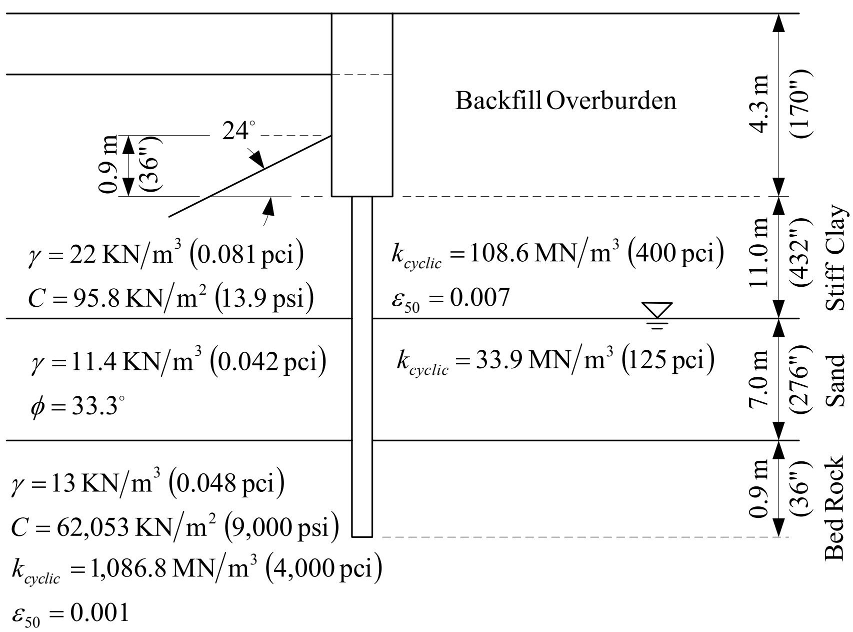

Figure 4-6: Soil Properties for Bridge 211 at Abutment 2

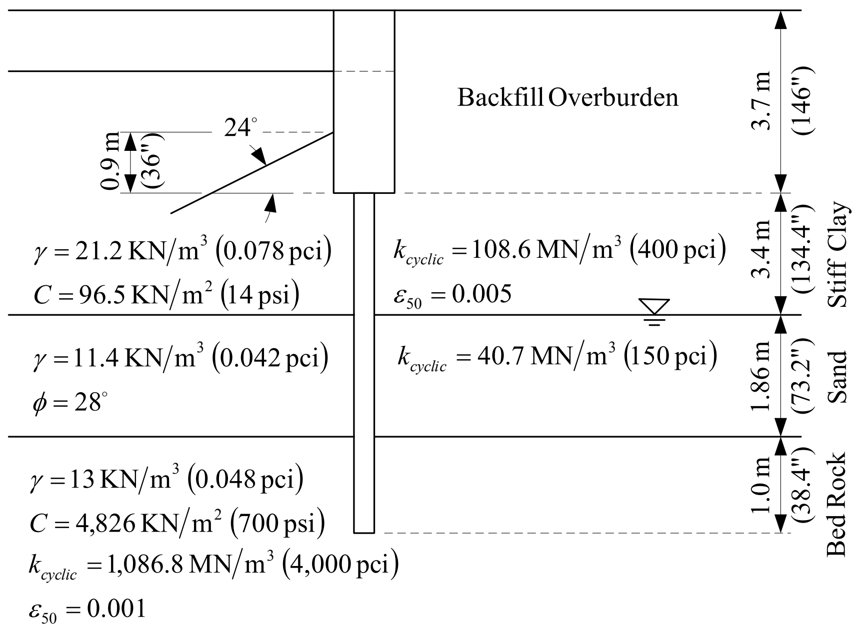

Figure 4-7: Soil Properties for Bridge 222 at Abutment 1

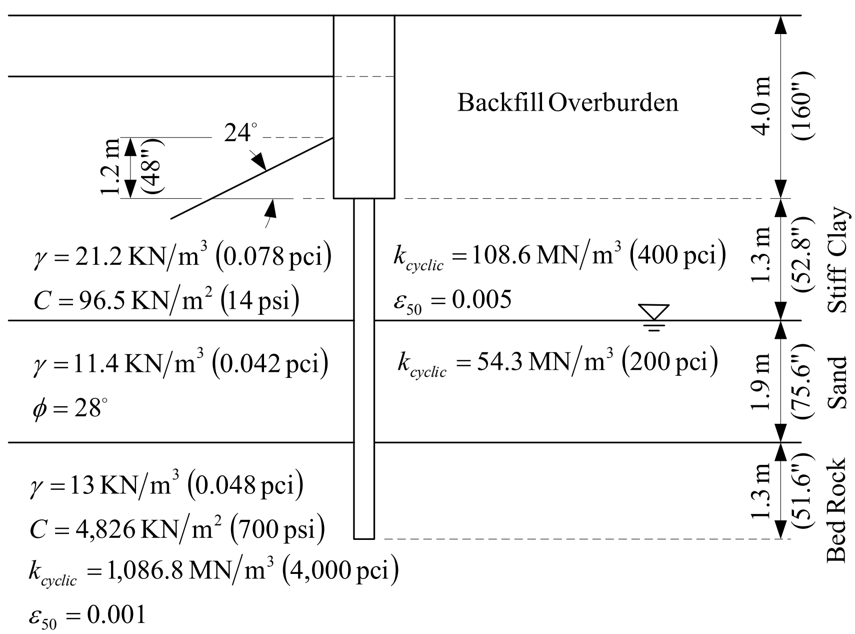

Figure 4-8: Soil Properties for Bridge 222 at Abutment 2

Sample loading curves for *H1* elements at 0 and 3 m (0′ and 10′) pile depth are presented in Figure 4-9. Unloading curves are not shown and only curves generated for abutment 2 of each bridge are presented.

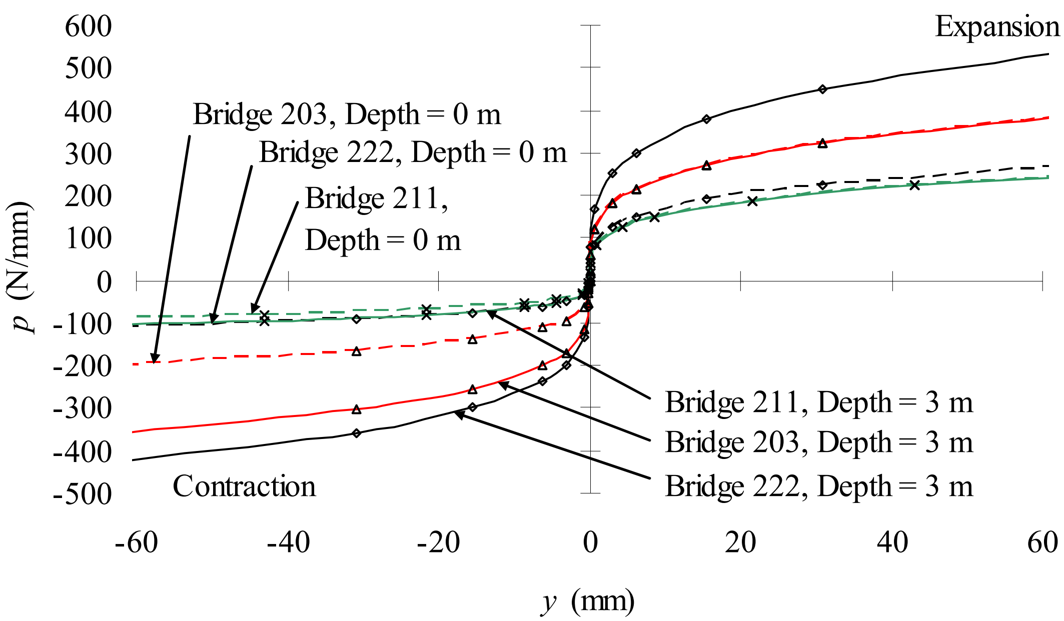

Figure 4-9: Sample of Loading Curves for *H1* Elements

As can be observed in Figure 4-9, due to the effects of downhill slopes and shallow soil overburden, soil stiffness and strength of the contraction case are smaller than those of the expansion case. This difference becomes less pronounced at a greater depth. At zero depth (at pile-abutment connection), the stiffness and strength of bridge 203 is the highest due to the largest soil overburden on both sides of the abutment. However, at the greater depth, the stiffness and strength of bridge 222 are the largest due to the smallest clay layer thickness. The stiffness and strength of bridge 211 are the weakest in any case, because its soil profile has a relatively shallow overburden and a thick clay layer.

***H2* Properties**

Properties of *H2* hysteresis elements were determined from a limit state of active, passive, and at-rest earth pressures. A lateral soil stiffness k_h, *i.e.* a slope of the line connecting the three limit states, was obtained from a linear fit of field collected data presented in Figures **4-10** to **4-12**, where the pressure and displacement magnitudes, which appear as vertical and horizontal scales, were taken from pressure cells and extensometers, respectively. Because pressure cells and extensometers were not installed at the same elevation, linear interpolation between two sets of extensometer data was performed to meet the pressure cell elevations.

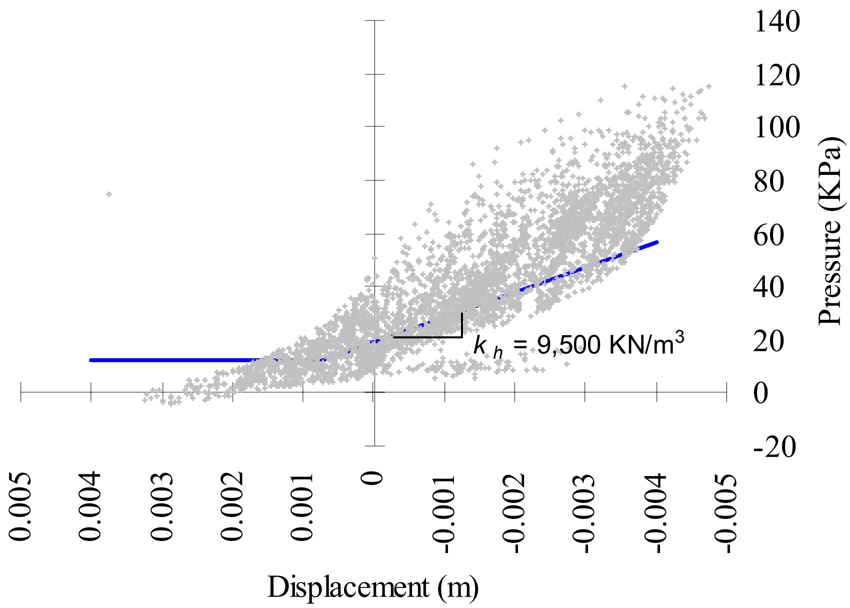

Figure **4-10**: Lateral Soil Stiffness for Bridge 203

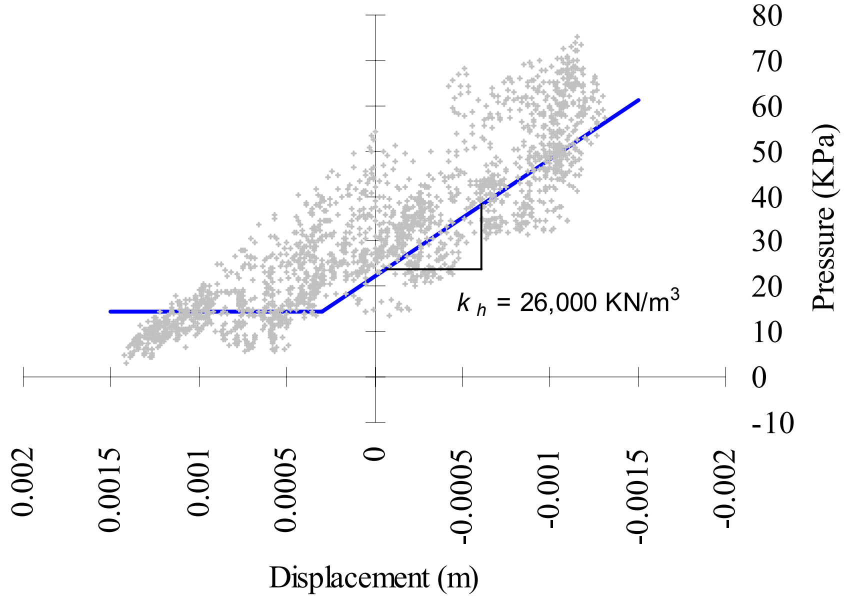

Figure **4-11**: Lateral Soil Stiffness for Bridge 211

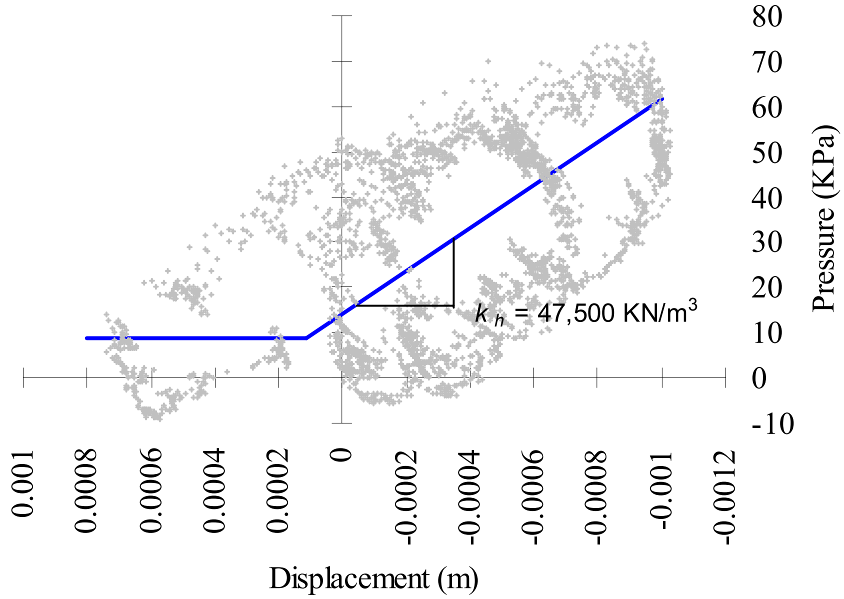

Figure **4-12**: Lateral Soil Stiffness for Bridge 222

The lateral soil stiffness, k_h, of each bridge from the best linear fits was slightly modified in order to gain a better correlation between the analysis results of the FE models and the field data (model calibration).

The difference in the lateral soil stiffness is observed, even though the pressure cell of each bridge is not comparably located at the same elevation. This difference reveals that lateral soil stiffness is inversely proportional to the bridge length. The explanation for this observation is that lateral soil stiffness is essentially a secant stiffness of a nonlinear stress-strain relation, which is generally smaller when deformation gets larger.

The lateral soil stiffness, k_h, as determined from the linear fit was used as a reference property of *H2* elements at the pressure cell elevation (hereafter defined as k_{ref}). In order to obtain lateral soil stiffness of *H2* elements at other elevations, $k_h(z)$, a polynomial interpolation (and extrapolation) between the pressure cell elevation ($k_h(z) = k_{ref}$) and soil surface elevation ($k_h(z) = 0$) was carried out and written as:

$$k_h(z) = k_{ref}\left(\frac{z}{h_{ref}}\right)^{0.5} \quad \textbf{(4-1)}$$

where h_{ref} is a reference depth measured from the soil surface to the pressure cell elevations and z is the depth of the interest. It is noted that a linear relationship, *i.e.* $k_h(z) = k_{ref}\left(z/h_{ref}\right)$, is not appropriate, because stiffness of gravel soil material is generally proportional to the square root of confinement [18].

***H3* Properties**

A property of *H3* element was based upon the moment-curvature relationship for abutment-backwall connection details. From Figure 2-4 in Chapter 2, a typical Ø16 mm @ 250 mm U-shape rebar is specified in the PennDOT standard IA joint detail [17]. This standard detail was used for bridge 222. However, some slight modification of a rebar spacing to 225 mm was employed for bridges 203 and 211. Figure 4-13 presents moment-curvature plots of the three bridges, using a strain compatibility approach and Whitney's equivalent stress block for computing ultimate moment capacities.

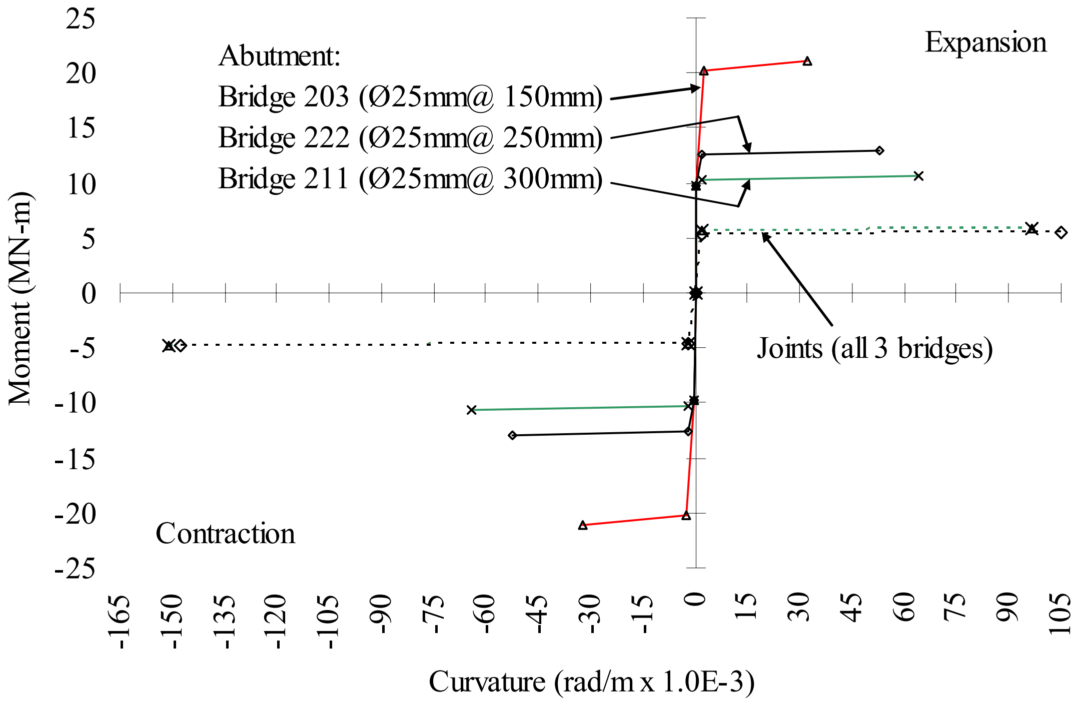

Figure 4-13: Moment-Curvatures of Abutment-Backwall Connection

Due to the unequal reinforcement arrangement and an effective concrete width of the abutment-backwall connections, calculated strength and its initial stiffness of these connections subjected to expansion movements are different from those subjected to contraction movements by a factor of approximately 1.2. In addition, the calculated initial rotational stiffness for abutments are 16 to 20 times higher than those of abutment-backwall connections, clearly indicating the connection weakness.

Conversion from moment curvature relationship, $M-\phi$, to moment-rotation relationship, $M-\theta$, is required to determine *H3* element properties. Based on the assumption of small deformation and constant moment over a joint length (*L*), this conversion can be written as [76 and 85]:

$$\theta=\int_0^L \frac{M}{EI}dx=\frac{M}{EI}L=\phi L \tag{4-2}$$

According to Paul [85], the joint length, *L*, is associated with the development length of an epoxy-coated reinforcement, which is equal to 0.4 m (16″) based on AASHTO [3]. By assuming a linear variation of rebar stresses over the development length, with a fully mobilized stress at the one end and zero stress at the other end, one half the development length was used as the joint length, *L* = 0.2 m (8″).

Properties of Other Substructure Components

The stiffness and strength of other substructure components, including abutment, backwall, pier, and piles, are significantly stronger than those of hysteresis elements. As a result, these components are expected to perform without cracking in a service condition. Section properties based on gross section assumptions can be used. Material and section properties of these components, as well as those of bearings, are shown in Table 4-4.

Table 4-4: Material and Section Properties of Various Substructure Components

Bridge	Component	Modulus MPa (ksi)	Area m^2 (in^2)	Moment of Inertia m^4 (in^4)
203	Abutment	21,760 (3,156)	16.80 (26,040)	2.081 (4,999,680)
	Backwall	25,124 (3,644)	16.80 (26,040)	2.081 (4,999,680)
	Continuity Diaphragm	25,124 (3,644)	5.03 (7,802)	2.378 (5,713,283)
	Pier	21,760 (3,156)	4.512 (6,994)	0.523 (1,255,904)
	Pile	200,000 (29,000)	0.112 (174.4)	6.19E-4 (1,488)
	Dowels at abutment 1	200,000 (29,000)	9.7E-4 (1.507)	2.17E-6 (5.22)
	Bearing at pier 1 span 1	2.7 (0.39)	108.7 (168,431)	1.17E-4 (281.5)
	Bearing at pier 1 span 2	2.7 (0.39)	108.7 (168,431)	1.17E-4 (281.5)
	Bearing at pier 2 span 2	2.7 (0.39)	108.7 (168,431)	1.17E-4 (281.5)
	Bearing at pier 2 span 3	2.7 (0.39)	72.4 (112,183)	1.41E-4 (338.4)
211	Abutment	21,760 (3,156)	16.80 (26,040)	2.081 (4,999,680)
	Backwall	25,124 (3,644)	16.80 (26,040)	2.081 (4,999,680)
	Pile (abutment 1 and 2)	200,000 (29,000)	0.155 (239.8)	8.52E-4 (2,046)
222	Abutment	21,760 (3,156)	16.80 (26,040)	2.081 (4,999,680)
	Backwall	25,124 (3,644)	16.80 (26,040)	2.081 (4,999,680)
	Pile (Abutment 1)	200,000 (29,000)	0.155 (239.8)	8.52E-4 (2,046)
	Pile (Abutment 2)	200,000 (29,000)	0.127 (196.2)	6.97E-4 (1,674)

For bridge 203 only, continuity diaphragms and elastomeric bearing pads were used to make a continuous structure. Figure 4-14 presents a typical modeling detail for the superstructure and substructure connectivity over the piers.

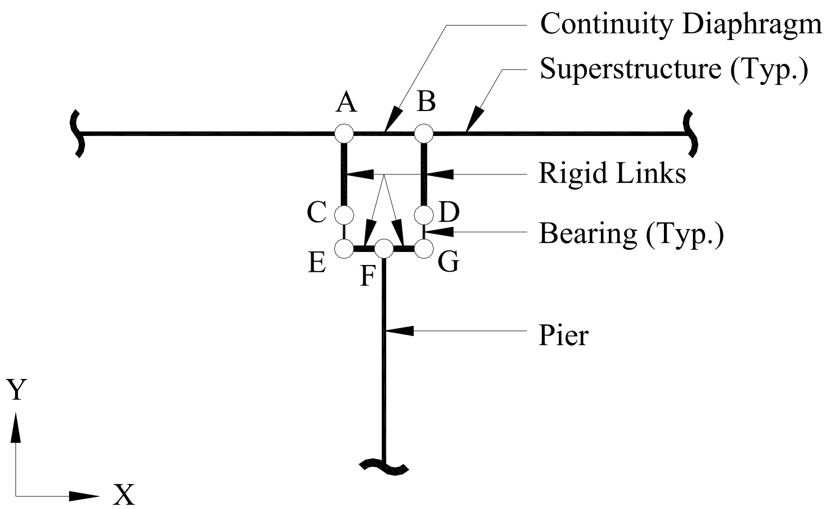

Figure 4-14: Typical Model at Super- and Sub-Structure Connection over Pier

An ANSYS BEAM3 element was typically used for all members shown above. For bearing members (segments C-E and D-G), the modulus of elasticity along the Y axis needs to be increased due to bulging restraint caused by the use of embedded steel shims, known as an effective compressive modulus of elasticity (E_c). According to AASHTO [3], this parameter can be calculated as:

$$E_c = 6GS^2 \tag{4-3}$$

where G is the shear modulus of elasticity of bearings and S is a shape factor, written as:

$$S = \frac{\text{shear area of bearings}}{\text{perimeter of bearings} \times \text{clear distance between adjacent steel shims}} \tag{4-4}$$

Modification of the input data in the FE models was applied to areas and moment of inertia, instead of elastic modulus, to account for bulging restraint effects. An equivalent area, A_e, is expressed as:

$$A_e = A_{bearing} \frac{E_c}{E} \tag{4-5}$$

where $A_{bearing}$ is the total actual bearing area and E is a nominal elastic modulus of bearings. An equivalent moment of inertia, determined from the equivalence of the lateral stiffness of bearings ($GA_{bearing}/H$) [120] and the lateral stiffness of classical beam ($12EI/H^3$) can be written as:

$$I_e = \frac{GA_{bearing}H^2}{12E} \tag{4-6}$$

where H is a bearing thickness. Note that values presented in Table 4-4 have appeared as equivalent properties (A_e and I_e).

Three-Dimensional Models

Properties of the 3-D models for substructures components are described here. Most beam and hysteresis element properties of the 3-D models can be taken from the 2-D models using additional consideration of the third dimension. An abutment and backwall for the 3-D models was constructed using ANSYS SHELL63 elements with a typical mesh size ranging from 300 to 450 mm (12″ to 18″). A sample mesh taken from bridge 222 at abutment 2 is presented in Figure 4-15.

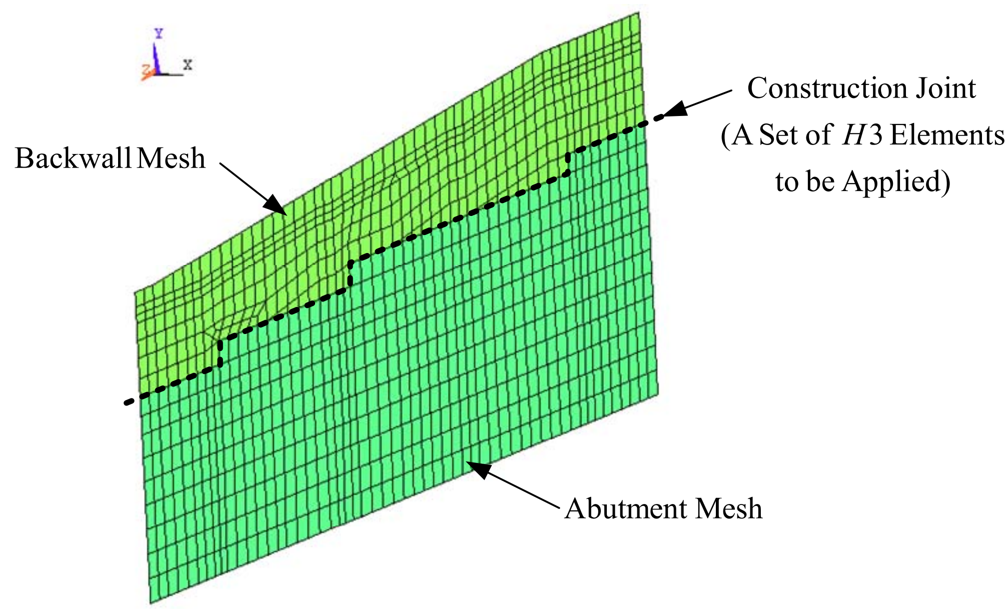

Figure 4-15: Sample Mesh of Bridge 222 Abutment and Backwall

A dotted thick line drawn through the mesh in Figure 4-15 represents a construction joint where there are two sets of coincided nodal points: one attached to the abutment component and the other one attached to the backwall. Along this line, a set of *H3* hysteresis elements and a coupling of every degree of freedom, except for rotation about the Z-axis, were applied to each pair of coincided nodal points. A property of *H3* hysteresis elements was calculated from the moment curvature relationship of the abutment-backwall connections similar to the 2-D models; however, the ratio of the distance between adjacent nodal points along the construction joint to the total joint length was used as a multiplier for each *H3* property of the 3-D models. Material properties of other substructure components for the 3-D models of all three instrumented bridges are summarized in Table 4-5.

Table 4-5: Material Properties for 3-D Substructure Models

Structure	Component	Elastic Modulus MPa (ksi)	Poisson's Ratio	Thermal Expansion Coefficient mm/mm/°C (in/in/°F)	Area mm^2 (in^2)	Inertia mm^4 (in^4)	Element Type
203	Abutment	21,760 (3,156)	0.2	9.0E-6 (5.0E-6)	-	-	SHELL63
	Backwall	25,124 (3,644)	0.2	9.0E-6 (5.0E-6)	-	-	SHELL63
	Continuity Diaphragm	25,124 (3,644)	0.2	9.0E-6 (5.0E-6)	-	-	SHELL63
	Pier	21,760 (3,156)	0.2	9.0E-6 (5.0E-6)	-	-	SHELL63
	Pile	200,000 (29,000)	0.3	-	1.41E-2 (21.8)	7.74E-5 (186)	BEAM4
	Dowels at abutment 1	200,000 (29,000)	0.3	-	1.14E-3 (1.767)	1.03E-7 (0.25)	BEAM4
	Bearing at abutment 1	2.7 (0.39)	0.4985	-	18.1 (28,046)	2.38E-5 (57.1)	BEAM4
	Bearing at pier 1 span 1	2.7 (0.39)	0.4985	-	27.2 (42,108)	2.93E-5 (70.4)	BEAM4
	Bearing at pier 1 span 2	2.7 (0.39)	0.4985	-	27.2 (42,108)	2.93E-5 (70.4)	BEAM4
	Bearing at pier 2 span 2	2.7 (0.39)	0.4985	-	27.2 (42,108)	2.93E-5 (70.4)	BEAM4
	Bearing at pier 2 span 3	2.7 (0.39)	0.4985	-	18.1 (28,046)	3.52E-5 (84.6)	BEAM4
	Pier Cap	21,760 (3,156)	0.2	9.0E-6 (5.0E-6)	-	-	SHELL63
	Pedestal	21,760 (3,156)	0.2	9.0E-6 (5.0E-6)	-	-	SHELL63
211 and 222	Abutment	21,760 (3,156)	0.2	9.0E-6 (5.0E-6)	-	-	SHELL63
	Backwall	25,124 (3,644)	0.2	9.0E-6 (5.0E-6)	-	-	SHELL63
	Pile	200,000 (29,000)	0.3	-	1.41E-2 (21.8)	7.74E-5 (186)	BEAM4

4.2.3 ANSYS Model Summary

Two-Dimensional Models

A number of nodes, elements, and active equations used in the three models are summarized in Table 4-6. ANSYS model plots of bridges 203, 211, and 222 are presented in Figures 4-16 to 4-18, respectively.

Table 4-6: Summary of 2-D Model Status

Bridge	No. of Nodes	No. of Elements	No. of Active Equations
203	225	225	397
211	255	254	405
222	215	214	333

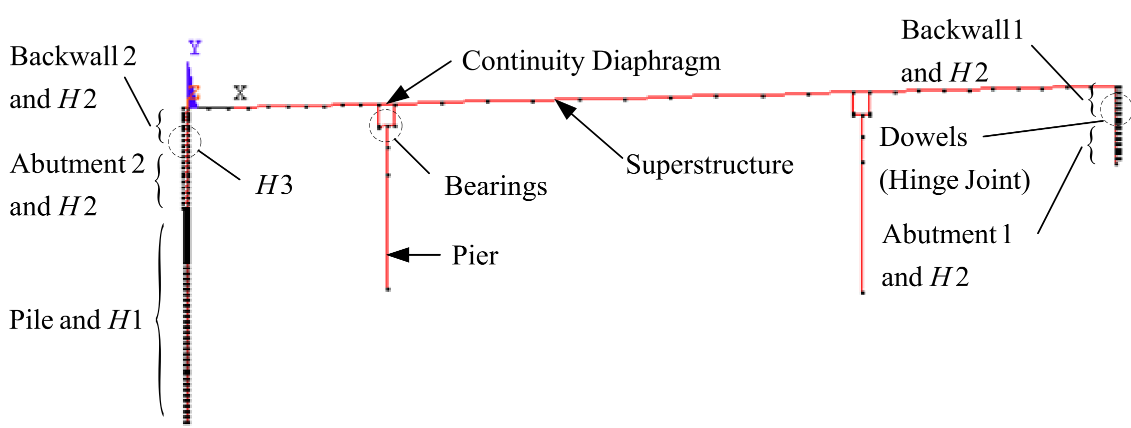

Figure 4-16: 2-D ANSYS Model for Bridge 203

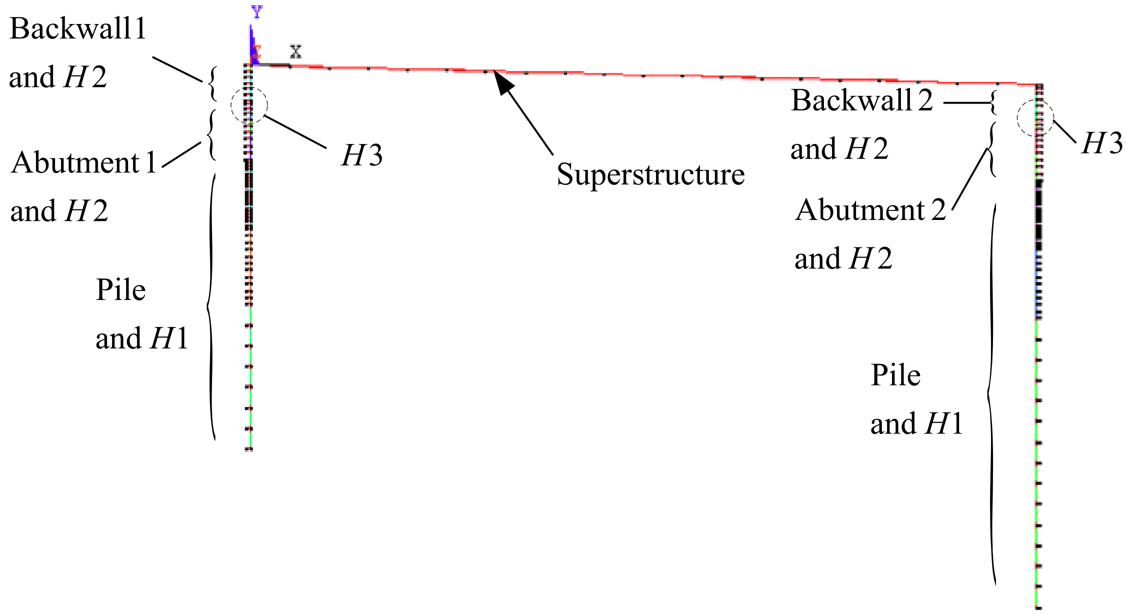

Figure 4-17: 2-D ANSYS Model for Bridge 211

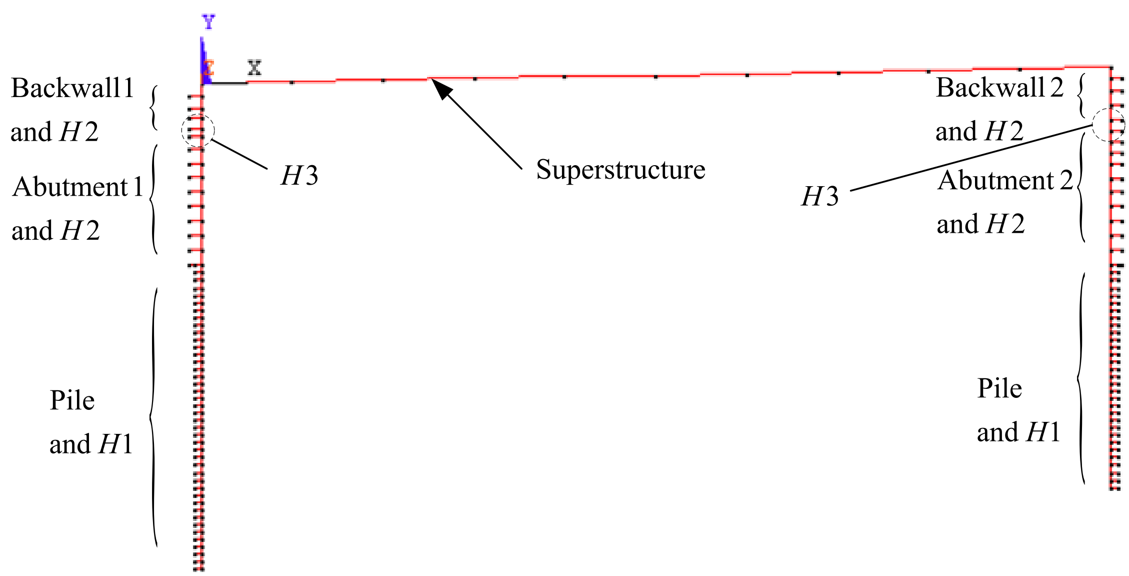

Figure 4-18: 2-D ANSYS Model for Bridge 222

Three-Dimensional Models

A number of nodes, elements, and active equations used in the three models are summarized in Table 4-7. ANSYS model plots of bridges 203, 211, and 222 are presented in Figures 4-19 to 4-21, respectively.

Table 4-7: Summary of 3-D Model Status

Bridge	No. of Nodes	No. of Elements	No. of Active Equations
203	15,374	16,062	82,004
211	22,566	21,865	109,859
222	11,215	11,583	51,537

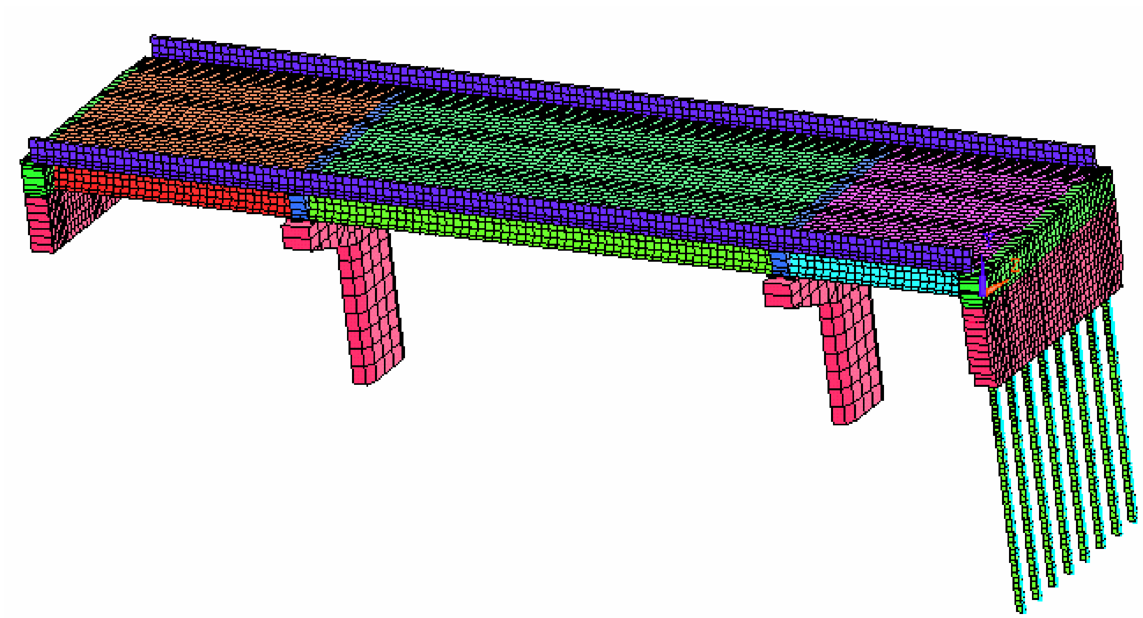

Figure 4-19: 3-D ANSYS Model for Bridge 203

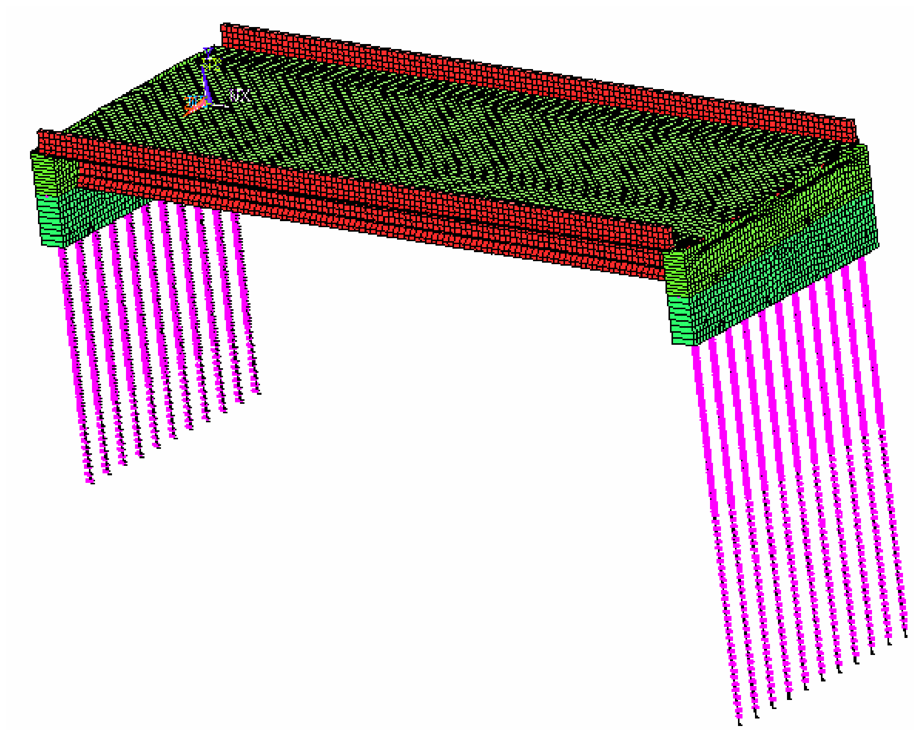

Figure 4-20: 3-D ANSYS Model for Bridge 211

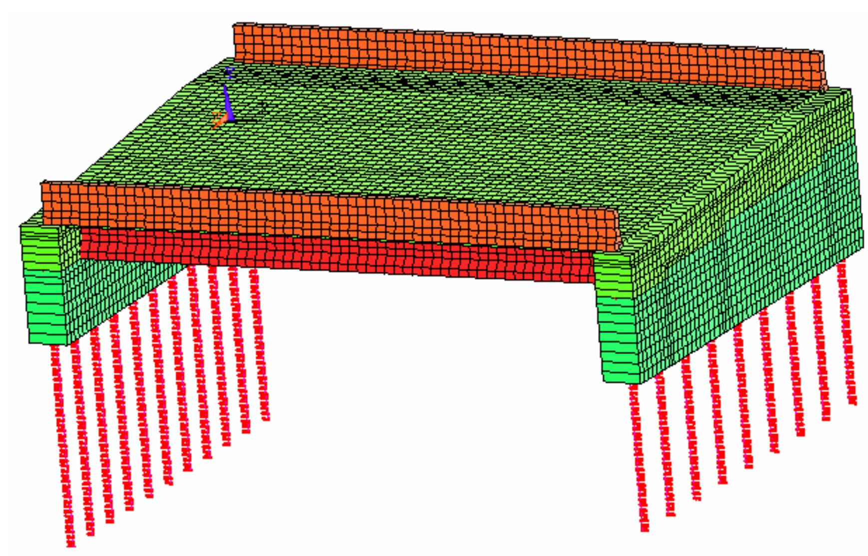

Figure 4-21: 3-D ANSYS Model of Bridge 222

4.3 Loadings

In this study there are three major loads to be considered: (1) earth pressures, (2) temperature, and (3) time-dependent loads. Because a starting analysis time of each model was set at the moment when a concrete abutment and backwall connection is cured (frame action begins), most self-weights occurred beforehand and no longer affected frame action behavior. As a result, self-weights were disregarded.

4.3.1 Earth Pressures

Earth pressures were applied to the supplementary step of the ANSYS analysis (See Chapter 3). At this first step, all *H2* hysteresis elements were artificially inactive by means of rigid body motion. An at-rest earth pressure, calculated by using the Jaky at-rest coefficient, *i.e.* $K_o = 1 - \sin\phi$, was applied to abutment and backwall elements. Figures 4-22 and 4-23 present a sample of bridge 222 earth pressures in the ANSYS 2-D and 3-D models.

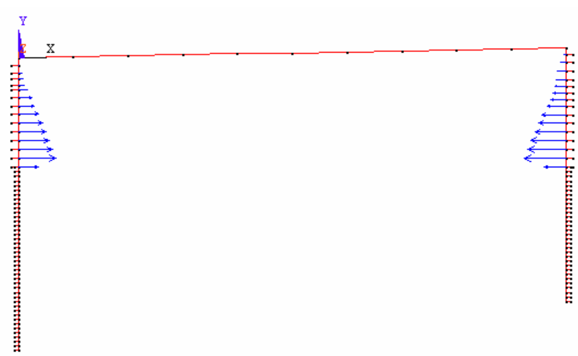

Figure 4-22: Earth Pressures of Bridge 222 (2-D Model)

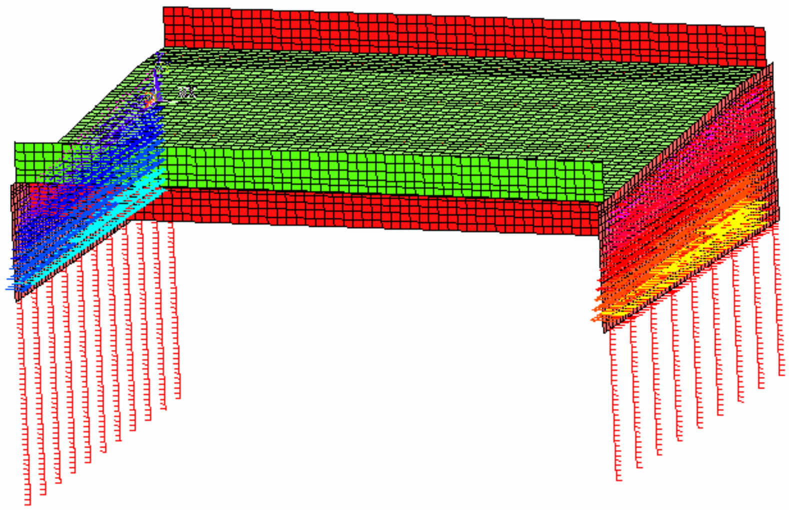

Figure 4-23: Earth Pressures of Bridge 222 (3-D Model)

After completion of the supplementary analysis step, the remaining time-history analysis steps followed. Earth pressures in the remaining steps were fully interacted with temperature and time-dependent loads, according to the characteristics of *H2* elements.

4.3.2 Temperature Loads

A record of ambient temperature has been taken from the weather station located in the vicinity of all three bridges. Figure 4-24 presents ambient temperature data from September 2002 to January 2006. The temperature time-history load and initial analysis time for each bridge are also presented in Figure 4-24.

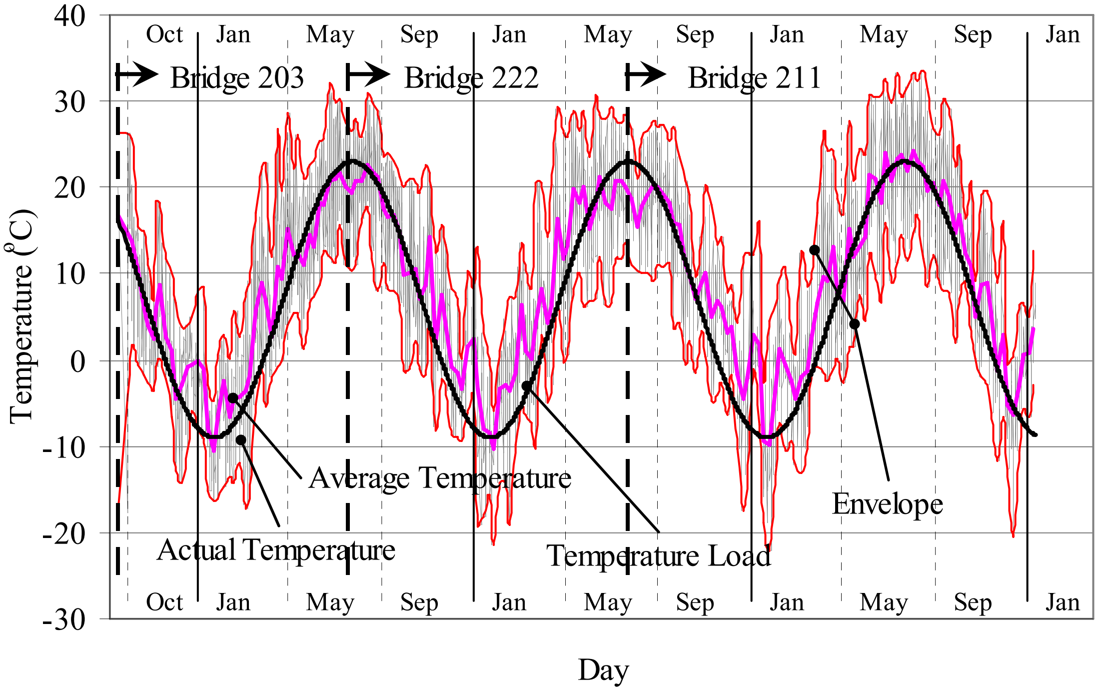

Figure 4-24: Temperature Loads for All Models

A sinusoidal function representing the temperature load is defined from the best fit to the average ambient temperature data in order to produce average bridge responses. This function is expressed as:

$$T(t) = T_m + A\sin(\omega t + \phi) \tag{4-7}$$

where T_m = Mean Temperature = 7 °C,

A = Amplitude of Temperature Fluctuation = 16 °C,

ω = Frequency = $2\pi/365.25$ = 0.017202 radian/day,

t = Analysis Time (day), and

ϕ = Phase lag (radian)

= {2.516, 1.561, 1.48} for bridges 203, 211, and 222, respectively.

The initial analysis time (t = 0) represents the condition when structural continuity has begun. The reference bridge temperatures for each bridge was determined from Equation 4-7 when t = 0. Therefore, it can be observed from Figure 4-24 that contraction movements are dominated for all three bridges.

4.3.3 Time-Dependent Loads

Prior to super- and sub-structure connection, time-dependent effects of creep, shrinkage, and steel relaxation on prestressed concrete girders have no influences on the overall IA bridge behavior, because girders are of an unrestraint condition. However, after this structural connection occurs, the remaining time-dependent strains need to be considered for the FE models. Each source of time-dependent effects is discussed and demonstrated using parameters from bridge 222. A preliminary investigation on the time-dependent effect sources obtained from several design recommendations is conducted and presented. Based on the AAEM method, the net time-dependent strains are determined and used as time-dependent loads for the FE models by means of equivalent temperatures. The net time-dependent strains for bridges 203 and 211, as well as their calculations using the AAEM method, are available in Appendix B.

Samples of creep coefficients, aging coefficients, and shrinkage strains from the design recommendations: AASHTO LRFD [3], ACI Committee 209 [5], CEB-FIP MC 90 [27], and Model B3 [16], are presented in Figures 4-25 to 4-27, respectively. Result comparisons between these design recommendations were intentionally conducted to cross-verify and select the most desirable design recommendation for detailed analyses.

Parameters used for determining these curves were taken from bridge 222 as an example. As can be observed in Figure 4-25, the creep coefficients using AASHTO and ACI appear to correlate well, because these two recommendations are based on a similar form of creep equation. Higher creep coefficients are observed from CEB-FIP and B3. The differences are made acceptable due to the fact that creep is a highly variable phenomenon with a coefficient of variation on the order of 15 to 20 percent [5]. Day 171, specified in Figure 4-25, represents the boundary event when changes in creep strains initiate to affect IA bridge behavior.

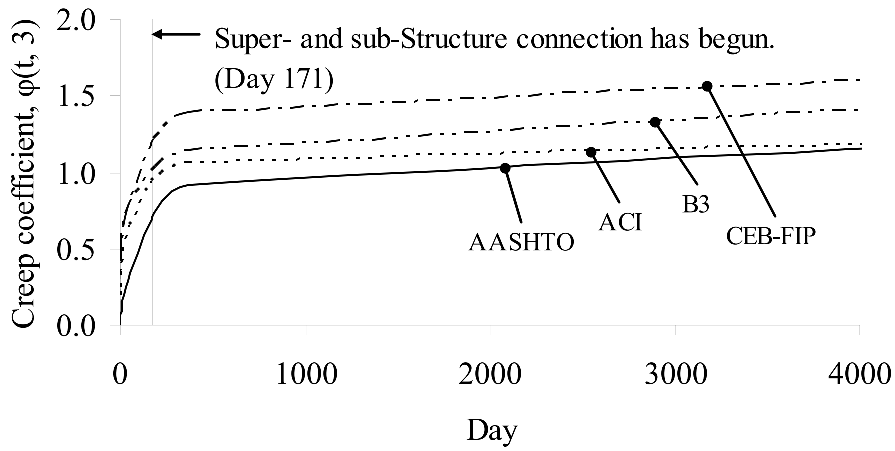

Figure 4-25: Creep Coefficients from Several Design Recommendations (Bridge 222)

As can be observed in Figure 4-26, the aging coefficients from ACI, CEB-FIP, and B3 appear as the same trend in which the aging coefficient from CEB-FIP is the smallest and the aging coefficient from B3 is the greatest. There is no aging coefficient available in AASHTO.

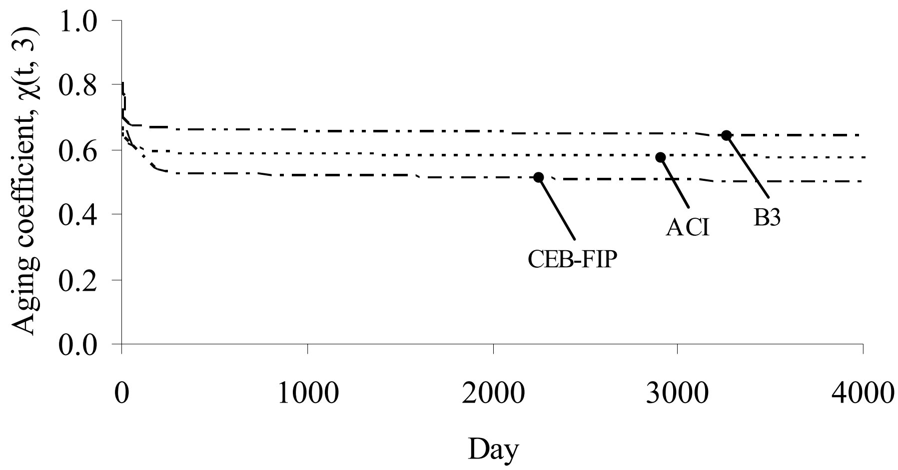

Figure 4-26: Aging Coefficients from Several Design Recommendations (Bridge 222)

As can be observed in Figure 4-27, shrinkage strains from AASHTO and ACI appear to correlate well, while shrinkage strains from CEB-FIP and B3 are relatively higher. Similar to creep phenomenon, shrinkage is also a highly variable phenomenon.

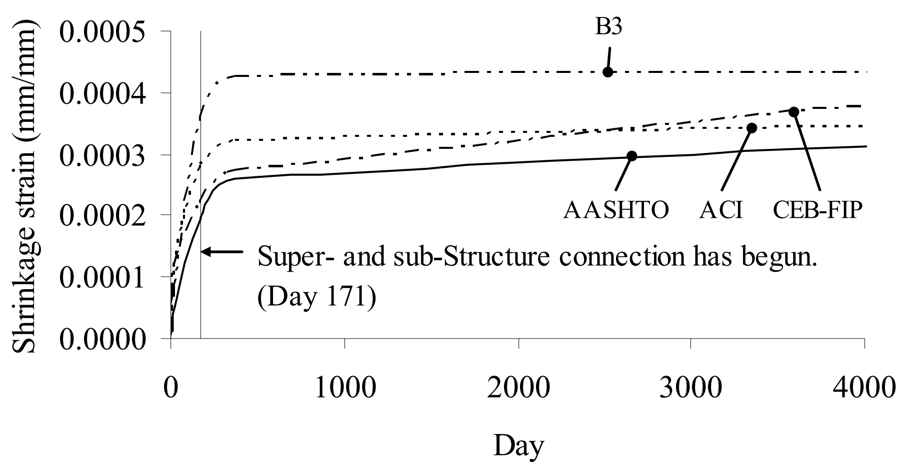

Figure 4-27: Shrinkage Strains from Several Design Recommendations (Bridge 222)

$\overline{E}(t,t_o)$ is a function of time in which magnitudes decrease logarithmically. Based on Equation 2-41 in Chapter 2, and using parameters from bridge 222, the $\overline{E}(t,t_o)$ for the girder at age of three days ($\overline{E}_{girder}(t,3)$), the girder at age of 171 days ($\overline{E}_{girder}(t,171)$), and the concrete slab at age of three days ($\overline{E}_{slab}(t,3)$) are presented in Figure 4-28. These three sets of $\overline{E}(t,t_o)$ serve as input parameters to determine time-dependent strains by using the AAEM method.

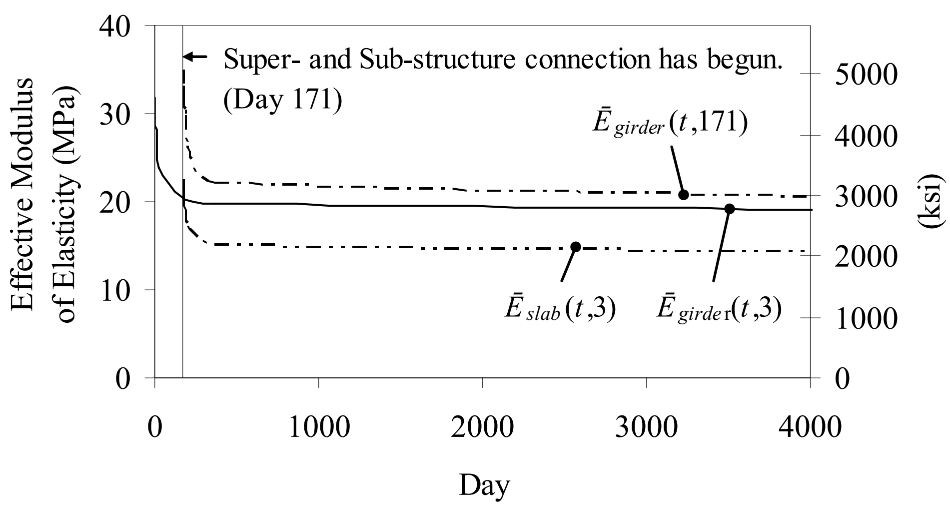

Figure 4-28: Age-Adjusted Effective Modulus (Bridge 222)

The selection of a design recommendation for detailed computation needs to be made. The AAEM method was applied to bridges 203, 211, and 222 and presented as a design calculation in Appendix B. Creep coefficients, aging coefficients, and shrinkage strains were determined using ACI, CEB-FIP, and B3, and are included in Appendix B. In general, results determined from these three design recommendations showed insignificant differences in outcomes. Therefore, given its relative ease of use, the ACI approach was selected for detailed computation.

Time-dependent strain results using ACI are summarized. The initial girder age of time-dependent strain computations corresponds to the age when superstructure and substructure were connected (Day 171 for bridge 222). Based on the AAEM method, time-dependent strains at the top and bottom fibers for the bridge 222 girder are presented in Figures **4-29** and **4-30**, respectively.

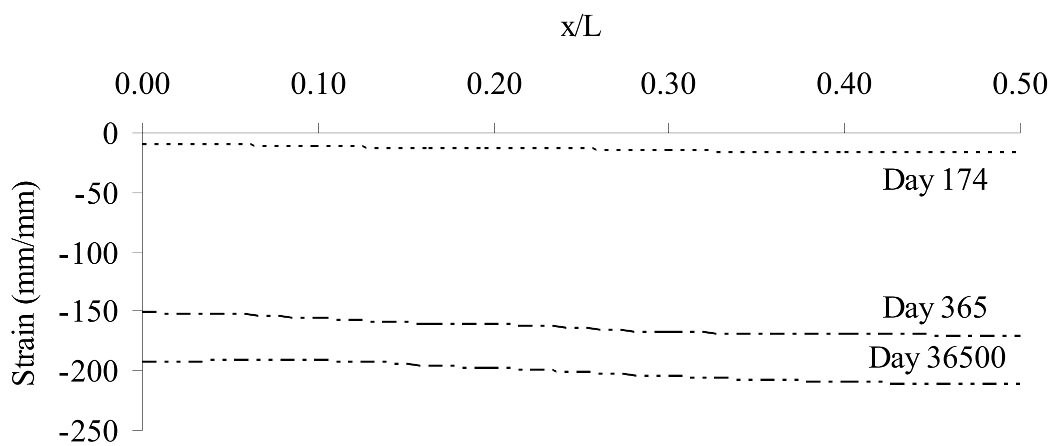

Figure **4-29**: Time-Dependent Strain at Top Fiber of Girder (Bridge 222)

Three samples days after the superstructure and substructure were connected (Days 174, 365, and 36500) are also presented in Figures **4-28** and **4-29**. Only the half-length of a girder is plotted to take advantage of symmetry. An unrestrained condition was applied to obtain these time-dependent strains. Detailed calculations to consider the effects of force redistribution due to structural continuity are provided in Appendix B.

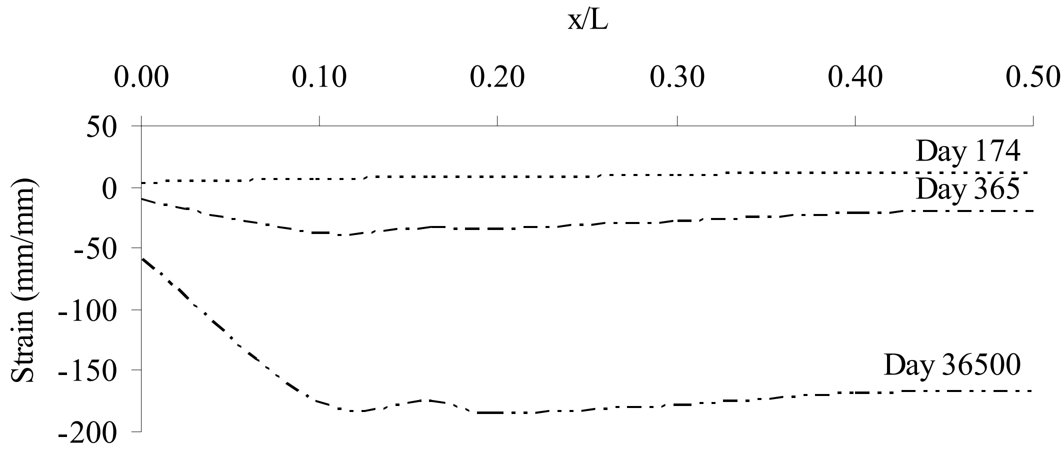

Figure 4-30: Time-Dependent Strain at Bottom Fiber of Girder (Bridge 222)

Time-dependent strains, determined by using the AAEM method, were imposed to a superstructure component by means of equivalent temperatures. Detailed calculations for equivalent temperatures are presented in Appendix B for all three instrumented bridges. The equivalent temperature is a function of the following parameters:

- *Time*: Absolute value of equivalent temperatures is increased when time is increased. The equivalent temperature sign is typically negative, representing a self-shortening deformation of superstructures.
- *Longitudinal position*: Magnitudes of equivalent temperatures are varied over a bridge span due to stress variations from self weight and de-bonding effects of prestressing strands.
- *Girder depth*: Similar to the longitudinal position parameter, equivalent temperatures are also varied through a girder depth.

Figure 4-31 presents a bridge 222 sample diagram for typical equivalent temperature distribution over a half superstructure element of the 2-D model.

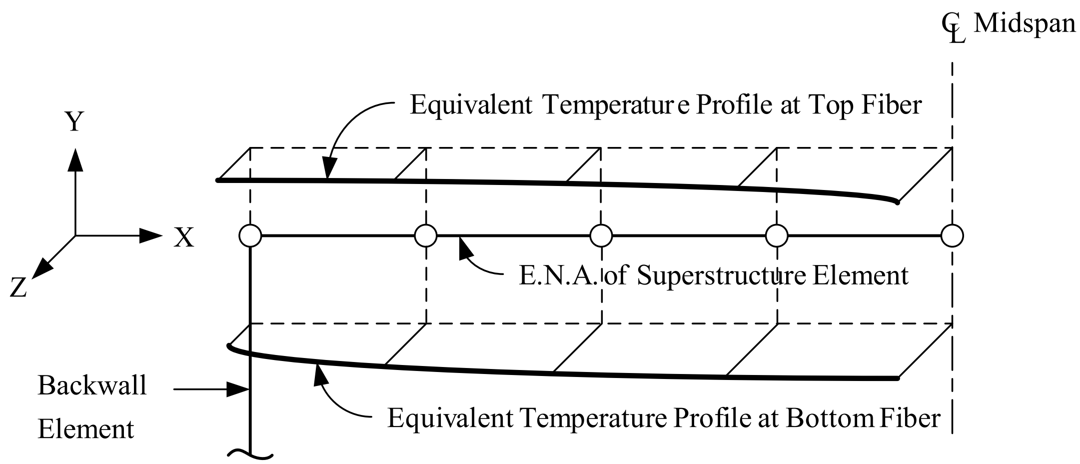

Figure 4-31: Equivalent Temperatures on 2-D Model

Equivalent temperatures for the 3-D models are varied from element to element. Figure 4-32 presents a sample contour plot of the equivalent temperatures on the full length of the bridge 222 interior girder and slab.

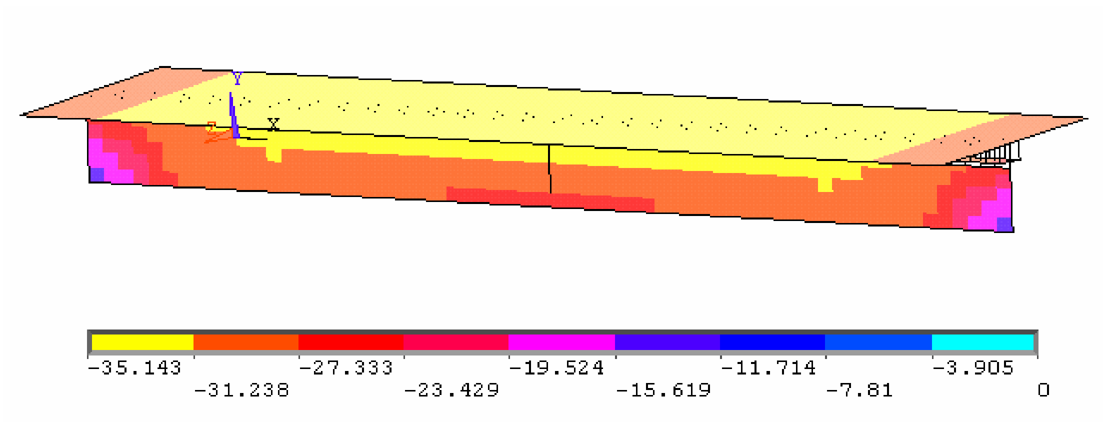

Figure 4-32: Equivalent Temperatures on 3-D Model (Bridge 222)

Calculated equivalent temperatures for interior and exterior girders in each 3-D FE model are different due to unequal effective slab widths. Detailed calculations for both girder types are also presented in Appendix B.

4.4 Types of Analysis and Convergence Criteria

4.4.1 Type of Analysis

Due to a significant simulation period for temperature cyclic loadings, a quasi-static analysis is adequate and acceptable for a time-history problem in the present study. In general, there are two widely accepted analysis methods for this time-history problem: explicit and implicit direct integration.

The choice of methods strongly depends upon a problem type [30]. In the explicit direct integration method, a small time-step size is required to ensure numerical stability, known as conditionally stable; thus, this method is generally appropriate for a high velocity problem. On the contrary, for the implicit method, there is no restriction for time-step size regarding numerical stability, known as unconditionally stable. Therefore, accuracy and convergence are the only main factors in selecting a time-step size, which is ideal for a low velocity problem. In this study the implicit method was adopted because a prolonged time-step size is required to cover a significantly long simulation time.

ANSYS [9] provides two alternate algorithms for the implicit direct integration: Newmark and Hilber-Hughes-Taylor (HHT). The HHT algorithm is essentially an improved Newmark version that yields more accurate results for high frequency modes. Because this improvement did not offer any advantage to the present problem, the Newmark algorithm was deemed sufficient.

There are several well-known solution methods available in ANSYS, including Newton-Raphson, modified Newton-Raphson, and initial stiffness for material nonlinearity analyses. Each method has both advantages and disadvantages concerning a computation time trade-off. ANSYS provides an option to select the most efficient method automatically, which was adopted in this study. A convergence accelerator available in ANSYS, known as line search [122], was also used to reduce computation time.

4.4.2 Convergence Criteria

Iterative processes are always encountered for all types of material nonlinearity solution methods. Convergence criteria are necessary to set a standard to terminate an iterative step for advancing to the next step. In a structural problem, a L2-norm is commonly implemented to compute a scalar number that represents residual quantities that could be force, moment, displacement, or rotation vectors. When a ratio of residual L2-norm to the reference L2-norm, *i.e.* $\left\|\{\Delta F\}\right\| / \left\|F_{ref}\right\|$ [9, 30, and 122], falls below a predefined tolerance, an analysis of the current iterative is said to converge, which allows the solver to progress to the next iterative step. In this study force and displacement quantities were monitored and set as convergence criteria. A tolerance of 0.001, suggested by Cook *et al* [30] for the 32-bit computer architecture and established as an ANSYS default, was used for both force and displacement convergence criteria.

Chapter 5

Condensed Hysteresis Model

5.1 General

A condensed hysteresis model is proposed to provide an alternative and simple IA bridge model that can be easily implemented. Only two unknowns within a condensed hysteresis model must be defined in order to reduce the significant computation time typically required for FE model analyses. Although condensed hysteresis models are intended to be simple, the complexity of influencing parameters: hysteretic and non-hysteretic (time-dependent) behaviors, are fully incorporated, using hysteresis elements and equivalent temperatures similar to what was employed in the FE models.

The outlined procedure and all hysteresis elements discussed in Chapter 3 are presented in more detail in this chapter. The Duhem hysteresis model is used for development of a soil-pile interaction hysteresis element, and the elasto-plastic hysteresis model is used for representing soil-abutment interaction and abutment-backwall connection hysteresis elements. In addition, the application of numerical schemes to solve a differential equation of each hysteresis element is provided. All hysteresis elements serve as a nonlinear hysteresis spring for a condensed hysteresis model.

A procedure to condense degrees of freedom by applying appropriate model assumptions, boundary conditions, and constraint equations is presented to construct a condensed hysteresis model. This procedure is initially carried out using linear spring elements to simplify the development procedure. Subsequently, replacement of linear springs by nonlinear hysteresis elements can be conveniently performed. Finally, a similar numerical solution method, commonly used in the FE approach, is discussed and applied to obtain a solution for a condensed hysteresis model. Implementation using MATLAB is also conducted and provided in Appendix C.

This chapter consists of five subsections. Section 5.2 describes the development procedure of a soil-pile interaction hysteresis element and the application of numerical schemes. Section 5.3 demonstrates the application of numerical schemes to the soil-abutment interaction and abutment-backwall connection hysteresis elements presented in Chapter 3. Section 5.4 presents the development procedure of a condensed hysteresis model. Model assumptions, boundary conditions, and constraint equations are provided in this section. Finally, Section 5.5 covers time-dependent effect consideration for condensed hysteresis models.

5.2 Development of a Soil-Pile Interaction Hysteresis Element

In this section a soil-pile interaction hysteresis element is developed. As outlined in Section 3.5.1, a transformation of a two-dimensional pile model into hysteresis elements, $\overline{K}_{22}$ and $\overline{K}_{33}$, at the pile head is required. The Duhem Model is used to provide a framework for hysteresis element development. The advantages of using the Duhem Model as opposed to other hysteresis models are to:

- provide capability to generate interior hysteresis loops and
- use an initial boundary value problem as a starting point.

which are necessary for the physical problem presented in this study. After differential equations are obtained, a numerical scheme can be applied.

In order to develop a soil-pile interaction hysteresis element at the pile head using the Duhem Model, the following four steps must be completed: (1) determine load-deformation curves at pile head; (2) develop tangent slope equations from load-deformation curves; (3) assign tangent slope equations to the Duhem equation to obtain differential equations that represent soil-pile interaction hysteresis model; and (4) apply a numerical solution scheme to the resulting differential equations to obtain results. All four steps are described in Sections **5.2.1** to **5.2.4**, respectively.

5.2.1 Load-Deformation Curves at Pile Head

Load-deformation curves at the pile head are typically used to determine foundation stiffness at a convenient interactive boundary between structural and geotechnical tasks. Foundation stiffness may be generated by using LPILE [**66**] - a geotechnical program based on the *p-y* curve method. Although load-deformation curves and foundation stiffness may be determined from any other nonlinear soil-pile interaction approach, ANSYS pile models (also based on the *p-y* curve method) as described in Section **3.2.1**, are consistently used to generate all load-deformation curves in this study.

Two types of load-deformation curves for condensed hysteresis models are required to determine nonlinear hysteresis elements, $\overline{K}_{22}$ and $\overline{K}_{33}$. The first type of load-deformation curve ($\overline{K}_{22}$) is a relationship between displacement and force reaction at the pile head. The second type of load-deformation curves is a relationship between rotation and moment reaction at the pile head ($\overline{K}_{33}$).

In order to generate load-deformation curves for both types, certain boundary conditions need to be specified at the pile head. For a displacement and force reaction curve, the rotational degree of freedom at the pile head needs to be restrained, while displacements are incrementally enforced to obtain corresponding incremental force reactions. Likewise, for a rotation and moment reaction curve, a translational degree of freedom at the pile head needs to be locked, while rotations are incrementally applied to obtain corresponding incremental moment reactions.

In this section, all load-deformation curves obtained from ANSYS pile models (see also Section **3.2** for ANSYS pile models) are presented and discussed. For each graph presented in Figures **5-1** to **5-4**, there are five curves, representing the ANSYS pile models for bridge 203, abutment 1 of bridge 211, abutment 2 of bridge 211, abutment 1 of bridge 222, and abutment 2 of bridge 222, respectively. The notations A1 and A2 stand for abutment 1 and abutment 2, respectively. Differences in displacement/rotation ranges on each graph are due to differences in corresponding free thermal expansion determined from each bridge length. Therefore, the displacement/rotation range for bridge 203 is the longest, while the displacement/rotation range for bridge 222 is the shortest. For contraction and expansion cases of all three instrumented bridges, displacement and force reaction curves are presented in Figures **5-1** and **5-2**, respectively.

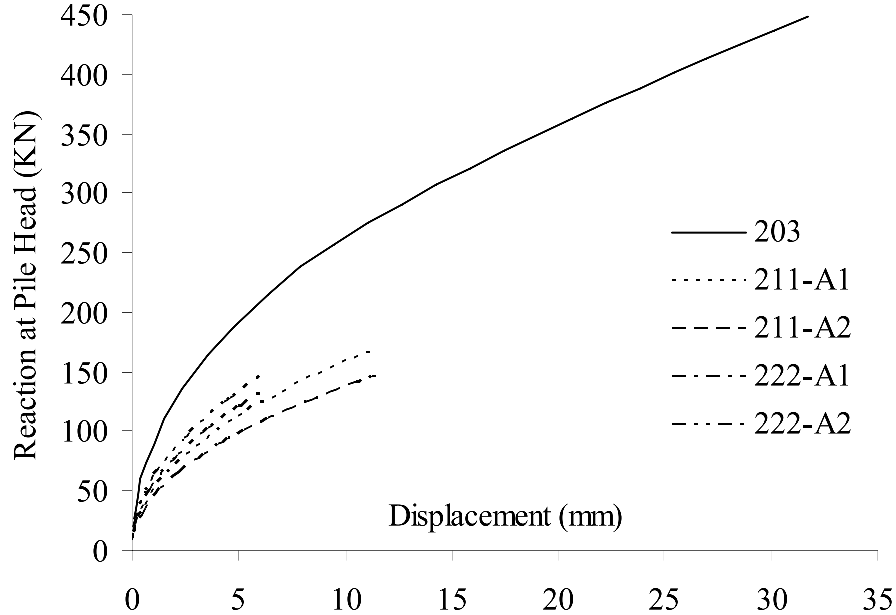

Figure 5-1: Displacement-Force Reaction Curve for Contraction Case

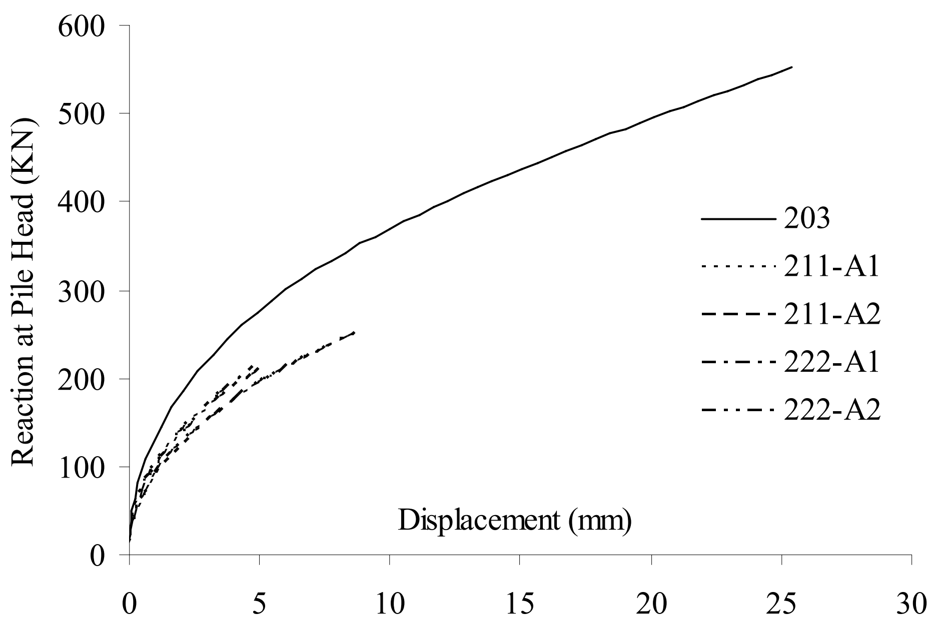

Figure 5-2: Displacement-Force Reaction Curve for Expansion Case

Similarly, for contraction and expansion cases of all three bridges, rotation and moment reaction curves are presented in Figures 5-3 and 5-4, respectively.

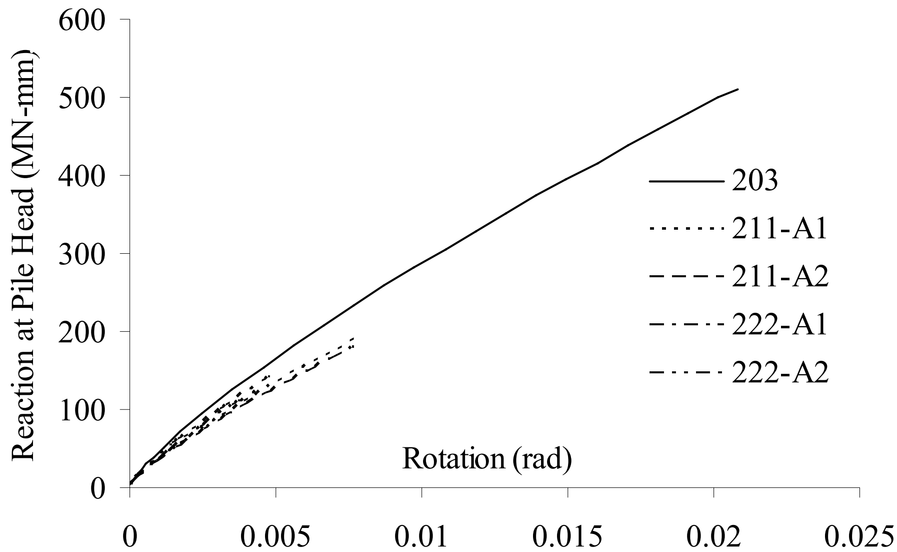

Figure 5-3: Rotation-Moment Reaction Curve for Contraction Case

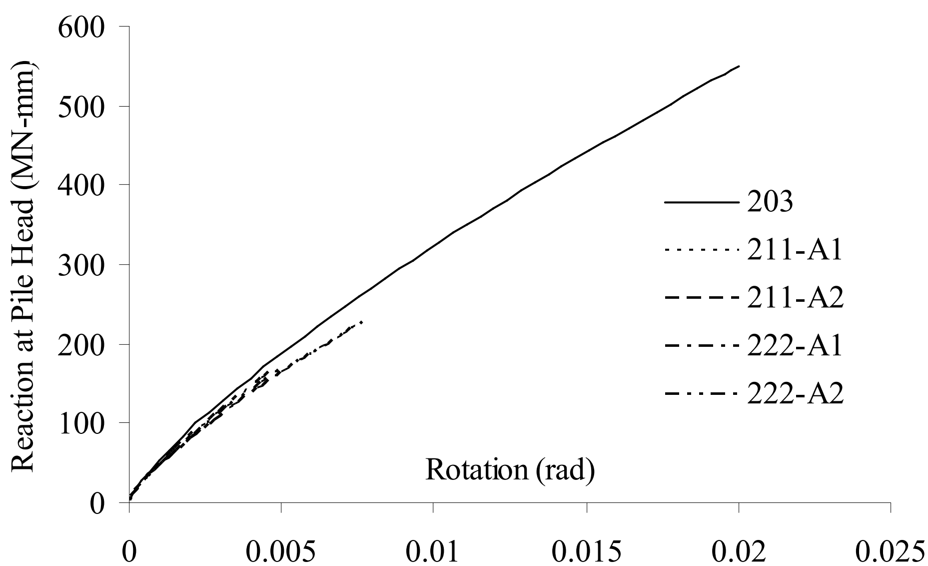

Figure 5-4: Rotation-Moment Reaction Curve for Expansion Case

It can be observed from Figures 5-1 to 5-4 that all load-deformation curves are to some degree nonlinear with softening as deformation increases. In terms of both strength and stiffness, bridge 203 piles are the strongest and bridge 211 piles are the weakest. The reaction magnitudes of bridge 211 (and 222) of two integral abutment piles are comparatively the same. All curves presented in this section are used to construct equations of load-deformation tangent slopes discussed in Section 5.2.2.

5.2.2 Equations for Load-Deformation Tangent Slopes

In this section a procedure to obtain equations of load-deformation tangent slopes is developed to construct a hysteresis element based on the Duhem Model. The load-deformation curves that are generated, using the ANSYS pile models as presented in Section 5.2.1, are used. Taking x as deformation (displacement/rotation) and y as load (force/moment reaction), a load-deformation tangent slope at any point of each load-deformation curve can be obtained from the ratio of incremental load (dy) to incremental deformation (dx). To determine an equation for load-deformation tangent slopes, deformations (x) versus load-deformation tangent slopes ($y' = dy/dx$) are plotted in Figures 5-5 to 5-8. Displacements versus displacement-force reaction tangent slopes for contraction and expansion cases are presented in Figures 5-5 and 5-6, respectively. Similarly, rotations versus rotation-moment reaction tangent slopes for contraction and expansion cases are presented in Figures 5-7 and 5-8, respectively. It is noted that natural logarithms are used for both axes to demonstrate a nearly straight line, which offers a better visualization for curve fittings.

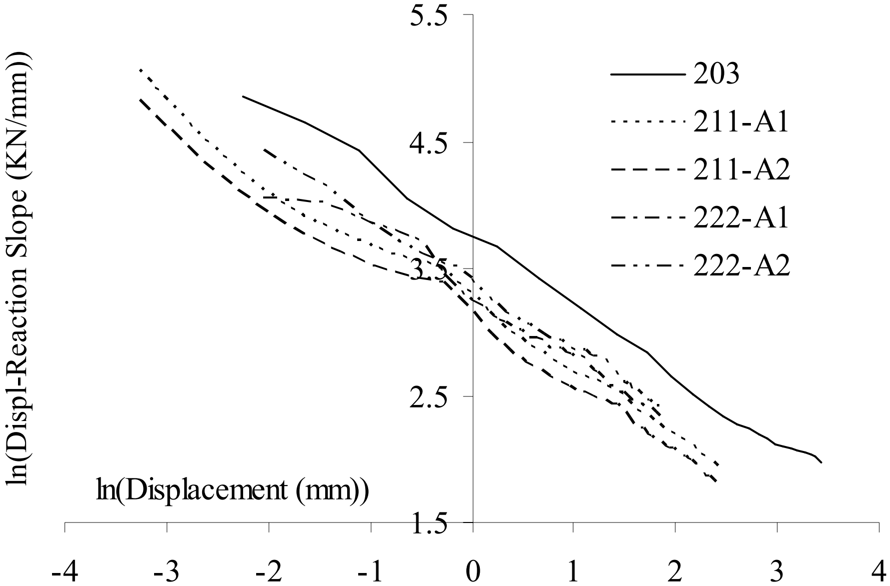

Figure 5-5: Displacement Versus Displacement-Force Reaction Tangent Slope in Natural Logarithm for Contraction Case

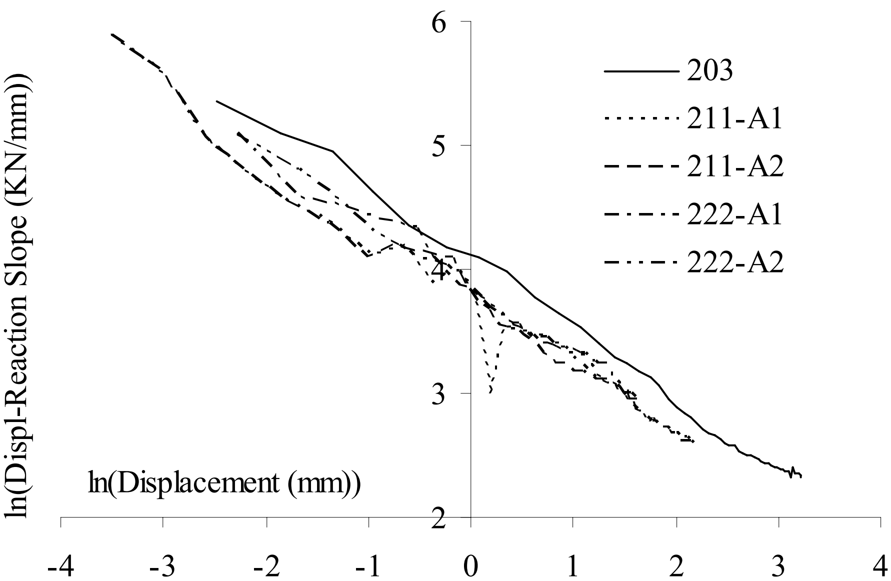

Figure 5-6: Displacement Versus Displacement-Force Reaction Tangent Slope in Natural Logarithm for Expansion Case

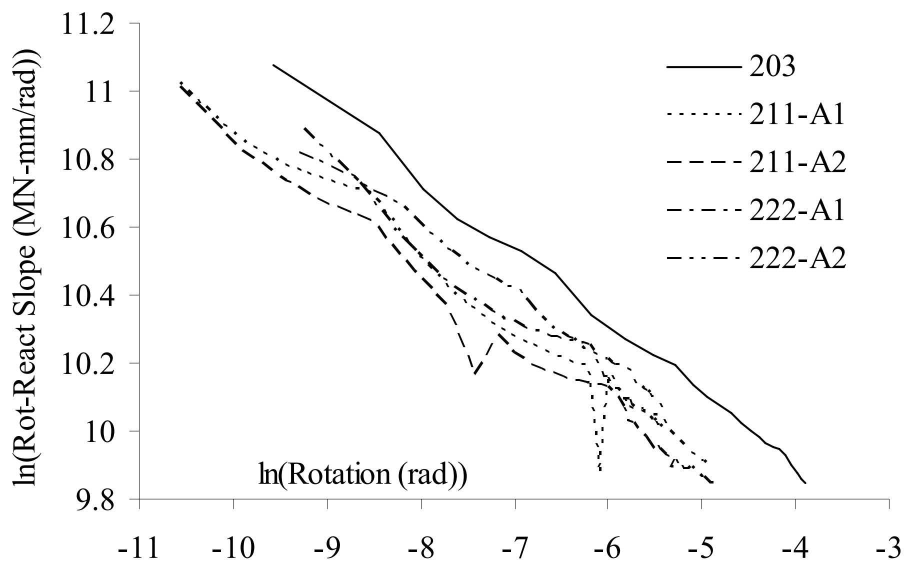

Figure 5-7: Rotation Versus Rotation-Moment Reaction Tangent Slope in Natural Logarithm for Contraction Case

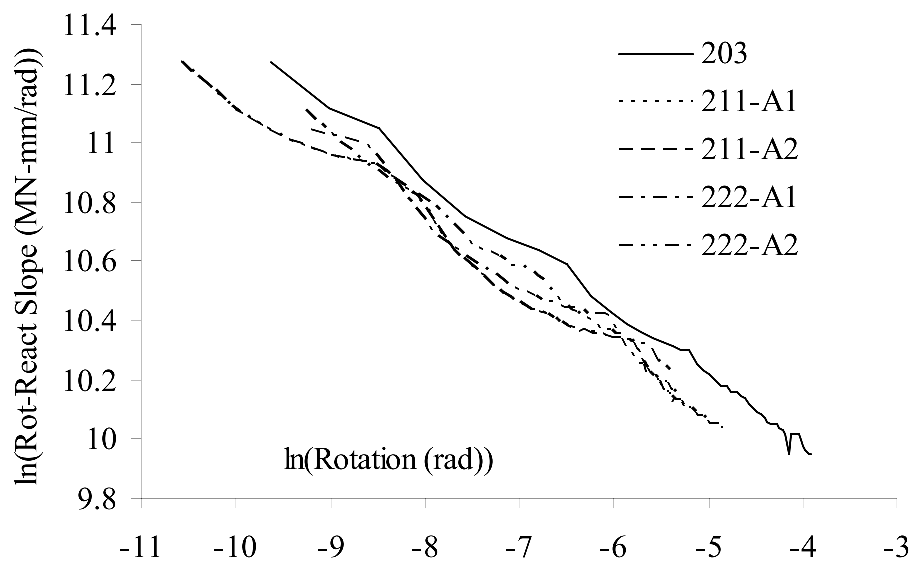

Figure 5-8: Rotation Versus Rotation-Moment Reaction Tangent Slope in Natural Logarithm for Expansion Case

After plotting deformations (x) versus load-deformation tangent slopes (y') on ln-ln scale, the results approximate a straight line. Therefore, linear regression can be employed to obtain the best fit equation in the form:

$$\ln(y') = m\ln(x) + C \tag{5-1}$$

where m is a slope of the linear regression equation (not a load-deformation tangent slope) and C is a coefficient value. Equation 5-1 can be rewritten as:

$$e^{\ln(y')} = e^{m\ln(x)+C} \tag{5-2}$$

$$y' = e^{C}x^{m} \tag{5-3}$$

Table 5-1 presents linear regression equations for displacement-force reaction tangent slopes in both forms along with R^2 values for all three bridges.

Table 5-1: Equations for Displacement-Force Reaction Tangent Slopes

Case	Bridge	$\ln(y') = m\ln(x) + C$	$y' = e^{C}x^{m}$	R^2
Contraction	203	$\ln(y') = -0.5\ \ln(x) + 3.653$	$y' = 38.572\ x^{-1/2}$	0.984
	211	$\ln(y') = -0.5\ \ln(x) + 3.092$	$y' = 22.027\ x^{-1/2}$	0.914
	222	$\ln(y') = -0.5\ \ln(x) + 3.315$	$y' = 27.534\ x^{-1/2}$	0.954
Expansion	203	$\ln(y') = -0.5\ \ln(x) + 3.917$	$y' = 50.263\ x^{-1/2}$	0.957
	211	$\ln(y') = -0.5\ \ln(x) + 3.703$	$y' = 40.561\ x^{-1/2}$	0.895
	222	$\ln(y') = -0.5\ \ln(x) + 3.809$	$y' = 45.124\ x^{-1/2}$	0.970

The parameters m obtained from the best fit varied from -0.56 to -0.456 with an average value of -0.523 with R^2 values ranging from 0.896 to 0.988. Therefore, to simplify further equation derivative/integration, it was accepted that m = -0.5 = -1/2 is taken for all equations with the corresponding R^2 values presented in Table 5-1. The maximum and average percent decreases of R^2 values between the cases before and after taking m = -0.5

are 2.54 and 0.13, respectively, indicating insensitivity to this change. A sample of linear regression lines overlaid onto Figure 5-5 is presented in Figure 5-9.

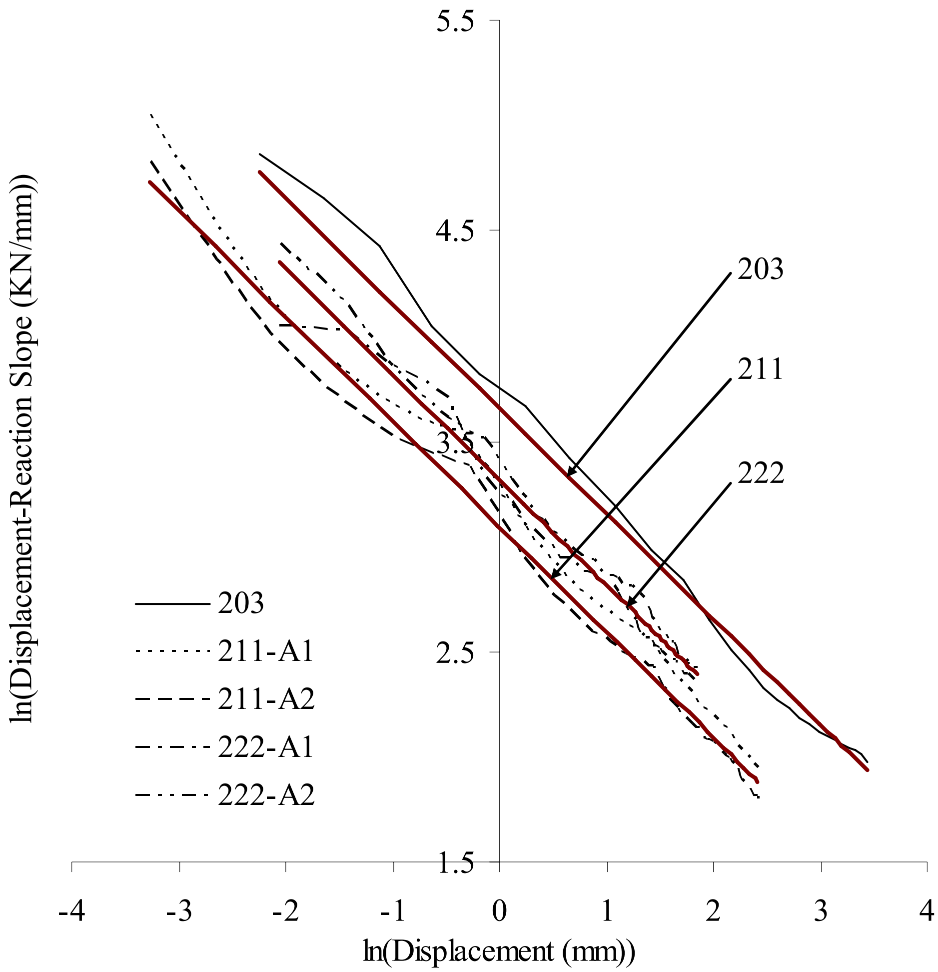

Figure 5-9: Linear Regression Equations of the Case Presented in Figure 5-5

Analytical integration with initial values of $x(0) = y(0) = 0$ to an equation for load-deformation tangent slopes can be performed to verify the load-deformation curve from ANSYS. For demonstration purposes, the first equation in Table 5-1 is integrated such that:

$$\int dy = \int \left(38.57167 x^{-1/2} \right) dx, \text{ and } \Rightarrow y = 2 \times 38.57167 x^{1/2} \quad (5\text{-}4)$$
$$x(0) = y(0) = 0.$$

A sample of the integrated slope equations overlaid onto Figure 5-1 is presented in Figure 5-10. The average R^2 value for the comparison between the load-deformation curves from ANSYS and the integrated tangent slope equations is 0.975.

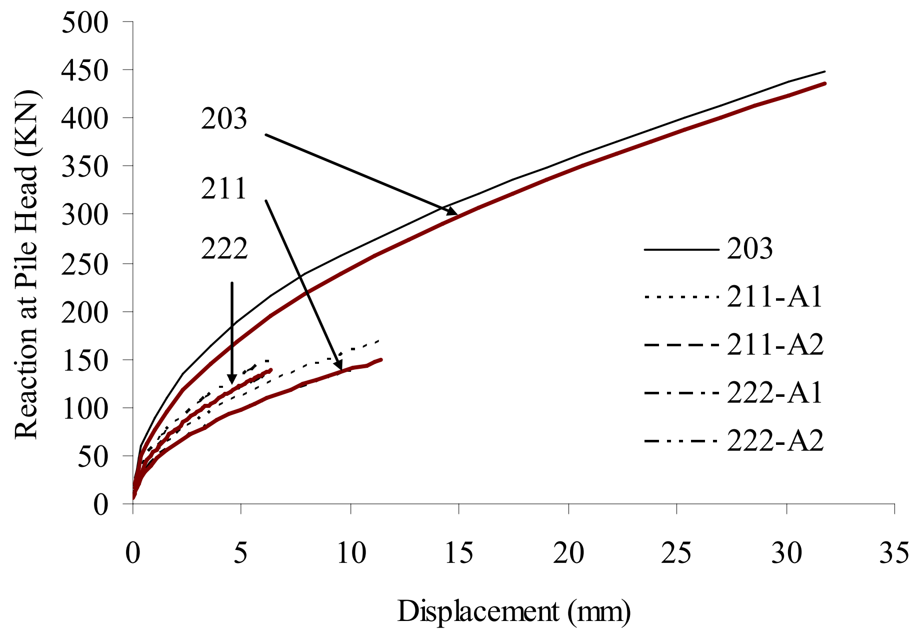

Figure 5-10: Integrated Slope Equations of the Case Presented in Figure 5-1

The same procedure is also applied to linear regression equations for rotation-moment reaction tangent slopes. Table 5-2 presents these equations in both forms for all three bridges.

Table 5-2: Equations for Rotation-Moment Reaction Tangent Slopes

Case	Bridge	$\ln(y') = m\ln(x) + C$	$y' = e^{C}x^{m}$	R^2
Contraction	203	$\ln(y') = -0.2\ \ln(x) + 9.115$	$y' = 9091.4\ x^{-1/5}$	0.9998
	211	$\ln(y') = -0.2\ \ln(x) + 8.883$	$y' = 7206.2\ x^{-1/5}$	0.9979
	222	$\ln(y') = -0.2\ \ln(x) + 8.972$	$y' = 7882.7\ x^{-1/5}$	0.9987
Expansion	203	$\ln(y') = -0.2\ \ln(x) + 9.214$	$y' = 10041.1\ x^{-1/5}$	0.9991
	211	$\ln(y') = -0.2\ \ln(x) + 9.094$	$y' = 8898.4\ x^{-1/5}$	0.9984
	222	$\ln(y') = -0.2\ \ln(x) + 9.149$	$y' = 9406.1\ x^{-1/5}$	0.9987

In this case the parameters m obtained from the best fit varied from -0.2291 to -0.1983 with an average value of -0.1929. Therefore, it was accepted that m = -0.2 = -1/5 is taken for all equations to simplify further equation derivative/integration. In addition, R^2 values obtained from the case after taking m = -0.2 as presented in Table 5-2 are almost 1.0, indicating insensitivity to this change. An equation for rotation-moment reaction tangent slopes, after taking integration and incorporating initial values of $x(0) = y(0) = 0$, is in the form:

$$y = \frac{5}{4}e^{C}x^{4/5} \tag{5-5}$$

It can be observed that all slope equations in Tables 5-1 and 5-2 are a C-Infinity function because their derivatives are not continuous at x = 0. However, all these slope equations are consistent with the *p-y* curve equation that appears in the form, $y = [\text{coeff}] \cdot x^{1/4}$ (See Equation 3-2). In addition, an absolute value of x is applied to the equations for displacement-force reaction tangent slopes to accommodate the negative sign of x for the unloading case. The general form of Equation 5-4 can be rewritten as:

$$y = [\text{coeff}]\,\text{sgn}(\dot{x})|x|^{1/2} \tag{5-6}$$

where $\dot{x}$ is a displacement rate $= \dfrac{dx}{dt}$,

sgn($\dot{x}$) is a signum function $= \begin{cases} -1, & \dot{x} < 0 \\ 0, & \dot{x} = 0 \\ 1, & \dot{x} > 0 \end{cases}$, and

coeff is a real number coefficient obtainable from curve fittings.

5.2.3 Equations for Soil-Pile Interaction Hysteresis Model

In this section the equations of load-deformation tangent slopes developed in Section 5.2.2 are applied to Equation 3-7. It is recalled from Section 3.5.1 in Chapter 3 that two nonlinear hysteresis springs need to be determined: $\overline{K}_{22}$ and $\overline{K}_{33}$. Because the procedure for determining nonlinear hysteresis spring stiffness is identical, only $\overline{K}_{22}$ is demonstrated in detail. The displacement-force reaction tangent slope relationship for the contraction case of $\overline{K}_{22}$ is presented as:

$$\frac{dy^C}{dx} = C_1|x|^{-1/2} \tag{5-7}$$

where x is a displacement, y is a force reaction, and C_1 is a coefficient value obtained from regression. Similarly, for the expansion case, the relationship for displacement-force reaction tangent slopes is written as:

$$\frac{dy^E}{dx} = C_2|x|^{-1/2} \tag{5-8}$$

where C_2 is a coefficient value obtained from the regression method. Substituting Equation 5-7 and Equation 5-8 into Equation 3-7 yields an initial boundary value problem as presented below:

$$\begin{aligned} &\frac{dy}{dt}(t) = \begin{cases} C_1 |x|^{-1/2}\dot{x}, \dot{x}(t) > 0 \\ C_2 |x|^{-1/2}\dot{x}, \dot{x}(t) < 0 \end{cases} \\ &y(0) = y_o \\ &x(0) = x_o \end{aligned} \tag{5-9}$$

where x_o and y_o are initial values for x and y respectively.

In order to ensure that the proposed equation for displacement-force reaction tangent slopes is bounded to an arbitrary positive constant λ, the Lipschitz condition needs to be satisfied. Referring to Equation 2-10,

$$\begin{aligned} (y_1 - y_2)[f_I(y_1, x) - f_I(y_2, x)] &\leq \lambda(x)(y_1 - y_2)^2 \\ (y_1 - y_2)[f_D(y_1, x) - f_D(y_2, x)] &\geq -\lambda(x)(y_1 - y_2)^2 \end{aligned},$$

as a starting point, substituting an increasing slope $f_I = \frac{dy^C}{dx} = C_1 x^{-1/2}$ and its integral equation $y = 2C_1 x^{1/2}$ into the first expression in Equation 2-10 leads to the following inequality:

$$\left(2C_1 x_1^{1/2} - 2C_1 x_2^{1/2}\right)\left(C_1 x_1^{-1/2} - C_2 x_2^{-1/2}\right) \overset{?}{\leq} \lambda\left(2C_1 x_1^{1/2} - 2C_1 x_2^{1/2}\right)^2 \tag{5-10}$$

where f_I is an increasing slope = a displacement-force reaction tangent slope for the contraction case, f_D is a decreasing slope = a displacement-force reaction tangent slope for the expansion case, and the subscripts 1 and 2 are used to distinguish 2 arbitrary sets of adjacent x and y values. By rearranging Equation **5-10**, the positive coefficient C_1 is cancelled out:

$$2-\frac{(x_1+x_2)}{(x_1x_2)^{1/2}}\overset{?}{\leq}2\lambda\left(x_1^{1/2}-x_2^{1/2}\right)^2 \qquad (\textbf{5-11})$$

The left-hand-side term in Equation **5-11** is rearranged such that:

$$\frac{-\left(x_1^{1/2}-x_2^{1/2}\right)^2}{(x_1x_2)^{1/2}}\overset{?}{\leq}2\lambda\left(x_1^{1/2}-x_2^{1/2}\right)^2 \qquad (\textbf{5-12})$$

since x_1 and x_2 must be positive (absolute values are required as expressed in Equation **5-6**), the term $\left(x_1^{1/2}-x_2^{1/2}\right)^2$ exists and is also positive:

$$\frac{-1}{2(x_1x_2)^{1/2}}\overset{?}{\leq}\lambda \qquad (\textbf{5-13})$$

which satisfies the Lipschitz condition because $(x_1x_2)^{1/2}$ is positive. Similarly, another proof for a decreasing curve (expansion case) can be performed, which yields the same result as in Equation **5-13**.

An initial boundary value problem for $\overline{K}_{33}$ is constructed from the equations for rotation-moment reaction tangent slopes as written below:

$$\begin{aligned}&\frac{dy}{dt}(t)=\begin{cases}C_3|x|^{-1/5}\dot{x}, \dot{x}(t)>0\\ C_4|x|^{-1/5}\dot{x}, \dot{x}(t)<0\end{cases}\\ &y(0)=y_o\\ &x(0)=x_o\end{aligned} \qquad (\textbf{5-14})$$

where x is a rotation, y is a moment reaction, C_3 and C_4 are coefficient values obtained from regression. A procedure to satisfy the Lipschitz condition is similar to the step presented from Equations 5-10 to 5-13. The finial results for increasing and decreasing curves are identical and written below:

$$\frac{-4\left(x_1^{1/5}-x_2^{1/5}\right)}{5(x_1x_2)^{1/5}\left(x_1^{4/5}-x_2^{4/5}\right)} \overset{?}{\leq} \lambda \qquad (5\text{-}15)$$

which also satisfies the Lipschitz condition because $\left(x_1^{1/5}-x_2^{1/5}\right)\Big/\left(x_1^{4/5}-x_2^{4/5}\right)$ and $(x_1x_2)^{1/5}$ are positive regardless of $x_1 > x_2$ or $x_1 < x_2$.

5.2.4 Numerical Scheme

In order to solve Equations 5-9 and 5-14, a numerical scheme is required. In this study the Euler forward method, one of the simply implemented numerical algorithms, is adopted. With respect to time, a standard equation of this method is expressed as [62]:

$$y(t+h) = y(t) + h \cdot \dot{y}(t) \qquad (5\text{-}16)$$

where y is a force reaction, $\dot{y}$ is a force reaction rate, and h is a time step.

In case of a monotonic increasing displacement, x, Equation 5-16 is substituted by the expression in Equation 5-9 for the contraction case ($\frac{dy}{dt} = \mathrm{C}_1|x|^{-1/2}\dot{x}$), leading to:

$$y(t+h) = y(t) + h \cdot \mathrm{C}_1|x(t)|^{-1/2}\frac{(x(t+h)-x(t))}{h} \qquad (5\text{-}17)$$

where a time step h on the right-hand-side term is cancelled out. It is observed that all variables on the right-hand-side term are known *a priori*, thus, $y(t+h)$ can be computed from each iterative step and then becomes $y(t)$ for subsequent iterative steps. The initial values in Equation **5-9** ($y(0) = y_o$ and $x(0) = x_o$) serve as the initial iterative step.

In case of unloading, the semi-group identity (Equation **2-6** in Chapter 2) is applied. This mathematical property has also been applied to the modified Ramberg-Osgood and hyperbolic hysteresis models, as can be observed in Equations **2-27**, **2-28**, **2-30**, and **2-31**. When the $\dot{x}(t)$ sign is reversed, the expression in Equation **5-9** for the expansion case ($\frac{dy}{dt} = \mathrm{C}_2 |x|^{-1/2} \dot{x}$) is taken. Additional parameters, $x_c(t_1)$ and $y_c(t_1)$ representing magnitudes of $x(t)$ and $y(t)$ at the time reversal t_1, are required to account for memory effects. The numerical solution for an unloading case is written as:

$$y(t+h) = y(t) + \mathrm{C}_2 |x(t) - x_c(t_1)|^{-1/2} \big(x(t+h) - x(t)\big), \text{for } t \geq t_1 \qquad \textbf{(5-18)}$$

Because the load-deformation equations are also taken as a hysteresis boundary, $y_c(t_1)$ cannot be smaller than zero for an unloading case ($\dot{x}(t) < 0$). In any case, if $y_c(t_1)$ appears to be smaller than zero, magnitudes of $x_c(t_1)$ and $y_c(t_1)$ need to be shifted, so as to enforce an unloading curve bounded by a hysteresis boundary as the following expressions:

$$\begin{aligned} x_c(t_1)_{shifted} &= x_c(t_1) + \left| \frac{y_c(t_1)}{2\mathrm{C}_2} \right|^2, \\ y_c(t_1)_{shifted} &= 0. \end{aligned} \qquad \textbf{(5-19)}$$

A step function is required to present a general form of a numerical scheme that can accommodate both unloading and reloading cases. Such a step function is written as:

$$S\left(\dot{x}(t)\right) = \begin{cases} \mathrm{C}_1, \dot{x}(t) \geq 0 \\ \mathrm{C}_2, \dot{x}(t) \leq 0 \end{cases} \tag{5-20}$$

and the general form of the numerical scheme is written as:

$$\begin{aligned} y(t+h) &= y(t) + S\left(x(t+h)-x(t)\right)\left(x(t+h)-x(t)\right) \\ &\times \left| x(t) - x_c(t_n) - \max\begin{pmatrix} \operatorname{sgn}\left(x(t+h)-x(t)\right)\operatorname{sgn}\left(y_c(t_n)\right) \\ \times \left| y_c(t_n) \big/ 2S\left(x(t+h)-x(t)\right) \right|^2, 0 \end{pmatrix} \right|^{-1/2}, \text{for } t \geq t_n \end{aligned} \tag{5-21}$$

where t_n is current time at the displacement reversal. Sample hysteresis loops in which applied displacements and model properties are taken from the last convergence case study in Section **3.2.4** is presented in Figure **5-11**. The dotted line represents a hysteresis loop determined analytically from Equation **5-6** and the continuous line represents a hysteresis loop determined numerically from Equation **5-21**. The maximum difference between these two methods is approximately 6 percent. In addition, a steady-state hysteresis loop can be observed.

A tangent slope that indicates the magnitude of the nonlinear spring, $\overline{K}_{22}$, can be obtained from:

$$\overline{K}_{22}\left(x(t+h), y(t+h)\right) = \frac{y(t+h)-y(t)}{x(t+h)-x(t)} \tag{5-22}$$

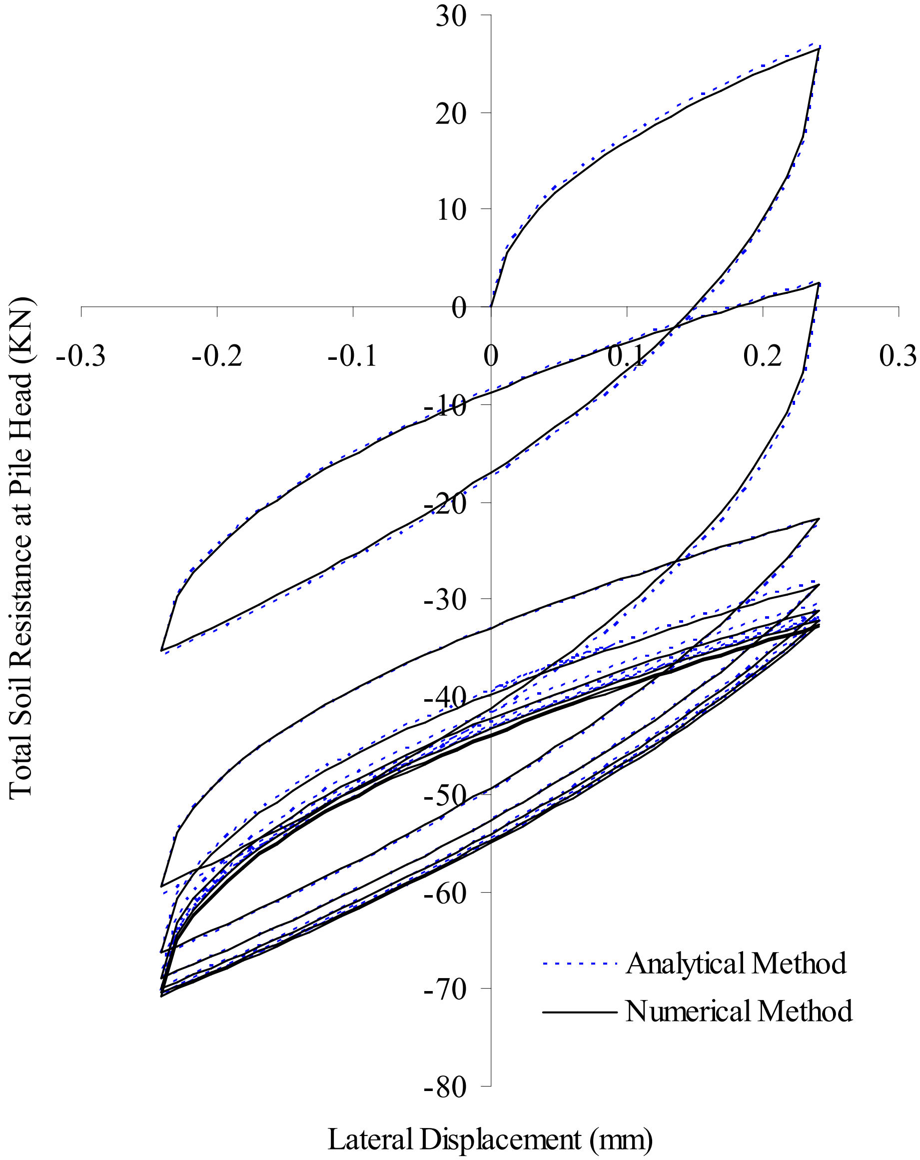

Figure 5-11: Displacement and Pile Head Resistance Hysteresis Loops

The same procedure can be used for numerical scheme of the nonlinear spring, $\overline{K}_{33}$. Therefore, the general form of this particular case is written as:

$$y(t+h) = y(t) + S\big(x(t+h) - x(t)\big)\big(x(t+h) - x(t)\big)$$
$$\times \left| x(t) - x_c(t_n) - \max\begin{pmatrix} \operatorname{sgn}\big(x(t+h) - x(t)\big)\operatorname{sgn}\big(y_c(t_n)\big) \\ \times \left| 4y_c(t_n) \big/ 5S\big(x(t+h) - x(t)\big) \right|^{5/4}, 0 \end{pmatrix} \right|^{-1/5}, \text{ for } t \geq t_n \tag{5-23}$$

where x and y stand for rotation and moment reaction, respectively. A step function used in Equation 5-23 is expressed as:

$$S\big(\dot{x}(t)\big) = \begin{cases} \mathrm{C}_3, \dot{x}(t) \geq 0 \\ \mathrm{C}_4, \dot{x}(t) \leq 0 \end{cases} \tag{5-24}$$

A tangent slope that indicates the magnitude of the nonlinear spring, $\overline{K}_{33}$, can be obtained from:

$$\overline{K}_{33}\big(x(t+h), y(t+h)\big) = \frac{y(t+h) - y(t)}{x(t+h) - x(t)} \tag{5-25}$$

The Euler forward method requires a small time step size to ensure accuracy and numerical stability. In this study, due to a few degrees of freedom being involved, analysis per iteration is very inexpensive, therefore, a considerably small time step can be assigned in order to avoid numerical instability.

5.3 Soil-Abutment Interaction and Abutment-Backwall Connection Hysteresis Elements

Similar to the numerical procedure for the soil-pile interaction hysteresis elements, the Euler forward method can be applied to soil-abutment interaction and abutment-backwall connection hysteresis elements. Differential equations for soil-abutment interaction and abutment-backwall connection hysteresis elements are referred to in Sections 3.5.2 and 3.5.3, respectively. In this section a similar procedure to obtain a general form of the numerical scheme presented in Section 5.2.4 is adopted in which a soil-abutment hysteresis element is used for demonstration. A numerical form for this hysteresis element derived from the differential equation (Equation 3-8) is written as:

$$
\begin{aligned}
&u(t+h) = u(t) + \left(x(t+h) - x(t)\right) \\
&\times \left[\begin{aligned} &H_3\left(x(t+h) - x(t)\right) \cdot H_4\left(u(t) - {\left(P_p - P_a\right)} \big/ {2K_a} \right) \\ &+ H_2\left(x(t+h) - x(t)\right) \cdot H_1\left(u(t) - {\left(P_p - P_a\right)} \big/ {2K_a} \right) \end{aligned} \right]
\end{aligned}
\qquad (5\text{-}26)
$$

where x is a displacement, u is a relative displacement of a spring attached to a Coulomb slip element, P_p is a passive force, P_a is an active force, and K_a is a linear spring derived from a lateral soil stiffness. The initial values, $x(0)$, are taken from Equation 3-11 and force reaction, y, is determined from Equation 3-12, written in a numerical form as:

$$
y(t+h) = K_a u(t+h) + \left(\frac{P_a + P_p}{2} \right) \qquad (5\text{-}27)
$$

Finally, a tangent slope that indicates the magnitude of the nonlinear spring for a soil-abutment interaction, $\overline{K}_a$, can be obtained from:

$$
\overline{K}_a\left(x(t+h), y(t+h)\right) = \frac{y(t+h) - y(t)}{x(t+h) - x(t)} \qquad (5\text{-}28)
$$

which also appears in a similar form as the tangent slopes for the soil-pile interaction, $\overline{K}_{22}$ and $\overline{K}_{33}$ (Equation 5-22 and Equation 5-25).

5.4 Constraint and Condensation Techniques

Constraint and condensation techniques are used as tools to transform a two-dimensional model to a condensed hysteresis model. A concept of these two techniques is extensively documented in many finite element textbooks [*e.g.* **30** and **122**]. As mentioned in Chapter 3, the desired end results of condensed hysteresis models are translational and rotational degrees of freedom at the pile-abutment connection. This location represents a point where structural and geotechnical designs are typically separated. In this study constraint and condensation techniques are used to eliminate all degrees of freedom, except for the translational and rotational degrees of freedoms at the pile head.

In order to make the explanation simpler, linear springs are initially used to present the procedure of constraints and condensations. This initial step along with model assumptions is presented in Section **5.4.1**. Discussed in Section **5.4.2**, a condensed hysteresis model is constructed by replacing linear springs with nonlinear hysteresis springs. Numerical techniques to obtain a solution for the condensed hysteresis model are presented in Section **5.4.3**.

5.4.1 Linear Springs

This section proposes a procedure to reduce degrees of freedom of a simplified 2-D model using constraint and condensation techniques. A set of linear springs is used to construct this 2-D model for this initial step. Figure **5-12** presents the 2-D model representing a single span IA bridge consisting of four translation springs, two rotational springs, five nodes, and three line elements. Detailed descriptions of this 2-D model and the procedure of constraints and condensations are presented in six subsections: (1) general 2-D model description; (2) 2-D model assumptions; (3) 2-D model boundary conditions; (4) constraint transformation matrix; (5) condensed stiffness matrix; and (6) condensed force vector.

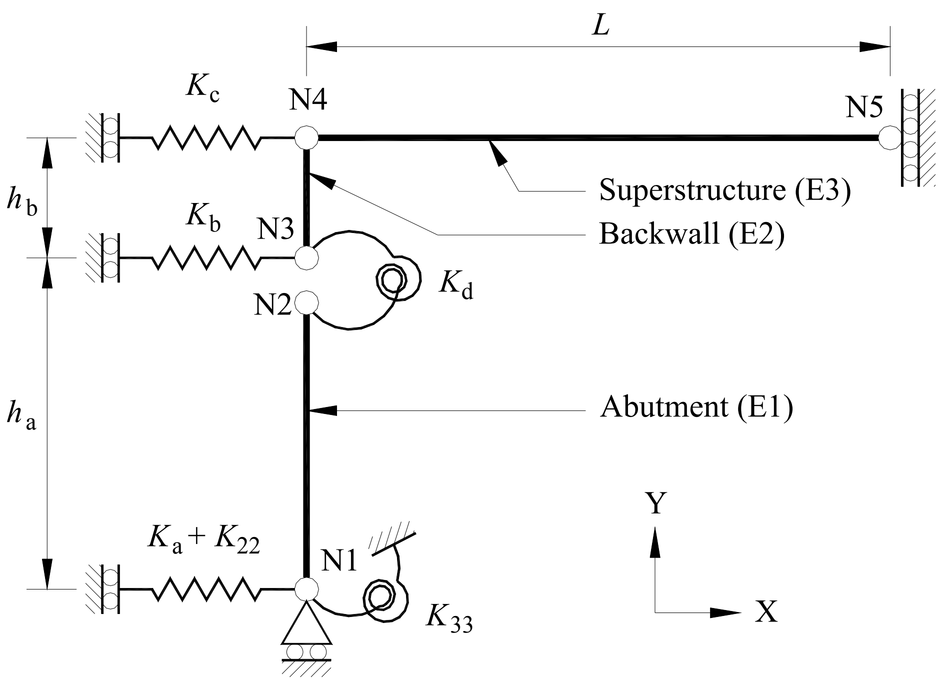

Figure 5-12: Schematic Representation of 2-D Model Prior to Condensation

General 2-D Model Description

General model descriptions and notations are referenced to Figure 5-12 and summarized in Table 5-3.

Table 5-3: 2-D Model Description and Notation

Notation	Description
L	Half the actual bridge length
h_a	Abutment height
h_b	Vertical dimension on backwall measured from the abutment-backwall connection to the elastic neutral axis of the superstructure
N_1 to N_5	Nodes of the 2-D model
E_1 to E_3	Elements of the 2-D model, representing abutment, backwall, and superstructure, respectively
K_a, K_b, and K_c	Linear springs, representing lateral stiffness of soil-abutment interaction
K_{22} and K_{33}	Linear springs, representing lateral and rotational stiffness of soil-pile interaction at the pile head
K_d	Linear spring, representing rotational stiffness of abutment-backwall connection

A standard finite element notation is adopted to define unknowns (degrees of freedom) of the 2-D model as presented in Table 5-4.

Table 5-4: Degrees of Freedom for 2-D Model

Notation	Description
u_1 to u_5	Lateral degrees of freedom for nodes 1 to 5
v_1 to v_5	Vertical degrees of freedom for nodes 1 to 5
θ_1 to θ_5	Rotational degrees of freedom for nodes 1 to 5

2-D Model Assumptions

The following assumptions are applied to the 2-D model to establish criteria for elimination of dependent degrees of freedom:

- The bridge is symmetrical about the superstructure mid-span, half of the structure is modeled.
- The axial deformation of steel H-piles is insignificant, a roller is placed at node 1.
- The coupled stiffness of soil-pile interaction, *i.e.* K_{23} and K_{32}, is insignificant, therefore, this two-coupled stiffness is ignored.
- The abutment and backwall components are sufficiently rigid relative to other elements for bending and axial deformation to be modeled as a rigid.

2-D Model Boundary Conditions

Based on the assumption of bridge symmetry, the boundary conditions at node 5 are $u_5 = \theta_5 = 0$. By neglecting pile axial deformation, the boundary condition at node 1 is $v_1 = 0$. Therefore, three degrees of freedom of the total 15x3 = 15 are eliminated after incorporating these three boundary conditions.

Constraint Transformation Matrix

Based on the assumption that the abutment and backwall are sufficiently rigid relative to other elements for axial deformation, the zero constraints at nodes 1 to 4 are $v_1 = v_2 = v_3 = v_4 = 0$. After incorporating these zero constraints, additional three degrees of freedom are eliminated, reducing a stiffness matrix size to nine.

Based on the assumption that the abutment and backwall are sufficiently rigid relative to other elements for bending, the non-zero constraints are $u_1 = u_2 + h_a\theta_2$, $\theta_1 = \theta_2$, $u_3 = u_4 + h_b\theta_4$, and $\theta_3 = \theta_4$. In addition, nodes 2 and 3 coincide, providing an additional non-zero constraint, $u_2 = u_3$. These non-zero constraints serve to construct the so-called constraint transformation matrix, C_{rc}. The reader is referred to Cook *et al* [30] for the detailed procedure to obtain C_{rc}. In this step, four degrees of freedom (u_1, θ_1, θ_4, and v_5) are kept and five degrees of freedom (u_2, θ_2, u_3, θ_3, and u_4) are eliminated. The constraint transformation matrix is written as:

$$C_{rc} = \begin{bmatrix} 1 & -h_a & 0 & 0 \\ 0 & 1 & 0 & 0 \\ 1 & -h_a & 0 & 0 \\ 0 & 0 & 1 & 0 \\ 1 & -h_a & -h_b & 0 \end{bmatrix} \tag{5-29}$$

The constraint transformation matrix is used for reducing a stiffness matrix size from nine to four. This procedure to apply this constraint transformation matrix will be presented in the condensed stiffness matrix and condensed force vector subsections.

Condensed Stiffness Matrix

A condensed stiffness matrix is derived from the global stiffness matrix of the 2-D model after incorporating the boundary conditions, constraints, and condensation to reduce a matrix size to two desirable unknowns, u_1 and θ_1. After the above defined boundary conditions and zero constraints are employed, the 2-D model stiffness matrix size is reduced to nine, defined as K in Equation 5-30. To apply the constraint transformation matrix, C_{rc}, to eliminate 5 additional degrees of freedom (u_1, θ_2, u_3, θ_3, and u_4), partitioning on K needs to be performed such that:

$$\mathrm{K} = \begin{bmatrix} \mathrm{K}_{rr} & \mathrm{K}_{rc} \\ \mathrm{K}_{cr} & \mathrm{K}_{cc} \end{bmatrix} \tag{5-30}$$

where $\mathrm{K}_{rr} = \begin{bmatrix} K_a + K_{22} & 0 & 0 & 0 \\ 0 & K_{33} & 0 & 0 \\ 0 & 0 & 4\mathrm{EI}/L & -6\mathrm{EI}/L^2 \\ 0 & 0 & -6\mathrm{EI}/L^2 & 12\mathrm{EI}/L^3 \end{bmatrix}$,

E = Reference elastic modulus of the superstructure,

A = Cross sectional area of the superstructure (composite),

I = Moment of inertia of the superstructure (composite),

$\mathrm{K}_{cc} = \begin{bmatrix} 0 & 0 & 0 & 0 & 0 \\ 0 & K_d & 0 & -K_d & 0 \\ 0 & 0 & K_b & 0 & 0 \\ 0 & -K_d & 0 & K_d & 0 \\ 0 & 0 & 0 & 0 & K_c + \mathrm{AE}/L \end{bmatrix}$,

K_{rc} = $[0]_{4x5}$, and

$\mathrm{K_{cr}} \quad = [0]_{5x4}$.

According to Cook *et al* [30], the stiffness matrix, after applying the constraint transformation matrix, K', is:

$$\mathrm{K}' = \mathrm{K_{rr}} + \mathrm{K_{rc}C_{rc}} + \mathrm{C_{rc}^T K_{cr}} + \mathrm{C_{rc}^T K_{cc} C_{rc}}$$

$$= \begin{bmatrix} \begin{matrix} K_a + K_b + K_c \\ + K_{22} + \dfrac{\mathrm{AE}}{L} \end{matrix} & & & Symm. \\ -h_a\begin{pmatrix} K_b \\ + K_c + \dfrac{\mathrm{AE}}{L} \end{pmatrix} & \begin{matrix} K_d + K_{33} \\ + h_a^2 \begin{pmatrix} K_b \\ + K_c + \dfrac{\mathrm{AE}}{L} \end{pmatrix} \end{matrix} & & \\ -h_b\left(K_c + \dfrac{\mathrm{AE}}{L}\right) & \begin{matrix} -K_d \\ + h_a h_b \left(K_c + \dfrac{\mathrm{AE}}{L}\right) \end{matrix} & \begin{matrix} K_d \\ + h_b^2\left(K_c + \dfrac{\mathrm{AE}}{L}\right) \\ + 4\mathrm{EI}/L \end{matrix} & \\ 0 & 0 & \dfrac{-6\mathrm{EI}}{L^2} & \dfrac{12\mathrm{EI}}{L^3} \end{bmatrix} \qquad (5\text{-}31)$$

At this point, the condensation technique can be employed. The first 2x2 of K' corresponding to u_1 and θ_1 are intended to be kept, while the last 2x2 of K' corresponding to θ_4 and v_5 are to be eliminated. Partitioning on K' needs to be performed such that:

$$\mathrm{K}' = \begin{bmatrix} \mathrm{K}'_{\mathrm{rr}} & \mathrm{K}'_{\mathrm{rc}} \\ \mathrm{K}'_{\mathrm{cr}} & \mathrm{K}'_{\mathrm{cc}} \end{bmatrix} \qquad (5\text{-}32)$$

where $\mathrm{K}'_{\mathrm{rr}} = \begin{array}{c} \begin{bmatrix} \mathrm{K_a} + \mathrm{K_b} + \mathrm{K_c} + \mathrm{K_{22}} + \mathrm{AE}/L & -h_a\left(K_b + K_c + \mathrm{AE}/L\right) \\ -h_a\left(K_b + K_c + \mathrm{AE}/L\right) & K_d + K_{33} + h_a^2\left(K_b + K_c + \mathrm{AE}/L\right) \end{bmatrix} \end{array} \begin{array}{c} u_1 \\ \theta_1 \end{array}$,

$\mathrm{K}'_{\mathrm{cr}} = \mathrm{K}'^{\,\mathrm{T}}_{\mathrm{rc}} = \begin{bmatrix} -h_b\left(K_c + \mathrm{AE}/L\right) & -K_d + h_a h_b\left(K_c + \mathrm{AE}/L\right) \\ 0 & 0 \end{bmatrix}$, and

$$\mathrm{K}'_{\mathrm{cc}} = \begin{bmatrix} K_d + h_b^2\left(K_c + \mathrm{AE}/L\right) + 4\mathrm{EI}/L & -6\mathrm{EI}/L^2 \\ -6\mathrm{EI}/L^2 & 12\mathrm{EI}/L^3 \end{bmatrix} \begin{matrix} \theta_4 \\ v_5 \end{matrix}.$$

According to Cook *et al* [30], a stiffness matrix, after applying matrix condensation representing a condensed stiffness matrix, K'', is determined from:

$$\mathrm{K}'' = \mathrm{K}'_{\mathrm{rr}} - \mathrm{K}'_{\mathrm{rc}}\mathrm{K}'^{-1}_{\mathrm{cc}}\mathrm{K}'_{\mathrm{cr}} \tag{5-33}$$

The condensed stiffness matrix, K'', appears in an awkward format. Thus, it is suggested that the condensation procedure is performed numerically by using Equation 5-31 as a starting point. Only 2x2 matrix operations are involved, making implementation easier.

The linear stiffness of three soil-abutment interaction springs (K_a, K_b, and K_c) is interconnected according to the relationship presented in Equation 4-1. This interconnection can be written in the following equations:

$$\begin{aligned} K_a &= \frac{k_h\left(h_a + h_b\right)B}{12\left(h_a + h_b\right)^{0.5}}\left(6\left(h_a + h_b\right)^{1.5} - 3h_a h_b{}^{0.5} - 6h_b{}^{1.5}\right) \\ K_b &= \frac{k_h\left(h_a + h_b\right)B}{12\left(h_a + h_b\right)^{0.5}}\left(2\left(h_a + h_b\right)^{1.5} + 3h_a h_b{}^{0.5} + 4h_b{}^{1.5}\right) \\ K_c &= \frac{k_h\left(h_a + h_b\right)B}{12\left(h_a + h_b\right)^{0.5}}\left(2h_b{}^{1.5}\right) \end{aligned} \tag{5-34}$$

where $k_h(z)$ is a lateral soil stiffness at depth z (Equation 4-1) and B is a abutment or backwall width.

Condensed Force Vector

The same approach used for reducing the stiffness matrix size is also applied to a global force vector of the 2-D model to obtain a condensed force vector. After the above defined boundary conditions and zero constraints are employed, the 2-D model force vector size is reduced to nine, defined as F in Equation 5-35. Partitioning on F needs to be performed such that:

$$\mathrm{F} = \begin{bmatrix} \mathrm{F_r} \\ \mathrm{F_c} \end{bmatrix} \tag{5-35}$$

where $\mathrm{F_r}$ $= [0]_{4\times 1}$,

$\mathrm{F_c}$ $= [0 \quad 0 \quad 0 \quad 0 \quad \text{-}\,\mathrm{AE}\alpha_{\mathrm{c}}\Delta T]^{\mathrm{T}}$,

α_c = Coefficient of thermal expansion, and

ΔT = Change in temperatures.

A force vector after applying the constraint transformation matrix, F', is determined from [30]:

$$\mathrm{F}' = \mathrm{F_r} + \mathrm{C_{rc}^T}\mathrm{F_c} = \begin{bmatrix} -\mathrm{AE}\alpha_{\mathrm{c}}\Delta T \\ h_a\mathrm{AE}\alpha_{\mathrm{c}}\Delta T \\ h_b\mathrm{AE}\alpha_{\mathrm{c}}\Delta T \\ 0 \end{bmatrix} \tag{5-36}$$

To obtain a condensed force vector, partitioning on F' needs to be performed such that:

$$\mathrm{F}' = \begin{bmatrix} \mathrm{F'_r} \\ \mathrm{F'_c} \end{bmatrix} \tag{5-37}$$

where $\mathrm{F}_{\mathrm{r}}' = \begin{bmatrix} -\mathrm{AE}\alpha_{\mathrm{c}}\Delta T \\ h_a\mathrm{AE}\alpha_{\mathrm{c}}\Delta T \end{bmatrix}$ and $\mathrm{F}_{\mathrm{c}}' = \begin{bmatrix} \mathrm{h}_{\mathrm{b}}\mathrm{AE}\alpha_{\mathrm{c}}\Delta T \\ 0 \end{bmatrix}$.

The condensed force vector, F'', is written as:

$$\mathrm{F}'' = \mathrm{F}_{\mathrm{r}}' - \mathrm{K}_{\mathrm{rc}}'\mathrm{K}_{\mathrm{cc}}'^{-1}\mathrm{F}_{\mathrm{c}}' \tag{5-38}$$

It is also suggested that the condensation procedure for the condensed force vector is performed numerically by using Equation **5-36** as a starting point. Only 2x1 vector operations are involved.

Although the proposed 2-D model is ideal for bridges 211 and 222, extension to bridge 203 can be performed by subdividing a superstructure component into three elements and imposing two rollers to the two new inner nodes. However, additional assumptions are provided to make use of the condensed matrix and force vector developed for a single span bridge. Such assumptions are listed as follows:

- The longitudinal displacement at abutment 1 (non-integral abutment) is insignificant due to foundations on the bedrock, the total bridge overall length is used as a length parameter, L_1, to the axial stiffness, AE/L, for the condensed stiffness matrix in Equation **5-31**.
- The zero rotation point is located about mid-way of span 3 (bridge span adjacent to the integral abutment). Half the magnitude of span 3 is used as a length parameter, L_2, to the bending stiffness, $12\mathrm{EI}/L^3$ and $6\mathrm{EI}/L^2$, for the condensed stiffness matrix in Equation **5-31**.

Figure **5-13** presents the two length parameters, L_1 and L_2, on a schematic elevation of bridge 203. These length parameters serve as the input for numerical computation.

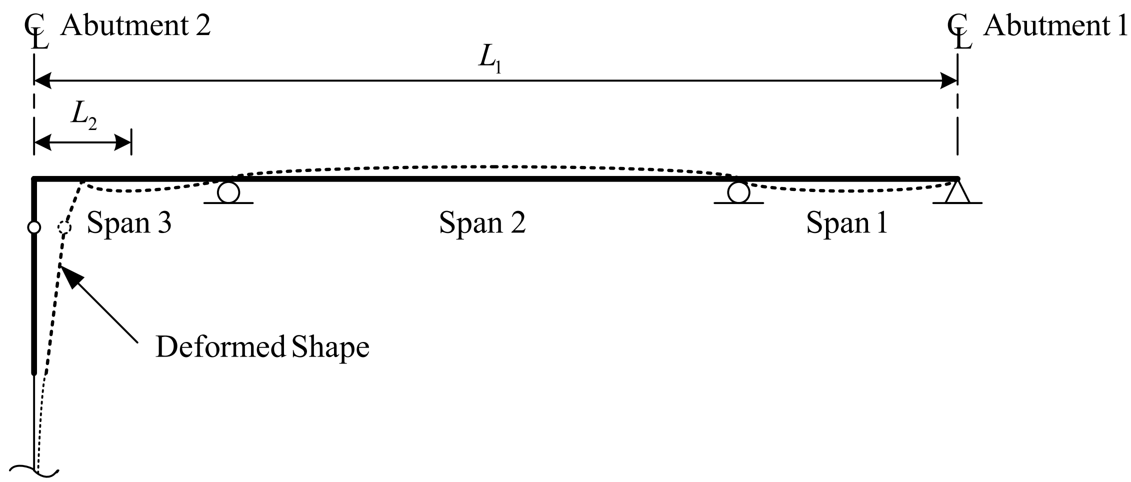

Figure 5-13: Modified Length Parameter for Condensed Hysteresis Model (Bridge 203)

5.4.2 Nonlinear Hysteresis Elements

All linear springs (K_{22}, K_{33}, K_a, K_b, K_c, and K_d) presented in Section 5.4.1 needs to be substituted by corresponding nonlinear hysteresis elements ($\overline{K}_{22}$, $\overline{K}_{33}$, $\overline{K}_a$, $\overline{K}_b$, $\overline{K}_c$, and $\overline{K}_d$) to construct a condensed hysteresis model. The numerical forms for soil-pile interaction hysteresis elements ($\overline{K}_{22}$ and $\overline{K}_{33}$) are presented in Equations 5-22 and 5-25, respectively. The differential equations for soil-abutment interaction hysteresis elements ($\overline{K}_a$, $\overline{K}_b$, and $\overline{K}_c$) and the abutment-backwall connection hysteresis element ($\overline{K}_d$) are provided in Sections 3.5.2 and 3.5.3. The procedure of incorporating the Euler forward method to obtain the numerical forms is demonstrated for $\overline{K}_a$ in Section 5.3. As a result, Equation 5-31 derived from the linear springs can be rewritten in Equation 5-39 for nonlinear hysteresis elements as:

$$\mathrm{K}' = \mathrm{K}_{rr} + \mathrm{K}_{rc}\mathrm{C}_{rc} + \mathrm{C}_{rc}^{T}\mathrm{K}_{cr} + \mathrm{C}_{rc}^{T}\mathrm{K}_{cc}\mathrm{C}_{rc}$$

$$= \begin{bmatrix} \begin{matrix}\overline{K}_a + \overline{K}_b + \overline{K}_c \\ + \overline{K}_{22} + \dfrac{\mathrm{AE}}{L}\end{matrix} & & & \mathit{Symm.} \\ -h_a\begin{pmatrix}\overline{K}_b \\ + \overline{K}_c + \dfrac{\mathrm{AE}}{L}\end{pmatrix} & \begin{matrix}\overline{K}_d + \overline{K}_{33} \\ + h_a^2\begin{pmatrix}\overline{K}_b \\ + \overline{K}_c + \dfrac{\mathrm{AE}}{L}\end{pmatrix}\end{matrix} & & \\ -h_b\left(\overline{K}_c + \dfrac{\mathrm{AE}}{L}\right) & \begin{matrix}-\overline{K}_d \\ + h_a h_b\left(\overline{K}_c + \dfrac{\mathrm{AE}}{L}\right)\end{matrix} & \begin{matrix}\overline{K}_d \\ + h_b^2\left(\overline{K}_c + \dfrac{\mathrm{AE}}{L}\right) \\ + 4\mathrm{EI}/L\end{matrix} & \\ 0 & 0 & \dfrac{-6\mathrm{EI}}{L^2} & \dfrac{12\mathrm{EI}}{L^3} \end{bmatrix} \quad (5\text{-}39)$$

Note that substituting nonlinear hysteresis elements into linear springs does not affect the condensed force vector in Equation 5-36.

5.4.3 Numerical Solution

Material nonlinearity is involved in condensed hysteresis models, thus, an iterative numerical solution method is required. The Euler forward method as described in Section 5.2.4 is applicable for a local level, that is, the method is employed to determine a tangent stiffness for each hysteresis element. For a global level, however, an iterative analysis of each time step is necessary to reduce numerical residuals or errors to a prescribed tolerance. With regard to a few degrees of freedom used, the Newton-Raphson method becomes one of the efficient solution methods because this method offers an exceptional convergence rate.

The procedure to obtain a solution for condensed hysteresis models using the Newton-Raphson method is described as follows:

1. load all input data, consisting of:
   - bridge dimension (h_a, h_b, L_1, and L_2),
   - bridge section properties (A, E, I, and B),
   - backfill properties (ϕ, γ, and k_{ref}),
   - coefficients for soil-pile interaction hysteresis elements (C_1, C_2, C_3, and C_4), and
   - connection properties (M_Y and θ_Y).
2. define a time step size and initial values (index number, i = 1), typically at-rest condition and initial spring stiffness are assigned,
3. begin the first computation cycle (i = 2), formation of stiffness matrices (K'_{rr}, K'_{rc}, K'_{cr}, and K'_{cc}), and incremental force vectors (dF'_r and dF'_c) are based on the initial values, and solve for incremental displacement vector $dU_{i=2}$ using Equation **5-39** and Equation **5-36**,
4. update stiffness matrices and incremental force vectors using a solution of the previous step; all nonlinear hysteresis elements ($\overline{K}_{22}$, $\overline{K}_{33}$, $\overline{K}_a$, $\overline{K}_b$, $\overline{K}_c$, and $\overline{K}_d$) are also updated using the Euler forward method during this step,
5. compute Euclidean norm using a new (current) and old (previous) incremental displacement vectors, defined as $\left\| dU_i^{\text{new}} - dU_i^{\text{old}} \right\| / \left\| U_i \right\|$ [**30**], if

the magnitude of this norm is smaller than a prescribed tolerance (tol = 0.001), skip step 6,

6. repeat steps 4 and 5,
7. compute a displacement vector using an incremental displacement solution obtained from the previous step, and
8. increase the index number i by 1, if i is smaller than prescribed number of steps, go back to step 4; otherwise, computation is complete.

The procedure described above is also illustrated in flowcharts presented in Figures **5-14** and **5-15**.

Based on the procedure presented in Figures **5-14** and **5-15**, an MATLAB code was implemented and provided in Appendix C. Additional consideration for the time-dependent effects described in Section **5.5** has been incorporated in the MATLAB implementation. Analysis results obtained from the condensed hysteresis models of all three instrumented bridges will be presented in Chapter 6, along with corresponding field collected data and analysis results from the FE models.

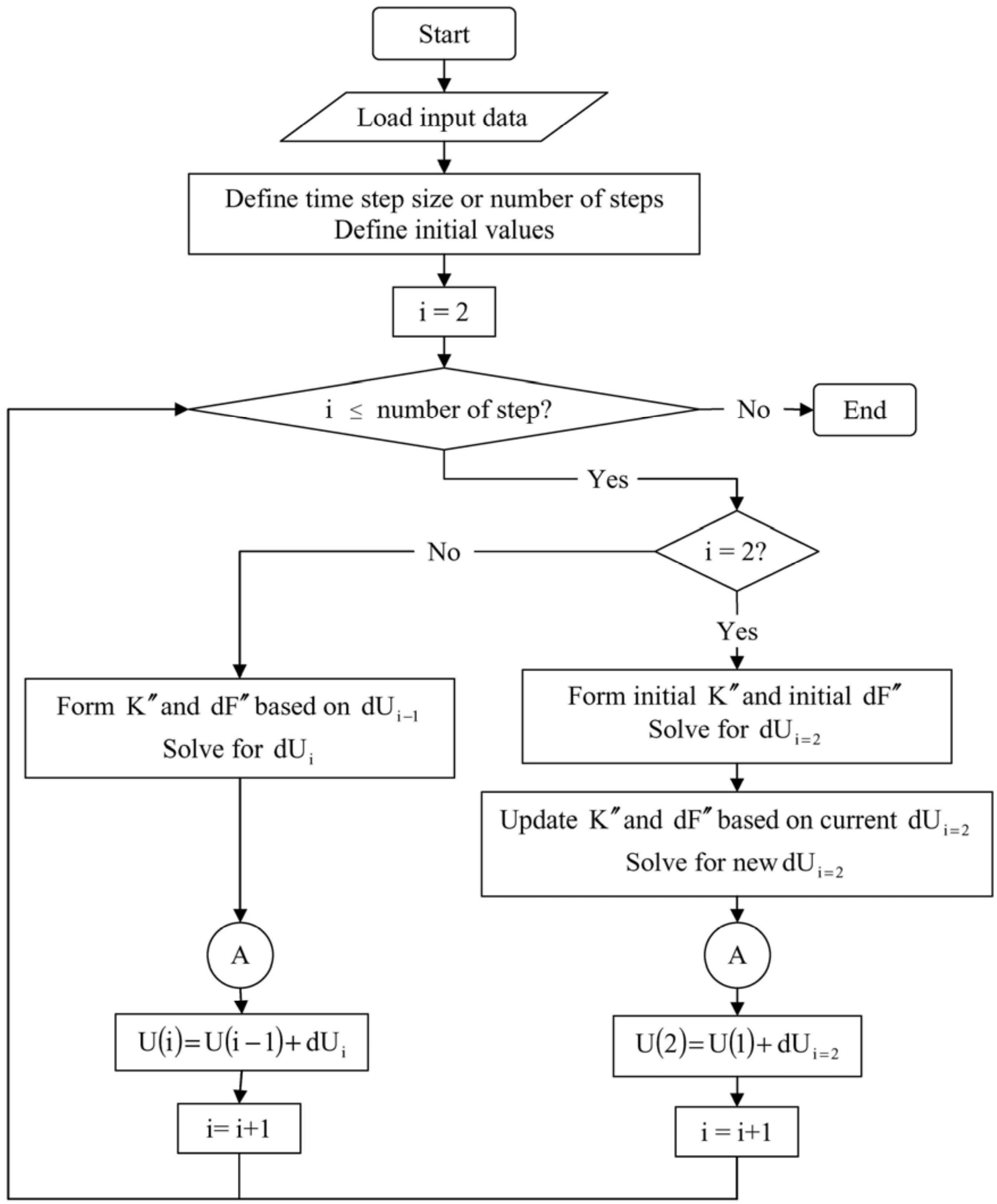

Figure 5-14: Numerical Solution Flowchart (1 of 2)

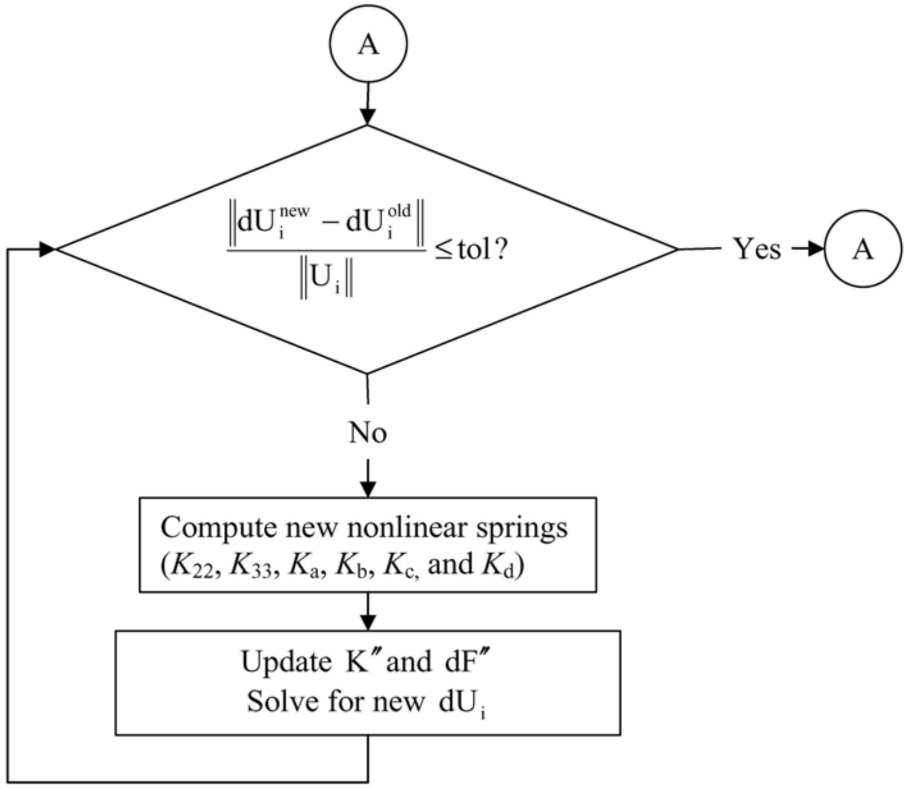

Figure 5-15: Numerical Solution Flowchart (2 of 2)

5.5 Consideration of Time-Dependent Effects on Condensed Hysteresis Model

In order to incorporate time-dependent effects into the condensed hysteresis models, additional implementation to the stiffness matrix (Equation 5-39) and force vector (Equation 5-36) need to be considered. The AAEM method, previously applied to the FE models, is also used for the condensed hysteresis models. There are two issues that need to be incorporated: superstructure modulus and equivalent temperature loads. These two issues are essentially the same as employed in the 2-D FE models.

The modulus of elasticity, E, appearing in the stiffness matrix (Equation 5-39) and force vector (Equation 5-36) is no longer constant, however, an age-adjusted effective modulus, $\overline{E}_c(t,t_o)$, determined by using the AAEM method, is replaced. This substitution can be easily incorporated into the Newton-Raphson method presented in Section 5.4.3 without any addition treatment.

Equivalent temperature loads based on the AAEM method (See also Section 4.3.3) can be incorporated into the total incremental temperature to form an incremental force vector. Therefore, the total incremental temperature is expressed as:

$$\Delta T_{\mathrm{total}} = \Delta T_{\mathrm{ambient}} + \Delta T_{\mathrm{equivalent}} \tag{5-40}$$

which is used in an incremental force vector formation. This modification does not affect the Newton-Raphson method. It is noted that equivalent temperature loads due to time-dependent curvatures are neglected to simplify a force vector formation.

Chapter 6

Measured and Predicted Responses

6.1 General

Measured response at bridges 203, 211, and 222 was initiated in November 2002, September 2004, and November 2003, respectively. Measured response, including 7-day averages and envelopes, are presented to convey the overall tendency and daily variation. Pressure cell and extensometer measurements, providing earth pressure and longitudinal abutment displacement data, are presented here. Predicted response is taken directly from FE and condensed hysteresis model nodes and elements that were placed at critical locations.

Comparison of predicted to measured behavior is performed to quantify accuracy of the FE and condensed hysteresis models. A 100-year simulation has been completed to study long-term IA bridge behavior. Eight load cases were established and analyzed to identify the relative magnitudes of hysteretic and non-hysteretic behaviors.

This chapter consists of four sections: Section 6.2 covers measured abutment soil pressure, predicted soil pressure, comparison of measured and predicted soil pressures, and FE model calibration for all three instrumented bridges. Section 6.3 presents measured abutment displacements, predicted abutment displacements, and comparison of measured and predicted abutment displacements. Analyses of the FE and condensed hysteresis models were also conducted and discussed in Section 6.3. Finally, Section 6.4

summarizes comparisons of measured and predicted responses and FE model accuracy for all three instrumented bridges.

6.2 Measured and Predicted Abutment Soil Pressures

Measured abutment soil pressure represents soil-abutment interaction behavior over the period of 39, 17, and 27 months for bridges 203, 211, and 222, respectively. Response at top and bottom pressure cell locations is presented. Graphs of measured and predicted abutment soil pressures are superimposed so as to facilitate comparison.

6.2.1 Bridge 203

Abutment 2 of bridge 203 is constructed as an integral abutment, therefore, the measured response at only abutment 2 is presented. Measured soil pressures from top and bottom pressure cells corresponding to channels 3-7 and 3-8 are compared with FE model predicted soil pressures. Lateral soil stiffness, k_h, for the FE and condensed hysteresis models has been altered from the magnitude obtained from the best fit of measured data to obtain better correlation between measured and predicted soil pressures (see Section **4.2.2**, *H2* properties). Lateral soil stiffness is the only parameter calibrated against measured data.

Measured and predicted soil pressures at the top and bottom abutment positions are presented in Figures **6-1** and **6-2**. It is observed in Figure **6-1** that the maximum percent difference between 2-D and 3-D predicted soil pressures is 3.5 and the average percent difference is 1.5. The correlation between average measured soil pressure and 2-D predicted soil pressure is 0.913, while the correlation between the average measured soil pressure and 3-D predicted soil pressure is 0.914. In addition, measured, 2-D predicted, and 3-D predicted soil pressures demonstrate the same trend.

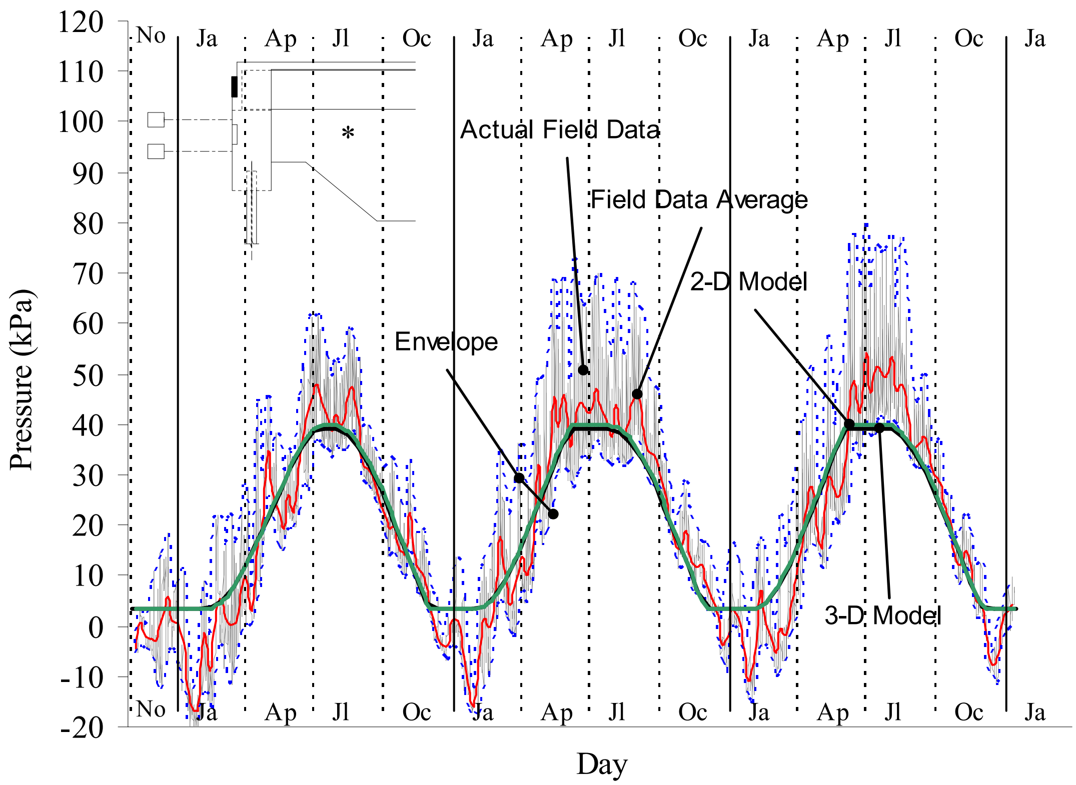

Figure 6-1: Top Elevation Pressure Cell Data and Predicted Results from FE Models (* Ref: Channel 3-7 in Figure A-3 for Instrumentation Location Detail)

It is observed in Figure 6-2 that the maximum percent difference between 2-D and 3-D predicted soil pressures is 2.8 and the average percent difference is 1.6. The correlation between average measured soil pressure and 2-D predicted soil pressure is 0.901, while the correlation between average measured soil pressure and 3-D predicted soil pressure is

0.901. In addition, measured, 2-D predicted, and 3-D predicted soil pressures demonstrate the same trend.

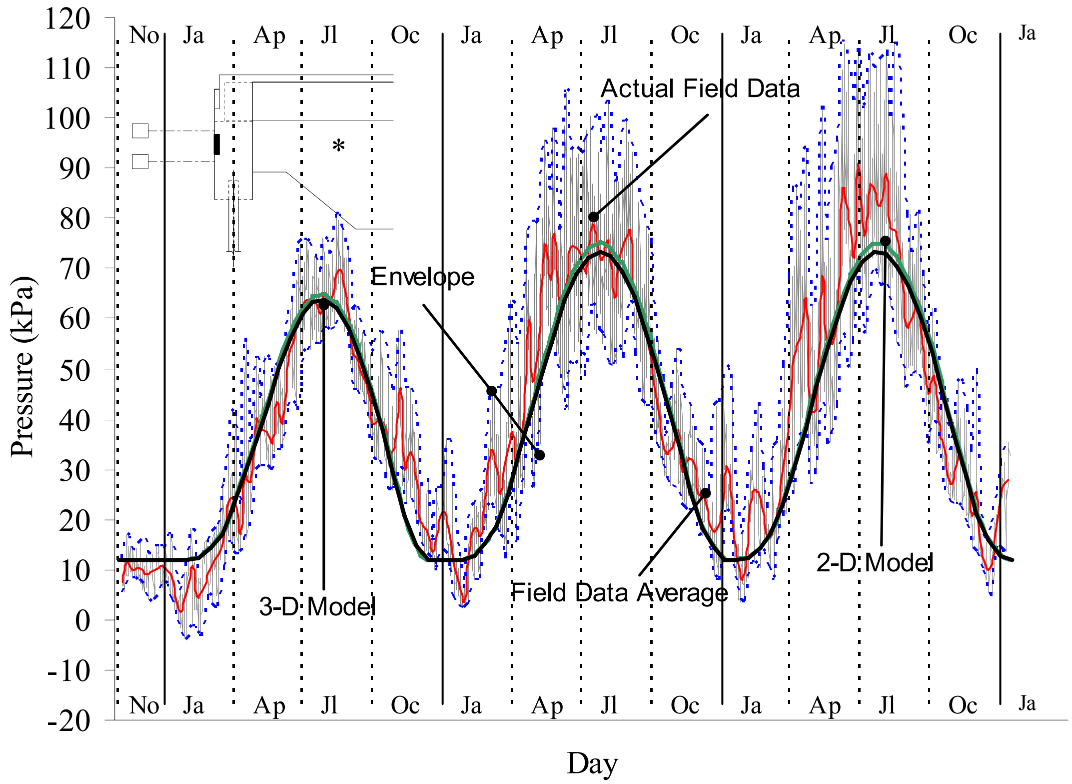

Figure 6-2: Bottom Elevation Pressure Cell Data and Predicted Results from FE Models (* Ref: Channel 3-8 in Figure A-3 for Instrumentation Location Detail)

Based on the percent differences and correlations between measured and predicted soil pressures presented above, it was determined that the elasto-plastic hysteresis model satisfactorily captures soil-abutment interaction behavior over the period of 39 months.

6.2.2 Bridge 211

Both abutments of bridge 211 are constructed as integral, therefore, the measured response at both abutments is presented. Measured soil pressures from top and bottom pressure cells, corresponding to channels 4-7 and 4-8 for abutment 1 and channels 2-7 and 2-8 for abutment 2, are compared with FE model predicted soil pressures. Lateral soil stiffness for the FE and condensed hysteresis models has been altered from the magnitude obtained from the best fit of measured data to obtain better correlation between measured and predicted soil pressures.

Measured and predicted soil pressures at the top and bottom abutment positions for abutment 1 are presented in Figures **6-3** and **6-4**. It is observed in Figure **6-3** that the maximum percent difference between 2-D and 3-D predicted soil pressures 72.6 and the average percent difference is 30. The correlation between average measured soil pressure and 2-D predicted soil pressure is 0.601, while the correlation between average measured soil pressure and 3-D predicted soil pressure is 0.516. The predicted soil pressure during September 2004 to December 2004 and May 2005 to November 2005 are inconsistent to the measured soil pressure due to the limits of active and passive earth pressure. These limits based on classical earth pressure theory do not incorporate effects of soil densification as a result of daily thermal abutment movements. In addition, the assumption of using an at-rest earth pressure as the initial loading condition may not be appropriate for bridge 211.

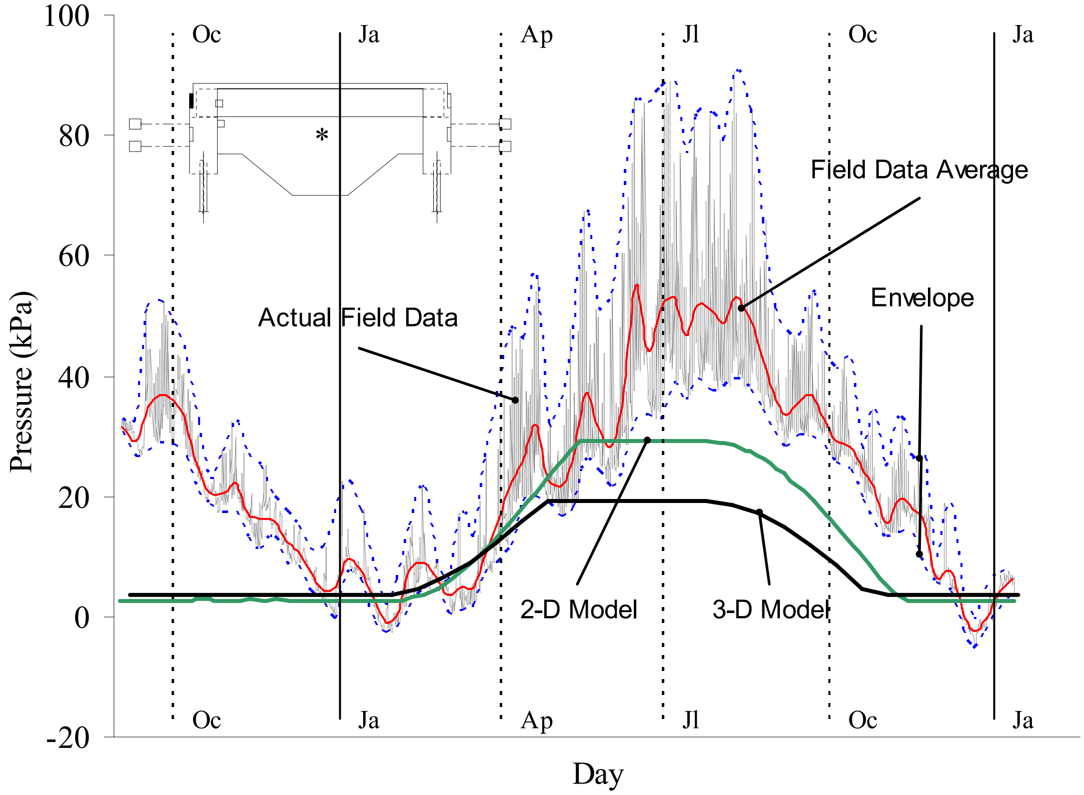

Figure 6-3: Top Elevation Pressure Cell Data and Predicted Results from FE Models (* Ref: Channel 4-7 in Figure A-7 for Instrumentation Location Detail at Abutment 1)

It is observed in Figure 6-4 that the maximum percent difference between 2-D and 3-D predicted soil pressures is 13.1 and the average percent difference is 3. The correlation between average measured soil pressure and 2-D predicted soil pressure is 0.574, while the correlation between average measured soil pressure and 3-D predicted soil pressure is 0.556. The same explanation for the inconsistency of measured and predicted response comparison, as described for the top pressure cell at abutment 1, is also applied here.

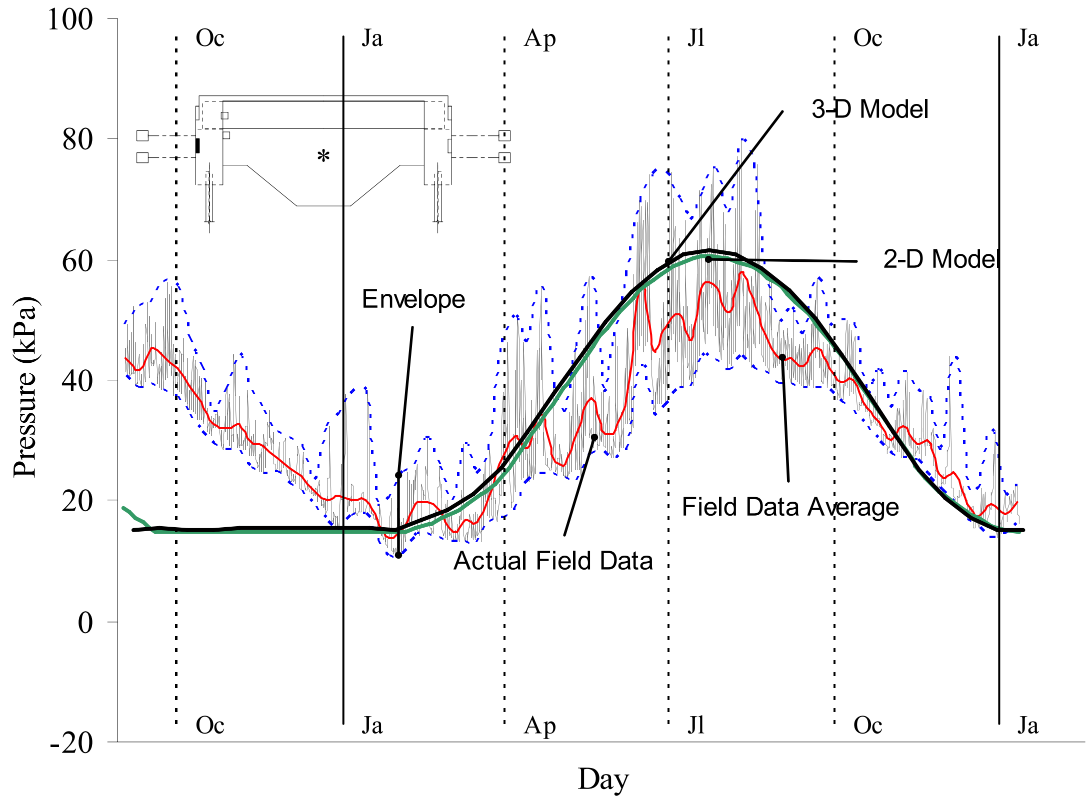

Figure 6-4: Bottom Elevation Pressure Cell Data and Predicted Results from FE Models (* Ref: Channel 4-8 in Figure A-7 for Instrumentation Location Detail at Abutment 1)

Measured and predicted soil pressures at the top and bottom abutment positions for abutment 2 are presented in Figures 6-5 and 6-6. It is observed in Figure 6-5 that the maximum percent difference between 2-D and 3-D predicted soil pressures is 58 and the average percent difference is 14.5. The correlation between average measured soil pressure and 2-D predicted soil pressure is 0.623, while the correlation between average measured soil pressure and 3-D predicted soil pressure is 0.563. The same explanation for the inconsistency of measured and predicted response comparison, as described for the top pressure cell at abutment 1, is also applied here.

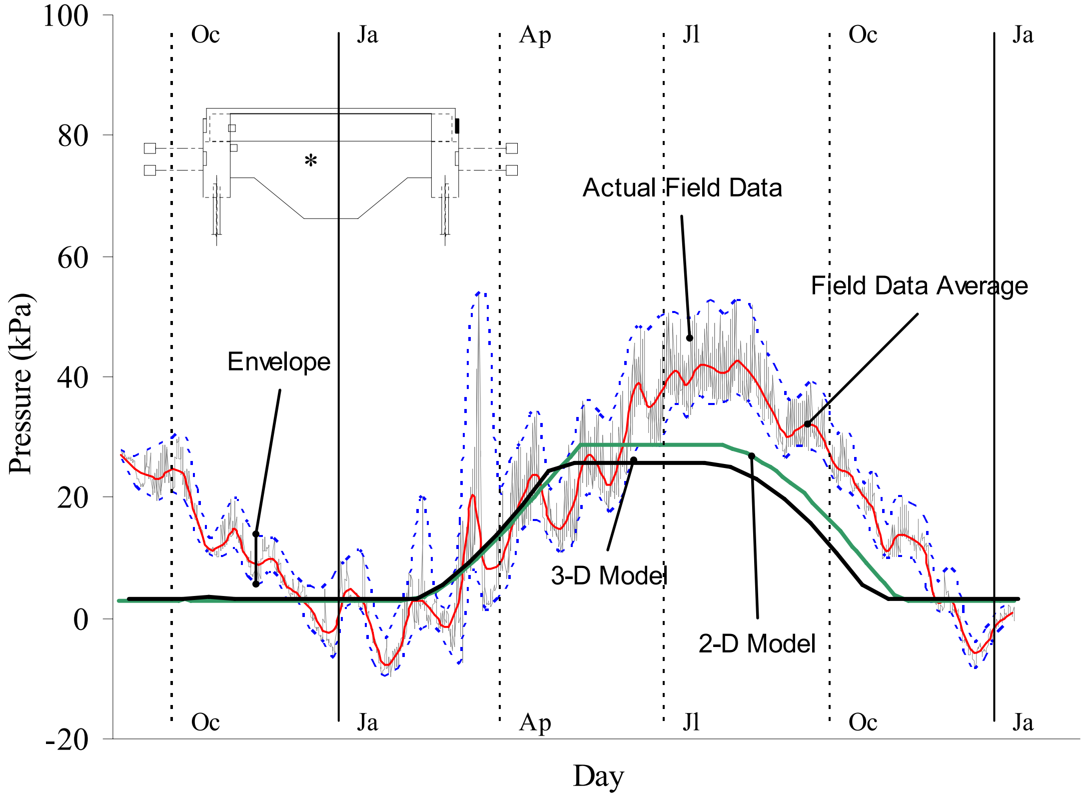

Figure 6-5: Top Elevation Pressure Cell Data and Predicted Results from FE Models (* Ref: Channel 2-7 in Figure A-6 for Instrumentation Location Detail at Abutment 2)

It is observed in Figure 6-6 that the maximum percent difference between 2-D and 3-D predicted soil pressures is 85 and the average percent difference is 44. The correlation between average measured soil pressure and 2-D predicted soil pressure is 0.739, while the correlation between average measured soil pressure and 3-D predicted soil pressure is 0.748. The same explanation for the inconsistency of measured and predicted response comparison, as described for the top pressure cell at abutment 1, is also applied here.

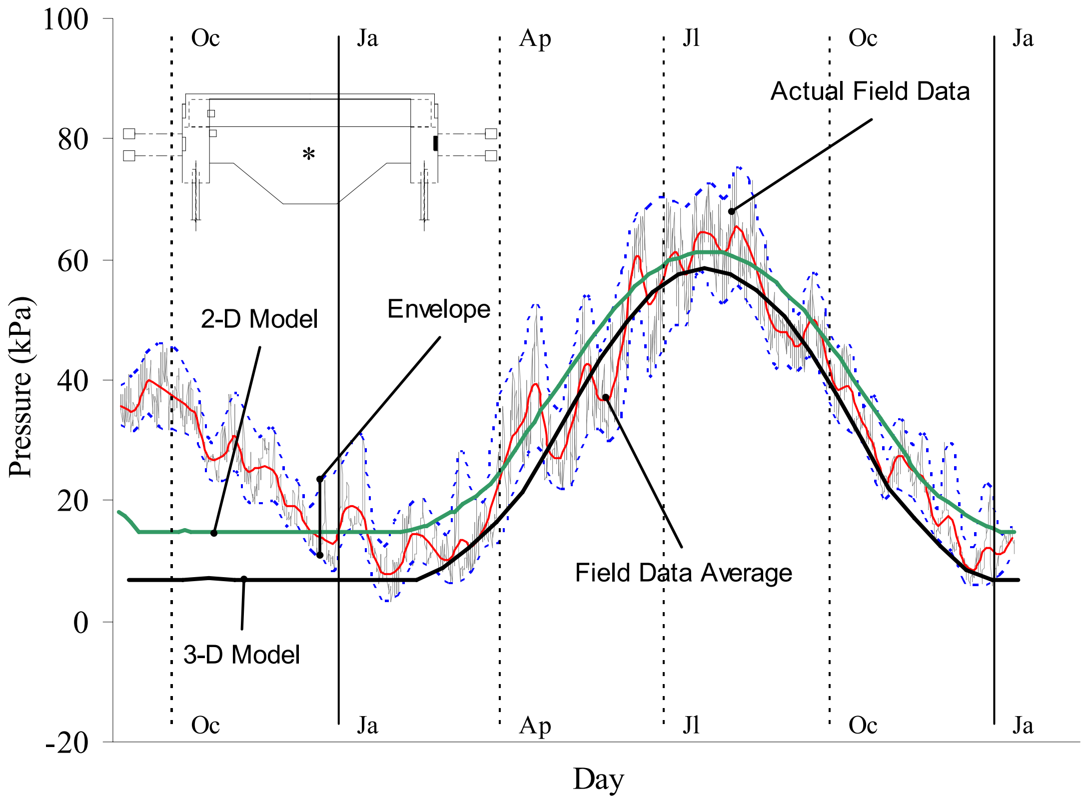

Figure 6-6: Bottom Elevation Pressure Cell Data and Predicted Results from FE Models (* Ref: Channel 2-8 in Figure A-6 for Instrumentation Location Detail at Abutment 2)

Based on the percent differences and correlations between measured and predicted soil pressures presented above, it was determined that the assumption of an at-rest earth pressure as the initial loading condition may not be appropriate. The elasto-plastic hysteresis model used in the bridge 211 FE models does not satisfactorily capture soil-abutment interaction behavior, as compared to the bridge 203 soil pressure prediction.

6.2.3 Bridge 222

Both abutments of bridge 211 is constructed as integral, therefore, the measured response at two abutments are presented. Measured soil pressures from top and bottom pressure cells, corresponding to channels 3-7 and 3-8 for abutment 1 and channels 2-3 and 2-4 for abutment 2, are compared with FE model predicted soil pressures.

Measured and predicted soil pressures at the top and bottom abutment positions for abutment 1 are presented in Figures 6-7 and 6-8.

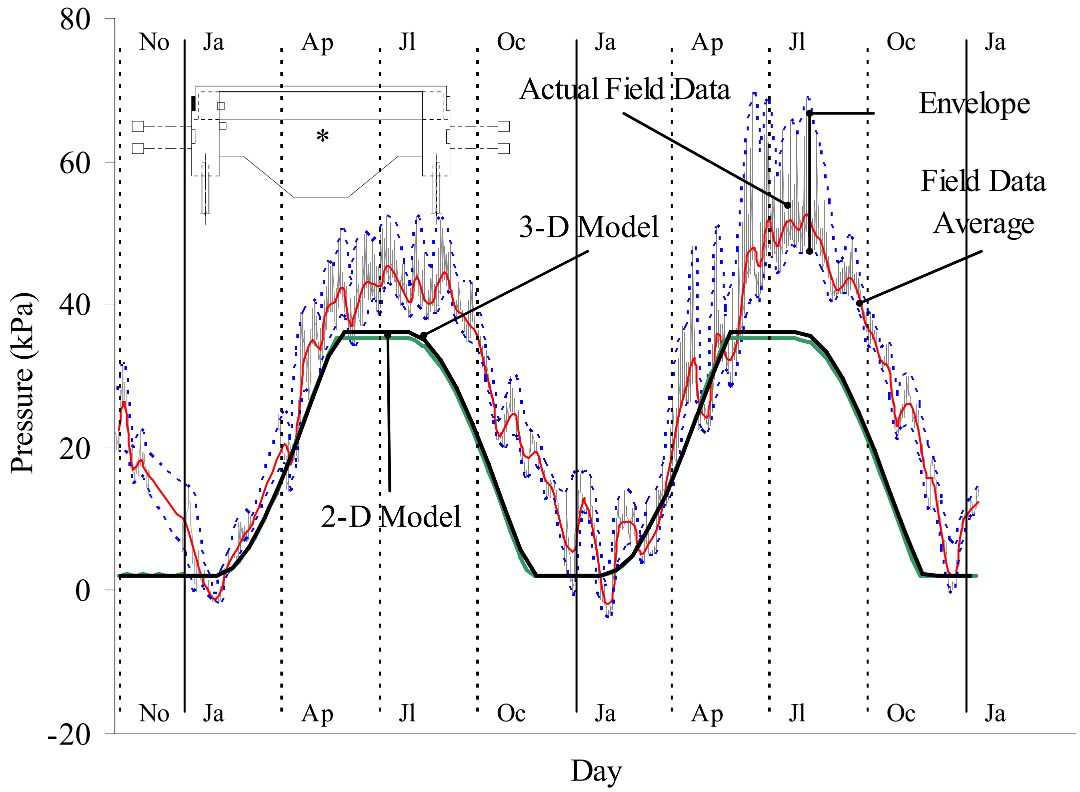

Figure 6-7: Top Elevation Pressure Cell Data and Predicted Results from FE Models
(* Ref: Channel 3-7 in Figure A-12 for Instrumentation Location Detail at Abutment 1)

It is observed in Figure 6-7 that the maximum percent difference between 2-D and 3-D predicted soil pressures is 20 and the average percent difference is 2.7. The correlation between average measured soil pressure and 2-D predicted soil pressure is 0.820, while the correlation between average measured soil pressure and 3-D predicted soil pressure is 0.832. In addition, measured, 2-D predicted, and 3-D predicted soil pressures demonstrate the same trend.

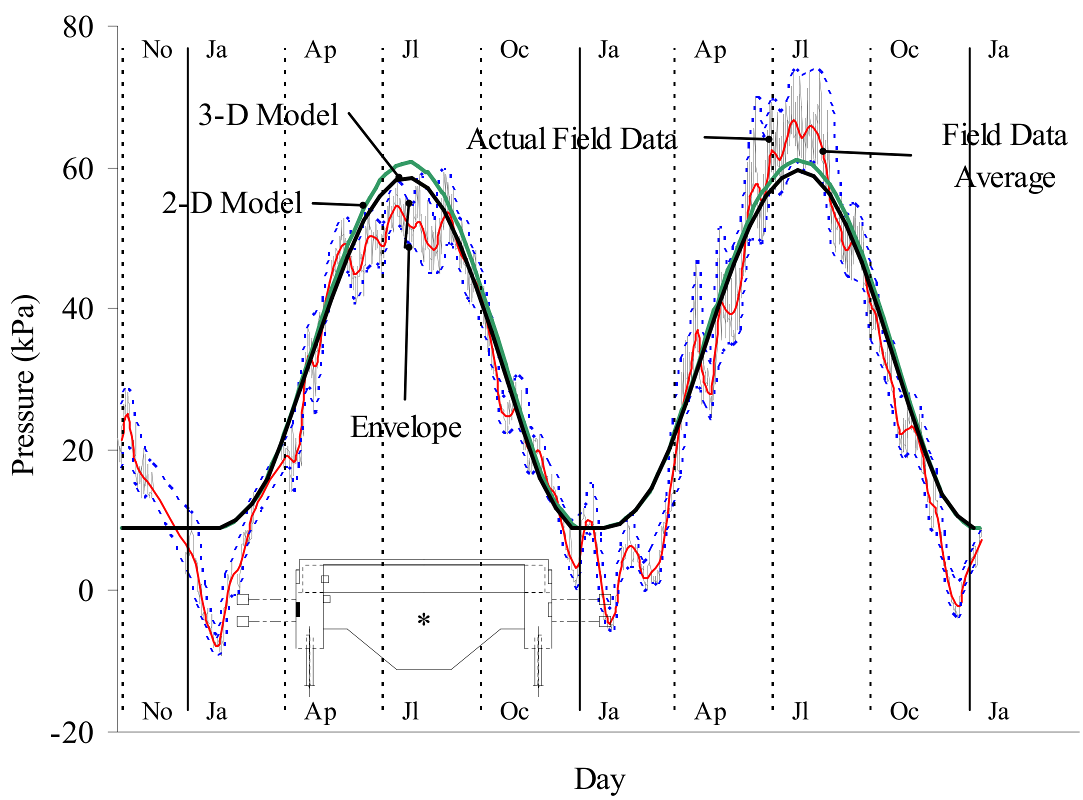

Figure 6-8: Bottom Elevation Pressure Cell Data and Predicted Results from FE Models (* Ref: Channel 3-8 in Figure A-12 for Instrumentation Location Detail at Abutment 1)

It is observed in Figure 6-8 that the maximum percent difference between 2-D and 3-D predicted soil pressures is 7.5 and the average percent difference is 2.3. The correlation between average measured soil pressure and 2-D predicted soil pressure is 0.929, while the correlation between average measured soil pressure and 3-D predicted soil pressure is 0.929. In addition, measured, 2-D predicted, and 3-D predicted soil pressures demonstrate the same trend.

Measured and predicted soil pressures at the top and bottom abutment positions for abutment 2 are presented in Figures 6-9 and 6-10.

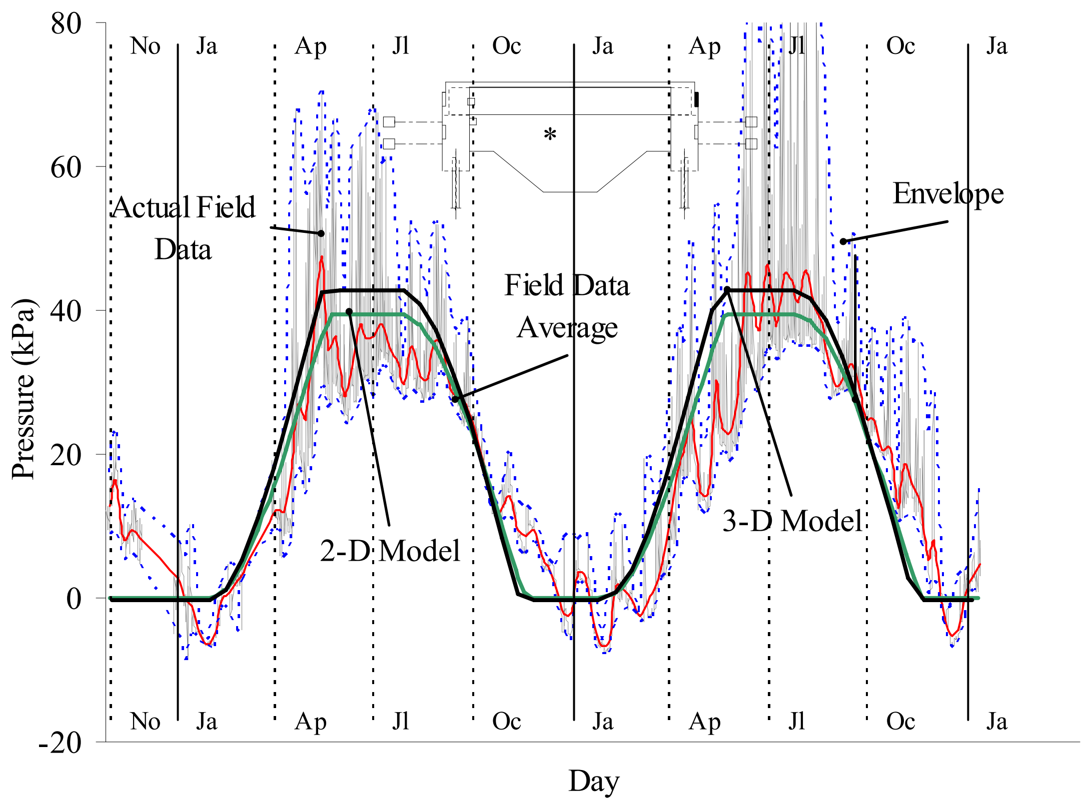

Figure 6-9: Top Elevation Pressure Cell Data and Predicted Results from FE Models (* Ref: Channel 2-3 in Figure A-11 for Instrumentation Location Detail at Abutment 2)

It is observed in Figure 6-9 that the maximum percent difference between 2-D and 3-D predicted soil pressures is 62 and the average percent difference is 10.9. The correlation between average measured soil pressure and 2-D predicted soil pressure is 0.846, while the correlation between average measured soil pressure and 3-D predicted soil pressure is

0.829. In addition, measured, 2-D predicted, and 3-D predicted soil pressures demonstrate the same trend.

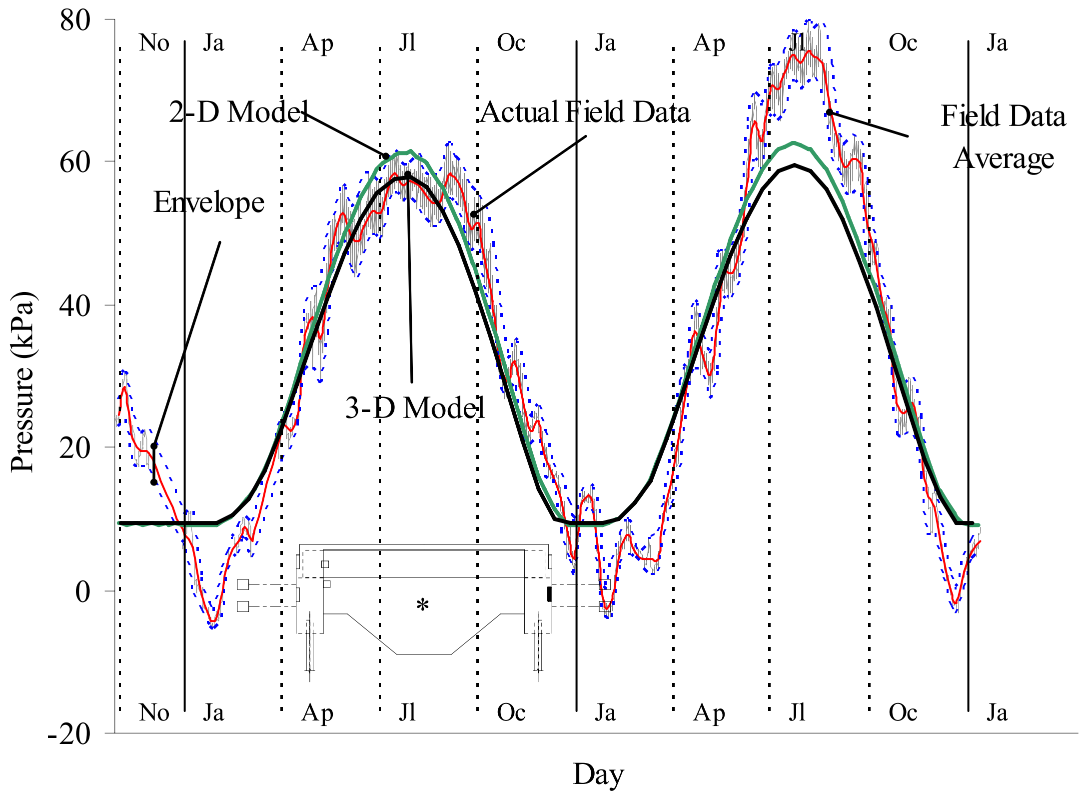

Figure **6-10**: Bottom Elevation Pressure Cell Data and Predicted Results from FE Models (* Ref: Channel 2-4 in Figure **A-11** for Instrumentation Location Detail at Abutment 2)

It is observed in Figure **6-10** that the maximum percent difference between 2-D and 3-D predicted soil pressures is 11.9 and the average percent difference is 4.3. The correlation between average measured soil pressure and 2-D predicted soil pressure is 0.916, while the correlation between average measured soil pressure and 3-D predicted soil pressure is 0.915. In addition, measured, 2-D predicted, and 3-D predicted soil pressures demonstrate the same trend.

Based on the percent differences and correlations between measured and predicted soil pressures presented above, it was determined that the elasto-plastic hysteresis model satisfactorily captures soil-abutment interaction behavior over the period of 27 months.

6.3 Measured and Predicted Abutment Displacements

Longitudinal abutment displacements represent the critical behavior for IA bridges subjected to temperature changes. Magnitudes of pile stresses, abutment moments, and redistributed superstructure moments depend directly on the magnitude of longitudinal abutment displacements. Measured and predicted abutment displacements at top and bottom extensometer locations are presented. Graphs of measured and predicted abutment displacements are superimposed so as to facilitate comparison. For the purposes of accurate comparison, the values of measured and predicted abutment displacements have been initialized with identical starting point established. This adjustment is required due to constraints on field instrumentation imposed by construction sequences that did not allow the measured data to have the same zero starting point as the FE models.

Extended simulation period for the FE and condensed hysteresis models have been carried out to study long-term IA bridge behavior. A 10-year simulation period is deemed sufficient to perform a comparison between 2-D and 3-D predicted abutment displacements. Next, a 100-year simulation period, indicating the PennDOT IA bridge design life, is conducted in the 2-D FE models to evaluate the relative magnitudes of hysteretic and non-hysteretic behaviors. The following 2-D FE model load cases are established and analyzed:

1. all hysteretic and non-hysteretic behaviors included,
2. all hysteretic and non-hysteretic behaviors excluded,
3. only hysteretic behavior included,
4. only non-hysteretic behavior included,
5. only soil-structure interaction hysteretic behavior included,
6. only abutment-backwall connection hysteretic behavior included,
7. only soil-abutment interaction hysteretic behavior included, and
8. only soil-structure interaction hysteretic behavior excluded.

Predicted condensed hysteresis model abutment displacements are also presented and compared with predicted 2-D and 3-D abutment displacements. Because displacement u_1 and rotation θ_1 at the pile head are available from the condensed hysteresis models, a comparison can be performed only at the bottom extensometer locations. The relationship, $u_E = u_1 - b \cdot \theta_1$, is used to transform predicted abutment displacements at the pile head locations to the bottom extensometer locations, where u_E is the predicted abutment displacement at the bottom extensometer locations, and b is the distance between the bottom extensometer and pile head locations (b = 1219 mm for all three instrumented bridges).

6.3.1 Bridge 203

Measured abutment displacements from top and bottom extensometers corresponding to channels 3-4 and 3-5 are compared with FE and condensed hysteresis model predicted abutment displacements. The positive magnitude of incremental abutment displacements means the abutment moving away from the backfill (bridge contraction) and the negative magnitude of incremental abutment displacements means the abutment moving toward the backfill (bridge expansion).

Measured and predicted abutment displacements at the top and bottom abutment positions over the period of 39 months are presented in Figures **6-11** and **6-12**. It is observed in Figure **6-11** that the maximum percent difference between 2-D and 3-D predicted abutment displacements is 2.6 and the average percent difference is 2.3. The correlation between average measured abutment displacement and 2-D predicted abutment displacement is 0.679, while the correlation between average measured abutment displacement and 3-D predicted abutment displacement is 0.679. 2-D and 3-D predicted abutment displacement amplitudes are approximately 1.6 times greater than the measured abutment displacement amplitudes. A different trend between measured and predicted abutment displacements is observed. The measured abutment displacement revealed the overall expansion trend, while the predicted abutment displacement showed the overall contraction trend.

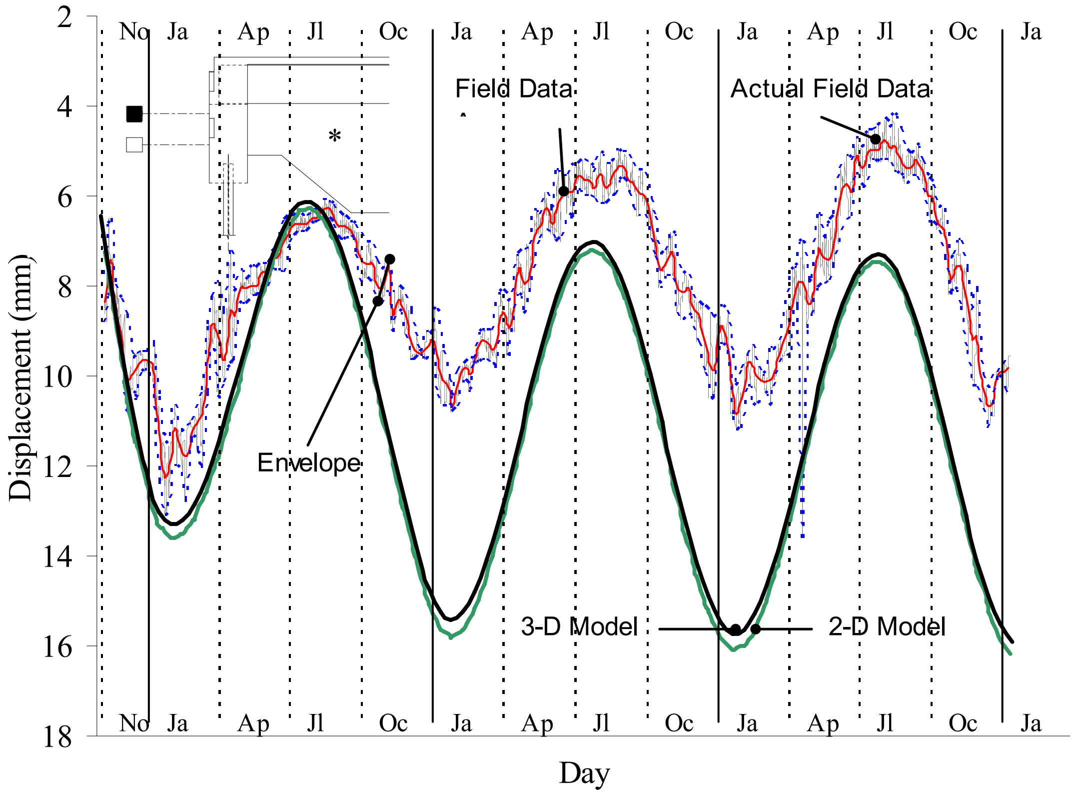

Figure 6-11: Top Elevation Extensometer Data and Predicted Results from FE Models
(* Ref: Channel 3-4 in Figure A-3 for Instrumentation Location Detail)

It is observed in Figure 6-12 that the maximum percent difference between 2-D and 3-D predicted abutment displacements is 15.4 and the average percent difference is 12.1. The maximum percent difference between 3-D and condensed hysteresis model predicted abutment displacements is 42.4 and the average percent difference is 31.3. The correlation between average measured abutment displacement and 2-D predicted abutment displacement is 0.882, the correlation between average measured abutment displacement and 3-D predicted abutment displacement is 0.899, and the correlation between average measured abutment displacement and condensed hysteresis model predicted abutment displacement is 0.107. Measured, 2-D predicted, 3-D predicted, and condensed hysteresis model predicted abutment displacements revealed the overall contraction trend. The 2-D, 3-D and condensed hysteresis model predicted abutment displacement amplitudes are approximately 1.05, 1.05, and 1.9 times greater than measured abutment displacement amplitude.

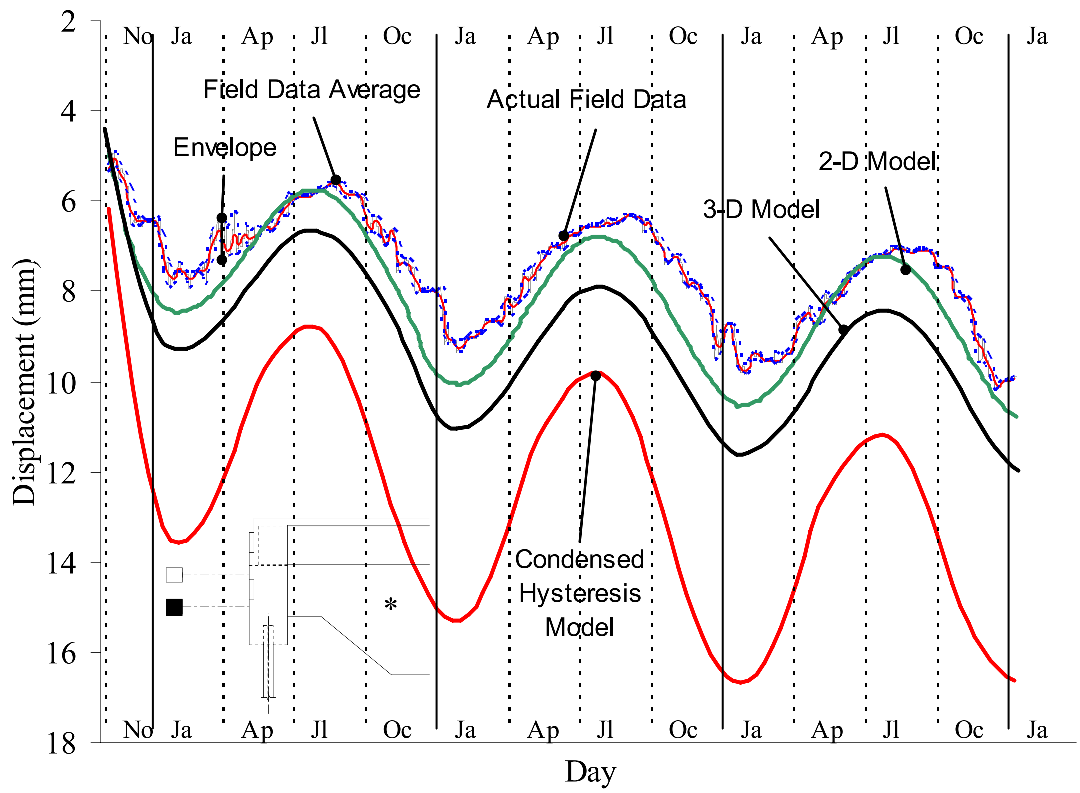

Figure 6-12: Bottom Extensometer Data and Results from FE and Condensed Models (* Ref: Channel 3-5 in Figure A-3 for Instrumentation Location Detail)

2-D and 3-D predicted abutment displacements at the top and bottom extensometer positions over the simulation period of 10 years are presented in Figures 6-13 and 6-14. A comparison between 2-D and 3-D predicted abutment displacements is conducted to present the validity of 2-D predicted abutment displacements for longer simulation period. It is observed in Figure 6-13 that the maximum percent difference between 2-D and 3-D predicted abutment displacements is 2.6 and the average percent difference is 1.7. The 2-D and 3-D predicted abutment displacements demonstrate the same trend, indicating the abutment moving away from the backfill. The logarithmic increase in adjacent displacement peaks is observed from 2-D and 3-D predicted abutment displacements as the number of years is increased.

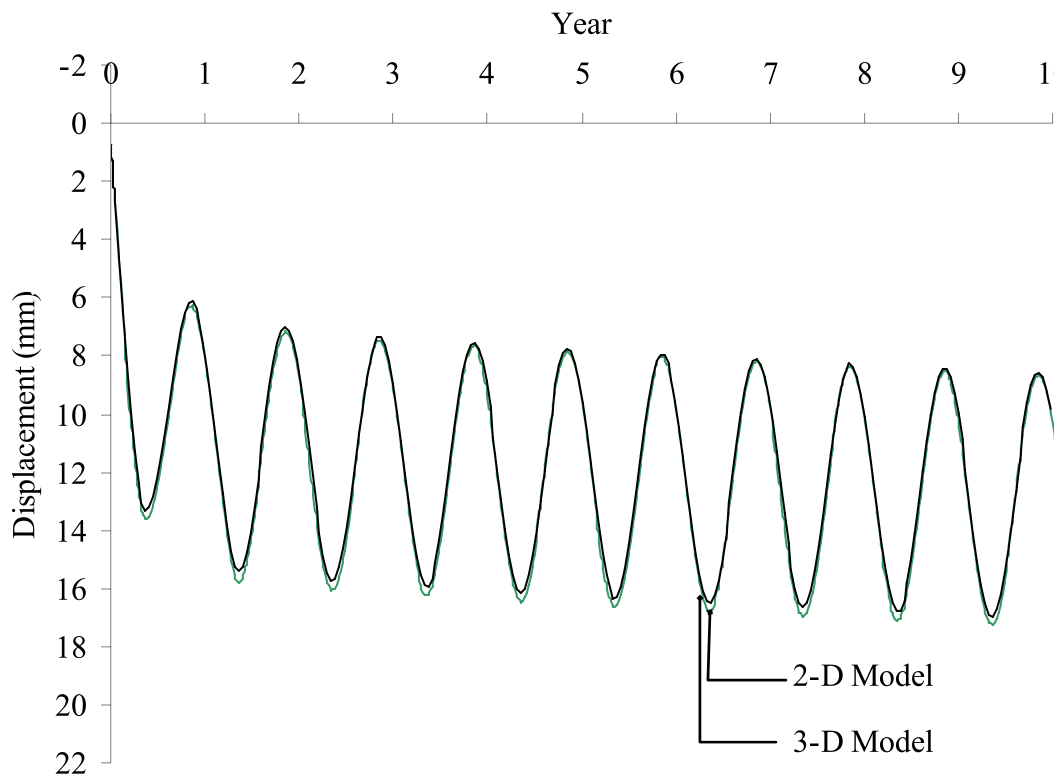

Figure 6-13: Predicted 10-Y Simulation Results from FE Models at Top Extensometer

It is observed in Figure 6-14 that the maximum percent difference between 2-D and 3-D predicted abutment displacements is 15.6 and the average percent difference is 11.9. The maximum percent difference between 3-D and condensed hysteresis model predicted displacements is 42.4 and the average percent difference is 24.8. The condensed hysteresis model predicted abutment displacement at the third cycle peak yields the highest magnitude of approximately 1.4 times greater than the 3-D predicted abutment displacement. The logarithmic increase in adjacent displacement peaks is observed from 2-D, 3-D, and condensed hysteresis model predicted abutment displacements as the number of years is increased.

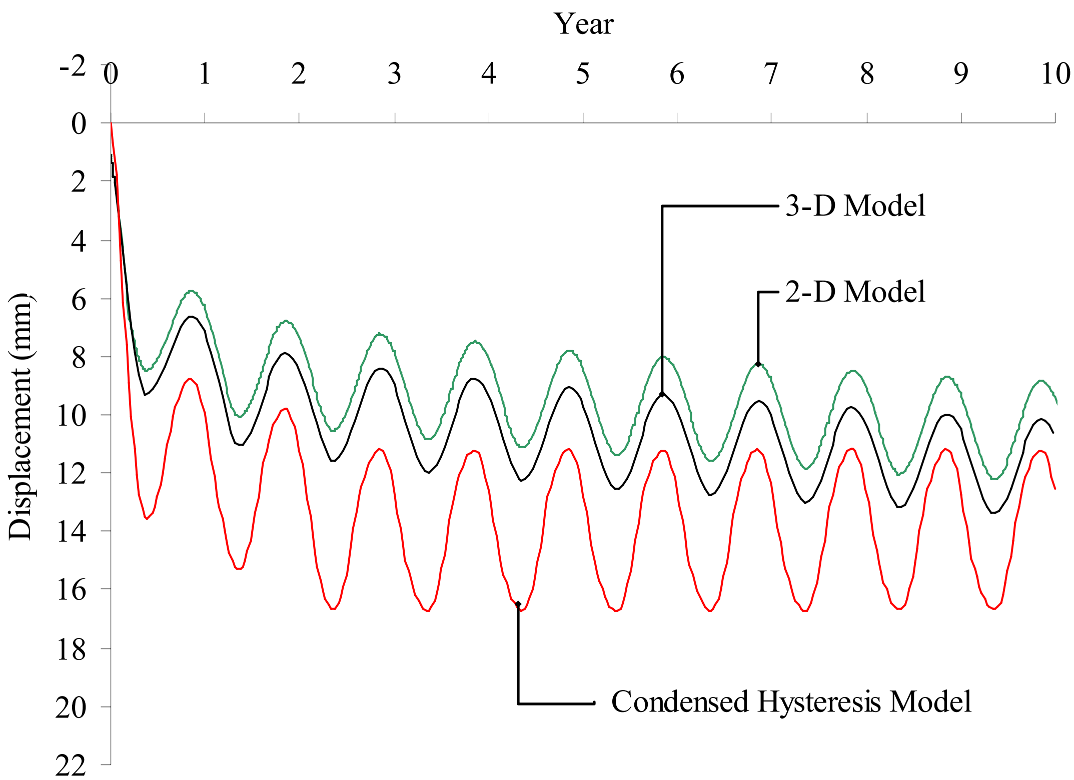

Figure 6-14: Predicted 10-Y Simulation Results from FE and Condensed Models at Bottom Extensometer

Analysis case 1 and analysis case 2 predicted abutment displacements at the top and bottom extensometer positions over the simulation period of 100 years are studied and presented in Figures 6-15 and 6-16 to quantify long-term effects of IA bridge behavior. The detailed descriptions of analysis case 1 and analysis case 2 are given below:

- case 1 - all hysteretic and non-hysteretic behaviors included and
- case 2 – all hysteretic and non-hysteretic behaviors excluded.

Analysis case 1 predicted abutment displacements represent bridge behaviors influenced by all pertinent long-term effects. Analysis case 2 predicted abutment displacements represent bridge behavior in which long-term effects are omitted. Therefore, the differences between these two analyses indicate the net quantity of long-term effects on bridge 203.

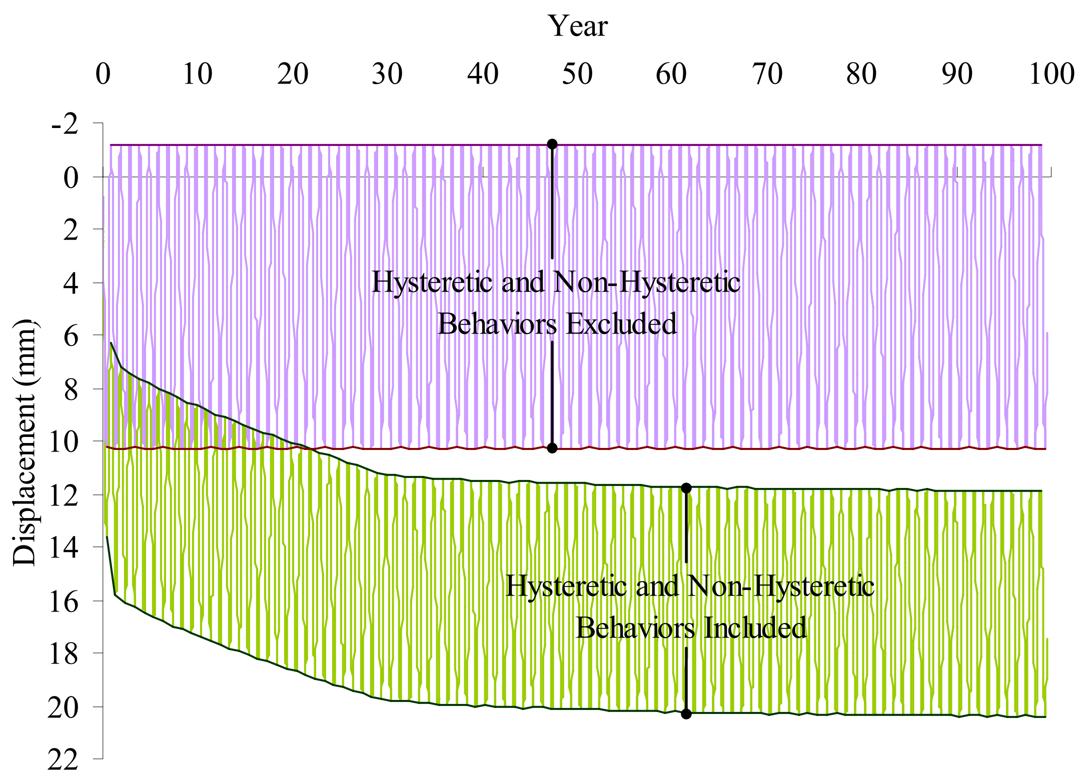

Figure 6-15: Predicted 100-Y Simulation Results from FE Model for Analysis Cases 1 and 2 at Top Extensometer

It is observed in Figure 6-15 that analysis case 1 predicted abutment displacement rate is relatively high at about the first 30 years. This predicted displacement rate gets smaller as the number of years is increased. However, analysis case 2 predicted abutment displacement rate is constant over the simulation period of 100 years. The maximum analysis case 1 and maximum analysis case 2 predicted abutment displacements at the end of the simulation period are 20.3 and 10.2 mm, indicating the ratio of long-term to short-term predicted abutment displacements of 2.0.

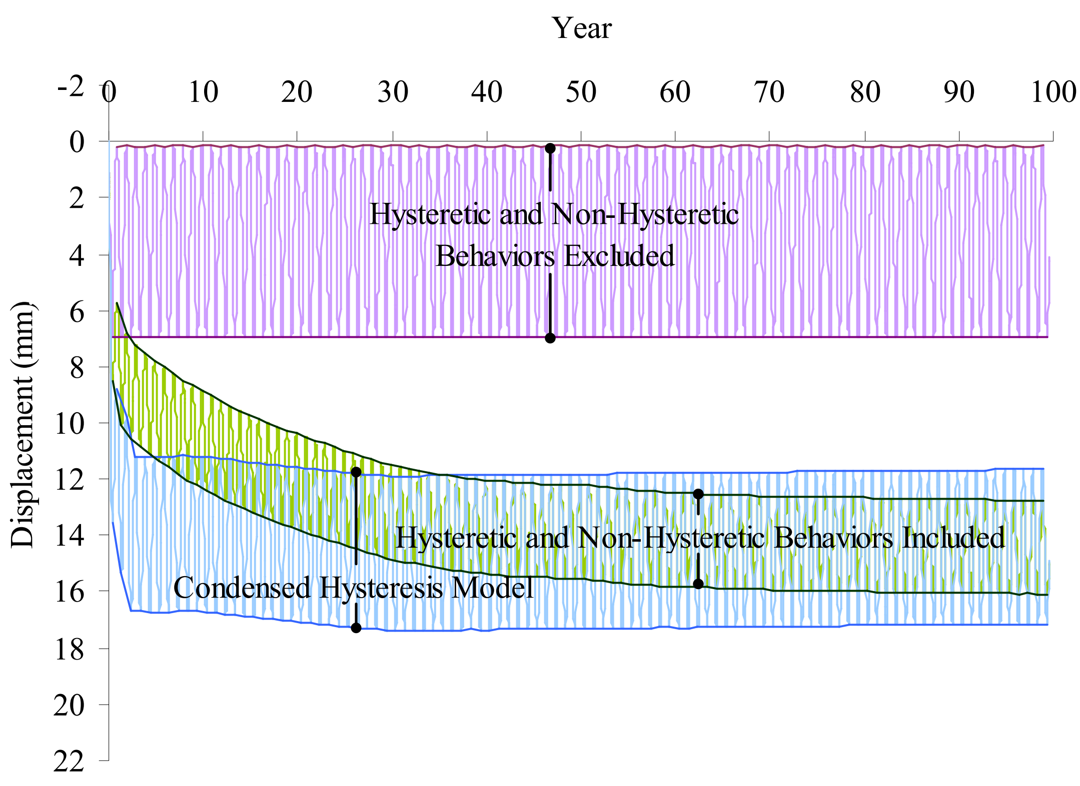

Figure 6-16: Predicted 100-Y Simulation Results from FE and Condensed Models for Analysis Cases 1 and 2 at Bottom Extensometer

It is observed in Figure **6-16** that analysis case 1 predicted abutment displacement rate is relatively high at about the first 30 years and gets smaller as the number of years is increased. However, analysis case 2 predicted abutment displacement rate is constant over the simulation period of 100 years. The maximum analysis case 1 and maximum analysis case 2 predicted abutment displacements at the end of the simulation period are 15.9 and 6.8 mm, indicating the ratio of long-term to short-term predicted abutment displacements of 2.3. In addition, condensed hysteresis model predicted abutment displacements at the bottom extensometer position are also presented in Figure **6-16**. The initial condensed hysteresis model predicted abutment displacement rate is significantly high at about the first 3 years. This predicted displacement rate becomes a nearly constant rate afterwards. The condensed hysteresis model predicted abutment displacement amplitude is approximately 1.7 times greater than the 2-D predicted abutment displacement amplitude. The ratio of condensed hysteresis model to 2-D predicted abutment displacements is 1.08.

Analysis case 3 and analysis case 4 predicted abutment displacements at the top and bottom extensometer positions are studied and presented in Figures **6-17** and **6-18** to evaluate the significance of hysteretic and non-hysteretic behaviors. The detailed description of analysis case 3 and analysis case 4 are given below:

- case 3 - only hysteretic behavior included and
- case 4 – only non-hysteretic behavior included.

Analysis case 3 predicted abutment displacements represent bridge behavior influenced by the combination of soil-structure interaction and abutment-backwall connection hysteretic components. Analysis case 4 predicted abutment displacements represent bridge behavior influenced by time-dependent effects. These predicted abutment displacements are compared with the analysis case 1 predicted abutment displacements to determine the relative magnitudes of hysteretic and non-hysteretic behaviors to the total long-term bridge behavior.

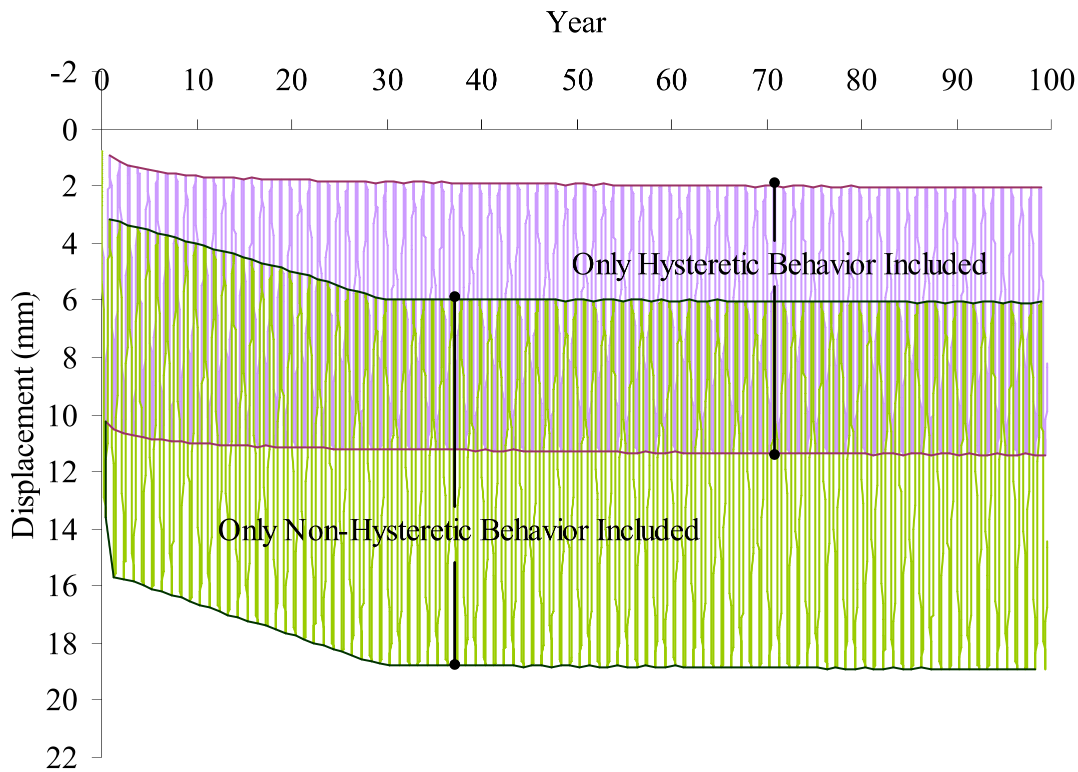

Figure 6-17: Predicted 100-Y Simulation Results from FE Model for Analysis Cases 3 and 4 at Top Extensometer

It is observed in Figure 6-17 that the maximum analysis case 3 and maximum analysis case 4 predicted abutment displacements at the end of the simulation period are 11.2 and 18.8 mm. Recalling that the maximum analysis case 1 predicted abutment displacement is 20.3 mm, it can be derived that the hysteretic and non-hysteretic behaviors are 55 and 93 percents proportional to the total long-term bridge behavior. Therefore, it is determined that predicted long-term abutment displacements near the girder elevation are strongly influenced by the non-hysteretic behavior.

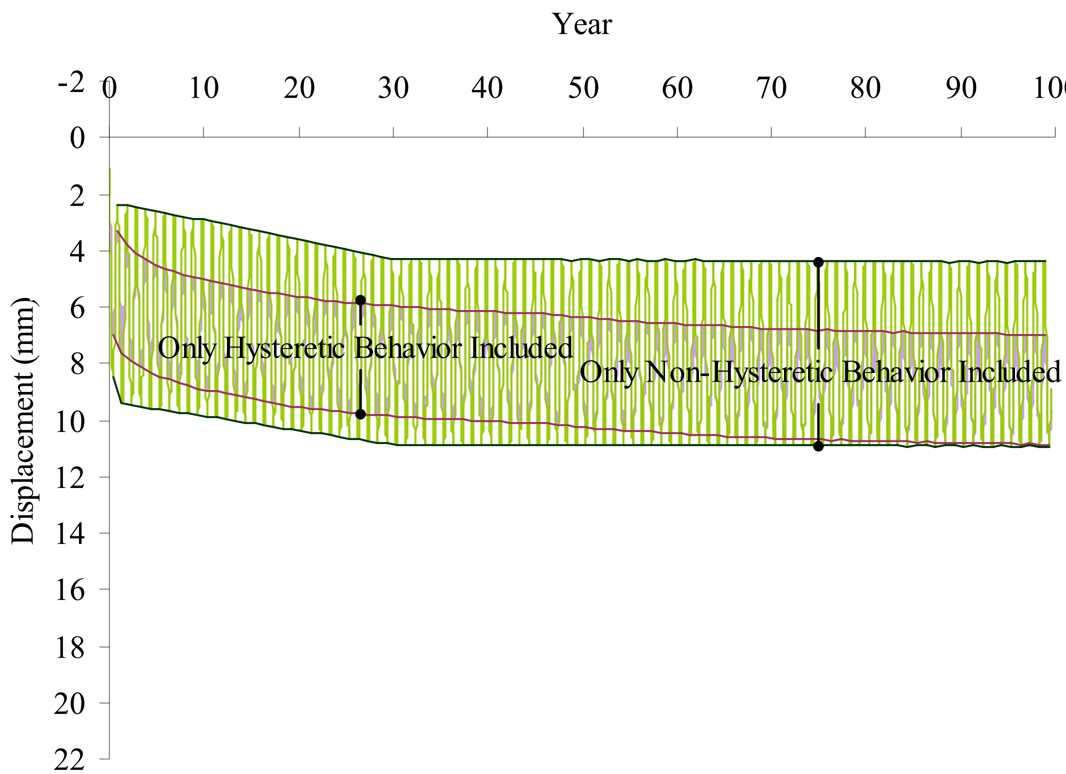

Figure 6-18: Predicted 100-Y Simulation Results from FE Model for Analysis Cases 3 and 4 at Bottom Extensometer

It is observed in Figure 6-18 that the maximum analysis case 3 and maximum analysis case 4 predicted abutment displacements at the end of the simulation period are 10.7 and 10.8 mm. Recalling that the maximum analysis case 1 predicted abutment displacement is 15.9 mm, it can be derived that the hysteretic and non-hysteretic behaviors are 67 and 68 percents proportional to the total long-term bridge behavior. Therefore, it is determined that predicted long-term abutment displacements near the abutment base elevation are equally influenced by both hysteretic and non-hysteretic behaviors.

Analysis case 5 and analysis case 6 predicted abutment displacements at the top and bottom extensometer positions are studied presented in Figures **6-19** and **6-20** to evaluate the significance of soil-structure interaction and abutment-backwall connection hysteretic behaviors. The detailed descriptions of analysis case 5 and analysis case 6 are given below:

- case 5 - only soil-structure interaction hysteretic behavior included and
- case 6 – only abutment-backwall connection hysteretic behavior included.

Analysis case 5 predicted abutment displacements represent bridge behavior influenced by soil-structure interaction hysteretic component. Analysis case 6 predicted abutment displacements represent bridge behavior influenced by abutment-backwall connection hysteretic component. These predicted abutment displacements are compared with the analysis case 2 and analysis case 3 predicted abutment displacements to determine the relative magnitudes of soil-structure interaction and abutment-backwall connection hysteretic behaviors to the total hysteretic behavior.

It is observed in Figure **6-19** that the maximum analysis case 5 and maximum analysis case 6 predicted abutment displacements at the end of the simulation period are 11.2 and 10.2 mm. Recalling that the maximum analysis case 2 and maximum analysis case 3 predicted abutment displacement are 10.2 and 11.2 mm, it can be derived that the total hysteretic behavior is fully dominated by the soil-structure interaction hysteretic component. However, it will be observed subsequently in the analysis case 8 that the abutment-backwall connection hysteretic component is capable of producing long-term effects when maximum resulting abutment displacements are high enough to make the structural connection yielded.

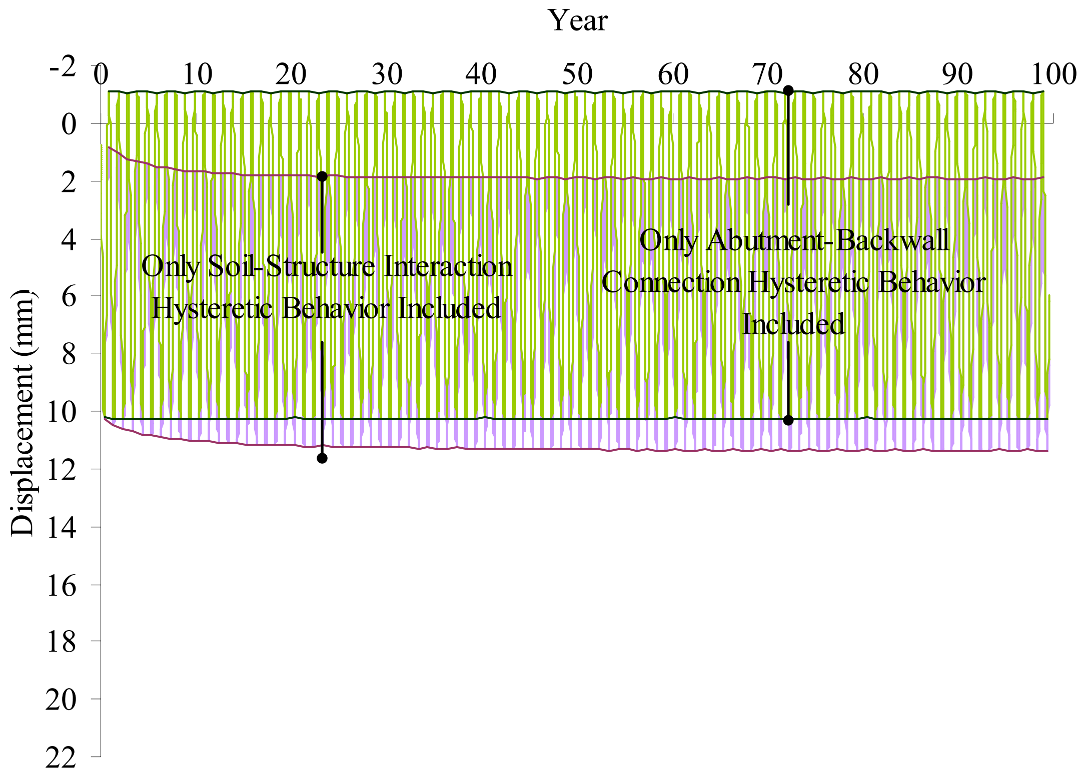

Figure 6-19: Predicted 100-Y Simulation Results from FE Model for Analysis Cases 5 and 6 at Top Extensometer

It is observed in Figure 6-20 that the maximum analysis case 5 and maximum analysis case 6 predicted abutment displacements at the end of the simulation period are 10.0 and 6.9 mm. Recalling that the maximum analysis case 2 and maximum analysis case 3 predicted abutment displacement are 6.8 and 10.7 mm, it can be derived that the total hysteretic behavior are strongly dominated by the soil-structure interaction hysteretic component. Similar to the implication given for the top elevation extensometer case, the abutment-backwall connection hysteretic component is capable of producing long-term effects when maximum resulting abutment displacements are high enough to make the structural connection yielded.

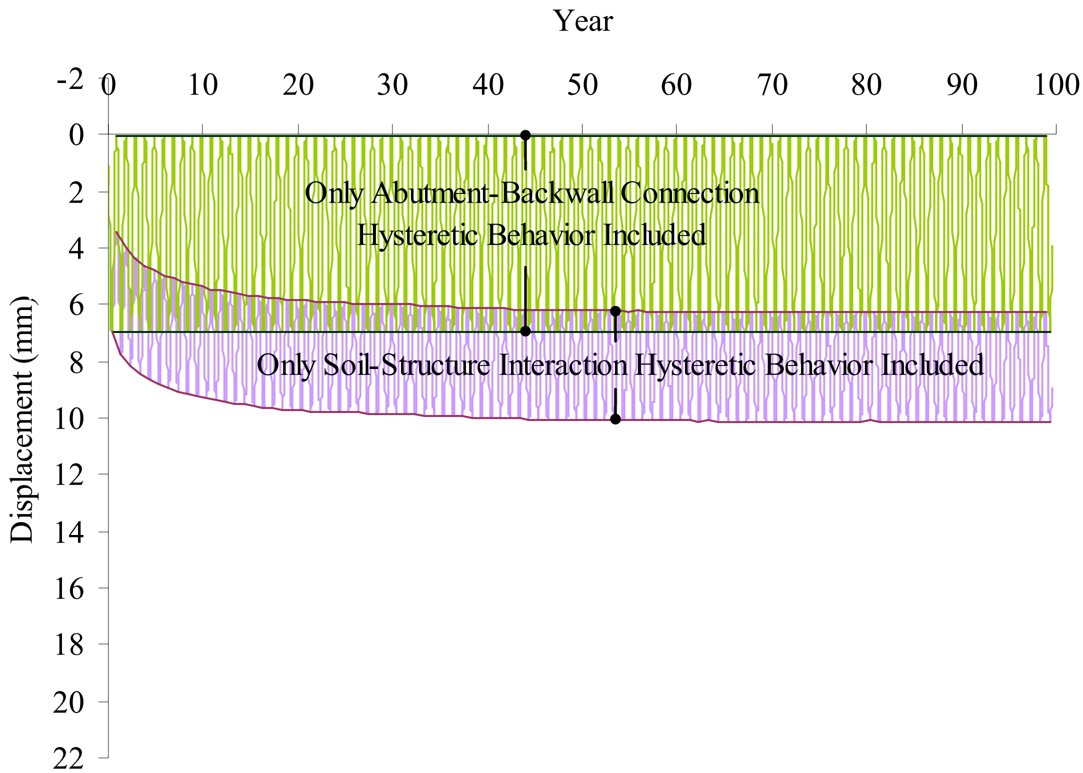

Figure 6-20: Predicted 100-Y Simulation Results from FE Model for Analysis Cases 5 and 6 at Bottom Extensometer

Analysis case 7 predicted abutment displacement at the top and bottom extensometer positions is studied and presented in Figures 6-21 and 6-22 to evaluate the significance of soil-pile interaction and soil-abutment interaction hysteretic behaviors. Analysis case 7 predicted abutment displacement represents bridge behavior influenced by soil-abutment interaction hysteretic component. This predicted abutment displacement is compared with the analysis case 2 predicted abutment displacement to determine the relative magnitudes of soil-pile interaction and soil-abutment interaction hysteretic behaviors to the soil-structure hysteretic behavior.

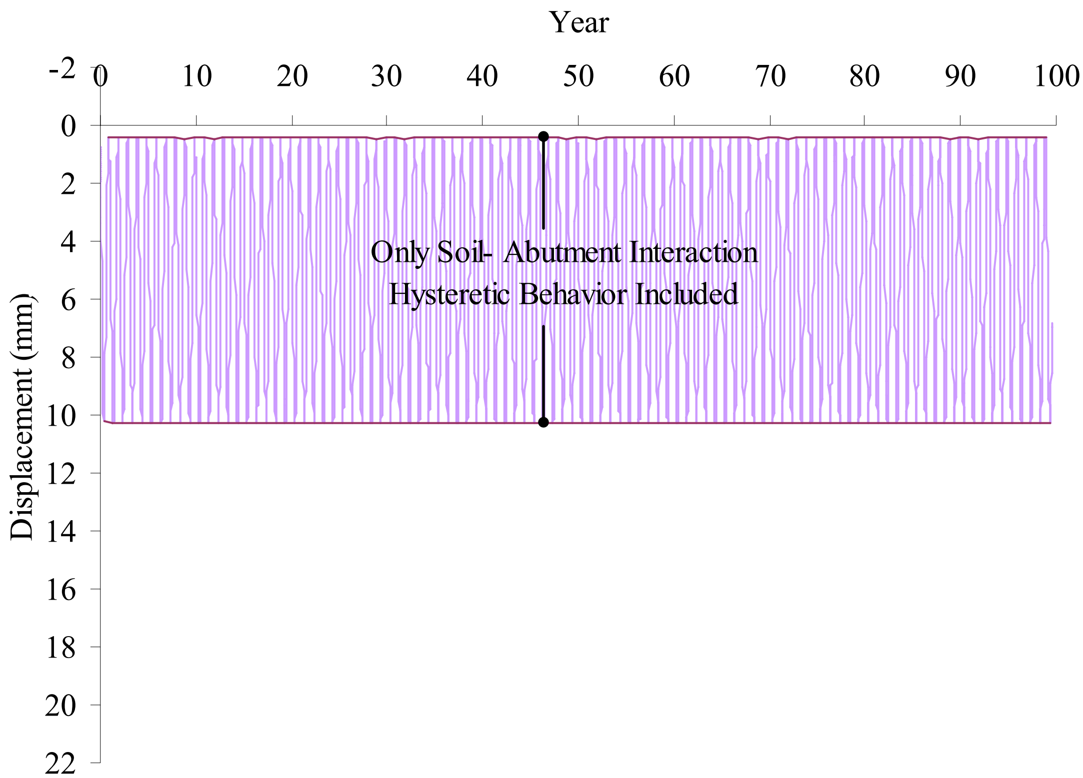

Figure 6-21: Predicted 100-Y Simulation Results from FE Model for Analysis Case 7 at Top Extensometer

It is observed in Figure 6-21 that the maximum analysis case 7 predicted abutment displacement at the end of the simulation period is the same as the maximum analysis case 2 predicted abutment displacement. However, the minimum analysis case 7 predicted abutment displacement is 1.6 mm different from the minimum analysis case 2 predicted abutment displacement. This difference indicates that abutment displacement amplitude is reduced due to the soil-abutment interaction hysteretic behavior, however, the soil-abutment interaction hysteretic behavior does not produce an adverse long-term displacement. The adverse long-term displacement is solely influenced by the soil-pile interaction hysteretic behavior.

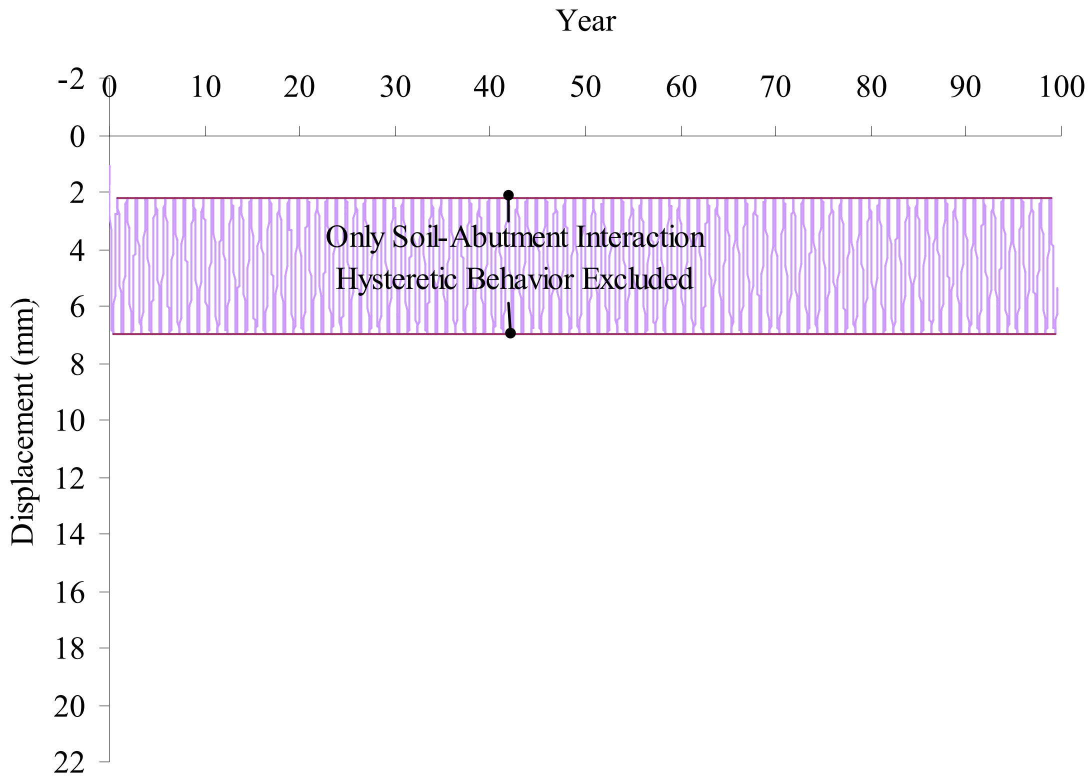

Figure 6-22: Predicted 100-Y Simulation Results from FE Model for Analysis Case 7 at Bottom Extensometer

It is observed in Figure 6-22 that the maximum analysis case 7 predicted abutment displacement at the end of the simulation period is the same as the maximum analysis case 2 predicted abutment displacement. However, the minimum analysis case 7 predicted abutment displacement is 2 mm different from the minimum analysis case 2 predicted abutment displacement. The same implication drawn from the top extensometer case is also applied to the bottom extensometer case.

Finally, analysis case 8 predicted abutment displacement at the top and bottom extensometer positions is studied and presented in Figures 6-23 and 6-24 to determine the influence of the abutment-backwall connection hysteretic behavior. Time-dependent effects are included here to produce additional abutment displacement to enforce a higher resulting rotation at the abutment-backwall connection, as compared to a resulting rotation produced by the analysis case 6 alone. When a resulting rotation is greater than the yielding capacity of the abutment-backwall connection, the influence of the abutment-backwall connection hysteretic behavior is initiated.

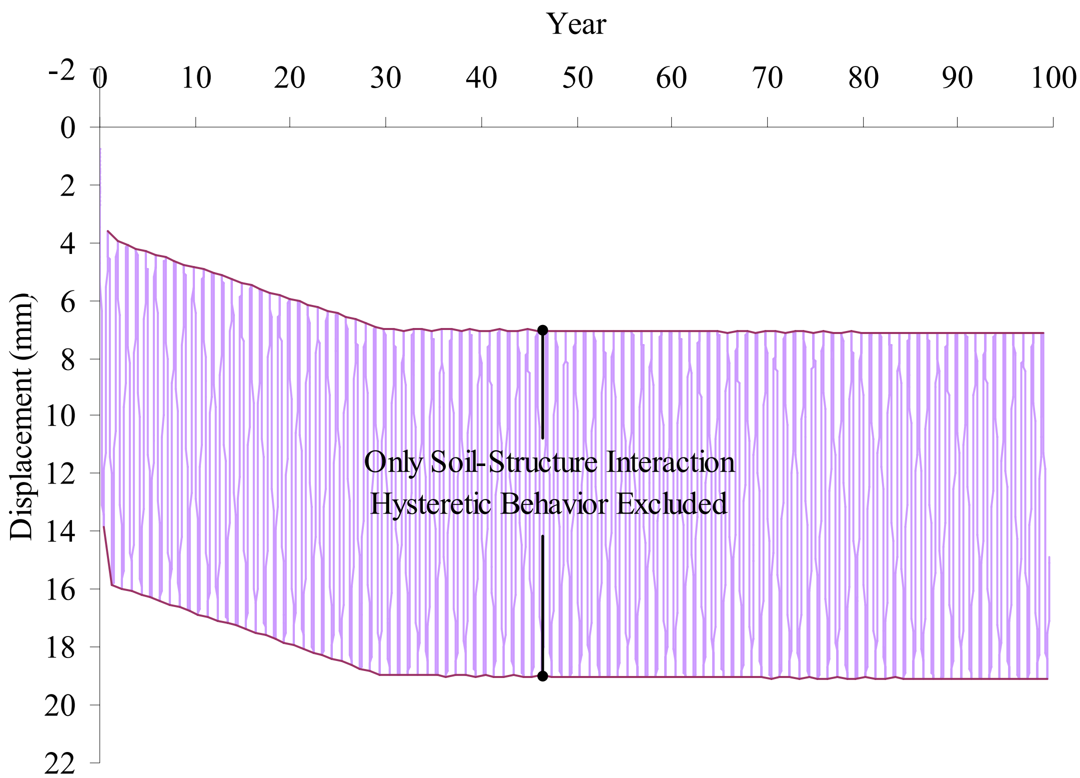

Figure 6-23: Predicted 100-Y Simulation Results from FE Model for Analysis Case 8 at Top Extensometer

It is observed in Figure 6-23 that the maximum analysis case 8 predicted abutment displacement at the end of the simulation period is 19.0 mm, which is nearly equal to the maximum analysis case 4 predicted abutment displacement. However, the minimum predicted analysis case 8 abutment displacement is 18 percent greater than the minimum analysis case 4 predicted abutment displacement. It is expected that this percent difference is greater for longer bridges.

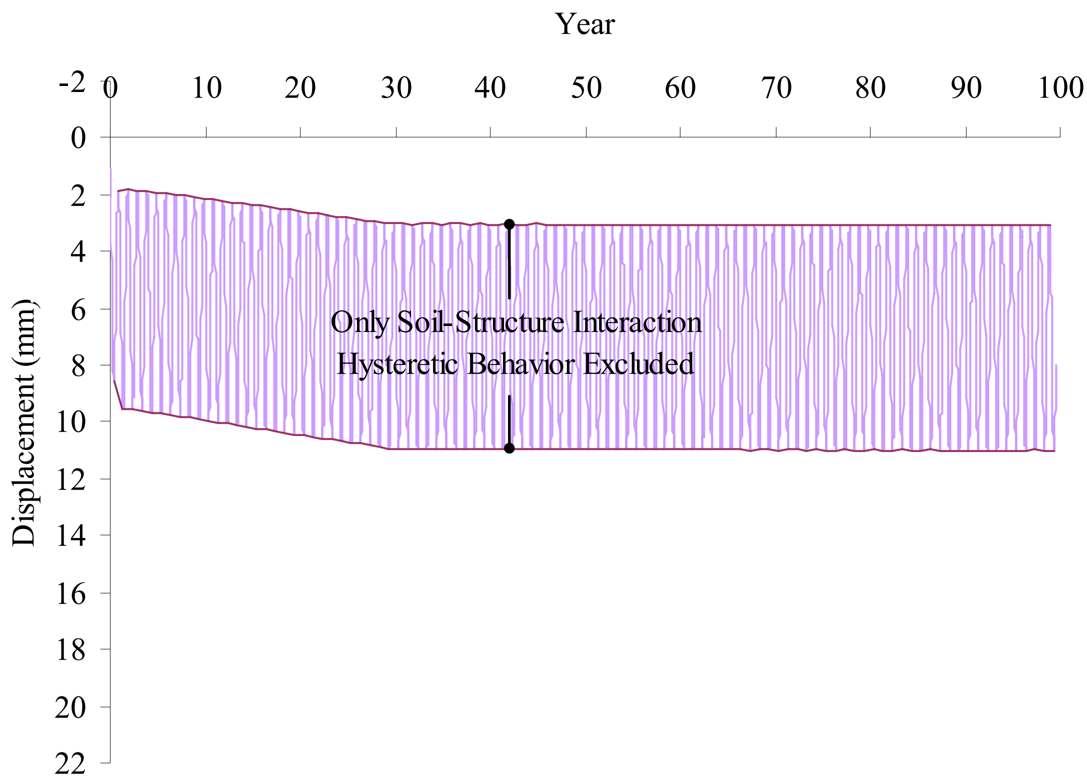

Figure 6-24: Predicted 100-Y Simulation Results from FE Model for Analysis Case 8 at Bottom Extensometer

It is observed in Figure 6-24 that the maximum analysis case 8 predicted abutment displacement at the end of the simulation period is 10.9 mm, which is nearly equal to the maximum analysis case 4 predicted abutment displacement. However, the minimum analysis case 8 predicted abutment displacement is 27 percent smaller than the minimum analysis case 4 predicted abutment displacement. It is expected that this percent difference is greater for longer bridges. On the other hand, the influence of the abutment-backwall connection hysteretic behavior for shorter bridges is negligible, which will be observed from predicted abutment displacements of the bridge 211 and bridge 222 FE models.

6.3.2 Bridge 211

Measured abutment displacements from top and bottom extensometers, corresponding to channels 4-5 and 4-6 for abutment 1 and channels 2-6 and 2-5 for abutment 2, are compared with FE and condensed hysteresis model predicted abutment displacements. The same sign convention used for bridge 203 displacements is also applied to the sign convention for bridge 211 displacements at abutment 1. However, the opposite sign convention is used for bridge 211 displacements at abutment 2.

Measured and predicted abutment displacements at the top and bottom extensometer positions of abutment 1 over the period of 17 months are presented in Figures **6-25** and **6-26**. It is observed in Figure **6-25** that the maximum percent difference between 2-D and 3-D predicted abutment displacements is 47 and the average percent difference is 27. The correlation between average measured abutment displacement and 2-D predicted abutment displacement is 0.845, while the correlation between average measured abutment displacement and 3-D predicted abutment displacement is 0.81. Measured, 2-D predicted, and 3-D predicted abutment displacements revealed the overall contraction trend. The 2-D and 3-D predicted abutment displacement amplitudes, between two adjacent peaks at the winter 2004 and summer 2004, are nearly equal to the measured abutment displacement amplitude.

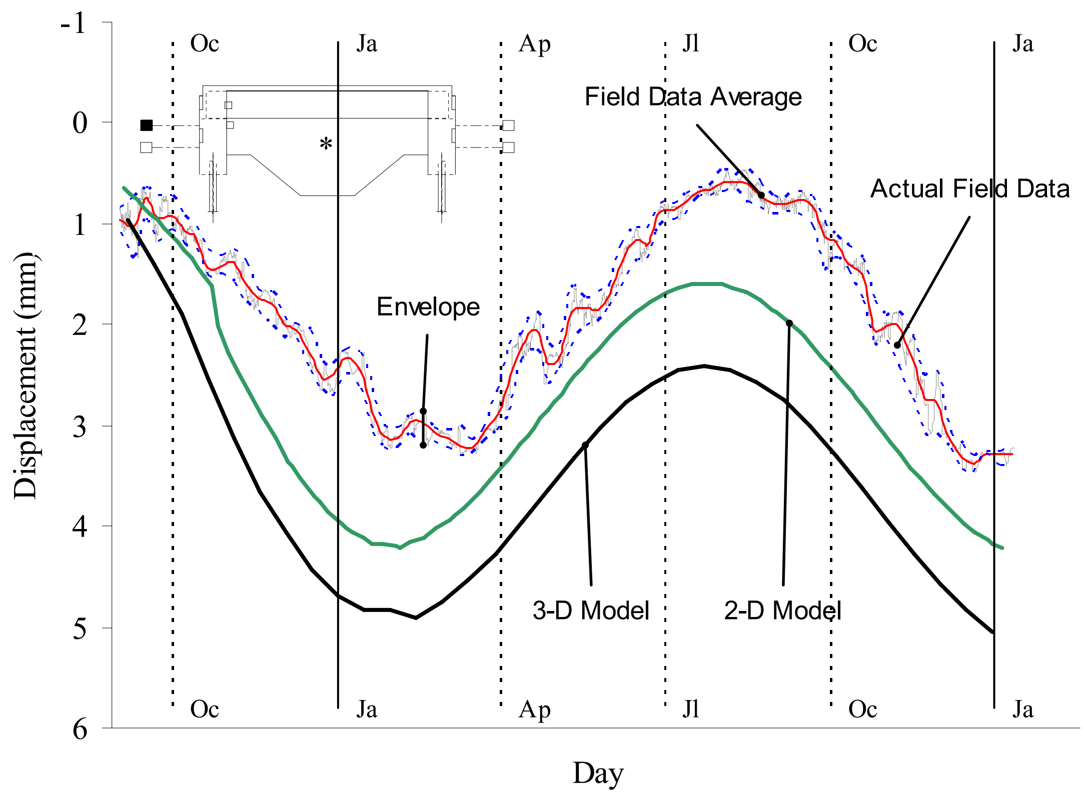

Figure 6-25: Top Elevation Extensometer Data and Predicted Results from FE Models (* Ref: Channel 4-5 in Figure A-7 for Instrumentation Location Detail at Abutment 1)

It is observed in Figure 6-26 that the maximum percent difference between 2-D and 3-D predicted abutment displacements is 47 and the average percent difference is 33. The maximum percent difference between 3-D and condensed hysteresis model predicted abutment displacement is 78 and the average percent difference is 50. The correlation between average measured abutment displacement and 2-D predicted abutment displacement is 0.806, the correlation between average measured abutment displacement and 3-D predicted abutment displacement is 0.913, and the correlation between average measured abutment displacement and condensed hysteresis model predicted abutment displacement is 0.735. Measured, 2-D predicted, 3-D predicted, and condensed hysteresis model predicted abutment displacements revealed the overall contraction trend. However, the measured abutment displacement rate is the greatest. The 2-D, 3-D, and condensed hysteresis model predicted abutment displacement amplitudes, between two adjacent peaks at the winter 2004 and summer 2004, are nearly equal to the measured abutment displacement amplitude.

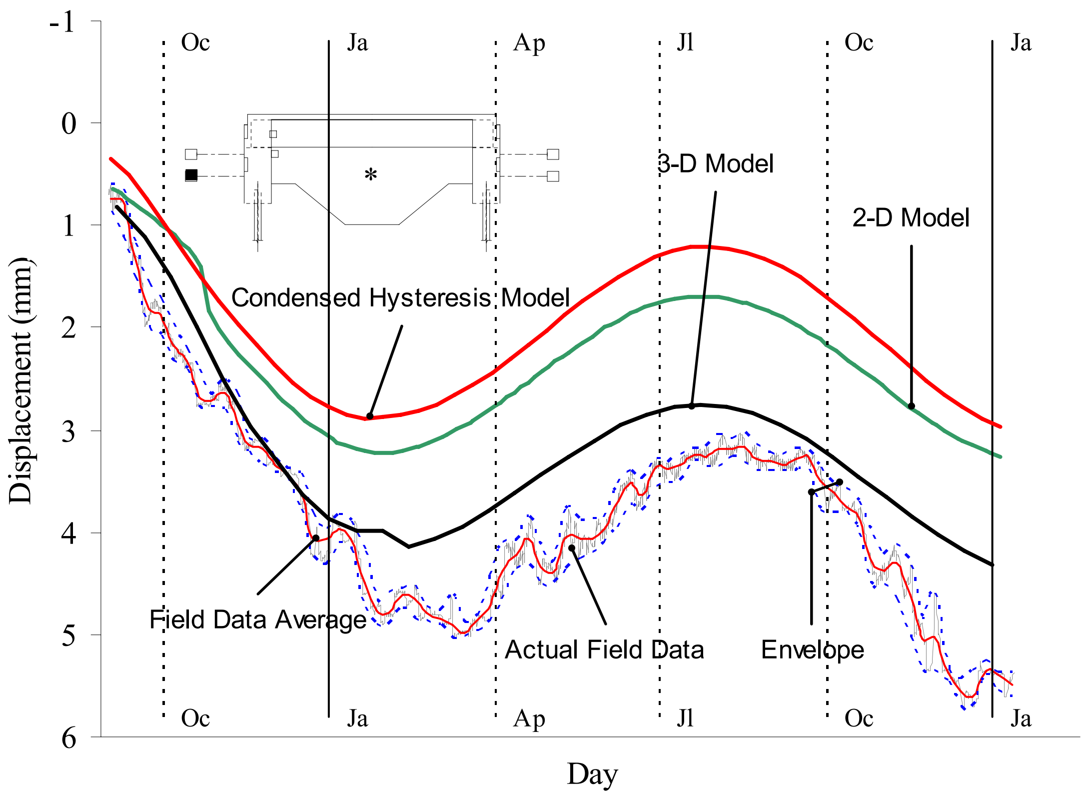

Figure 6-26: Bottom Extensometer Data and Results from FE and Condensed Models (* Ref: Channel 4-6 in Figure A-7 for Instrumentation Location Detail at Abutment 1)

Measured and predicted abutment displacements at the top and bottom extensometer positions of abutment 2 over the period of 17 months are presented in Figures 6-27 and 6-28. It is observed in Figure 6-27 that the maximum percent difference between 2-D and 3-D predicted abutment displacements is 22 and the average percent difference is 7. The correlation between average measured abutment displacement and 2-D predicted abutment displacement is 0.594, while the correlation between average measured abutment displacement and 3-D predicted abutment displacement is 0.629. The 2-D and 3-D predicted abutment displacements revealed the overall contraction trend, while the overall expansion trend is observed from measured abutment displacement. The 2-D and 3-D predicted abutment displacement amplitudes, between two adjacent peaks at the winter 2004 and summer 2004, are approximately 1.1 times greater than the measured abutment displacement amplitude.

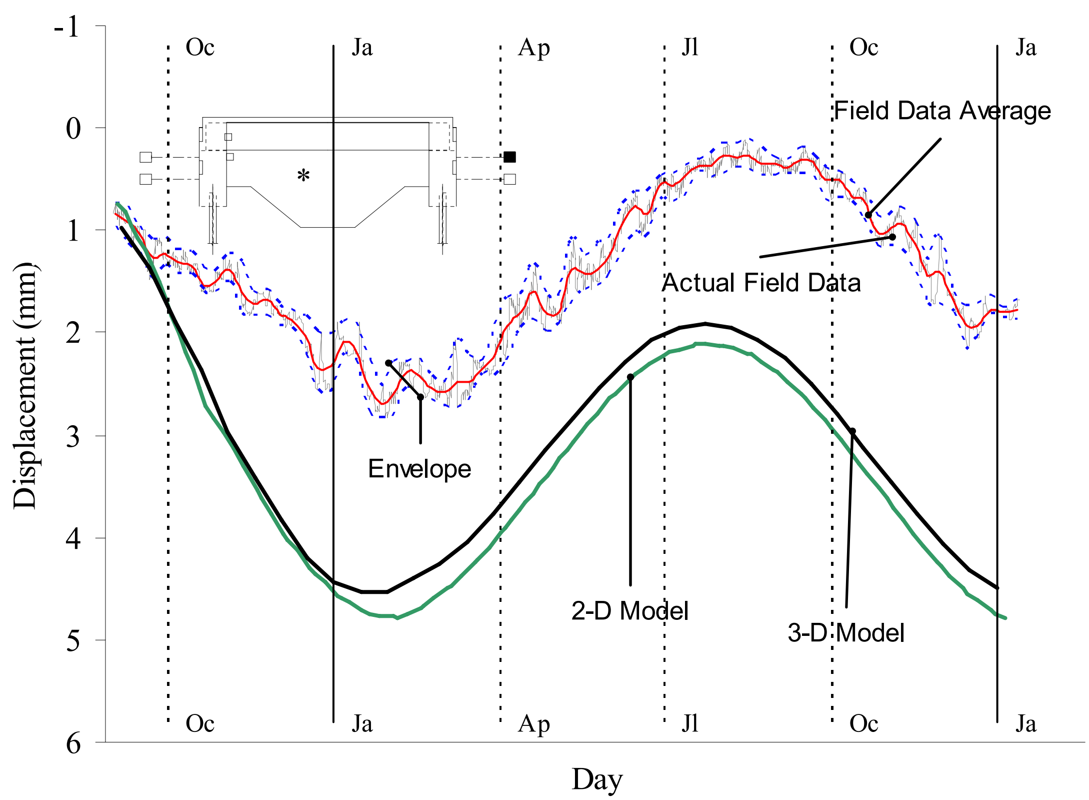

Figure 6-27: Top Elevation Extensometer Data and Predicted Results from FE Models (* Ref: Channel 2-6 in Figure A-6 for Instrumentation Location Detail at Abutment 2)

It is observed in Figure 6-28 that the maximum percent difference between 2-D and 3-D predicted abutment displacements is 20 and the average percent difference is 3.5. The maximum percent difference between 3-D and condensed hysteresis model predicted abutment displacement is 76 and the average percent difference is 41.

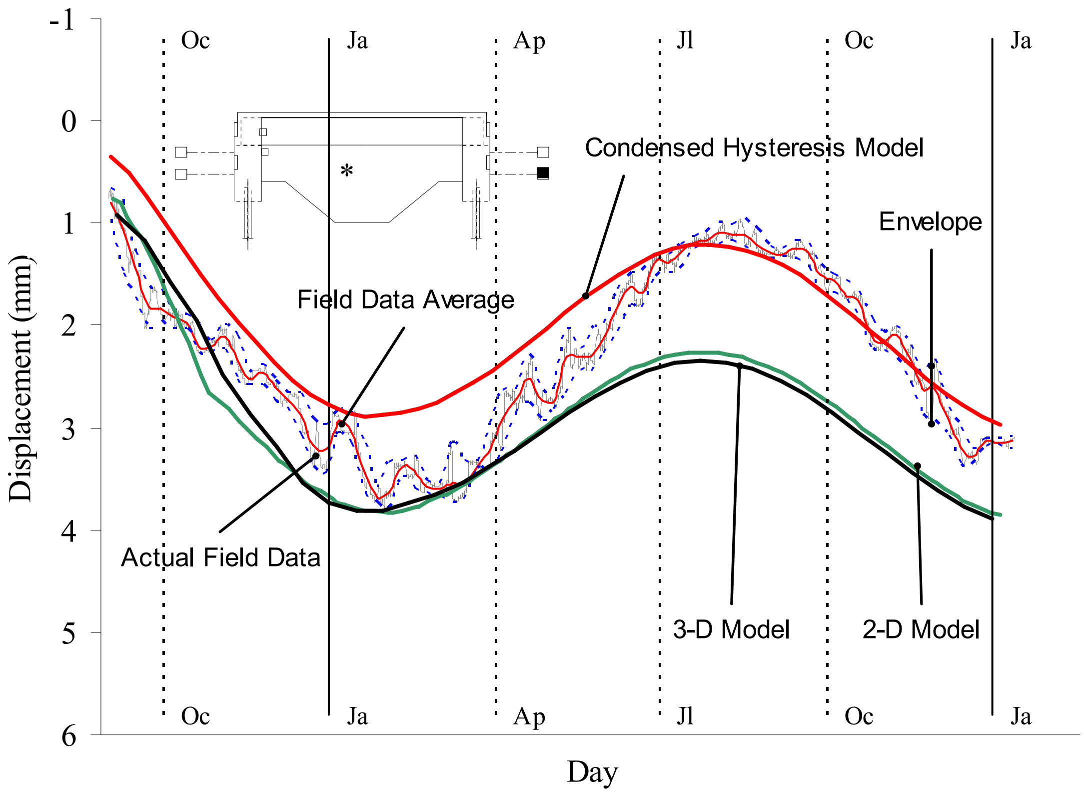

Figure 6-28: Bottom Extensometer Data and Results from FE and Condensed Models (* Ref: Channel 2-5 in Figure A-6 for Instrumentation Location Detail at Abutment 2)

The correlation between average measured abutment displacement and 2-D predicted abutment displacement is 0.712, the correlation between average measured abutment displacement and 3-D predicted abutment displacement is 0.641, and the correlation between average measured abutment displacement and condensed hysteresis model predicted abutment displacement is 0.818. Measured, 2-D predicted, 3-D predicted, and condensed hysteresis model predicted abutment displacements revealed the overall contraction trend. The 2-D, 3-D, and condensed hysteresis model predicted abutment displacement amplitudes, between two adjacent peaks at the winter 2004 and summer 2004, are approximately 0.6 times smaller than the measured abutment displacement amplitude.

2-D and 3-D predicted abutment displacements at the top and bottom extensometer positions over the simulation period of 10 years are presented in Figures 6-29 and 6-30. Note that A1 and A2 represent abutment 1 and abutment 2, respectively.

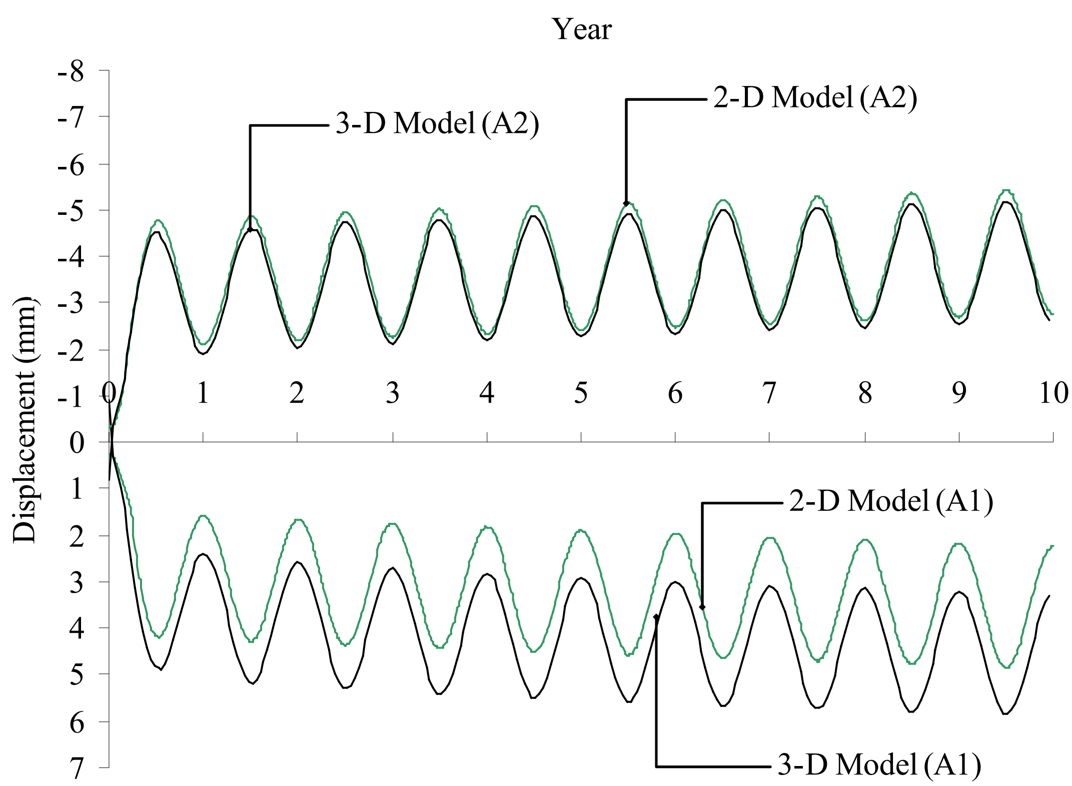

Figure 6-29: Predicted 10-Y Simulation Results from FE Models at Top Extensometer

It is observed in Figure 6-29 that the maximum percent differences between 2-D and 3-D predicted abutment displacements are 47 for abutment 1 and 21.5 for abutment 2. The average percent differences are 28 for abutment 1 and 5.5 for abutment 2. 2-D and 3-D predicted abutment displacements demonstrate the same trend, indicating that the abutments moving away from the backfill. The logarithmic increase in adjacent abutment displacement peaks is observed as the number of years is increased.

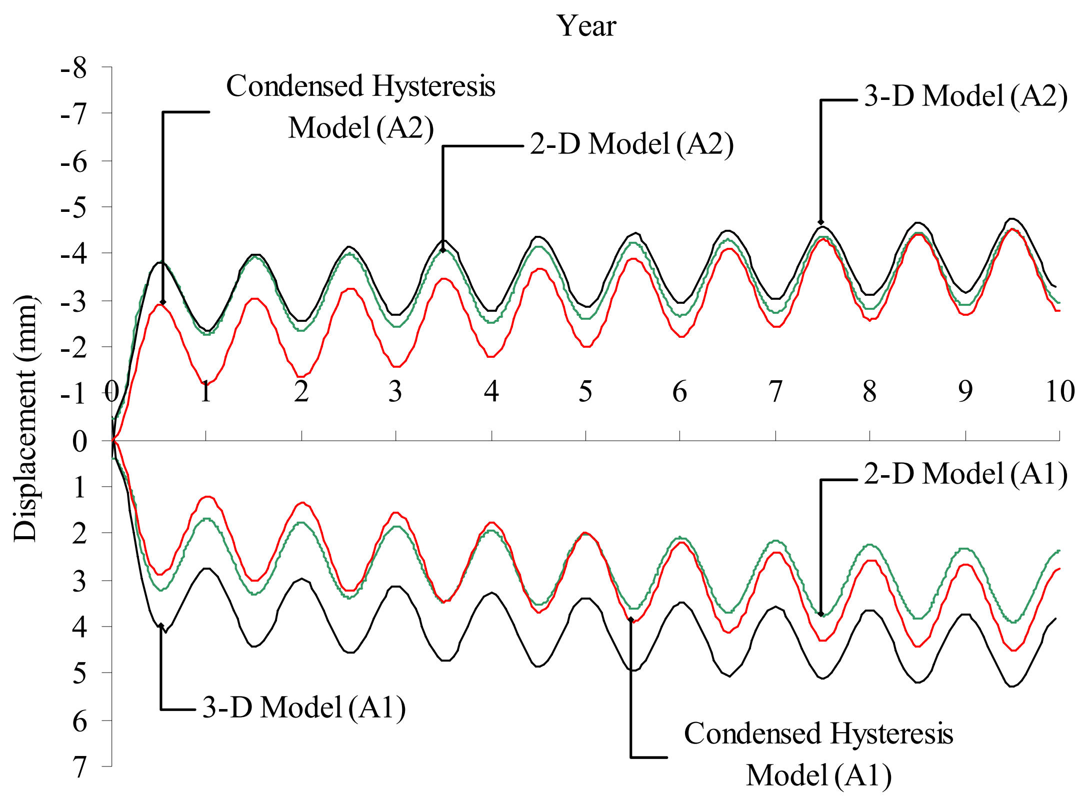

Figure 6-30: Predicted 10-Y Simulation Results from FE and Condensed Models at Bottom Extensometer

It is observed in Figure 6-30 that the maximum percent differences between 2-D and 3-D predicted abutment displacements are 51 for abutment 1 and 20 for abutment 2, while the average percent differences are 38 for abutment 1 and 6.3 for abutment 2. The maximum percent differences between 3-D and condensed hysteresis model predicted abutment displacements are 78 for abutment 1 and 76 for abutment 2, while the average percent differences are 37 for abutment 1 and 25 for abutment 2. The logarithmic increase in adjacent abutment displacement peaks is observed as the number of years is increased.

Analysis case 1 and analysis case 2 predicted abutment displacements at the top and bottom extensometer positions over the simulation period of 100 years are studied and presented in Figures **6-31** and **6-32** to determine long-term effects of IA bridge behavior.

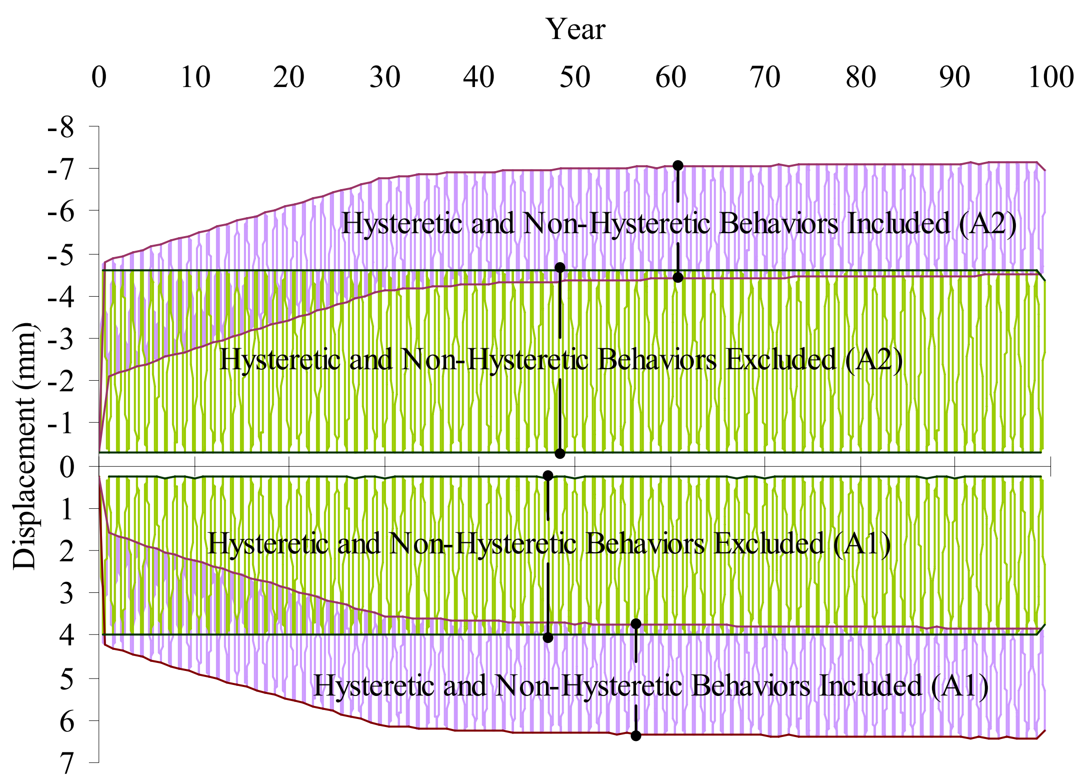

Figure **6-31**: Predicted 100-Y Simulation Results from FE Model for Analysis Cases 1 and 2 at Top Extensometer

It is observed in Figure 6-31 that the analysis case 1 predicted abutment displacement rate is relatively high at about the first 30 years and gets smaller as the number of years is increased. However, the analysis case 2 predicted abutment displacement rate is constant over the simulation period of 100 years. The maximum analysis case 1 and maximum analysis case 2 predicted abutment displacements at the end of the simulation period are 6.4 and 3.9 mm for abutment 1 (7.0 and 4.6 mm for abutment 2). These predicted abutment displacements indicate the ratios of long-term to short-term predicted abutment displacements of 1.6 and 1.5 for abutment 1 and abutment 2, respectively.

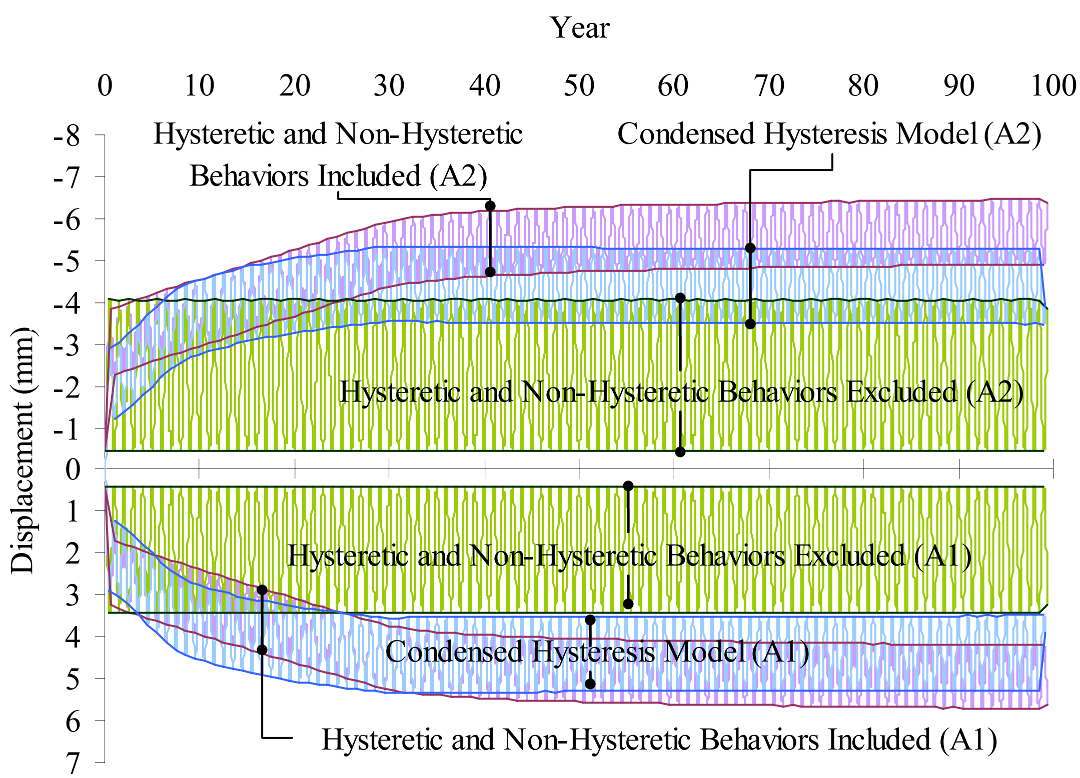

Figure 6-32: Predicted 100-Y Simulation Results from FE and Condensed Models for Analysis Cases 1 and 2 at Bottom Extensometer

It is observed in Figure 6-32 that the analysis case 1 predicted abutment displacement rate is relatively high at about the first 30 years and gets smaller as the number of years is increased. However, the analysis case 2 predicted abutment displacement rate is constant over the simulation period of 100 years. The maximum analysis case 1 and maximum analysis case 2 predicted abutment displacements at the end of the simulation period are 5.7 and 3.4 mm for abutment 1 (6.4 and 4.0 mm for abutment 2). These predicted abutment displacements indicate the ratios of long-term to short-term predicted abutment displacements of 1.7 and 1.6 for abutment 1 and abutment 2, respectively. In addition, condensed hysteresis model predicted abutment displacement at the bottom extensometer position is also presented. The percent differences between 2-D and condensed hysteresis model predicted abutment displacement amplitudes are 12.5 for abutment 1 and 19.4 for abutment 2. The percent differences between 2-D and condensed hysteresis model predicted abutment displacements are 9.2 for abutment 1 and 20.7 for abutment 2.

Analysis case 3 and analysis case 4 predicted abutment displacements at the top and bottom extensometer positions are studied and presented in Figures 6-33 and 6-34 to determine the relative magnitudes of hysteretic and non-hysteretic behavior. It is observed in Figure 6-33 that the maximum analysis case 3 and maximum analysis case 4 predicted abutment displacements at the end of the simulation period are 4.4 and 5.4 mm for abutment 1 (5.6 and 5.9 mm for abutment 2). Recalling that the maximum analysis case 1 predicted abutment displacement is 6.4 mm for abutment 1 and 7 mm for abutment 2, it can be derived that the hysteretic and non-hysteretic behaviors are 69 and 84 percent proportional to the total long-term behavior for abutment 1 (80 and 84 percents for abutment 2). Unlike the implication for bridge 203, predicted abutment displacements for bridge 211 indicate that hysteretic behavior has the influence on the total long-term abutment displacements near the girder elevation as significant as non-hysteretic behavior. This is because the girder age at erection for bridge 211 was 268 days, while the girder age at erection for bridge 203 was 115 days.

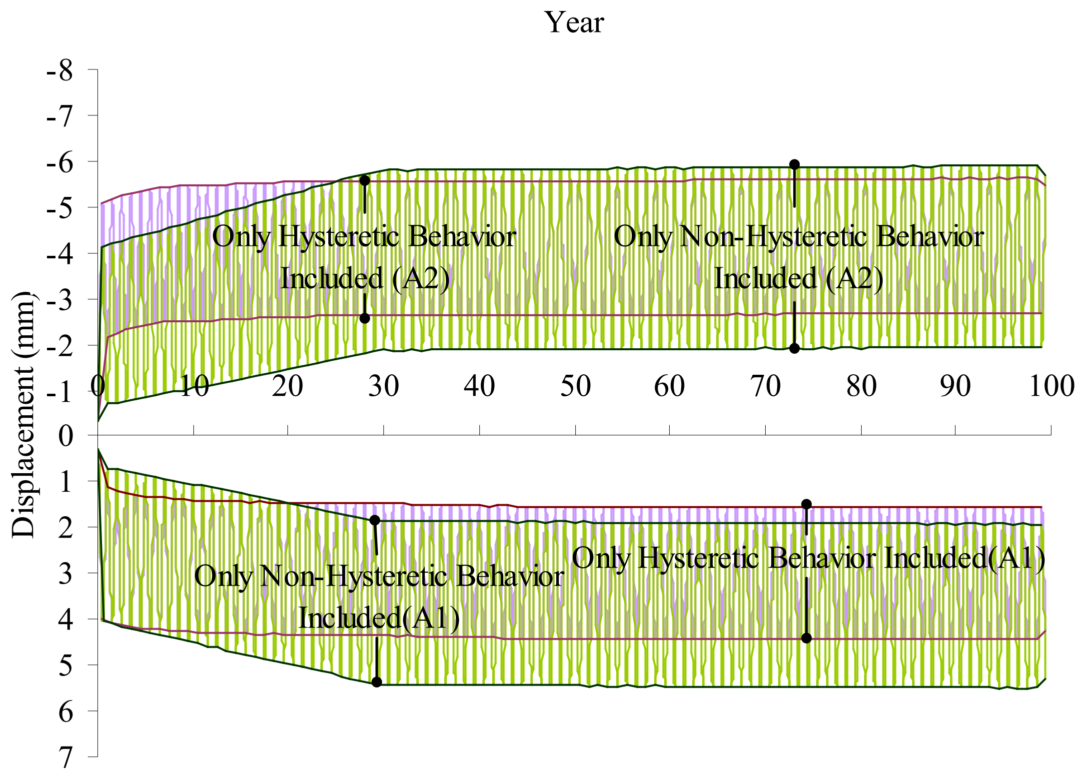

Figure 6-33: Predicted 100-Y Simulation Results from FE Model for Analysis Cases 3 and 4 at Top Extensometer

It is observed in Figure 6-34 that the maximum analysis case 3 and maximum analysis case 4 predicted abutment displacements at the end of the simulation period are 4.3 and 4.1 mm for abutment 1 (5.5 and 4.5 mm for abutment 2). Recalling that the maximum analysis case 1 predicted abutment displacement is 5.7 mm for abutment 1 and 6.4 mm for abutment 2, it can be derived that the hysteretic and non-hysteretic behaviors are 79 and 72 percent proportional to the total long-term behavior for abutment 1 (86 and 70 percents for abutment 2). Therefore, it is determined that predicted long-term abutment displacements near the abutment base elevation are equally influenced by both hysteretic and non-hysteretic behaviors.

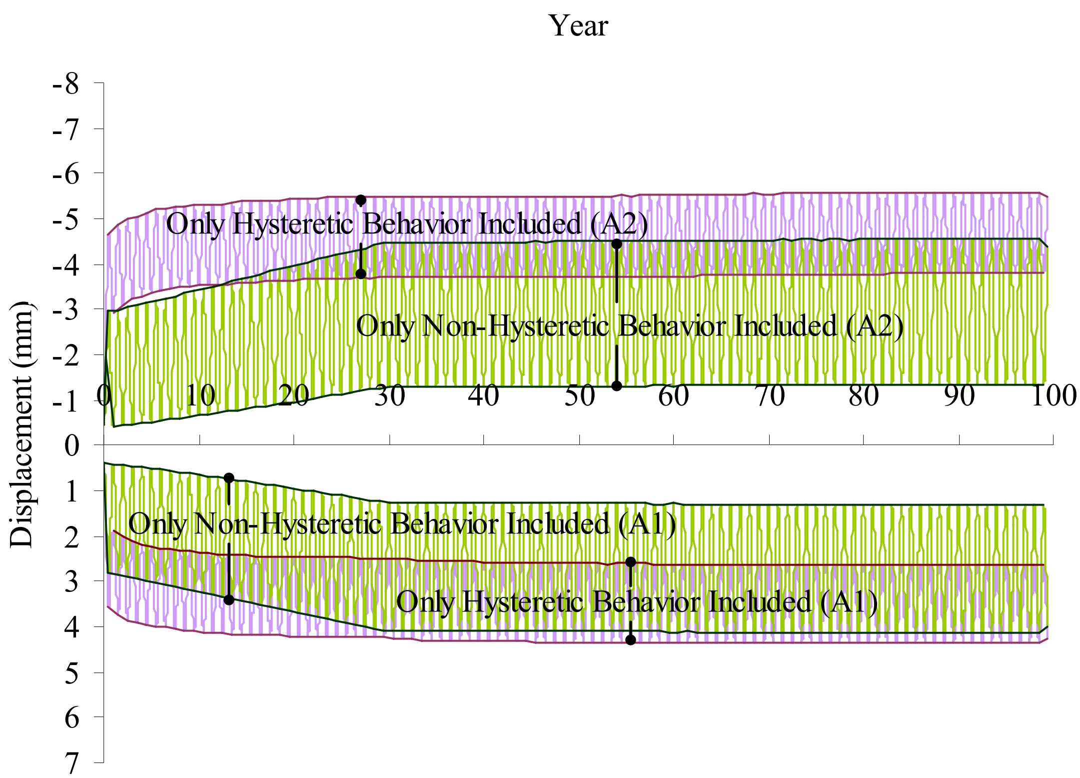

Figure 6-34: Predicted 100-Y Simulation Results from FE Model for Analysis Cases 3 and 4 at Bottom Extensometer

Analysis case 5 and analysis case 6 predicted abutment displacements are studied and presented in Figures 6-35 and 6-36 to determine the relative magnitudes of soil-structure interaction and abutment-backwall connection hysteretic behaviors. It is observed in Figure 6-35 that the maximum analysis case 5 and maximum analysis case 6 predicted abutment displacements at the end of the simulation period are 4.4 and 3.9 mm for abutment 1 (5.6 and 4.6 mm for abutment 2). Recalling that the maximum analysis case 2 and maximum analysis case 3 predicted abutment displacement are 3.9 and 4.4 mm for abutment 1 (4.6 and 5.6 mm for abutment 2), it can be derived that the total hysteretic behavior is fully dominated by the soil-structure interaction hysteretic behavior.

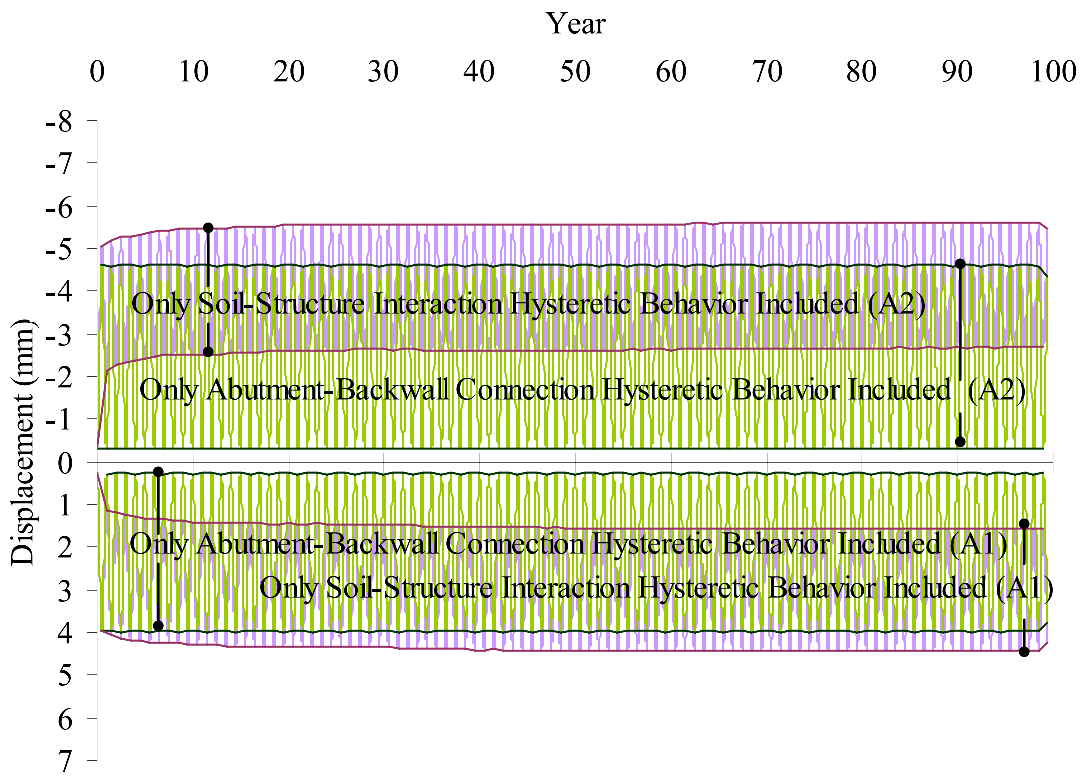

Figure 6-35: Predicted 100-Y Simulation Results from FE Model for Analysis Cases 5 and 6 at Top Extensometer

It is observed in Figure 6-36 that the maximum analysis case 5 and maximum analysis case 6 predicted abutment displacements at the end of the simulation period are 4.3 and 3.4 mm for abutment 1 (5.5 and 4.0 mm for abutment 2). Recalling that the maximum analysis case 2 and maximum analysis case 3 predicted abutment displacement are 3.4

and 4.3 mm for abutment 1 (4.0 and 5.5 mm for abutment 2), it can be derived that the total hysteretic behavior is fully dominated by the soil-structure interaction hysteretic behavior.

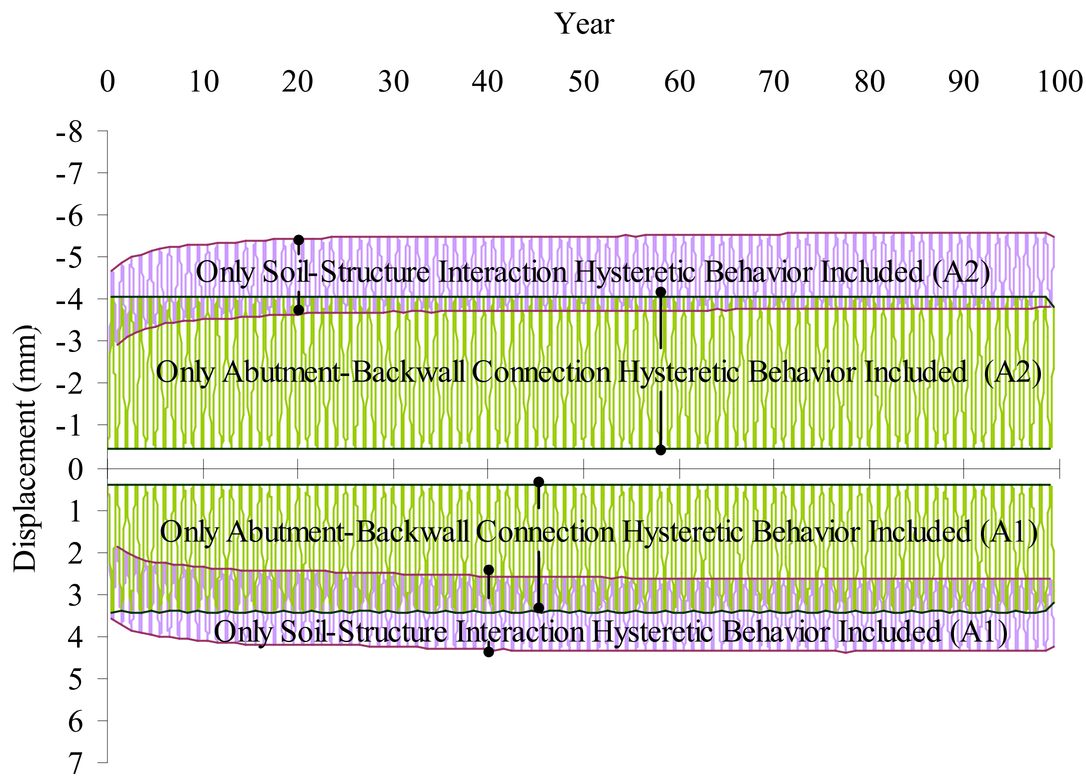

Figure 6-36: Predicted 100-Y Simulation Results from FE Model for Analysis Cases 5 and 6 at Bottom Extensometer

Analysis case 7 predicted abutment displacement for bridge 211 indicate the same implication as for bridge 203. It is determined that soil-abutment interaction hysteretic behavior affects only the minimum predicted abutment displacement envelope, while the adverse long-term abutment displacement is solely influenced by the soil-pile interaction hysteretic behavior.

Finally, analysis case 8 predicted abutment displacements at the top and bottom extensometer positions are studied and presented in Figures 6-37 and 6-38 to investigate the influence of the abutment-backwall connection hysteretic behavior.

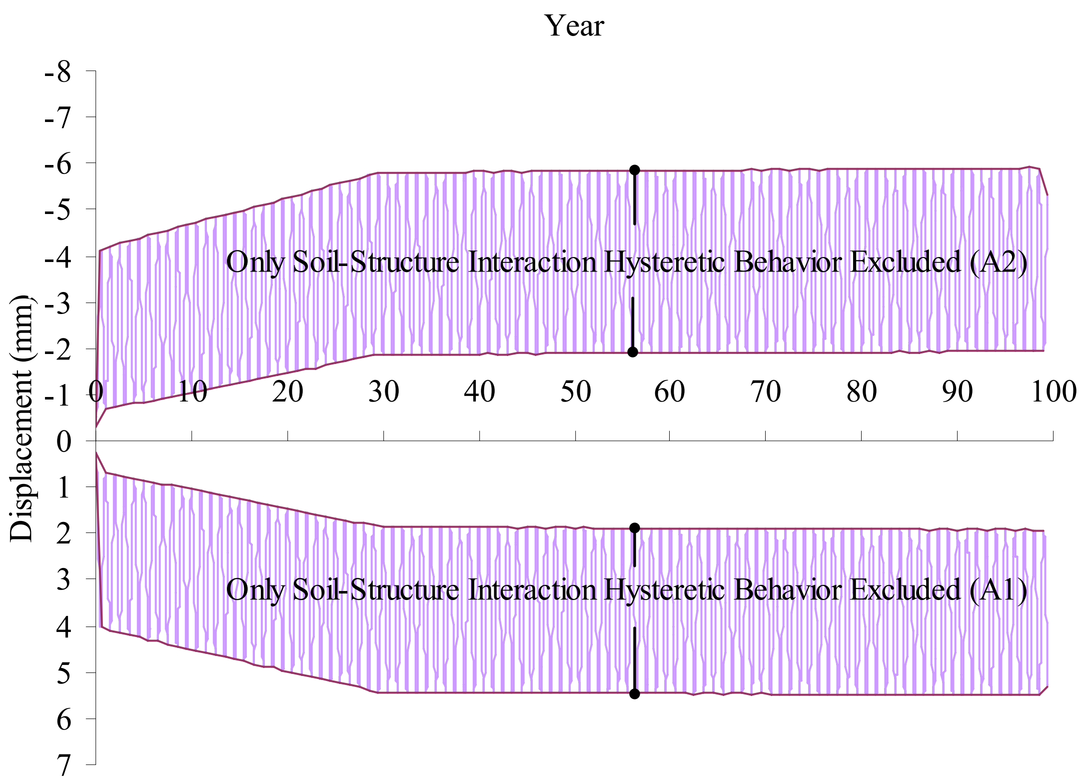

Figure 6-37: Predicted 100-Y Simulation Results from FE Model for Analysis Case 8 at Top Extensometer

It is observed in Figure 6-37 that the maximum analysis case 8 predicted abutment displacements at the end of the simulation period are 5.4 mm for abutment 1 and 5.9 mm for abutment 2, which are identical to the maximum analysis case 4 predicted abutment displacements. The minimum analysis case 7 predicted abutment displacements at the end of the simulation period are approximately 5 percent different from the minimum analysis case 4 predicted abutment displacements. These predicted abutment displacements indicate that the influence from the abutment-backwall connection hysteretic behavior is negligible.

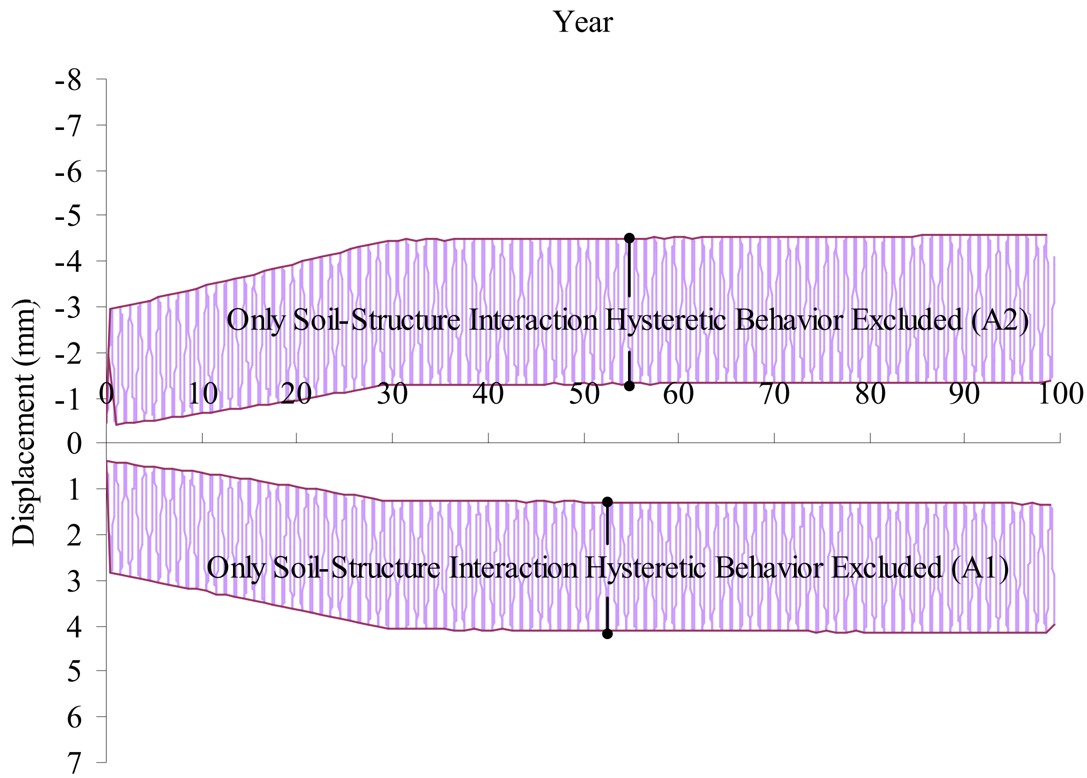

Figure 6-38: Predicted 100-Y Simulation Results from FE Model for Analysis Case 8 at Bottom Extensometer

It is observed in Figure 6-38 that the maximum analysis case 8 predicted abutment displacements at the end of the simulation period are 4.1 mm for abutment 1 and 4.5 mm for abutment 2, which are identical to the maximum analysis case 4 predicted abutment displacements. The minimum analysis case 8 predicted abutment displacements at the end of the simulation period are approximately 7 percent different from the minimum analysis case 4 predicted abutment displacements. Therefore, the same implication as described for the top extensometer is also applied here.

6.3.3 Bridge 222

Measured abutment displacements from top and bottom extensometers, corresponding to channels 3-5 and 3-6 for abutment 1 and channels 2-1 and 2-2 for abutment 2, are compared with FE and condensed hysteresis model predicted abutment displacements. The same sign convention used for bridge 211 displacements is also applied to the sign convention for bridge 222 displacements.

Measured and predicted abutment displacements at the top and bottom extensometer positions of abutment 1 over the period of 27 months are presented in Figures **6-39** and **6-40**. It is observed in Figure **6-39** that the maximum percent difference between 2-D and 3-D predicted abutment displacements is 13.5 and the average percent difference is 7.4. The correlation between average measured abutment displacement and 2-D predicted abutment displacement is 0.645, while the correlation between average measured abutment displacement and 3-D predicted abutment displacement is 0.651. The 2-D and 3-D predicted abutment displacement amplitudes are approximately 1.15 times greater than the measured abutment displacement amplitude. A different trend between measured and predicted abutment displacements is observed. The measured abutment displacement revealed the overall expansion trend, while the predicted abutment displacement demonstrated the overall contraction trend.

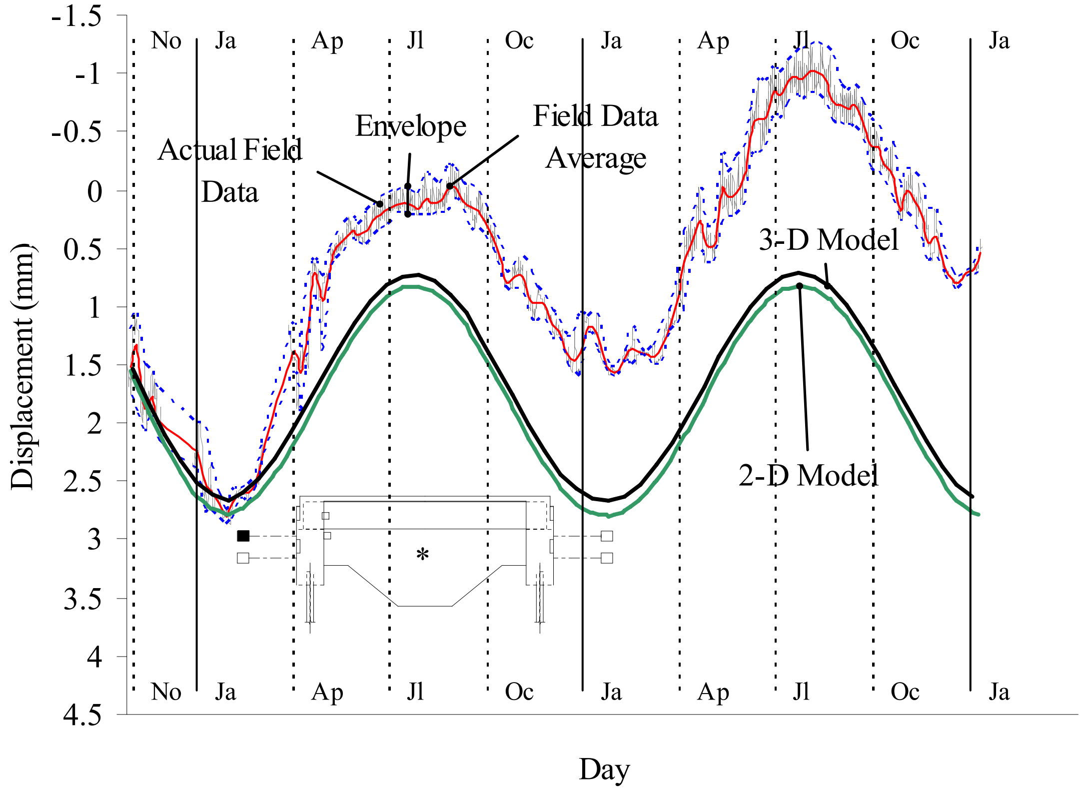

Figure 6-39: Top Elevation Extensometer Data and Predicted Results from FE Models (* Ref: Channel 3-5 in Figure A-12 for Instrumentation Location Detail at Abutment 1)

It is observed in Figure 6-40 that the maximum percent difference between 2-D and 3-D predicted abutment displacements is 5.4 and the average percent difference is 3.1. The maximum percent difference between 3-D and condensed hysteresis model predicted abutment displacements is 5.3 and the average percent difference is 2.8. The correlation between average measured abutment displacement and 2-D predicted abutment displacement is 0.241, the correlation between average measured abutment displacement and 3-D predicted abutment displacement is 0.255, and the correlation between average measured abutment displacement and condensed hysteresis model predicted abutment displacement is 0.202. Measured, 2-D predicted, 3-D predicted, and condensed hysteresis model predicted abutment displacements revealed the overall contraction trend. However, the measured abutment displacement rate is the greatest. The 2-D predicted, 3-D predicted, and condensed hysteresis model predicted abutment displacement amplitudes are approximately 1.1 times greater than the measured abutment displacement amplitude.

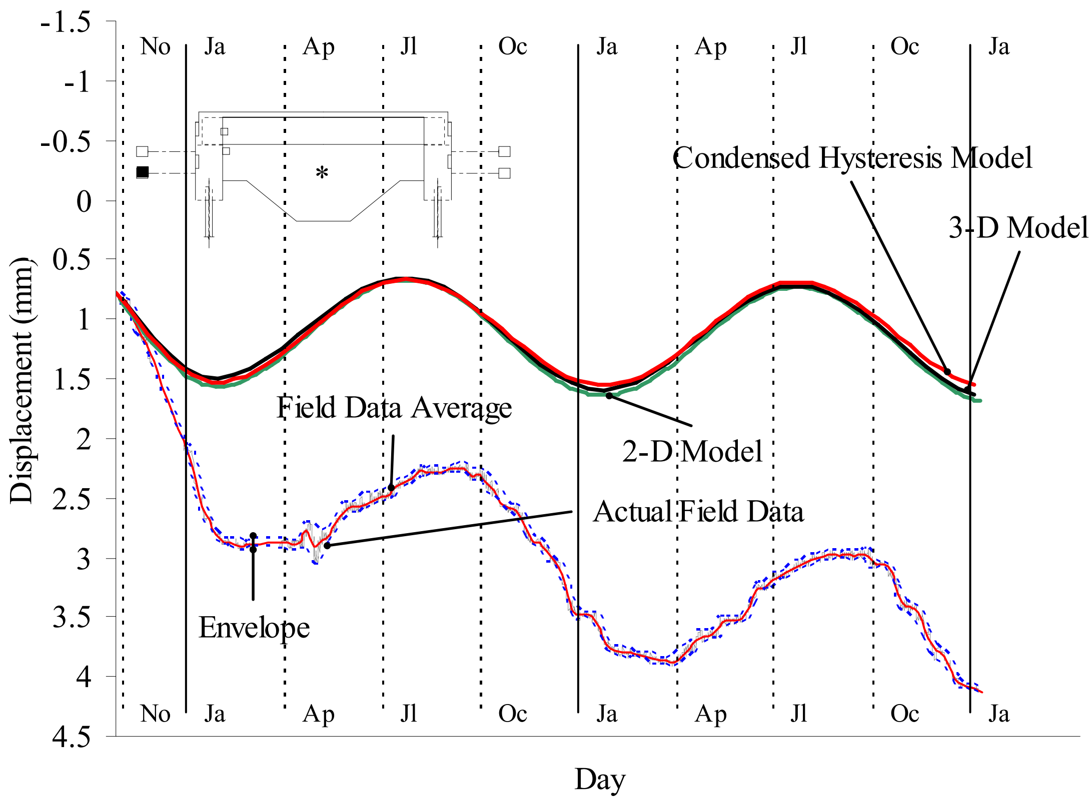

Figure 6-40: Bottom Extensometer Data and Results from FE and Condensed Models
(* Ref: Channel 3-6 in Figure A-12 for Instrumentation Location Detail at Abutment 1)

Measured and predicted abutment displacements at the top and bottom extensometer positions of abutment 2 over the period of 27 months are presented in Figures 6-41 and 6-42. It is observed in Figure 6-41 that the maximum percent difference between 2-D and 3-D predicted abutment displacements is 3.6 and the average percent difference is 1.4. The correlation between average measured abutment displacement and

2-D predicted abutment displacement is 0.312, while the correlation between average measured abutment displacement and 3-D predicted abutment displacement is 0.282. A different trend between measured and predicted abutment displacements is observed. The measured abutment displacement revealed the overall expansion trend, while the predicted abutment displacement demonstrated the overall contraction trend. Lag in measured abutment displacement peaks of approximately two months is observed, which leads to the poor correlations between measured and predicted abutment displacements.

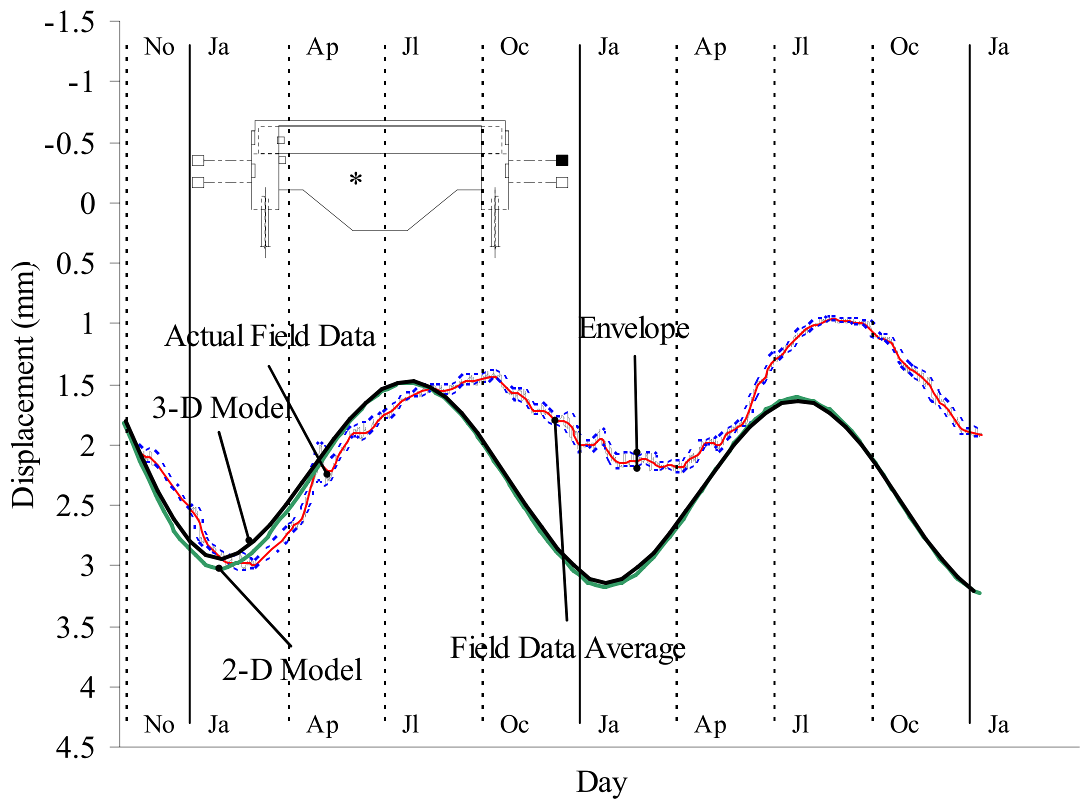

Figure 6-41: Top Elevation Extensometer Data and Predicted Results from FE Models (* Ref: Channel 2-1 in Figure A-11 for Instrumentation Location Detail at Abutment 2)

It is observed in Figure 6-42 that the maximum percent difference between 2-D and 3-D predicted abutment displacements is 7.4 and the average percent difference is 3.3. The maximum percent difference between 3-D and condensed hysteresis model predicted abutment displacements is 76 and the average percent difference is 46.

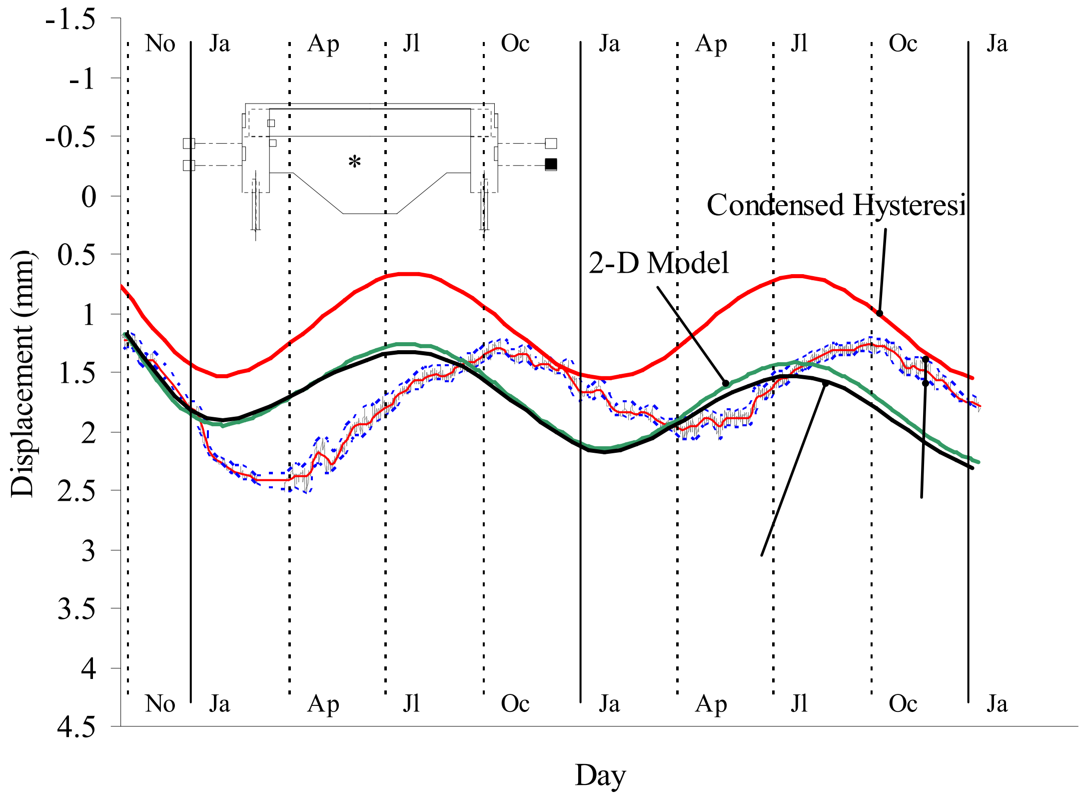

Figure 6-42: Bottom Extensometer Data and Results from FE and Condensed Models (* Ref: Channel 2-2 in Figure A-11 for Instrumentation Location Detail at Abutment 2)

The correlation between average measured abutment displacement and 2-D predicted abutment displacement is 0.041, the correlation between average measured abutment displacement and 3-D predicted abutment displacement is 0.018, and the correlation between average measured abutment displacement and condensed hysteresis model predicted abutment displacement is 0.116. Lag in measured abutment displacement peaks of approximately two months is observed, which leads to the poor correlations between measured and predicted abutment displacements. The 2-D predicted, 3-D predicted, and condensed hysteresis model predicted abutment displacement amplitudes are nearly equal to the measured abutment displacement amplitude.

2-D and 3-D predicted abutment displacements at the top and bottom extensometer positions over the simulation period of 10 years are presented in Figures 6-43 and 6-44.

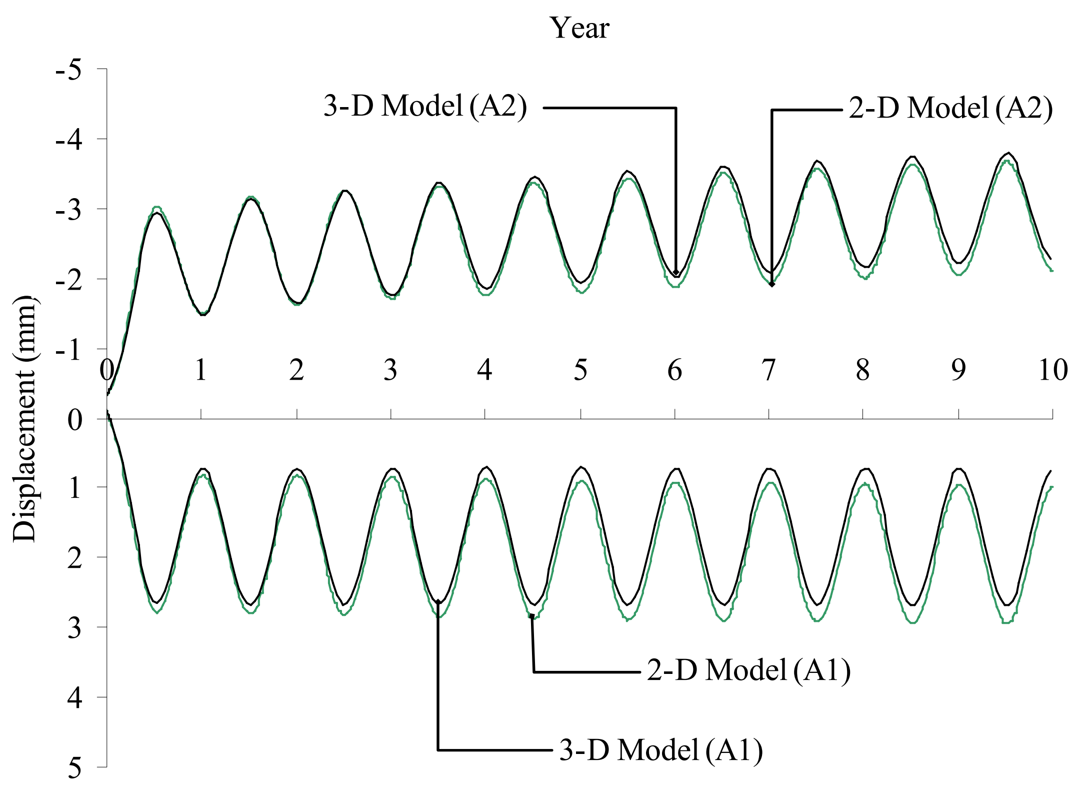

Figure 6-43: Predicted 10-Y Simulation Results from FE Models at Top Extensometer

It is observed in Figure 6-43 that the maximum percent differences between 2-D and 3-D predicted abutment displacements are 27.5 for abutment 1 and 7.8 for abutment 2, while the average percent differences are 12.1 for abutment 1 and 3.5 for abutment 2. The 2-D and 3-D predicted abutment displacements demonstrate the same trend, indicating the abutments moving away from the backfill. The logarithmic increase in adjacent abutment displacement peaks is observed as the number of years is increased.

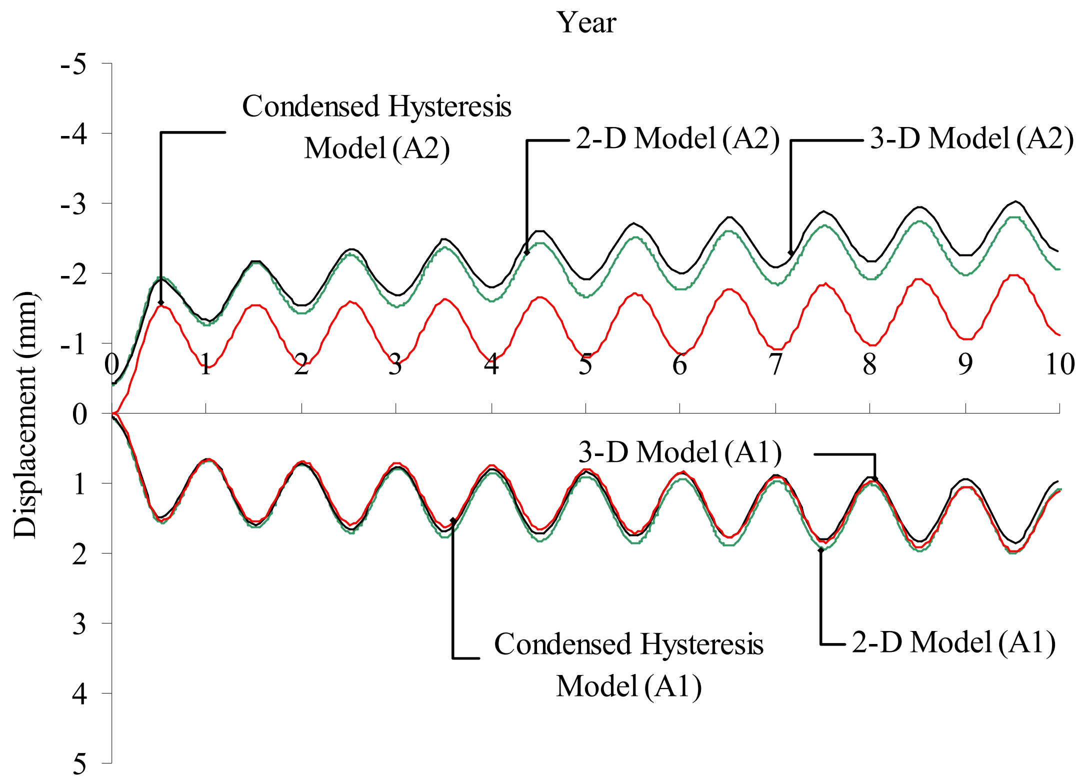

Figure 6-44: Predicted 10-Y Simulation Results from FE and Condensed Models at Bottom Extensometer

It is observed in Figure 6-44 that the maximum percent differences between 2-D and 3-D predicted abutment displacements are 13.5 for abutment 1 and 14.1 for abutment 2, while the average percent differences are 7.4 for abutment 1 and 7.7 for abutment 2. The maximum percent differences between 3-D and condensed hysteresis model predicted abutment displacements are 15.7 for abutment 1 and 83 for abutment 2, while the average percent differences are 4.4 for abutment 1 and 56 for abutment 2. Abutment 1 and abutment 2 of bridge 222 are supported by 11 and 9 piles, respectively. An average value of 10 piles was used as a parameter in the condensed hysteresis model. Although the 2-D and 3-D predicted abutment displacements of abutment 2 are greater than those of abutment 1 as determined from corresponding pile stiffness, the measured abutment displacement demonstrates the opposite behavior. This inconsistency is a result of uncertainties of actual soil properties and imperfect bridge configurations that easily degrade a small abutment displacement range predicted by the bridge 222 model based on estimated soil properties and perfect bridge configurations.

Analysis case 1 and analysis case 2 predicted abutment displacements at the top and bottom extensometer positions over the simulation period of 100 years are studied are presented Figures **6-45** and **6-46** to determine long-term effects of IA bridge behavior. It is observed in Figure **6-45** that the analysis case 1 predicted abutment displacement rate is relatively high at about the first 30 years and gets smaller as the number of years is increased. However, the analysis case 2 predicted abutment displacement rate is constant over the simulation period of 100 years. The maximum analysis case 1 and maximum analysis case 2 predicted abutment displacements at the end of the simulation period are 3.6 and 2.0 mm for abutment 1 (4.5 and 2.6 mm for abutment 2). These predicted abutment displacements indicate the ratios of long-term to short-term predicted abutment displacements of 1.8 and 1.7 for abutment 1 and abutment 2, respectively.

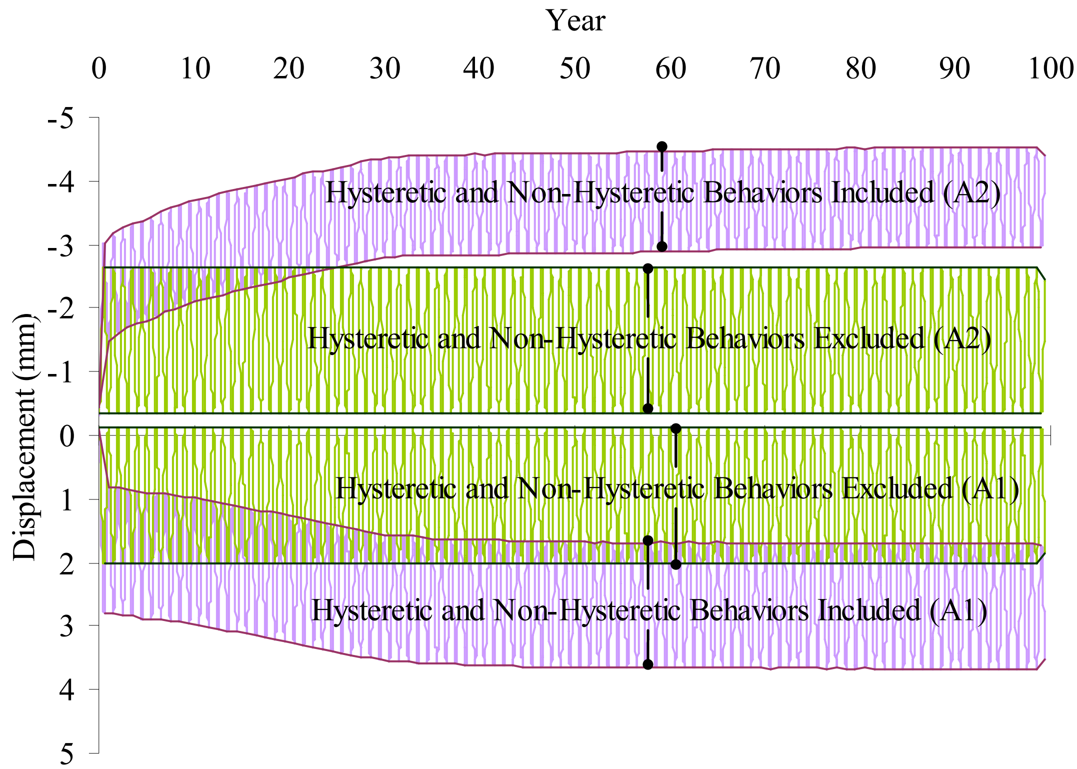

Figure 6-45: Predicted 100-Y Simulation Results from FE Model for Analysis Cases 1 and 2 at Top Extensometer

It is observed in Figure 6-46 that the analysis case 1 predicted abutment displacement rate is relatively high at about the first 30 years and gets smaller as the number of years is increased. However, the analysis case 2 predicted abutment displacement rate is constant over the simulation period of 100 years. The maximum analysis case 1 and maximum analysis case 2 predicted abutment displacements at the end of the simulation period are 3.2 and 1.4 mm for abutment 1 (4.0 and 2.0 mm for abutment 2). These predicted abutment displacements indicate the ratios of long-term to short-term predicted abutment displacements of 2.3 and 2.0 for abutment 1 and abutment 2, respectively. In addition, the maximum percent differences between 2-D and condensed hysteresis model predicted abutment displacement amplitudes are 0.0 for abutment 1 and 22 for abutment 2. The maximum percent differences between 2-D and condensed hysteresis model predicted abutment displacements are 12 for abutment 1 and 13 for abutment 2.

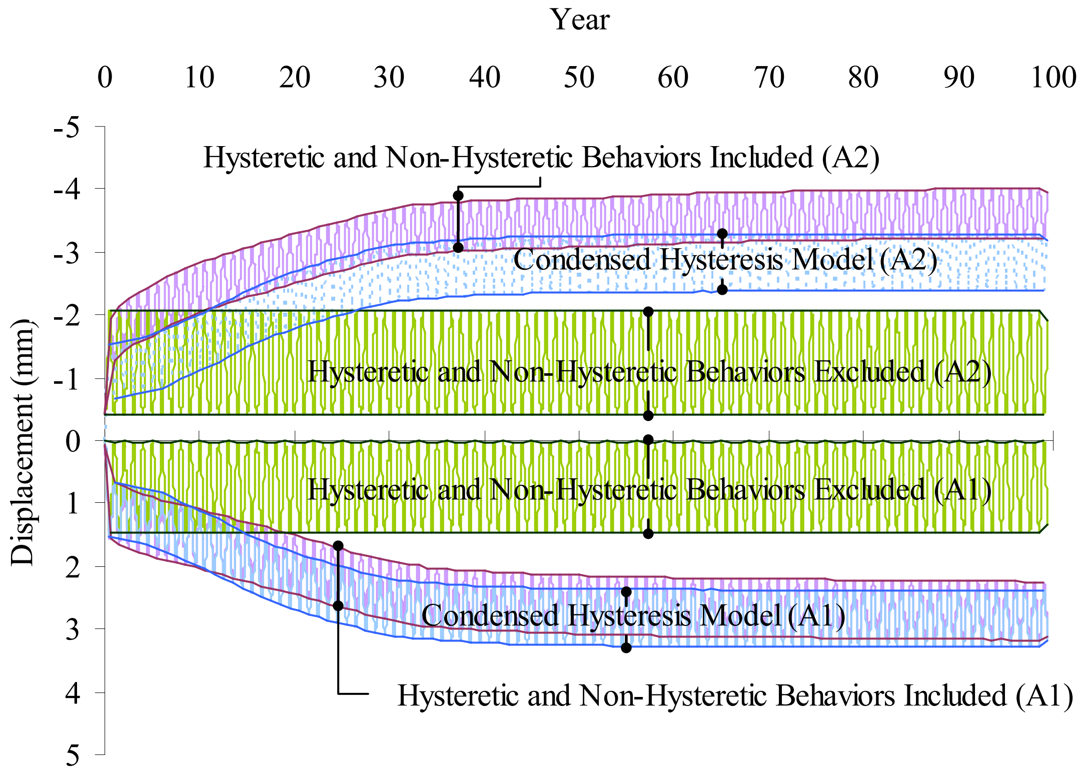

Figure 6-46: Predicted 100-Y Simulation Results from FE and Condensed Models for Analysis Cases 1 and 2 at Bottom Extensometer

Analysis case 3 and analysis case 4 predicted abutment displacements at the top and bottom extensometer positions are studied and presented in Figures 6-47 and 6-48 to determine the relative magnitudes of hysteretic and non-hysteretic behaviors. It is observed in Figure 6-47 that the maximum analysis case 3 and maximum analysis case 4 predicted abutment displacements at the end of the simulation period are 2.2 and 3.3 mm for abutment 1 (3.0 and 3.8 for abutment 2). Recalling that the maximum analysis case 1 predicted displacement is 3.6 mm for abutment 1 and 4.5 mm for abutment 2, it can be derived that the hysteretic and non-hysteretic behaviors are 61 and 92 percents proportional to the total long-term behavior for abutment 1 (67 and 84 percents for abutment 2). Similar to the implication for bridge 203, it is determined that predicted long-term abutment displacements near the girder elevation are strongly influenced by the non-hysteretic behavior.

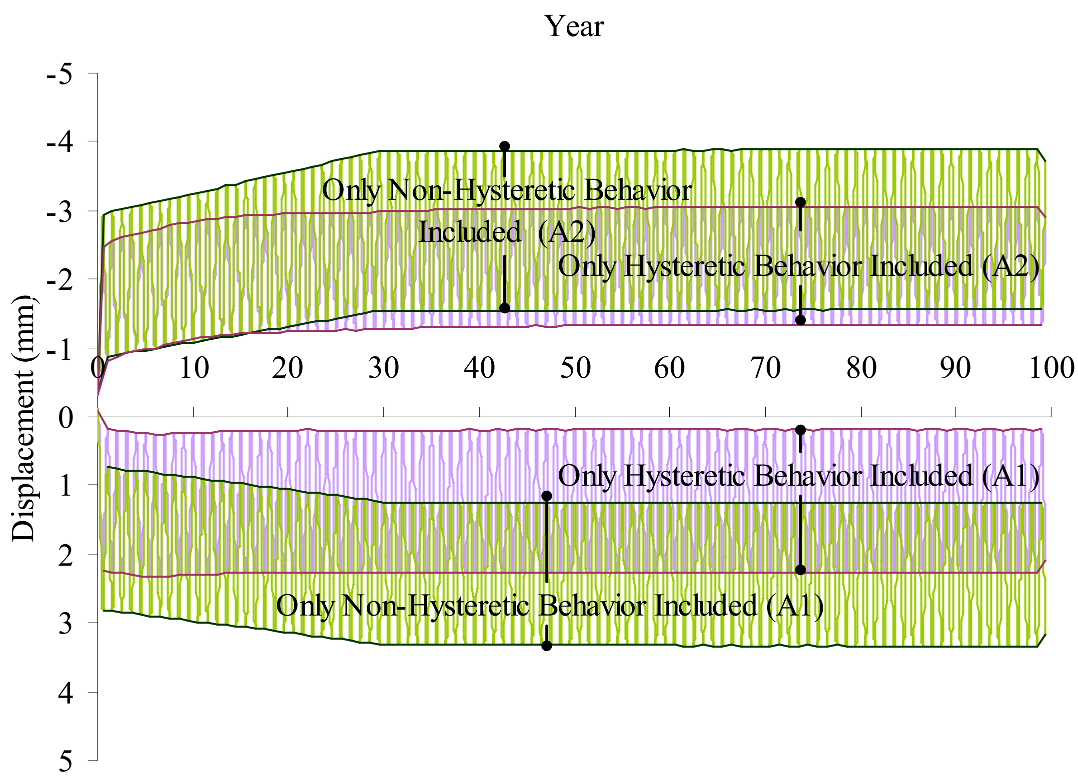

Figure 6-47: Predicted 100-Y Simulation Results from FE Model for Analysis Cases 3 and 4 at Top Extensometer

It is observed in Figure 6-48 that the maximum analysis case 3 and maximum analysis case 4 predicted abutment displacements at the end of simulation period are 2.2 and 2.2 mm for abutment 1 (2.9 and 2.8 mm for abutment 2). Recalling that the maximum analysis case 1 predicted abutment displacement is 3.2 mm for abutment 1 and 4.0 mm for abutment 2, it can be derived that the hysteretic and non-hysteretic behaviors are 69 and 69 percents proportional to the total long-term behavior for abutment 1 (73 and 70 percents for abutment 2). Similar to the implication for bridge 203, it is determined that predicted long-term abutment displacements near the abutment base elevation are equally influenced by both hysteretic and non-hysteretic behaviors.

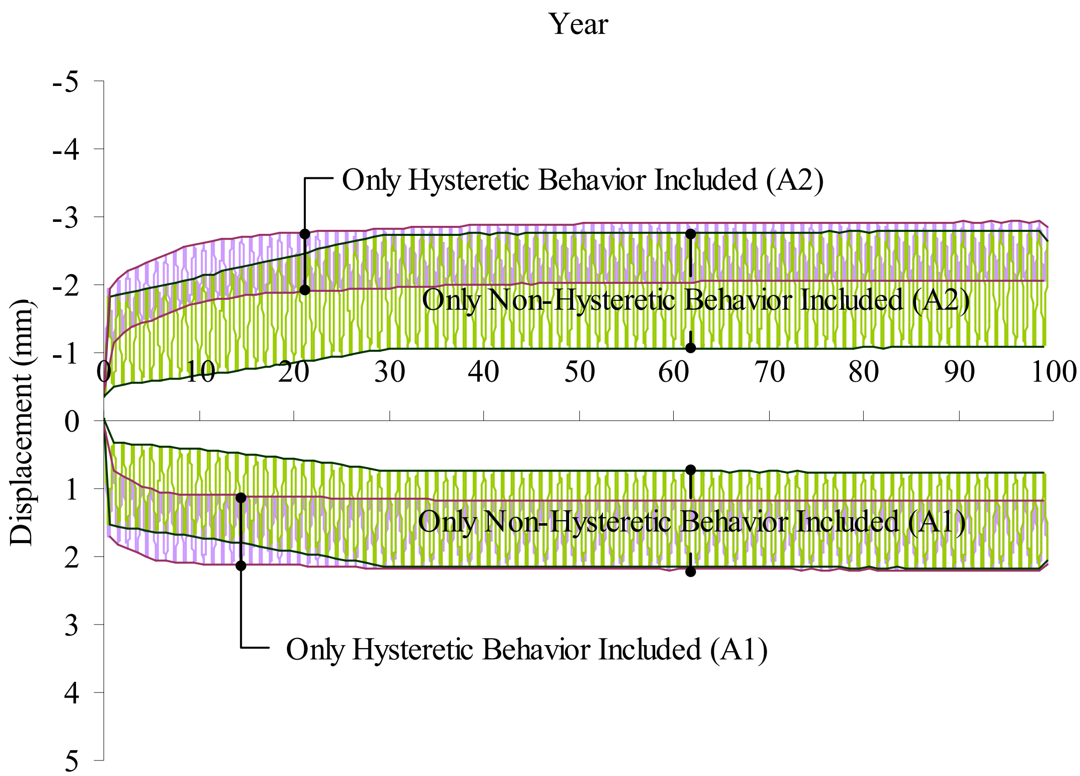

Figure 6-48: Predicted 100-Y Simulation Results from FE Model for Analysis Cases 3 and 4 at Bottom Extensometer

Analysis case 5 and analysis case 6 predicted abutment displacements at the top and bottom extensometer positions are studied and presented in Figures 6-49 and 6-50 to determine the relative magnitudes of soil-structure interaction and abutment-backwall connection hysteretic behaviors. It is observed in Figure 6-49 that the maximum analysis case 5 and maximum analysis case 6 predicted abutment displacements at the end of simulation period are 2.2 and 2.0 mm for abutment 1 (3.0 and 2.6 mm for abutment 2). Recalling that the maximum analysis case 2 and maximum analysis case 3 predicted abutment displacements are 2.0 and 2.2 mm for abutment 1 (2.6 and 3.0 for abutment 2), it can be derived that the total hysteretic behavior is fully dominated by the soil-structure interaction hysteretic behavior.

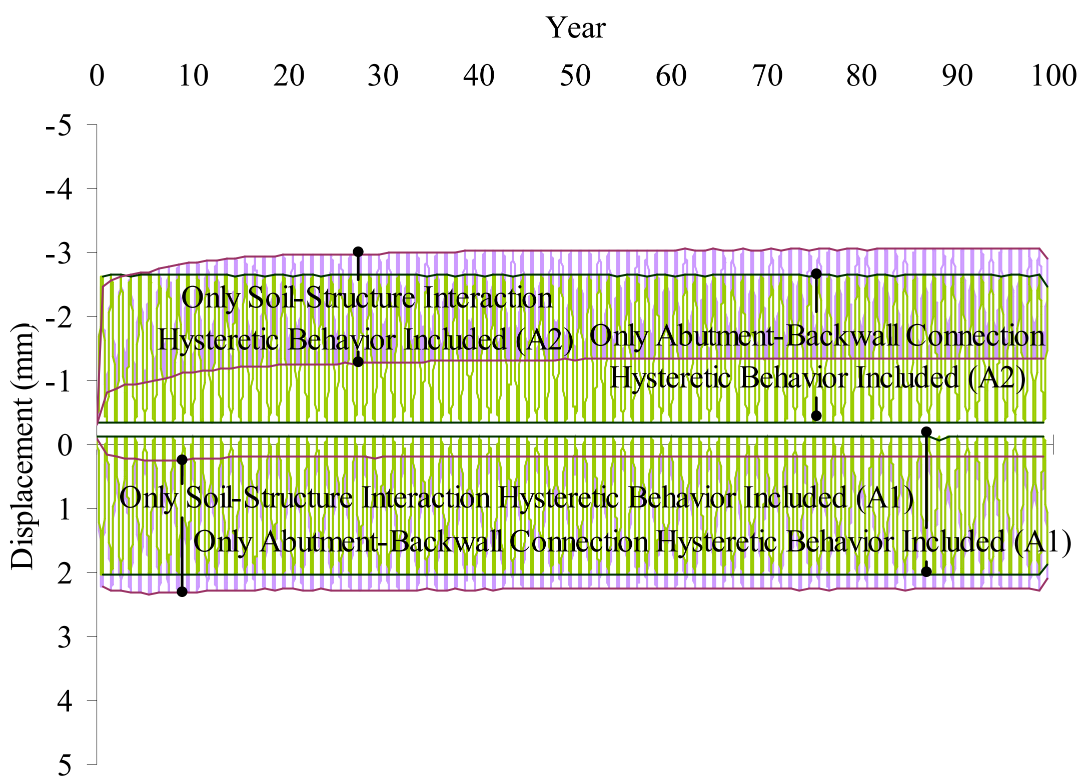

Figure 6-49: Predicted 100-Y Simulation Results from FE Model for Analysis Cases 5 and 6 at Top Extensometer

It is observed in Figure 6-50 that the maximum analysis case 5 and maximum analysis case 6 predicted abutment displacements at the end of the simulation period are 2.2 and 1.4 mm for abutment 1 (2.9 and 2.0 mm for abutment 2). Recalling that the maximum analysis case 2 and maximum analysis case 3 predicted abutment displacements are 1.4 and 2.2 mm for abutment 1 (2.0 and 3.0 mm for abutment 2), it can be derived that the total hysteretic behavior is fully dominated by the soil-structure interaction hysteretic behavior.

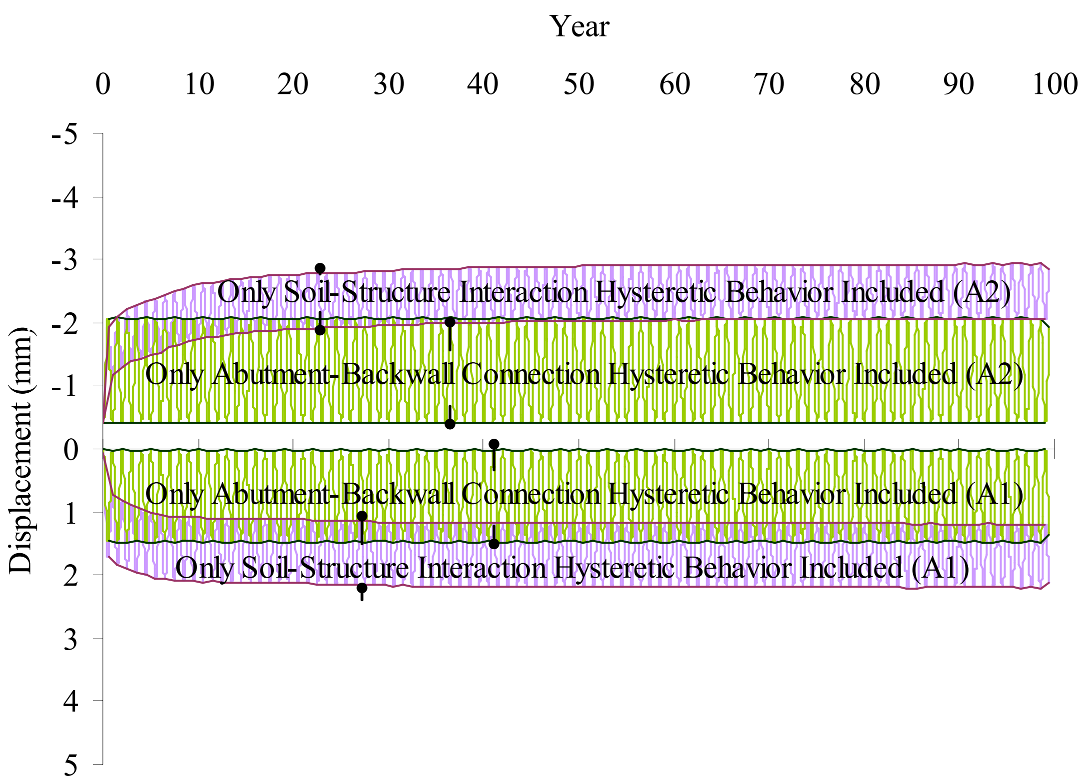

Figure 6-50: Predicted 100-Y Simulation Results from FE Model for Analysis Cases 5 and 6 at Bottom Extensometer

The analysis cases 7 and 8 are not provided here because the predicted abutment displacements are the same as those from the analysis case 4. This indicates that the abutment-backwall connection hysteretic behavior has no influence on the long-term behavior of bridge 222.

6.4 Summary

This section summarizes FE and condensed hysteresis model accuracy and predicted response. The correlation between measured and FE model predicted soil pressures of bridges 203 and 222 ranges from 0.82 to 0.916. The correlation between measured and FE model predicted soil pressures of bridge 211 are relatively inconsistent with the values ranging from 0.516 to 0.748. This inconsistency, particularly during the abutments moving away from the backfill, is a result from the assumption of an at-rest earth pressure as the initial loading condition. The correlation between measured and FE model predicted abutment displacements of bridges 203 and 211 ranges from 0.594 to 0.913. The correlation between measured and FE model predicted abutment displacements of bridge 222 are inconsistent due to a significant lag in abutment displacement peaks of approximately 2 months. The major predicted abutment displacements at the end of the simulation period are presented as follows:

- The ratios of the long-term to short-term predicted abutment displacements (the ratios of the analysis case 1 to analysis case 2 predicted abutment displacements) are presented in Table **6-1**.

Table 6-1: Ratios of Long-Term to Short-Term Displacements

Displacement Location	Bridge				
	203	211		222	
		Abutment 1	Abutment 2	Abutment 1	Abutment 2
Top Elevation	2	1.6	1.5	1.8	1.7
Bottom Elevation	2.3	1.7	1.6	2.3	2

- The ratios of the condensed hysteresis model to 2-D FE predicted abutment displacements are presented in Table 6-2.

Table 6-2: Ratios of Displacements Results Predicted by 2-D FE and Condensed Models

Displacement Location	Bridge				
	203	211		222	
		Abutment 1	Abutment 2	Abutment 1	Abutment 2
Bottom Elevation	1.08	0.93	0.81	1.03	0.83

- The ratios of the analysis case 3 predicted abutment displacement (only hysteretic behavior included) to analysis case 2 predicted abutment displacement (short-term) are presented in Table 6-3.

Table 6-3: Ratios of Predicted Hysteretic Displacements to Short-Term Displacements

Displacement Location	Bridge				
	203	211		222	
		Abutment 1	Abutment 2	Abutment 1	Abutment 2
Top Elevation	1.1	1.1	1.2	1.1	1.15
Bottom Elevation	1.6	1.3	1.4	1.6	1.45

According to the predicted ratios presented in Tables 6-1 and 6-3, it can be observed that long-term behavior of bridge 203, the longest bridge with the tallest abutment, is as significant as long-term behavior of bridge 222, the shortest bridge with a moderate abutment height. However, these predicted ratios indicate the smallest influence on long-term behavior of bridge 211 due to its girder age at erection of 268 days, as compared to the bridge 203 and bridge 222 girder ages of 115 and 171 days. Therefore, bridge 211 has relatively less amount of remaining time dependent effects. Higher predicted ratios for bridge 211 are expected, if its girder age at erection is similar to those of bridges 203 and 222. On the basis of similarity in bridge 203 and bridge 222 predicted ratios and difference in remaining time-dependent effects, no certain pattern to identify the relationship between long-term behavior and bridge geometry is observed.

Chapter 7

Summary, Conclusions and Recommendations

7.1 Summary

The significance of hysteretic behavior on long-term IA bridge behavior was evaluated using hysteresis elements derived from available mathematical and physical hysteresis models. In addition, the non-hysteresis, time-dependent effects of concrete creep, concrete shrinkage, and prestressing steel relaxation, on IA bridges were incorporated to this study. The two major sources influencing long-term behavior of IA bridges are soil-structure interaction and yielding of abutment reinforcing at joints. These influences were identified on the basis of measured bridge response at the three instrumented bridges. Three hysteresis element types were used in the FE and condensed hysteresis models for all three bridges to represent soil-pile interaction, soil-abutment interaction, and abutment-backwall connection hysteretic behaviors. The AAEM method was used to represent non-hysteretic behavior by means by equivalent temperatures. 2-D and 3-D FE models were constructed for efficiency and accuracy purposes. The development procedure of condensed hysteresis models was established and the condensed hysteresis models for the three instrumented bridges were constructed to provide an alternate and efficient approach. Predicted FE model response was compared against the measured bridge response to evaluate FE model accuracy. Eight different load cases, varying from the load case that all hysteretic and non-hysteretic behaviors are included (long-term behavior) through the load case that all hysteretic and non-hysteretic behaviors are excluded (short-term behavior), were established. The FE models incorporating each of these eight different cases were analyzed under a 100 year simulation to evaluate the individual influence of the hysteretic and non-hysteretic behavior on IA bridge long-term abutment displacements.

7.2 Conclusions

The study objectives are to: predict steady-state and long-term IA bridge behavior, develop condensed hysteresis models, quantify the significance of hysteretic behavior, correlate hysteretic behavior with bridge lengths and abutment heights, and recommend a methodology to predict steady-state and long-term IA bridge behavior. The ultimate goal of this research is to demonstrate the importance of long-term IA bridge responses influenced by hysteretic behavior in addition to time-dependent effects of creep and shrinkage on IA bridges. The following conclusions are drawn from the present study:

- After model calibration, correlations between measured and predicted soil pressures are from 0.82 to 0.916. The correlations between measured and predicted abutment displacements ranging from 0.516 to 0.913 for bridges 203 and 211 are observed, while the maximum correlation between measured and predicted abutment displacements for bridge 222 is 0.651 due to 2 month lag in measured abutment displacement peaks.

- Measured and 2-D predicted, 3-D predicted, and condensed hysteresis model predicted response revealed that increasing rate of long-term abutment displacements after 100 year simulation approaches, but not reaches, steady-state. The ratios of the long-term to short-term abutment displacements after 100-year simulation are from 1.5 to 2.3 times, indicating the significance of hysteretic and non-hysteretic behavior.
- The development procedure of condensed hysteresis models was established. The ratios of the condensed hysteresis model to 2-D predicted abutment displacements after 100-year simulation are from 0.81 to 1.08. These predicted ratios indicate that condensed hysteresis models are a valid approach with respect to its relative simplicity and efficiency, as compared to the FE models.
- The ratios of the predicted abutment displacements from the load case that only hysteretic behavior component is included to the predicted short-term abutment displacements are 1.6 and 1.2 at the top and bottom extensometers. These predicted ratios indicate that the influence of hysteretic behavior on abutment displacements is greater at a location near an abutment base.
- The ratios of the predicted abutment displacements from the load case that only hysteretic behavior is included to the predicted short-term abutment displacements from the three instrumented bridges reveal no apparent correlation between hysteretic behavior to bridge geometry. It is recommended that a parametric study be conducted to establish a general correlation between these parameters.
- A condensed hysteresis model is recommended as an alternative approach to predict a long-term abutment displacement and rotation at the pile head due to simpler

development procedure, more efficient computation time, and relatively accurate response prediction.

7.3 Recommendations for Further Research

The following studies that would provide additional useful information to better predict long-term bridge behavior through a hysteresis model approach are:

- a nonlinear soil-abutment interaction hysteresis model,
- a step-by-step based approach with a nonlinear viscoelastic constitutive law for predicting time-dependent effects,
- a parametric study to determine a general correlation between bridge geometry and hysteretic behavior, and a general correlation between soil-pile properties and condensed model hysteresis elements, and
- a statistical based approach to determine load and resistance coefficients of variation to develop load and resistance factors for IA bridge design.

References

1. AASHTO Guide Specification (1989) "Thermal Effects in Concrete Bridge Superstructures," American Association of State Highway and Transportation Officials.

2. AASHTO Guide Specification (1999) "Seismic Isolation Design," American Association of State Highway and Transportation Officials, 2nd Edition.

3. AASHTO LRFD Bridge Design Specification (2004), American Association of State Highway and Transportation Officials.

4. Abendroth, R. E. and Greimann, L. F. (1990) "Pile Behavior Established from Model Tests," *Journal of Geotechnical Engineering*, ASCE, V. 116, No. 4, pp. 571-588.

5. ACI Committee 209 (2004) "Prediction of Creep, Shrinkage, and Temperature Effects in Concrete Structures," *ACI Manual of Concrete Practice Part 1*, American Concrete Institute.

6. Alampalli, S. and Yannotti, A. P. (1998) "In-Service Performance of Integral Bridges and Jointless Decks," *Transportation Research Record 1624*, Transportation Research Board, National Research Council, Washington D.C., pp. 1-7.

7. Amde, A. M., Chini, S. A., and Mafi, M. (1997) "Model Study of H-Piles Subjected to Combined Loading," *Technical Note: Geotechnical and Geological Engineering*, Springer Netherlands, V. 15, pp. 343-355.

8. Anderssen, R. S., Götz, I. G., and Hoffmann, K. (1998) "The Global Behavior of Elastoplastic and Viscoelastic Materials with Hysteresis-Type State Equations," *SIAM J. Appl. Math.*, V. 58, No. 2, pp. 703-723.

9. ANSYS Release 10.0, ANSYS University Advanced, ANSYS, Inc.

10. Arockiasamy, A., Butrieng, N., and Sivakumar, M. (2004) "State-of-the-Art of Integral Abutment Bridges: Design and Practice," *Journal of Bridge Engineering*, ASCE, V. 9, No. 5, pp. 497-506.

11. Arockiasamy, M. and Sivakumar, M. (2005) "Time-Dependent Behavior of Continuous Composite Integral Abutment Bridges," *Practice Periodical on Structural Design and Construction*, ASCE, V. 10, No. 3, pp. 161-170.

12. Arsoy, S. (2000) "Experimental and Analytical Investigations of Piles and Abutments of Integral Bridges," *Ph.D. Thesis*, Virginia Polytechnic Institute and State University.

13. Banks, H. T., Pinter, G. A., Potter, L. K., Gaitens, M. J., and Yanyo, L. C. (1999) "Modeling of Nonlinear Hysteresis in Elastomers," *CRSC-TR99-09*, CRSC Technical Reports, North Carolina State University.

14. Bažant, Z. P. (1988) "Mathematical Modeling of Creep and Shrinkage of Concrete," *John Wiley& Sons*.

15. Bažant, Z. P. and Baweja, S. (1995) "Creep and Shrinkage Prediction Model for Analysis and Design of Concrete Structures: Model B3 – RILEM Recommendations," *Materials and Structures*, V. 28, pp. 357-365.

16. Bažant, Z. P. and Baweja, S. (2000) "Creep and Shrinkage Prediction Model for Analysis and Design of Concrete Structures: Model B3 – Short Form," *Adam Neville Symposium: Creep and Shrinkage: Structural Design Effects*, American Concrete Institute, pp. 85-100.

17. BD-667M (2005) "Standard Integral Abutment Drawings," Bureau of Design, Commonwealth of Pennsylvania, Department of Transportation.

18. Boulanger, R. W., Curras, C. J., Kutter, B. L., Wilson, D. W., and Abghari, A. (1999) "Seismic Soil-Pile-Structure Interaction Experiments and Analyses," *Journal of Geotechnical and Geoenvironmental Engineering*, ASCE, V. 125, No. 9, pp. 750-759.

19. Briaud, J. (2001) "Introduction to Soil Moduli," *Geotechnical News*, GEOSPEC, Bitech Publishing, Vancouver, B.C., June.

20. Bridge Detail Sheets (2005) "Integral Abutments Adjacent PC Beams," Structures and Design and Construction Division, State of New York, Department of Transportation, Dwg. No. BD-ID1.

21. Bridge Manual Part II: Standard Details (2005) "Integral Abutments: Abutment Reinforcement," Commonwealth of Massachusetts, Massachusetts Highway Department, Dwg. No. 12.2.5.

22. Bridge Manual Standard Drawing Plates (2004) "Integral Abutments for Prestressed Concrete Superstructure," Bureau of Structural Engineering, New Jersey Department of Transportation, Dwg. Plate 2.9-3.

23. Brokate, M. and Sprekels, J. (1989) "Existence and Optimal Control of Mechanical Process with Hysteresis in Viscous Solids," *IMA Journal of Applied Mathematics*, V. 43, pp. 219-229.

24. Brokate, M. and Sprekels, J. (1996) "Hysteresis and Phase Transitions," *Applied Mathematical Sciences 121*, Springer-Verlag Berlin Heidelberg.

25. Cai, Z. and Bathurst, R. J. (1995) "Seismic Response Analysis of Geosynthetic Reinforced Soil Segmental Retaining Walls by Finite Element Method," *Computers and Geotechnics*, Elsevier, V. 17, pp. 523-546.

26. CDOT Bridge Design Manual (1999) "Section 7: Substructure," Corolado Department of Transportation.

27 Comite Euro-Internationale du Beton (1990) "CEB-FIP Model Code 1990," *Buletin D'Information No. 213/214*, Lausanne, Switzerland.

28. Cheng, F. Y. (2001) "Matrix Analysis of Structural Dynamics: Application and Earthquake Engineering," *Marcel Dekker, Inc*., New York.

29. ConnDOT Bridge Design Manual (2003) "Section 5.11: Requirements for Abutments," Connecticut Department of Transportation.

30. Cook, R. D., Malkus, D. S., and Plesha, M. E. (1989) "Concepts and Applications of Finite Element Analysis," *John Wiley& Sons*, 3rd Edition.

31. Cousins, T. E. (2005) "Investigation of Long-Term Prestress Losses in Pretensioned High Performance Concrete Structures," *Report No. FHWA/VTRC 05-CR20*, Virginia Transportation Research Council, Virginia Department of Transportation.

32. Das, B. M. (1999) "Principles of Foundation Engineering," *PWS Publishing*, 4th Edition.

33. Delattre, L. (2001) "A Century of Design Methods for Retaining Walls – The French Point of View: I. Calculation – Based Approaches – Conventional and Subgrade Reaction Methods," *BLPC-2001/234*, Laboratoire Central des Ponts et Chaussées.

34. Dicleli, M. (2000) "Simplified Model for Computer-Aided Analysis of Integral Bridges," *Journal of Bridge Engineering*, ASCE, V. 5, No. 3, pp. 240-248.

35. Dicleli, M. and Albhaisi, S. M. (2003) "Maximum Length of Integral Bridges Supported on Steel H-Piles Driven in Sand," *Engineering Structures*, Elsevier, V. 25, pp. 1491-1504.

36. Dicleli, M. and Albhaisi, S. M. (2004) "Effect of Cyclic Thermal Loading on the Performance of Steel H-Piles in Integral Bridges with Stub-Abutments," *Journal of Constructional Steel Research*, Elsevier, V. 60, pp. 161-182.

37. Dunker, K. F. and Abu-Hawash, A. (2005) "Expanding the Use of Integral Abutments in Iowa," *Proceedings of the 2005 Mid-Continent Transportation Research Symposium*, Iowa State University, Ames, Iowa, August 2005.

38. Elbadry, M. M. and Ghali, A. (2001) "Analysis of Time-Dependent Effects in Concrete Structures Using Conventional Linear Computer Programs," *Can. J. Civ. Eng.*, V. 28, pp. 190-200.

39. EM 1110-2-2504 (1994) "Design of Sheet Pile Walls," *Engineering Manual*, US Army Corps of Engineers, Department of the Army, Washington, D.C.

40. England, G. L., Tsang, N. C. M., and Bush, D. I. (2000) "Integral Bridges: A Fundamental Approach to the Time-Temperature Loading Problem," *Thomas Telford*.

41. Faraji, S., Ting, J. M., Crovo, D. S., and Ernst, H. (2001) "Nonlinear Analysis of Integral Bridges: Finite-Element Model," *Journal of Geotechnical and Geoenvironmental Engineering*, ASCE, V. 127, No. 5, pp. 454-461.

42. Fanourakis, G. C. and Ballim, Y. (2003) "Predicting Creep Deformation of Concrete: A Comparison of Results from Different Investigations," *Proceedings: 11th FIG Symposium on Deformation Measurements*, Santorini, Greece.

43. Fennema, J. L. (2003) "Prediction and Measured Response of Integral Abutment Bridges," *M.S. Thesis*, The Pennsylvania State University.

44. Fennema, J. L., Laman, J. A., and Linzell, D. G. (2005) "Predicted and Measured Response of an Integral Abutment Bridge," *Journal of Bridge Engineering*, ASCE, V. 10, No. 6, pp. 666-677.

45. Flynn, D., McNamara, H., O'Kane, P., and Pokrovskiĭ, A. V. (2003) "Application of the Preisach Model in Soil-Moisture Hysteresis," *Preprint of Boole Centre for Research in Informatics (BCRI) 15/03*, Department of Applied Mathematics, University College Cork.

46. Gardner, N. J. (2004) "Comparison of Prediction for Drying Shrinkage and Creep of Normal-Strength Concretes," *Can. J. Civ. Eng.*, V. 31, pp. 767-775.

47. Ghali, A., Favre, R., and Elbadry, M. (2002) "Concrete Structures: Stresses and Deformation," *Spon Press*, London, 3rd Edition.

48. Gorbet, R. B. (1997) "Control of Hysteretic Systems with Preisach Representations," *Ph.D. Thesis*, The University of Waterloo.

49. Haukaas, T. and Kiureghian, A. D. (2004) "Finite Element Reliability and Sensitivity Methods for Performance-Based Engineering," *PEER Report 2003/14*,

Pacific Earthquake Engineering Research Center, University of California, Berkeley.

50. Hinkle, J. D. and Peterson, L. D. (2002) "Physics and Modeling Issues in Interface Microslip Mechanics," *CU-CAS-02-23*, Center for Aerospace Structures, University of Colorado at Boulder.

51. Huang, J., Shield, C. K., and French, C. (2005) "Time-Dependent Behavior of a Concrete Integral Abutment Bridge," *Transportation Research Record: Journal of the Transportation Research Board*, Transportation Research Board of the National Academies, Washington D.C., pp. 299-309.

52. Hwang, J. S. (1996) "Evaluation of Equivalent Linear Analysis Methods of Bridge Isolation," *Journal of Structural Engineering*, ASCE, V. 122, No. 8, pp. 972-976.

53. Ilki, A. and Kumbasar, N. (2000) "Hysteresis Model for Reinforced Concrete Members," *14th Engineering Mechanics Conference*, Department of Civil Engineering, The University of Texas at Austin, May 21-24.

54. IowaDOT Bridge Design Manual and Commentary (2004) "Section 6: Bridge Substructure Design," Iowa Department of Transportation.

55. Jirásek, M. and Bažant, Z. P. (2002) "Inelastic Analysis of Structures," *John Wiley& Sons*, New York.

56. Khodair, Y. A. and Hassiotis, S. (2003) "Analysis of Pile Soil Interaction," *The 16th ASCE Engineering Mechanics Conference*, University of Washington, Seattle, July 16-18.

57. Koskinen, M. "Soil-Structure-Interaction of Jointless Bridges on Piles," Geotechnical Laboratory, Tampere University of Technology, Finland, pp. 1091-1096.

58. Krasnosel'skiĭ, M. A. and Pokrovskiĭ, A. V. (1989) "System with Hysteresis: Translated from the Russian By Marek Niezgodka," *Springer-Verlag Berlin Heidelberg*.

59. Kunin, J. and Alampalli, S. (2000) "Integral Abutment Bridges: Current Practice in United States and Canada," *Journal of Performance of Constructed Facilities*, ASCE, V. 14, No. 3, pp. 104-111.

60. Laman, J. A., Linzell, D. G., Leighty, C. A., and Fennema, J. L. (2003) "Methodology to Predict Movement and Stresses in Integral Abutment Bridges," *Report No. FHWA-PA-2002-039-97-04(80)*, Pennsylvania Transportation Research Council.

61. Laman, J. A., Pugasap, K., and Kim, W. (2006) "Field Monitoring of Integral Abutment Bridges," *Interim Report to Federal Highway Administration*, Pennsylvania Transportation Research Council.

62. Lee, H. J. and Schiesser, W. E. (2004) "Ordinary and Partial Differential Equation Routines in C, C++, Fortran, Java®, Maple®, and MATLAB®," Chapman& Hall/CRC.

63. Leighty, C. A., Fennema, J. L., and Laman, J. A. (2003) "Integral Abutment Bridges: Methodology to Predict Movement and Stresses," *The Sixth Annual PTI Conference*, The Pennsylvania Transportation Institute, July 16-17.

64. Lin, S. and Liao, J. (1999) "Permanent Strains of Piles in Sand Due to Cyclic Lateral Loads," *Journal of Geotechnical and Geoenvironmental Engineering*, ASCE, V. 125, No. 9, pp. 798-802.

65. Lin, T. Y. and Burns, N. H. (1982) "Design of Prestressed Concrete Structures," *John Wiley& Sons*, New York.

66. Lpile Plus Version 4.0, ENSOFT Incorporated.

67. Lubarda, V. A. (2002) "Elastoplasticity Theory," *CRC Press LLC*.

68. Ma, F., Zhang, H., Bockstedte, A., Foliente, G. C., and Paevere, P. (2004) "Parameter Analysis of the Differential Model of Hysteresis," *ASME Journal of Applied Mechanics*, V. 71, pp. 342-349.

69. Macki, J. W., Nistri, P., and Zecca, P. (1993) "Mathematical Models for Hysteresis," *SIAM Review*, Society for Industrial and Applied Mathematics, V. 35, No. 1, pp. 94-123.

70. Mayergoyz, I. (2003) "Mathematical Models of Hysteresis and Their Applications," *Elsevier*.

71. Monaco, P. and Marchetti, S. (2004) "Evaluation of the Coefficient of Subgrade Reaction for Design of Multi-Propped Diaphragm Walls from DMT Moduli," *Proceedings: International Site Characterization*, ISC'2 – Porto – Portugal.

72. Montana Structures Manual, Part II "Chapter 19: Substructures and Bearings," Montana Department of Transportation.

73. Mostaghel, N. (1999) "Analytical Description of Pinching, Degrading Hysteretic Stystems," *Journal of Engineering Mechanics*, ASCE, V. 125, No. 2, pp. 216-224.

74. NAVFAC DM7-02 (1986) "Foundation& Earth Structures," *Design Manual 7.02*, Naval Facilities Engineering Command, Alexandria, Virginia.

75. Ndon, U. J. and Bergeson, K. L. (1995) "Thermal Expansion of Concretes: Case Study in Iowa," *Journal of Materials in Civil Engineering*, ASCE, V. 7, No. 4, pp. 246–251.

76. NEHRP Recommended Provisions for Seismic Regulations for New Buildings and Other Structures and Commentary: FEMA 368 and FEMA 369 (2000), *Chapter 13: Commentary – Seismically Isolated Structures Design Requirements*.

77. Neville, A. M., Dilger, W. H., and Brooks, J. J. (1983) "Creep of Plain and Structural Concrete," *Construction Press*, London and New York.

78. Ni, Y. Q., Ying, Z. G., Ko, J. M., and Zhu, W. Q. (2002) "Random Response of Integrable Duhem Hysteretic Systems under Non-White Excitation," *International Journal of Non-Linear Mechanics*, V. 37, pp. 1407-1419.

79. NJDOT Design Manual for Bridges and Structures (2002) "Section 15: Integral Abutment Bridges," New Jersy Department of Transportation, 4th Edition.

80. NYDOT Bridge Manual (2002) "Section 11: Substructures," New York State Department of Transportation, Structures Design and Construction Division, 3rd Edition.

81. O'Brien, F. J. and Flanagan, J. W. (1996) "Relief of Creep/Shrinkage Stresses in Integrally Constructed Bridges," *Bridge Management 3*, Edited by J. E. Harding G. A. R. Parke and M. J. Ryall, E& FN Spon, London, pp. 164-172.

82. Oh, J. and Bernstein, D. S. (2003) "Analysis of the Semilinear Duhem Model for Rate-Independent Hysteresis," *Proceedings of the 42nd IEEE Conference on Decision and Control*, Maui, Hawaii, December 2003.

83. OhioDOT Bridge Design Manual (2004) "Section 303: Substructures," Ohio Department of Transportation.

84. O'Neil, P. V. (1995) "Advanced Engineering Mathematics," *PWS Publishing Company*.

85. Paul, M. D. (2003) "Thermally Induced Superstructure Stress in Prestressed Girder Integral Abutment Bridges," *M.S. Thesis*, The Pennsylvania State University.

86. Paual, M. D., Laman, J. A., and Linzell, D. G. (2005) "Thermally Induced Superstructure Stresses in Prestressed Girder Integral Abutment Bridges," *Transportation Research Record: Journal of the Transportation Research Board*, Transportation Research Board of the National Academies, Washington D.C., pp. 287-297.

87. PCI (2001) "The State of the Art of Precast/Prestressed Integral Bridges," Precast/Prestressed Concrete Institute.

88. PennDOT Design Manual Part 4 (2000) "Structures: Procedures-Design-Plans Presentation," Commonwealth of Pennsylvania, Department of Transportation, V. 1.

89. Pokrovskiĭ, A. V., http://euclid.ucc.ie/hysteresis/node1.htm "System with Hysteresis," Department of Applied Mathematics, University College Cork, Accessed November 4, 2005.

90. Prevost, J. H. and Popescu, R. (1996) "Constitutive Relations for Soil Materials," *Electronic Journal of Geotechnical Engineering*, V. 1.

91. Pugasap, K., Leighty, C. A., and Laman, J. A. (2004) "Hysteresis Phenomenon in Integral Abutment Bridges: Field Data Evaluation," *The Seventh Annual PTI Conference*, The Pennsylvania Transportation Institute, August 11-12.

92. Reese, L. C. (1984) "Handbook on Design of Piles and Drilled Shafts Under Lateral Load," *Report No. FHWA-IP-84-11*, U.S. Department of Transportation.

93. Sain, P. M. (1997) "Models for Hysteresis and Application to Structural Control," *Proceedings American Control Conference*, June 1997, pp. 16-20.

94. SAP2000 Advanced Version 9.09, Structural Analysis Program, Computers and Strcutures, Inc.

95. Shames, I. H. and Cozzarelli, F. A. (1992) "Elastic and Inelastic Stress Analysis," Prentice Hall.

96. Soltani, A. A. and Kukreti, A. R. (1992) "Performance Evaluation of Integral Abutment Bridges," *Transportation Research Record No. 1371*, National Research Council, Washington D.C.

97. Spencer, B. F. (1986) "Reliability of Randomly Excited Hysteretic Structures," *Lecture Notes in Engineering 21*, Springer-Verlag Berlin Heidelberg.

98. Springman, S. M. and Norrish, A. R. M. (1993) "Soil-Structure Interaction: Centrifuge Modelling of Integral Bridge Abutments," *Proc. Of the Henderson Colloquium – Towards Joint-Free Bridges*, International Association for Bridge and Structural Engineering, Pembroke College, July 1993, pp. 251-263.

99. STAAD Pro 2004, Research Engineers International.

100. Taciroglu, E., Rha, C., Stewart, J. P., and Wallace, J. W. (2003) "Robust Numerical Models for Cyclic Response of Columns Embedded in Soil," *The 16th*

ASCE Engineering Mechanics Conference, University of Washington, Seattle, July 16-18.

101. Tadros, M.K., Al-Omaishi, N., Seguirant, S. J., and Gallt, J. G. (2003) "Prestress losses in Pretensioned High-Strength Concrete Bridge Girders," *NCHRP Report 496*, National Cooperative Highway Research Program, Washington D.C.

102. Tan, R. Y. and Huang, M. C. (2000) "System Identification of a Bridge with Lead-Rubber Bearings," *Computers& Structures*, Elsevier, V. 74, pp. 267-280.

103. Terzaghi, K. (1955) "Evaluation of Coefficients of Subgrade Reaction," *Géotechnique*, Thomas Telford, V. 5, No. 4, pp. 297-326.

104. Thomson, T. A. and Lutenegger, A. J. (1998) "Passive Earth Pressure Tests on an Integral Bridge Abutment," *Proceedings: Fourth International Conference on Case Histories in Geotechnical Engineering*, St. Louis, Missouri, March 9-12.

105. Thyagarajan, R. S. (1989) "Modeling and Analysis of Hysteretic Structural Behavior," *Report No. EERL 89-03*, Earthquake Engineering Research Laboratory, California Institute of Technology.

106. Tsang, N. C. M., England, G. L., and Dunstan, T. (2002) "Soil/Structure Interaction of Integral Bridge with Full Height Abutments," *15th ASCE Engineering Mechanics Conference*, Columbia University, New York, June 2-5.

107. Valdman, J. (2001) "Mathematical and Numerical Analysis of Elastoplastic Material with Multi-Surface Stress-Strain Relation," *Ph.D. Dissertation*, Christian-Albrechts-Universität zu Kiel.

108. Visintin, A. (1993) "Models of Hysteresis," *Pitman Research Notes in Mathematics Series 286*, Longman Scientific& Technical.

109. Visintin, A. (1994) "Differential Models of Hysteresis," *Applied Mathematical Science 111*, Springer-Verlag Berlin Heidelberg.

110. Visintin, A. (2002) "On Hysteresis in Elasto-Plasticity and in Ferromagnetism," *Int. J. Nonlinear Mechanics*, V. 37, pp. 1283-1298.

111. Wan, S., Loh, C. H., and Peng, S. Y. (2000) "Experimental and Theoretical Study on Softening and Pinching Effects of Bridge Column," *Soil Dynamics and Earthquake Engineering*, Elsevier, V. 21, pp. 75-81.

112. Wang, S. and Reese, L. C. (1993) "COM624P – Laterally Loaded Pile Analysis Program for the Microcomputer," *Report No. FHWA-SA-91-048*, U.S. Department of Transportation.

113. Wasserman, E. P. (1987) "Jointless Bridge Decks," *Engineering Journal*, AISC, V. 24, No. 3, pp. 93-100.

114. Wasserman, E. P. and Walker, J. H. (1996) "Integral Abutments for Steel Bridges," *American Iron and Steel Institute Highway Structures Design Handbook*, V. 2, Chap. 5.

115. Wen, Y. K. (1976) "Method for Random Vibration of Hysteretic Systems," *Journal of The Engineering Mechanics Division*, V. 102, No. EM2, pp. 249-263.

116. Wolde-Tinsae, A. M., Greimann, L. F., and Johnson, B. V. (1983) "Performance of Integral Bridge Abutments," *IABSE Proceddings*, pp. 58-83.

117. Wolde-Tinsae, A. M., Klinger, J. E., and White, E. J. (1988) "Performance of Jointless Bridges," *Journal of Performance of Constructed Facilities*, ASCE, V. 2, No. 2, pp. 111-125.

118. WvDOT Bridge Design Manual Section 3: Design (2004) "Section 3.9: Jointless Bridge Abutments," West Virginia Department of Transportation.

119. Xanthakos, P. P. (1995) "Bridge Substructure and Foundation Design," *Prentice Hall*.

120. Yazdani, N., Eddy, S., and Cai, C. S. (2000) "Effect of Bearing Pads on Precast Prestressed Concrete Bridges," *Journal of Bridge Engineering*, ASCE, V. 5, No. 3, pp. 224-232.

121. Zhang, Y., Cofer, W. F., and McLean, D. I. (1999) "Analytical Evaluation of Retrofit Strategies for Multicolumn Bridges," *Journal of Bridge Engineering*, ASCE, V. 4, No. 2, pp. 143-150.

122. Zienkiewicz, O. C. and Taylor, R. L. (1991) "The Finite Element Method: Volume 2, Solid and Fluid Mechanics, Dynamics and Non-Linearity," *McGraw-Hill*, 4th Edition.

Appendix A

Bridge Description and Instrumentation Plan

This appendix provides pertinent information of three instrumented IA bridges used in this study. Lengths and number of spans for each bridge are described. Number of instruments, types, and locations are discussed. All these information are also provided graphically in a drawing and symbol format. Gage designations, labeled as a CHx-xx series, are presented in the drawings along with their descriptions. The following sections are arranged in an arithmetic order, i.e. bridge 203, bridge 211, and bridge 222.

A.1 Bridge 203

Bridge 203 is a 3-span composite slab on 4 prestressed concrete I-girders with spans of 14.3, 26.8, and 11.3 m (47, 88, and 37 ft). As presented in Figures **A-1** to **A-3**, the instrumentation consists of 16 strain gages on 4 girders, 30 strain gages on 2 piles, 4 tilt meters on 4 girders, 4 tilt meters on 1 abutment, 3 extensometers on 1 abutment, 3 pressure cells on 1 abutment, and 4 sister bar gages embedded in 1 approach slab. The total instruments for this bridge are 64 gages. It should be noted that the abutment on the south side is stub and rest on the bed rock, therefore, it is considered as a rigid foundation. With this respect, no instrumentation was planned for this abutment.

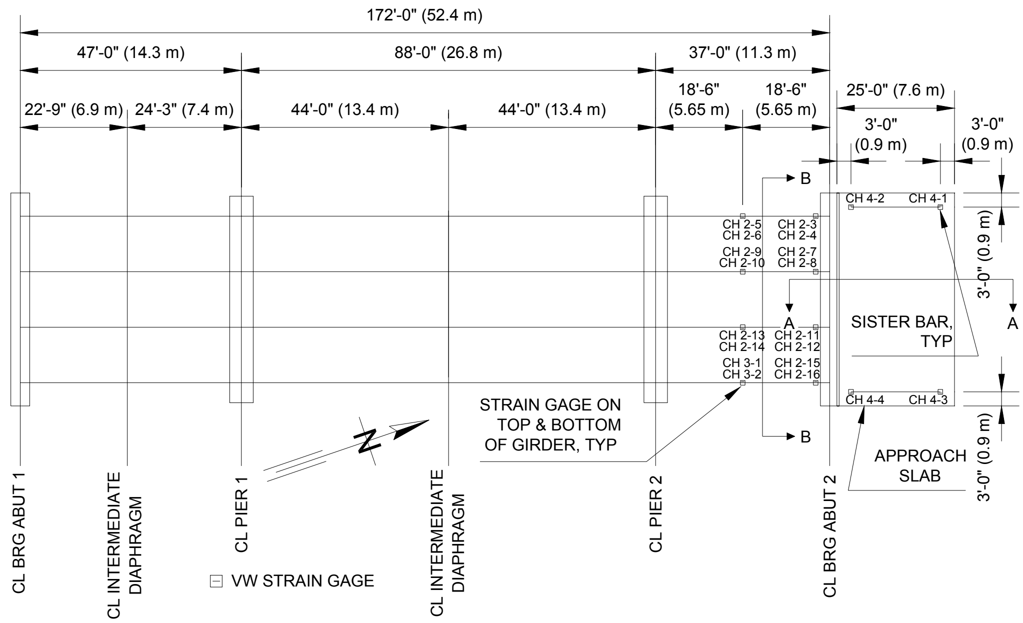

Figure A-1: Bridge 203 – Instrumentation Plan View

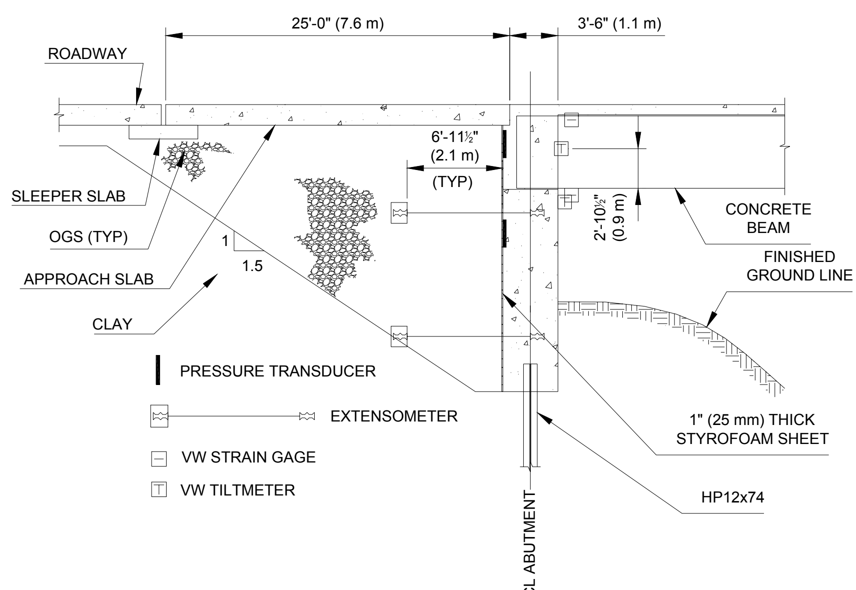

Figure A-2: Bridge 203 – Section A

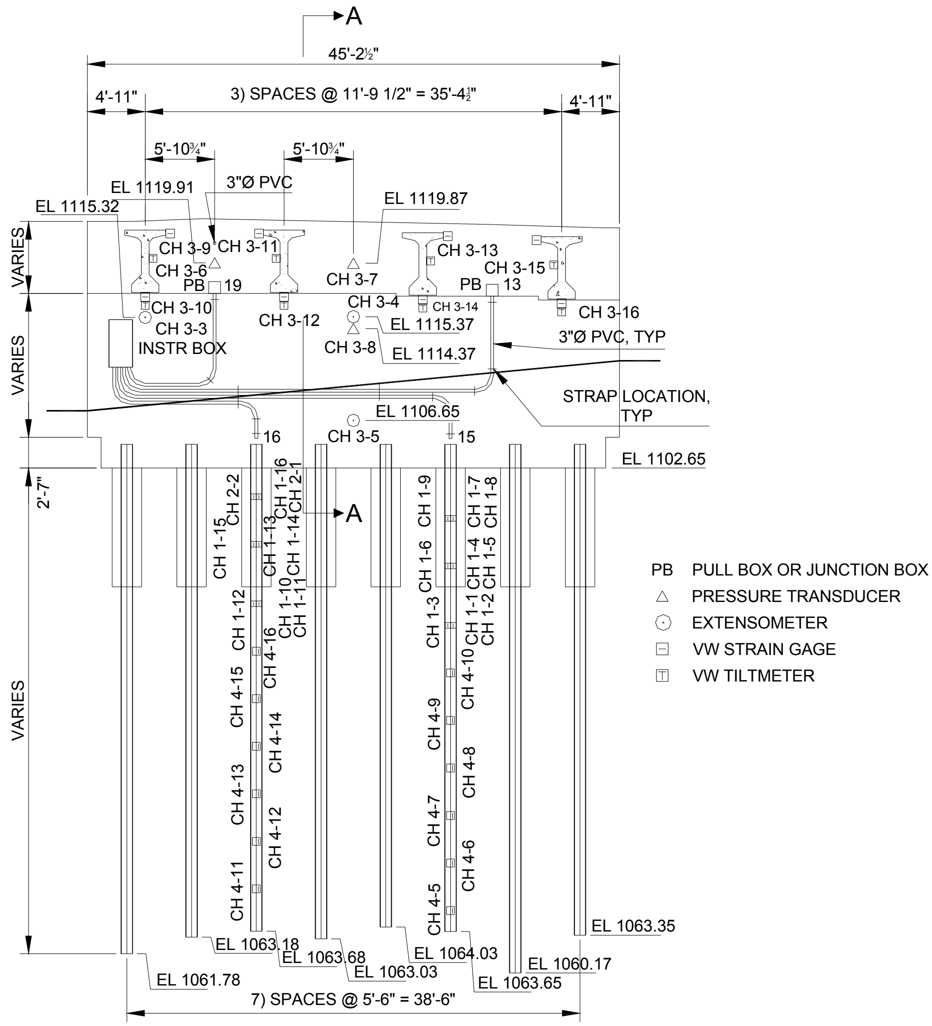

Figure A-3: Bridge 203 – Section B

A.2 Bridge 211

Bridge 211 is a single span composite slab on 4 prestressed concrete I-girders with a span length of 34.7 m (114 ft). As presented in Figures A-4 to A-8, the instrumentation consists of 16 strain gages on 4 girders, 24 strain gages on 4 piles, 4 tilt meters on 2 girders, 4 tilt meters on 2 abutments, 4 extensometers on 2 abutments, 4 pressure cells on 2 abutments, and 8 sister bar gages embedded in 2 approach slabs. The total instruments for this bridge are 64 gages.

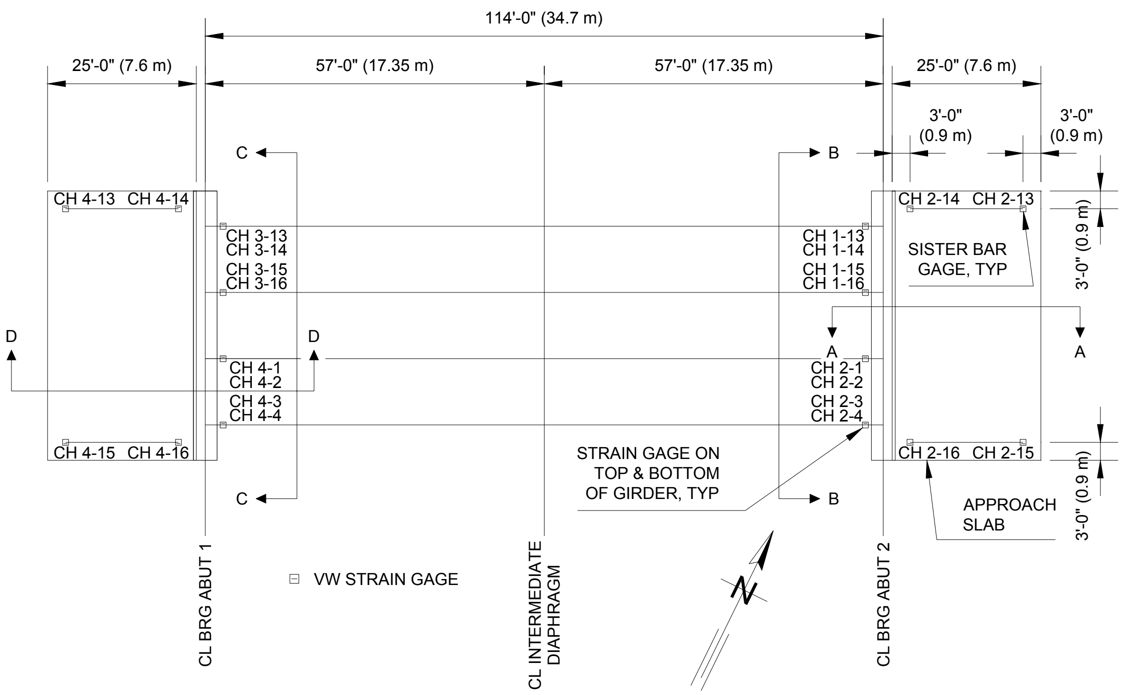

Figure A-4: Bridge 211 – Instrumentation Plan View

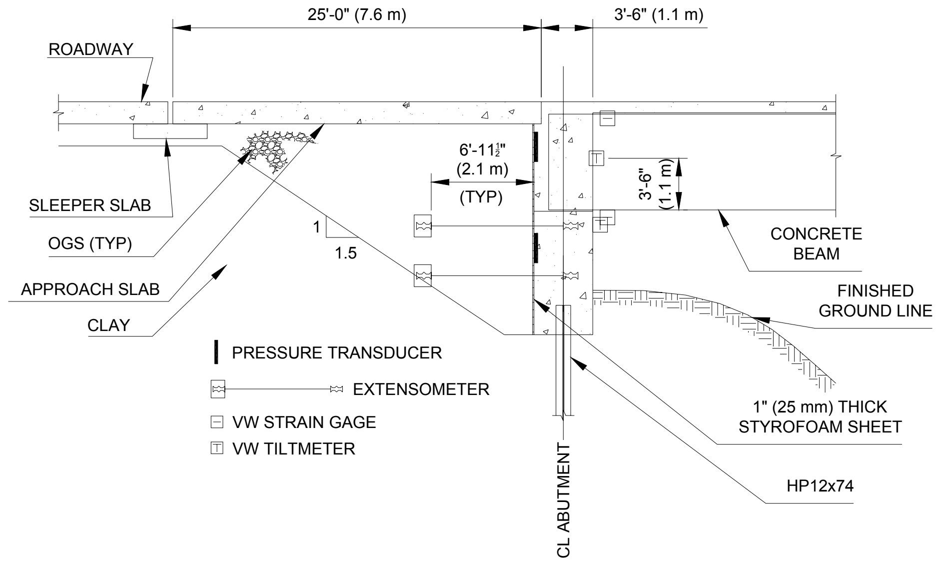

Figure A-5: Bridge 211 – Section A

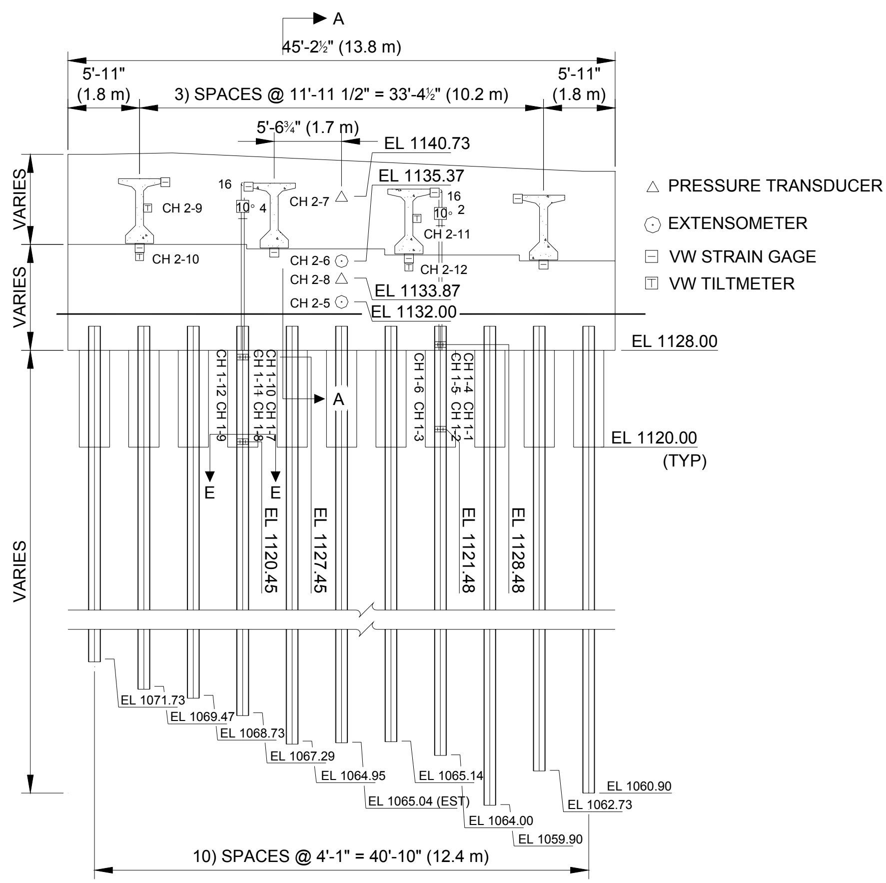

Figure A-6: Bridge 211 – Section B

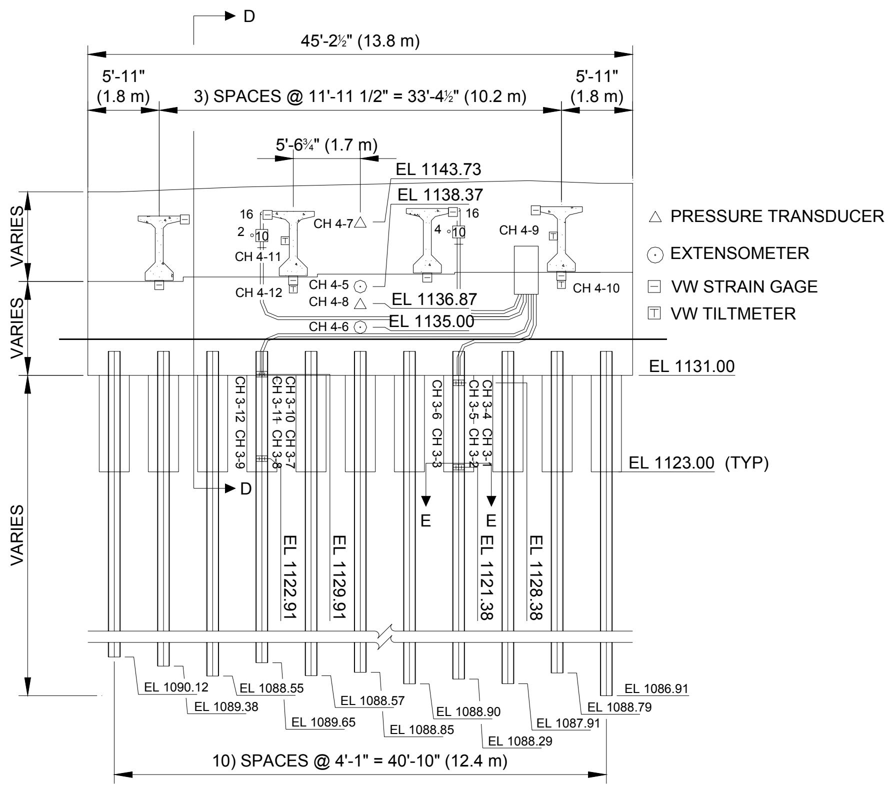

Figure A-7: Bridge 211 – Section C

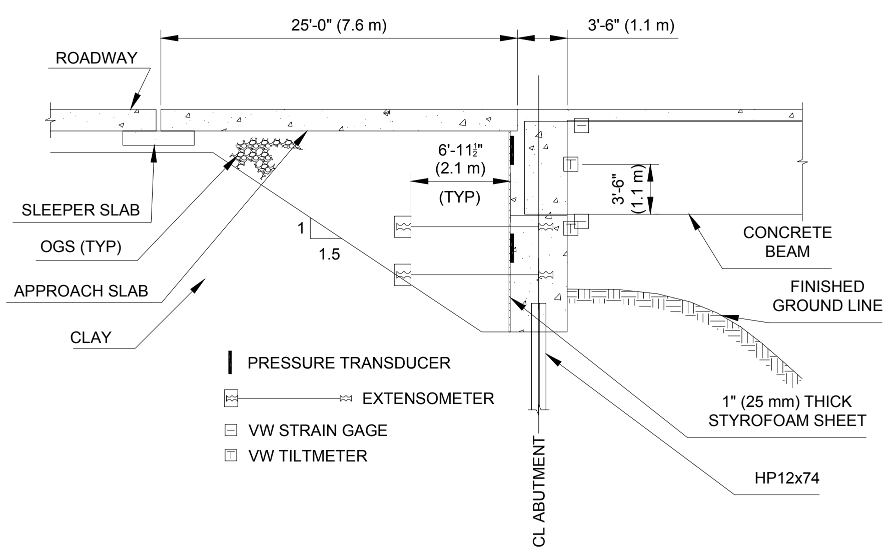

Figure A-8: Bridge 211 – Section D

A.3 Bridge 222

Bridge 222 is a single span composite slab on 4 prestressed concrete I-girders with a span length of 18.7 m (61.5 ft) at the centerline of the bridge. As presented in Figures A-9 to A-13, the instrumentation consists of 8 strain gages on 2 girders, 24 strain gages on 4 piles, 2 tilt meters on 2 girders, 2 tilt meters on 1 abutment, 4 extensometers on 2 abutments, 4 pressure cells on 2 abutments, and 4 sister bar gages embedded in 1 approach slab. The total instruments for this bridge are 48 gages.

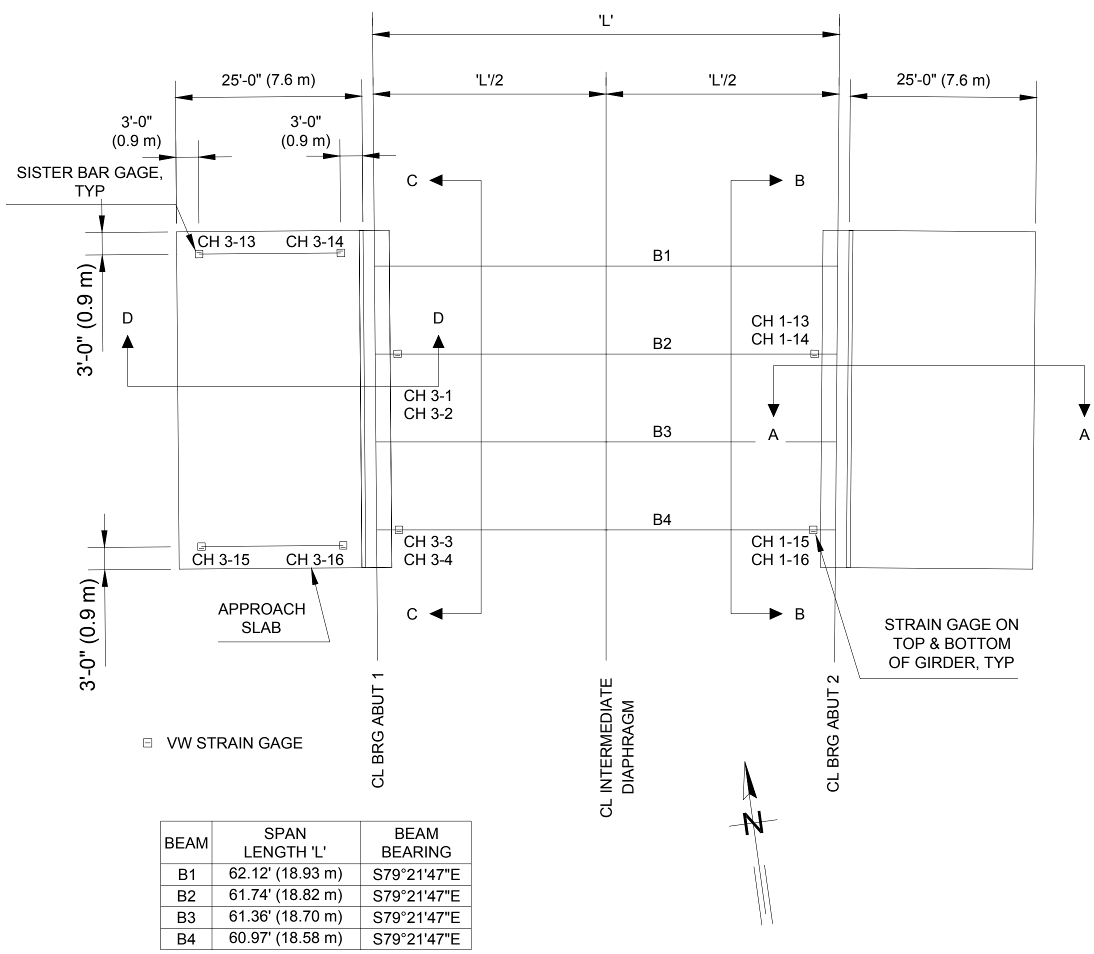

BEAM	SPAN LENGTH 'L'	BEAM BEARING
B1	62.12' (18.93 m)	S79°21'47"E
B2	61.74' (18.82 m)	S79°21'47"E
B3	61.36' (18.70 m)	S79°21'47"E
B4	60.97' (18.58 m)	S79°21'47"E

Figure A-9: Bridge 222 – Instrumentation Plan View

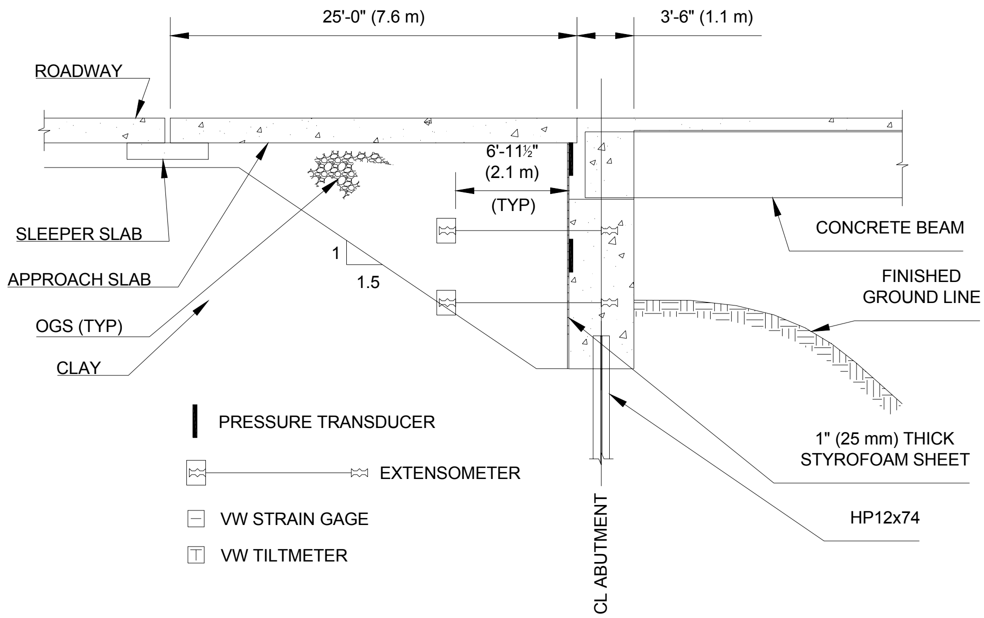

Figure A-10: Bridge 222 – Section A

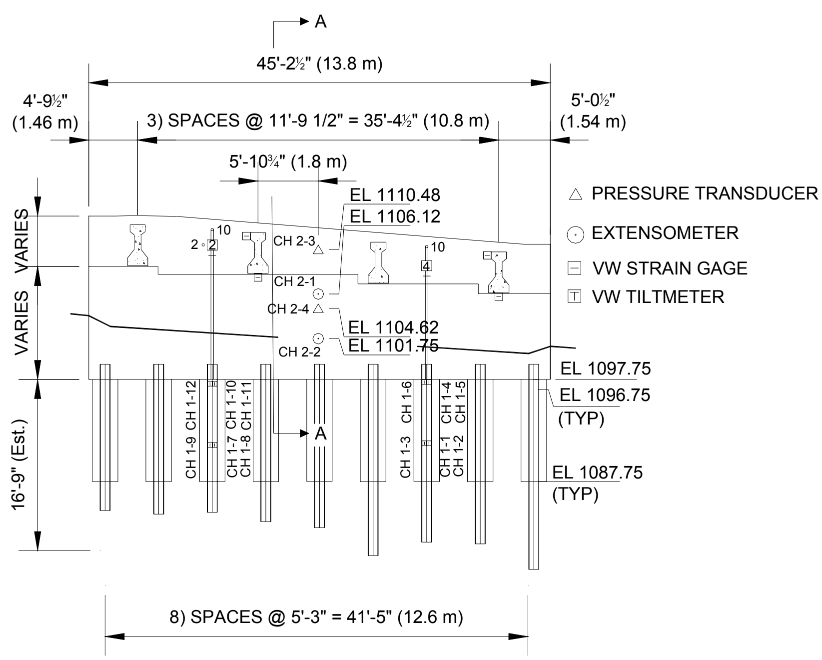

Figure A-11: Bridge 222 – Section B

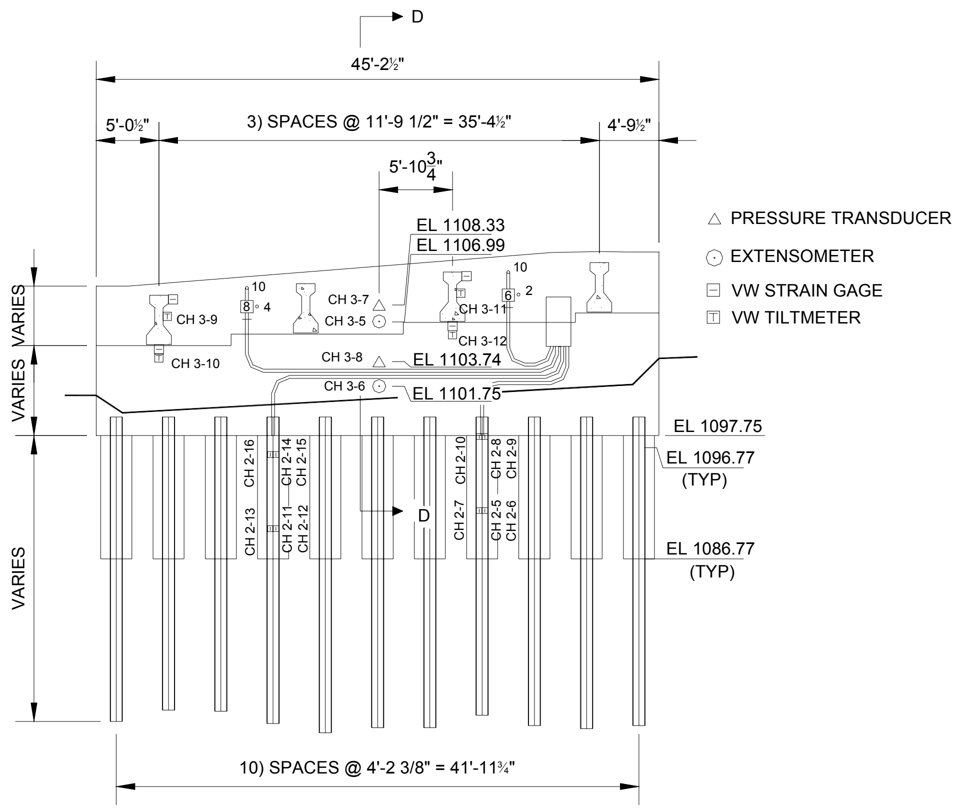

Figure A-12: Bridge 222 – Section C

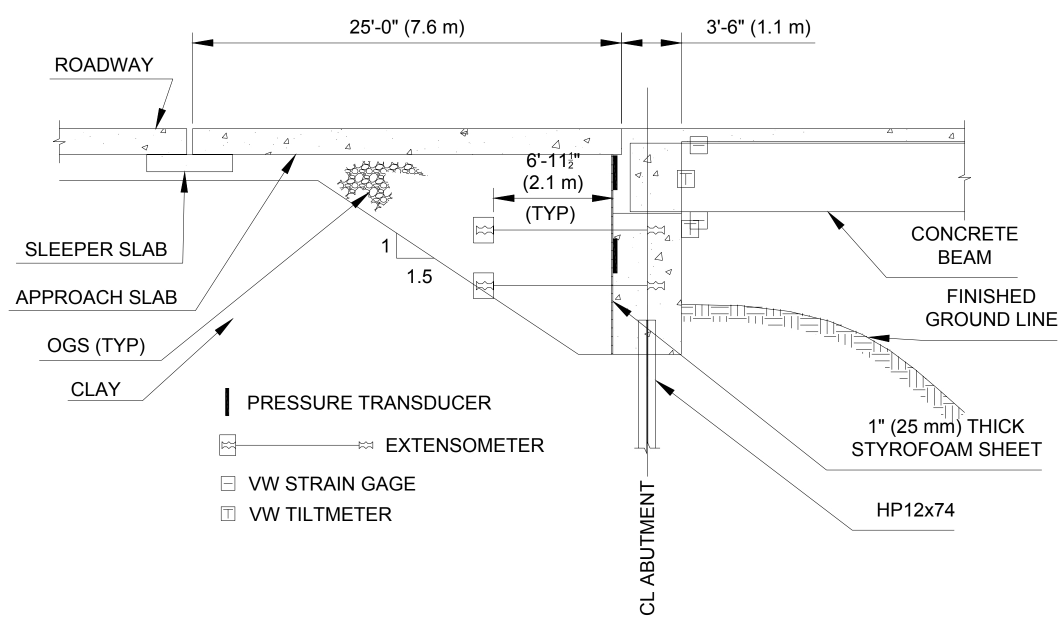

Figure A-13: Bridge 222 – Section D

All gages used in this study are a vibrating wire based. This gage type possesses an important characteristic as required for long-term monitoring, including repeatability and stability. Detailed description for gage types, installation procedure, bridge locations, and bridge reinforcement details are excluded from the scope of this study. However, this information can be found in Laman *et al* [**60**].

Appendix B

Calculation of Time-Dependent Strains

This appendix provides time-dependent strain design calculations of all three instrumented bridges based on the age-adjusted effective modulus method (AAEM). The design calculation spreadsheet consists of 9 pages. The first page deals with section properties, pages 2 to 3 present curves of creep, shrinkage, and aging coefficients for a girder member, page 4 provides results of time-dependent strains under an unrestrained boundary condition, pages 5 to 7 presents curves of creep, shrinkage, and aging coefficient for aging girder and slab members, and finally pages 8 to 9 provides results of time-dependent strains under a restrained boundary condition. It is noted that the design calculations are also presented in an arithmetic order.

B.1 Bridge 203

Bridge 203 consists of three spans. Referring to Appendix A, span 1 is placed between abutment 1 and pier 1, span 2 is placed between pier 1 and pier 2, and span 3 (integral abutment span) is placed between pier 2 and abutment 2.

B.1.1 Span 1

Interior Girder

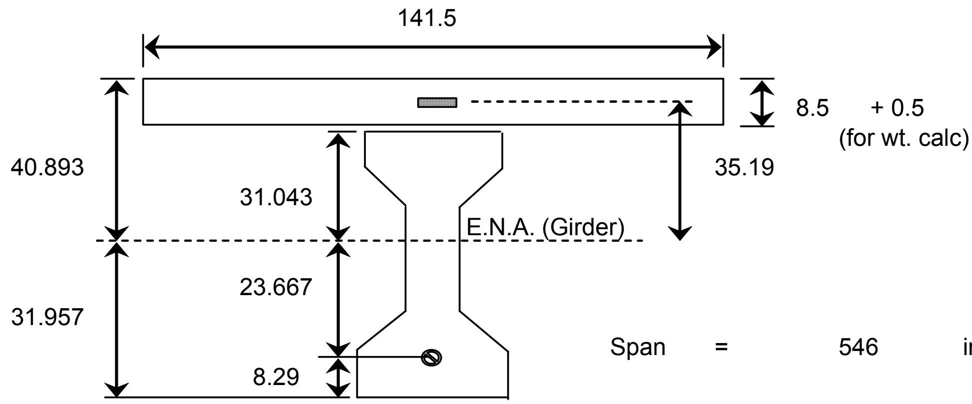

Span = 546 in

Concrete properties:

Girder:

A	=	1013	in^2
I	=	521162.6	in^4
$E_c(3)$	=	4628.4	ksi
$E_c(28)$	=	5098.2	ksi

Slab:

$E_c(3)$	=	3272.8	ksi
$E_c(28)$	=	3605.0	ksi

Prestress strand properties:

A	=	0.153	in^2
No.	=	28	
Jacking	=	30.982	k/strand
E_{ps}	=	28500	ksi
$A_{s\text{-}slab}$	=	9.412	in^2
E_s	=	29000	ksi

Section Properties at t = 3 days (midspan):

	Properties of area			Properties of transformed area		
	A	B	I	$A*E/E_{ref}$	$B*E/E_{ref}$	$I*E/E_{ref}$
Girder	1013	0	521162.6	1013	0	521162.6
Strand	4.284	101.4	2399.6	26.4	624.3	14775.8
				1039.4	624.3	535938.4

Relaxation loss from t = 0 to 3 days:

Δf_{RE}	=	-2.664	ksi
f_{pi}	=	199.833	ksi

Applied forces at transfer:

x/L	e (in)	No. of strands	A	B	I	N (kips)	M (kips-in)
0.000	0.000	0	1013.0	0.0	521162.6	0.0	0.0
0.100	22.777	22	1033.7	472.1	531915.4	-672.6	-14141.0
0.176	22.777	22	1033.7	472.1	531915.4	-672.6	-13421.3
0.200	23.667	28	1039.4	624.3	535938.4	-856.1	-18163.8
0.300	23.667	28	1039.4	624.3	535938.4	-856.1	-17508.4
0.400	23.667	28	1039.4	624.3	535938.4	-856.1	-17115.2
0.500	23.667	28	1039.4	624.3	535938.4	-856.1	-16984.1

Strains and curvatures at transfer:

x/L	ε_o in/inx10^6	ψ 1/inx10^6
0.000	0.0	0.0
0.100	-138.0	-5.6
0.176	-138.2	-5.3
0.200	-173.7	-7.1
0.300	-173.8	-6.9
0.400	-173.9	-6.7
0.500	-174.0	-6.6

Strain at the strand level (midspan) =	-331.2	in/inx10^6
Elastic shortening loss =	-9.440	ksi
Stress of prestress strand =	190.393	ksi
% initial loss =	5.98	%

Creep coefficients, Φ(t, 3):

Model	Day 3.01	4	7	28	124	365	10950	36500
AASHTO	0.003	0.050	0.107	0.284	0.638	0.959	1.425	1.460
ACI	0.009	0.126	0.259	0.565	0.886	1.072	1.334	1.359
CEB-FIP	0.070	0.280	0.423	0.725	1.110	1.405	1.820	1.839
B3	0.000	0.362	0.505	0.728	0.961	1.131	1.722	1.967

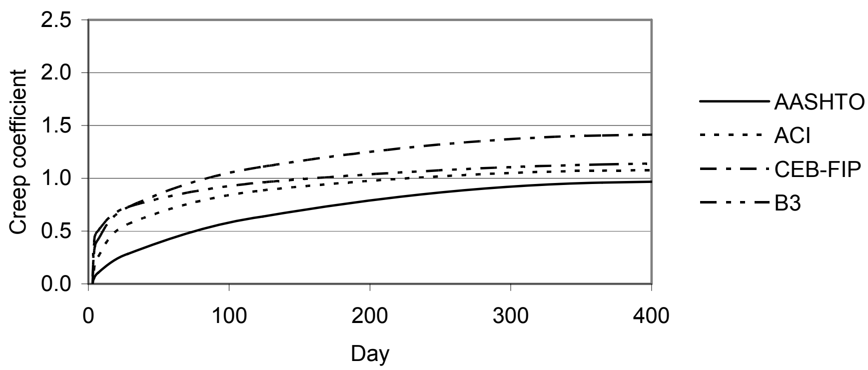

Shrinkage, $\varepsilon_{sh}(t)$:

Model	Day 3.01	4	7	28	124	365	10950	36500
AASHTO	0.000007	0.000010	0.000017	0.000062	0.000182	0.000283	0.000388	0.000391
ACI	0.000000	0.000007	0.000026	0.000120	0.000264	0.000334	0.000383	0.000384
CEB-FIP	0.000034	0.000047	0.000066	0.000123	0.000207	0.000283	0.000503	0.000523
B3	0.000000	0.000004	0.000014	0.000087	0.000326	0.000430	0.000432	0.000432

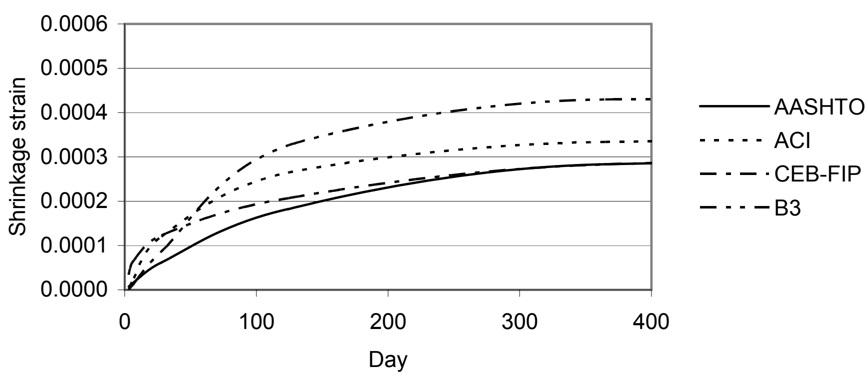

Aging coefficients, χ(t, 3):

Model	Day							
	3.01	4	7	28	124	365	10950	36500
AASHTO	N/A	N/A	N/A	N/A	N/A	N/A	N/A	N/A
ACI	0.710	0.658	0.642	0.621	0.604	0.594	0.567	0.558
CEB-FIP	0.808	0.777	0.769	0.648	0.568	0.536	0.478	0.475
B3	0.731	0.702	0.693	0.682	0.671	0.660	0.614	0.597

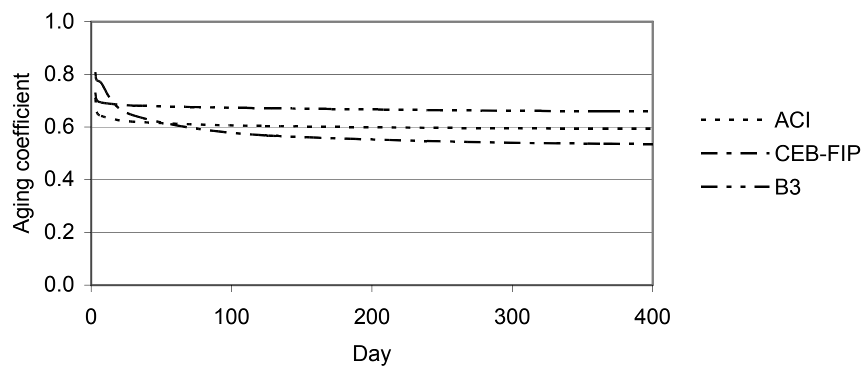

Use engineering recommendation model: **ACI**

Time-dependent restrained forces at t = 124 days (ΔN and ΔM):

$\Phi(124,3)$ =	0.886			$\chi(124,3)$ =	0.604	
Ec(124,3) =	3015.9	ksi	*(Age-adjusted elastic modulus)*			
$\varepsilon sh(124)$ =	0.000264			λ =	0.705	
Ω =	0.064			χ_r =	0.827	
A (mid) =	1053.5	in^2		B (mid) =	958.1	in^3
I (mid) =	543838	in^4				

x/L	Creep		Shrinkage		Relaxation		Total	
	ΔN	ΔM	ΔN	ΔM	ΔN	ΔM	ΔN	ΔM
0.000	0.0	0.0	808.0	0.0	0.0	0.0	808.0	0.0
0.100	373.4	7825.1	808.0	0.0	-6.5	-147.0	1175.0	7678.1
0.176	373.8	7418.0	808.0	0.0	-6.5	-147.0	1175.4	7271.0
0.200	469.9	9911.4	808.0	0.0	-8.2	-194.4	1269.7	9717.0
0.300	470.4	9543.4	808.0	0.0	-8.2	-194.4	1270.1	9349.0
0.400	470.6	9322.6	808.0	0.0	-8.2	-194.4	1270.4	9128.2
0.500	470.7	9248.9	808.0	0.0	-8.2	-194.4	1270.5	9054.6

Strains and curvatures at t = 124 days

x/L	$\Delta\varepsilon_o(t)$	$\Delta\psi(t)$
	in/inx10^6	1/inx10^6
0.000	-264.5	0.0
0.100	-370.0	-4.2
0.176	-370.2	-4.0
0.200	-394.9	-5.2
0.300	-395.2	-5.0
0.400	-395.4	-4.9
0.500	-395.5	-4.8

Strain inc. at the strand level (mid) =	-509.7	in/inx10^6
Time-dependent inc. losses =	-14.525	ksi
Stress of prestress strand =	175.868	ksi
% losses =	13.15	%

Strains and curvatures - Summary for simple span case at x/L = 0.500

Strain, $\varepsilon_o(t)$ using ACI, CEB-FIP, and B3 respectively

Day								
3	3.01	4	7	28	124	365	10950	36500
-174.0	-175.5	-201.3	-241.3	-381.0	-569.5	-664.1	-748.5	-752.9
-171.7	-216.4	-262.7	-303.6	-405.3	-544.5	-662.1	-933.3	-955.0
-174.0	-174.0	-236.5	-269.4	-373.8	-639.2	-763.7	-850.9	-885.8

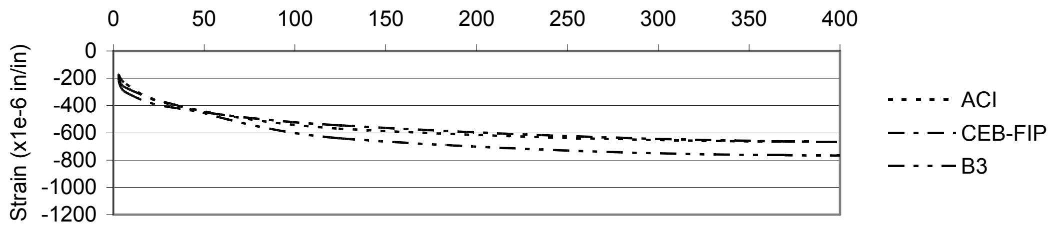

Curvature, $\psi(t)$ using ACI, CEB-FIP, and B3 respectively

Day								
3	3.01	4	7	28	124	365	10950	36500
-6.6	-6.7	-7.4	-8.2	-9.9	-11.5	-12.4	-13.7	-13.8
-6.6	-7.0	-8.2	-9.0	-10.7	-12.7	-14.2	-16.0	-16.1
-6.6	-6.6	-8.9	-9.7	-10.9	-11.7	-12.5	-15.6	-16.8

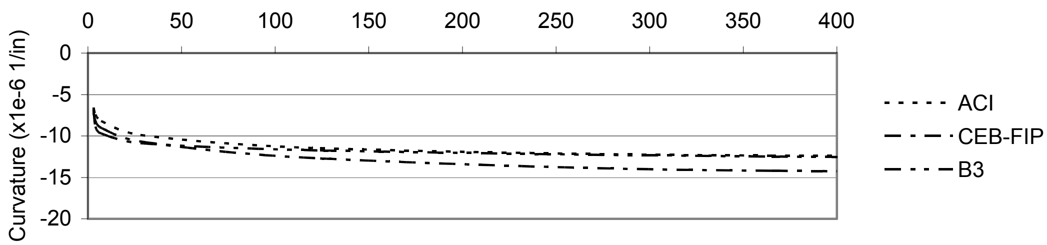

Stress of prestress strand using ACI, CEB-FIP, and B3 respectively

Day								
3	3.01	4	7	28	124	365	10950	36500
190.4	190.3	189.1	187.4	182.3	175.9	172.6	169.3	169.1
190.5	189.0	186.8	185.1	181.1	175.7	171.4	162.4	161.8
190.4	190.4	187.1	185.6	181.9	173.7	169.7	165.1	163.2

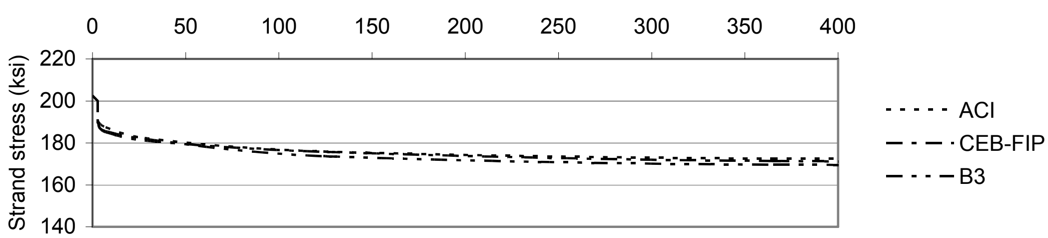

% prestress losses using ACI, CEB-FIP, and B3 respectively

Day								
3	3.01	4	7	28	124	365	10950	36500
6.0	6.0	6.6	7.4	10.0	13.2	14.8	16.4	16.5
5.9	6.7	7.7	8.6	10.6	13.2	15.4	19.8	20.1
6.0	6.0	7.6	8.3	10.2	14.2	16.2	18.5	19.4

Effect of concrete deck placed at t = 124 days

Section Properties at t = 124 days when deck is not hardened yet (midspan):

	Properties of area			Properties of transformed area		
	A	B	I	A^*E/E_{ref}	B^*E/E_{ref}	I^*E/E_{ref}
Girder	1013	0	521162.6	1013	0	521162.6
Strand	4.284	101.4	2399.6	23.9	566.8	13414.1
				1036.9	566.8	534576.7

Applied forces due to concrete deck placement:

x/L	A	B	I	ΔN (kips)	ΔM (kips-in)
0.000	1013.0	0.0	521162.6	0.0	0.0
0.100	1031.8	428.6	530924.5	0.0	1483.0
0.176	1031.8	428.6	530924.5	0.0	2387.8
0.200	1036.9	566.8	534576.7	0.0	2636.5
0.300	1036.9	566.8	534576.7	0.0	3460.4
0.400	1036.9	566.8	534576.7	0.0	3954.7
0.500	1036.9	566.8	534576.7	0.0	4119.5

Strains and curvatures at deck placement:

x/L	$\Delta\varepsilon_o$ in/inx10^6	$\Delta\psi$ 1/inx10^6
0.000	0.0	0.0
0.100	-0.2	0.5
0.176	-0.4	0.9
0.200	-0.5	1.0
0.300	-0.7	1.3
0.400	-0.8	1.5
0.500	-0.8	1.5

Strain at the strand level (midspan) =	35.0	in/inx10^6
Elastic stress gain =	0.997	ksi
Stress of prestress strand =	176.865	ksi
% losses =	12.66	%

Creep coefficients of girder, Φ(t, 124):

Model	Day							
	124.01	125	127	131	152	365	10950	36500
ACI	0.006	0.087	0.155	0.232	0.406	0.696	0.920	0.938
CEB-FIP	0.033	0.131	0.181	0.233	0.350	0.613	0.883	0.894
B3	0.000	0.148	0.198	0.243	0.331	0.505	0.806	0.925

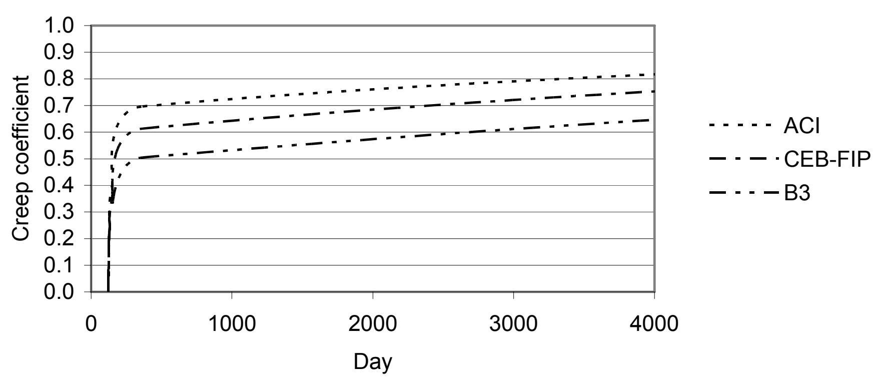

Aging coefficients of girder, χ(t, 124):

Model	Day							
	124.01	125	127	131	152	365	10950	36500
ACI	0.545	0.725	0.767	0.800	0.854	0.914	0.921	0.915
CEB-FIP	0.812	0.860	0.899	0.909	0.909	0.883	0.820	0.817
B3	0.548	0.737	0.781	0.816	0.873	0.935	0.932	0.923

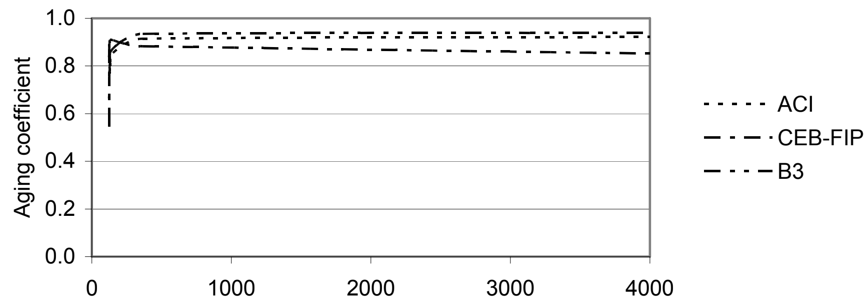

Creep coefficients of concrete deck slab, Φ(t, 3):

Model	Day							
	3.01	4	6	10	31	244	10829	36379
ACI	0.008	0.115	0.205	0.308	0.538	0.923	1.220	1.243
CEB-FIP	0.092	0.367	0.510	0.656	0.989	1.779	2.809	2.860
B3	0.000	0.360	0.470	0.563	0.731	1.043	1.703	1.950

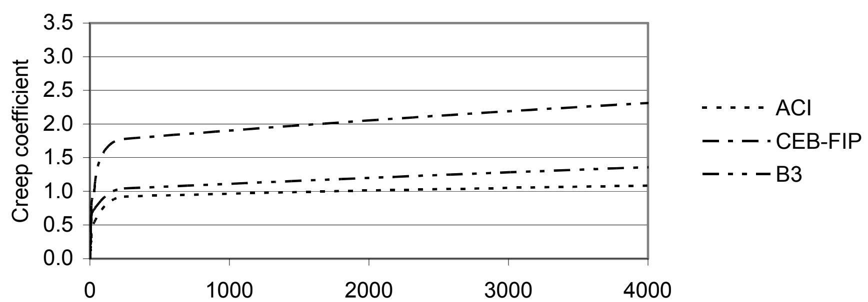

Aging coefficients of concrete deck slab, χ(t, 3):

Model	Day							
	3.01	4	6	10	31	244	10829	36379
ACI	0.695	0.630	0.615	0.603	0.583	0.558	0.530	0.522
CEB-FIP	0.809	0.794	0.809	0.781	0.699	0.574	0.644	0.650
B3	0.731	0.701	0.694	0.688	0.679	0.662	0.612	0.595

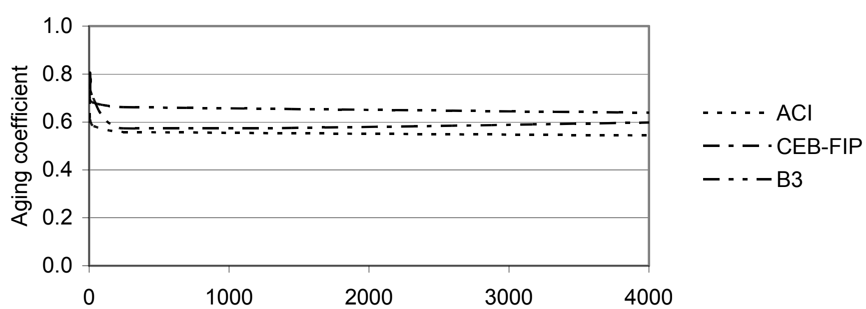

Shrinkage of concrete deck slab, $\varepsilon_{sh}(t)$:

Model	Day							
	3.01	4	6	10	31	244	10829	36379
ACI	0.000000	0.000004	0.000012	0.000025	0.000075	0.000181	0.000221	0.000222
CEB-FIP	0.000016	0.000024	0.000031	0.000042	0.000070	0.000153	0.000502	0.000584
B3	0.000000	0.000001	0.000004	0.000009	0.000037	0.000273	0.000432	0.000432

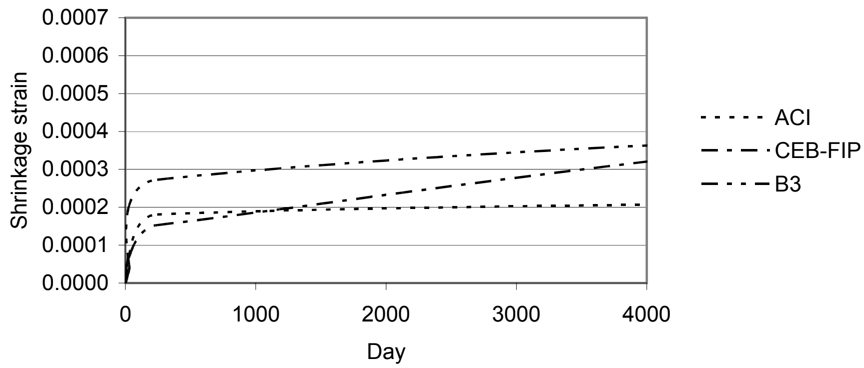

Time-dependent effect at t = 36500 days:

Girder:

$\Delta\Phi(36500,3)$ = 0.474

$\Delta\varepsilon sh(36500)$ = 0.00012

$\Phi(36500,124)$ = 0.938

$\chi(36500,124)$ = 0.915

$Ec(36500,124)$ = 2742.7 ksi

Slab:

$\Phi(36379,3)$ = 1.243

$\chi(36379,3)$ = 0.522

$Ec(36379,3)$ = 1985.0 ksi

$\varepsilon sh(36379)$ = 0.000222

Strand:

λ = 0.705

χ_r = 0.814

Ω = 0.069

Stresses and curvatures prior to composite action

x/L	Restrained		Time-dependence		Change in stresses			
	σ_{top}	σ_{bot}	σ_{top}	σ_{bot}	$\Delta\sigma_{top}$	$\Delta\sigma_{bot}$	$\Delta\sigma$	$\Delta\psi$
0.000	0.798	0.798	-0.798	-0.798	0.000	0.000	0.000	0.000
0.100	0.700	1.646	-0.719	-1.524	-0.019	0.122	0.051	0.002
0.176	0.725	1.621	-0.744	-1.501	-0.019	0.121	0.050	0.002
0.200	0.671	1.869	-0.701	-1.695	-0.030	0.174	0.071	0.003
0.300	0.694	1.847	-0.723	-1.674	-0.030	0.173	0.070	0.003
0.400	0.707	1.834	-0.737	-1.662	-0.030	0.172	0.070	0.003
0.500	0.711	1.829	-0.741	-1.658	-0.030	0.172	0.070	0.003

Section Properties at t = 36500 days when composite action starts (midspan):

	Properties of area			Properties of transformed area		
	A	B	I	$A*E/E_{ref}$	$B*E/E_{ref}$	$I*E/E_{ref}$
Girder	1013	0	521162.6	1013	0	521162.6
Strand	4.284	101.4	2399.6	44.5	1053.5	24934.4
Deck	1203	-44072	1622185	870	-31896	1174002
Rebars	9.41	-331.2	11655.9	99.5	-3502.1	123242.5
				2027	-34344	1843342

Note *: neglected the duration of 3-day concrete deck hardening*

Time-dependent restrained forces at t = 36500 days (ΔN and ΔM):

x/L	Creep		Shrinkage		Relaxation		Total	
	ΔN	ΔM	ΔN	ΔM	ΔN	ΔM	ΔN	ΔM
0.000	0.0	0.0	862.8	-19435.6	0.0	0.0	862.8	-19435.6
0.100	167.8	2742.6	862.8	-19435.6	-9.7	-221.1	1020.9	-16914.0
0.176	168.5	2099.6	862.8	-19435.6	-9.7	-221.1	1021.6	-17557.1
0.200	209.8	3046.2	862.8	-19435.6	-12.4	-292.4	1060.2	-16681.7
0.300	210.6	2465.6	862.8	-19435.6	-12.4	-292.4	1061.1	-17262.3
0.400	211.1	2117.3	862.8	-19435.6	-12.4	-292.4	1061.5	-17610.6
0.500	211.3	2001.2	862.8	-19435.6	-12.4	-292.4	1061.7	-17726.7

Strains and curvatures at t = 36500 days

x/L	$\Delta\varepsilon_o(t)$	$\Delta\psi(t)$
	in/inx10^6	1/inx10^6
0.000	-136.5	1.2
0.100	-187.4	-0.2
0.176	-184.4	0.0
0.200	-196.9	-0.4
0.300	-194.3	-0.2
0.400	-192.7	-0.1
0.500	-192.2	-0.1

Strain inc. at the strand level (mid) =	-194.0	in/inx10^6
Time-dependent inc. losses =	-5.528	ksi
Stress of prestress strand =	171.337	ksi
% losses =	15.39	%

Time-dependent strain at top fiber along the length of the girder:

x/L	Day							
	124.01	125	127	131	152	365	10950	36500
0.000	0.0	-3.0	-8.8	-19.2	-57.9	-148.3	-186.3	-187.2
0.100	-0.1	-3.6	-9.7	-20.5	-59.6	-147.3	-179.9	-180.3
0.176	-0.1	-3.9	-10.3	-21.4	-61.2	-150.3	-184.3	-184.9
0.200	-0.1	-4.0	-10.4	-21.5	-61.3	-149.3	-181.4	-181.8
0.300	-0.1	-4.3	-10.9	-22.3	-62.7	-152.0	-185.3	-185.9
0.400	-0.1	-4.4	-11.3	-22.8	-63.6	-153.6	-187.7	-188.3
0.500	-0.1	-4.5	-11.4	-23.0	-63.8	-154.1	-188.5	-189.1

Time-dependent strain at bottom fiber along the length of the girder:

x/L	Day							
	124.01	125	127	131	152	365	10950	36500
0.000	0.0	0.6	1.7	3.6	8.2	-43.4	-95.4	-96.9
0.100	0.1	1.4	2.9	4.9	7.4	-78.9	-187.0	-193.0
0.176	0.1	2.0	4.0	6.5	10.3	-73.1	-178.3	-184.0
0.200	0.1	2.1	4.0	6.5	9.4	-82.9	-201.9	-208.7
0.300	0.2	2.6	5.0	7.9	12.0	-77.8	-194.3	-200.9
0.400	0.2	3.0	5.6	8.8	13.6	-74.7	-189.7	-196.1
0.500	0.2	3.1	5.8	9.1	14.1	-73.7	-188.2	-194.6

Strains and curvatures - Summary for simple span case at x/L = 0.500

Strain, $\varepsilon_o(t)$ using ACI, CEB-FIP, and B3 respectively

Day								
124	124.01	125	127	131	152	365	10950	36500
0.0	0.0	-0.3	-1.7	-5.0	-20.1	-109.0	-188.3	-192.2
0.0	-2.8	-3.8	-5.7	-8.8	-22.1	-126.6	-411.6	-442.5
0.0	0.0	0.7	-0.2	-2.5	-16.0	-150.2	-265.6	-300.4

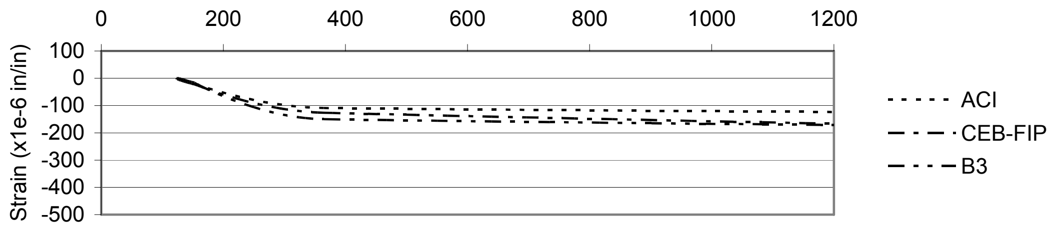

Curvature, $\psi(t)$ using ACI, CEB-FIP, and B3 respectively

Day								
124	124.01	125	127	131	152	365	10950	36500
0.0	0.0	0.1	0.2	0.4	1.1	1.1	0.0	-0.1
0.0	0.2	0.4	0.5	0.6	0.8	-0.1	-0.5	0.1
0.0	0.0	0.1	0.2	0.2	0.5	1.7	1.2	0.1

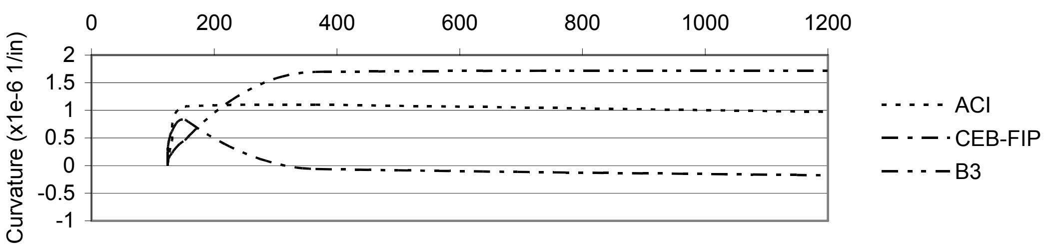

Stress of prestress strand using ACI, CEB-FIP, and B3 respectively

Day								
124	124.01	125	127	131	152	365	10950	36500
176.9	176.9	176.9	177.0	177.0	177.0	174.5	171.5	171.3
176.6	176.7	176.8	176.8	176.8	176.6	173.0	164.6	164.1
174.7	174.7	174.8	174.8	174.8	174.5	171.6	167.9	166.2

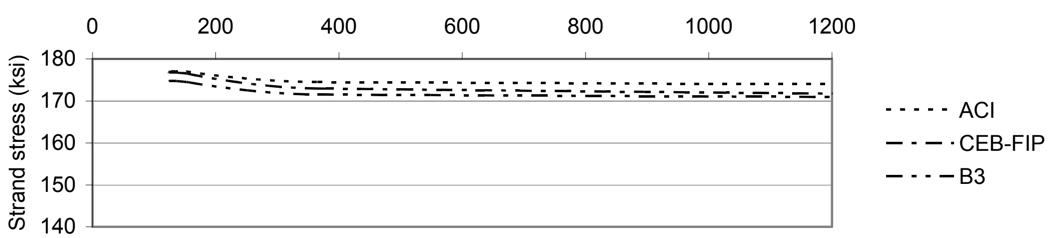

% prestress losses using ACI, CEB-FIP, and B3 respectively

Day								
124	124.01	125	127	131	152	365	10950	36500
12.7	12.7	12.6	12.6	12.6	12.6	13.8	15.3	15.4
12.8	12.7	12.7	12.7	12.7	12.8	14.6	18.7	19.0
13.7	13.7	13.7	13.7	13.7	13.8	15.3	17.1	17.9

End of Calculation

Three samples of time-dependent strains with respect to the time-line (127, 365, and 36,500 days) at the top fiber of interior girders are shown in Figure B-1.

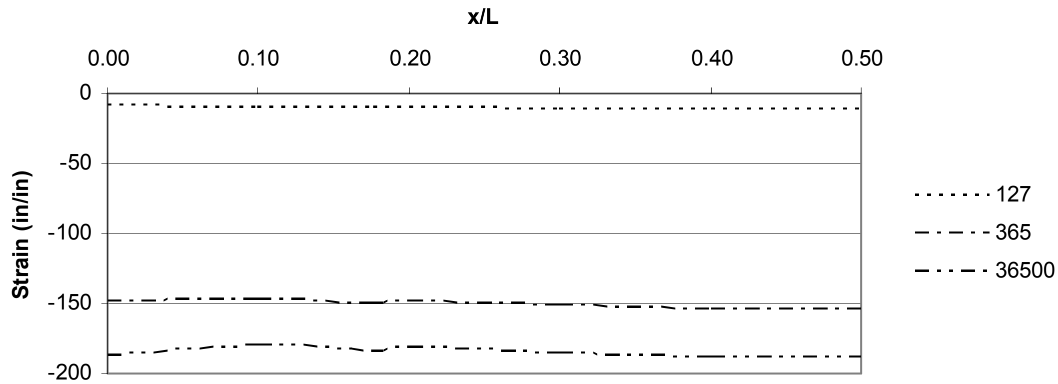

Figure B-1: Time-Dependent Strains at Top Fiber (Bridge 203 – Span 1 – Int. Girder)

Three samples of time-dependent strains with respect to the time-line (127, 365, and 36,500 days) at the bottom fiber of interior girders are shown in Figure B-2.

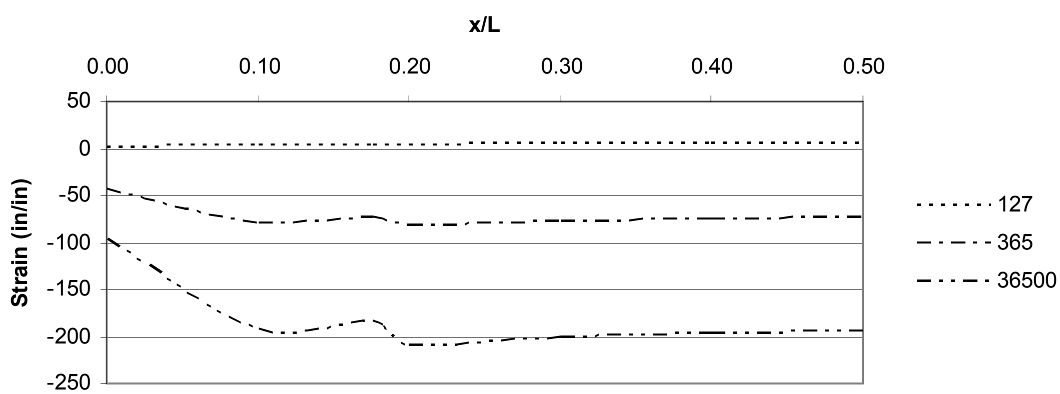

Figure B-2: Time-Dependent Strains at Bottom Fiber (Bridge 203 – Span 1 – Int. Girder)

Exterior Girder

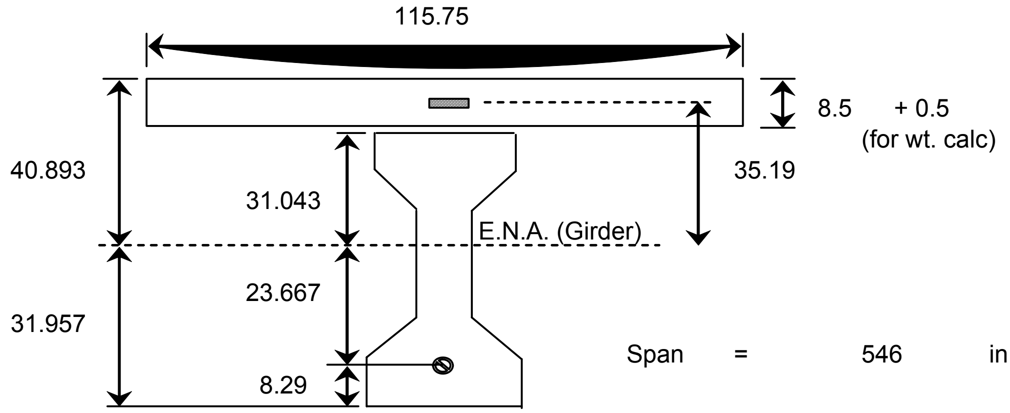

Span = 546 in

Concrete properties:

Girder:

A	=	1013	in^2
I	=	521162.6	in^4
$E_c(3)$	=	4628.4	ksi
$E_c(28)$	=	5098.2	ksi

Slab:

$E_c(3)$	=	3272.8	ksi
$E_c(28)$	=	3605.0	ksi

Prestress strand properties:

A	=	0.153	in^2
No.	=	28	
Jacking	=	30.982	k/strand
E_{ps}	=	28500	ksi
$A_{s\text{-}slab}$	=	9.412	in^2
E_s	=	29000	ksi

Section Properties at t = 3 days (midspan):

	Properties of area			Properties of transformed area		
	A	B	I	$A*E/E_{ref}$	$B*E/E_{ref}$	$I*E/E_{ref}$
Girder	1013	0	521162.6	1013	0	521162.6
Strand	4.284	101.4	2399.6	26.4	624.3	14775.8
				1039.4	624.3	535938.4

Relaxation loss from t = 0 to 3 days:

Δf_{RE}	=	-2.664	ksi
f_{pi}	=	199.833	ksi

Applied forces at transfer:

x/L	e (in)	No. of strands	A	B	I	N (kips)	M (kips-in)
0.000	0.000	0	1013.0	0.0	521162.6	0.0	0.0
0.100	22.777	22	1033.7	472.1	531915.4	-672.6	-14141.0
0.176	22.777	22	1033.7	472.1	531915.4	-672.6	-13421.3
0.200	23.667	28	1039.4	624.3	535938.4	-856.1	-18163.8
0.300	23.667	28	1039.4	624.3	535938.4	-856.1	-17508.4
0.400	23.667	28	1039.4	624.3	535938.4	-856.1	-17115.2
0.500	23.667	28	1039.4	624.3	535938.4	-856.1	-16984.1

Strains and curvatures at transfer:

x/L	ε_o in/inx10^6	ψ 1/inx10^6
0.000	0.0	0.0
0.100	-138.0	-5.6
0.176	-138.2	-5.3
0.200	-173.7	-7.1
0.300	-173.8	-6.9
0.400	-173.9	-6.7
0.500	-174.0	-6.6

Strain at the strand level (midspan) =	-331.2	in/inx10^6
Elastic shortening loss =	-9.440	ksi
Stress of prestress strand =	190.393	ksi
% initial loss =	5.98	%

Creep coefficients, $\Phi(t, 3)$:

Model	Day							
	3.01	4	7	28	124	365	10950	36500
AASHTO	0.003	0.050	0.107	0.284	0.638	0.959	1.425	1.460
ACI	0.009	0.126	0.259	0.565	0.886	1.072	1.334	1.359
CEB-FIP	0.070	0.280	0.423	0.725	1.110	1.405	1.820	1.839
B3	0.000	0.362	0.505	0.728	0.961	1.131	1.722	1.967

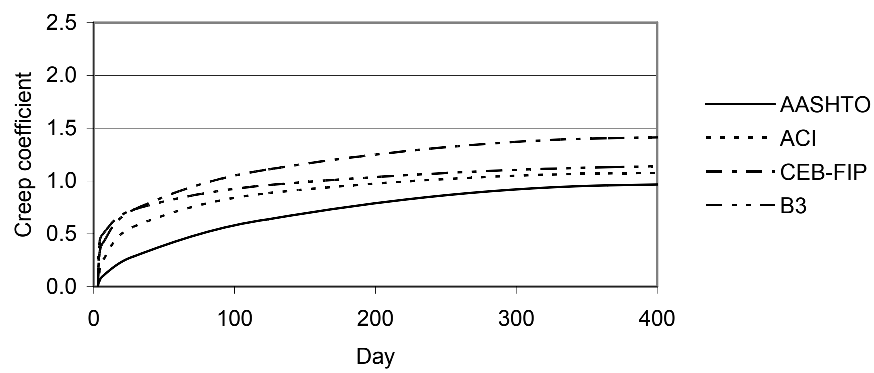

Shrinkage, $\varepsilon_{sh}(t)$:

Model	Day							
	3.01	4	7	28	124	365	10950	36500
AASHTO	0.000007	0.000010	0.000017	0.000062	0.000182	0.000283	0.000388	0.000391
ACI	0.000000	0.000007	0.000026	0.000120	0.000264	0.000334	0.000383	0.000384
CEB-FIP	0.000034	0.000047	0.000066	0.000123	0.000207	0.000283	0.000503	0.000523
B3	0.000000	0.000004	0.000014	0.000087	0.000326	0.000430	0.000432	0.000432

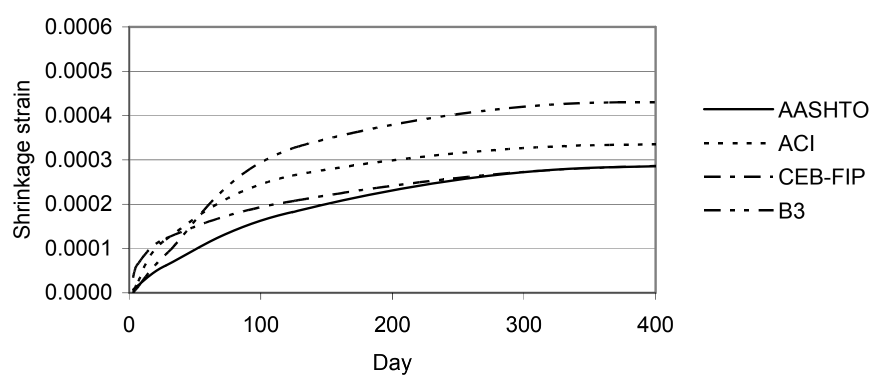

Aging coefficients, χ(t, 3):

Model	Day							
	3.01	4	7	28	124	365	10950	36500
AASHTO	N/A	N/A	N/A	N/A	N/A	N/A	N/A	N/A
ACI	0.710	0.658	0.642	0.621	0.604	0.594	0.567	0.558
CEB-FIP	0.808	0.777	0.769	0.648	0.568	0.536	0.478	0.475
B3	0.731	0.702	0.693	0.682	0.671	0.660	0.614	0.597

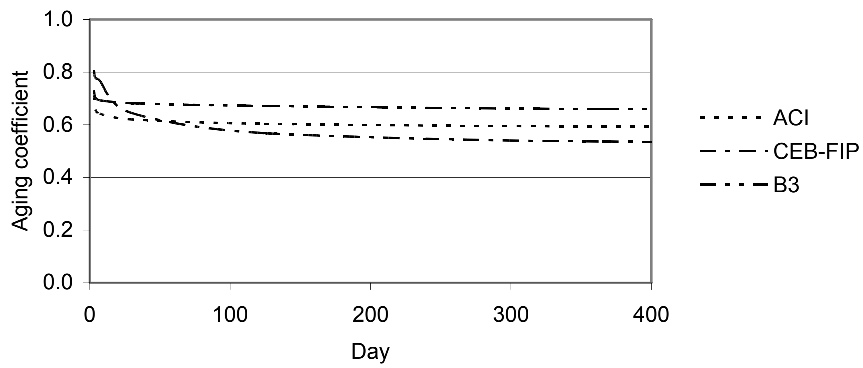

Use engineering recommendation model: **ACI**

Time-dependent restrained forces at t = 124 days (ΔN and ΔM):

Φ(124,3) =	0.886		χ(124,3) =		0.604	
Ec(124,3) =	3015.9	ksi	*(Age-adjusted elastic modulus)*			
εsh(124) =	0.000264		λ	=	0.705	
Ω =	0.064		χ_r	=	0.827	
A (mid) =	1053.5	in^2	B (mid)	=	958.1	in^3
I (mid) =	543838	in^4				

x/L	Creep		Shrinkage		Relaxation		Total	
	ΔN	ΔM	ΔN	ΔM	ΔN	ΔM	ΔN	ΔM
0.000	0.0	0.0	808.0	0.0	0.0	0.0	808.0	0.0
0.100	373.4	7825.1	808.0	0.0	-6.5	-147.0	1175.0	7678.1
0.176	373.8	7418.0	808.0	0.0	-6.5	-147.0	1175.4	7271.0
0.200	469.9	9911.4	808.0	0.0	-8.2	-194.4	1269.7	9717.0
0.300	470.4	9543.4	808.0	0.0	-8.2	-194.4	1270.1	9349.0
0.400	470.6	9322.6	808.0	0.0	-8.2	-194.4	1270.4	9128.2
0.500	470.7	9248.9	808.0	0.0	-8.2	-194.4	1270.5	9054.6

Strains and curvatures at t = 124 days

x/L	$\Delta\varepsilon_o(t)$	$\Delta\psi(t)$
	in/inx10^6	1/inx10^6
0.000	-264.5	0.0
0.100	-370.0	-4.2
0.176	-370.2	-4.0
0.200	-394.9	-5.2
0.300	-395.2	-5.0
0.400	-395.4	-4.9
0.500	-395.5	-4.8

Strain inc. at the strand level (mid) =	-509.7	in/inx10^6
Time-dependent inc. losses =	-14.525	ksi
Stress of prestress strand =	175.868	ksi
% losses =	13.15	%

Strains and curvatures - Summary for simple span case at x/L = 0.500

Strain, $\varepsilon_o(t)$ using ACI, CEB-FIP, and B3 respectively

Day								
3	3.01	4	7	28	124	365	10950	36500
-174.0	-175.5	-201.3	-241.3	-381.0	-569.5	-664.1	-748.5	-752.9
-171.7	-216.4	-262.7	-303.6	-405.3	-544.5	-662.1	-933.3	-955.0
-174.0	-174.0	-236.5	-269.4	-373.8	-639.2	-763.7	-850.9	-885.8

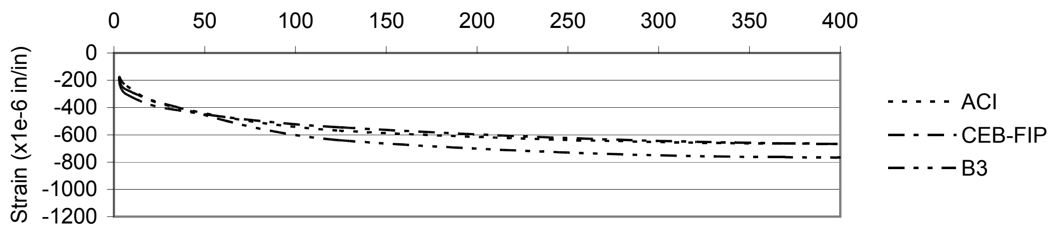

Curvature, $\psi(t)$ using ACI, CEB-FIP, and B3 respectively

Day								
3	3.01	4	7	28	124	365	10950	36500
-6.6	-6.7	-7.4	-8.2	-9.9	-11.5	-12.4	-13.7	-13.8
-6.6	-7.0	-8.2	-9.0	-10.7	-12.7	-14.2	-16.0	-16.1
-6.6	-6.6	-8.9	-9.7	-10.9	-11.7	-12.5	-15.6	-16.8

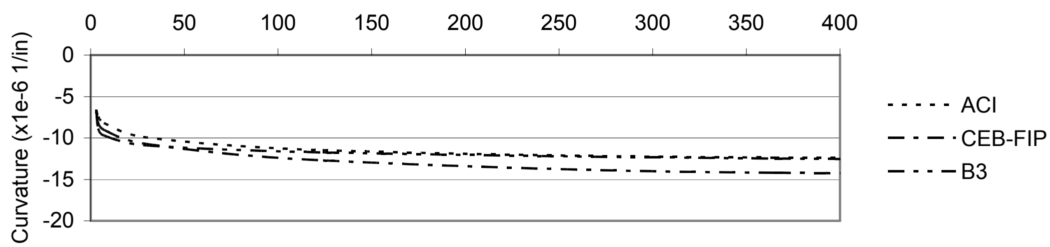

Stress of prestress strand using ACI, CEB-FIP, and B3 respectively

Day								
3	3.01	4	7	28	124	365	10950	36500
190.4	190.3	189.1	187.4	182.3	175.9	172.6	169.3	169.1
190.5	189.0	186.8	185.1	181.1	175.7	171.4	162.4	161.8
190.4	190.4	187.1	185.6	181.9	173.7	169.7	165.1	163.2

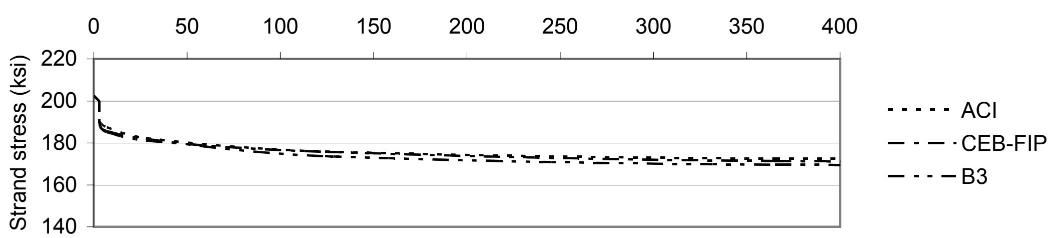

% prestress losses using ACI, CEB-FIP, and B3 respectively

Day								
3	3.01	4	7	28	124	365	10950	36500
6.0	6.0	6.6	7.4	10.0	13.2	14.8	16.4	16.5
5.9	6.7	7.7	8.6	10.6	13.2	15.4	19.8	20.1
6.0	6.0	7.6	8.3	10.2	14.2	16.2	18.5	19.4

Effect of concrete deck placed at t = 124 days

Section Properties at t = 124 days when deck is not hardened yet (midspan):

	Properties of area			Properties of transformed area		
	A	B	I	A^*E/E_{ref}	B^*E/E_{ref}	I^*E/E_{ref}
Girder	1013	0	521162.6	1013	0	521162.6
Strand	4.284	101.4	2399.6	23.9	566.8	13414.1
				1036.9	566.8	534576.7

Applied forces due to concrete deck placement:

x/L	A	B	I	ΔN (kips)	ΔM (kips-in)
0.000	1013.0	0.0	521162.6	0.0	0.0
0.100	1031.8	428.6	530924.5	0.0	1213.1
0.176	1031.8	428.6	530924.5	0.0	1953.3
0.200	1036.9	566.8	534576.7	0.0	2156.7
0.300	1036.9	566.8	534576.7	0.0	2830.6
0.400	1036.9	566.8	534576.7	0.0	3235.0
0.500	1036.9	566.8	534576.7	0.0	3369.8

Strains and curvatures at deck placement:

x/L	$\Delta\varepsilon_o$ in/inx10^6	$\Delta\psi$ 1/inx10^6
0.000	0.0	0.0
0.100	-0.2	0.4
0.176	-0.3	0.7
0.200	-0.4	0.8
0.300	-0.6	1.0
0.400	-0.6	1.2
0.500	-0.7	1.2

Strain at the strand level (midspan) =	28.6	in/inx10^6
Elastic stress gain =	0.815	ksi
Stress of prestress strand =	176.683	ksi
% losses =	12.75	%

Creep coefficients of girder, Φ(t, 124):

Model	Day							
	124.01	125	127	131	152	365	10950	36500
ACI	0.006	0.087	0.155	0.232	0.406	0.696	0.920	0.938
CEB-FIP	0.033	0.131	0.181	0.233	0.350	0.613	0.883	0.894
B3	0.000	0.148	0.198	0.243	0.331	0.505	0.806	0.925

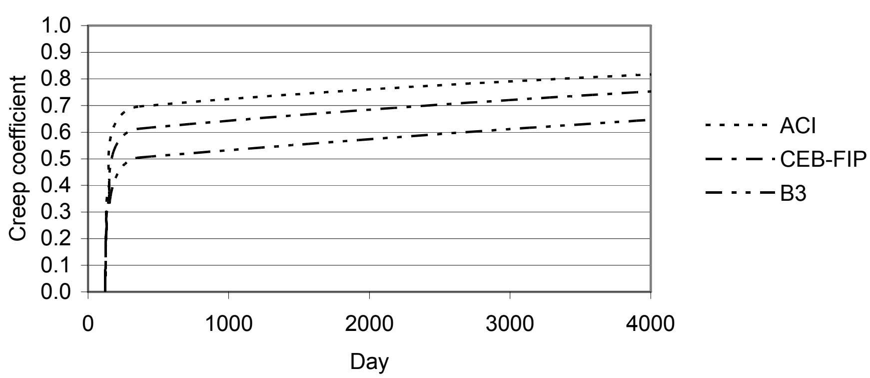

Aging coefficients of girder, χ(t, 124):

Model	Day							
	124.01	125	127	131	152	365	10950	36500
ACI	0.545	0.725	0.767	0.800	0.854	0.914	0.921	0.915
CEB-FIP	0.812	0.860	0.899	0.909	0.909	0.883	0.820	0.817
B3	0.548	0.737	0.781	0.816	0.873	0.935	0.932	0.923

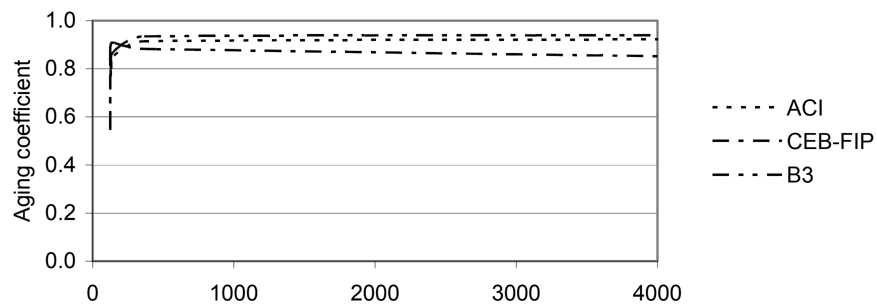

Creep coefficients of concrete deck slab, Φ(t, 3):

Model	Day							
	3.01	4	6	10	31	244	10829	36379
ACI	0.008	0.115	0.205	0.308	0.538	0.923	1.220	1.243
CEB-FIP	0.092	0.367	0.510	0.656	0.989	1.779	2.809	2.860
B3	0.000	0.360	0.470	0.563	0.731	1.043	1.703	1.950

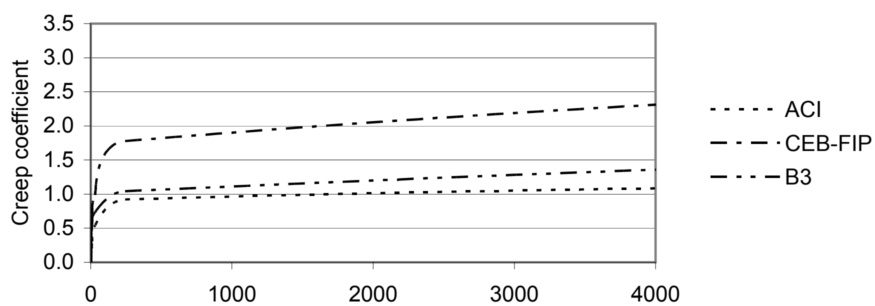

Aging coefficients of concrete deck slab, χ(t, 3):

Model	Day							
	3.01	4	6	10	31	244	10829	36379
ACI	0.695	0.630	0.615	0.603	0.583	0.558	0.530	0.522
CEB-FIP	0.809	0.794	0.809	0.781	0.699	0.574	0.644	0.650
B3	0.731	0.701	0.694	0.688	0.679	0.662	0.612	0.595

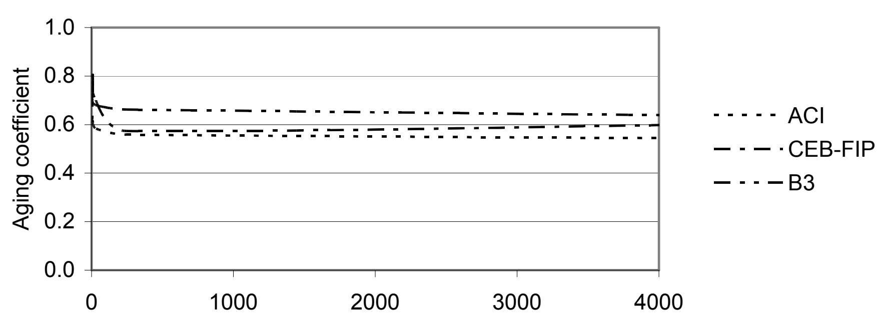

Shrinkage of concrete deck slab, $\varepsilon_{sh}(t)$:

Model	Day							
	3.01	4	6	10	31	244	10829	36379
ACI	0.000000	0.000004	0.000012	0.000025	0.000075	0.000181	0.000221	0.000222
CEB-FIP	0.000016	0.000024	0.000031	0.000042	0.000070	0.000153	0.000502	0.000584
B3	0.000000	0.000001	0.000004	0.000009	0.000037	0.000273	0.000432	0.000432

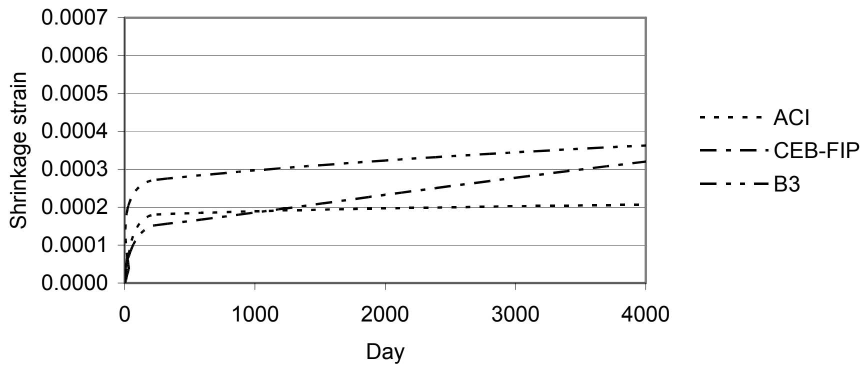

Time-dependent effect at t = 36500 days:

Girder:			*Slab:*		
$\Delta\Phi(36500,3)$ =	0.474		$\Phi(36379,3)$ =	1.243	
$\Delta\varepsilon sh(36500)$ =	0.00012		$\chi(36379,3)$ =	0.522	
$\Phi(36500,124)$ =	0.938		Ec(36379,3) =	1985.0	ksi
$\chi(36500,124)$ =	0.915		$\varepsilon sh(36379)$ =	0.000222	
Ec(36500,124) =	2742.7	ksi			
Strand:					
λ =	0.705		Ω =	0.071	
χ_r =	0.810				

Stresses and curvatures prior to composite action

x/L	Restrained		Time-dependence		Change in stresses			
	σ_{top}	σ_{bot}	σ_{top}	σ_{bot}	$\Delta\sigma_{top}$	$\Delta\sigma_{bot}$	$\Delta\sigma$	$\Delta\psi$
0.000	0.798	0.798	-0.798	-0.798	0.000	0.000	0.000	0.000
0.100	0.700	1.646	-0.719	-1.524	-0.019	0.122	0.051	0.002
0.176	0.725	1.621	-0.744	-1.501	-0.019	0.121	0.050	0.002
0.200	0.671	1.869	-0.701	-1.695	-0.030	0.174	0.071	0.003
0.300	0.694	1.847	-0.723	-1.674	-0.030	0.173	0.070	0.003
0.400	0.707	1.834	-0.737	-1.662	-0.030	0.172	0.070	0.003
0.500	0.711	1.829	-0.741	-1.658	-0.030	0.172	0.070	0.003

Section Properties at t = 36500 days when composite action starts (midspan):

	Properties of area			Properties of transformed area		
	A	B	I	A^*E/E_{ref}	B^*E/E_{ref}	I^*E/E_{ref}
Girder	1013	0	521162.6	1013	0	521162.6
Strand	4.284	101.4	2399.6	44.5	1053.5	24934.4
Deck	984	-36052	1326982	712	-26092	960359
Rebars	9.41	-331.2	11655.9	99.5	-3502.1	123242.5
				1869	-28540	1629698

Note *: neglected the duration of 3-day concrete deck hardening*

Time-dependent restrained forces at t = 36500 days (ΔN and ΔM):

x/L	Creep		Shrinkage		Relaxation		Total	
	ΔN	ΔM	ΔN	ΔM	ΔN	ΔM	ΔN	ΔM
0.000	0.0	0.0	766.3	-15898.7	0.0	0.0	766.3	-15898.7
0.100	167.7	2876.4	766.3	-15898.7	-9.7	-220.0	924.3	-13242.3
0.176	168.3	2314.9	766.3	-15898.7	-9.7	-220.0	924.9	-13803.7
0.200	209.5	3282.4	766.3	-15898.7	-12.3	-290.9	963.5	-12907.2
0.300	210.3	2775.7	766.3	-15898.7	-12.3	-290.9	964.3	-13413.9
0.400	210.7	2471.6	766.3	-15898.7	-12.3	-290.9	964.7	-13718.0
0.500	210.9	2370.3	766.3	-15898.7	-12.3	-290.9	964.9	-13819.3

Strains and curvatures at t = 36500 days

x/L	$\Delta\varepsilon_o(t)$	$\Delta\psi(t)$
	in/inx10^6	1/inx10^6
0.000	-134.9	1.1
0.100	-186.4	-0.3
0.176	-183.8	-0.2
0.200	-196.4	-0.6
0.300	-194.2	-0.4
0.400	-192.9	-0.3
0.500	-192.5	-0.3

Strain inc. at the strand level (mid) =	-199.1	in/inx10^6
Time-dependent inc. losses =	-5.674	ksi
Stress of prestress strand =	171.010	ksi
% losses =	15.55	%

Time-dependent strain at top fiber along the length of the girder:

x/L	Day							
	124.01	125	127	131	152	365	10950	36500
0.000	0.0	-2.9	-8.3	-18.1	-54.6	-142.3	-180.0	-180.9
0.100	-0.1	-3.3	-9.1	-19.3	-56.1	-140.6	-172.4	-172.8
0.176	-0.1	-3.6	-9.6	-20.1	-57.6	-143.5	-176.7	-177.3
0.200	-0.1	-3.7	-9.8	-20.2	-57.7	-142.3	-173.4	-173.8
0.300	-0.1	-4.0	-10.3	-21.0	-59.0	-144.8	-177.3	-177.8
0.400	-0.1	-4.2	-10.5	-21.4	-59.8	-146.4	-179.7	-180.3
0.500	-0.1	-4.2	-10.6	-21.5	-60.0	-146.9	-180.5	-181.1

Time-dependent strain at bottom fiber along the length of the girder:

x/L	Day							
	124.01	125	127	131	152	365	10950	36500
0.000	0.0	0.6	1.6	3.3	7.2	-45.3	-97.4	-98.9
0.100	0.1	1.2	2.4	4.1	5.6	-82.2	-190.9	-197.0
0.176	0.1	1.7	3.4	5.5	8.1	-77.1	-183.2	-189.0
0.200	0.1	1.8	3.4	5.4	7.1	-87.1	-207.1	-214.0
0.300	0.1	2.2	4.2	6.6	9.3	-82.7	-200.3	-207.0
0.400	0.2	2.5	4.7	7.3	10.6	-80.0	-196.2	-202.8
0.500	0.2	2.6	4.9	7.6	11.0	-79.1	-194.9	-201.4

Strains and curvatures - Summary for simple span case at x/L = 0.500

Strain, $\varepsilon_o(t)$ using ACI, CEB-FIP, and B3 respectively

Day

124	124.01	125	127	131	152	365	10950	36500
0.0	0.0	-0.4	-1.9	-5.2	-20.1	-108.9	-188.6	-192.5
0.0	-2.7	-3.8	-5.6	-8.8	-21.9	-126.5	-409.1	-439.1
0.0	0.0	0.4	-0.6	-2.9	-16.3	-148.6	-262.3	-297.2

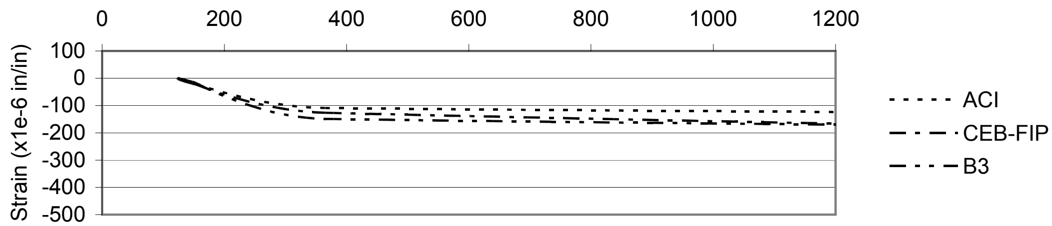

Curvature, $\psi(t)$ using ACI, CEB-FIP, and B3 respectively

Day

124	124.01	125	127	131	152	365	10950	36500
0.0	0.0	0.1	0.2	0.4	1.0	0.9	-0.2	-0.3
0.0	0.2	0.4	0.4	0.6	0.7	-0.2	-0.9	-0.3
0.0	0.0	0.1	0.1	0.2	0.4	1.5	0.7	-0.3

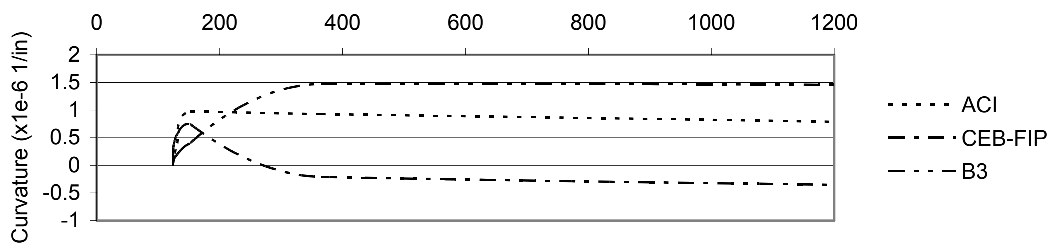

Stress of prestress strand using ACI, CEB-FIP, and B3 respectively

Day

124	124.01	125	127	131	152	365	10950	36500
176.7	176.7	176.7	176.8	176.8	176.8	174.2	171.2	171.0
176.5	176.5	176.6	176.6	176.6	176.3	172.7	164.2	163.7
174.5	174.5	174.6	174.6	174.6	174.3	171.3	167.5	165.8

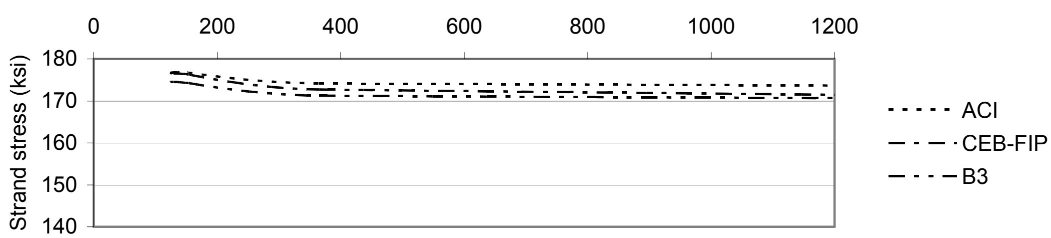

% prestress losses using ACI, CEB-FIP, and B3 respectively

Day

124	124.01	125	127	131	152	365	10950	36500
12.7	12.7	12.7	12.7	12.7	12.7	14.0	15.5	15.5
12.9	12.8	12.8	12.8	12.8	12.9	14.7	18.9	19.1
13.8	13.8	13.8	13.8	13.8	13.9	15.4	17.3	18.1

End of Calculation

Three samples of time-dependent strains with respect to the time-line (127, 365, and 36,500 days) at the top fiber of interior girders are shown in Figure B-3.

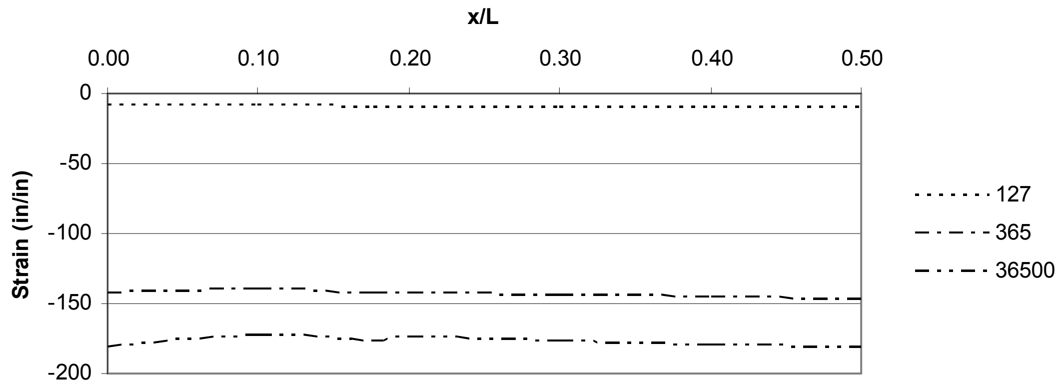

Figure B-3: Time-Dependent Strains at Top Fiber (Bridge 203 – Span 1 – Ext. Girder)

Three samples of time-dependent strains with respect to the time-line (127, 365, and 36,500 days) at the bottom fiber of interior girders are shown in Figure B-4.

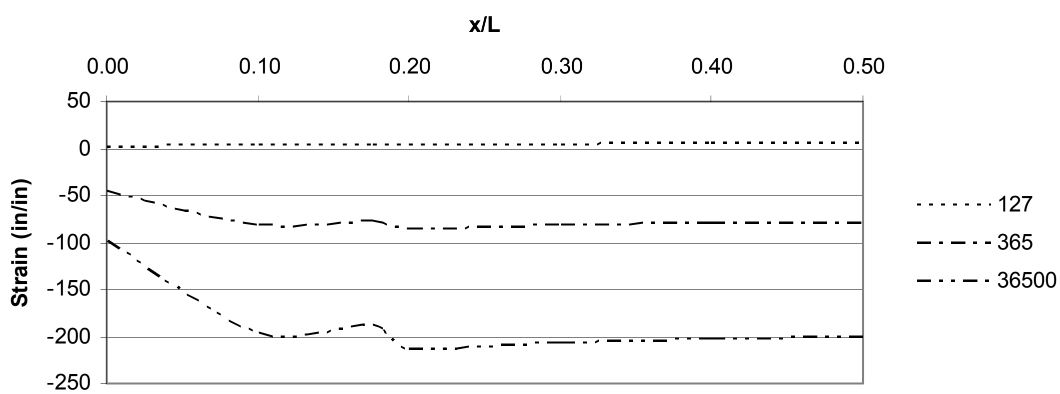

Figure B-4: Type Caption Here

B.1.2 Span 2

Interior Girder

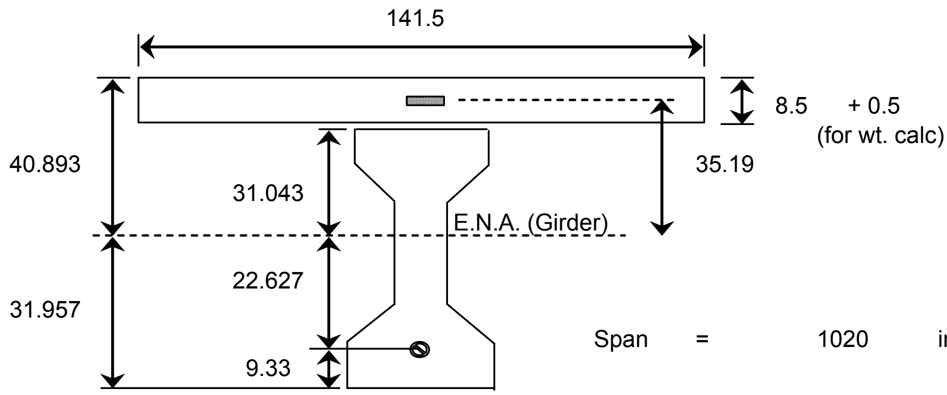

Span = 1020 in

Concrete properties:

Girder:

A	=	1013	in^2
I	=	521162.6	in^4
$E_c(3)$	=	4628.4	ksi
$E_c(28)$	=	5098.2	ksi

Slab:

$E_c(3)$	=	3272.8	ksi
$E_c(28)$	=	3605.0	ksi

Prestress strand properties:

A	=	0.153	in^2
No.	=	48	
Jacking	=	30.982	k/strand
E_{ps}	=	28500	ksi
$A_{s\text{-}slab}$	=	9.412	in^2
E_s	=	29000	ksi

Section Properties at t = 3 days (midspan):

	Properties of area			Properties of transformed area		
	A	B	I	$A*E/E_{ref}$	$B*E/E_{ref}$	$I*E/E_{ref}$
Girder	1013	0	521162.6	1013	0	521162.6
Strand	7.344	166.2	3760.0	45.2	1023.2	23152.7
				1058.2	1023.2	544315.3

Relaxation loss from t = 0 to 3 days:

Δf_{RE}	=	-2.664	ksi
f_{pi}	=	199.833	ksi

Applied forces at transfer:

x/L	e (in)	No. of strands	A	B	I	N (kips)	M (kips-in)
0.000	0.000	0	1013.0	0.0	521162.6	0.0	0.0
0.094	21.517	36	1046.9	729.8	536865.2	-1100.7	-19783.3
0.141	22.387	42	1052.6	885.8	540993.7	-1284.1	-23201.5
0.200	22.627	48	1058.2	1023.2	544315.3	-1467.6	-25887.8
0.300	22.627	48	1058.2	1023.2	544315.3	-1467.6	-23600.7
0.400	22.627	48	1058.2	1023.2	544315.3	-1467.6	-22228.4
0.500	22.627	48	1058.2	1023.2	544315.3	-1467.6	-21770.9

Strains and curvatures at transfer:

x/L	ε_o in/inx10^6	ψ 1/inx10^6
0.000	0.0	0.0
0.094	-221.8	-7.7
0.141	-256.1	-8.8
0.200	-290.2	-9.7
0.300	-291.1	-8.8
0.400	-291.6	-8.3
0.500	-291.8	-8.1

Strain at the strand level (midspan) =	-474.9	in/inx10^6
Elastic shortening loss =	-13.536	ksi
Stress of prestress strand =	186.297	ksi
% initial loss =	8.00	%

Creep coefficients, Φ(t, 3):

Model	Day							
	3.01	4	7	28	136	365	10950	36500
AASHTO	0.003	0.050	0.107	0.284	0.666	0.959	1.425	1.460
ACI	0.009	0.126	0.259	0.565	0.904	1.072	1.334	1.359
CEB-FIP	0.070	0.280	0.423	0.725	1.136	1.405	1.820	1.839
B3	0.000	0.362	0.505	0.728	0.976	1.131	1.722	1.967

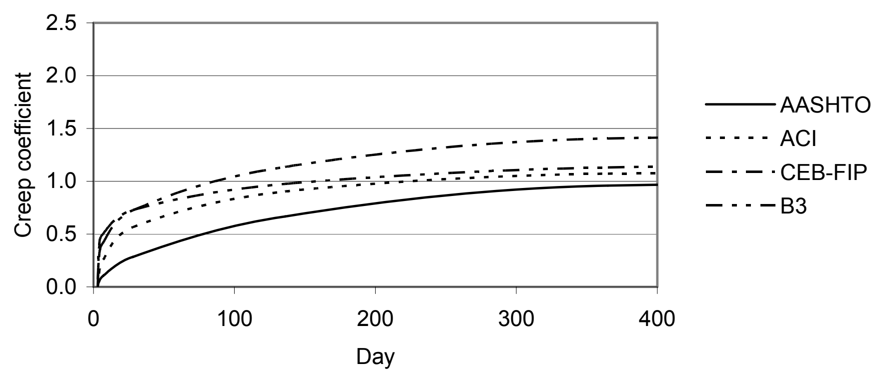

Shrinkage, $\varepsilon_{sh}(t)$:

Model	Day							
	3.01	4	7	28	136	365	10950	36500
AASHTO	0.000007	0.000010	0.000017	0.000062	0.000191	0.000283	0.000388	0.000391
ACI	0.000000	0.000007	0.000026	0.000120	0.000272	0.000334	0.000383	0.000384
CEB-FIP	0.000034	0.000047	0.000066	0.000123	0.000213	0.000283	0.000503	0.000523
B3	0.000000	0.000004	0.000014	0.000087	0.000343	0.000430	0.000432	0.000432

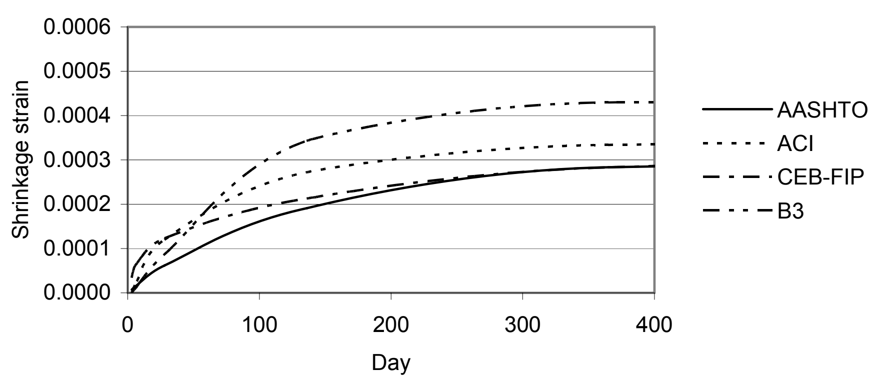

Aging coefficients, χ(t, 3):

Model	Day							
	3.01	4	7	28	136	365	10950	36500
AASHTO	N/A	N/A	N/A	N/A	N/A	N/A	N/A	N/A
ACI	0.710	0.658	0.642	0.621	0.603	0.594	0.567	0.558
CEB-FIP	0.808	0.777	0.769	0.648	0.562	0.535	0.477	0.474
B3	0.731	0.702	0.693	0.682	0.670	0.660	0.614	0.597

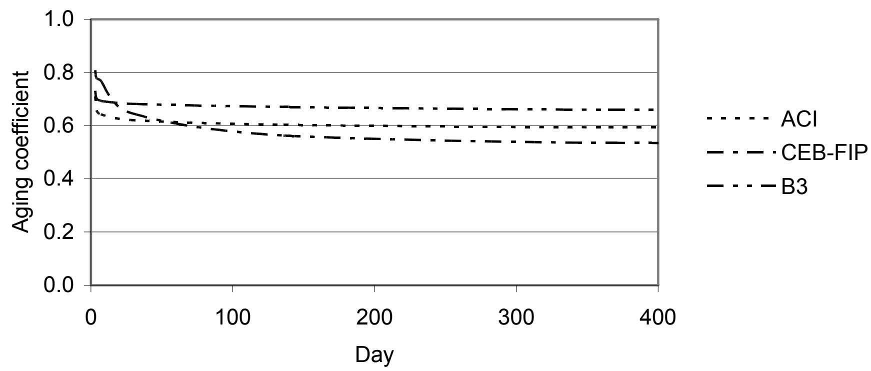

Use engineering recommendation model: **ACI**

Time-dependent restrained forces at t = 136 days (ΔN and ΔM):

Φ(136,3) =	0.904		χ(136,3) =	0.603	
Ec(136,3) =	2996.3	ksi	*(Age-adjusted elastic modulus)*		
εsh(136) =	0.000272		λ =	0.690	
Ω =	0.080		χ_r =	0.783	
A (mid) =	1082.9	in^2	B (mid) =	1580.6	in^3
I (mid) =	556927	in^4			

x/L	Creep		Shrinkage		Relaxation		Total	
	ΔN	ΔM	ΔN	ΔM	ΔN	ΔM	ΔN	ΔM
0.000	0.0	0.0	826.0	0.0	0.0	0.0	826.0	0.0
0.094	608.3	10808.2	826.0	0.0	-10.2	-220.5	1424.1	10587.7
0.141	702.5	12482.3	826.0	0.0	-12.0	-267.6	1516.6	12214.7
0.200	796.0	13729.0	826.0	0.0	-13.7	-309.2	1608.3	13419.9
0.300	798.4	12445.7	826.0	0.0	-13.7	-309.2	1610.7	12136.6
0.400	799.8	11675.8	826.0	0.0	-13.7	-309.2	1612.2	11366.6
0.500	800.3	11419.1	826.0	0.0	-13.7	-309.2	1612.7	11110.0

Strains and curvatures at t = 136 days

x/L	$\Delta\varepsilon_o(t)$	$\Delta\psi(t)$
	in/inx10^6	1/inx10^6
0.000	-272.1	0.0
0.094	-440.2	-5.6
0.141	-463.3	-6.2
0.200	-486.0	-6.7
0.300	-487.9	-5.9
0.400	-489.0	-5.4
0.500	-489.4	-5.3

Strain inc. at the strand level (mid) =	-608.6	in/inx10^6
Time-dependent inc. losses =	-17.344	ksi
Stress of prestress strand =	168.953	ksi
% losses =	16.57	%

Strains and curvatures - Summary for simple span case at x/L = 0.500

Strain, $\varepsilon_o(t)$ using ACI, CEB-FIP, and B3 respectively

Day								
3	3.01	4	7	28	136	365	10950	36500
-291.8	-294.2	-332.2	-385.5	-553.7	-781.2	-879.7	-986.0	-992.4
-288.0	-339.6	-406.9	-461.6	-591.2	-777.0	-907.9	-1211.0	-1233.4
-291.8	-291.8	-391.8	-438.7	-562.9	-863.5	-981.3	-1119.9	-1175.8

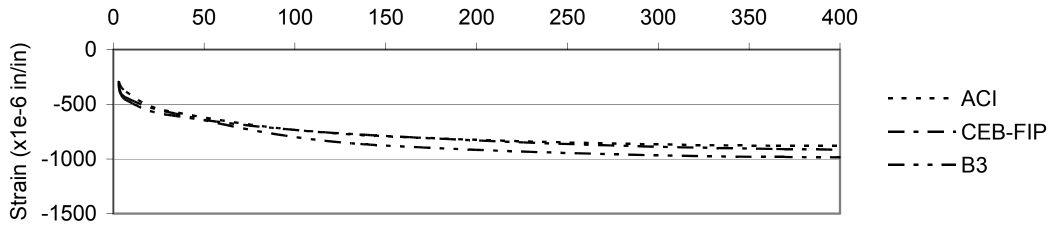

Curvature, $\psi(t)$ using ACI, CEB-FIP, and B3 respectively

Day								
3	3.01	4	7	28	136	365	10950	36500
-8.1	-8.2	-9.0	-9.8	-11.6	-13.4	-14.2	-15.5	-15.6
-8.0	-8.4	-9.8	-10.7	-12.5	-14.8	-16.2	-18.0	-18.0
-8.1	-8.1	-10.6	-11.5	-12.8	-13.5	-14.2	-17.3	-18.6

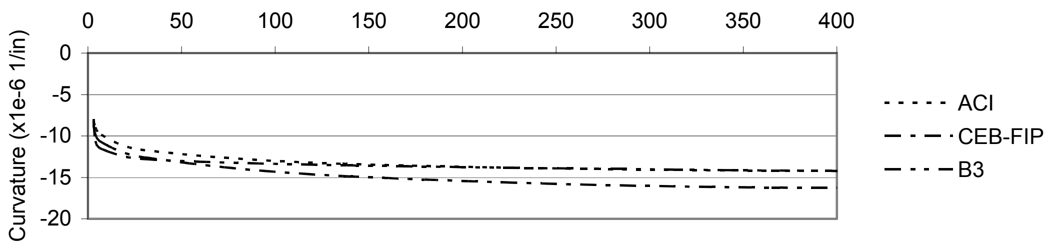

Stress of prestress strand using ACI, CEB-FIP, and B3 respectively

Day								
3	3.01	4	7	28	136	365	10950	36500
186.3	186.2	184.6	182.5	176.5	169.0	165.6	161.8	161.5
186.5	184.7	181.9	179.8	174.9	168.1	163.5	153.7	153.1
186.3	186.3	181.8	179.9	175.6	166.5	162.7	156.7	154.3

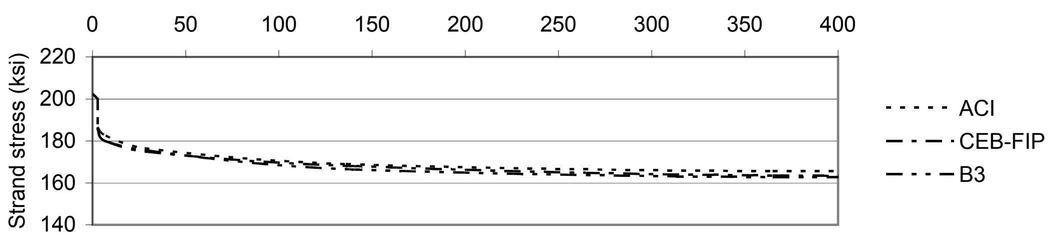

% prestress losses using ACI, CEB-FIP, and B3 respectively

Day								
3	3.01	4	7	28	136	365	10950	36500
8.0	8.1	8.8	9.9	12.8	16.6	18.2	20.1	20.2
7.9	8.8	10.2	11.2	13.6	17.0	19.3	24.1	24.4
8.0	8.0	10.2	11.2	13.3	17.8	19.6	22.6	23.8

Effect of concrete deck placed at t = 136 days

Section Properties at t = 136 days when deck is not hardened yet (midspan):

	Properties of area			Properties of transformed area		
	A	B	I	$A*E/E_{ref}$	$B*E/E_{ref}$	$I*E/E_{ref}$
Girder	1013	0	521162.6	1013	0	521162.6
Strand	7.344	166.2	3760.0	41.1	928.9	21019.0
				1054.1	928.9	542181.6

Applied forces due to concrete deck placement:

x/L	A	B	I	ΔN (kips)	ΔM (kips-in)
0.000	1013.0	0.0	521162.6	0.0	0.0
0.094	1043.8	662.5	535418.1	0.0	4903.0
0.141	1048.9	804.2	539166.1	0.0	6972.4
0.200	1054.1	928.9	542181.6	0.0	9201.0
0.300	1054.1	928.9	542181.6	0.0	12076.4
0.400	1054.1	928.9	542181.6	0.0	13801.6
0.500	1054.1	928.9	542181.6	0.0	14376.6

Strains and curvatures at deck placement:

x/L	$\Delta\varepsilon_o$ in/inx10^6	$\Delta\psi$ 1/inx10^6
0.000	0.0	0.0
0.094	-1.1	1.8
0.141	-1.9	2.5
0.200	-2.9	3.3
0.300	-3.9	4.4
0.400	-4.4	5.0
0.500	-4.6	5.2

Strain at the strand level (midspan) =	113.3	in/inx10^6
Elastic stress gain =	3.228	ksi
Stress of prestress strand =	172.181	ksi
% losses =	14.97	%

Creep coefficients of girder, Φ(t, 136):

Model	Day							
	136.01	137	139	143	164	365	10950	36500
ACI	0.006	0.086	0.153	0.230	0.402	0.684	0.912	0.930
CEB-FIP	0.032	0.128	0.178	0.229	0.344	0.596	0.868	0.878
B3	0.000	0.143	0.192	0.235	0.321	0.485	0.780	0.895

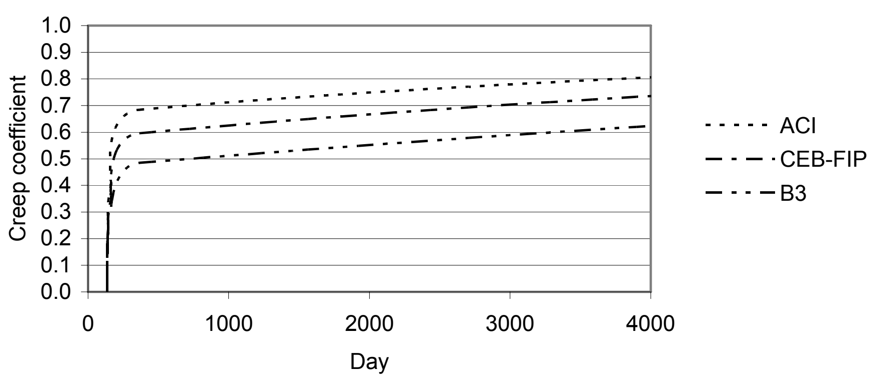

Aging coefficients of girder, χ(t, 136):

Model	Day							
	136.01	137	139	143	164	365	10950	36500
ACI	0.543	0.724	0.767	0.800	0.855	0.915	0.923	0.918
CEB-FIP	0.812	0.860	0.899	0.909	0.909	0.888	0.823	0.821
B3	0.546	0.736	0.781	0.816	0.873	0.935	0.934	0.924

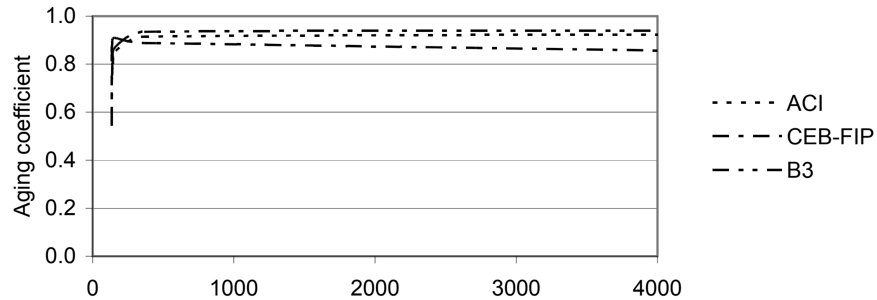

Creep coefficients of concrete deck slab, Φ(t, 3):

Model	Day							
	3.01	4	6	10	31	232	10817	36367
ACI	0.008	0.115	0.205	0.308	0.538	0.915	1.220	1.243
CEB-FIP	0.092	0.367	0.510	0.656	0.989	1.757	2.809	2.860
B3	0.000	0.360	0.470	0.563	0.731	1.035	1.703	1.949

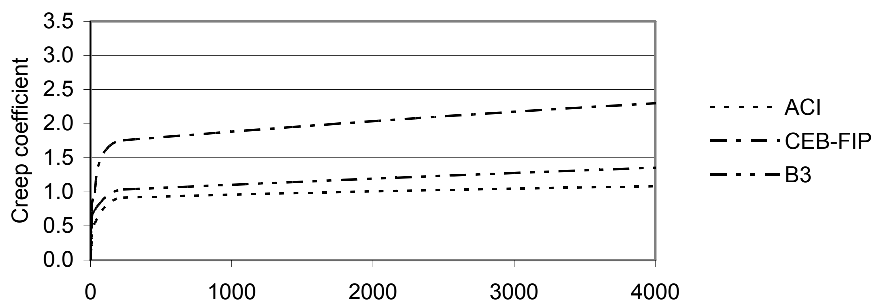

Aging coefficients of concrete deck slab, χ(t, 3):

Model	Day							
	3.01	4	6	10	31	232	10817	36367
ACI	0.695	0.630	0.615	0.603	0.583	0.559	0.530	0.522
CEB-FIP	0.809	0.794	0.809	0.781	0.699	0.577	0.644	0.650
B3	0.731	0.701	0.694	0.688	0.679	0.663	0.612	0.595

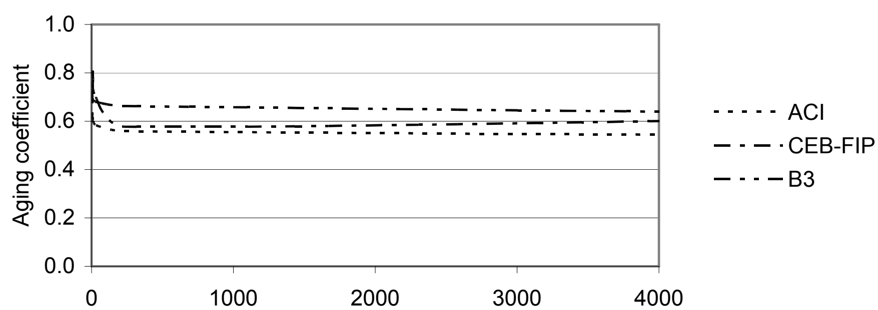

Shrinkage of concrete deck slab, $\varepsilon_{sh}(t)$:

Model	Day							
	3.01	4	6	10	31	232	10817	36367
ACI	0.000000	0.000004	0.000012	0.000025	0.000075	0.000179	0.000221	0.000222
CEB-FIP	0.000016	0.000024	0.000031	0.000042	0.000070	0.000150	0.000502	0.000584
B3	0.000000	0.000001	0.000004	0.000009	0.000037	0.000263	0.000432	0.000432

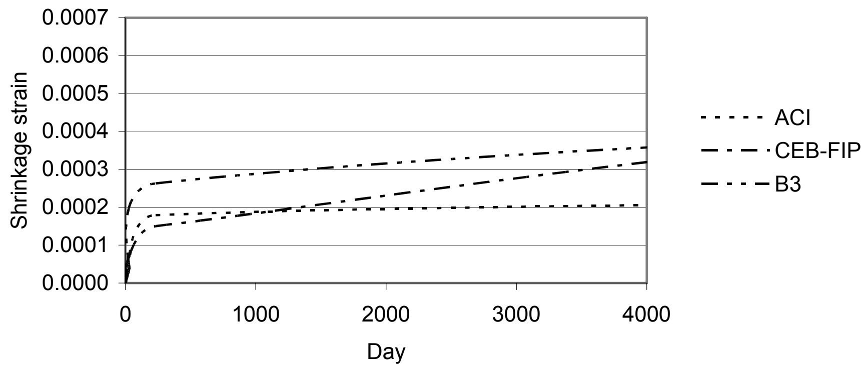

Time-dependent effect at t = 36500 days:

Girder:

$\Delta\Phi(36500,3)$ =	0.456	
$\Delta\varepsilon sh(36500)$ =	0.000112	
$\Phi(36500,136)$ =	0.930	
$\chi(36500,136)$ =	0.918	
Ec(36500,136) =	2750.1	ksi

Slab:

$\Phi(36367,3)$ =	1.243	
$\chi(36367,3)$ =	0.522	
Ec(36367,3) =	1985.0	ksi
$\varepsilon sh(36367)$ =	0.000222	

Strand:

λ = 0.690 Ω = 0.070

χ_r = 0.808

Stresses and curvatures prior to composite action

x/L	Restrained		Time-dependence		Change in stresses			
	σ_{top}	σ_{bot}	σ_{top}	σ_{bot}	$\Delta\sigma_{top}$	$\Delta\sigma_{bot}$	$\Delta\sigma$	$\Delta\psi$
0.000	0.815	0.815	-0.815	-0.815	0.000	0.000	0.000	0.000
0.094	0.772	2.079	-0.801	-1.852	-0.029	0.226	0.097	0.004
0.141	0.765	2.274	-0.808	-1.986	-0.042	0.289	0.121	0.005
0.200	0.783	2.443	-0.836	-2.094	-0.053	0.349	0.145	0.006
0.300	0.862	2.367	-0.914	-2.026	-0.052	0.341	0.142	0.006
0.400	0.910	2.321	-0.961	-1.984	-0.051	0.336	0.140	0.006
0.500	0.925	2.306	-0.976	-1.971	-0.051	0.335	0.139	0.006

Section Properties at t = 36500 days when composite action starts (midspan):

	Properties of area			Properties of transformed area		
	A	B	I	$A*E/E_{ref}$	$B*E/E_{ref}$	$I*E/E_{ref}$
Girder	1013	0	521162.6	1013	0	521162.6
Strand	7.344	166.2	3760.0	76.1	1722.1	38965.5
Deck	1203	-44072	1622185	868	-31810	1170846
Rebars	9.41	-331.2	11655.9	99.2	-3492.7	122911.2
				2056	-33581	1853885

Note *: neglected the duration of 3-day concrete deck hardening*

Time-dependent restrained forces at t = 36500 days (ΔN and ΔM):

x/L	Creep		Shrinkage		Relaxation		Total	
	ΔN	ΔM	ΔN	ΔM	ΔN	ΔM	ΔN	ΔM
0.000	0.0	0.0	842.3	-19435.5	0.0	0.0	842.3	-19435.5
0.094	257.9	2033.7	842.3	-19435.5	-15.5	-333.4	1084.7	-17735.3
0.141	297.0	1649.6	842.3	-19435.5	-18.1	-404.7	1121.2	-18190.7
0.200	336.2	1009.3	842.3	-19435.5	-20.7	-467.5	1157.8	-18893.7
0.300	340.6	-953.2	842.3	-19435.5	-20.7	-467.5	1162.2	-20856.2
0.400	343.2	-2130.7	842.3	-19435.5	-20.7	-467.5	1164.9	-22033.8
0.500	344.1	-2523.3	842.3	-19435.5	-20.7	-467.5	1165.7	-22426.3

Strains and curvatures at t = 36500 days

x/L	$\Delta\varepsilon_o(t)$	$\Delta\psi(t)$
	in/inx10^6	1/inx10^6
0.000	-130.5	1.4
0.094	-195.5	-0.1
0.141	-200.7	-0.1
0.200	-204.8	0.0
0.300	-197.0	0.5
0.400	-192.3	0.8
0.500	-190.7	0.9

Strain inc. at the strand level (mid) =	-169.3	in/inx10^6
Time-dependent inc. losses =	-4.826	ksi
Stress of prestress strand =	167.355	ksi
% losses =	17.35	%

Time-dependent strain at top fiber along the length of the girder:

x/L	Day							
	136.01	137	139	143	164	365	10950	36500
0.000	0.0	-3.0	-8.8	-19.2	-57.7	-145.7	-185.1	-185.9
0.094	-0.2	-4.8	-11.8	-23.7	-65.0	-153.8	-190.1	-190.8
0.141	-0.2	-5.5	-13.1	-25.5	-68.1	-158.7	-196.1	-196.9
0.200	-0.3	-6.2	-14.5	-27.6	-71.6	-164.4	-203.7	-204.6
0.300	-0.3	-7.3	-16.3	-30.3	-76.3	-173.3	-217.0	-218.3
0.400	-0.4	-7.9	-17.4	-31.9	-79.2	-178.7	-225.1	-226.6
0.500	-0.4	-8.1	-17.7	-32.5	-80.1	-180.5	-227.7	-229.3

Time-dependent strain at bottom fiber along the length of the girder:

x/L	Day							
	136.01	137	139	143	164	365	10950	36500
0.000	0.0	0.6	1.8	3.8	8.9	-34.1	-85.7	-87.2
0.094	0.2	3.5	6.6	10.2	15.9	-65.5	-191.9	-199.2
0.141	0.3	4.7	8.6	13.2	20.4	-63.1	-195.9	-203.7
0.200	0.4	5.9	10.8	16.3	25.4	-59.1	-196.8	-204.9
0.300	0.5	7.7	13.9	21.0	33.7	-43.2	-172.8	-180.2
0.400	0.6	8.8	15.8	23.9	38.8	-33.6	-158.4	-165.5
0.500	0.6	9.1	16.4	24.8	40.4	-30.5	-153.6	-160.5

Strains and curvatures - Summary for simple span case at x/L = 0.500

Strain, $\varepsilon_o(t)$ using ACI, CEB-FIP, and B3 respectively

Day								
136	136.01	137	139	143	164	365	10950	36500
0.0	0.2	1.6	1.5	-0.3	-12.5	-96.3	-186.1	-190.7
0.0	-2.2	-1.5	-2.6	-5.2	-17.8	-125.2	-431.1	-462.4
0.0	0.0	3.7	3.7	2.2	-9.6	-133.1	-284.8	-333.5

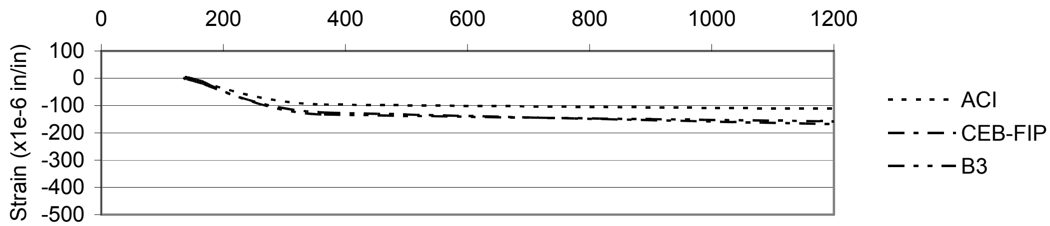

Curvature, ψ(t) using ACI, CEB-FIP, and B3 respectively

Day								
136	136.01	137	139	143	164	365	10950	36500
0.0	0.0	0.2	0.5	0.8	1.7	2.1	1.0	0.9
0.0	0.3	0.6	0.7	0.9	1.3	0.6	0.4	1.0
0.0	0.0	0.3	0.5	0.6	1.0	2.4	1.8	0.6

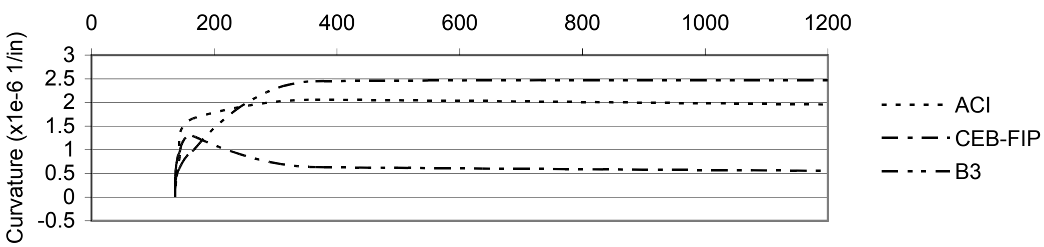

Stress of prestress strand using ACI, CEB-FIP, and B3 respectively

Day								
136	136.01	137	139	143	164	365	10950	36500
172.2	172.2	172.4	172.5	172.7	172.9	170.8	167.5	167.4
171.0	171.1	171.3	171.4	171.5	171.3	167.9	159.0	158.5
169.7	169.7	170.0	170.1	170.2	170.1	167.5	162.7	160.6

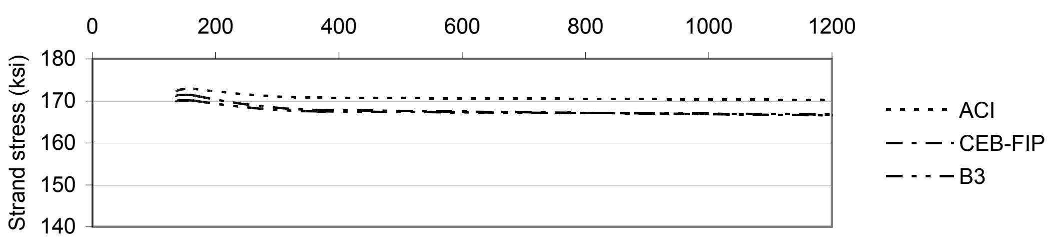

% prestress losses using ACI, CEB-FIP, and B3 respectively

Day								
136	136.01	137	139	143	164	365	10950	36500
15.0	15.0	14.9	14.8	14.7	14.6	15.7	17.3	17.4
15.6	15.5	15.4	15.4	15.3	15.4	17.1	21.5	21.7
16.2	16.2	16.0	16.0	16.0	16.0	17.3	19.6	20.7

End of Calculation

Three samples of time-dependent strains with respect to the time-line (139, 365, and 36,500 days) at the top fiber of interior girders are shown in Figure B-5.

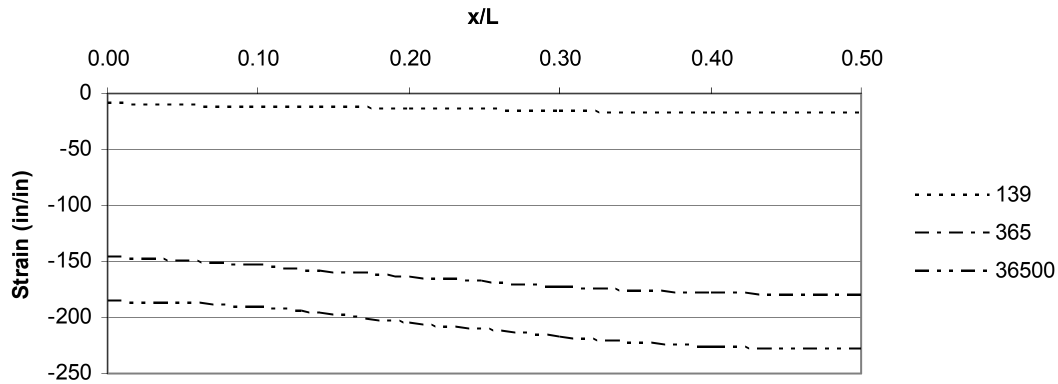

Figure B-5: Time-Dependent Strains at Top Fiber (Bridge 203 – Span 2 – Int. Girder)

Three samples of time-dependent strains with respect to the time-line (139, 365, and 36,500 days) at the bottom fiber of interior girders are shown in Figure B-6.

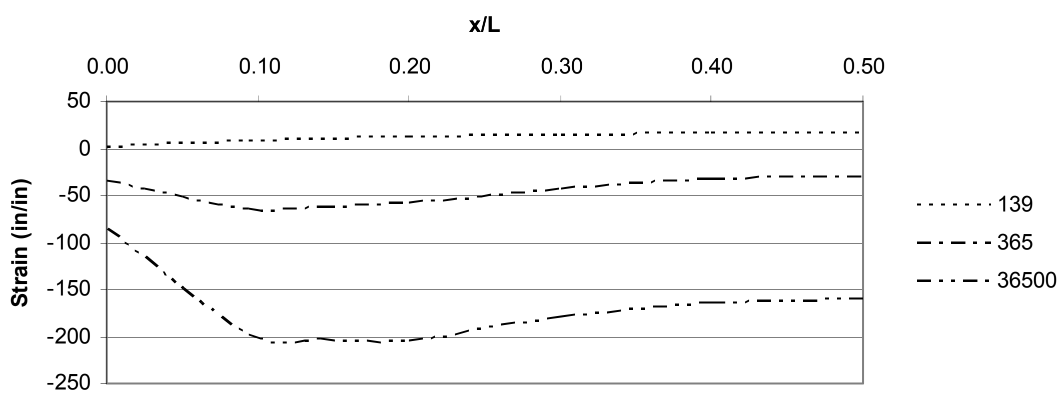

Figure B-6: Time-Dependent Strains at Bottom Fiber (Bridge 203 – Span 2 – Int. Girder)

Exterior Girder

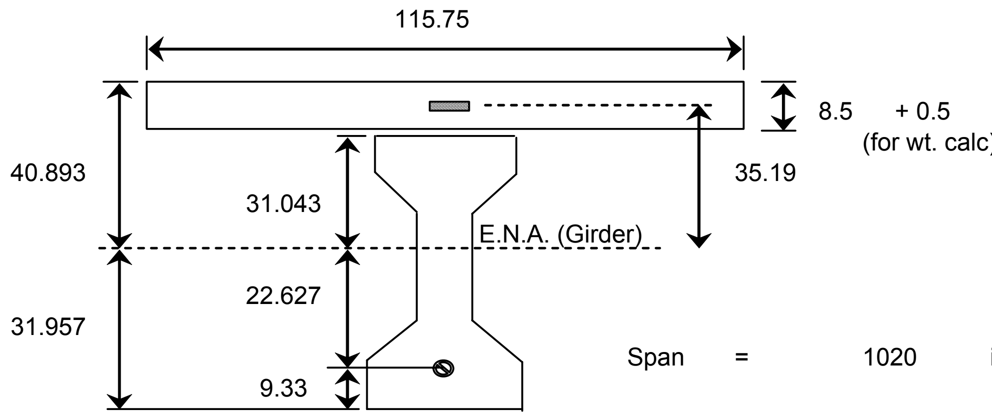

Span = 1020 in

Concrete properties:

Girder:

A	=	1013	in^2
I	=	521162.6	in^4
$E_c(3)$	=	4628.4	ksi
$E_c(28)$	=	5098.2	ksi

Slab:

$E_c(3)$	=	3272.8	ksi
$E_c(28)$	=	3605.0	ksi

Prestress strand properties:

A	=	0.153	in^2
No.	=	48	
Jacking	=	30.982	k/strand
E_{ps}	=	28500	ksi
$A_{s\text{-}slab}$	=	9.412	in^2
E_s	=	29000	ksi

Section Properties at t = 3 days (midspan):

	Properties of area			Properties of transformed area		
	A	B	I	A^*E/E_{ref}	B^*E/E_{ref}	I^*E/E_{ref}
Girder	1013	0	521162.6	1013	0	521162.6
Strand	7.344	166.2	3760.0	45.2	1023.2	23152.7
				1058.2	1023.2	544315.3

Relaxation loss from t = 0 to 3 days:

Δf_{RE}	=	-2.664	ksi
f_{pi}	=	199.833	ksi

Applied forces at transfer:

x/L	e (in)	No. of strands	A	B	I	N (kips)	M (kips-in)
0.000	0.000	0	1013.0	0.0	521162.6	0.0	0.0
0.094	21.517	36	1046.9	729.8	536865.2	-1100.7	-19783.3
0.141	22.387	42	1052.6	885.8	540993.7	-1284.1	-23201.5
0.200	22.627	48	1058.2	1023.2	544315.3	-1467.6	-25887.8
0.300	22.627	48	1058.2	1023.2	544315.3	-1467.6	-23600.7
0.400	22.627	48	1058.2	1023.2	544315.3	-1467.6	-22228.4
0.500	22.627	48	1058.2	1023.2	544315.3	-1467.6	-21770.9

Strains and curvatures at transfer:

x/L	ε_o in/inx10^6	ψ 1/inx10^6
0.000	0.0	0.0
0.094	-221.8	-7.7
0.141	-256.1	-8.8
0.200	-290.2	-9.7
0.300	-291.1	-8.8
0.400	-291.6	-8.3
0.500	-291.8	-8.1

Strain at the strand level (midspan) =	-474.9	in/inx10^6
Elastic shortening loss =	-13.536	ksi
Stress of prestress strand =	186.297	ksi
% initial loss =	8.00	%

Creep coefficients, Φ(t, 3):

Model	Day							
	3.01	4	7	28	136	365	10950	36500
AASHTO	0.003	0.050	0.107	0.284	0.666	0.959	1.425	1.460
ACI	0.009	0.126	0.259	0.565	0.904	1.072	1.334	1.359
CEB-FIP	0.070	0.280	0.423	0.725	1.136	1.405	1.820	1.839
B3	0.000	0.362	0.505	0.728	0.976	1.131	1.722	1.967

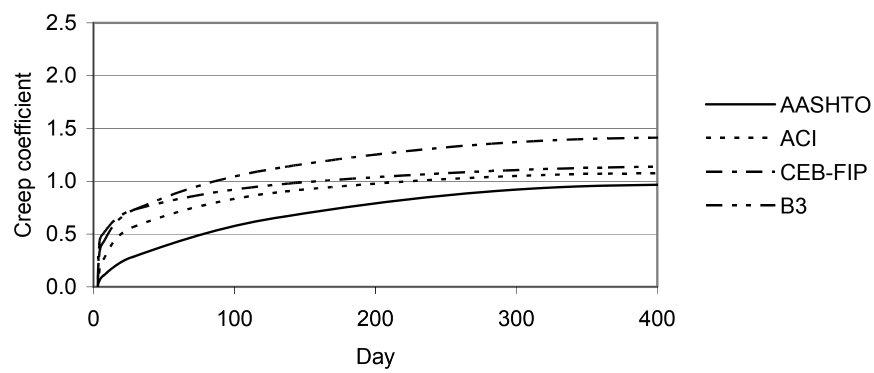

Shrinkage, $\varepsilon_{sh}(t)$:

Model	Day							
	3.01	4	7	28	136	365	10950	36500
AASHTO	0.000007	0.000010	0.000017	0.000062	0.000191	0.000283	0.000388	0.000391
ACI	0.000000	0.000007	0.000026	0.000120	0.000272	0.000334	0.000383	0.000384
CEB-FIP	0.000034	0.000047	0.000066	0.000123	0.000213	0.000283	0.000503	0.000523
B3	0.000000	0.000004	0.000014	0.000087	0.000343	0.000430	0.000432	0.000432

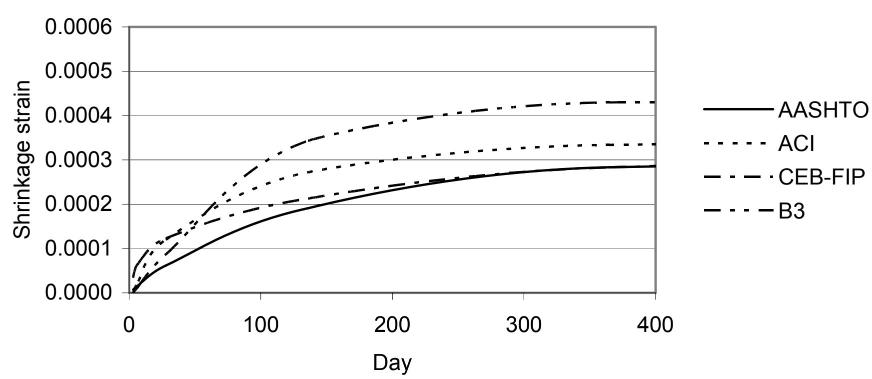

Aging coefficients, χ(t, 3):

Model	Day							
	3.01	4	7	28	136	365	10950	36500
AASHTO	N/A	N/A	N/A	N/A	N/A	N/A	N/A	N/A
ACI	0.710	0.658	0.642	0.621	0.603	0.594	0.567	0.558
CEB-FIP	0.808	0.777	0.769	0.648	0.562	0.535	0.477	0.474
B3	0.731	0.702	0.693	0.682	0.670	0.660	0.614	0.597

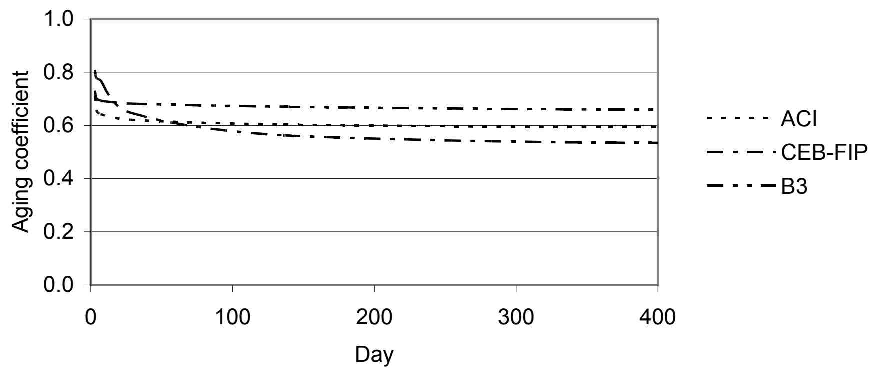

Use engineering recommendation model: **ACI**

Time-dependent restrained forces at t = 136 days (ΔN and ΔM):

Φ(136,3)	=	0.904		χ(136,3)	=	0.603
Ec(136,3)	=	2996.3	ksi	*(Age-adjusted elastic modulus)*		
εsh(136)	=	0.000272		λ	=	0.690
Ω	=	0.080		χ_r	=	0.783
A (mid)	=	1082.9	in^2	B (mid)	=	1580.6 in^3
I (mid)	=	556927	in^4			

x/L	Creep		Shrinkage		Relaxation		Total	
	ΔN	ΔM	ΔN	ΔM	ΔN	ΔM	ΔN	ΔM
0.000	0.0	0.0	826.0	0.0	0.0	0.0	826.0	0.0
0.094	608.3	10808.2	826.0	0.0	-10.2	-220.5	1424.1	10587.7
0.141	702.5	12482.3	826.0	0.0	-12.0	-267.6	1516.6	12214.7
0.200	796.0	13729.0	826.0	0.0	-13.7	-309.2	1608.3	13419.9
0.300	798.4	12445.7	826.0	0.0	-13.7	-309.2	1610.7	12136.6
0.400	799.8	11675.8	826.0	0.0	-13.7	-309.2	1612.2	11366.6
0.500	800.3	11419.1	826.0	0.0	-13.7	-309.2	1612.7	11110.0

Strains and curvatures at t = 136 days

x/L	$\Delta\varepsilon_o(t)$	$\Delta\psi(t)$
	$in/inx10^6$	$1/inx10^6$
0.000	-272.1	0.0
0.094	-440.2	-5.6
0.141	-463.3	-6.2
0.200	-486.0	-6.7
0.300	-487.9	-5.9
0.400	-489.0	-5.4
0.500	-489.4	-5.3

Strain inc. at the strand level (mid) =	-608.6	$in/inx10^6$
Time-dependent inc. losses =	-17.344	ksi
Stress of prestress strand =	168.953	ksi
% losses =	16.57	%

Strains and curvatures - Summary for simple span case at x/L = 0.500

Strain, $\varepsilon_o(t)$ using ACI, CEB-FIP, and B3 respectively

Day								
3	3.01	4	7	28	136	365	10950	36500
-291.8	-294.2	-332.2	-385.5	-553.7	-781.2	-879.7	-986.0	-992.4
-288.0	-339.6	-406.9	-461.6	-591.2	-777.0	-907.9	-1211.0	-1233.4
-291.8	-291.8	-391.8	-438.7	-562.9	-863.5	-981.3	-1119.9	-1175.8

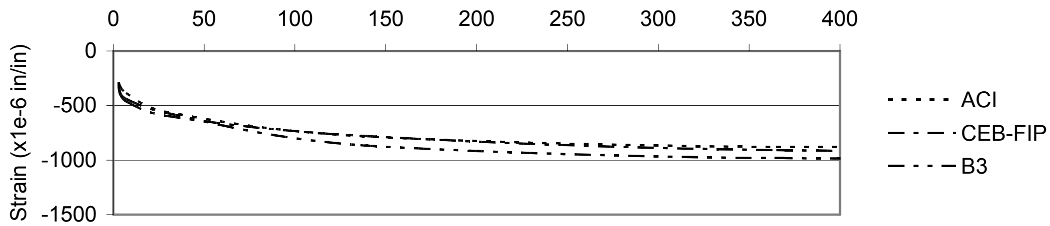

Curvature, ψ(t) using ACI, CEB-FIP, and B3 respectively

Day								
3	3.01	4	7	28	136	365	10950	36500
-8.1	-8.2	-9.0	-9.8	-11.6	-13.4	-14.2	-15.5	-15.6
-8.0	-8.4	-9.8	-10.7	-12.5	-14.8	-16.2	-18.0	-18.0
-8.1	-8.1	-10.6	-11.5	-12.8	-13.5	-14.2	-17.3	-18.6

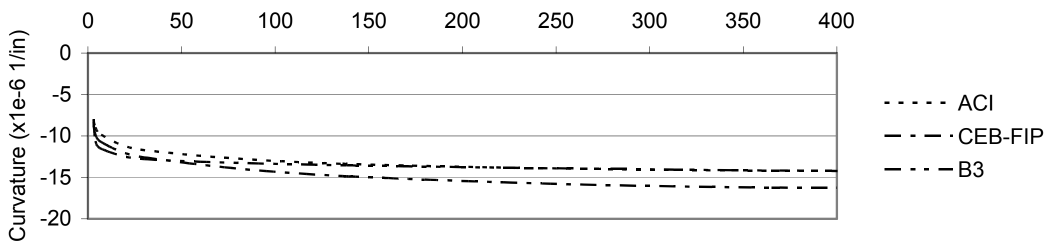

Stress of prestress strand using ACI, CEB-FIP, and B3 respectively

Day								
3	3.01	4	7	28	136	365	10950	36500
186.3	186.2	184.6	182.5	176.5	169.0	165.6	161.8	161.5
186.5	184.7	181.9	179.8	174.9	168.1	163.5	153.7	153.1
186.3	186.3	181.8	179.9	175.6	166.5	162.7	156.7	154.3

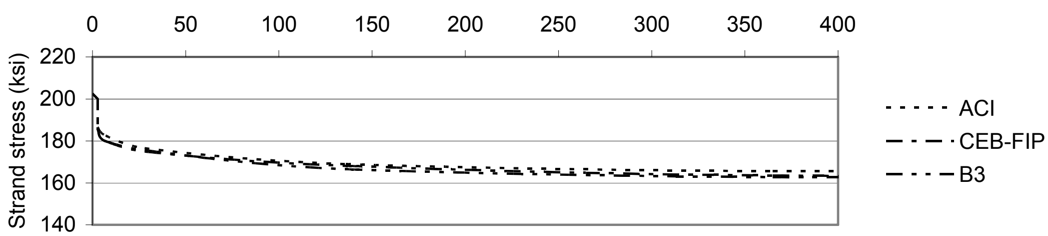

% prestress losses using ACI, CEB-FIP, and B3 respectively

Day								
3	3.01	4	7	28	136	365	10950	36500
8.0	8.1	8.8	9.9	12.8	16.6	18.2	20.1	20.2
7.9	8.8	10.2	11.2	13.6	17.0	19.3	24.1	24.4
8.0	8.0	10.2	11.2	13.3	17.8	19.6	22.6	23.8

Effect of concrete deck placed at t = 136 days

Section Properties at t = 136 days when deck is not hardened yet (midspan):

	Properties of area			Properties of transformed area		
	A	B	I	A^*E/E_{ref}	B^*E/E_{ref}	I^*E/E_{ref}
Girder	1013	0	521162.6	1013	0	521162.6
Strand	7.344	166.2	3760.0	41.1	928.9	21019.0
				1054.1	928.9	542181.6

Applied forces due to concrete deck placement:

x/L	A	B	I	ΔN (kips)	ΔM (kips-in)
0.000	1013.0	0.0	521162.6	0.0	0.0
0.094	1043.8	662.5	535418.1	0.0	4010.7
0.141	1048.9	804.2	539166.1	0.0	5703.6
0.200	1054.1	928.9	542181.6	0.0	7526.6
0.300	1054.1	928.9	542181.6	0.0	9878.7
0.400	1054.1	928.9	542181.6	0.0	11290.0
0.500	1054.1	928.9	542181.6	0.0	11760.4

Strains and curvatures at deck placement:

x/L	$\Delta\varepsilon_o$ in/inx10^6	$\Delta\psi$ 1/inx10^6
0.000	0.0	0.0
0.094	-0.9	1.5
0.141	-1.6	2.1
0.200	-2.4	2.7
0.300	-3.2	3.6
0.400	-3.6	4.1
0.500	-3.8	4.3

Strain at the strand level (midspan) =	92.7	in/inx10^6
Elastic stress gain =	2.641	ksi
Stress of prestress strand =	171.594	ksi
% losses =	15.26	%

Creep coefficients of girder, Φ(t, 136):

Model	Day							
	136.01	137	139	143	164	365	10950	36500
ACI	0.006	0.086	0.153	0.230	0.402	0.684	0.912	0.930
CEB-FIP	0.032	0.128	0.178	0.229	0.344	0.596	0.868	0.878
B3	0.000	0.143	0.192	0.235	0.321	0.485	0.780	0.895

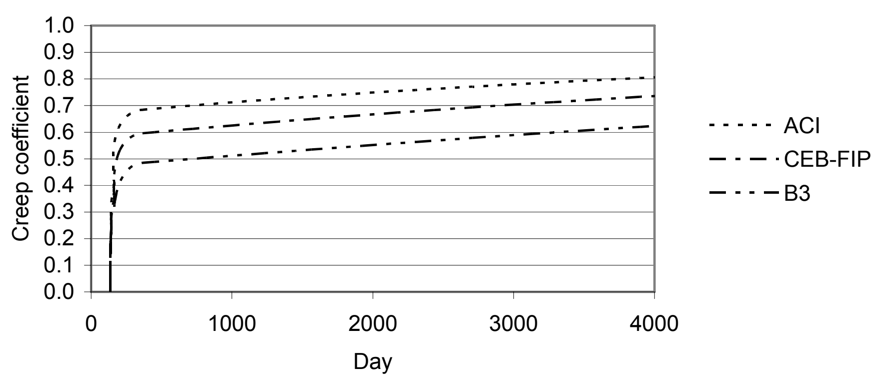

Aging coefficients of girder, χ(t, 136):

Model	Day							
	136.01	137	139	143	164	365	10950	36500
ACI	0.543	0.724	0.767	0.800	0.855	0.915	0.923	0.918
CEB-FIP	0.812	0.860	0.899	0.909	0.909	0.888	0.823	0.821
B3	0.546	0.736	0.781	0.816	0.873	0.935	0.934	0.924

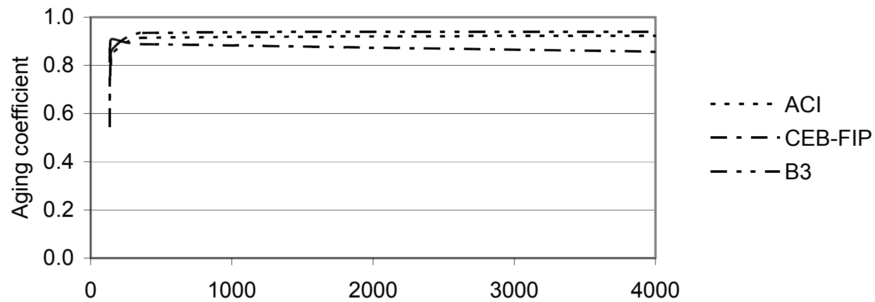

Creep coefficients of concrete deck slab, Φ(t, 3):

Model	Day							
	3.01	4	6	10	31	232	10817	36367
ACI	0.008	0.115	0.205	0.308	0.538	0.915	1.220	1.243
CEB-FIP	0.092	0.367	0.510	0.656	0.989	1.757	2.809	2.860
B3	0.000	0.360	0.470	0.563	0.731	1.035	1.703	1.949

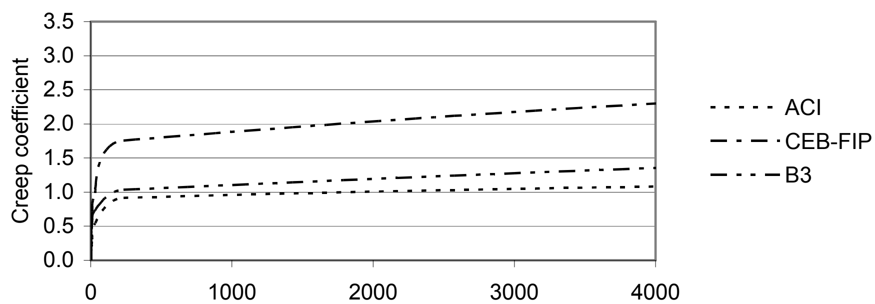

Aging coefficients of concrete deck slab, χ(t, 3):

Model	Day							
	3.01	4	6	10	31	232	10817	36367
ACI	0.695	0.630	0.615	0.603	0.583	0.559	0.530	0.522
CEB-FIP	0.809	0.794	0.809	0.781	0.699	0.577	0.644	0.650
B3	0.731	0.701	0.694	0.688	0.679	0.663	0.612	0.595

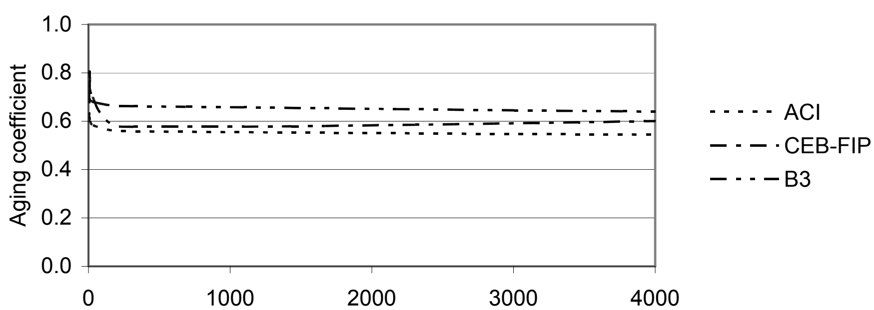

Shrinkage of concrete deck slab, $\varepsilon_{sh}(t)$:

Model	Day							
	3.01	4	6	10	31	232	10817	36367
ACI	0.000000	0.000004	0.000012	0.000025	0.000075	0.000179	0.000221	0.000222
CEB-FIP	0.000016	0.000024	0.000031	0.000042	0.000070	0.000150	0.000502	0.000584
B3	0.000000	0.000001	0.000004	0.000009	0.000037	0.000263	0.000432	0.000432

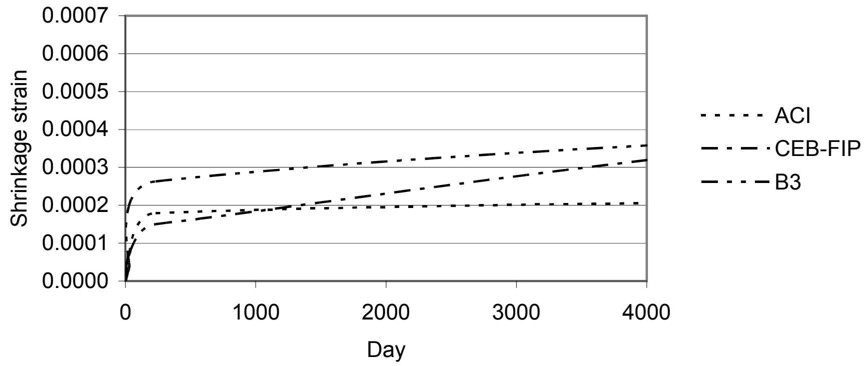

Time-dependent effect at t = 36500 days:

Girder:

$\Delta\Phi(36500,3)$ = 0.456
$\Delta\varepsilon sh(36500)$ = 0.000112
$\Phi(36500,136)$ = 0.930
$\chi(36500,136)$ = 0.918
$Ec(36500,136)$ = 2750.1 ksi

Slab:

$\Phi(36367,3)$ = 1.243
$\chi(36367,3)$ = 0.522
$Ec(36367,3)$ = 1985.0 ksi
$\varepsilon sh(36367)$ = 0.000222

Strand:

λ = 0.690
χ_r = 0.795
Ω = 0.075

Stresses and curvatures prior to composite action

x/L	Restrained		Time-dependence		Change in stresses			
	σ_{top}	σ_{bot}	σ_{top}	σ_{bot}	$\Delta\sigma_{top}$	$\Delta\sigma_{bot}$	$\Delta\sigma$	$\Delta\psi$
0.000	0.815	0.815	-0.815	-0.815	0.000	0.000	0.000	0.000
0.094	0.772	2.079	-0.801	-1.852	-0.029	0.226	0.097	0.004
0.141	0.765	2.274	-0.808	-1.986	-0.042	0.289	0.121	0.005
0.200	0.783	2.443	-0.836	-2.094	-0.053	0.349	0.145	0.006
0.300	0.862	2.367	-0.914	-2.026	-0.052	0.341	0.142	0.006
0.400	0.910	2.321	-0.961	-1.984	-0.051	0.336	0.140	0.006
0.500	0.925	2.306	-0.976	-1.971	-0.051	0.335	0.139	0.006

Section Properties at t = 36500 days when composite action starts (midspan):

	Properties of area			Properties of transformed area		
	A	B	I	$A*E/E_{ref}$	$B*E/E_{ref}$	$I*E/E_{ref}$
Girder	1013	0	521162.6	1013	0	521162.6
Strand	7.344	166.2	3760.0	76.1	1722.1	38965.5
Deck	984	-36052	1326982	710	-26021	957777
Rebars	9.41	-331.2	11655.9	99.2	-3492.7	122911.2
				1898	-27792	1640816

***Note** : neglected the duration of 3-day concrete deck hardening*

Time-dependent restrained forces at t = 36500 days (ΔN and ΔM):

x/L	Creep		Shrinkage		Relaxation		Total	
	ΔN	ΔM	ΔN	ΔM	ΔN	ΔM	ΔN	ΔM
0.000	0.0	0.0	745.8	-15898.7	0.0	0.0	745.8	-15898.7
0.094	257.4	2469.7	745.8	-15898.7	-15.3	-328.2	987.9	-13757.2
0.141	296.1	2265.6	745.8	-15898.7	-17.8	-398.4	1024.1	-14031.5
0.200	334.8	1818.1	745.8	-15898.7	-20.3	-460.2	1060.3	-14540.8
0.300	338.7	108.2	745.8	-15898.7	-20.3	-460.2	1064.2	-16250.6
0.400	341.1	-917.7	745.8	-15898.7	-20.3	-460.2	1066.6	-17276.5
0.500	341.9	-1259.6	745.8	-15898.7	-20.3	-460.2	1067.4	-17618.5

Strains and curvatures at t = 36500 days

x/L	$\Delta\varepsilon_o(t)$	$\Delta\psi(t)$
	in/inx10^6	1/inx10^6
0.000	-128.8	1.2
0.094	-196.2	-0.3
0.141	-202.3	-0.3
0.200	-207.3	-0.3
0.300	-200.9	0.2
0.400	-197.1	0.5
0.500	-195.8	0.6

Strain inc. at the strand level (mid) =	-182.5	in/inx10^6
Time-dependent inc. losses =	-5.203	ksi
Stress of prestress strand =	166.391	ksi
% losses =	17.83	%

Time-dependent strain at top fiber along the length of the girder:

x/L	Day							
	136.01	137	139	143	164	365	10950	36500
0.000	0.0	-2.9	-8.3	-18.1	-54.4	-139.4	-178.4	-179.3
0.094	-0.1	-4.5	-11.1	-22.2	-61.1	-146.3	-181.8	-182.5
0.141	-0.2	-5.1	-12.2	-23.9	-64.0	-150.9	-187.4	-188.1
0.200	-0.2	-5.8	-13.5	-25.8	-67.2	-156.2	-194.6	-195.5
0.300	-0.3	-6.8	-15.2	-28.3	-71.6	-164.8	-207.7	-209.0
0.400	-0.3	-7.3	-16.2	-29.8	-74.3	-170.0	-215.6	-217.1
0.500	-0.4	-7.5	-16.5	-30.4	-75.2	-171.7	-218.3	-219.9

Time-dependent strain at bottom fiber along the length of the girder:

x/L	Day							
	136.01	137	139	143	164	365	10950	36500
0.000	0.0	0.6	1.6	3.4	7.8	-36.1	-87.8	-89.3
0.094	0.2	2.9	5.5	8.5	12.5	-71.5	-199.4	-206.9
0.141	0.3	3.9	7.2	10.9	16.2	-70.5	-205.3	-213.3
0.200	0.3	5.0	9.0	13.5	20.2	-68.1	-208.2	-216.5
0.300	0.4	6.4	11.6	17.5	27.3	-54.2	-186.9	-194.6
0.400	0.5	7.3	13.2	19.9	31.5	-46.0	-174.2	-181.4
0.500	0.5	7.6	13.8	20.7	32.9	-43.2	-169.9	-177.1

Strains and curvatures - Summary for simple span case at x/L = 0.500

Strain, $\varepsilon_o(t)$ using ACI, CEB-FIP, and B3 respectively

Day								
136	136.01	137	139	143	164	365	10950	36500
0.0	0.1	1.0	0.5	-1.7	-14.5	-99.6	-191.1	-195.8
0.0	-2.2	-2.0	-3.4	-6.1	-19.2	-127.7	-432.6	-463.1
0.0	0.0	2.6	2.4	0.7	-11.5	-133.9	-285.5	-335.0

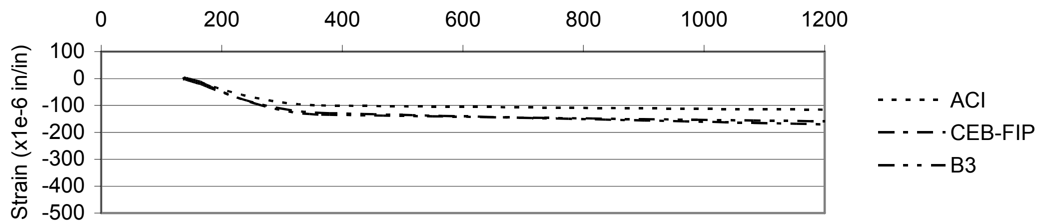

Curvature, ψ(t) using ACI, CEB-FIP, and B3 respectively

Day								
136	136.01	137	139	143	164	365	10950	36500
0.0	0.0	0.2	0.4	0.7	1.5	1.8	0.7	0.6
0.0	0.3	0.5	0.7	0.8	1.1	0.4	-0.1	0.4
0.0	0.0	0.3	0.4	0.5	0.8	2.1	1.2	0.0

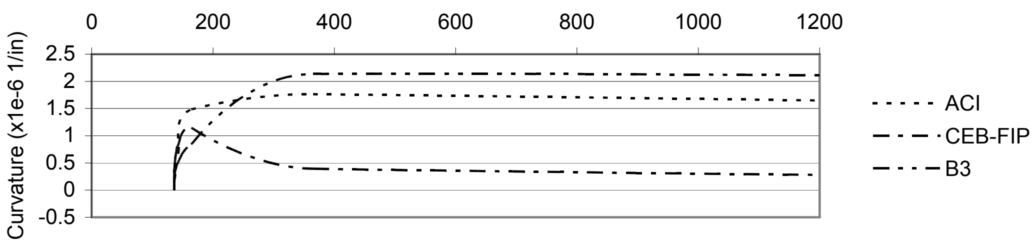

Stress of prestress strand using ACI, CEB-FIP, and B3 respectively

Day								
136	136.01	137	139	143	164	365	10950	36500
171.6	171.6	171.8	171.9	172.0	172.1	169.9	166.6	166.4
170.5	170.6	170.8	170.8	170.9	170.7	167.1	158.1	157.6
169.1	169.1	169.4	169.5	169.5	169.4	166.7	161.8	159.6

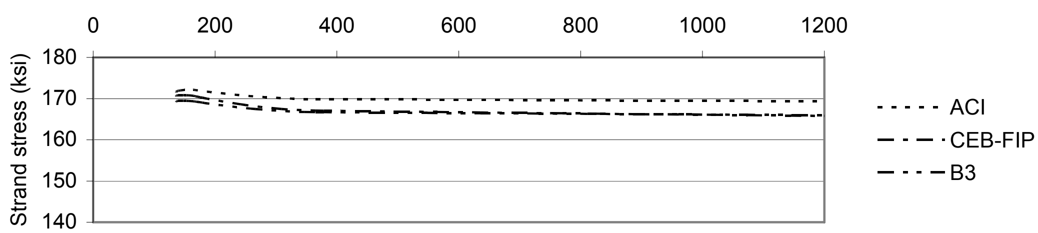

% prestress losses using ACI, CEB-FIP, and B3 respectively

Day								
136	136.01	137	139	143	164	365	10950	36500
15.3	15.3	15.2	15.1	15.1	15.0	16.1	17.7	17.8
15.8	15.8	15.7	15.6	15.6	15.7	17.5	21.9	22.2
16.5	16.5	16.3	16.3	16.3	16.4	17.7	20.1	21.2

End of Calculation

Three samples of time-dependent strains with respect to the time-line (139, 365, and 36,500 days) at the top fiber of interior girders are shown in Figure Figure **B-7**.

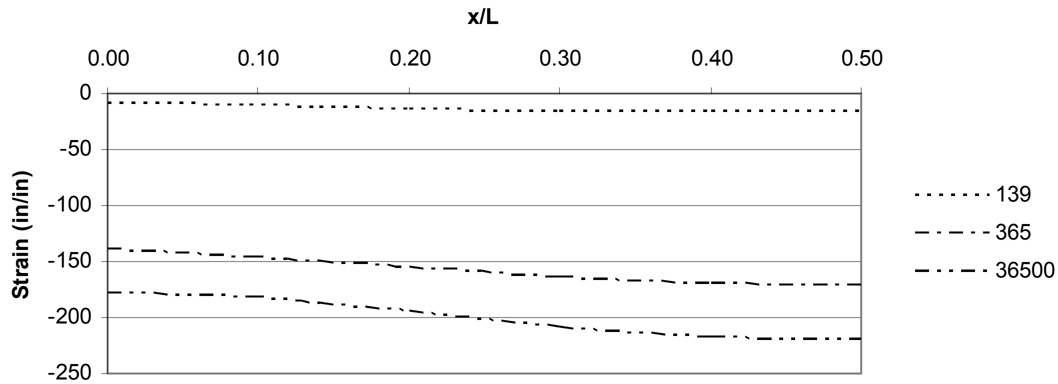

Figure **B-7**: Time-Dependent Strains at Top Fiber (Bridge 203 – Span 2 – Ext. Girder)

Three samples of time-dependent strains with respect to the time-line (139, 365, and 36,500 days) at the bottom fiber of interior girders are shown in Figure **B-8**.

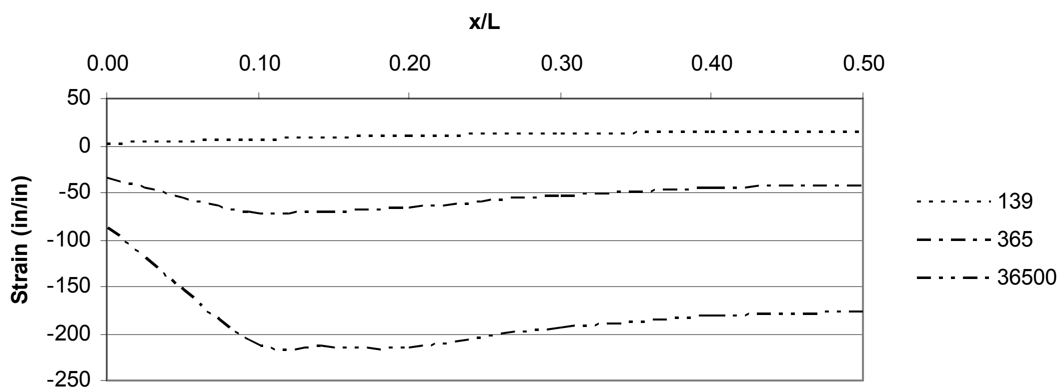

Figure **B-8**: Time-Dependent Strains at Bottom Fiber (Bridge 203 – Span 2 – Ext. Girder)

B.1.3 Span 3

Interior Girder

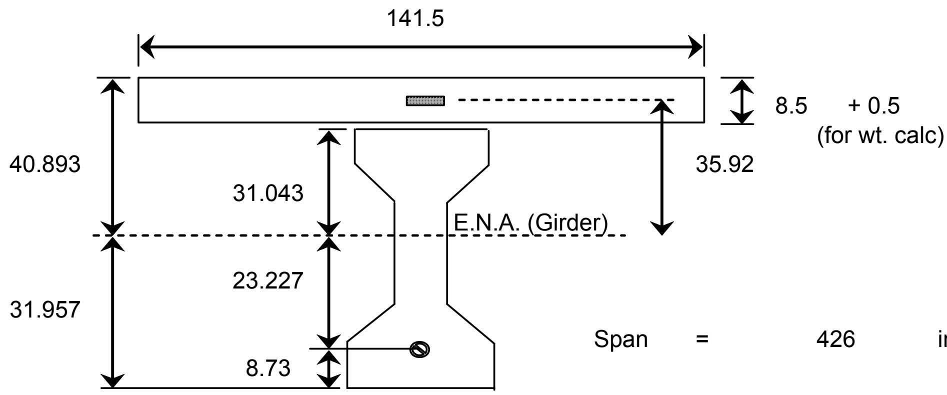

Span = 426 in

Concrete properties:

Girder:

A	=	1013	in^2
I	=	521162.6	in^4
$E_c(3)$	=	4628.4	ksi
$E_c(28)$	=	5098.2	ksi

Slab:

$E_c(3)$	=	3272.8	ksi
$E_c(28)$	=	3605.0	ksi

Prestress strand properties:

A	=	0.153	in^2
No.	=	30	
Jacking	=	30.982	k/strand
E_{ps}	=	28500	ksi
$A_{s\text{-}slab}$	=	20.764	in^2
E_s	=	29000	ksi

Section Properties at t = 3 days (midspan):

	Properties of area			Properties of transformed area		
	A	B	I	$A*E/E_{ref}$	$B*E/E_{ref}$	$I*E/E_{ref}$
Girder	1013	0	521162.6	1013	0	521162.6
Strand	4.59	106.6	2476.3	28.3	656.5	15248.0
				1041.3	656.5	536410.6

Relaxation loss from t = 0 to 3 days:

Δf_{RE}	=	-2.664	ksi
f_{pi}	=	199.833	ksi

Applied forces at transfer:

x/L	e (in)	No. of strands	A	B	I	N (kips)	M (kips-in)
0.000	0.000	0	1013.0	0.0	521162.6	0.0	0.0
0.100	22.287	24	1035.6	503.9	532393.7	-733.8	-15635.8
0.225	22.287	24	1035.6	503.9	532393.7	-733.8	-14961.0
0.275	23.227	30	1041.3	656.5	536410.6	-917.2	-19713.8
0.300	23.227	30	1041.3	656.5	536410.6	-917.2	-19629.0
0.400	23.227	30	1041.3	656.5	536410.6	-917.2	-19389.6
0.500	23.227	30	1041.3	656.5	536410.6	-917.2	-19309.8

Strains and curvatures at transfer:

x/L	ε_o in/inx10^6	ψ 1/inx10^6
0.000	0.0	0.0
0.100	-150.1	-6.2
0.225	-150.2	-5.9
0.275	-185.5	-7.7
0.300	-185.5	-7.7
0.400	-185.5	-7.6
0.500	-185.6	-7.6

Strain at the strand level (midspan) =	-360.9	in/inx10^6
Elastic shortening loss =	-10.287	ksi
Stress of prestress strand =	189.546	ksi
% initial loss =	6.40	%

Creep coefficients, Φ(t, 3):

Model	Day							
	3.01	4	7	28	115	365	10950	36500
AASHTO	0.003	0.050	0.107	0.284	0.616	0.959	1.425	1.460
ACI	0.009	0.126	0.259	0.565	0.871	1.072	1.334	1.359
CEB-FIP	0.070	0.280	0.423	0.725	1.089	1.405	1.820	1.839
B3	0.000	0.362	0.505	0.728	0.949	1.131	1.722	1.967

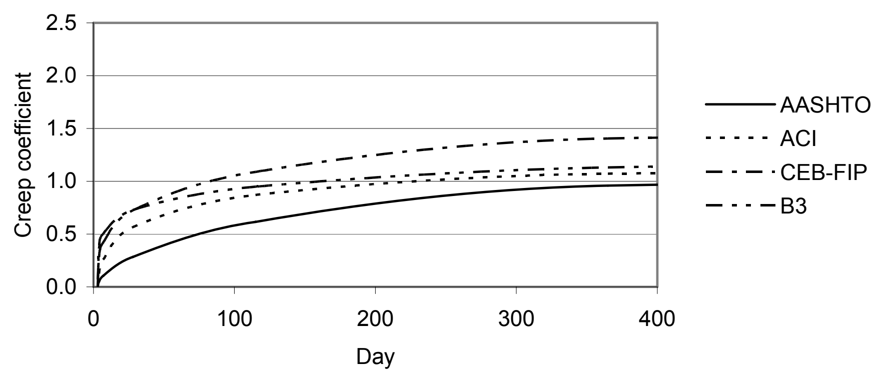

Shrinkage, $\varepsilon_{sh}(t)$:

Model	Day							
	3.01	4	7	28	115	365	10950	36500
AASHTO	0.000007	0.000010	0.000017	0.000062	0.000174	0.000283	0.000388	0.000391
ACI	0.000000	0.000007	0.000026	0.000120	0.000258	0.000334	0.000383	0.000384
CEB-FIP	0.000034	0.000047	0.000066	0.000123	0.000202	0.000283	0.000503	0.000523
B3	0.000000	0.000004	0.000014	0.000087	0.000312	0.000430	0.000432	0.000432

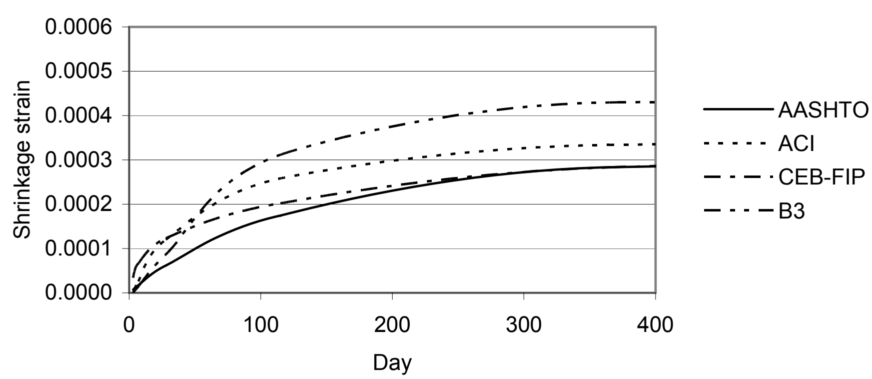

Aging coefficients, χ(t, 3):

Model	Day							
	3.01	4	7	28	115	365	10950	36500
AASHTO	N/A	N/A	N/A	N/A	N/A	N/A	N/A	N/A
ACI	0.710	0.658	0.642	0.621	0.604	0.594	0.567	0.558
CEB-FIP	0.808	0.777	0.769	0.648	0.573	0.537	0.478	0.475
B3	0.731	0.702	0.693	0.682	0.672	0.660	0.614	0.597

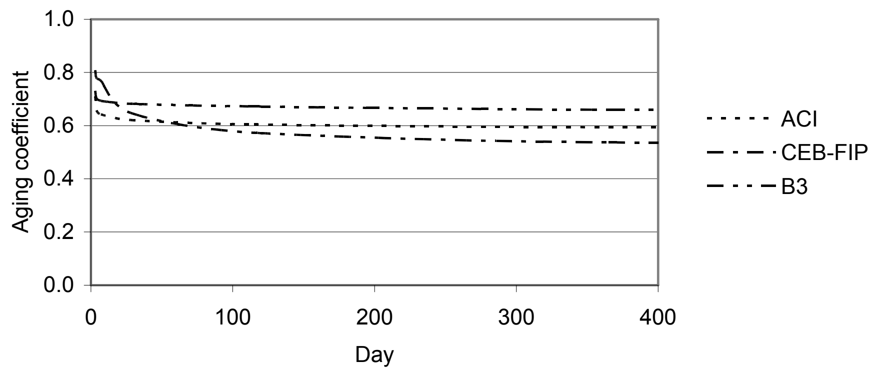

Use engineering recommendation model: **ACI**

Time-dependent restrained forces at t = 115 days (ΔN and ΔM):

Φ(115,3) =	0.871		χ(115,3) =		0.604	
Ec(115,3) =	3032.5	ksi	*(Age-adjusted elastic modulus)*			
εsh(115) =	0.000258		λ	=	0.702	
Ω =	0.066		χ_r	=	0.821	
A (mid) =	1056.1	in^2	B (mid)	=	1002.0	in^3
I (mid) =	544435	in^4				

x/L	Creep		Shrinkage		Relaxation		Total	
	ΔN	ΔM	ΔN	ΔM	ΔN	ΔM	ΔN	ΔM
0.000	0.0	0.0	792.5	0.0	0.0	0.0	792.5	0.0
0.100	401.4	8536.5	792.5	0.0	-6.8	-152.5	1187.1	8384.0
0.225	401.8	8159.5	792.5	0.0	-6.8	-152.5	1187.5	8007.0
0.275	496.1	10614.6	792.5	0.0	-8.6	-198.7	1280.0	10415.9
0.300	496.1	10567.6	792.5	0.0	-8.6	-198.7	1280.1	10368.9
0.400	496.3	10434.8	792.5	0.0	-8.6	-198.7	1280.3	10236.1
0.500	496.3	10390.6	792.5	0.0	-8.6	-198.7	1280.3	10191.9

Strains and curvatures at t = 115 days

x/L	$\Delta\varepsilon_o(t)$	$\Delta\psi(t)$
	$in/inx10^6$	$1/inx10^6$
0.000	-258.0	0.0
0.100	-370.3	-4.6
0.225	-370.6	-4.4
0.275	-394.4	-5.6
0.300	-394.4	-5.6
0.400	-394.6	-5.5
0.500	-394.6	-5.4

Strain inc. at the strand level (mid) =	-521.1	$in/inx10^6$
Time-dependent inc. losses =	-14.852	ksi
Stress of prestress strand =	174.694	ksi
% losses =	13.73	%

Strains and curvatures - Summary for simple span case at x/L = 0.500

Strain, $\varepsilon_o(t)$ using ACI, CEB-FIP, and B3 respectively

Day								
3	3.01	4	7	28	115	365	10950	36500
-185.6	-187.2	-214.1	-255.4	-397.8	-580.2	-684.8	-771.2	-775.8
-183.1	-228.5	-276.8	-319.0	-423.3	-557.8	-685.7	-959.7	-981.4
-185.6	-185.6	-251.7	-285.8	-392.1	-643.3	-784.6	-876.4	-913.2

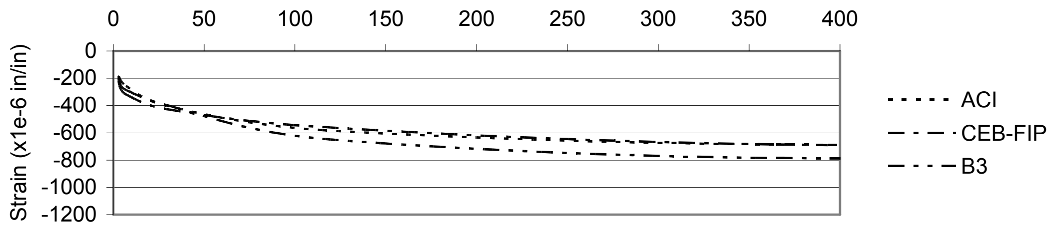

Curvature, ψ(t) using ACI, CEB-FIP, and B3 respectively

Day								
3	3.01	4	7	28	115	365	10950	36500
-7.6	-7.6	-8.4	-9.3	-11.2	-13.0	-14.1	-15.6	-15.7
-7.5	-7.9	-9.3	-10.2	-12.1	-14.4	-16.2	-18.3	-18.4
-7.6	-7.6	-10.1	-11.0	-12.4	-13.4	-14.3	-17.8	-19.3

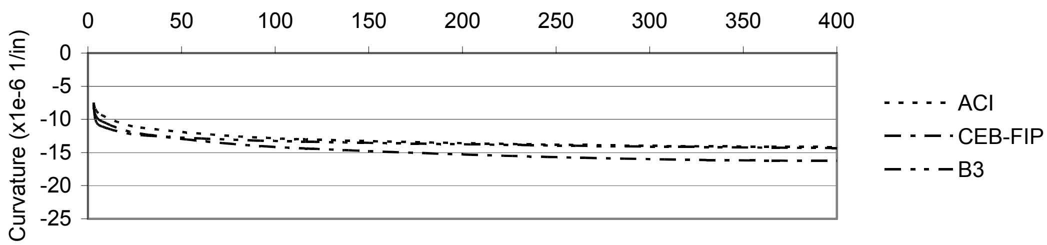

Stress of prestress strand using ACI, CEB-FIP, and B3 respectively

Day								
3	3.01	4	7	28	115	365	10950	36500
189.5	189.5	188.2	186.4	181.1	174.7	171.0	167.5	167.3
189.7	188.1	185.8	184.0	179.7	174.4	169.6	160.3	159.7
189.5	189.5	186.0	184.4	180.5	172.7	168.0	163.1	161.1

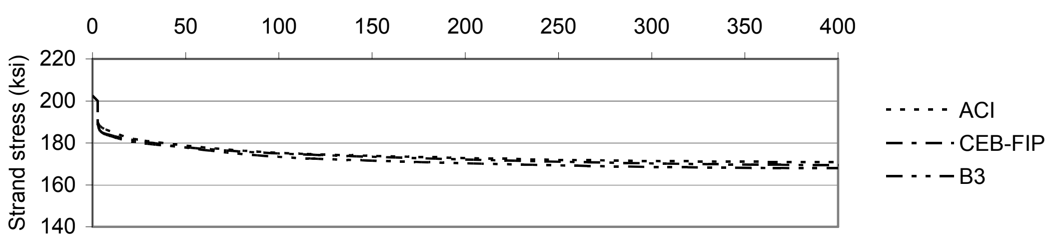

% prestress losses using ACI, CEB-FIP, and B3 respectively

Day								
3	3.01	4	7	28	115	365	10950	36500
6.4	6.4	7.1	8.0	10.6	13.7	15.6	17.3	17.4
6.3	7.1	8.3	9.2	11.2	13.9	16.3	20.8	21.1
6.4	6.4	8.2	8.9	10.9	14.7	17.0	19.5	20.5

Effect of concrete deck placed at t = 115 days

Section Properties at t = 115 days when deck is not hardened yet (midspan):

	Properties of area			Properties of transformed area		
	A	B	I	A^*E/E_{ref}	B^*E/E_{ref}	I^*E/E_{ref}
Girder	1013	0	521162.6	1013	0	521162.6
Strand	4.59	106.6	2476.3	25.7	596.0	13842.8
				1038.7	596.0	535005.4

Applied forces due to concrete deck placement:

x/L	A	B	I	ΔN (kips)	ΔM (kips-in)
0.000	1013.0	0.0	521162.6	0.0	0.0
0.100	1033.5	457.5	531358.6	0.0	902.8
0.225	1033.5	457.5	531358.6	0.0	1751.1
0.275	1038.7	596.0	535005.4	0.0	1999.9
0.300	1038.7	596.0	535005.4	0.0	2106.5
0.400	1038.7	596.0	535005.4	0.0	2407.4
0.500	1038.7	596.0	535005.4	0.0	2507.7

Strains and curvatures at deck placement:

x/L	$\Delta\varepsilon_o$ in/inx10^6	$\Delta\psi$ 1/inx10^6
0.000	0.0	0.0
0.100	-0.1	0.3
0.225	-0.3	0.6
0.275	-0.4	0.7
0.300	-0.4	0.8
0.400	-0.5	0.9
0.500	-0.5	0.9

Strain at the strand level (midspan) =	20.8	in/inx10^6
Elastic stress gain =	0.594	ksi
Stress of prestress strand =	175.288	ksi
% losses =	13.44	%

Creep coefficients of girder, Φ(t, 115):

Model	Day							
	115.01	116	118	122	143	365	10950	36500
ACI	0.006	0.087	0.156	0.234	0.409	0.705	0.927	0.945
CEB-FIP	0.033	0.132	0.184	0.237	0.355	0.627	0.896	0.907
B3	0.000	0.152	0.203	0.249	0.339	0.521	0.827	0.949

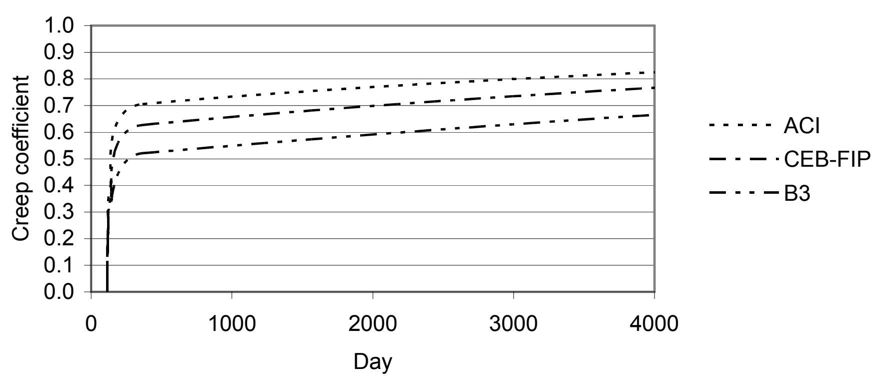

Aging coefficients of girder, χ(t, 115):

Model	Day							
	115.01	116	118	122	143	365	10950	36500
ACI	0.547	0.725	0.768	0.801	0.854	0.914	0.919	0.913
CEB-FIP	0.812	0.860	0.899	0.908	0.908	0.878	0.816	0.814
B3	0.549	0.737	0.782	0.816	0.873	0.934	0.931	0.921

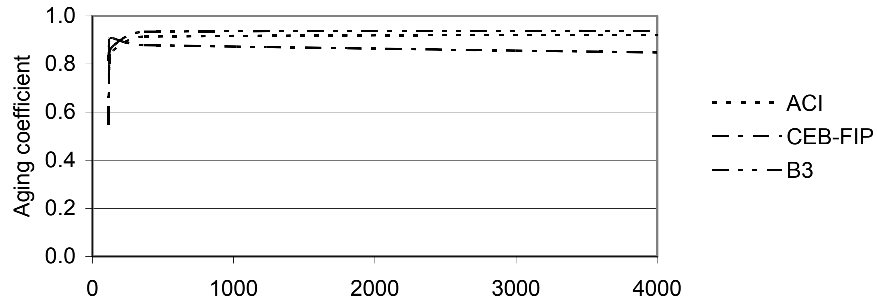

Creep coefficients of concrete deck slab, Φ(t, 3):

Model	Day							
	3.01	4	6	10	31	253	10838	36388
ACI	0.008	0.115	0.205	0.308	0.538	0.928	1.220	1.243
CEB-FIP	0.092	0.367	0.510	0.656	0.989	1.794	2.809	2.860
B3	0.000	0.360	0.470	0.563	0.731	1.049	1.703	1.950

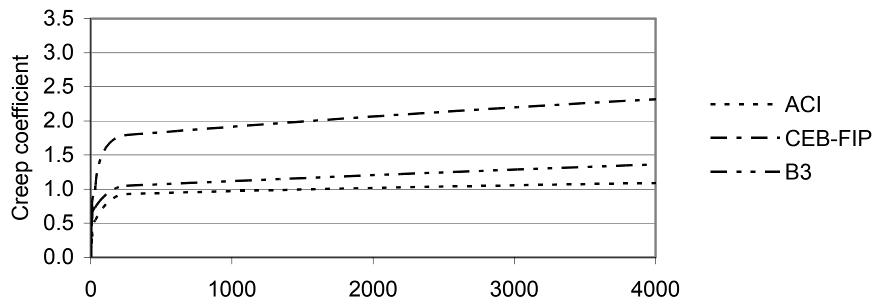

Aging coefficients of concrete deck slab, χ(t, 3):

Model	Day							
	3.01	4	6	10	31	253	10838	36388
ACI	0.695	0.630	0.615	0.603	0.583	0.558	0.530	0.522
CEB-FIP	0.809	0.794	0.809	0.781	0.699	0.571	0.644	0.650
B3	0.731	0.701	0.694	0.688	0.679	0.662	0.612	0.595

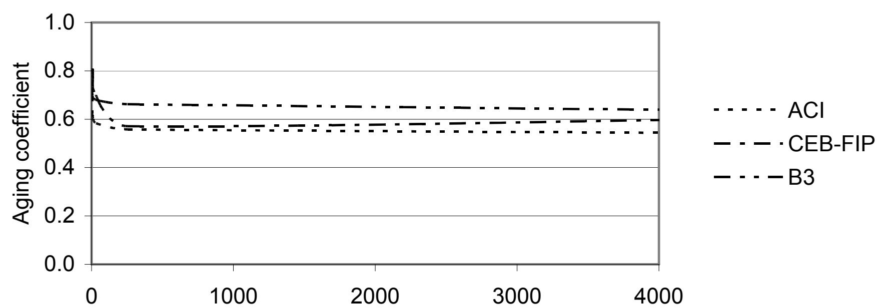

Shrinkage of concrete deck slab, $\varepsilon_{sh}(t)$:

Model	Day							
	3.01	4	6	10	31	253	10838	36388
ACI	0.000000	0.000004	0.000012	0.000025	0.000075	0.000182	0.000221	0.000222
CEB-FIP	0.000016	0.000024	0.000031	0.000042	0.000070	0.000155	0.000502	0.000584
B3	0.000000	0.000001	0.000004	0.000009	0.000037	0.000280	0.000432	0.000432

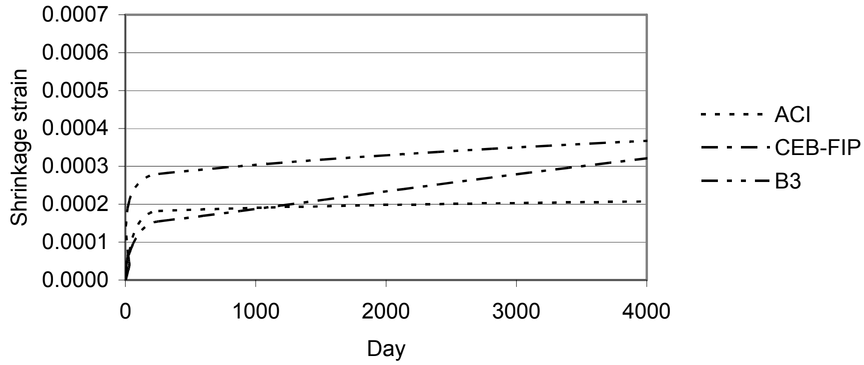

Time-dependent effect at t = 36500 days:

Girder:			*Slab:*		
$\Delta\Phi(36500,3)$ =	0.488		$\Phi(36388,3)$ =	1.243	
$\Delta\varepsilon sh(36500)$ =	0.000126		$\chi(36388,3)$ =	0.522	
$\Phi(36500,115)$ =	0.945		Ec(36388,3) =	1985.0	ksi
$\chi(36500,115)$ =	0.913		$\varepsilon sh(36388)$ =	0.000222	
Ec(36500,115) =	2736.7	ksi			
Strand:					
λ =	0.702		Ω =	0.078	
χ_r =	0.792				

Stresses and curvatures prior to composite action

x/L	Restrained		Time-dependence		Change in stresses			
	σ_{top}	σ_{bot}	σ_{top}	σ_{bot}	$\Delta\sigma_{top}$	$\Delta\sigma_{bot}$	$\Delta\sigma$	$\Delta\psi$
0.000	0.782	0.782	-0.782	-0.782	0.000	0.000	0.000	0.000
0.100	0.670	1.702	-0.689	-1.569	-0.019	0.133	0.056	0.002
0.225	0.693	1.679	-0.712	-1.548	-0.019	0.131	0.055	0.002
0.275	0.640	1.923	-0.670	-1.737	-0.031	0.186	0.076	0.003
0.300	0.643	1.920	-0.673	-1.734	-0.031	0.186	0.076	0.003
0.400	0.651	1.912	-0.681	-1.727	-0.030	0.185	0.076	0.003
0.500	0.653	1.909	-0.684	-1.724	-0.030	0.185	0.076	0.003

Section Properties at t = 36500 days when composite action starts (midspan):

	Properties of area			Properties of transformed area		
	A	B	I	A*E/E$_{ref}$	B*E/E$_{ref}$	I*E/E$_{ref}$
Girder	1013	0	521162.6	1013	0	521162.6
Strand	4.59	106.6	2476.3	47.8	1110.3	25788.1
Deck	1203	-44072	1622185	872	-31966	1176597
Rebars	20.76	-745.9	26793.7	220.0	-7904.0	283926.7
				2153	-38760	2007474

***Note** : neglected the duration of 3-day concrete deck hardening*

Time-dependent restrained forces at t = 36500 days (ΔN and ΔM):

x/L	Creep		Shrinkage		Relaxation		Total	
	ΔN	ΔM	ΔN	ΔM	ΔN	ΔM	ΔN	ΔM
0.000	0.0	0.0	880.0	-19435.6	0.0	0.0	880.0	-19435.6
0.100	187.3	3509.2	880.0	-19435.6	-10.4	-232.5	1056.9	-16158.8
0.225	188.0	2899.5	880.0	-19435.6	-10.4	-232.5	1057.6	-16768.5
0.275	229.9	3867.1	880.0	-19435.6	-13.0	-302.8	1096.9	-15871.3
0.300	230.1	3791.2	880.0	-19435.6	-13.0	-302.8	1097.0	-15947.3
0.400	230.4	3576.7	880.0	-19435.6	-13.0	-302.8	1097.4	-16161.7
0.500	230.5	3505.2	880.0	-19435.6	-13.0	-302.8	1097.5	-16233.2

Strains and curvatures at t = 36500 days

x/L	$\Delta\varepsilon_o(t)$	$\Delta\psi(t)$
	in/inx10^6	1/inx10^6
0.000	-137.1	0.8
0.100	-196.0	-0.9
0.225	-193.1	-0.7
0.275	-205.6	-1.1
0.300	-205.3	-1.1
0.400	-204.3	-1.0
0.500	-203.9	-1.0

Strain inc. at the strand level (mid) =	-226.8	in/inx10^6
Time-dependent inc. losses =	-6.463	ksi
Stress of prestress strand =	168.826	ksi
% losses =	16.63	%

Time-dependent strain at top fiber along the length of the girder:

x/L	Day							
	115.01	116	118	122	143	365	10950	36500
0.000	0.0	-2.9	-8.3	-18.0	-53.8	-137.7	-170.1	-170.9
0.100	-0.1	-3.2	-8.8	-18.7	-54.5	-134.2	-160.1	-160.4
0.225	-0.1	-3.4	-9.3	-19.4	-55.9	-136.8	-164.0	-164.3
0.275	-0.1	-3.5	-9.4	-19.6	-56.0	-135.8	-161.2	-161.4
0.300	-0.1	-3.6	-9.5	-19.7	-56.2	-136.1	-161.7	-161.9
0.400	-0.1	-3.7	-9.6	-20.0	-56.7	-137.1	-163.0	-163.3
0.500	-0.1	-3.7	-9.7	-20.1	-56.8	-137.4	-163.5	-163.7

Time-dependent strain at bottom fiber along the length of the girder:

x/L	Day							
	115.01	116	118	122	143	365	10950	36500
0.000	0.0	0.5	1.5	3.1	6.3	-55.4	-109.2	-110.7
0.100	0.0	0.9	1.9	3.1	3.0	-101.2	-217.3	-223.9
0.225	0.1	1.5	2.9	4.6	5.8	-95.8	-209.2	-215.5
0.275	0.1	1.6	3.0	4.6	4.9	-106.0	-232.8	-240.2
0.300	0.1	1.6	3.1	4.8	5.3	-105.3	-231.8	-239.1
0.400	0.1	1.8	3.5	5.3	6.2	-103.4	-229.0	-236.3
0.500	0.1	1.9	3.6	5.5	6.5	-102.8	-228.1	-235.3

Strains and curvatures - Summary for simple span case at x/L = 0.500

Strain, $\varepsilon_o(t)$ using ACI, CEB-FIP, and B3 respectively

				Day				
115	115.01	116	118	122	143	365	10950	36500
0.0	0.0	-0.6	-2.2	-5.7	-21.3	-118.0	-199.7	-203.9
0.0	-2.7	-4.0	-6.0	-9.2	-23.0	-136.7	-417.9	-447.3
0.0	0.0	0.2	-0.9	-3.5	-17.7	-162.8	-281.8	-319.6

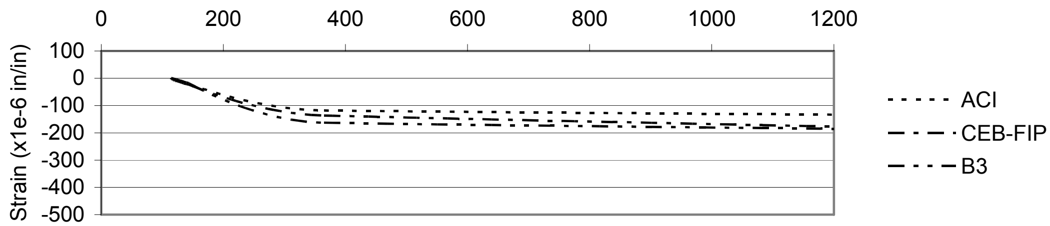

Curvature, ψ(t) using ACI, CEB-FIP, and B3 respectively

				Day				
115	115.01	116	118	122	143	365	10950	36500
0.0	0.0	0.1	0.2	0.4	0.9	0.5	-0.9	-1.0
0.0	0.2	0.3	0.4	0.5	0.7	-0.7	-2.0	-1.5
0.0	0.0	0.1	0.1	0.1	0.3	1.0	-0.2	-1.4

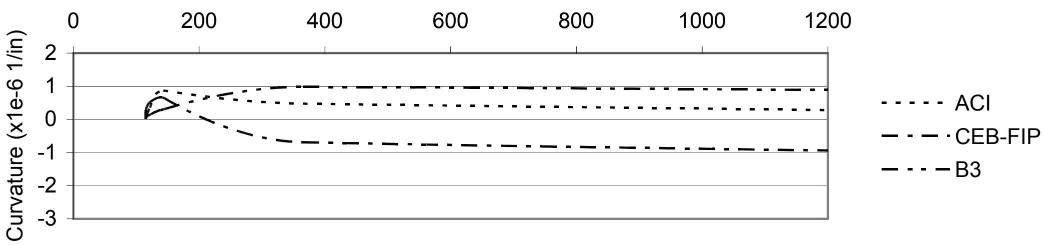

Stress of prestress strand using ACI, CEB-FIP, and B3 respectively

				Day				
115	115.01	116	118	122	143	365	10950	36500
175.3	175.3	175.3	175.3	175.4	175.3	172.2	169.0	168.8
175.0	175.0	175.1	175.1	175.0	174.7	170.6	161.7	161.2
173.2	173.2	173.3	173.3	173.2	172.9	169.3	165.1	163.2

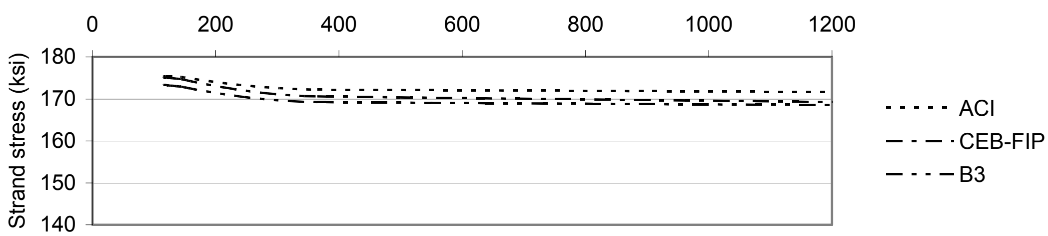

% prestress losses using ACI, CEB-FIP, and B3 respectively

				Day				
115	115.01	116	118	122	143	365	10950	36500
13.4	13.4	13.4	13.4	13.4	13.5	14.9	16.5	16.6
13.6	13.6	13.5	13.5	13.6	13.7	15.7	20.1	20.4
14.4	14.4	14.4	14.4	14.4	14.6	16.4	18.5	19.4

End of Calculation

Three samples of time-dependent strains with respect to the time-line (118, 365, and 36,500 days) at the top fiber of interior girders are shown in Figure B-9.

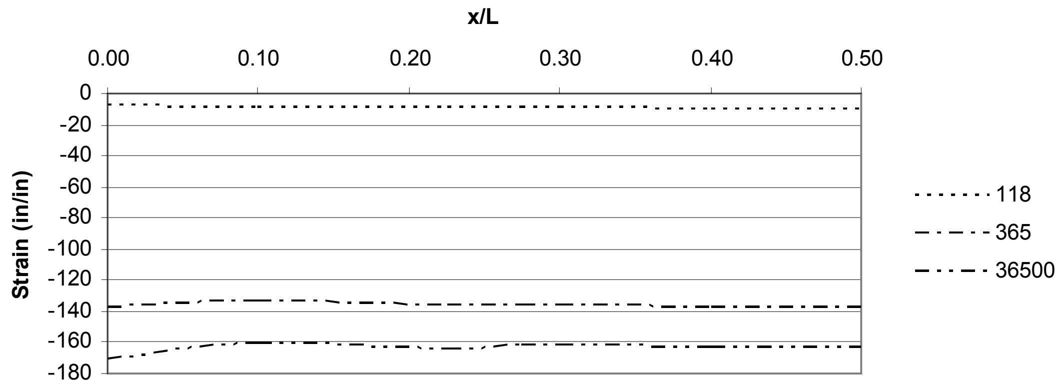

Figure B-9: Time-Dependent Strains at Top Fiber (Bridge 203 – Span 3 – Int. Girder)

Three samples of time-dependent strains with respect to the time-line (118, 365, and 36,500 days) at the bottom fiber of interior girders are shown in Figure B-10.

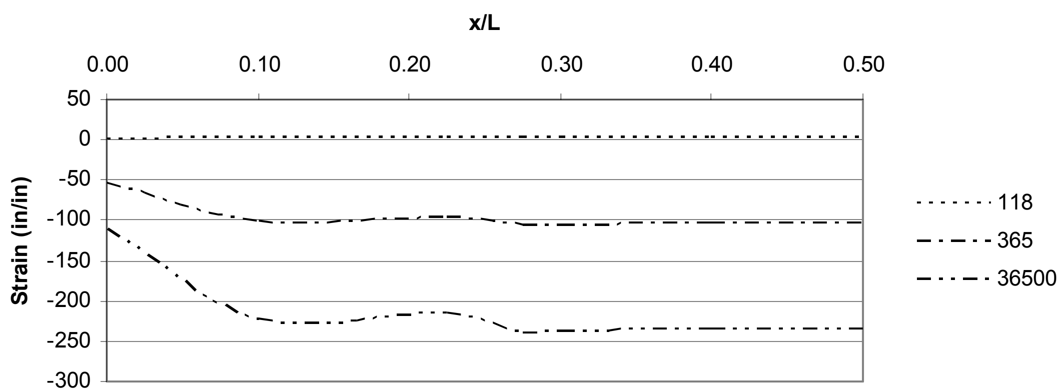

Figure B-10: Time-Dependent Strains at Bottom Fiber
(Bridge 203 – Span 3 – Int. Girder)

Exterior Girder

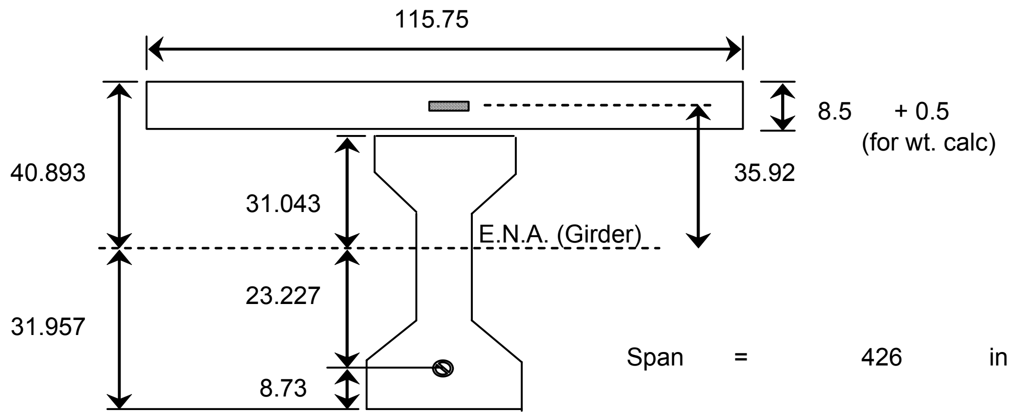

Span = 426 in

Concrete properties:

Girder:

A	=	1013	in^2
I	=	521162.6	in^4
$E_c(3)$	=	4628.4	ksi
$E_c(28)$	=	5098.2	ksi

Slab:

$E_c(3)$	=	3272.8	ksi
$E_c(28)$	=	3605.0	ksi

Prestress strand properties:

A	=	0.153	in^2
No.	=	30	
Jacking	=	30.982	k/strand
E_{ps}	=	28500	ksi
$A_{s\text{-}slab}$	=	20.764	in^2
E_s	=	29000	ksi

Section Properties at t = 3 days (midspan):

	Properties of area			Properties of transformed area		
	A	B	I	$A*E/E_{ref}$	$B*E/E_{ref}$	$I*E/E_{ref}$
Girder	1013	0	521162.6	1013	0	521162.6
Strand	4.59	106.6	2476.3	28.3	656.5	15248.0
				1041.3	656.5	536410.6

Relaxation loss from t = 0 to 3 days:

Δf_{RE}	=	-2.664	ksi
f_{pi}	=	199.833	ksi

Applied forces at transfer:

x/L	e (in)	No. of strands	A	B	I	N (kips)	M (kips-in)
0.000	0.000	0	1013.0	0.0	521162.6	0.0	0.0
0.100	22.287	24	1035.6	503.9	532393.7	-733.8	-15635.8
0.225	22.287	24	1035.6	503.9	532393.7	-733.8	-14961.0
0.275	23.227	30	1041.3	656.5	536410.6	-917.2	-19713.8
0.300	23.227	30	1041.3	656.5	536410.6	-917.2	-19629.0
0.400	23.227	30	1041.3	656.5	536410.6	-917.2	-19389.6
0.500	23.227	30	1041.3	656.5	536410.6	-917.2	-19309.8

Strains and curvatures at transfer:

x/L	ε_o in/inx10^6	ψ 1/inx10^6
0.000	0.0	0.0
0.100	-150.1	-6.2
0.225	-150.2	-5.9
0.275	-185.5	-7.7
0.300	-185.5	-7.7
0.400	-185.5	-7.6
0.500	-185.6	-7.6

Strain at the strand level (midspan) =	-360.9	in/inx10^6
Elastic shortening loss =	-10.287	ksi
Stress of prestress strand =	189.546	ksi
% initial loss =	6.40	%

Creep coefficients, Φ(t, 3):

Model	Day							
	3.01	4	7	28	115	365	10950	36500
AASHTO	0.003	0.050	0.107	0.284	0.616	0.959	1.425	1.460
ACI	0.009	0.126	0.259	0.565	0.871	1.072	1.334	1.359
CEB-FIP	0.070	0.280	0.423	0.725	1.089	1.405	1.820	1.839
B3	0.000	0.362	0.505	0.728	0.949	1.131	1.722	1.967

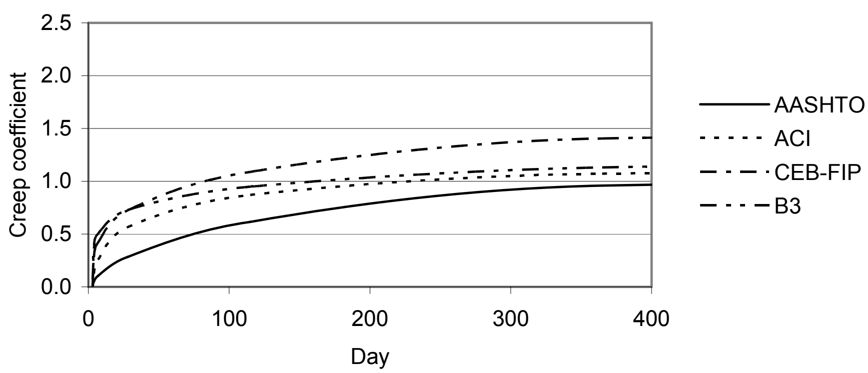

Shrinkage, $\varepsilon_{sh}(t)$:

Model	Day							
	3.01	4	7	28	115	365	10950	36500
AASHTO	0.000007	0.000010	0.000017	0.000062	0.000174	0.000283	0.000388	0.000391
ACI	0.000000	0.000007	0.000026	0.000120	0.000258	0.000334	0.000383	0.000384
CEB-FIP	0.000034	0.000047	0.000066	0.000123	0.000202	0.000283	0.000503	0.000523
B3	0.000000	0.000004	0.000014	0.000087	0.000312	0.000430	0.000432	0.000432

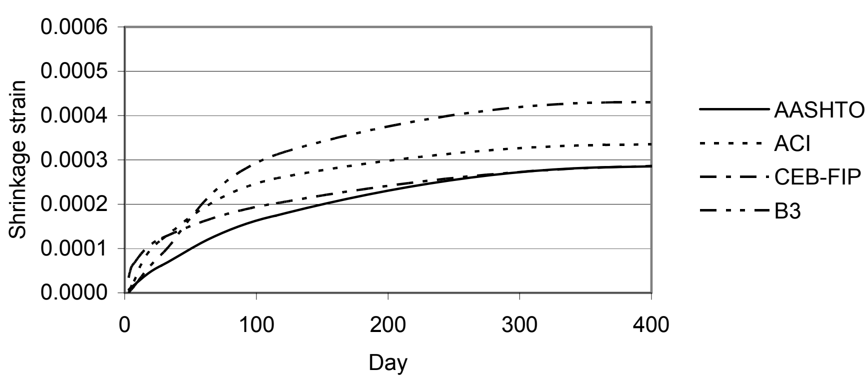

Aging coefficients, χ(t, 3):

Model	Day							
	3.01	4	7	28	115	365	10950	36500
AASHTO	N/A	N/A	N/A	N/A	N/A	N/A	N/A	N/A
ACI	0.710	0.658	0.642	0.621	0.604	0.594	0.567	0.558
CEB-FIP	0.808	0.777	0.769	0.648	0.573	0.537	0.478	0.475
B3	0.731	0.702	0.693	0.682	0.672	0.660	0.614	0.597

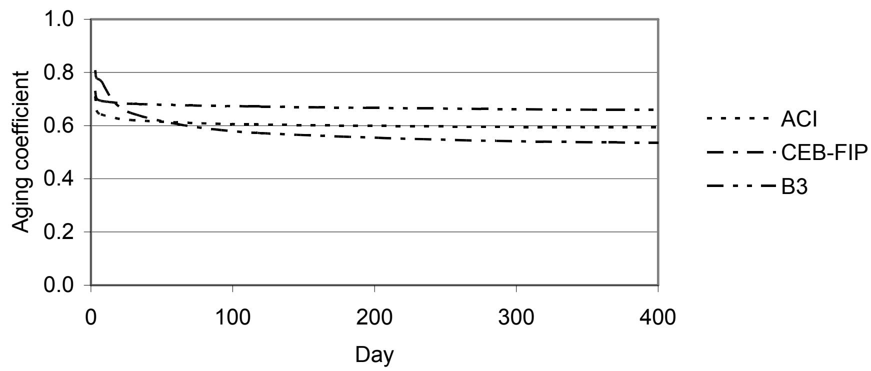

Use engineering recommendation model: **ACI**

Time-dependent restrained forces at t = 115 days (ΔN and ΔM):

Φ(115,3) =	0.871		χ(115,3) =	0.604	
Ec(115,3) =	3032.5	ksi	*(Age-adjusted elastic modulus)*		
εsh(115) =	0.000258		λ =	0.702	
Ω =	0.066		χ_r =	0.821	
A (mid) =	1056.1	in^2	B (mid) =	1002.0	in^3
I (mid) =	544435	in^4			

x/L	Creep		Shrinkage		Relaxation		Total	
	ΔN	ΔM	ΔN	ΔM	ΔN	ΔM	ΔN	ΔM
0.000	0.0	0.0	792.5	0.0	0.0	0.0	792.5	0.0
0.100	401.4	8536.5	792.5	0.0	-6.8	-152.5	1187.1	8384.0
0.225	401.8	8159.5	792.5	0.0	-6.8	-152.5	1187.5	8007.0
0.275	496.1	10614.6	792.5	0.0	-8.6	-198.7	1280.0	10415.9
0.300	496.1	10567.6	792.5	0.0	-8.6	-198.7	1280.1	10368.9
0.400	496.3	10434.8	792.5	0.0	-8.6	-198.7	1280.3	10236.1
0.500	496.3	10390.6	792.5	0.0	-8.6	-198.7	1280.3	10191.9

Strains and curvatures at t = 115 days

x/L	$\Delta\varepsilon_o(t)$	Δψ(t)
	$in/inx10^6$	$1/inx10^6$
0.000	-258.0	0.0
0.100	-370.3	-4.6
0.225	-370.6	-4.4
0.275	-394.4	-5.6
0.300	-394.4	-5.6
0.400	-394.6	-5.5
0.500	-394.6	-5.4

Strain inc. at the strand level (mid) =	-521.1	$in/inx10^6$
Time-dependent inc. losses =	-14.852	ksi
Stress of prestress strand =	174.694	ksi
% losses =	13.73	%

Strains and curvatures - Summary for simple span case at x/L = 0.500

Strain, $\varepsilon_o(t)$ using ACI, CEB-FIP, and B3 respectively

Day								
3	3.01	4	7	28	115	365	10950	36500
-185.6	-187.2	-214.1	-255.4	-397.8	-580.2	-684.8	-771.2	-775.8
-183.1	-228.5	-276.8	-319.0	-423.3	-557.8	-685.7	-959.7	-981.4
-185.6	-185.6	-251.7	-285.8	-392.1	-643.3	-784.6	-876.4	-913.2

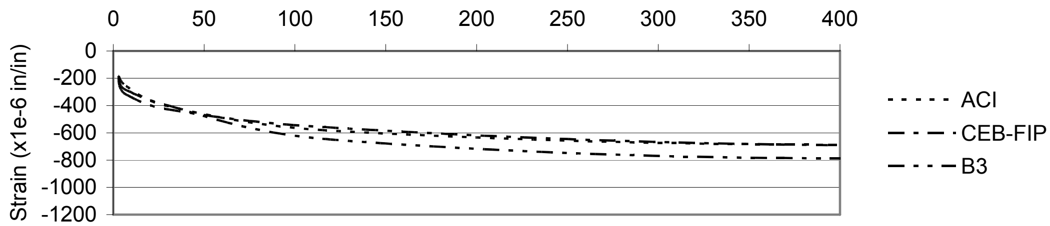

Curvature, ψ(t) using ACI, CEB-FIP, and B3 respectively

Day								
3	3.01	4	7	28	115	365	10950	36500
-7.6	-7.6	-8.4	-9.3	-11.2	-13.0	-14.1	-15.6	-15.7
-7.5	-7.9	-9.3	-10.2	-12.1	-14.4	-16.2	-18.3	-18.4
-7.6	-7.6	-10.1	-11.0	-12.4	-13.4	-14.3	-17.8	-19.3

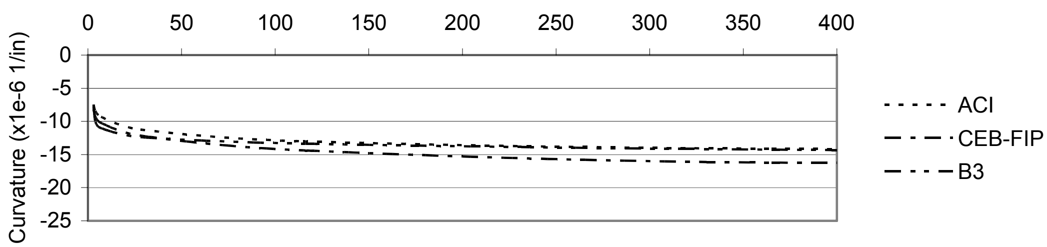

Stress of prestress strand using ACI, CEB-FIP, and B3 respectively

Day								
3	3.01	4	7	28	115	365	10950	36500
189.5	189.5	188.2	186.4	181.1	174.7	171.0	167.5	167.3
189.7	188.1	185.8	184.0	179.7	174.4	169.6	160.3	159.7
189.5	189.5	186.0	184.4	180.5	172.7	168.0	163.1	161.1

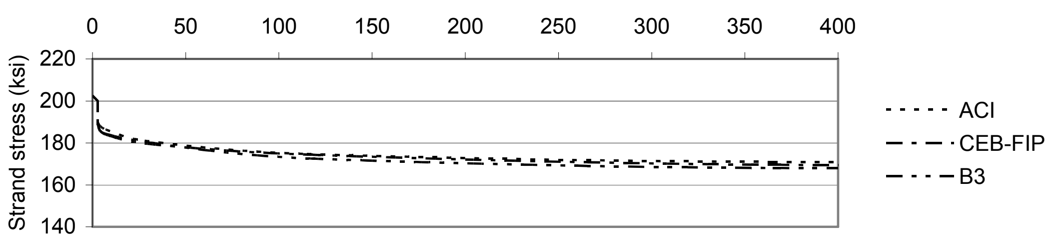

% prestress losses using ACI, CEB-FIP, and B3 respectively

Day								
3	3.01	4	7	28	115	365	10950	36500
6.4	6.4	7.1	8.0	10.6	13.7	15.6	17.3	17.4
6.3	7.1	8.3	9.2	11.2	13.9	16.3	20.8	21.1
6.4	6.4	8.2	8.9	10.9	14.7	17.0	19.5	20.5

Effect of concrete deck placed at t = 115 days

Section Properties at t = 115 days when deck is not hardened yet (midspan):

	Properties of area			Properties of transformed area		
	A	B	I	A^*E/E_{ref}	B^*E/E_{ref}	I^*E/E_{ref}
Girder	1013	0	521162.6	1013	0	521162.6
Strand	4.59	106.6	2476.3	25.7	596.0	13842.8
				1038.7	596.0	535005.4

Applied forces due to concrete deck placement:

x/L	A	B	I	ΔN (kips)	ΔM (kips-in)
0.000	1013.0	0.0	521162.6	0.0	0.0
0.100	1033.5	457.5	531358.6	0.0	738.5
0.225	1033.5	457.5	531358.6	0.0	1432.4
0.275	1038.7	596.0	535005.4	0.0	1636.0
0.300	1038.7	596.0	535005.4	0.0	1723.1
0.400	1038.7	596.0	535005.4	0.0	1969.3
0.500	1038.7	596.0	535005.4	0.0	2051.4

Strains and curvatures at deck placement:

x/L	$\Delta\varepsilon_o$ in/inx10^6	$\Delta\psi$ 1/inx10^6
0.000	0.0	0.0
0.100	-0.1	0.3
0.225	-0.2	0.5
0.275	-0.3	0.6
0.300	-0.4	0.6
0.400	-0.4	0.7
0.500	-0.4	0.8

Strain at the strand level (midspan) =	17.0	in/inx10^6
Elastic stress gain =	0.486	ksi
Stress of prestress strand =	175.180	ksi
% losses =	13.49	%

Creep coefficients of girder, Φ(t, 115):

Model	Day							
	115.01	116	118	122	143	365	10950	36500
ACI	0.006	0.087	0.156	0.234	0.409	0.705	0.927	0.945
CEB-FIP	0.033	0.132	0.184	0.237	0.355	0.627	0.896	0.907
B3	0.000	0.152	0.203	0.249	0.339	0.521	0.827	0.949

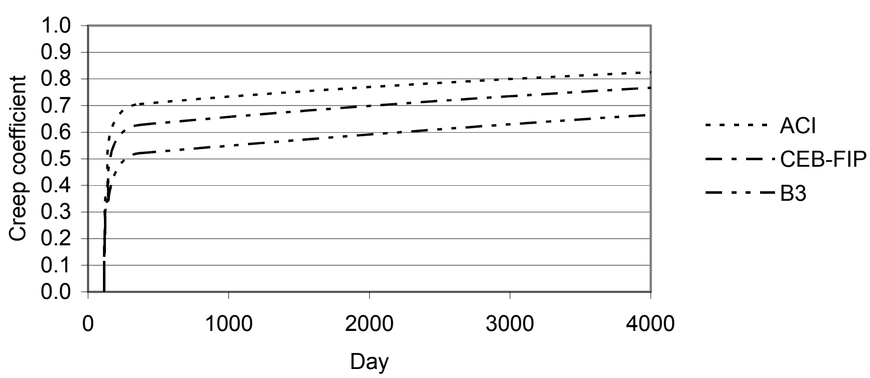

Aging coefficients of girder, χ(t, 115):

Model	Day							
	115.01	116	118	122	143	365	10950	36500
ACI	0.547	0.725	0.768	0.801	0.854	0.914	0.919	0.913
CEB-FIP	0.812	0.860	0.899	0.908	0.908	0.878	0.816	0.814
B3	0.549	0.737	0.782	0.816	0.873	0.934	0.931	0.921

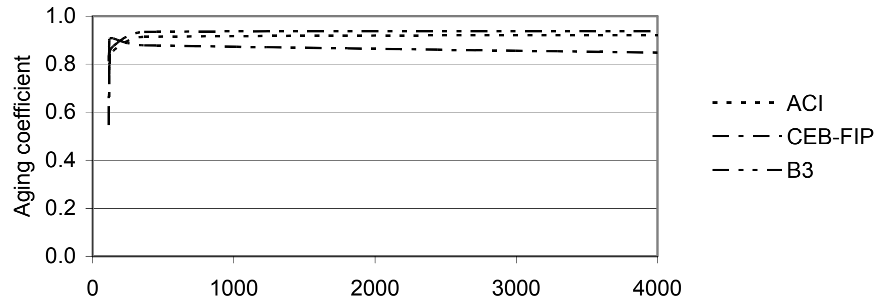

Creep coefficients of concrete deck slab, Φ(t, 3):

Model	Day							
	3.01	4	6	10	31	253	10838	36388
ACI	0.008	0.115	0.205	0.308	0.538	0.928	1.220	1.243
CEB-FIP	0.092	0.367	0.510	0.656	0.989	1.794	2.809	2.860
B3	0.000	0.360	0.470	0.563	0.731	1.049	1.703	1.950

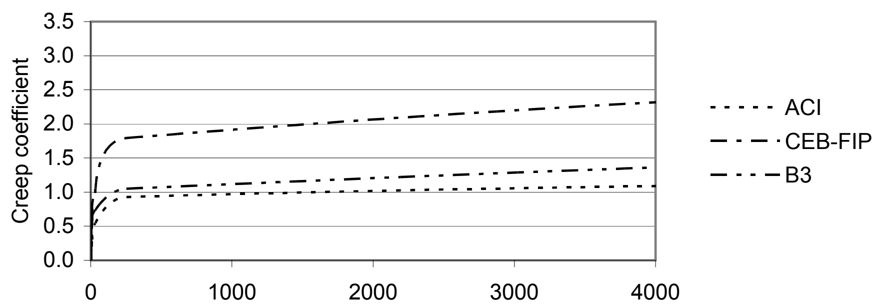

Aging coefficients of concrete deck slab, χ(t, 3):

Model	Day							
	3.01	4	6	10	31	253	10838	36388
ACI	0.695	0.630	0.615	0.603	0.583	0.558	0.530	0.522
CEB-FIP	0.809	0.794	0.809	0.781	0.699	0.571	0.644	0.650
B3	0.731	0.701	0.694	0.688	0.679	0.662	0.612	0.595

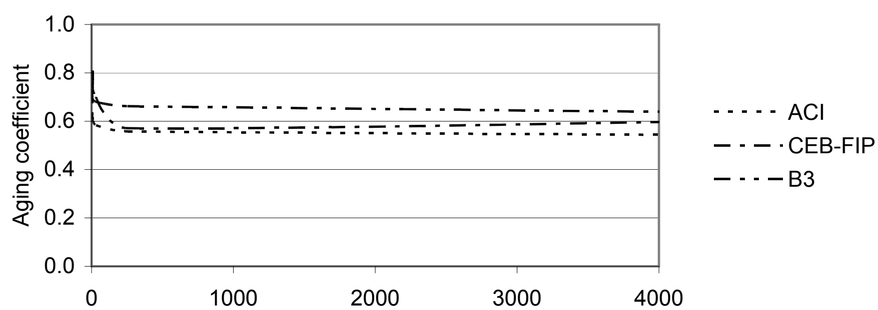

Shrinkage of concrete deck slab, $\varepsilon_{sh}(t)$:

Model	Day							
	3.01	4	6	10	31	253	10838	36388
ACI	0.000000	0.000004	0.000012	0.000025	0.000075	0.000182	0.000221	0.000222
CEB-FIP	0.000016	0.000024	0.000031	0.000042	0.000070	0.000155	0.000502	0.000584
B3	0.000000	0.000001	0.000004	0.000009	0.000037	0.000280	0.000432	0.000432

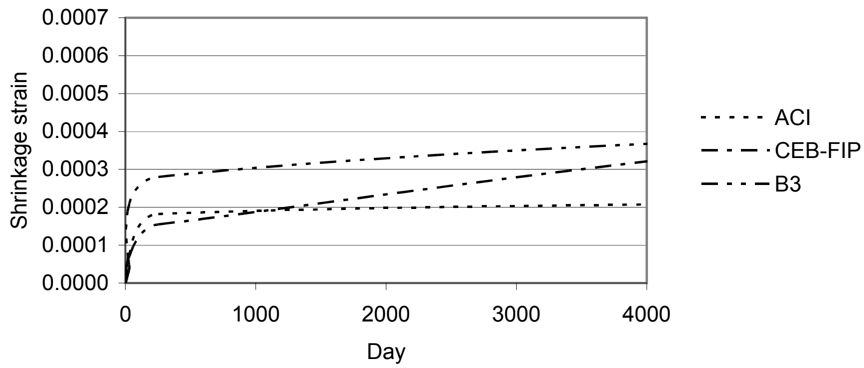

Time-dependent effect at t = 36500 days:

Girder:

$\Delta\Phi(36500,3)$ = 0.488
$\Delta\varepsilon sh(36500)$ = 0.000126
$\Phi(36500,115)$ = 0.945
$\chi(36500,115)$ = 0.913
Ec(36500,115) = 2736.7 ksi

Slab:

$\Phi(36388,3)$ = 1.243
$\chi(36388,3)$ = 0.522
Ec(36388,3) = 1985.0 ksi
$\varepsilon sh(36388)$ = 0.000222

Strand:

λ = 0.702
Ω = 0.080
χ_r = 0.789

Stresses and curvatures prior to composite action

x/L	Restrained		Time-dependence		Change in stresses			
	σ_{top}	σ_{bot}	σ_{top}	σ_{bot}	$\Delta\sigma_{top}$	$\Delta\sigma_{bot}$	$\Delta\sigma$	$\Delta\psi$
0.000	0.782	0.782	-0.782	-0.782	0.000	0.000	0.000	0.000
0.100	0.670	1.702	-0.689	-1.569	-0.019	0.133	0.056	0.002
0.225	0.693	1.679	-0.712	-1.548	-0.019	0.131	0.055	0.002
0.275	0.640	1.923	-0.670	-1.737	-0.031	0.186	0.076	0.003
0.300	0.643	1.920	-0.673	-1.734	-0.031	0.186	0.076	0.003
0.400	0.651	1.912	-0.681	-1.727	-0.030	0.185	0.076	0.003
0.500	0.653	1.909	-0.684	-1.724	-0.030	0.185	0.076	0.003

Section Properties at t = 36500 days when composite action starts (midspan):

	Properties of area			Properties of transformed area		
	A	B	I	A^*E/E_{ref}	B^*E/E_{ref}	I^*E/E_{ref}
Girder	1013	0	521162.6	1013	0	521162.6
Strand	4.59	106.6	2476.3	47.8	1110.3	25788.1
Deck	984	-36052	1326982	714	-26149	962481
Rebars	20.76	-745.9	26793.7	220.0	-7904.0	283926.7
				1994	-32943	1793359

Note *: neglected the duration of 3-day concrete deck hardening*

Time-dependent restrained forces at t = 36500 days (ΔN and ΔM):

x/L	Creep		Shrinkage		Relaxation		Total	
	ΔN	ΔM	ΔN	ΔM	ΔN	ΔM	ΔN	ΔM
0.000	0.0	0.0	783.5	-15898.7	0.0	0.0	783.5	-15898.7
0.100	187.2	3591.0	783.5	-15898.7	-10.4	-231.7	960.3	-12539.4
0.225	187.9	3058.1	783.5	-15898.7	-10.4	-231.7	961.0	-13072.3
0.275	229.7	4047.0	783.5	-15898.7	-13.0	-301.8	1000.3	-12153.5
0.300	229.8	3980.7	783.5	-15898.7	-13.0	-301.8	1000.4	-12219.9
0.400	230.1	3793.3	783.5	-15898.7	-13.0	-301.8	1000.6	-12407.2
0.500	230.2	3730.8	783.5	-15898.7	-13.0	-301.8	1000.7	-12469.7

Strains and curvatures at t = 36500 days

x/L	$\Delta\varepsilon_o(t)$	$\Delta\psi(t)$
	in/inx10^6	1/inx10^6
0.000	-135.1	0.7
0.100	-194.3	-1.0
0.225	-191.8	-0.9
0.275	-204.4	-1.3
0.300	-204.1	-1.3
0.400	-203.2	-1.2
0.500	-203.0	-1.2

Strain inc. at the strand level (mid) =	-230.5	in/inx10^6
Time-dependent inc. losses =	-6.570	ksi
Stress of prestress strand =	168.610	ksi
% losses =	16.73	%

Time-dependent strain at top fiber along the length of the girder:

x/L	Day							
	115.01	116	118	122	143	365	10950	36500
0.000	0.0	-2.7	-7.7	-16.8	-50.3	-130.7	-162.3	-163.1
0.100	0.0	-2.9	-8.2	-17.4	-50.8	-126.6	-151.3	-151.5
0.225	-0.1	-3.2	-8.6	-18.1	-52.1	-129.1	-155.1	-155.4
0.275	-0.1	-3.3	-8.7	-18.2	-52.1	-127.9	-152.0	-152.1
0.300	-0.1	-3.3	-8.8	-18.3	-52.3	-128.2	-152.4	-152.6
0.400	-0.1	-3.4	-9.0	-18.6	-52.8	-129.1	-153.7	-153.9
0.500	-0.1	-3.4	-9.0	-18.7	-52.9	-129.4	-154.2	-154.4

Time-dependent strain at bottom fiber along the length of the girder:

x/L	Day							
	115.01	116	118	122	143	365	10950	36500
0.000	0.0	0.5	1.3	2.7	5.2	-57.6	-111.7	-113.3
0.100	0.0	0.8	1.5	2.5	1.4	-104.4	-221.1	-227.7
0.225	0.1	1.2	2.4	3.7	3.7	-99.6	-213.9	-220.3
0.275	0.1	1.3	2.4	3.7	2.8	-110.0	-237.7	-245.2
0.300	0.1	1.3	2.5	3.8	3.1	-109.4	-236.9	-244.3
0.400	0.1	1.5	2.8	4.3	3.9	-107.8	-234.4	-241.8
0.500	0.1	1.6	2.9	4.4	4.1	-107.2	-233.6	-240.9

Strains and curvatures - Summary for simple span case at x/L = 0.500

Strain, $\varepsilon_o(t)$ using ACI, CEB-FIP, and B3 respectively

Day

115	115.01	116	118	122	143	365	10950	36500
0.0	0.0	-0.6	-2.3	-5.7	-20.9	-117.0	-198.8	-203.0
0.0	-2.6	-3.8	-5.7	-9.0	-22.5	-135.8	-414.0	-442.4
0.0	0.0	0.0	-1.2	-3.7	-17.8	-160.5	-277.4	-315.1

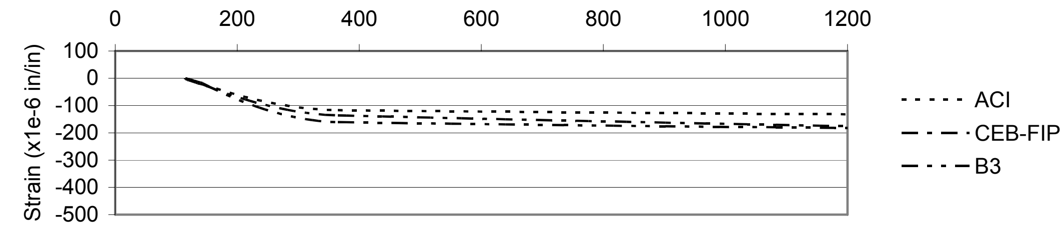

Curvature, ψ(t) using ACI, CEB-FIP, and B3 respectively

Day

115	115.01	116	118	122	143	365	10950	36500
0.0	0.0	0.1	0.2	0.3	0.8	0.3	-1.1	-1.2
0.0	0.2	0.3	0.4	0.5	0.6	-0.8	-2.4	-2.0
0.0	0.0	0.1	0.1	0.1	0.3	0.7	-0.6	-1.8

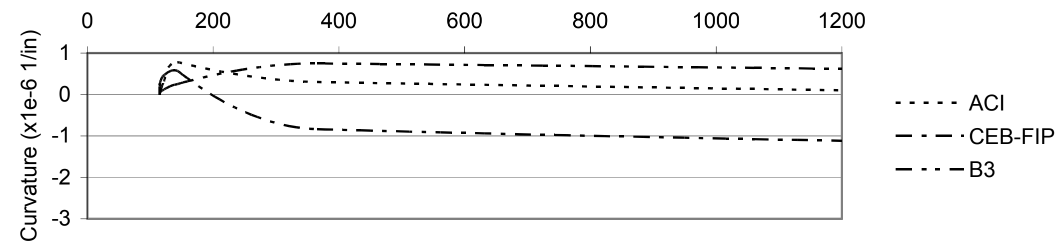

Stress of prestress strand using ACI, CEB-FIP, and B3 respectively

Day

115	115.01	116	118	122	143	365	10950	36500
175.2	175.2	175.2	175.2	175.2	175.1	172.0	168.8	168.6
174.9	174.9	175.0	175.0	174.9	174.6	170.4	161.5	160.9
173.1	173.1	173.2	173.2	173.1	172.8	169.1	164.8	162.9

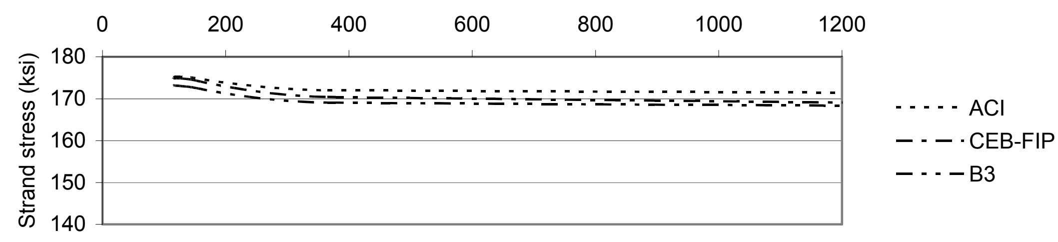

% prestress losses using ACI, CEB-FIP, and B3 respectively

Day

115	115.01	116	118	122	143	365	10950	36500
13.5	13.5	13.5	13.5	13.5	13.5	15.0	16.6	16.7
13.6	13.6	13.6	13.6	13.6	13.8	15.8	20.3	20.5
14.5	14.5	14.5	14.5	14.5	14.7	16.5	18.6	19.5

End of Calculation

Three samples of time-dependent strains with respect to the time-line (118, 365, and 36,500 days) at the top fiber of interior girders are shown in Figure B-11.

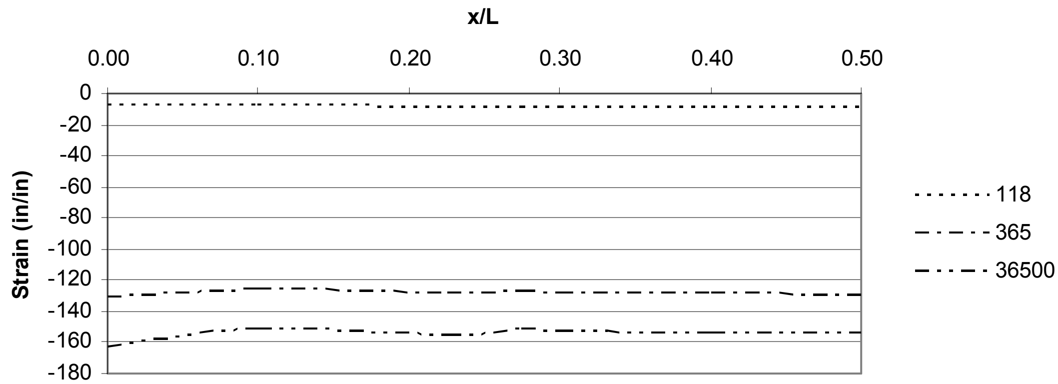

Figure B-11: Time-Dependent Strains at Top Fiber (Bridge 203 – Span 3 – Ext. Girder)

Three samples of time-dependent strains with respect to the time-line (118, 365, and 36,500 days) at the bottom fiber of interior girders are shown in Figure B-12

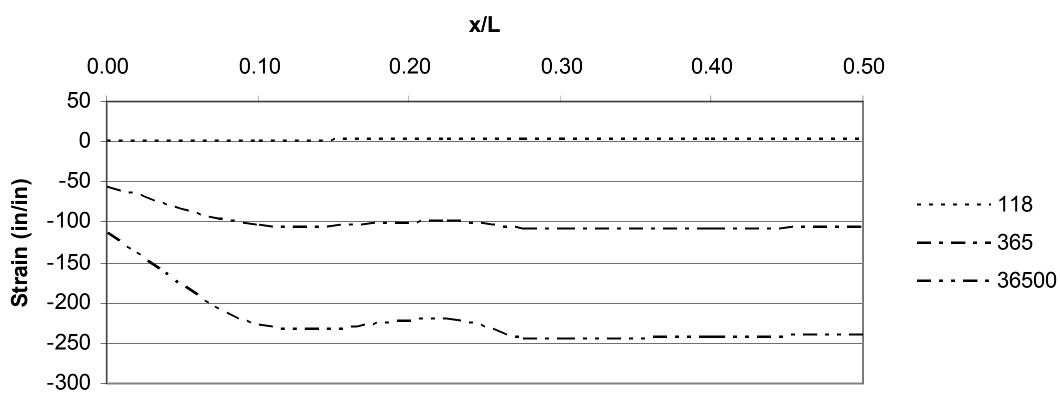

Figure B-12: Time-Dependent Strains at Bottom Fiber
(Bridge 203 – Span 3 – Ext. Girder)

B.2 Bridge 211

Interior Girder

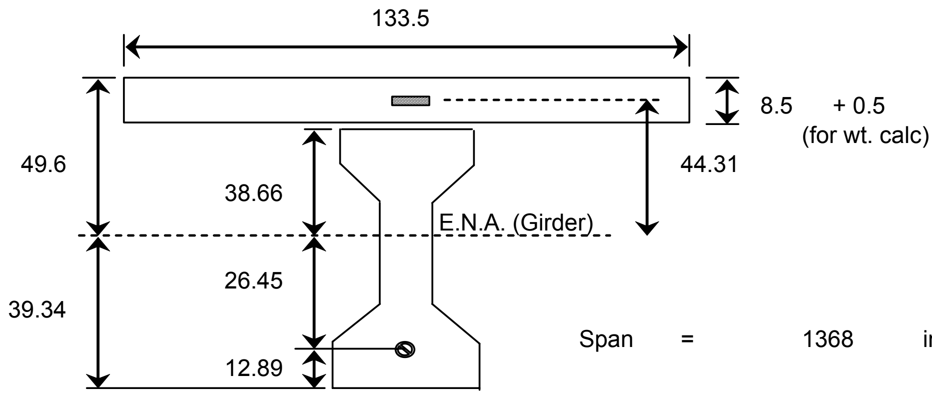

Span = 1368 in

Concrete properties:

Girder:

A	=	1133	in^2
I	=	898985	in^4
$E_c(3)$	=	4628.4	ksi
$E_c(28)$	=	5098.2	ksi

Slab:

$E_c(3)$	=	3272.8	ksi
$E_c(28)$	=	3605.0	ksi

Prestress strand properties:

A	=	0.153	in^2
No.	=	70	
Jacking	=	30.98	k/strand
E_{ps}	=	28500	ksi
$A_{s\text{-}slab}$	=	6.12	in^2
E_s	=	29000	ksi

Section Properties at t = 3 days (midspan):

	Properties of area			Properties of transformed area		
	A	B	I	$A*E/E_{ref}$	$B*E/E_{ref}$	$I*E/E_{ref}$
Girder	1133	0	898985	1133	0	898985
Strand	10.71	283.3	7492.7	65.9	1744.3	46137.7
				1198.9	1744.3	945122.7

Relaxation loss from t = 0 to 3 days:

Δf_{RE}	=	-2.663	ksi
f_{pi}	=	199.820	ksi

Applied forces at transfer:

x/L	e (in)	No. of strands	A	B	I	N (kips)	M (kips-in)
0.000	0.000	0	1133.0	0.0	898985	0.0	0.0
0.044	29.273	54	1183.9	1489.2	942580	-1650.9	-44468.0
0.088	29.516	58	1187.6	1612.8	946590	-1773.2	-44973.5
0.132	30.024	64	1193.3	1810.3	953338	-1956.6	-48230.5
0.300	26.450	70	1198.9	1744.3	945123	-2140.1	-37279.2
0.400	26.450	70	1198.9	1744.3	945123	-2140.1	-34518.3
0.500	26.450	70	1198.9	1744.3	945123	-2140.1	-33598.0

Strains and curvatures at transfer:

x/L	ε_o in/inx10^6	ψ 1/inx10^6
0.000	0.0	0.0
0.044	-289.0	-9.7
0.088	-309.4	-9.7
0.132	-338.7	-10.3
0.300	-374.3	-7.8
0.400	-375.2	-7.2
0.500	-375.5	-7.0

Strain at the strand level (midspan) =	-560.3	in/inx10^6
Elastic shortening loss =	-15.969	ksi
Stress of prestress strand =	183.852	ksi
% initial loss =	9.20	%

Creep coefficients, Φ(t, 3):

Model	Day							
	3.01	4	7	28	268	365	10950	36500
AASHTO	0.003	0.051	0.109	0.289	0.878	0.965	1.429	1.463
ACI	0.009	0.126	0.259	0.566	1.027	1.074	1.337	1.363
CEB-FIP	0.071	0.281	0.425	0.727	1.327	1.408	1.822	1.840
B3	0.000	0.362	0.505	0.728	1.084	1.132	1.722	1.967

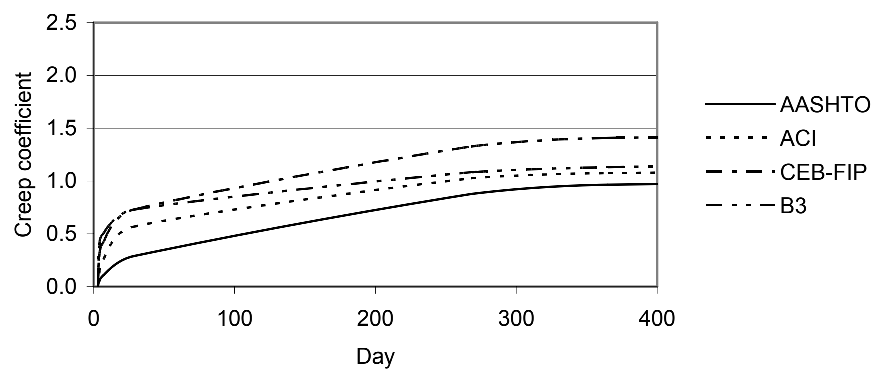

Shrinkage, $\varepsilon_{sh}(t)$:

Model	Day							
	3.01	4	7	28	268	365	10950	36500
AASHTO	0.000008	0.000010	0.000017	0.000063	0.000261	0.000287	0.000391	0.000394
ACI	0.000000	0.000007	0.000026	0.000121	0.000321	0.000336	0.000385	0.000386
CEB-FIP	0.000034	0.000047	0.000067	0.000124	0.000261	0.000285	0.000503	0.000523
B3	0.000000	0.000004	0.000014	0.000089	0.000422	0.000430	0.000432	0.000432

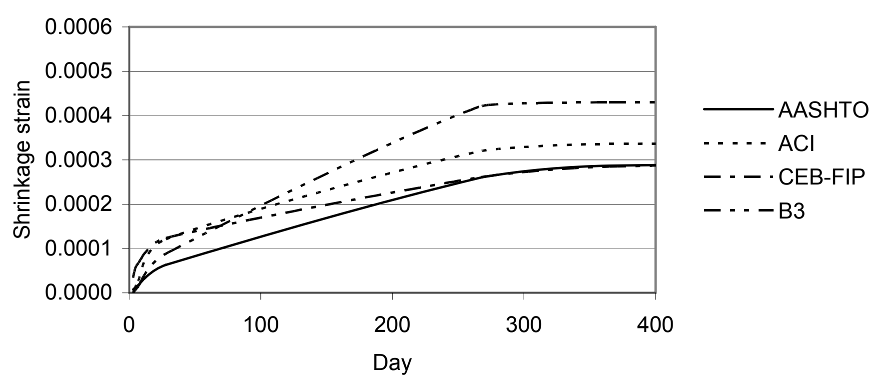

Aging coefficients, χ(t, 3):

Model	Day							
	3.01	4	7	28	268	365	10950	36500
AASHTO	N/A	N/A	N/A	N/A	N/A	N/A	N/A	N/A
ACI	0.710	0.658	0.643	0.622	0.598	0.595	0.568	0.559
CEB-FIP	0.808	0.777	0.769	0.648	0.521	0.518	0.467	0.465
B3	0.731	0.702	0.693	0.682	0.663	0.660	0.614	0.597

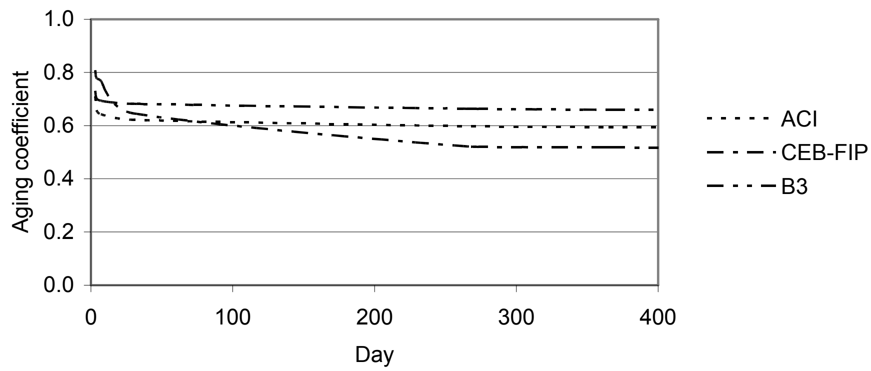

Use engineering recommendation model: **ACI**

Time-dependent restrained forces at t = 268 days (ΔN and ΔM):

Φ(268,3)	=	1.027		χ(268,3)	=	0.598
Ec(268,3)	=	2868.2	ksi	*(Age-adjusted elastic modulus)*		
εsh(268)	=	0.000321		λ	=	0.681
Ω	=	0.101		χ_r	=	0.732
A (mid)	=	1239.4	in^2	B (mid)	=	2814.9 in^3
I (mid)	=	973438	in^4			

x/L	Creep		Shrinkage		Relaxation		Total	
	ΔN	ΔM	ΔN	ΔM	ΔN	ΔM	ΔN	ΔM
0.000	0.0	0.0	1041.6	0.0	0.0	0.0	1041.6	0.0
0.044	964.3	25773.5	1041.6	0.0	-16.9	-495.0	1989.0	25278.5
0.088	1032.1	25778.2	1041.6	0.0	-18.2	-536.1	2055.5	25242.1
0.132	1129.9	27232.8	1041.6	0.0	-20.0	-601.7	2151.4	26631.1
0.300	1248.6	20731.0	1041.6	0.0	-21.9	-579.8	2268.3	20151.2
0.400	1251.7	19055.7	1041.6	0.0	-21.9	-579.8	2271.4	18476.0
0.500	1252.7	18497.3	1041.6	0.0	-21.9	-579.8	2272.4	17917.6

Strains and curvatures at t = 268 days

x/L	$\Delta\varepsilon_o(t)$	$\Delta\psi(t)$
	in/inx10^6	1/inx10^6
0.000	-320.5	0.0
0.044	-555.5	-7.7
0.088	-570.9	-7.5
0.132	-591.5	-7.7
0.300	-625.8	-5.4
0.400	-628.0	-4.8
0.500	-628.8	-4.6

Strain inc. at the strand level (mid) =	-750.4	in/inx10^6
Time-dependent inc. losses =	-21.388	ksi
Stress of prestress strand =	162.464	ksi
% losses =	19.76	%

Strains and curvatures - Summary for simple span case at x/L = 0.500

Strain, $\varepsilon_o(t)$ using ACI, CEB-FIP, and B3 respectively

Day

3	3.01	4	7	28	268	365	10950	36500
-375.5	-378.6	-425.1	-487.7	-676.2	-1004.3	-1032.9	-1154.6	-1162.4
-370.7	-427.0	-509.2	-573.5	-722.8	-1036.7	-1082.5	-1405.9	-1428.5
-375.5	-375.5	-501.4	-558.0	-697.3	-1111.7	-1133.3	-1306.3	-1376.3

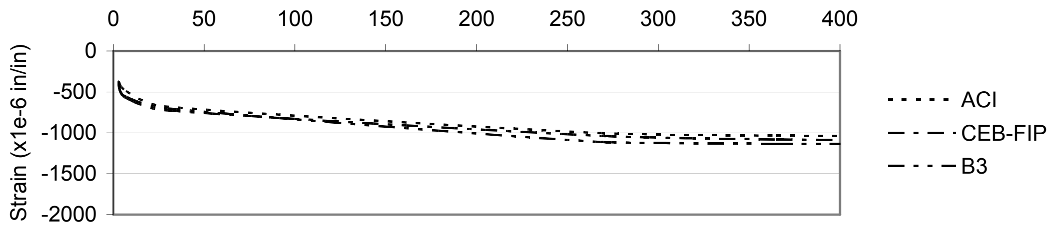

Curvature, ψ(t) using ACI, CEB-FIP, and B3 respectively

Day

3	3.01	4	7	28	268	365	10950	36500
-7.0	-7.0	-7.7	-8.4	-9.8	-11.6	-11.8	-12.7	-12.8
-6.9	-7.3	-8.4	-9.1	-10.5	-13.2	-13.5	-14.7	-14.7
-7.0	-7.0	-9.1	-9.8	-10.7	-11.5	-11.7	-14.1	-15.1

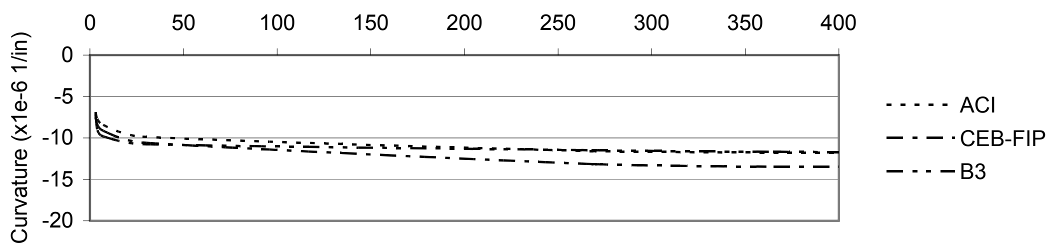

Stress of prestress strand using ACI, CEB-FIP, and B3 respectively

Day

3	3.01	4	7	28	268	365	10950	36500
183.9	183.7	181.9	179.6	173.1	162.5	161.5	157.3	157.0
184.1	182.2	179.0	176.6	171.3	160.4	158.8	148.7	148.0
183.9	183.9	178.7	176.5	171.9	159.5	158.7	152.0	149.2

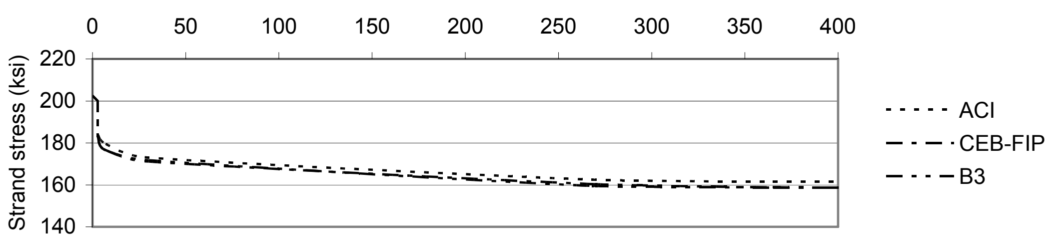

% prestress losses using ACI, CEB-FIP, and B3 respectively

Day

3	3.01	4	7	28	268	365	10950	36500
9.2	9.3	10.2	11.3	14.5	19.8	20.2	22.3	22.4
9.1	10.0	11.6	12.8	15.4	20.8	21.6	26.6	26.9
9.2	9.2	11.7	12.8	15.1	21.2	21.6	24.9	26.3

Effect of concrete deck placed at t = 268 days

Section Properties at t = 268 days when deck is not hardened yet (midspan):

	Properties of area			Properties of transformed area		
	A	B	I	$A*E/E_{ref}$	$B*E/E_{ref}$	$I*E/E_{ref}$
Girder	1133	0	898985	1133	0	898985
Strand	10.71	283.3	7492.7	59.9	1583.6	41885.7
				1192.9	1583.6	940870.7

Applied forces due to concrete deck placement:

x/L	A	B	I	ΔN (kips)	ΔM (kips-in)
0.000	1133.0	0.0	898985.0	0.0	0.0
0.044	1179.2	1352.0	938562.2	0.0	4092.6
0.088	1182.6	1464.2	942202.5	0.0	7809.8
0.132	1187.7	1643.5	948328.9	0.0	11151.4
0.300	1192.9	1583.6	940870.7	0.0	20494.3
0.400	1192.9	1583.6	940870.7	0.0	23422.0
0.500	1192.9	1583.6	940870.7	0.0	24398.0

Strains and curvatures at deck placement:

x/L	$\Delta\varepsilon_o$ in/inx10^6	$\Delta\psi$ 1/inx10^6
0.000	0.0	0.0
0.044	-1.0	0.9
0.088	-2.0	1.6
0.132	-3.2	2.3
0.300	-5.7	4.3
0.400	-6.5	4.9
0.500	-6.8	5.1

Strain at the strand level (midspan) =	128.1	in/inx10^6
Elastic stress gain =	3.650	ksi
Stress of prestress strand =	166.114	ksi
% losses =	17.96	%

Creep coefficients of girder, Φ(t, 268):

Model	Day							
	268.01	269	271	275	298	365	10950	36500
ACI	0.006	0.081	0.145	0.218	0.389	0.544	0.861	0.878
CEB-FIP	0.029	0.114	0.158	0.203	0.311	0.429	0.764	0.772
B3	0.000	0.093	0.123	0.148	0.197	0.244	0.480	0.560

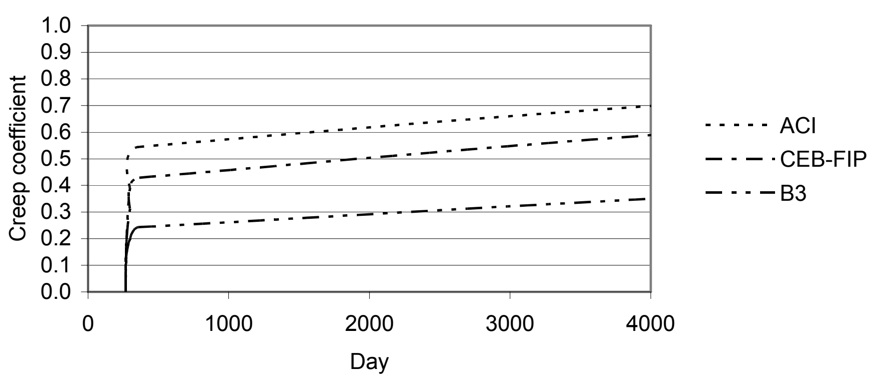

Aging coefficients of girder, χ(t, 268):

Model	Day							
	268.01	269	271	275	298	365	10950	36500
ACI	0.528	0.719	0.764	0.800	0.860	0.908	0.941	0.938
CEB-FIP	0.812	0.860	0.899	0.909	0.913	0.919	0.817	0.816
B3	0.533	0.731	0.778	0.815	0.877	0.928	0.945	0.936

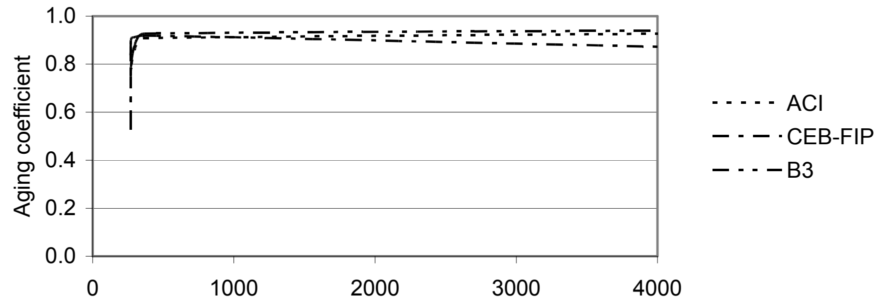

Creep coefficients of concrete deck slab, Φ(t, 3):

Model	Day							
	3.01	4	6	10	33	100	10685	36235
ACI	0.008	0.115	0.205	0.308	0.551	0.771	1.219	1.243
CEB-FIP	0.092	0.367	0.510	0.656	1.009	1.406	2.809	2.860
B3	0.000	0.360	0.470	0.563	0.740	0.902	1.701	1.949

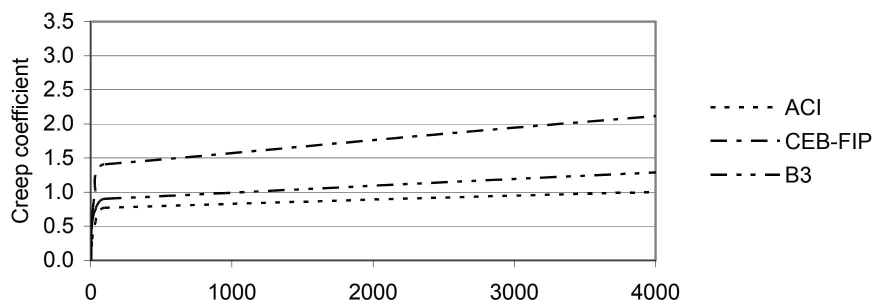

Aging coefficients of concrete deck slab, χ(t, 3):

Model	Day							
	3.01	4	6	10	33	100	10685	36235
ACI	0.695	0.630	0.615	0.603	0.582	0.566	0.530	0.522
CEB-FIP	0.809	0.794	0.809	0.781	0.694	0.634	0.644	0.650
B3	0.731	0.701	0.694	0.688	0.679	0.671	0.613	0.595

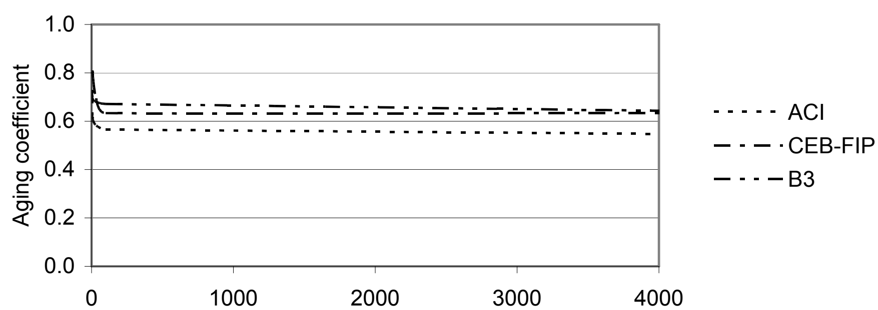

Shrinkage of concrete deck slab, $\varepsilon_{sh}(t)$:

Model	Day							
	3.01	4	6	10	33	100	10685	36235
ACI	0.000000	0.000004	0.000012	0.000025	0.000079	0.000142	0.000221	0.000222
CEB-FIP	0.000016	0.000024	0.000031	0.000042	0.000072	0.000111	0.000501	0.000584
B3	0.000000	0.000001	0.000004	0.000009	0.000040	0.000126	0.000432	0.000432

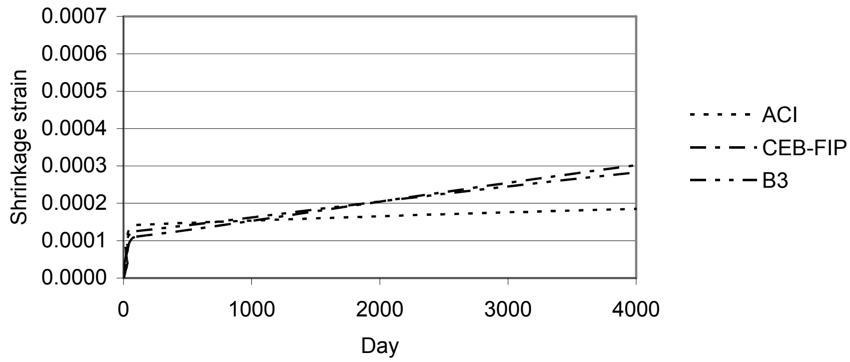

Time-dependent effect at t = 36500 days:

Girder:			*Slab:*		
$\Delta\Phi(36500,3)$ =	0.336		$\Phi(36235,3)$ =	1.243	
$\Delta\varepsilon sh(36500)$ =	6.59E-05		$\chi(36235,3)$ =	0.522	
$\Phi(36500,268)$ =	0.878		$Ec(36235,3)$ =	1984.9	ksi
$\chi(36500,268)$ =	0.938		$\varepsilon sh(36235)$ =	0.000222	
$Ec(36500,268)$ =	2795.4	ksi			
Strand:					
λ =	0.681		Ω =	0.079	
χ_r =	0.784				

Stresses and curvatures prior to composite action

x/L	Restrained		Time-dependence		Change in stresses			
	σ_{top}	σ_{bot}	σ_{top}	σ_{bot}	$\Delta\sigma_{top}$	$\Delta\sigma_{bot}$	$\Delta\sigma$	$\Delta\psi$
0.000	0.919	0.919	-0.919	-0.919	0.000	0.000	0.000	0.000
0.044	0.662	2.898	-0.738	-2.464	-0.076	0.435	0.177	0.007
0.088	0.722	2.958	-0.806	-2.483	-0.084	0.475	0.193	0.007
0.132	0.745	3.108	-0.847	-2.561	-0.102	0.548	0.220	0.008
0.300	1.130	2.929	-1.195	-2.405	-0.065	0.523	0.226	0.008
0.400	1.205	2.858	-1.269	-2.343	-0.064	0.515	0.223	0.007
0.500	1.230	2.834	-1.293	-2.322	-0.064	0.512	0.222	0.007

Section Properties at t = 36500 days when composite action starts (midspan):

	Properties of area			Properties of transformed area		
	A	B	I	A^*E/E_{ref}	B^*E/E_{ref}	I^*E/E_{ref}
Girder	1133	0	898985	1133	0	898985
Strand	10.71	283.3	7492.7	109.2	2888.1	76390.0
Deck	1135	-51461	2340585	806	-36541	1661975
Rebars	6.12	-271.2	12015.9	63.5	-2813.2	124653.3
				2111	-36466	2762003

***Note** : neglected the duration of 3-day concrete deck hardening*

Time-dependent restrained forces at t = 36500 days (ΔN and ΔM):

x/L	Creep		Shrinkage		Relaxation		Total	
	ΔN	ΔM	ΔN	ΔM	ΔN	ΔM	ΔN	ΔM
0.000	0.0	0.0	709.3	-22693.6	0.0	0.0	709.3	-22693.6
0.044	269.6	5137.6	709.3	-22693.6	-19.8	-580.4	959.0	-18136.4
0.088	290.5	3319.3	709.3	-22693.6	-21.3	-628.5	978.5	-20002.8
0.132	318.7	2065.7	709.3	-22693.6	-23.5	-705.5	1004.5	-21333.4
0.300	362.1	-4214.7	709.3	-22693.6	-25.7	-679.8	1045.6	-27588.1
0.400	366.1	-6076.5	709.3	-22693.6	-25.7	-679.8	1049.7	-29449.9
0.500	367.5	-6697.2	709.3	-22693.6	-25.7	-679.8	1051.1	-30070.6

Strains and curvatures at t = 36500 days

x/L	$\Delta\varepsilon_o(t)$	$\Delta\psi(t)$
	in/inx10^6	1/inx10^6
0.000	-94.5	1.6
0.044	-160.9	0.2
0.088	-158.8	0.5
0.132	-159.5	0.7
0.300	-149.5	1.6
0.400	-145.0	1.9
0.500	-143.5	2.0

Strain inc. at the strand level (mid) =	-90.7	in/inx10^6
Time-dependent inc. losses =	-2.584	ksi
Stress of prestress strand =	163.530	ksi
% losses =	19.24	%

Time-dependent strain at top fiber along the length of the girder:

x/L	Day							
	268.01	269	271	275	298	365	10950	36500
0.000	0.0	-2.9	-8.4	-18.2	-57.4	-105.7	-174.7	-175.8
0.044	-0.1	-3.9	-10.2	-20.9	-61.5	-110.0	-170.5	-170.8
0.088	-0.2	-4.9	-11.9	-23.5	-66.1	-116.4	-182.0	-182.7
0.132	-0.2	-5.8	-13.4	-25.7	-70.1	-122.0	-191.3	-192.3
0.300	-0.4	-8.3	-17.9	-32.5	-82.4	-139.8	-226.7	-228.8
0.400	-0.5	-9.0	-19.3	-34.6	-86.1	-145.2	-236.8	-239.2
0.500	-0.5	-9.3	-19.8	-35.3	-87.3	-146.9	-240.2	-242.7

Time-dependent strain at bottom fiber along the length of the girder:

x/L	Day							
	268.01	269	271	275	298	365	10950	36500
0.000	0.0	0.7	2.1	4.4	12.3	13.9	-28.7	-30.1
0.044	0.1	2.2	4.3	7.2	12.8	2.4	-143.3	-153.0
0.088	0.2	3.7	7.0	11.1	19.7	11.6	-130.5	-139.9
0.132	0.3	5.0	9.2	14.4	25.1	18.5	-124.1	-133.6
0.300	0.6	8.9	16.3	24.9	44.1	45.3	-78.5	-86.6
0.400	0.7	10.1	18.4	28.2	49.9	53.7	-62.7	-70.3
0.500	0.7	10.5	19.1	29.3	51.8	56.5	-57.4	-64.9

Strains and curvatures - Summary for simple span case at x/L = 0.500

Strain, $\varepsilon_o(t)$ using ACI, CEB-FIP, and B3 respectively

Day

268	268.01	269	271	275	298	365	10950	36500
0.0	0.2	1.8	1.9	0.7	-9.7	-33.5	-138.2	-143.5
0.0	-2.1	-1.4	-2.4	-4.6	-16.4	-47.2	-373.2	-404.6
0.0	0.0	2.5	2.5	1.5	-7.0	-33.8	-236.6	-298.0

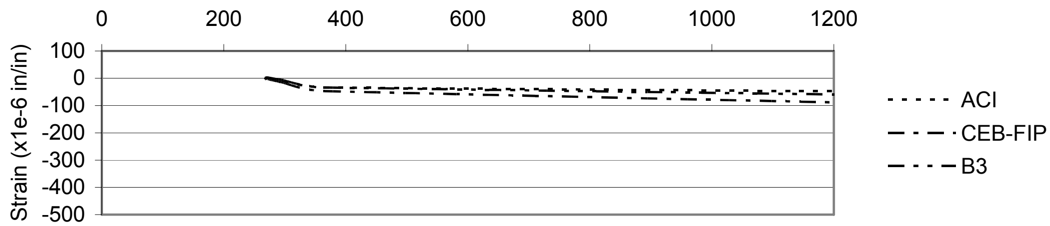

Curvature, ψ(t) using ACI, CEB-FIP, and B3 respectively

Day

268	268.01	269	271	275	298	365	10950	36500
0.0	0.0	0.2	0.4	0.7	1.6	2.3	2.1	2.0
0.0	0.2	0.5	0.6	0.8	1.2	1.4	1.8	2.3
0.0	0.0	0.2	0.3	0.4	0.8	1.5	1.9	0.8

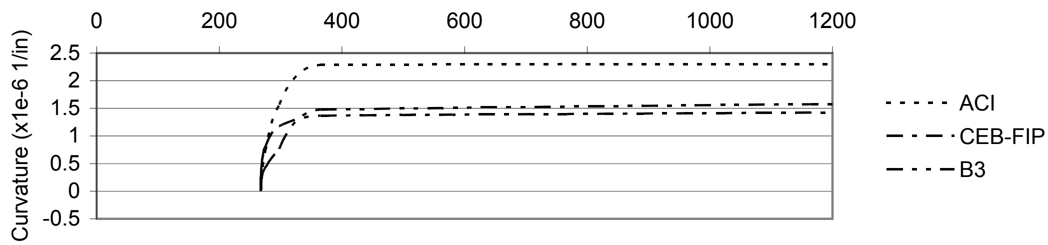

Stress of prestress strand using ACI, CEB-FIP, and B3 respectively

Day

268	268.01	269	271	275	298	365	10950	36500
166.1	166.1	166.3	166.5	166.7	167.0	166.9	163.7	163.5
163.6	163.7	163.9	164.0	164.1	164.0	163.3	154.3	153.8
163.1	163.1	163.4	163.4	163.5	163.5	163.3	157.8	155.3

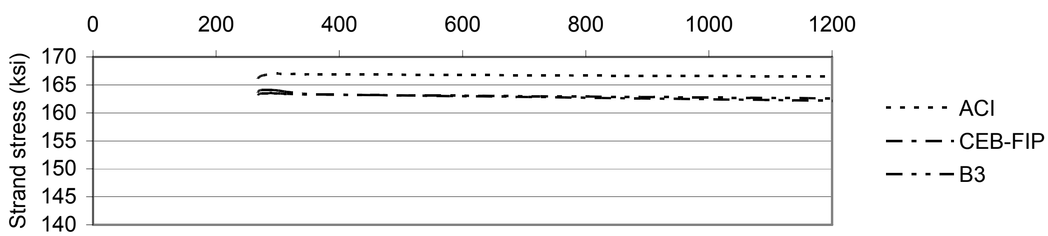

% prestress losses using ACI, CEB-FIP, and B3 respectively

Day

268	268.01	269	271	275	298	365	10950	36500
18.0	18.0	17.9	17.8	17.7	17.5	17.6	19.1	19.2
19.2	19.1	19.0	19.0	19.0	19.0	19.3	23.8	24.0
19.4	19.4	19.3	19.3	19.3	19.2	19.4	22.1	23.3

End of Calculation

Three samples of time-dependent strains with respect to the time-line (271, 365, and 36,500 days) at the top fiber of interior girders are shown in Figure B-13.

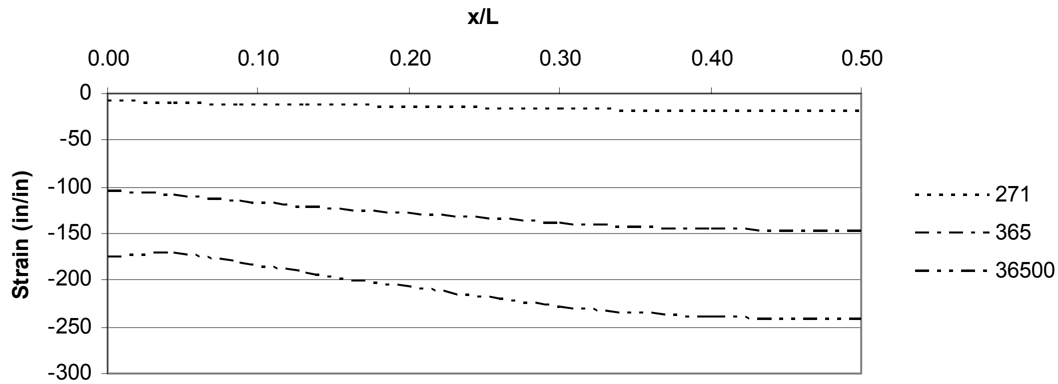

Figure B-13: Time-Dependent Strains at Top Fiber (Bridge 211 – Int. Girder)

Three samples of time-dependent strains with respect to the time-line (271, 365, and 36,500 days) at the bottom fiber of interior girders are shown in Figure B-14.

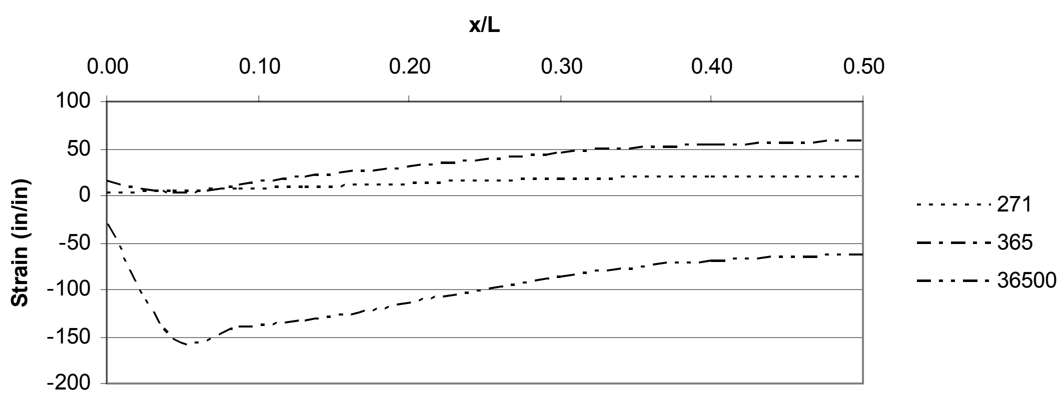

Figure B-14: Time-Dependent Strains at Bottom Fiber (Bridge 211 – Int. Girder)

Exterior Girder

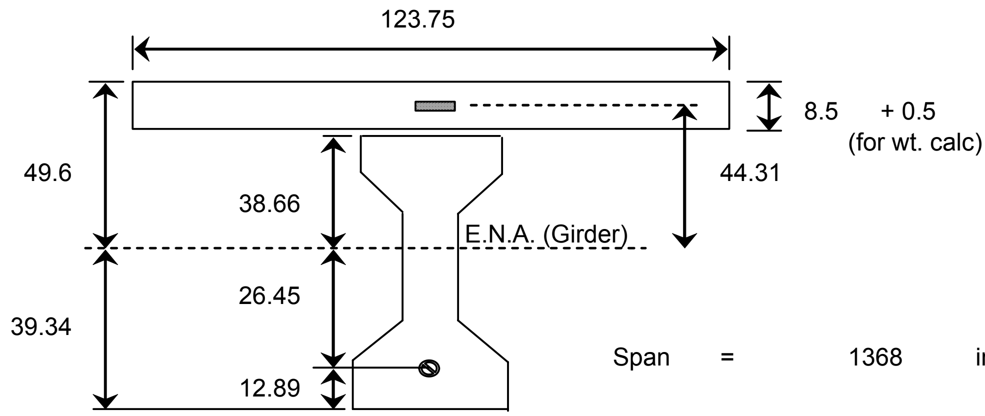

Span = 1368 in

Concrete properties:

Girder:

A	=	1133	in^2
I	=	898985	in^4
$E_c(3)$	=	4628.4	ksi
$E_c(28)$	=	5098.2	ksi

Slab:

$E_c(3)$	=	3272.8	ksi
$E_c(28)$	=	3605.0	ksi

Prestress strand properties:

A	=	0.153	in^2
No.	=	70	
Jacking	=	30.98	k/strand
E_{ps}	=	28500	ksi
$A_{s\text{-}slab}$	=	6.12	in^2
E_s	=	29000	ksi

Section Properties at t = 3 days (midspan):

	Properties of area			Properties of transformed area		
	A	B	I	$A{*}E/E_{ref}$	$B{*}E/E_{ref}$	$I{*}E/E_{ref}$
Girder	1133	0	898985	1133	0	898985
Strand	10.71	283.3	7492.7	65.9	1744.3	46137.7
				1198.9	1744.3	945122.7

Relaxation loss from t = 0 to 3 days:

Δf_{RE}	=	-2.663	ksi
f_{pi}	=	199.820	ksi

Applied forces at transfer:

x/L	e (in)	No. of strands	A	B	I	N (kips)	M (kips-in)
0.000	0.000	0	1133.0	0.0	898985	0.0	0.0
0.044	29.273	54	1183.9	1489.2	942580	-1650.9	-44468.0
0.088	29.516	58	1187.6	1612.8	946590	-1773.2	-44973.5
0.132	30.024	64	1193.3	1810.3	953338	-1956.6	-48230.5
0.300	26.450	70	1198.9	1744.3	945123	-2140.1	-37279.2
0.400	26.450	70	1198.9	1744.3	945123	-2140.1	-34518.3
0.500	26.450	70	1198.9	1744.3	945123	-2140.1	-33598.0

Strains and curvatures at transfer:

x/L	ε_o in/inx10^6	ψ 1/inx10^6
0.000	0.0	0.0
0.044	-289.0	-9.7
0.088	-309.4	-9.7
0.132	-338.7	-10.3
0.300	-374.3	-7.8
0.400	-375.2	-7.2
0.500	-375.5	-7.0

Strain at the strand level (midspan) =	-560.3	in/inx10^6
Elastic shortening loss =	-15.969	ksi
Stress of prestress strand =	183.852	ksi
% initial loss =	9.20	%

Creep coefficients, Φ(t, 3):

Model	Day							
	3.01	4	7	28	268	365	10950	36500
AASHTO	0.003	0.051	0.109	0.289	0.878	0.965	1.429	1.463
ACI	0.009	0.126	0.259	0.566	1.027	1.074	1.337	1.363
CEB-FIP	0.071	0.281	0.425	0.727	1.327	1.408	1.822	1.840
B3	0.000	0.362	0.505	0.728	1.084	1.132	1.722	1.967

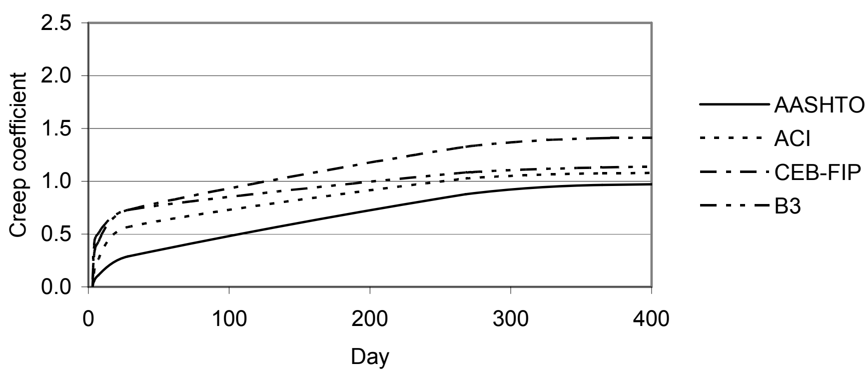

Shrinkage, $\varepsilon_{sh}(t)$:

Model	Day							
	3.01	4	7	28	268	365	10950	36500
AASHTO	0.000008	0.000010	0.000017	0.000063	0.000261	0.000287	0.000391	0.000394
ACI	0.000000	0.000007	0.000026	0.000121	0.000321	0.000336	0.000385	0.000386
CEB-FIP	0.000034	0.000047	0.000067	0.000124	0.000261	0.000285	0.000503	0.000523
B3	0.000000	0.000004	0.000014	0.000089	0.000422	0.000430	0.000432	0.000432

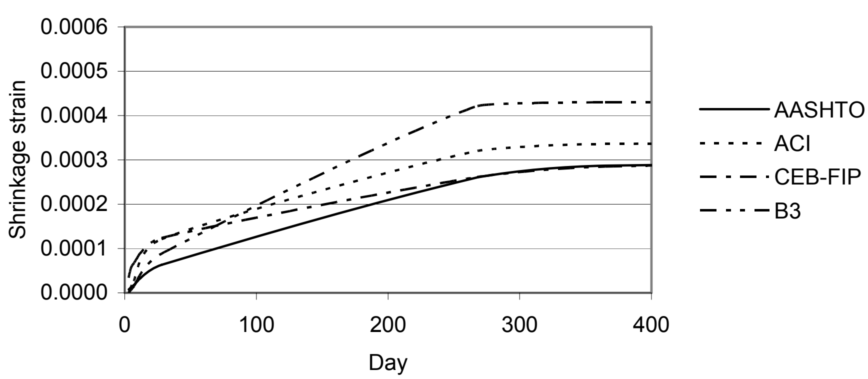

Aging coefficients, χ(t, 3):

Model	Day							
	3.01	4	7	28	268	365	10950	36500
AASHTO	N/A	N/A	N/A	N/A	N/A	N/A	N/A	N/A
ACI	0.710	0.658	0.643	0.622	0.598	0.595	0.568	0.559
CEB-FIP	0.808	0.777	0.769	0.648	0.521	0.518	0.467	0.465
B3	0.731	0.702	0.693	0.682	0.663	0.660	0.614	0.597

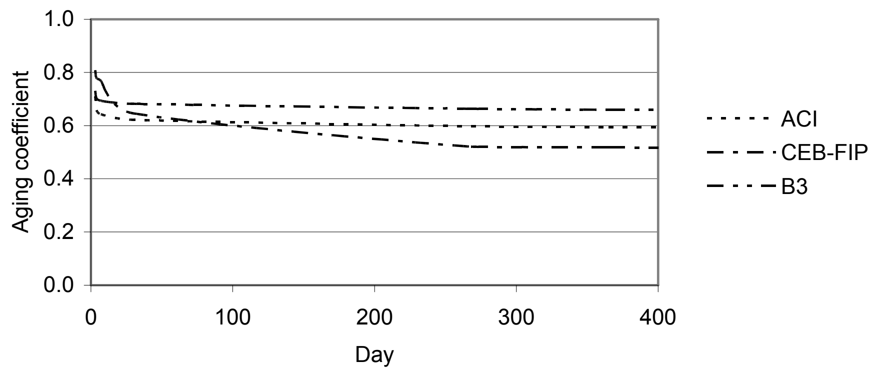

Use engineering recommendation model: **ACI**

Time-dependent restrained forces at t = 268 days (ΔN and ΔM):

Φ(268,3)	=	1.027		χ(268,3)	=	0.598	
Ec(268,3)	=	2868.2	ksi	*(Age-adjusted elastic modulus)*			
εsh(268)	=	0.000321		λ	=	0.681	
Ω	=	0.101		χ_r	=	0.732	
A (mid)	=	1239.4	in^2	B (mid)	=	2814.9	in^3
I (mid)	=	973438	in^4				

x/L	Creep		Shrinkage		Relaxation		Total	
	ΔN	ΔM	ΔN	ΔM	ΔN	ΔM	ΔN	ΔM
0.000	0.0	0.0	1041.6	0.0	0.0	0.0	1041.6	0.0
0.044	964.3	25773.5	1041.6	0.0	-16.9	-495.0	1989.0	25278.5
0.088	1032.1	25778.2	1041.6	0.0	-18.2	-536.1	2055.5	25242.1
0.132	1129.9	27232.8	1041.6	0.0	-20.0	-601.7	2151.4	26631.1
0.300	1248.6	20731.0	1041.6	0.0	-21.9	-579.8	2268.3	20151.2
0.400	1251.7	19055.7	1041.6	0.0	-21.9	-579.8	2271.4	18476.0
0.500	1252.7	18497.3	1041.6	0.0	-21.9	-579.8	2272.4	17917.6

Strains and curvatures at t = 268 days

x/L	$\Delta\varepsilon_o(t)$	Δψ(t)
	in/inx10^6	1/inx10^6
0.000	-320.5	0.0
0.044	-555.5	-7.7
0.088	-570.9	-7.5
0.132	-591.5	-7.7
0.300	-625.8	-5.4
0.400	-628.0	-4.8
0.500	-628.8	-4.6

Strain inc. at the strand level (mid) =	-750.4	in/inx10^6
Time-dependent inc. losses =	-21.388	ksi
Stress of prestress strand =	162.464	ksi
% losses =	19.76	%

Strains and curvatures - Summary for simple span case at x/L = 0.500

Strain, $\varepsilon_o(t)$ using ACI, CEB-FIP, and B3 respectively

Day

3	3.01	4	7	28	268	365	10950	36500
-375.5	-378.6	-425.1	-487.7	-676.2	-1004.3	-1032.9	-1154.6	-1162.4
-370.7	-427.0	-509.2	-573.5	-722.8	-1036.7	-1082.5	-1405.9	-1428.5
-375.5	-375.5	-501.4	-558.0	-697.3	-1111.7	-1133.3	-1306.3	-1376.3

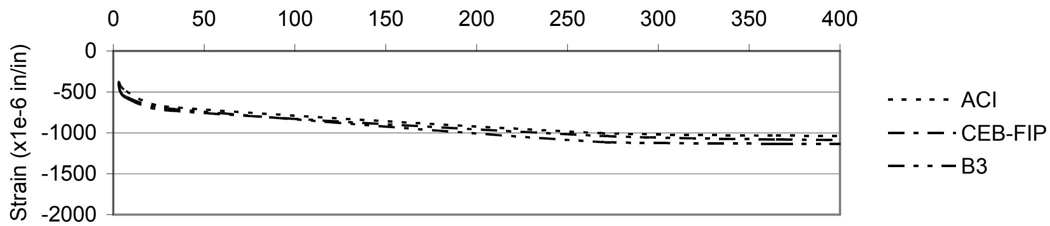

Curvature, ψ(t) using ACI, CEB-FIP, and B3 respectively

Day

3	3.01	4	7	28	268	365	10950	36500
-7.0	-7.0	-7.7	-8.4	-9.8	-11.6	-11.8	-12.7	-12.8
-6.9	-7.3	-8.4	-9.1	-10.5	-13.2	-13.5	-14.7	-14.7
-7.0	-7.0	-9.1	-9.8	-10.7	-11.5	-11.7	-14.1	-15.1

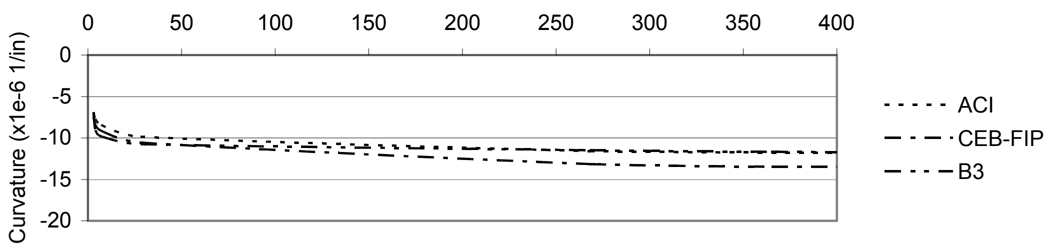

Stress of prestress strand using ACI, CEB-FIP, and B3 respectively

Day

3	3.01	4	7	28	268	365	10950	36500
183.9	183.7	181.9	179.6	173.1	162.5	161.5	157.3	157.0
184.1	182.2	179.0	176.6	171.3	160.4	158.8	148.7	148.0
183.9	183.9	178.7	176.5	171.9	159.5	158.7	152.0	149.2

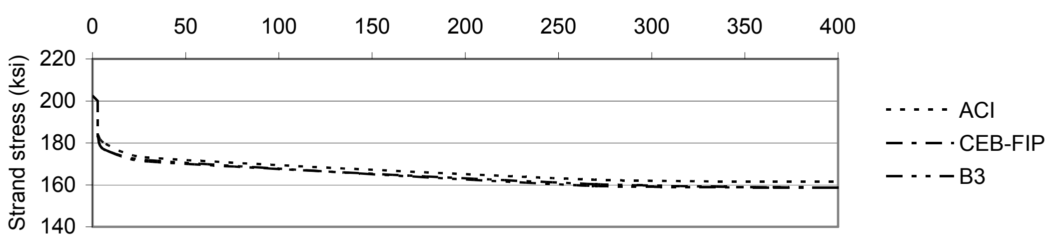

% prestress losses using ACI, CEB-FIP, and B3 respectively

Day

3	3.01	4	7	28	268	365	10950	36500
9.2	9.3	10.2	11.3	14.5	19.8	20.2	22.3	22.4
9.1	10.0	11.6	12.8	15.4	20.8	21.6	26.6	26.9
9.2	9.2	11.7	12.8	15.1	21.2	21.6	24.9	26.3

Effect of concrete deck placed at t = 268 days

Section Properties at t = 268 days when deck is not hardened yet (midspan):

	Properties of area			Properties of transformed area		
	A	B	I	$A*E/E_{ref}$	$B*E/E_{ref}$	$I*E/E_{ref}$
Girder	1133	0	898985	1133	0	898985
Strand	10.71	283.3	7492.7	59.9	1583.6	41885.7
				1192.9	1583.6	940870.7

Applied forces due to concrete deck placement:

x/L	A	B	I	ΔN (kips)	ΔM (kips-in)
0.000	1133.0	0.0	898985.0	0.0	0.0
0.044	1179.2	1352.0	938562.2	0.0	3793.7
0.088	1182.6	1464.2	942202.5	0.0	7239.4
0.132	1187.7	1643.5	948328.9	0.0	10337.0
0.300	1192.9	1583.6	940870.7	0.0	18997.5
0.400	1192.9	1583.6	940870.7	0.0	21711.4
0.500	1192.9	1583.6	940870.7	0.0	22616.1

Strains and curvatures at deck placement:

x/L	$\Delta\varepsilon_o$ in/inx10^6	$\Delta\psi$ 1/inx10^6
0.000	0.0	0.0
0.044	-0.9	0.8
0.088	-1.9	1.5
0.132	-3.0	2.1
0.300	-5.3	4.0
0.400	-6.0	4.5
0.500	-6.3	4.7

Strain at the strand level (midspan) =	118.7	in/inx10^6
Elastic stress gain =	3.383	ksi
Stress of prestress strand =	165.847	ksi
% losses =	18.09	%

Creep coefficients of girder, Φ(t, 268):

Model	Day							
	268.01	269	271	275	298	365	10950	36500
ACI	0.006	0.081	0.145	0.218	0.389	0.544	0.861	0.878
CEB-FIP	0.029	0.114	0.158	0.203	0.311	0.429	0.764	0.772
B3	0.000	0.093	0.123	0.148	0.197	0.244	0.480	0.560

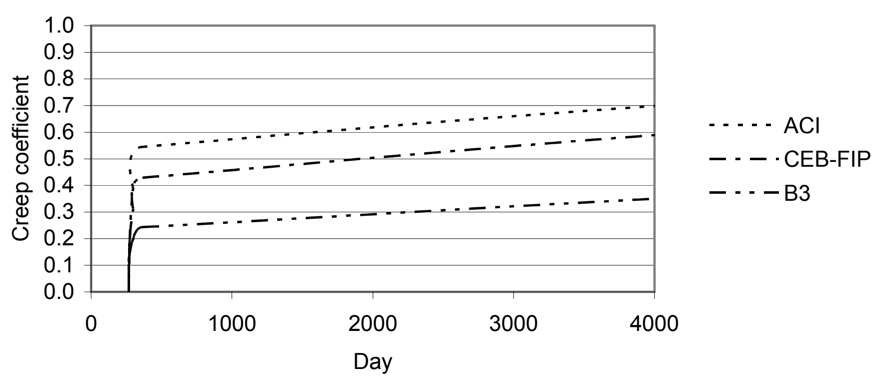

Aging coefficients of girder, χ(t, 268):

Model	Day							
	268.01	269	271	275	298	365	10950	36500
ACI	0.528	0.719	0.764	0.800	0.860	0.908	0.941	0.938
CEB-FIP	0.812	0.860	0.899	0.909	0.913	0.919	0.817	0.816
B3	0.533	0.731	0.778	0.815	0.877	0.928	0.945	0.936

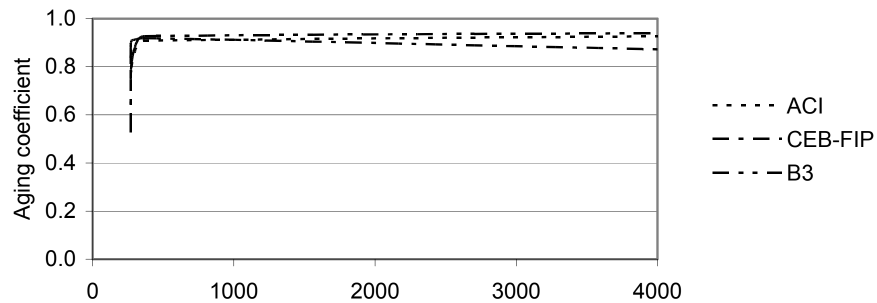

Creep coefficients of concrete deck slab, Φ(t, 3):

Model	Day							
	3.01	4	6	10	33	100	10685	36235
ACI	0.008	0.115	0.205	0.308	0.551	0.771	1.219	1.243
CEB-FIP	0.092	0.367	0.510	0.656	1.009	1.406	2.809	2.860
B3	0.000	0.360	0.470	0.563	0.740	0.902	1.701	1.949

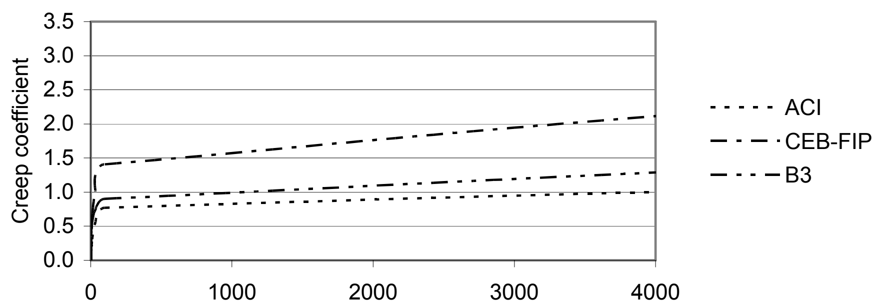

Aging coefficients of concrete deck slab, χ(t, 3):

Model	Day							
	3.01	4	6	10	33	100	10685	36235
ACI	0.695	0.630	0.615	0.603	0.582	0.566	0.530	0.522
CEB-FIP	0.809	0.794	0.809	0.781	0.694	0.634	0.644	0.650
B3	0.731	0.701	0.694	0.688	0.679	0.671	0.613	0.595

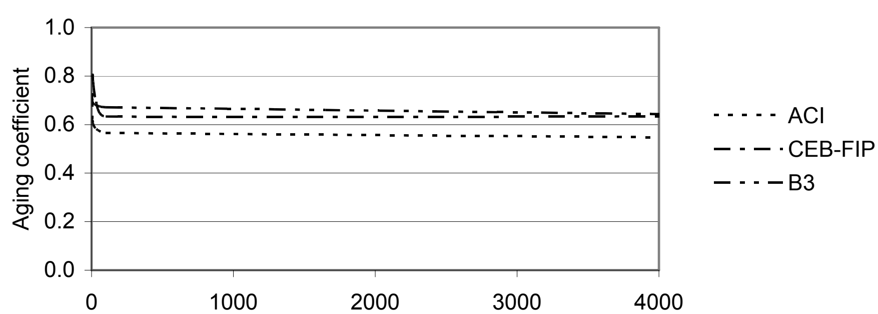

Shrinkage of concrete deck slab, $\varepsilon_{sh}(t)$:

Model	Day							
	3.01	4	6	10	33	100	10685	36235
ACI	0.000000	0.000004	0.000012	0.000025	0.000079	0.000142	0.000221	0.000222
CEB-FIP	0.000016	0.000024	0.000031	0.000042	0.000072	0.000111	0.000501	0.000584
B3	0.000000	0.000001	0.000004	0.000009	0.000040	0.000126	0.000432	0.000432

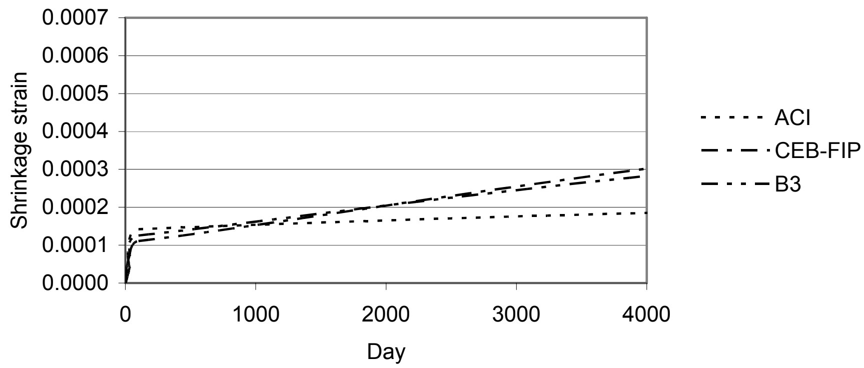

Time-dependent effect at t = 36500 days:

Girder:

$\Delta\Phi(36500,3)$ = 0.336
$\Delta\varepsilon sh(36500)$ = 6.59E-05
$\Phi(36500,268)$ = 0.878
$\chi(36500,268)$ = 0.938
Ec(36500,268) = 2795.4 ksi

Slab:

$\Phi(36235,3)$ = 1.243
$\chi(36235,3)$ = 0.522
Ec(36235,3) = 1984.9 ksi
$\varepsilon sh(36235)$ = 0.000222

Strand:

λ = 0.681
χ_r = 0.779
Ω = 0.081

Stresses and curvatures prior to composite action

x/L	Restrained		Time-dependence		Change in stresses			
	σ_{top}	σ_{bot}	σ_{top}	σ_{bot}	$\Delta\sigma_{top}$	$\Delta\sigma_{bot}$	$\Delta\sigma$	$\Delta\psi$
0.000	0.919	0.919	-0.919	-0.919	0.000	0.000	0.000	0.000
0.044	0.662	2.898	-0.738	-2.464	-0.076	0.435	0.177	0.007
0.088	0.722	2.958	-0.806	-2.483	-0.084	0.475	0.193	0.007
0.132	0.745	3.108	-0.847	-2.561	-0.102	0.548	0.220	0.008
0.300	1.130	2.929	-1.195	-2.405	-0.065	0.523	0.226	0.008
0.400	1.205	2.858	-1.269	-2.343	-0.064	0.515	0.223	0.007
0.500	1.230	2.834	-1.293	-2.322	-0.064	0.512	0.222	0.007

Section Properties at t = 36500 days when composite action starts (midspan):

	Properties of area			Properties of transformed area		
	A	B	I	$A*E/E_{ref}$	$B*E/E_{ref}$	$I*E/E_{ref}$
Girder	1133	0	898985	1133	0	898985
Strand	10.71	283.3	7492.7	109.2	2888.1	76390.0
Deck	1052	-47703	2169643	747	-33872	1540595
Rebars	6.12	-271.2	12015.9	63.5	-2813.2	124653.3
				2053	-33797	2640623

Note *: neglected the duration of 3-day concrete deck hardening*

Time-dependent restrained forces at t = 36500 days (ΔN and ΔM):

x/L	Creep		Shrinkage		Relaxation		Total	
	ΔN	ΔM	ΔN	ΔM	ΔN	ΔM	ΔN	ΔM
0.000	0.0	0.0	672.7	-21036.2	0.0	0.0	672.7	-21036.2
0.044	269.4	5275.7	672.7	-21036.2	-19.7	-576.2	922.4	-16336.7
0.088	290.1	3581.9	672.7	-21036.2	-21.1	-624.0	941.7	-18078.4
0.132	318.1	2438.4	672.7	-21036.2	-23.3	-700.4	967.5	-19298.3
0.300	360.9	-3524.5	672.7	-21036.2	-25.5	-674.9	1008.1	-25235.6
0.400	364.8	-5287.7	672.7	-21036.2	-25.5	-674.9	1012.0	-26998.9
0.500	366.1	-5875.5	672.7	-21036.2	-25.5	-674.9	1013.3	-27586.6

Strains and curvatures at t = 36500 days

x/L	$\Delta\varepsilon_o(t)$	$\Delta\psi(t)$
	in/inx10^6	1/inx10^6
0.000	-93.7	1.6
0.044	-160.5	0.1
0.088	-158.9	0.4
0.132	-160.0	0.6
0.300	-151.3	1.5
0.400	-147.2	1.8
0.500	-145.8	1.9

Strain inc. at the strand level (mid) =	-96.3	in/inx10^6
Time-dependent inc. losses =	-2.745	ksi
Stress of prestress strand =	163.103	ksi
% losses =	19.45	%

Time-dependent strain at top fiber along the length of the girder:

x/L	Day							
	268.01	269	271	275	298	365	10950	36500
0.000	0.0	-2.8	-8.1	-17.8	-56.0	-103.4	-171.7	-172.8
0.044	-0.1	-3.8	-9.9	-20.3	-60.0	-107.4	-166.8	-167.1
0.088	-0.2	-4.8	-11.6	-22.9	-64.5	-113.7	-178.2	-178.8
0.132	-0.2	-5.6	-13.1	-25.1	-68.4	-119.1	-187.3	-188.3
0.300	-0.4	-8.1	-17.4	-31.7	-80.3	-136.6	-222.7	-224.8
0.400	-0.4	-8.8	-18.8	-33.7	-84.0	-141.8	-232.7	-235.2
0.500	-0.5	-9.1	-19.2	-34.4	-85.2	-143.6	-236.0	-238.6

Time-dependent strain at bottom fiber along the length of the girder:

x/L	Day							
	268.01	269	271	275	298	365	10950	36500
0.000	0.0	0.7	2.0	4.3	11.9	13.2	-29.6	-31.1
0.044	0.1	2.0	4.1	6.7	11.9	1.0	-145.5	-155.2
0.088	0.2	3.5	6.6	10.4	18.3	9.6	-133.6	-143.1
0.132	0.3	4.6	8.6	13.5	23.4	15.9	-128.0	-137.5
0.300	0.6	8.3	15.2	23.4	41.1	41.1	-84.7	-93.0
0.400	0.6	9.5	17.3	26.4	46.6	49.0	-69.6	-77.4
0.500	0.7	9.9	17.9	27.4	48.4	51.6	-64.6	-72.2

Strains and curvatures - Summary for simple span case at x/L = 0.500

Strain, $\varepsilon_o(t)$ using ACI, CEB-FIP, and B3 respectively

Day

268	268.01	269	271	275	298	365	10950	36500
0.0	0.2	1.5	1.5	0.1	-10.7	-34.7	-140.4	-145.8
0.0	-2.1	-1.6	-2.7	-5.0	-17.0	-48.0	-373.9	-405.0
0.0	0.0	2.2	2.2	1.1	-7.4	-34.0	-236.1	-297.9

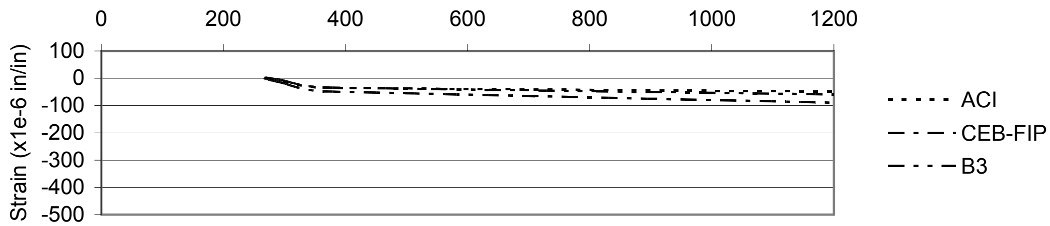

Curvature, ψ(t) using ACI, CEB-FIP, and B3 respectively

Day

268	268.01	269	271	275	298	365	10950	36500
0.0	0.0	0.2	0.4	0.7	1.5	2.2	1.9	1.9
0.0	0.2	0.5	0.6	0.8	1.1	1.3	1.6	2.1
0.0	0.0	0.2	0.3	0.4	0.7	1.4	1.7	0.7

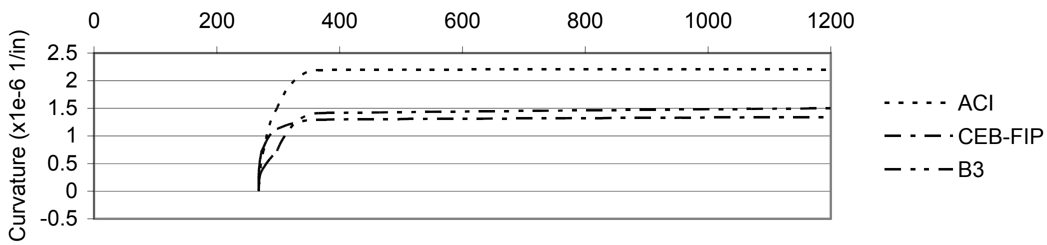

Stress of prestress strand using ACI, CEB-FIP, and B3 respectively

Day

268	268.01	269	271	275	298	365	10950	36500
165.8	165.9	166.1	166.2	166.4	166.7	166.5	163.3	163.1
163.4	163.5	163.7	163.8	163.8	163.8	163.0	154.0	153.4
162.9	162.9	163.1	163.2	163.2	163.2	163.0	157.4	154.9

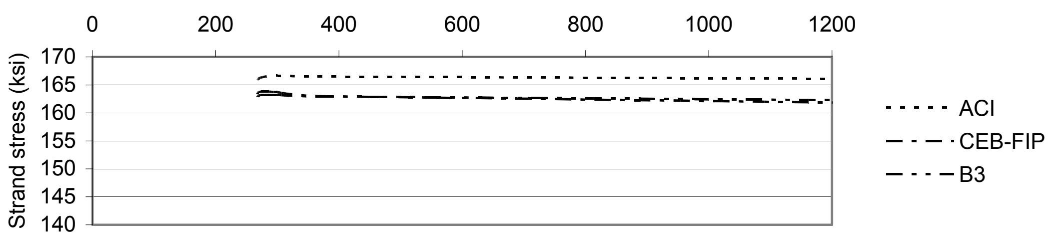

% prestress losses using ACI, CEB-FIP, and B3 respectively

Day

268	268.01	269	271	275	298	365	10950	36500
18.1	18.1	18.0	17.9	17.8	17.7	17.8	19.4	19.4
19.3	19.3	19.2	19.1	19.1	19.1	19.5	24.0	24.2
19.6	19.6	19.5	19.4	19.4	19.4	19.5	22.3	23.5

End of Calculation

Three samples of time-dependent strains with respect to the time-line (271, 365, and 36,500 days) at the top fiber of interior girders are shown in Figure **B-15**.

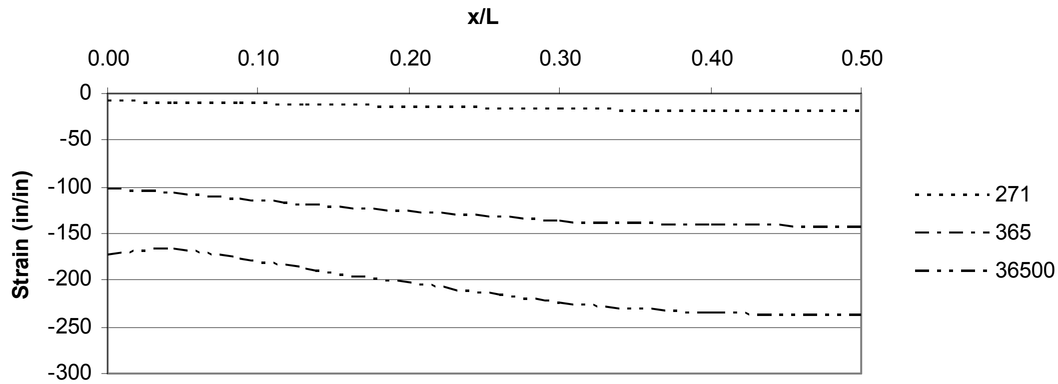

Figure **B-15**: Time-Dependent Strains at Top Fiber (Bridge 211 – Ext. Girder)

Three samples of time-dependent strains with respect to the time-line (271, 365, and 36,500 days) at the bottom fiber of interior girders are shown in Figure **B-16**.

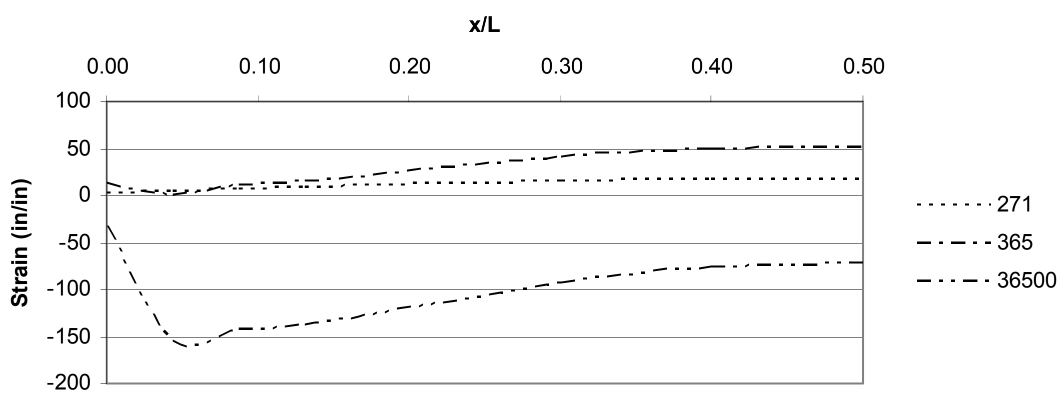

Figure **B-16**: Time-Dependent Strains at Bottom Fiber (Bridge 211 – Ext. Girder)

B.3 Bridge 222

Interior Girder

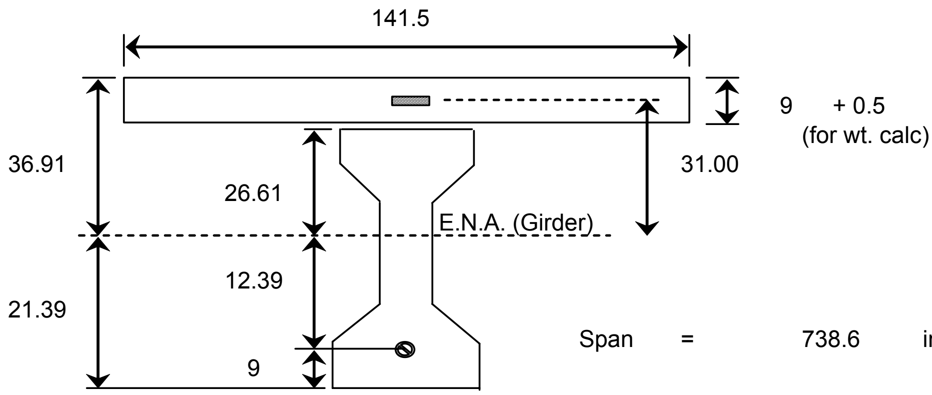

Span = 738.6 in

Concrete properties:

Girder:

A	=	708	in^2
I	=	172712.4	in^4
$E_c(3)$	=	4628.4	ksi
$E_c(28)$	=	5098.2	ksi

Slab:

$E_c(3)$	=	3272.8	ksi
$E_c(28)$	=	3605.0	ksi

Prestress strand properties:

A	=	0.153	in^2
No.	=	40	
Jacking	=	33.82	k/strand
E_{ps}	=	28500	ksi
$A_{s\text{-}slab}$	=	7.878	in^2
E_s	=	29000	ksi

Section Properties at t = 3 days (midspan):

	Properties of area			Properties of transformed area		
	A	B	I	A^*E/E_{ref}	B^*E/E_{ref}	I^*E/E_{ref}
Girder	708	0	172712.4	708	0	172712.4
Strand	6.12	75.8	939.5	37.7	466.9	5785.1
				745.7	466.9	178497.5

Relaxation loss from t = 0 to 3 days:

Δf_{RE}	=	-3.691	ksi
f_{pi}	=	217.354	ksi

Applied forces at transfer:

x/L	e (in)	No. of strands	A	B	I	N (kips)	M (kips-in)
0.000	0.000	0	708.0	0.0	172712.4	0.0	0.0
0.097	11.323	30	736.3	320.0	176336.1	-997.7	-9821.6
0.162	11.566	34	740.0	370.5	176997.4	-1130.7	-10796.3
0.195	12.074	38	743.8	432.3	177931.5	-1263.7	-12626.8
0.300	12.390	40	745.7	466.9	178497.5	-1330.2	-12960.9
0.400	12.390	40	745.7	466.9	178497.5	-1330.2	-12458.0
0.500	12.390	40	745.7	466.9	178497.5	-1330.2	-12290.4

Strains and curvatures at transfer:

x/L	ε_o in/inx10^6	ψ 1/inx10^6
0.000	0.0	0.0
0.097	-287.8	-11.5
0.162	-323.9	-12.5
0.195	-358.7	-14.5
0.300	-376.2	-14.7
0.400	-376.6	-14.1
0.500	-376.7	-13.9

Strain at the strand level (midspan) =	-548.8	in/inx10^6
Elastic shortening loss =	-15.642	ksi
Stress of prestress strand =	201.713	ksi
% initial loss =	8.75	%

Creep coefficients, Φ(t, 3):

Model	Day							
	3.01	4	7	28	171	365	10950	36500
AASHTO	0.003	0.044	0.094	0.254	0.688	0.915	1.404	1.440
ACI	0.009	0.124	0.255	0.556	0.932	1.055	1.313	1.338
CEB-FIP	0.069	0.274	0.415	0.711	1.180	1.384	1.808	1.827
B3	0.000	0.362	0.505	0.727	1.011	1.131	1.722	1.967

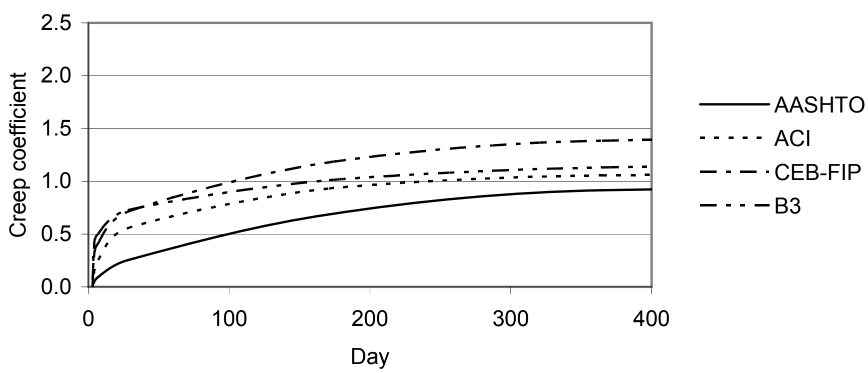

Shrinkage, $\varepsilon_{sh}(t)$:

Model	Day							
	3.01	4	7	28	171	365	10950	36500
AASHTO	0.000006	0.000008	0.000014	0.000053	0.000193	0.000261	0.000368	0.000372
ACI	0.000000	0.000007	0.000025	0.000116	0.000278	0.000321	0.000368	0.000369
CEB-FIP	0.000034	0.000047	0.000065	0.000120	0.000220	0.000273	0.000498	0.000522
B3	0.000000	0.000003	0.000012	0.000075	0.000358	0.000427	0.000432	0.000432

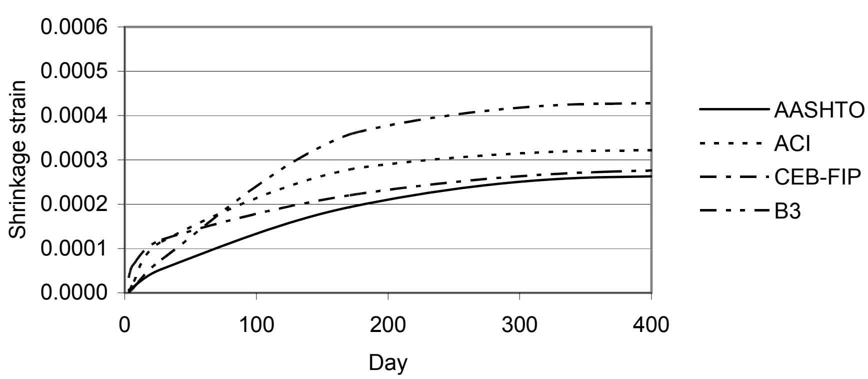

Aging coefficients, χ(t, 3):

Model	Day							
	3.01	4	7	28	171	365	10950	36500
AASHTO	N/A	N/A	N/A	N/A	N/A	N/A	N/A	N/A
ACI	0.707	0.653	0.636	0.615	0.594	0.587	0.560	0.551
CEB-FIP	0.808	0.776	0.766	0.644	0.543	0.527	0.468	0.466
B3	0.731	0.702	0.693	0.682	0.668	0.660	0.614	0.597

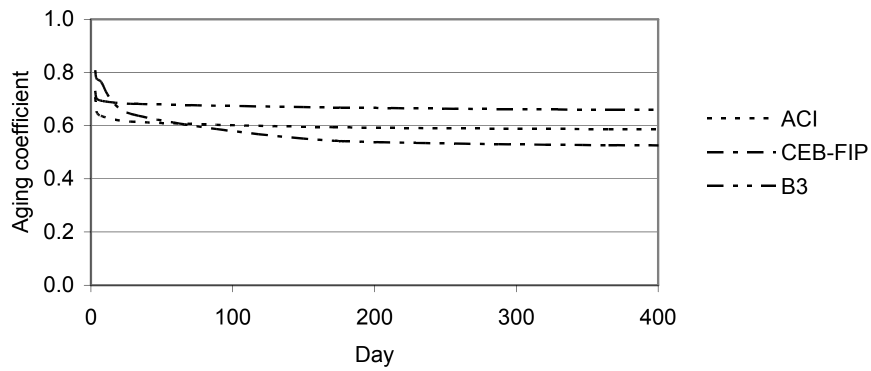

Use engineering recommendation model: **ACI**

Time-dependent restrained forces at t = 171 days (ΔN and ΔM):

Φ(171,3) =	0.932		χ(171,3) =		0.594	
Ec(171,3) =	2979.8	ksi	*(Age-adjusted elastic modulus)*			
εsh(171) =	0.000278		λ	=	0.747	
Ω =	0.079		χ_r	=	0.804	
A (mid) =	766.5	in^2	B (mid)	=	725.2	in^3
I (mid) =	181698	in^4				

x/L	Creep		Shrinkage		Relaxation		Total	
	ΔN	ΔM	ΔN	ΔM	ΔN	ΔM	ΔN	ΔM
0.000	0.0	0.0	587.5	0.0	0.0	0.0	587.5	0.0
0.097	565.8	5521.9	587.5	0.0	-12.9	-145.9	1140.4	5376.0
0.162	636.8	5996.4	587.5	0.0	-14.6	-168.9	1209.7	5827.5
0.195	705.3	6936.5	587.5	0.0	-16.3	-197.1	1276.4	6739.5
0.300	739.8	7053.1	587.5	0.0	-17.2	-212.9	1310.1	6840.3
0.400	740.5	6760.6	587.5	0.0	-17.2	-212.9	1310.8	6547.8
0.500	740.8	6663.2	587.5	0.0	-17.2	-212.9	1311.1	6450.3

Strains and curvatures at t = 171 days

x/L	$\Delta\varepsilon_o(t)$	$\Delta\psi(t)$
	in/inx10^6	1/inx10^6
0.000	-278.5	0.0
0.097	-503.2	-8.7
0.162	-528.8	-9.2
0.195	-551.8	-10.5
0.300	-563.7	-10.4
0.400	-564.6	-9.8
0.500	-564.9	-9.7

Strain inc. at the strand level (mid) =	-684.5	in/inx10^6
Time-dependent inc. losses =	-19.509	ksi
Stress of prestress strand =	182.203	ksi
% losses =	17.57	%

Strains and curvatures - Summary for simple span case at x/L = 0.500

Strain, $\varepsilon_o(t)$ using ACI, CEB-FIP, and B3 respectively

Day

3	3.01	4	7	28	171	365	10950	36500
-376.7	-379.8	-425.6	-487.1	-671.0	-941.6	-1018.5	-1136.5	-1143.4
-371.9	-427.9	-508.6	-571.6	-717.8	-958.6	-1070.2	-1404.9	-1430.0
-376.7	-376.7	-503.4	-558.8	-688.0	-1036.8	-1136.3	-1313.1	-1383.4

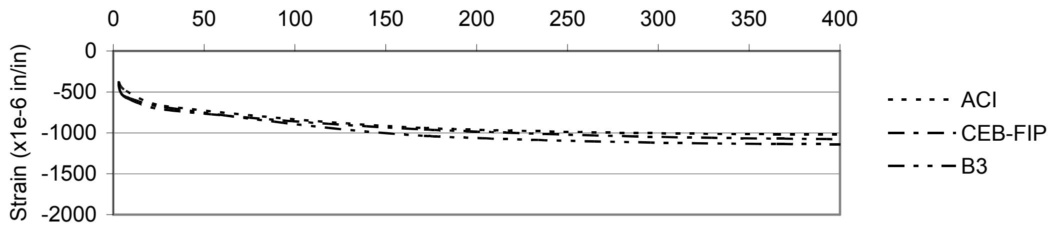

Curvature, ψ(t) using ACI, CEB-FIP, and B3 respectively

Day

3	3.01	4	7	28	171	365	10950	36500
-13.9	-14.0	-15.4	-16.9	-20.1	-23.6	-24.7	-26.9	-27.1
-13.7	-14.5	-16.9	-18.4	-21.5	-26.2	-28.2	-31.5	-31.5
-13.9	-13.9	-18.3	-19.9	-22.1	-24.0	-24.9	-30.5	-32.8

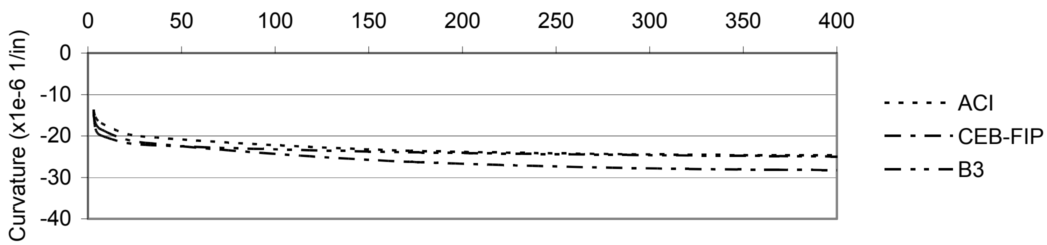

Stress of prestress strand using ACI, CEB-FIP, and B3 respectively

Day

3	3.01	4	7	28	171	365	10950	36500
201.7	201.6	199.8	197.5	191.1	182.2	179.6	175.5	175.2
201.9	200.0	196.9	194.6	189.3	180.8	176.9	166.2	165.5
201.7	201.7	196.6	194.4	190.0	179.3	176.2	169.2	166.4

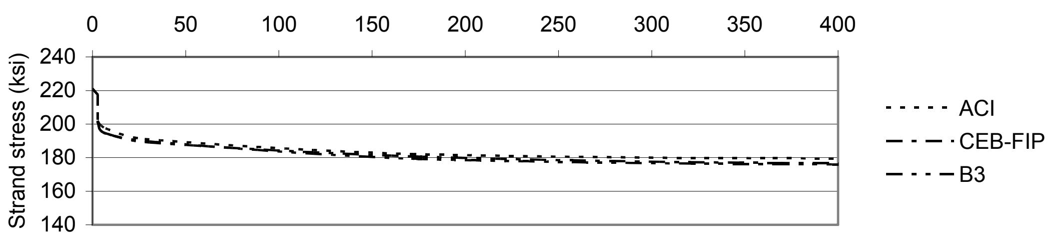

% prestress losses using ACI, CEB-FIP, and B3 respectively

Day

3	3.01	4	7	28	171	365	10950	36500
8.7	8.8	9.6	10.6	13.5	17.6	18.7	20.6	20.7
8.7	9.5	10.9	12.0	14.4	18.2	20.0	24.8	25.1
8.7	8.7	11.1	12.1	14.1	18.9	20.3	23.5	24.7

Effect of concrete deck placed at t = 171 days

Section Properties at t = 171 days when deck is not hardened yet (midspan):

	Properties of area			Properties of transformed area		
	A	B	I	$A*E/E_{ref}$	$B*E/E_{ref}$	$I*E/E_{ref}$
Girder	708	0	172712.4	708	0	172712.4
Strand	6.12	75.8	939.5	34.2	423.9	5251.9
				742.2	423.9	177964.3

Applied forces due to concrete deck placement:

x/L	A	B	I	ΔN (kips)	ΔM (kips-in)
0.000	708.0	0.0	172712.4	0.0	0.0
0.097	733.7	290.5	176002.1	0.0	2800.2
0.162	737.1	336.3	176602.5	0.0	4331.0
0.195	740.5	392.4	177450.5	0.0	4995.6
0.300	742.2	423.9	177964.3	0.0	6684.0
0.400	742.2	423.9	177964.3	0.0	7638.8
0.500	742.2	423.9	177964.3	0.0	7957.1

Strains and curvatures at deck placement:

x/L	$\Delta\varepsilon_o$ $in/inx10^6$	$\Delta\psi$ $1/inx10^6$
0.000	0.0	0.0
0.097	-1.2	3.1
0.162	-2.2	4.8
0.195	-2.9	5.5
0.300	-4.2	7.4
0.400	-4.8	8.4
0.500	-5.0	8.8

Strain at the strand level (midspan) =	103.8	$in/inx10^6$
Elastic stress gain =	2.958	ksi
Stress of prestress strand =	185.162	ksi
% losses =	16.23	%

Creep coefficients of girder, Φ(t, 171):

Model	Day							
	171.01	172	174	178	199	365	10950	36500
ACI	0.006	0.084	0.150	0.226	0.394	0.651	0.893	0.910
CEB-FIP	0.031	0.123	0.171	0.219	0.329	0.550	0.830	0.840
B3	0.000	0.132	0.176	0.216	0.295	0.432	0.715	0.821

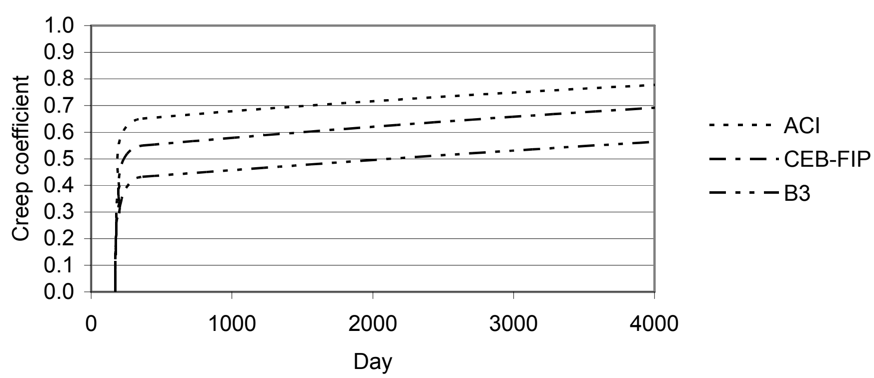

Aging coefficients of girder, χ(t, 171):

Model	Day							
	171.01	172	174	178	199	365	10950	36500
ACI	0.538	0.722	0.766	0.800	0.855	0.915	0.929	0.925
CEB-FIP	0.812	0.860	0.899	0.909	0.911	0.900	0.829	0.827
B3	0.541	0.733	0.779	0.815	0.873	0.934	0.937	0.928

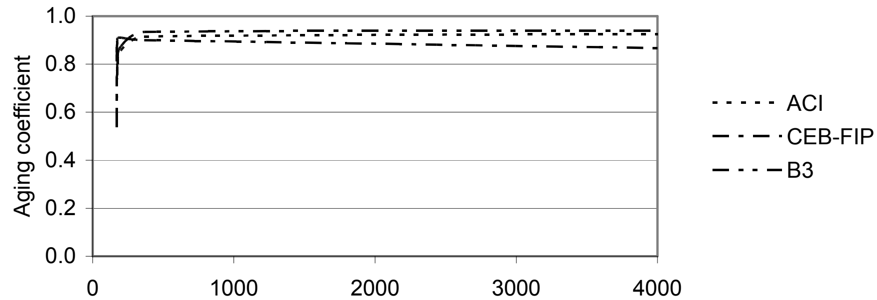

Creep coefficients of concrete deck slab, Φ(t, 3):

Model	Day							
	3.01	4	6	10	31	197	10782	36332
ACI	0.008	0.115	0.205	0.307	0.537	0.887	1.217	1.241
CEB-FIP	0.091	0.361	0.501	0.645	0.972	1.661	2.792	2.845
B3	0.000	0.360	0.470	0.562	0.730	1.007	1.702	1.949

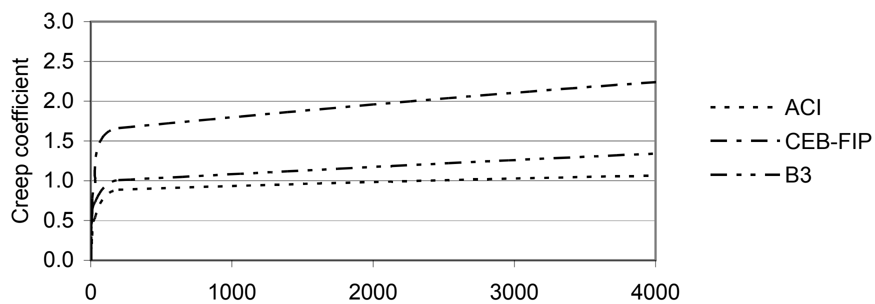

Aging coefficients of concrete deck slab, χ(t, 3):

Model	Day							
	3.01	4	6	10	31	197	10782	36332
ACI	0.695	0.630	0.614	0.602	0.581	0.556	0.531	0.523
CEB-FIP	0.809	0.793	0.807	0.779	0.697	0.585	0.642	0.649
B3	0.731	0.701	0.694	0.688	0.679	0.661	0.615	0.599

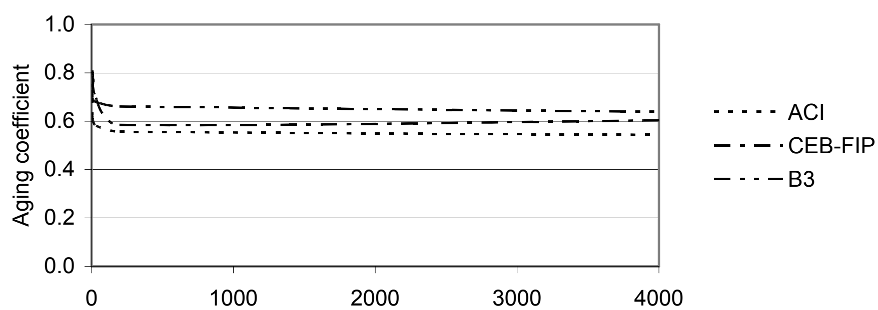

Shrinkage of concrete deck slab, $\varepsilon_{sh}(t)$:

Model	Day							
	3.01	4	6	10	31	197	10782	36332
ACI	0.000000	0.000004	0.000011	0.000024	0.000071	0.000163	0.000208	0.000209
CEB-FIP	0.000016	0.000023	0.000031	0.000041	0.000068	0.000137	0.000492	0.000579
B3	0.000000	0.000001	0.000004	0.000008	0.000033	0.000212	0.000432	0.000432

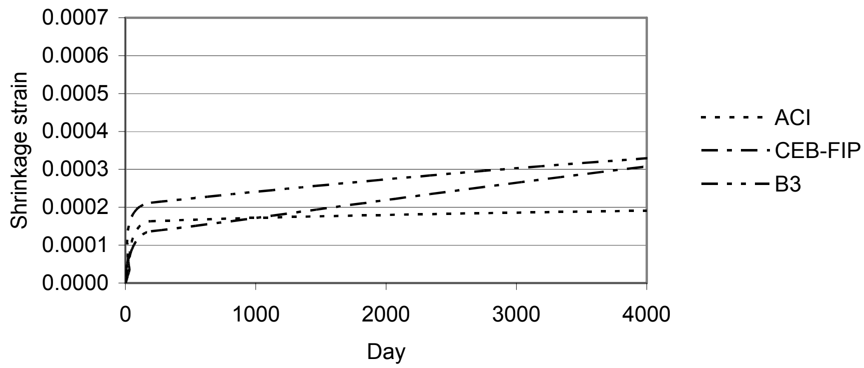

Time-dependent effect at t = 36500 days:

Girder:			*Slab:*		
$\Delta\Phi(36500,3)$ =	0.406		$\Phi(36332,3)$ =	1.241	
$\Delta\varepsilon sh(36500)$ =	9.06E-05		$\chi(36332,3)$ =	0.523	
$\Phi(36500,171)$ =	0.910		$Ec(36332,3)$ =	1984.8	ksi
$\chi(36500,171)$ =	0.925		$\varepsilon sh(36332)$ =	0.000209	
$Ec(36500,171)$ =	2768.0	ksi			
Strand:					
λ =	0.747		Ω =	0.065	
χ_r =	0.837				

Stresses and curvatures prior to composite action

x/L	Restrained		Time-dependence		Change in stresses			
	σ_{top}	σ_{bot}	σ_{top}	σ_{bot}	$\Delta\sigma_{top}$	$\Delta\sigma_{bot}$	$\Delta\sigma$	$\Delta\psi$
0.000	0.830	0.830	-0.830	-0.830	0.000	0.000	0.000	0.000
0.097	0.778	2.313	-0.809	-2.055	-0.030	0.258	0.129	0.006
0.162	0.805	2.472	-0.846	-2.162	-0.040	0.309	0.154	0.007
0.195	0.757	2.685	-0.815	-2.311	-0.058	0.374	0.182	0.009
0.300	0.788	2.748	-0.856	-2.342	-0.068	0.407	0.195	0.010
0.400	0.834	2.713	-0.902	-2.310	-0.068	0.403	0.193	0.010
0.500	0.849	2.701	-0.917	-2.299	-0.068	0.402	0.193	0.010

Section Properties at t = 36500 days when composite action starts (midspan):

	Properties of area			Properties of transformed area		
	A	B	I	$A*E/E_{ref}$	$B*E/E_{ref}$	$I*E/E_{ref}$
Girder	708	0	172712.4	708	0	172712.4
Strand	6.12	75.8	939.5	63.0	780.7	9673.2
Deck	1274	-41274	1346291	913	-29595	965353
Rebars	7.88	-244.2	7571.2	82.5	-2558.7	79322.3
				1767	-31373	1227060

Note *: neglected the duration of 3-day concrete deck hardening*

Time-dependent restrained forces at t = 36500 days (ΔN and ΔM):

x/L	Creep		Shrinkage		Relaxation		Total	
	ΔN	ΔM	ΔN	ΔM	ΔN	ΔM	ΔN	ΔM
0.000	0.0	0.0	706.4	-17140.2	0.0	0.0	706.4	-17140.2
0.097	209.1	624.5	706.4	-17140.2	-17.8	-201.3	897.7	-16717.0
0.162	235.3	26.7	706.4	-17140.2	-20.2	-233.1	921.6	-17346.6
0.195	259.5	24.8	706.4	-17140.2	-22.5	-271.9	943.4	-17387.3
0.300	273.5	-770.4	706.4	-17140.2	-23.7	-293.7	956.3	-18204.4
0.400	275.2	-1344.4	706.4	-17140.2	-23.7	-293.7	957.9	-18778.4
0.500	275.7	-1535.8	706.4	-17140.2	-23.7	-293.7	958.4	-18969.8

Strains and curvatures at t = 36500 days

x/L	$\Delta\varepsilon_o(t)$	$\Delta\psi(t)$
	in/inx10^6	1/inx10^6
0.000	-107.3	2.3
0.097	-180.2	0.3
0.162	-181.5	0.4
0.195	-187.7	0.3
0.300	-183.8	0.7
0.400	-178.9	1.0
0.500	-177.3	1.1

Strain inc. at the strand level (mid) =	-164.3	in/inx10^6
Time-dependent inc. losses =	-4.682	ksi
Stress of prestress strand =	180.479	ksi
% losses =	18.35	%

Time-dependent strain at top fiber along the length of the girder:

x/L	Day							
	171.01	172	174	178	199	365	10950	36500
0.000	0.0	-3.4	-9.9	-21.5	-64.1	-148.4	-189.7	-190.4
0.097	-0.1	-4.9	-12.4	-25.2	-70.1	-154.4	-190.1	-190.5
0.162	-0.2	-5.7	-13.8	-27.3	-73.6	-159.9	-197.4	-197.9
0.195	-0.2	-6.0	-14.4	-28.2	-75.0	-161.7	-198.7	-199.2
0.300	-0.3	-6.9	-16.0	-30.5	-79.0	-168.0	-207.5	-208.2
0.400	-0.3	-7.4	-16.8	-31.8	-81.3	-172.0	-213.3	-214.1
0.500	-0.3	-7.5	-17.1	-32.3	-82.0	-173.3	-215.2	-216.1

Time-dependent strain at bottom fiber along the length of the girder:

x/L	Day							
	171.01	172	174	178	199	365	10950	36500
0.000	0.0	0.8	2.2	4.6	11.8	-9.4	-57.6	-59.1
0.097	0.2	3.3	6.3	10.2	17.4	-35.0	-166.8	-174.2
0.162	0.3	4.7	8.8	13.8	23.3	-28.6	-164.5	-172.0
0.195	0.3	5.2	9.6	15.0	24.9	-29.7	-173.1	-181.1
0.300	0.4	6.7	12.3	19.0	31.6	-19.9	-161.9	-169.7
0.400	0.5	7.6	13.9	21.4	35.8	-12.7	-151.0	-158.6
0.500	0.5	7.9	14.5	22.2	37.2	-10.2	-147.4	-154.8

Strains and curvatures - Summary for simple span case at x/L = 0.500

Strain, $\varepsilon_o(t)$ using ACI, CEB-FIP, and B3 respectively

Day

171	171.01	172	174	178	199	365	10950	36500
0.0	0.2	2.2	2.9	2.2	-6.6	-70.1	-172.3	-177.3
0.0	-1.5	-0.1	-0.7	-2.8	-14.5	-104.7	-440.1	-473.5
0.0	0.0	4.3	4.6	3.4	-7.2	-105.1	-300.7	-365.4

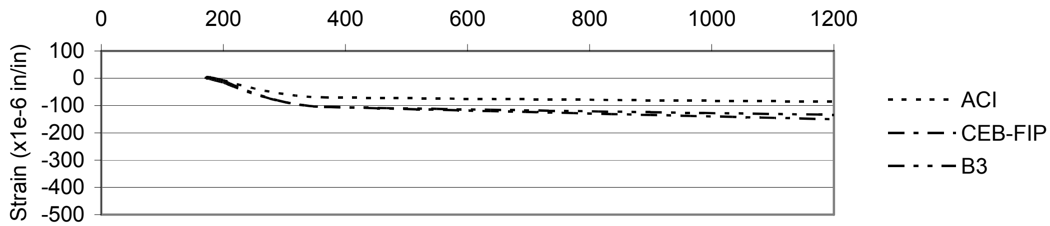

Curvature, $\psi(t)$ using ACI, CEB-FIP, and B3 respectively

Day

171	171.01	172	174	178	199	365	10950	36500
0.0	0.0	0.3	0.5	0.9	2.0	2.8	1.2	1.1
0.0	0.4	0.7	0.9	1.2	1.6	1.0	0.2	1.3
0.0	0.0	0.3	0.5	0.6	1.0	2.8	2.2	0.3

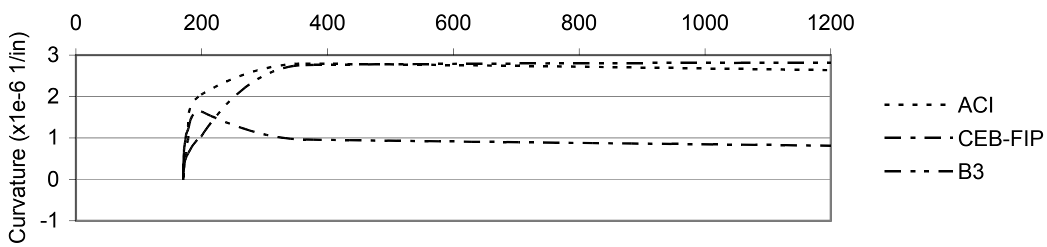

Stress of prestress strand using ACI, CEB-FIP, and B3 respectively

Day

171	171.01	172	174	178	199	365	10950	36500
185.2	185.2	185.3	185.4	185.6	185.7	184.2	180.7	180.5
183.4	183.5	183.7	183.7	183.7	183.6	180.8	170.9	170.4
182.3	182.3	182.5	182.6	182.6	182.5	180.3	174.5	172.0

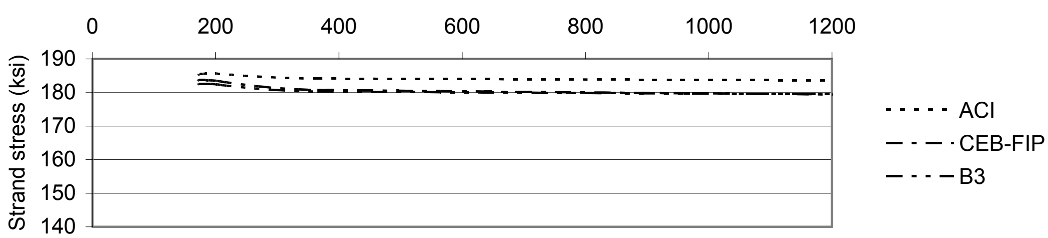

% prestress losses using ACI, CEB-FIP, and B3 respectively

Day

171	171.01	172	174	178	199	365	10950	36500
16.2	16.2	16.2	16.1	16.1	16.0	16.7	18.3	18.4
17.0	17.0	16.9	16.9	16.9	17.0	18.2	22.7	22.9
17.5	17.5	17.4	17.4	17.4	17.5	18.4	21.1	22.2

End of Calculation

Three samples of time-dependent strains with respect to the time-line (174, 365, and 36,500 days) at the top fiber of interior girders are shown in Figure **B-17**.

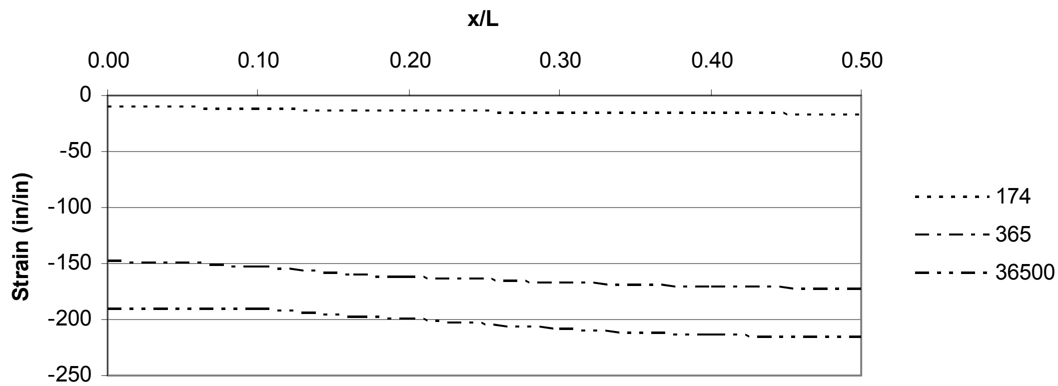

Figure **B-17**: Time-Dependent Strains at Top Fiber (Bridge 222 – Int. Girder

Three samples of time-dependent strains with respect to the time-line (174, 365, and 36,500 days) at the bottom fiber of interior girders are shown in Figure **B-18**.

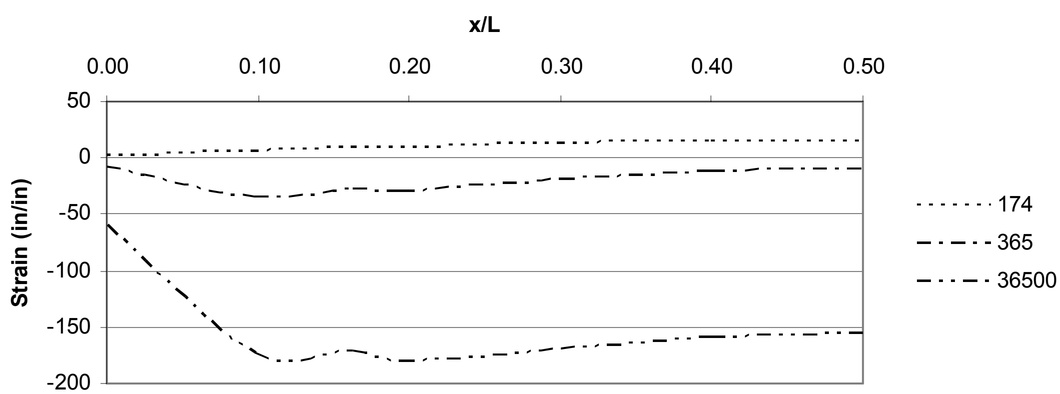

Figure **B-18**: Time-Dependent Strains at Bottom Fiber (Bridge 222 – Int. Girder)

Exterior Girder

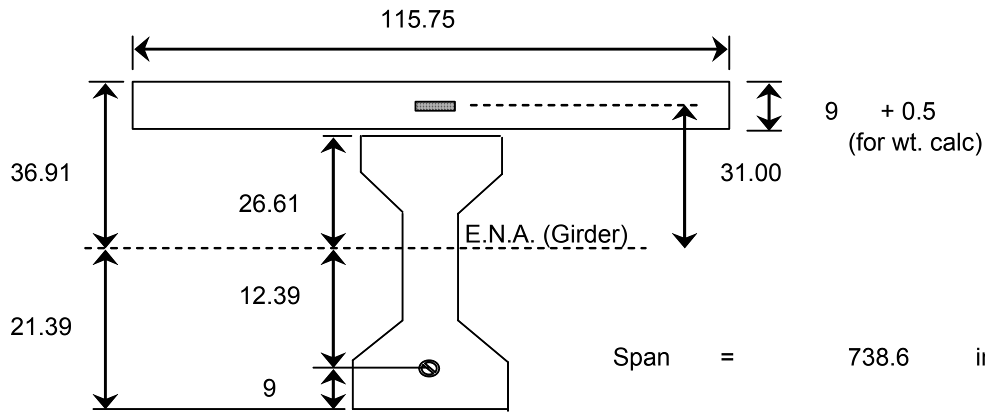

Span = 738.6 in

Concrete properties:

Girder:

A	=	708	in^2
I	=	172712.4	in^4
$E_c(3)$	=	4628.4	ksi
$E_c(28)$	=	5098.2	ksi

Slab:

$E_c(3)$	=	3272.8	ksi
$E_c(28)$	=	3605.0	ksi

Prestress strand properties:

A	=	0.153	in^2
No.	=	40	
Jacking	=	33.82	k/strand
E_{ps}	=	28500	ksi
$A_{s\text{-}slab}$	=	7.878	in^2
E_s	=	29000	ksi

Section Properties at t = 3 days (midspan):

	Properties of area			Properties of transformed area		
	A	B	I	$A*E/E_{ref}$	$B*E/E_{ref}$	$I*E/E_{ref}$
Girder	708	0	172712.4	708	0	172712.4
Strand	6.12	75.8	939.5	37.7	466.9	5785.1
				745.7	466.9	178497.5

Relaxation loss from t = 0 to 3 days:

Δf_{RE}	=	-3.691	ksi
f_{pi}	=	217.354	ksi

Applied forces at transfer:

x/L	e (in)	No. of strands	A	B	I	N (kips)	M (kips-in)
0.000	0.000	0	708.0	0.0	172712.4	0.0	0.0
0.097	11.323	30	736.3	320.0	176336.1	-997.7	-9821.6
0.162	11.566	34	740.0	370.5	176997.4	-1130.7	-10796.3
0.195	12.074	38	743.8	432.3	177931.5	-1263.7	-12626.8
0.300	12.390	40	745.7	466.9	178497.5	-1330.2	-12960.9
0.400	12.390	40	745.7	466.9	178497.5	-1330.2	-12458.0
0.500	12.390	40	745.7	466.9	178497.5	-1330.2	-12290.4

Strains and curvatures at transfer:

x/L	ε_o in/inx10^6	ψ 1/inx10^6
0.000	0.0	0.0
0.097	-287.8	-11.5
0.162	-323.9	-12.5
0.195	-358.7	-14.5
0.300	-376.2	-14.7
0.400	-376.6	-14.1
0.500	-376.7	-13.9

Strain at the strand level (midspan) =	-548.8	in/inx10^6
Elastic shortening loss =	-15.642	ksi
Stress of prestress strand =	201.713	ksi
% initial loss =	8.75	%

Creep coefficients, Φ(t, 3):

Model	Day							
	3.01	4	7	28	171	365	10950	36500
AASHTO	0.003	0.044	0.094	0.254	0.688	0.915	1.404	1.440
ACI	0.009	0.124	0.255	0.556	0.932	1.055	1.313	1.338
CEB-FIP	0.069	0.274	0.415	0.711	1.180	1.384	1.808	1.827
B3	0.000	0.362	0.505	0.727	1.011	1.131	1.722	1.967

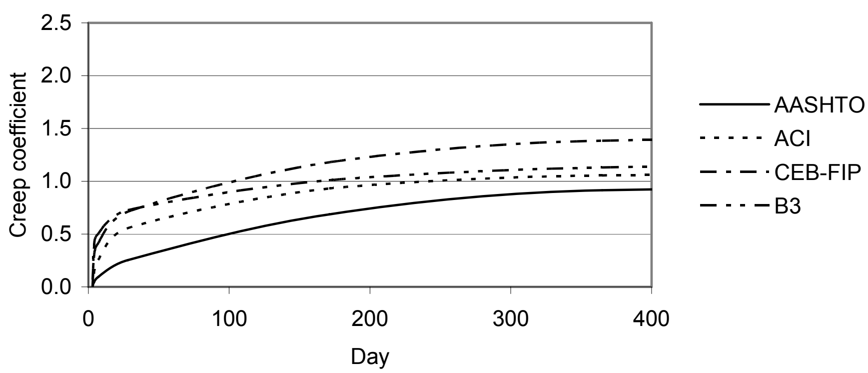

Shrinkage, $\varepsilon_{sh}(t)$:

Model	Day							
	3.01	4	7	28	171	365	10950	36500
AASHTO	0.000006	0.000008	0.000014	0.000053	0.000193	0.000261	0.000368	0.000372
ACI	0.000000	0.000007	0.000025	0.000116	0.000278	0.000321	0.000368	0.000369
CEB-FIP	0.000034	0.000047	0.000065	0.000120	0.000220	0.000273	0.000498	0.000522
B3	0.000000	0.000003	0.000012	0.000075	0.000358	0.000427	0.000432	0.000432

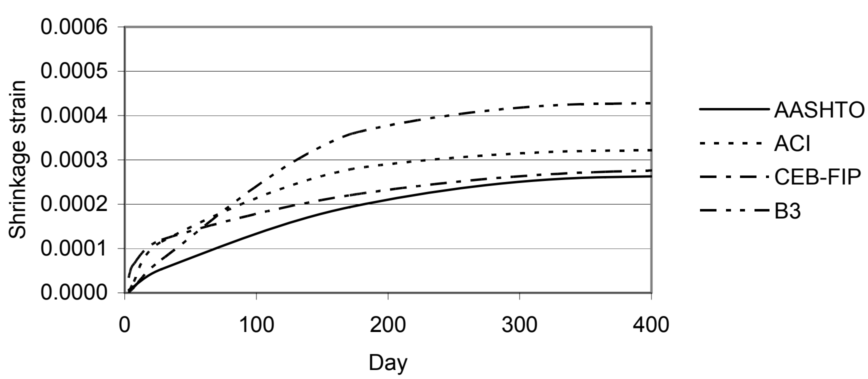

Aging coefficients, $\chi(t, 3)$:

Model	Day							
	3.01	4	7	28	171	365	10950	36500
AASHTO	N/A	N/A	N/A	N/A	N/A	N/A	N/A	N/A
ACI	0.707	0.653	0.636	0.615	0.594	0.587	0.560	0.551
CEB-FIP	0.808	0.776	0.766	0.644	0.543	0.527	0.468	0.466
B3	0.731	0.702	0.693	0.682	0.668	0.660	0.614	0.597

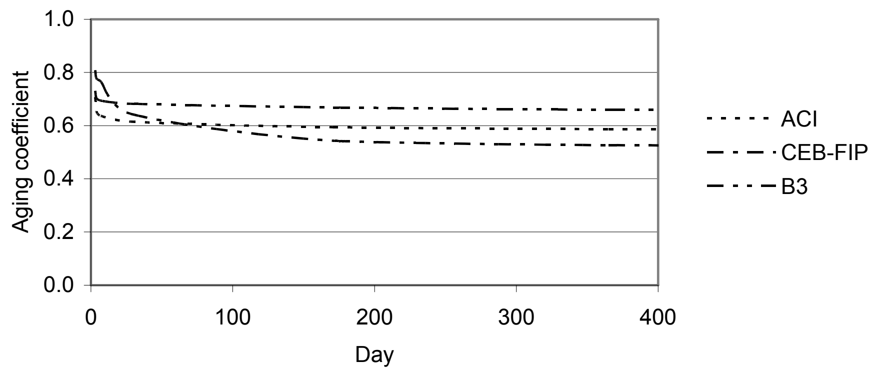

Use engineering recommendation model: **ACI**

Time-dependent restrained forces at t = 171 days (ΔN and ΔM):

$\Phi(171,3)$ = 0.932 $\chi(171,3)$ = 0.594

$E_c(171,3)$ = 2979.8 ksi *(Age-adjusted elastic modulus)*

$\varepsilon_{sh}(171)$ = 0.000278 λ = 0.747

Ω = 0.079 χ_r = 0.804

A (mid) = 766.5 in^2 B (mid) = 725.2 in^3

I (mid) = 181698 in^4

x/L	Creep		Shrinkage		Relaxation		Total	
	ΔN	ΔM	ΔN	ΔM	ΔN	ΔM	ΔN	ΔM
0.000	0.0	0.0	587.5	0.0	0.0	0.0	587.5	0.0
0.097	565.8	5521.9	587.5	0.0	-12.9	-145.9	1140.4	5376.0
0.162	636.8	5996.4	587.5	0.0	-14.6	-168.9	1209.7	5827.5
0.195	705.3	6936.5	587.5	0.0	-16.3	-197.1	1276.4	6739.5
0.300	739.8	7053.1	587.5	0.0	-17.2	-212.9	1310.1	6840.3
0.400	740.5	6760.6	587.5	0.0	-17.2	-212.9	1310.8	6547.8
0.500	740.8	6663.2	587.5	0.0	-17.2	-212.9	1311.1	6450.3

Strains and curvatures at t = 171 days

x/L	$\Delta\varepsilon_o(t)$	$\Delta\psi(t)$
	in/inx10^6	1/inx10^6
0.000	-278.5	0.0
0.097	-503.2	-8.7
0.162	-528.8	-9.2
0.195	-551.8	-10.5
0.300	-563.7	-10.4
0.400	-564.6	-9.8
0.500	-564.9	-9.7

Strain inc. at the strand level (mid) = -684.5 in/inx10^6

Time-dependent inc. losses = -19.509 ksi

Stress of prestress strand = 182.203 ksi

% losses = 17.57 %

Strains and curvatures - Summary for simple span case at x/L = 0.500

Strain, $\varepsilon_o(t)$ using ACI, CEB-FIP, and B3 respectively

Day								
3	3.01	4	7	28	171	365	10950	36500
-376.7	-379.8	-425.6	-487.1	-671.0	-941.6	-1018.5	-1136.5	-1143.4
-371.9	-427.9	-508.6	-571.6	-717.8	-958.6	-1070.2	-1404.9	-1430.0
-376.7	-376.7	-503.4	-558.8	-688.0	-1036.8	-1136.3	-1313.1	-1383.4

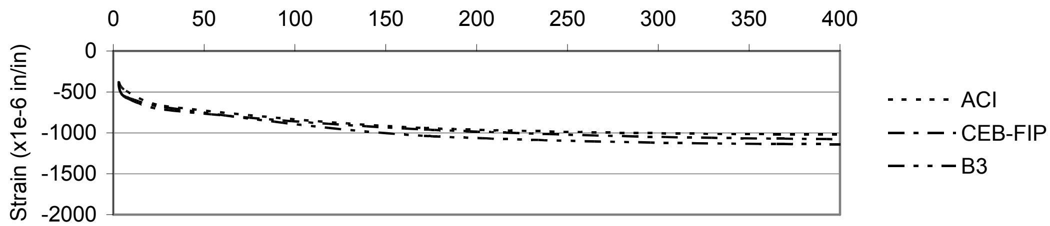

Curvature, $\psi(t)$ using ACI, CEB-FIP, and B3 respectively

Day								
3	3.01	4	7	28	171	365	10950	36500
-13.9	-14.0	-15.4	-16.9	-20.1	-23.6	-24.7	-26.9	-27.1
-13.7	-14.5	-16.9	-18.4	-21.5	-26.2	-28.2	-31.5	-31.5
-13.9	-13.9	-18.3	-19.9	-22.1	-24.0	-24.9	-30.5	-32.8

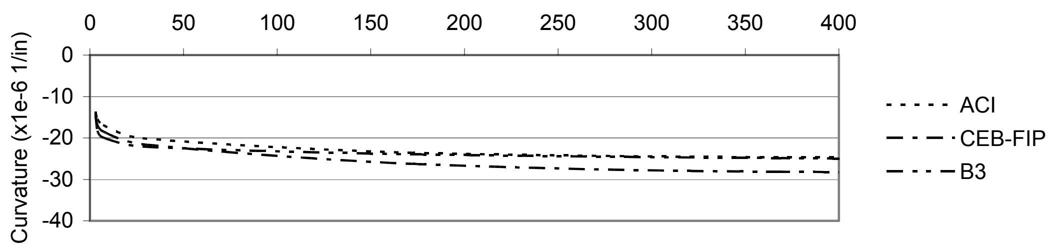

Stress of prestress strand using ACI, CEB-FIP, and B3 respectively

Day								
3	3.01	4	7	28	171	365	10950	36500
201.7	201.6	199.8	197.5	191.1	182.2	179.6	175.5	175.2
201.9	200.0	196.9	194.6	189.3	180.8	176.9	166.2	165.5
201.7	201.7	196.6	194.4	190.0	179.3	176.2	169.2	166.4

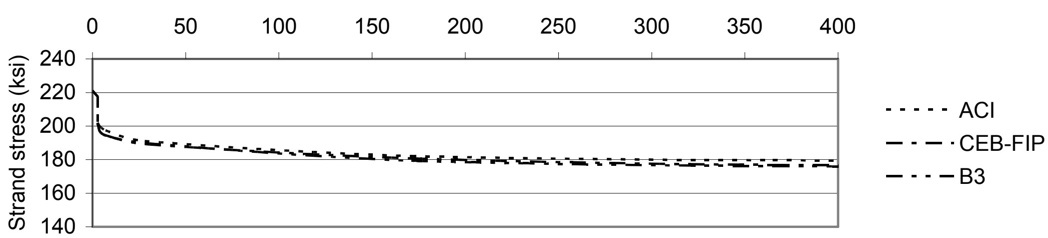

% prestress losses using ACI, CEB-FIP, and B3 respectively

Day								
3	3.01	4	7	28	171	365	10950	36500
8.7	8.8	9.6	10.6	13.5	17.6	18.7	20.6	20.7
8.7	9.5	10.9	12.0	14.4	18.2	20.0	24.8	25.1
8.7	8.7	11.1	12.1	14.1	18.9	20.3	23.5	24.7

Effect of concrete deck placed at t = 171 days

Section Properties at t = 171 days when deck is not hardened yet (midspan):

	Properties of area			Properties of transformed area		
	A	B	I	$A*E/E_{ref}$	$B*E/E_{ref}$	$I*E/E_{ref}$
Girder	708	0	172712.4	708	0	172712.4
Strand	6.12	75.8	939.5	34.2	423.9	5251.9
				742.2	423.9	177964.3

Applied forces due to concrete deck placement:

x/L	A	B	I	ΔN (kips)	ΔM (kips-in)
0.000	708.0	0.0	172712.4	0.0	0.0
0.097	733.7	290.5	176002.1	0.0	2290.7
0.162	737.1	336.3	176602.5	0.0	3542.9
0.195	740.5	392.4	177450.5	0.0	4086.5
0.300	742.2	423.9	177964.3	0.0	5467.6
0.400	742.2	423.9	177964.3	0.0	6248.7
0.500	742.2	423.9	177964.3	0.0	6509.1

Strains and curvatures at deck placement:

x/L	$\Delta\varepsilon_o$ in/inx10^6	$\Delta\psi$ 1/inx10^6
0.000	0.0	0.0
0.097	-1.0	2.6
0.162	-1.8	3.9
0.195	-2.4	4.5
0.300	-3.4	6.0
0.400	-3.9	6.9
0.500	-4.1	7.2

Strain at the strand level (midspan) =	84.9	in/inx10^6
Elastic stress gain =	2.420	ksi
Stress of prestress strand =	184.623	ksi
% losses =	16.48	%

Creep coefficients of girder, Φ(t, 171):

Model	Day							
	171.01	172	174	178	199	365	10950	36500
ACI	0.006	0.084	0.150	0.226	0.394	0.651	0.893	0.910
CEB-FIP	0.031	0.123	0.171	0.219	0.329	0.550	0.830	0.840
B3	0.000	0.132	0.176	0.216	0.295	0.432	0.715	0.821

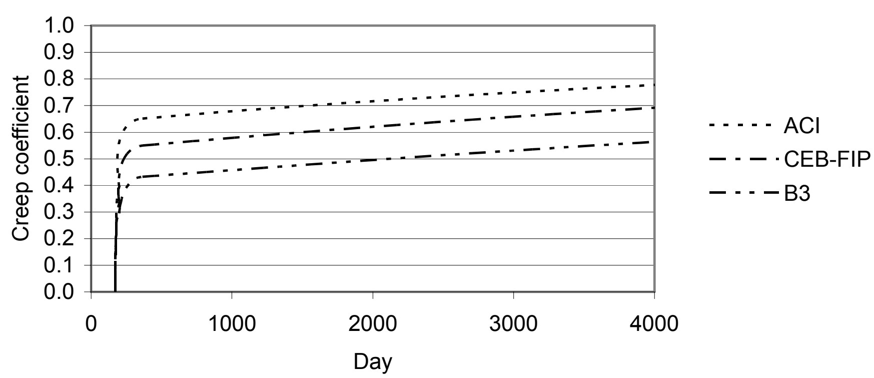

Aging coefficients of girder, χ(t, 171):

Model	Day							
	171.01	172	174	178	199	365	10950	36500
ACI	0.538	0.722	0.766	0.800	0.855	0.915	0.929	0.925
CEB-FIP	0.812	0.860	0.899	0.909	0.911	0.900	0.829	0.827
B3	0.541	0.733	0.779	0.815	0.873	0.934	0.937	0.928

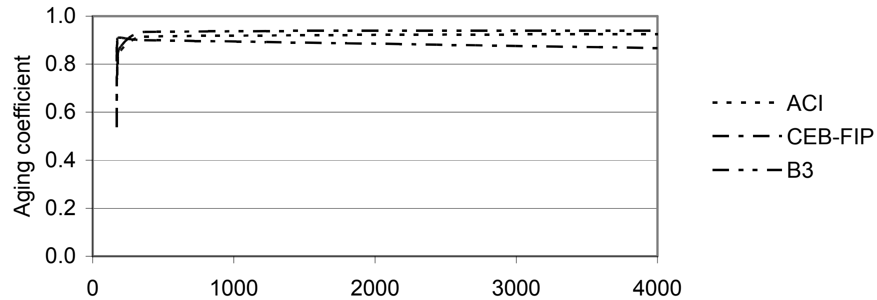

Creep coefficients of concrete deck slab, Φ(t, 3):

Model	Day							
	3.01	4	6	10	31	197	10782	36332
ACI	0.008	0.115	0.205	0.307	0.537	0.887	1.217	1.241
CEB-FIP	0.091	0.361	0.501	0.645	0.972	1.661	2.792	2.845
B3	0.000	0.360	0.470	0.562	0.730	1.007	1.702	1.949

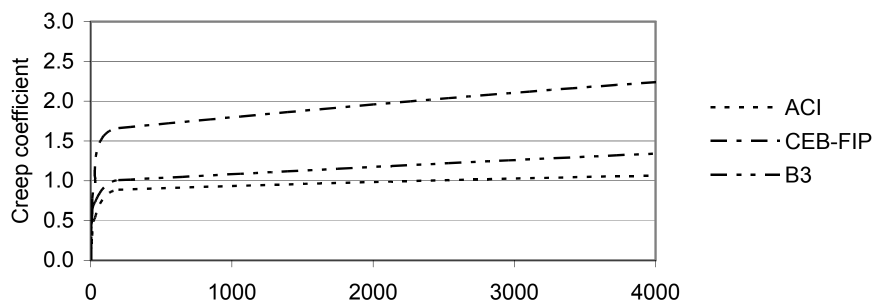

Aging coefficients of concrete deck slab, χ(t, 3):

Model	Day							
	3.01	4	6	10	31	197	10782	36332
ACI	0.695	0.630	0.614	0.602	0.581	0.556	0.531	0.523
CEB-FIP	0.809	0.793	0.807	0.779	0.697	0.585	0.642	0.649
B3	0.731	0.701	0.694	0.688	0.679	0.661	0.615	0.599

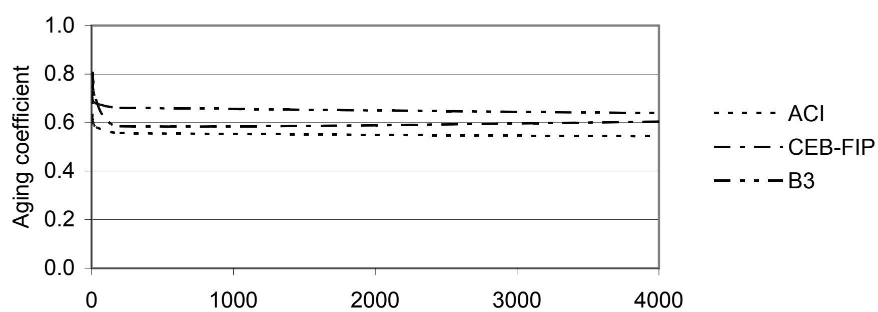

Shrinkage of concrete deck slab, $\varepsilon_{sh}(t)$:

Model	Day							
	3.01	4	6	10	31	197	10782	36332
ACI	0.000000	0.000004	0.000011	0.000024	0.000071	0.000163	0.000208	0.000209
CEB-FIP	0.000016	0.000023	0.000031	0.000041	0.000068	0.000137	0.000492	0.000579
B3	0.000000	0.000001	0.000004	0.000008	0.000033	0.000212	0.000432	0.000432

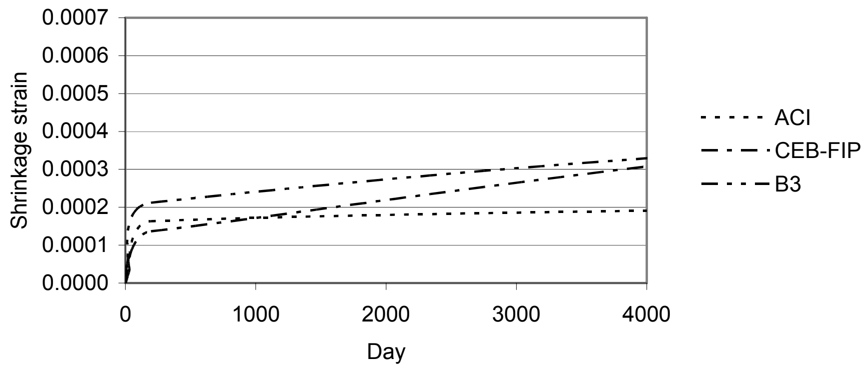

Time-dependent effect at t = 36500 days:

Girder:			*Slab:*		
$\Delta\Phi(36500,3)$ =	0.406		$\Phi(36332,3)$ =	1.241	
$\Delta\varepsilon sh(36500)$ =	9.06E-05		$\chi(36332,3)$ =	0.523	
$\Phi(36500,171)$ =	0.910		Ec(36332,3) =	1984.8	ksi
$\chi(36500,171)$ =	0.925		$\varepsilon sh(36332)$ =	0.000209	
Ec(36500,171) =	2768.0	ksi			
Strand:					
λ =	0.747		Ω =	0.069	
χ_r =	0.827				

Stresses and curvatures prior to composite action

x/L	Restrained		Time-dependence		Change in stresses			
	σ_{top}	σ_{bot}	σ_{top}	σ_{bot}	$\Delta\sigma_{top}$	$\Delta\sigma_{bot}$	$\Delta\sigma$	$\Delta\psi$
0.000	0.830	0.830	-0.830	-0.830	0.000	0.000	0.000	0.000
0.097	0.778	2.313	-0.809	-2.055	-0.030	0.258	0.129	0.006
0.162	0.805	2.472	-0.846	-2.162	-0.040	0.309	0.154	0.007
0.195	0.757	2.685	-0.815	-2.311	-0.058	0.374	0.182	0.009
0.300	0.788	2.748	-0.856	-2.342	-0.068	0.407	0.195	0.010
0.400	0.834	2.713	-0.902	-2.310	-0.068	0.403	0.193	0.010
0.500	0.849	2.701	-0.917	-2.299	-0.068	0.402	0.193	0.010

Section Properties at t = 36500 days when composite action starts (midspan):

	Properties of area			Properties of transformed area		
	A	B	I	A^*E/E_{ref}	B^*E/E_{ref}	I^*E/E_{ref}
Girder	708	0	172712.4	708	0	172712.4
Strand	6.12	75.8	939.5	63.0	780.7	9673.2
Deck	1042	-33763	1101294	747	-24210	789679
Rebars	7.88	-244.2	7571.2	82.5	-2558.7	79322.3
				1601	-25988	1051387

***Note** : neglected the duration of 3-day concrete deck hardening*

Time-dependent restrained forces at t = 36500 days (ΔN and ΔM):

x/L	Creep		Shrinkage		Relaxation		Total	
	ΔN	ΔM	ΔN	ΔM	ΔN	ΔM	ΔN	ΔM
0.000	0.0	0.0	610.2	-14021.1	0.0	0.0	610.2	-14021.1
0.097	208.7	871.9	610.2	-14021.1	-17.6	-199.0	801.3	-13348.2
0.162	234.6	408.0	610.2	-14021.1	-19.9	-230.4	824.9	-13843.5
0.195	258.6	462.7	610.2	-14021.1	-22.3	-268.8	846.5	-13827.2
0.300	272.2	-186.0	610.2	-14021.1	-23.4	-290.4	858.9	-14497.5
0.400	273.6	-676.6	610.2	-14021.1	-23.4	-290.4	860.4	-14988.1
0.500	274.1	-840.1	610.2	-14021.1	-23.4	-290.4	860.8	-15151.6

Strains and curvatures at t = 36500 days

x/L	$\Delta\varepsilon_o(t)$	$\Delta\psi(t)$
	in/inx10^6	1/inx10^6
0.000	-106.3	2.1
0.097	-181.8	0.0
0.162	-184.6	0.2
0.195	-191.2	0.0
0.300	-188.7	0.3
0.400	-184.7	0.6
0.500	-183.4	0.7

Strain inc. at the strand level (mid) =	-175.0	in/inx10^6
Time-dependent inc. losses =	-4.988	ksi
Stress of prestress strand =	179.635	ksi
% losses =	18.73	%

Time-dependent strain at top fiber along the length of the girder:

x/L	Day							
	171.01	172	174	178	199	365	10950	36500
0.000	0.0	-3.3	-9.5	-20.7	-61.7	-143.6	-184.2	-185.0
0.097	-0.1	-4.7	-11.9	-24.2	-67.3	-148.7	-183.3	-183.7
0.162	-0.2	-5.4	-13.2	-26.2	-70.7	-154.0	-190.2	-190.7
0.195	-0.2	-5.7	-13.8	-27.0	-72.0	-155.6	-191.3	-191.7
0.300	-0.3	-6.5	-15.2	-29.2	-75.7	-161.6	-199.7	-200.4
0.400	-0.3	-7.0	-16.1	-30.4	-77.9	-165.4	-205.5	-206.3
0.500	-0.3	-7.2	-16.4	-30.8	-78.6	-166.7	-207.4	-208.2

Time-dependent strain at bottom fiber along the length of the girder:

x/L	Day							
	171.01	172	174	178	199	365	10950	36500
0.000	0.0	0.7	2.1	4.4	11.2	-10.7	-59.2	-60.6
0.097	0.2	2.8	5.4	8.8	14.7	-39.8	-173.3	-180.8
0.162	0.2	4.0	7.5	11.8	19.5	-35.1	-173.2	-181.0
0.195	0.3	4.4	8.2	12.8	20.8	-36.8	-182.7	-190.9
0.300	0.4	5.7	10.4	16.1	26.3	-28.8	-173.9	-182.0
0.400	0.4	6.4	11.8	18.1	29.9	-22.6	-164.4	-172.2
0.500	0.4	6.7	12.2	18.8	31.1	-20.5	-161.2	-168.9

Strains and curvatures - Summary for simple span case at x/L = 0.500

Strain, $\varepsilon_o(t)$ using ACI, CEB-FIP, and B3 respectively

Day								
171	171.01	172	174	178	199	365	10950	36500
0.0	0.2	1.6	1.7	0.6	-9.2	-74.1	-178.2	-183.4
0.0	-1.6	-0.8	-1.7	-4.0	-16.3	-107.7	-443.2	-476.1
0.0	0.0	3.2	3.2	1.8	-9.3	-107.2	-303.2	-368.7

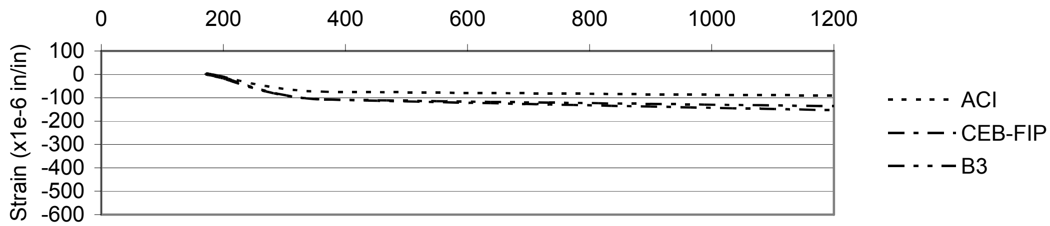

Curvature, ψ(t) using ACI, CEB-FIP, and B3 respectively

Day								
171	171.01	172	174	178	199	365	10950	36500
0.0	0.0	0.2	0.5	0.9	1.9	2.5	0.8	0.7
0.0	0.4	0.7	0.9	1.1	1.5	0.7	-0.4	0.6
0.0	0.0	0.3	0.4	0.5	0.9	2.5	1.6	-0.4

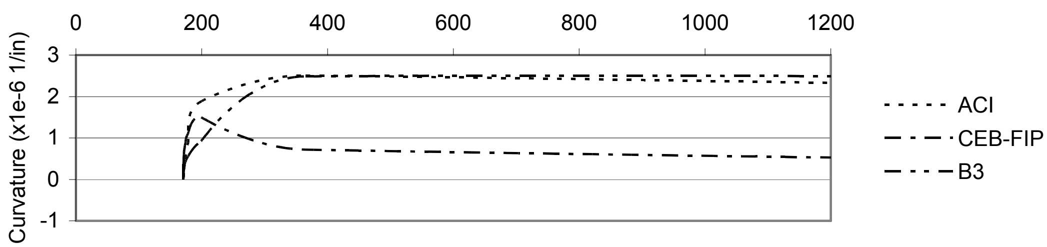

Stress of prestress strand using ACI, CEB-FIP, and B3 respectively

Day								
171	171.01	172	174	178	199	365	10950	36500
184.6	184.6	184.8	184.8	184.9	185.0	183.4	179.8	179.6
182.9	183.0	183.1	183.2	183.2	183.0	180.1	170.2	169.6
181.8	181.8	182.0	182.0	182.0	181.8	179.6	173.7	171.1

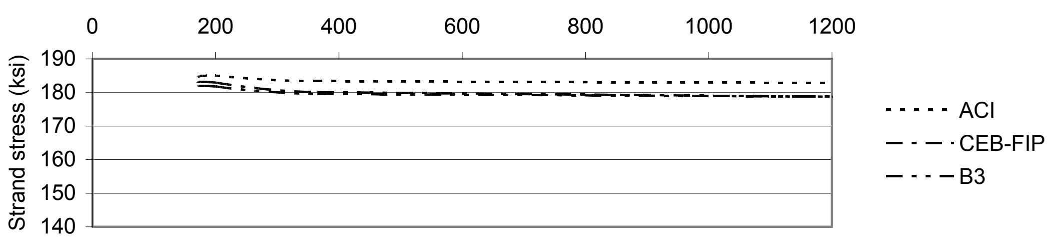

% prestress losses using ACI, CEB-FIP, and B3 respectively

Day								
171	171.01	172	174	178	199	365	10950	36500
16.5	16.5	16.4	16.4	16.3	16.3	17.0	18.6	18.7
17.2	17.2	17.1	17.1	17.1	17.2	18.5	23.0	23.3
17.8	17.8	17.7	17.7	17.7	17.7	18.8	21.4	22.6

End of Calculation

Three samples of time-dependent strains with respect to the time-line (174, 365, and 36,500 days) at the top fiber of interior girders are shown in Figure **B-19**.

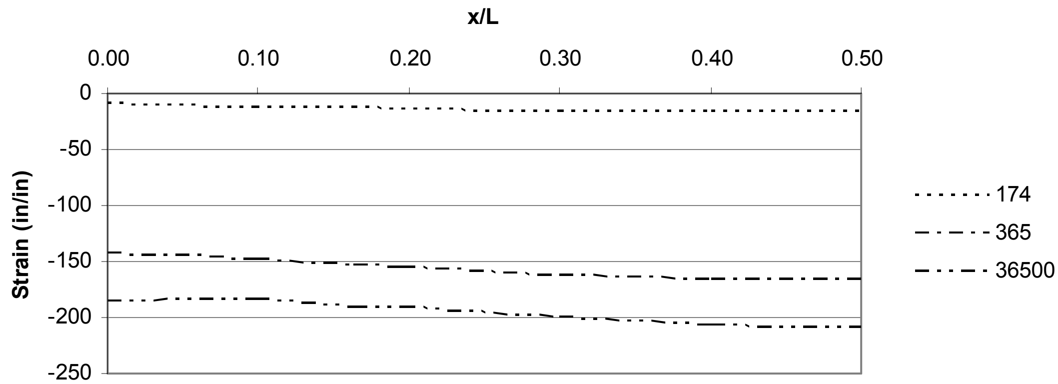

Figure **B-19**: Time-Dependent Strains at Top Fiber (Bridge 222 – Ext. Girder)

Three samples of time-dependent strains with respect to the time-line (174, 365, and 36,500 days) at the bottom fiber of interior girders are shown in Figure **B-20**.

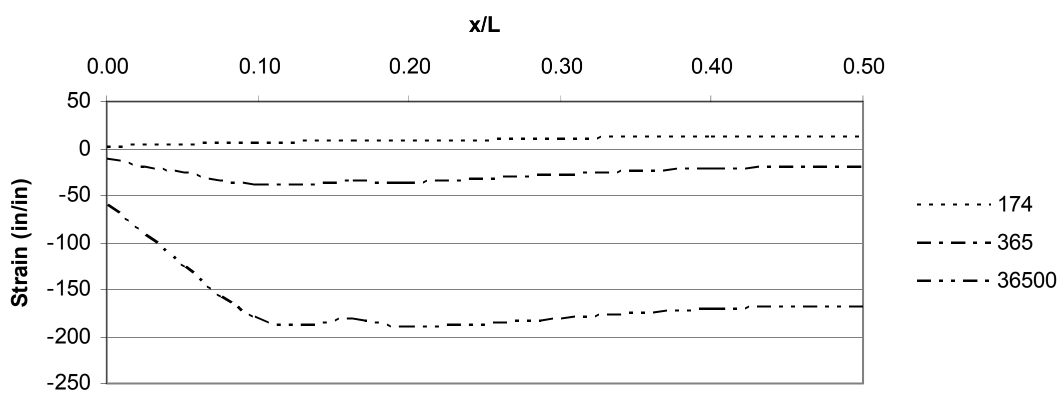

Figure **B-20**: Time-Dependent Strains at Bottom Fiber (Bridge 222 – Ext. Girder)

Appendix C

MATLAB Code for Condensed Hysteresis Model

Main Function

```
function U = runmodel(h)
% Main function
% h is time step size

mat = loadmat;  % load all material input data
atemp = loadatemp;  % load all air temperature input parameters
aaem = loadaaem;  % load time-dependent effect parameters
step = round(atemp.t_end/h);  % number of iterative steps
txt = sprintf('Total number of looping = %d', step);
disp(txt);
k = 1;  % for progress print out
mat.h = h;
U = zeros(step,2);  % for u1 and o1
U2 = zeros(step,2);  % for o4 and v5
dU = zeros(4,1);
tol = 0.00075;  % tolerance for use with CNorm
cntrl = 5000;  % max number of iterative analysis per each load step
prntxt = 1000;
Kn = setIntVal;  % initial values
Kn = getSoilProp(mat, Kn);  % compute soil properties for Ka, Kb, and Kc
for i = 2:step  % main looping
   mat.i = i;
   if i == 2  % first step, use initial slope
      Kn.Ka = Kn.kha;
      Kn.Kb = Kn.khb;
      Kn.Kc = Kn.khc;
      Kn.Kd = mat.Kd;
      Kn.K22 = 1e12;  % theoretically this stiffness is infinity at x = 0
      Kn.K33 = 1e12;  % theoretically this stiffness is infinity at x = 0
      Krr = formKrr(mat, Kn);  % form first partition of condensed stiffness matrix
      Kcr = formKcr(mat, Kn);  % form second and third partitions of condensed stiffness
matrix
      Kcc = formKcc(mat, Kn);  % form forth partition of condensed stiffness matrix
```

```
        Kcm = Krr - transpose(Kcr)*inv(Kcc)*Kcr;  % condense 4x4 matrix to 2x2 matrix
        Kn = getDT(mat, Kn, atemp, aaem);  % compute total incremental temperature
(ambient + time-dependence)
        Fr = formFr(mat, atemp, Kn.T-Kn.Ti);  % form first partition of condensed RHS
force vector
        Fc = formFc(mat, atemp, Kn.T-Kn.Ti);  % form second partition of condensed RHS
force vector
        Fcm = Fr - transpose(Kcr)*inv(Kcc)*Fc;  % condense 4x1 vector to 2x1 vector
        dU(1:2) = Kcm\Fcm;  % solve for displacements based on initial stiffness
        U(i,1) = U(i-1,1) + dU(1);
        U(i,2) = U(i-1,2) + dU(2);
        % Back condesation to obtain dU2 = inv(Kcc)*(Fc - Kcr*transpose(U(mat.i,:)))
        dU(3:4) = inv(Kcc)*(Fc - Kcr*dU(1:2));  % solve for o4 and v5 (only o4, the first
term, is needed)
        U2(i,1) = U2(i-1,1) + dU(3);
        U2(i,2) = U2(i-1,2) + dU(4);
        Kn.flagI = sign(U(i,1) - U(i-1,1));  % set switching flag for storing the most updated
xc and yc
        Kn.flagI2 = sign(U(i,2) - U(i-1,2));
        [dUi, Kn] = getNewResult(mat, Kn, atemp, aaem, U, U2);  % solve for
displacements based on updated stiffness
        j = 0;
        % iterative analysis to reduce errors to prescribed tolerance
        nrmref = max(norm(norm(U(i,:)),norm(U2(i,:))),1e-16);
        while (norm(dU-dUi)/nrmref > tol) & (j < cntrl)
          dU = dUi;
          U(i,1) = U(i-1,1) + dU(1);
          U(i,2) = U(i-1,2) + dU(2);
          U2(i,1) = U2(i-1,1) + dU(3);
          U2(i,2) = U2(i-1,2) + dU(4);
          nrmref = max(norm(norm(U(i,:)),norm(U2(i,:))),1e-16);
          [dUi, Kn] = getNewResult(mat, Kn, atemp, aaem, U, U2);
          j = j + 1;
          if j >= cntrl
            txt = sprintf('Overflow at loop %d and time %0.5g with CNORM = %0.5g',...
              i, (i-1)*h, norm(dU-dUi)/max(norm(U(i,:)),1e-16));
            disp(txt);
          end
        end
        dU = dUi;
        Kn.Ti = Kn.T;
    else
        U(i,1) = U(i-1,1) + dU(1);
        U(i,2) = U(i-1,2) + dU(2);
        U2(i,1) = U2(i-1,1) + dU(3);
```

```
        U2(i,2) = U2(i-1,2) + dU(4);
        %Kn.flagI = sign(U(i,1) - U(i-1,1));
        %Kn.flagI2 = sign(U(i,2) - U(i-1,2));
        [dUi, Kn] = getNewResult(mat, Kn, atemp, aaem, U, U2);
        j = 0;
        nrmref = max(norm(norm(U(i,:)),norm(U2(i,:))),1e-16);
        while (norm(dU-dUi)/max(norm(U(i,:)),1e-16) > tol) & (j < cntrl)
            dU = dUi;
            U(i,1) = U(i-1,1) + dU(1);
            U(i,2) = U(i-1,2) + dU(2);
            U2(i,1) = U2(i-1,1) + dU(3);
            U2(i,2) = U2(i-1,2) + dU(4);
            nrmref = max(norm(norm(U(i,:)),norm(U2(i,:))),1e-16);
            [dUi, Kn] = getNewResult(mat, Kn, atemp, aaem, U, U2);
            j = j + 1;
            if j >= cntrl
                txt = sprintf('Overflow at loop %d and time %0.5g with CNORM = %0.5g',...
                    i, (i-1)*h, norm(dU-dUi)/max(norm(U(i,:)),1e-16));
                disp(txt);
            end
        end
        dU = dUi;
        Kn.Ti = Kn.T;
    end
    if i == k*prntxt
        txt = sprintf('  Looping # %d', i);
        disp(txt);
        k = k + 1;
    end
end
abc = 1;
% End of main function
```

Function for solving iterative analysis step

```
function [dUi, Kn] = getNewResult(mat, Kn, atemp, aaem, U, U2)
% Function for solving iterative analysis step

dUi = zeros(4,1);
% Compute tangent stiffness of K22
if mat.i == 2
    yt = 0;
```

```
    Kn.yc = 0;
    xth = U(2,1);
    xt = U(1,1);
    Kn.xc = 0;
else
    yt = Kn.yt;
    xth = U(mat.i,1);
    xt = U(mat.i-1,1);
end
Kn.flag = sign(xth - xt);
if Kn.flag ~= Kn.flagI  % indicate point of displacement reversal
    Kn.xc = xt;
    Kn.yc = yt;
    Kn.flagI = Kn.flag;
end
Kn.yt = duhemK22(yt, Kn.yc, xth, xt, Kn.xc, mat.C1, mat.C2);
Kn.K22 = (Kn.yt - yt)/(xth - xt);
% Compute tangent stiffness of K33
if mat.i == 2
    yt2 = 0;
    Kn.yc2 = 0;
    xth2 = U(2,2);
    xt2 = U(1,2);
    Kn.xc2 = 0;
else
    yt2 = Kn.yt2;
    xth2 = U(mat.i,2);
    xt2 = U(mat.i-1,2);
end
Kn.flag2 = sign(xth2 - xt2);
if Kn.flag2 ~= Kn.flagI2  % indicate point of rotation reversal
    Kn.xc2 = xt2;
    Kn.yc2 = yt2;
    Kn.flagI2 = Kn.flag2;
end
Kn.yt2 = duhemK33(yt2, Kn.yc2, xth2, xt2, Kn.xc2, mat.C3, mat.C4);
Kn.K33 = (Kn.yt2 - yt2)/(xth2 - xt2);
% Compute tangent stiffness of Ka
if mat.i == 2
    xt = -U(1,1) + (2*Kn.poa - Kn.paa - Kn.ppa)/2/Kn.kha;   % Note: sign of all
displacement is flipped
    xth = xt - U(2,1) + U(1,1);
    ut = xt;
    Kn.uta = ut;
    yt = Kn.kha*ut + (Kn.paa + Kn.ppa)/2;
```

```
else
   yt = Kn.yta;
   ut = Kn.uta;
   xt = -U(mat.i-1,1);
   xth = xt - U(mat.i,1) + U(mat.i-1,1);
end
Kn.uta = elastoK(ut, xth, xt, Kn.kha, Kn.paa, Kn.ppa);
Kn.yta = Kn.kha*Kn.uta + (Kn.paa + Kn.ppa)/2;
Kn.Ka = (Kn.yta - yt)/(xth - xt);
% Compute tangent stiffness of Kb
if mat.i == 2
   % apply constrint equation to obtain displacement at Kb elevation
   uuth = U(2,1) - mat.ha*U(2,2);
   uut = U(1,1) - mat.ha*U(1,2);
   % u2 = u1 - ha*o1
   xt = -uut + (2*Kn.pob - Kn.pab - Kn.ppb)/2/Kn.khb;
   xth = xt - uuth + uut;
   ut = xt;
   Kn.utb = ut;
   yt = Kn.khb*ut + (Kn.pab + Kn.ppb)/2;
else
   % aaply constraint equation
   uuth = U(mat.i,1) - mat.ha*U(mat.i,2);
   uut = U(mat.i-1,1) - mat.ha*U(mat.i-1,2);
   % u2 = u1 - ha*o1
   yt = Kn.ytb;
   ut = Kn.utb;
   xt = -uut;
   xth = xt - uuth + uut;
end
Kn.utb = elastoK(ut, xth, xt, Kn.khb, Kn.pab, Kn.ppb);
Kn.ytb = Kn.khb*Kn.utb + (Kn.pab + Kn.ppb)/2;
Kn.Kb = (Kn.ytb - yt)/(xth - xt);
% Compute tangent stiffness of Kc
if mat.i == 2
   % apply constraint equation to obtain displacement at Kc elevation
   uut = uut - mat.hb*U2(1,1);
   uuth = uuth - mat.hb*U2(2,1);
   % u4 = u2 - hb*o4
   xt = -uut + (2*Kn.poc - Kn.pac - Kn.ppc)/2/Kn.khc;
   xth = xt - uuth + uut;
   ut = xt;
   Kn.utc = ut;
   yt = Kn.khc*ut + (Kn.pac + Kn.ppc)/2;
else
```

```
    uut = uut - mat.hb*U2(mat.i-1,1);
    uuth = uuth - mat.hb*U2(mat.i,1);
    % u1 = u2 + h2*o2
    yt = Kn.ytc;
    ut = Kn.utc;
    xt = -uut;
    xth = xt - uuth + uut;
end
Kn.utc = elastoK(ut, xth, xt, Kn.khc, Kn.pac, Kn.ppc);
Kn.ytc = Kn.khc*Kn.utc + (Kn.pac + Kn.ppc)/2;
Kn.Kc = (Kn.ytc - yt)/(xth - xt);
% Compute tangent stiffness of Kd
if mat.i == 2
    xt = U(1,2) - U2(1,1);
    xth = U(2,2) - U2(2,1);
    ut = xt;
    Kn.utd = ut;
yt = mat.Kd*ut;
else
    yt = Kn.ytd;
    ut = Kn.utd;
    xt = U(mat.i-1,2) - U2(mat.i-1,1);
    xth = U(mat.i,2) - U2(mat.i-1,1);
end
Kn.utd = elastoK(ut, xth, xt, mat.Kd, 0, 2*mat.Md);
Kn.ytd = mat.Kd*Kn.utd;
Kn.Kd = (Kn.ytd - yt)/(xth - xt);
% iterative analysis
if mat.i > 2
    Kn = getDT(mat, Kn, atemp, aaem);
end
Krr = formKrr(mat, Kn);
Kcr = formKcr(mat, Kn);
Kcc = formKcc(mat, Kn);
Kcm = Krr - transpose(Kcr)*inv(Kcc)*Kcr;
Fr = formFr(mat, atemp, Kn.T-Kn.Ti);
Fc = formFc(mat, atemp, Kn.T-Kn.Ti);
Fcm = Fr - transpose(Kcr)*inv(Kcc)*Fc;
dUi(1:2) = Kcm\Fcm;
dUi(3:4) = inv(Kcc)*(Fc - Kcr*dUi(1:2));
```

Function for setting initial values for all nonlinear hysteresis springs

```
function Kn = setIntVal
% Function for setting initial values for all nonlinear hysteresis springs (and total temperature)

% initial values of K22
Kn.xc = 0;
Kn.yt = 0;
Kn.yc = 0;
% initial values of K33
Kn.xc2 = 0;
Kn.yt2 = 0;
Kn.yc2 = 0;
% initial values of Ka
Kn.yta = 0;
Kn.uta = 0;
% initial values of Kb
Kn.ytb = 0;
Kn.utb = 0;
% initial values of Kc
Kn.ytc = 0;
Kn.utc = 0;
% initial values of Kd
Kn.ytd = 0;
Kn.utd = 0;
Kn.xtd = 0;
% initial values total temperature
Kn.T = 0;
Kn.Ti = 0;
```

Function for loading material properties

```
function mat = loadmat()
% Function for loading material properties
% The order of input data file should follow:
% A = area of composite superstructure component
% E = reference elastic modulus of composite superstructure component
% I = moment of inertia of composite superstructure component
% L1 = superstructure length to be used in stiffness term "AE/L"
```

```
% L2 = superstructure length to be used in stiffness terms "12EI/L^3" and "6EI/L^2"
% ha = abutment height
% hb = backwall height (distance from construction joint to E.N.A. of composite
superstructure component
% kref = lateral soil-abutment modulus of subgrade reaction at the pile head location
% B = soil-abutment interaction width
% phi = backfill interal friction angle (degree)
% gamma = unit weight of backfill
% C1 = coefficient for pile head displacement-force reaction tangential slope (K22) of
contraction case
% C2 = coefficient for pile head displacement-force reaction tangential slope (K22) of
expansion case
% C3 = coefficient for pile head rotation-moment reaction tangential slope (K33) of
contraction case
% C4 = coefficient for pile head rotation-moment reaction tangential slope (K33) of
expansion case
% Kd = stiffness of cold joint
% Md = yielding moment of cold joint
% Note 1: all input units need to be consistent.
% Note 2: rotational mode of IA bridge movements during contraction is to be resisted by
soil on backfill side,
% thus, C4 should be used for contraction movement and C3 should be used for
expansion movement.

temp = load('mat.dat');
mat.A = temp(1);
mat.E = temp(2);
mat.I = temp(3);
mat.L1 = temp(4);
mat.L2 = temp(5);
mat.ha = temp(6);
mat.hb = temp(7);
mat.kref = temp(8);
mat.B = temp(9);
mat.phi = temp(10);
mat.gamma = temp(11);
mat.C1 = temp(12);
mat.C2 = temp(13);
mat.C3 = temp(14);
mat.C4 = temp(15);
mat.Kd = temp(16);
mat.Md = temp(17);
```

Function for loading air temperature parameters

```
function atemp = loadatemp()
% Function for loading air temperature parameters
% t_end = duration of analysis time (initial time is always set to zero)
% Tm = mean temperature (= 7 C for this thesis)
% A = amplitude of temperature fluctuation (= 16 C for this thesis)
% phase = phase lag, radian (= 2.51622, 1.561486, and 1.479774 for bridges 203, 211,
and 222 respectively)
% alfa = coefficient of thermal expansion (=9x10-6 /C for this thesis)
% Note: Only air temperature is assigned for this function. Time unit is day. Temperature
unit is celcius.

temp = load('atemp.dat');
atemp.t_end = temp(1);
atemp.Tm = temp(2);
atemp.A = temp(3);
atemp.phase = temp(4);
atemp.alfa = temp(5);
```

Function for loading days, time-dependent elastic modulus, and equivalent temperature

```
function aaem = loadaaem()
% Function for loading days, time-dependent elastic modulus, and equivalent temperature
% day = day function
% Ec = time-dependent elastic modulus based on the AAEM method
% Eqtemp = equivalent temperature based on the AAEM method

temp = load('aaem.dat');
aaem.day = temp(:,1);
aaem.Ec = temp(:,2);
aaem.Eqtemp = temp(:,3);
```

Function for computing soil properties for K_a, K_b, and K_c

```
function Kn = getSoilProp(mat, Kn)
% Function for computing soil properties for Ka, Kb, and Kc

K_a = (1-sin(mat.phi*pi/180))/(1+sin(mat.phi*pi/180));
K_p = 1/K_a;
K_o = 1 - sin(mat.phi*pi/180);
% properties for Ka
Kn.kha = getKh(mat, 1);
Kn.poa = K_o*mat.gamma*mat.B*(mat.hb + 3/4*mat.ha)*mat.ha/2;
Kn.paa = Kn.poa*K_a/K_o;
Kn.ppa = Kn.poa*K_p/K_o;
% properties for Kb
Kn.khb = getKh(mat, 2);
Kn.pob = K_o*mat.gamma*mat.B*((mat.hb + 1/4*mat.ha)*mat.ha/2 + 3/4*mat.hb*mat.hb/2);
Kn.pab = Kn.pob*K_a/K_o;
Kn.ppb = Kn.pob*K_p/K_o;
% properties for Kc
Kn.khc = getKh(mat, 3);
Kn.poc = K_o*mat.gamma*mat.B*1/2*mat.hb/2*mat.hb/2;
Kn.pac = Kn.poc*K_a/K_o;
Kn.ppc = Kn.poc*K_p/K_o;
```

Function for computing initial stiffness of soil-abutment interaction springs

```
function Kh = getKh(mat, flag)
% Function for computing initial stiffness of soil-abutment interaction springs
% flag = 1 means Ka (spring at pile head location)
%      = 2 means Kb (spring at abutment-backwall connection)
%      = 3 means Kc (spring at E.N.A. of superstructure componenet)

switch flag
case 1,
   Kh = mat.kref*mat.B*(6*(mat.ha+mat.hb)^1.5 - 3*mat.ha*mat.hb^0.5 - 6*mat.hb^1.5)/(12*(mat.ha + mat.hb)^0.5);
case 2,
   Kh = mat.kref*mat.B*(2*(mat.ha+mat.hb)^1.5 + 3*mat.ha*mat.hb^0.5 + 4*mat.hb^1.5)/(12*(mat.ha + mat.hb)^0.5);
case 3,
```

```
   Kh = mat.kref*mat.B*2*mat.hb^1.5/(12*(mat.ha + mat.hb)^0.5);
end
```

Function for computing incremental temperature

```
function Kn = getDT(mat, Kn, atemp, aaem)
% Function for computing incremental temperature

t = (mat.i - 1)*mat.h;
T1 = atemp.A*sin(2*pi/365.25*t + atemp.phase) - atemp.A*sin(atemp.phase);
if t < aaem.day(1)
   Kn.T = T1;
   Kn.Ec = mat.E;
elseif t < aaem.day(2)
   Kn.T = T1 + aaem.Eqtemp(1) + (aaem.Eqtemp(2) - aaem.Eqtemp(1))*(t - aaem.day(1))/(aaem.day(2) - aaem.day(1));
   Kn.Ec = aaem.Ec(1) + (aaem.Ec(2) - aaem.Ec(1))*(t - aaem.day(1))/(aaem.day(2) - aaem.day(1));
elseif t < aaem.day(3)
   Kn.T = T1 + aaem.Eqtemp(2) + (aaem.Eqtemp(3) - aaem.Eqtemp(2))*(t - aaem.day(2))/(aaem.day(3) - aaem.day(2));
   Kn.Ec = aaem.Ec(2) + (aaem.Ec(3) - aaem.Ec(2))*(t - aaem.day(2))/(aaem.day(3) - aaem.day(2));
elseif t < aaem.day(4)
   Kn.T = T1 + aaem.Eqtemp(3) + (aaem.Eqtemp(4) - aaem.Eqtemp(3))*(t - aaem.day(3))/(aaem.day(4) - aaem.day(3));
   Kn.Ec = aaem.Ec(3) + (aaem.Ec(4) - aaem.Ec(3))*(t - aaem.day(3))/(aaem.day(4) - aaem.day(3));
elseif t < aaem.day(5)
   Kn.T = T1 + aaem.Eqtemp(4) + (aaem.Eqtemp(5) - aaem.Eqtemp(4))*(t - aaem.day(4))/(aaem.day(5) - aaem.day(4));
   Kn.Ec = aaem.Ec(4) + (aaem.Ec(5) - aaem.Ec(4))*(t - aaem.day(4))/(aaem.day(5) - aaem.day(4));
elseif t < aaem.day(6)
   Kn.T = T1 + aaem.Eqtemp(5) + (aaem.Eqtemp(6) - aaem.Eqtemp(5))*(t - aaem.day(5))/(aaem.day(6) - aaem.day(5));
   Kn.Ec = aaem.Ec(5) + (aaem.Ec(6) - aaem.Ec(5))*(t - aaem.day(5))/(aaem.day(6) - aaem.day(5));
elseif t < aaem.day(7)
   Kn.T = T1 + aaem.Eqtemp(6) + (aaem.Eqtemp(7) - aaem.Eqtemp(6))*(t - aaem.day(6))/(aaem.day(7) - aaem.day(6));
   Kn.Ec = aaem.Ec(6) + (aaem.Ec(7) - aaem.Ec(6))*(t - aaem.day(6))/(aaem.day(7) -
```

```
aaem.day(6));
elseif t < aaem.day(8)
   Kn.T = T1 + aaem.Eqtemp(7) + (aaem.Eqtemp(8) - aaem.Eqtemp(7))*(t - aaem.day(7))/(aaem.day(8) - aaem.day(7));
   Kn.Ec = aaem.Ec(7) + (aaem.Ec(8) - aaem.Ec(7))*(t - aaem.day(7))/(aaem.day(8) - aaem.day(7));
else
   Kn.T = T1 + aaem.Eqtemp(8);
   Kn.Ec = aaem.Ec(8);
end
```

Function for forming the first partition of 4x4 condensed stiffness matrix

```
function Krr = formKrr(mat, Kn)
% Function for forming the first partition of 4x4 condensed stiffness matrix
% see function "loadmat" for all notations

a11 = Kn.Ka + Kn.Kb + Kn.Kc + Kn.K22 + mat.A*mat.E/mat.L1;
a12 = -mat.ha*(Kn.Kb + Kn.Kc + mat.A*mat.E/mat.L1);
a22 = Kn.Kd + Kn.K33 + mat.ha^2*(Kn.Kb + Kn.Kc + mat.A*mat.E/mat.L1);
Krr = [a11, a12; a12, a22];
```

Function for forming the second and the third partitions of 4x4 condensed stiffness matrix

```
function Kcr = formKcr(mat, Kn)
% Function for forming the second and the third partitions of 4x4 condensed stiffness matrix

a11 = -mat.hb*(Kn.Kc + mat.A*mat.E/mat.L1);
a12 = -Kn.Kd + mat.ha*mat.hb*(Kn.Kc + mat.A*mat.E/mat.L1);
Kcr = [a11, a12; 0, 0];
```

Function for forming the forth partition of 4x4 condensed stiffness matrix

```
function Kcc = formKcc(mat, Kn)
% Function for forming the forth partition of 4x4 condensed stiffness matrix

a11 = Kn.Kd + mat.hb^2*(Kn.Kc + mat.A*mat.E/mat.L1) + 4*mat.E*mat.I/mat.L2;
a12 = -6*mat.E*mat.I/mat.L2^2;
a22 = 12*mat.E*mat.I/mat.L2^3;
Kcc = [a11, a12; a12, a22];
```

Function for forming the first partition of 4x1 condense right-hand-side force vector

```
function Fr = formFr(mat, atemp, dT)
% Function for forming the first partition of 4x1 condense right-hand-side force vector

a1 = -mat.A*mat.E*atemp.alfa*dT;
a2 = mat.ha*mat.A*mat.E*atemp.alfa*dT;
Fr = [a1; a2];
```

Function for forming the second partition of 4x1 condensed right-hand-side force vector

```
function Fc = formFc(mat, atemp, dT)
% Function for forming the second partition of 4x1 condensed right-hand-side force
vector

a1 = mat.hb*mat.A*mat.E*atemp.alfa*dT;
a2 = 0;
Fc = [a1; a2];
```

Function for calculating load-deformation curve based on duhem model

```
function yth = duhemK22(yt, yc, xth, xt, xc, c1, c2)
% Function to calculate load-deformation curve based on duhem model
%      yth = duhemK22(yt, yc, xth, xt, xc, c1, c2)
% yth is to be solved of current iteration (load)
% yt is load of previous iteration
% yc is load at current reversal
% xth is displacement of current iteration (known)
% xt is displacement of previous iteration
% xc is displacement at current reversal
% c1 is coefficient of increasing curve (contraction case)
% c2 is coefficient of decreasing curve (expansion case)

if xth-xt >= 0  % increasing curve
   c = c1;
else  % decreasing curve
   c = c2;
end
xc_add = max(sign(xth-xt)*sign(yc)*(abs(yc/2/c))^2,0);    % account for hysteresis boundary
yth = yt + c*(xth-xt)*(abs(xth-xc-xc_add))^(-0.5);
```

Function for calculating load-deformation curve based on duhem model

```
function yth = duhemK33(yt, yc, xth, xt, xc, c3, c4)
% Function to calculate load-deformation curve based on duhem model
%      yth = duhemK33(yt, yc, xth, xt, xc, c3, c4)
% yth is to be solved of current iteration (load)
% yt is moment of previous iteration
% yc is moment at current reversal
% xth is rotation of current iteration (known)
% xt is rotation of previous iteration
% xc is rotation at current reversal
% c3 is coefficient of decreasing curve (contraction case)
% c4 is coefficient of increasing curve (expansion case)
% Note: These two coefficients are opposite to the case K22

if xth-xt >= 0  % increasing curve
   c = c4;
```

```
else  % decreasing curve
   c = c3;
end
xc_add = max(sign(xth-xt)*sign(yc)*(abs(4*yc/5/c))^(5/4),0);  % account for hysteresis boundary
yth = yt + c*(xth-xt)*(abs(xth-xc-xc_add))^(-0.2);
```

Function for calculating load-deformation curve based on duhem model

```
function uth = elastoK(ut, xth, xt, kh, pa, pp)
% Function to calculate load-deformation curve based on duhem model
%      uth = elastoK(ut, xth, xt, kh, po, pa, pp)
% uth is to be solved of current iteration (load)
% ut is load of previous iteration
% xth is displacement of current iteration (known)
% xt is displacement of previous iteration
% kh is initial slope
% pa is active load
% pp is passive load

if (ut + (pp-pa)/2/kh) >= 0  % Heaviside's unit step function H1
   H1 = 1;
else
   H1 = 0;
end
if (xth - xt) >= 0  % Heaviside's unit step function H2
   H2 = 0;
else
   H2 = 1;
end
if (xth - xt) > 0  % Heaviside's unit step function H3
   H3 = 1;
else
   H3 = 0;
end
if (ut - (pp-pa)/2/kh) > 0  % Heaviside's unit step function H4
   H4 = 0;
else
   H4 = 1;
end
uth = ut + (xth - xt)*(H3*H4 + H2*H1);
```

VITA

Kongsak Pugasap

Place and Date of Birth

- Bangkok, Thailand, 1974

Education

- Ph.D. in Civil Engineering, Pennsylvania State University, 2006.
- M.Eng. in Structural Engineering, Asian Institute of Technology, Thailand, 1998.
- B.Eng. in Irrigation Engineering, Kasetsart University, 1995.

Employment

- Research Assistant, Pennsylvania State University, 2002-2006.
- Structural Engineer, Pyramid Development International Corp., Ltd., Thailand, 1999-2002.
- Research Assistant, Asian Institute of Technology, Thailand, 1998-1999.
- Civil Engineer, Pyramid Development International Corp., Ltd., 1995-1996.

Publications

- Pugasap, K., Leighty, C. A., and Laman, J. A. (2004) “Hysteresis Phenomenon in Integral Abutment Bridges: Field Data Evaluation,” *The Seventh Annual PTI Conference*, The Pennsylvania Transportation Institute, August 11-12.
- Kanok-Nukulchai, W. and Pugasap, K. (1999) “Development of a Finite Element Program Based on Object-Oriented Programming,” *The 5th National Convention on Civil Engineering Conference*, Bangkok, Thailand.
- Pugasap, K. (1998) “A New General-Purposed Finite Element Program Based on Object-Oriented Programming,” *AIT Thesis*, Thailand.